8-26-91
E5728

NASA Conference Publication 3107

Space Photovoltaic Research and Technology–1989

Proceedings of a conference held at
NASA Lewis Research Center
Cleveland, Ohio
November 7–9, 1989

NASA

NASA Conference Publication 3107

Space Photovoltaic Research and Technology–1989

Proceedings of a conference held at
NASA Lewis Research Center
Cleveland, Ohio
November 7–9, 1989

NASA
National Aeronautics and
Space Administration
Office of Management
Scientific and Technical
Information Division
1991

Contents

Foreword
Dennis Flood, Chief, Photovoltaic Branch, NASA Lewis Research Center vii

Overview

The OAST Space Power Program
Gary L. Bennett, Code RP, NASA Headquarters..... 3

Air Force Advanced Photovoltaics Technology
James S. Cloyd, Wright-Patterson Air Force Base..... 18

Session 1—Multi-Junction Cell Technology

Progress Toward the Development of Dual Junction GaAs/Ge Solar Cells
D.R. Lillington, D.D. Krut, B.T. Cavicchi, E. Ralph and Lt. M. Chung..... 29

Status of GaAs/Ge Solar Cells
P.A. Iles, F. Ho and Y.C.M. Yeh..... 42

Graded-Bandgap AlGaAs Solar Cells for AlGaAs/Ge Cascade Cells
M.L. Timmons, R. Venkatasubramanian, T.S. Colpitts, J.S. Hills,
J.A. Hutchby. P.A. Iles and C.L. Chu..... 48

AlGaAs Top Solar Cell for Mechanical Attachment in a Multi-Junction Tandem Concentrator Solar Cell Stack
L.C. DiNetta, M.H. Hannon, J.B. McNeely and A.M. Barnett 60

Progress Toward a 30%-Efficient, Monolithic, Three-Junction, Two-Terminal Concentrator Solar Cell for Space Applications
L.D. Partain, B-C. Chung, G.F. Virshup, J.C. Schultz, H.F. MacMillan,
M. Ladle Ristow, M.S. Kuryla and K.A. Bertness..... 73

Tandem Concentrator Solar Cells with 30% (AMO) Power Conversion Efficiency
J.E. Avery, L.M. Fraas, V.S. Sundaram, D.J. Brinker, J.M. Gee and M.J. O'Neill 77

Progress in GaAs/$CuInSe_2$ Tandem Junction Solar Cells
N.P. Kim, R.M. Burgess, R.A. Mickelsen, B.J. Stanbery,
R.W. McClelland, B.D. King and R.P. Gale..... 88

InP/$Ga_{0.47}In_{0.53}As$ Monolithic, Two-Junction, Three-Terminal Tandem Solar Cells
M.W. Wanlass, T.A. Gessert, G.S. Horner, K.A. Emery and T.J. Coutts..... 102

Preceding Page Blank

Session 2—GaAs Cells

Phase Equilibrium Modeling for High Temperature Metallization on GaAs Solar Cells
M.A. Chung, J.E. Davison and S.R. Smith 119

GaAs Solar Cell Photoresponse Modeling Using PC-1D V2.1
D.A. Huber, L.C. Olsen, G. Dunham and F.W. Addis 126

High-Efficiency, Radiation-Resistant GaAs Space Cells
K.A. Bertness, M. Ladle Ristow, M. Grounner, M.S. Kuryla, and J.G. Werthen..... 136

Thermal Annealing of GaAs Concentrator Solar Cells
H.B. Curtis and D.J. Brinker 140

Burst Annealing of High Temperature GaAs Solar Cells
P.R. Brothers and W.E. Horne..... 154

Session 3—System Studies

An Approach for Configuring Space Photovoltaic Tandem Arrays Based on Cell Layer Performance
C.S. Flora and P.A. Dillard 167

Review of Thin Film Solar Cell Technology and Applications for Ultra-Light Spacecraft Solar Arrays
Geoffrey A. Landis 180

Performance, Size, Mass and Cost Estimates for Projected 1KW EOL Si, InP and GaAs Arrays
Luther W. Slifer, Jr..... 204

Dual-Purpose Self-Deliverable Lunar Surface PV Electrical Power System
Jack H. Arnold, David W. Harris, Eldon R. Cross and Dennis Flood 212

Feasibility of Solar Power for Mars
Joseph Appelbaum and Geoffrey A. Landis..... 223

Session 4—InP Cells

Recent Advances in the ITO/InP Solar Cell
T.A. Gessert, X. Li, M.W. Wanlass and T.J. Coutts 257

Semiconductor Structural Damage Attendant to Contact Formation in III-V Solar Cells
Navid S. Fatemi and Victor G. Weizer..... 270

The Effect of Process Conditions on the Performance of Epitaxial InP Solar Cells
J.M. Borrego and S.K. Ghandi 280

Effects of Proton Irradiation on the Performance of InP/GaAs Solar Cells
I. Weinberg, C.K. Swartz, D.J. Brinker and D.M. Wilt 289

Key Factors Limiting the Open Circuit Voltage of n^+pp^+ Indium Phosphide Solar Cells
Chandra Goradia, William Thesling and Irving Weinberg 298

Determination of Series Resistance of Indium Phosphide Solar Cells
R.K. Jain and I. Weinberg 311

Investigation of Anodic and Chemical Oxides Grown on p-type InP with Applications to Surface Passivation for n^+-p Solar Cell Fabrication
Maria Faur, Mircea Faur, Manju Goradia, Chandra Goradia,
Phillip Jenkins, Douglas Jayne and Irving Weinberg 316

A Comparative Study of Performance Parameters of n^+-p InP Solar Cells Made by Closed-Ampoule Sulfur Diffusion into Cd- and Zn-doped p-type InP Substrates
Mircea Faur, Maria Faur, Chandra Goradia, Manju Goradia,
Ralph D. Thomas, David J. Brinker, Navid Fatemi and Frank Honecy 332

Session 5—Non-Solar Direct Conversion

Radioisotope Thermal Photovoltaic Application of the GaSb Solar Cell
M.D. Morgan, W.E. Horne and A.C. Day 349

GaP Betavoltaic Cells as a Power Source
F.S. Pool, P. Stella and B. Anspaugh 359

Low Cost Space Power Generation
Randall B. Olsen 371

Session 6—Solar Cell and Array Development

Spaceflight Performance of Several Types of Silicon Solar Cells on the LIPS III Satellite
J. Silver and D. Warfield 385

Annealing Characteristics of Irradiated Hydrogenated Amorphous Silicon Solar Cells
J.S. Payson, S. Abdulaziz, Y. Li and J.R. Woodyard 389

Optimization and Performance of Space Station Freedom Solar Cells
S. Khemthong, N. Hansen and M. Bower 400

Thermal Cycle Testing of Space Station Freedom Solar Array Blanket Coupons
Bryan K. Smith and David A. Scheiman 410

The Advanced Photovoltaic Solar Array (APSA) Technology Status and Performance
Paul M. Stella and Richard M. Kurland 421

Integral Bypass Diodes in an Amorphous Silicon Alloy Photovoltaic Module
J.J. Hanak and H. Flaisher 433

Mini-Dome Fresnel Lens Photovoltaic Concentrator Development
Mark J. O'Neill and Michael F. Piszczor, Jr. 443

Workshop Summaries

Mechanical vs. Monolithic Multijunction Cells
John Fan 463

Strategy in Space Flight Experiments
Dean Marvin and James Severns 469

Non-Solar Direct Conversion
W.E. Horne 474

Indium Phosphide Solar Cells
I. Weinberg 484

Space Cell Theory and Modeling
James Hutchby 487

Invited Paper

Cryogenic Reactant Storage for Lunar Base Regenerative Fuel Cells
Lisa Kohout 495

Foreword

Dennis Flood
Chief, Photovoltaic Branch
NASA Lewis Research Center
Cleveland, Ohio

This Tenth Space Photovoltaic Research and Technology Conference marks a milestone in the series. A quick review of its contents will reveal that much that was speculation at the first such conference fifteen years ago has now become reality. For the first time, a multiple bandgap device has been reported with an efficiency above 30% under concentration in the AM0 spectrum. At the same time, the speculation that 40% efficiency appears feasible did not even raise a hint of controversy, nor was it dismissed as a frivolous idea. Discussion of approaches for achieving that level of performance are included in this volume.

But perhaps of even more significance, much that is reported in this volume was not a matter of speculation at that first meeting. Some truly new technology elements have been introduced into the field of photovoltaic power generation in space in the intervening years, and significant progress has been made on them in a relatively short period of time. A major case in point is the development of high efficiency InP solar cells with their accompanying high degree of resistance to radiation damage. Efficiencies above 20% AM0 are now assured in large (>4 sq.cm) area devices, and laboratory radiation damage tests with both electrons and protons show significantly less degradation in such cells than in any other single crystal material thus far. InP solar cells, of course, are not a new idea, and easily predate the beginning of this conference series. Their possible use in space was not a matter of speculation or interest 15 years ago, however, and now such use seems assured.

There are certainly other examples which could be cited. They can be found in the collection of papers that follow. The Tenth SPRAT contained more outstanding results on a wider range of solar cell types than any in the series thus far. The excitement does not stop there, however. This conference introduced some interesting speculations, and presented preliminary experimental results on the use of solar cells to convert energy from sources other than the sun. Who knows what the Twentieth SPRAT may bring?

The efforts of many persons here at Lewis Research Center went into making this conference run smoothly and should be acknowledged. In particular, Cliff Swartz who served as General Chairman, Don Chubb, who served as Logistics Chairman and who will chair the 11th meeting, and Brian Good, who worked hard to put all the manuscripts into publishable format, deserve our sincere appreciation for its success. We look forward to hearing in this forum for many more years of the outstanding progress that is yet to come.

Overview

The OAST Space Power Program

Gary L. Bennett
National Aeronautics and Space Administration
Washington, D.C.

The NASA Office of Aeronautics and Space Technology (OAST) space power program has been established to provide the technology base to meet power system requirements for future space missions, including growth Space Station, Earth orbiting spacecraft, lunar and planetary bases, and solar system exploration. The program spans photovoltaic energy conversion, chemical energy conversion, thermal energy conversion, power management, thermal management and focused initiatives on high-capacity power, surface power and space nuclear power.

Introduction

Within the National Aeronautics and Space Administration (NASA) the Office of Aeronautics and Space Technology (OAST) is responsible for planning and managing NASA's aeronautics, space, and transatmospheric research and technology (R&T) programs. A primary function of OAST is to ensure that the programs are aligned toward providing the technology required to meet national needs in aviation and space (OAST 1989). The space R&T program is divided into the R&T Base and three focused programs: the Civil Space Technology Initiative (CSTI), Pathfinder, and the In-Space Technology Experiments. This paper will focus on the space power program contained in the R&T Base, CSTI and Pathfinder. Program management for the OAST space power program resides in the OAST Propulsion, Power and Energy Division.

Space Energy Conversion R&T

The objective of the space energy conversion R&T program is to provide the technology base to meet power system requirements for future space missions, including growth Space Station, Earth orbiting spacecraft, lunar and planetary bases, and solar system exploration. Power system requirements will range from a few kilowatts to megawatts, and system lifetimes from two to more than ten years. System configurations must be available for single user requirements, as well as for utility type applications, and must include a variety of power generation, storage, distribution, and management options. The program elements are

- Photovoltaic Energy Conversion
- Chemical Energy Conversion
- Thermal Energy Conversion

Preceding Page Blank

- Power Management
- Thermal Management

The program elements will be discussed in the following sections.

Photovoltaic Energy Conversion

The photovoltaic energy conversion program will provide the technology for photovoltaic arrays with improved conversion efficiency, reduced mass, reduced cost, and increased operating life for advanced space missions. Specific long-range goals are to develop the technology base for photovoltaic arrays with specific power of 300 W/kg, with substantial reductions in size, cost, and increases in end-of-life (EOL) power capability. Establishment of this technology will have a significant impact on all near-Earth manned and unmanned space missions, as well as interplanetary missions from near Sun to several astronomical units. This technology is also applicable to missions with power requirements from hundreds of watts to hundreds of kilowatts. Areas covered include advanced photovoltaic device research and technology development, thin film cells, light-weight solar array technology and high-power array technology for planar, as well as concentrator, concepts and configurations (OAST 1989).

The OAST-sponsored research on photovoltaic energy conversion is carried out through two NASA centers: Lewis Research Center (LeRC) and the Jet Propulsion Laboratory (JPL). The LeRC work is focused primarily on advanced solar cell technology while the JPL work is focused primarily on high-performance solar arrays. The two programs are complementary with LeRC providing the advanced, high-efficiency, radiation-resistant solar cells needed for the JPL high-performance array work (Flood et al. 1989).

The development of a high-efficiency, light-weight, rugged, radiation-resistant solar cell is an essential element of the NASA goals to achieve 300 W/kg for a deployable planar array and 300 W/m^2 at 100 W/kg in concentrator arrays. To achieve this development LeRC is focusing on indium phosphide (InP) and gallium arsenide (GaAs) and LeRC is also beginning to investigate thin-film cell technology (Flood et al. 1989).

The objectives of the InP solar cell program are to (Flood et al. 1989)

- Demonstrate a cell structure capable of achieving 20% air mass zero (AM0) efficiency with $\leq$1% degradation in power after 10 years in geosynchronous Earth orbit (GEO)
- Fabricate InP cells on alternative substrates
- Demonstrate high-efficiency, ultra-thin InP cells with improved radiation resistance (compared to GaAs and silicon)

Recently LeRC has accomplished the following in the InP program (Flood et al. 1989):

- Achieved an efficiency of 18.8% in an n/p homojunction structure
- Achieved an efficiency >17% in a cell produced by sputtering indium tin oxide (ITO) onto InP
- Fabricated some InP on alternative substrates (efficiencies 10%)
- Initiated fabrication of ultra-thin InP cells

The objectives of the GaAs solar cell program are to (Flood et al. 1989)

- Develop high-efficiency concentrator cells
- Demonstrate feasibility of the point contact junction geometry in GaAs
- Develop a v-grooved cell geometry with improved efficiency and radiation resistance (compared to the standard cell geometry)

Recently LeRC has accomplished the following in the GaAs program (Flood et al. 1989):

- Achieved an efficiency >22% with prism-covered cells operating at 100 Suns and 373 K
- Developed a domed mini-Fresnel lens that offers the possibility of raising the specific power of radiation-resistant arrays from $\leq$30 W/kg to about 60 to 90 W/kg
- Developed an understanding of the requirements that must be met to demonstrate a point-contact GaAs cell
- Grew a p-n junction on a v-groove surface geometry

The objective of the JPL advanced photovoltaic solar array (APSA) program is to develop an ultra-light-weight, high-performance, advanced deployable photovoltaic array design that will be suitable for a broad range of long-term NASA and U. S. commercial space applications for the period beyond 1990. The near-term goal is to achieve a specific power of 130 W/kg and the long term goal is to achieve 300 W/kg. Under the JPL program a flexible blanket array has been built based on the 55-μm silicon solar cell. The specific power of this array is 130 W/kg for a 5.3 kWe beginning of life (BOL) deployable wing (Flood et al. 1989).

The APSA design is based on near-term technology and prior experience (Flood et al. 1989):

- Patterned after the Canadian Telecommunications Satellite (CTS) and the Solar Array Flight Experiment (SAFE) solar array designs

- Consists of a flat-pack, fold-out, flexible blanket planar array
- Uses thin (55-μm), high-performance (~13.5% efficient) silicon solar cell modules
- Uses a flexible, printed-circuit blanket electrical harness
- Uses a graphite/epoxy blanket box structure
- Uses a light-weight version of the continuous longeron lattice mast deployment system
- Builds on the LeRC work on high-efficiency cells

The APSA program is now moving into a ground testing phase and will then move on toward the long-term goal of 300 W/kg. APSA clearly offers the capability to meet a wide range of mission requirements including Earth Observing System (EOS) and solar electric propulsion (SEP).

Chemical Energy Conversion

The chemical energy conversion program has been established to provide the technology base for advanced electrochemical energy conversion and storage systems required to support the low- to high-power needs of future manned and unmanned space applications, the cycle life requirements of low-Earth orbit (LEO) systems and storage life requirements of new long-duration unmanned planetary missions. Included in this program element is the development of high-performance, long-life, cost-effective systems for primary and secondary (rechargeable) power applications, advanced fuel cells, and thermal electrochemical converter concepts (OAST 1989).

The OAST chemical energy conversion program is being carried out at LeRC and JPL. LeRC is focusing primarily on nickel-hydrogen batteries (individual pressure vessel or IPV and bipolar) and advanced fuel cells. LeRC is also involved in a planned flight experiment to test a sodium-sulfur battery design. JPL is focusing primarily on lithium rechargeable batteries, having successfully transferred its lithium primary battery technology to the Air Force for use on the Centaur upper stage. Both LeRC and JPL are studying advanced battery concepts that offer even higher specific energies. The long-term goal is to achieve 100 W-h/kg. As an approximate rule-of-thumb, the nickel-hydrogen batteries are useful for power requirements $\geq$1 kWe and the lithium rechargeable batteries are useful for power requirements $\leq$1 kWe.

The objectives of the LeRC nickel-hydrogen (NiH_2) battery program are to develop improved specific energy cells (at least two times the state of the art) and improved specific volume (at least 20% better than the state of the art) cells. The approach is to optimize the design using computer-aided design (CAD) tools and to develop the technology for light-weight nickel electrodes and to optimize the potassium hydroxide (KOH) concentration. The design will be verified by testing boiler plate and flight-weight cells. This work will support future energy storage on Space

Station, Earth Observing System, Hubble Space Telescope, communication satellites and exploratory rovers.

In 1988 LeRC and Hughes won an IR&D 100 Award for their advanced design IPV NiH_2 cell. A key factor was the use of a 26% KOH solution that improves the cycle life about ten times that of the state-of-the-art (Lim and Verzwyvelt 1987). LeRC has successfully tested 26% KOH NiH_2 cells for >5600 h and has developed a light-weight nickel electrode for a high-energy density NiH_2 cell with LEO performance verified at 80% depth of discharge (DOD).

The JPL work on lithium batteries complements planned future planetary space missions which require batteries with enhanced energy storage capability, long active shelf life, long cycle life and a high degree of safety and reliability for powers $\leq$1 kWe. A JPL review of advanced electrochemical systems has led to a focus on the organic electrolyte system Li-TiS_2 (Subbarao et al. 1989). Such a battery system offers a 2 to 3-fold increase in energy storage capability over nickel-cadmium (NiCd) and NiH_2 batteries with a 35% to 50% reduction in battery mass and volume for 5- to 10-year lifetimes. To date JPL has developed a better controlled synthetic process for TiS_2 and has developed a fabrication process for thinner and larger electrodes.

LeRC has been investigating new catalyst systems for improved alkaline fuel cells. Studies of a new gold-platinum cathode catalyst have shown more than two times the surface area of the reference cathode catalyst (Martin and Manzo 1988). This work will continue and is integral to the surface power program to be described in a subsequent section.

Thermal Energy Conversion

The thermal energy conversion program has these goals (OAST 1989):

- Develop the technology base to provide advanced high-efficiency, high- temperature (1050 - 1400 K), long-life solar dynamic Stirling/Brayton power systems for a wide range of NASA and commercial space power requirements (specific goals include specific powers of 8 to 20 W/kg)

- Develop new thermoelectric materials with significantly higher figure of merit values to improve the efficiency of a space thermoelectric power system toward >10%

- Investigate and demonstrate the feasibility of a high-power, long-life alkali metal thermal-to-electric (AMTEC) electrode which will enable the projected efficiencies of 20% or greater to be achieved for >10,000 h

LeRC is managing an advanced solar dynamic space power program with the objective of developing small and light-weight solar dynamic systems which show significant improvement in efficiency and specific mass over the baseline design derived

from Space Station technology. Technology advancements to the receiver/thermal energy storage subsystem offer the highest payoff because these are the heaviest components. Accordingly LeRC is aiming at developing a receiver with half the specific mass of the current state-of-the-art. In the first phase of this effort receivers for both Brayton and Stirling heat engines are being developed (Kesseli and Lacy 1989 and Heidenreich et al. 1989). Separately under this program LeRC is developing long lived ($\geq$10 y), light-weight, and more reflective space solar concentrators than the state-of-the-art. The concentrator program is focused on concentrator concept development and the resolution of those critical technology issues that will lead to durable, highly specular, and light-weight reflector elements (Naujokas and Savino 1989).

LeRC has been evaluating free piston Stirling engines for potential use in a wide variety of space power missions. A space power demonstrator engine (SPDE) was built by Mechanical Technology Incorporated (MTI) with the following accomplishments (Dochat and Dhar 1989):

- Operation at design stroke, pressure and temperature (T_H = 650 K; T_C = 325 K)
- Demonstrated 28 kW indicated power versus 28.8 kW goal
- Achieved 22% indicated efficiency versus 28% goal
- Demonstrated 17 kW electrical power versus 25 kW goal
- Demonstrated excellent dynamic balance
- Measured 0.03 mm casing motion amplitude at design point versus 0.07 mm maximum permissible
- Stable operation over entire operating range
- Good data correlation with MTI's HFAST Stirling engine harmonic code
- Demonstrated 87% linear alternator efficiency on dynamometer test rig

Near the conclusion of the SPDE program, the SPDE was divided into two 12.5-kWe single cylinder engines to be used as test beds for critical Stirling technology development. Work is under way now to develop a 1050 K space Stirling engine (SSE) with an EOL power of 25 kWe and an efficiency of >25% for a lifetime of 60,000 h. Much of the Stirling work is now being carried out under the CSTI program, which will be described in a subsequent section.

The AMTEC is a thermally regenerative electrochemical device for the direct conversion of heat to electrical energy. AMTEC can operate at T_H's ranging from 900 to 1300 K with predicted device efficiencies of 15% to 30%. Experimentally, AMTEC has demonstrated an energy conversion efficiency of 19% and stable electrode performance at 0.4 to 0.5 W/cm^2 for 1500 h. AMTEC offers the potential of doubling

or tripling the conversion efficiency of static conversion systems which is important for mass-sensitive space missions. Current efforts are focused on testing the recirculating test cell (RTC) which is a laboratory mockup of a flight-type AMTEC converter (Underwood et al. 1989).

The advanced thermoelectric program is aimed at developing thermoelectric materials with improved figures of merit. (The figure of merit, Z, is equal to S^2/pk, where S is the Seebeck coefficient, p is the electrical resistivity and k is the thermal conductivity.) The silicon-germanium (SiGe) alloy used on the radioisotope thermoelectric generators (RTGs) on the two Voyager spacecraft and the Galileo spacecraft has a figure of merit of about $0.6 \times 10^{-3}K^{-1}$. As in the case of AMTEC, improved SiGe alloys with higher figures of merit can lead to substantial mass and cost savings for space nuclear power systems. Recent experimental and theoretical studies on n-type gallium-phosphide(GaP)-doped SiGe indicate 20% to 30% gains in the figure of merit (Vandersande et al. 1987 and Fleurial et al. 1989). Parallel improvements in the p-leg will be necessary to raise the overall figure of merit. Recent theoretical work indicates that reducing the thermal conductivity through the addition of inert particles to the SiGe may enable achievement of higher figures of merit.

Power Management

The power management program will develop the electrical/electronic technologies needed to provide safe, effective and light-weight systems to control, distribute, and condition electric power for future planetary, lunar, and Earth-orbital space missions. These missions will require (1) automation, (2) the ability to operate in hostile environments, (3) higher performance, (4) lower specific mass, and (5) the development of an "electric utility" approach to dramatically reduce cost and increase the adaptability of power systems to programmatic changes in direction. Of particular interest is the development of technologies to achieve power densities of 0.6 W/cm^3 for spacecraft power distribution, switching and control functions. Such high-density power technology is crucial to constraining the power system to 15% to 20% of the overall system mass and volume. The power management program also includes power beaming (OAST 1989).

LeRC is working on power management and distribution (PMAD) systems technology to ensure that this technology is available to meet the demanding requirements of the exploration initiative and other advanced missions. This work involves mission studies to identify the requirements and focused projects to resolve critical issues. For the former, LeRC is now: (1) studying lunar base scenarios to identify technical constraints in growing from a 20-kWe outpost to a mature multimegawatt base and (2) developing an understanding of the relation of PMAD system masses to their requirements through design analyses of Space Station Freedom and existing space power systems. For the latter LeRC is extending its development of the light-weight, versatile and safe 20-kHz alternating current distribution technology, and developing

smart, fault-tolerant systems to greatly enhance PMAD reliability. A smart diagnostics system using neural nets has been successfully installed on a DC PMAD breadboard at LeRC. A theoretical structure has been developed to connect total system costs, including costs of mission failure, to the degree of redundancy (Faymon et al. 1987).

Separately, LeRC has been working to develop high-temperature power electronics. This is critical to reducing the size of the electronics radiator which grows rapidly as power levels rise. It is also very important on the lunar surface where the day temperatures are comparable to the limits of existing electronics and in other applications, such as the SP-100 space nuclear reactor, where the electronics must operate in a hot environment. Silicon carbide (SiC) offers the potential for high-temperature diodes and metal oxide semiconductor (MOS) field effect transistor (FET) power switches. LeRC has demonstrated a SiC diode and developed and characterized advanced materials at a temperature of about 870 K. LeRC is also working on high-temperature dielectrics and insulators, and LeRC is developing intercalated graphite for application to high-thermal-conductivity circuit boards.

JPL has been focusing on the development of high-density intelligent or "smart" power device technology. Program targets are low mass and low volume, high-efficiency, generic power building blocks applicable to a wide range of PMAD implementations. The overall objective is to achieve PMAD power densities of >0.6 W/cm^3 (a 20-fold improvement over the state of the art in space PMAD applications). The short-term goal is to develop hybrid smart modules containing the required basic power functions. A longer term goal is to upgrade these functions into monolithic power integrated circuits (PICs) technology. This effort offers the potential for up to 80% reductions in mass and volume and up to 90% reductions in the piece parts count in a typical PMAD system. JPL has completed breadboard testing of (1) a coreless Hall effect current sensor, (2) a low-voltage synchronous rectifier, and (3) MOS-controlled thyristor (MCT)/FET and gate turn-off thyristor (GTO)/FET high-power, high-performance switches. JPL is proceeding with the development of a monolithic synchronous rectifier and hybridization of a 20-kVA MCT/FET switching module (Klein and Theisinger 1987 and Rippel 1987, 1989a and 1989b).

Both LeRC and Langley Research Center (LaRC) are working on power beaming. LaRC has been pursuing the use of lasers to transmit power (Kwon and Lee 1989). Beam power may provide an alternative to nuclear and photovoltaic/chemical power sources for bases or rovers on the surfaces of the Moon and Mars. To date LaRC has produced 14 W of continuous wave (CW) power at 1.3 μm from a solar-simulator-pumped iodide laser and LaRC has operated the world's first solar-pumped iodide laser amplifier. A recent LeRC study has shown that a nuclear electric propulsion (NEP) cargo vehicle sent to Mars could be used to provide beamed power to a number of surface bases or installations (Cull and Faymon 1989).

Thermal Management

The objectives of the thermal management program are to (OAST 1989):

- Develop the thermal management technology for advanced high capacity and high-performance thermal management systems for future NASA space missions
- Enhance the understanding of fluid behavior and dynamics in a reduced gravity environment to establish reliable predictive models and data bases for the development of advanced space systems.
- Develop, analyze, and test various thermal energy management concepts and components for application to future spacecraft and space facilities

The thermal management program includes the following technology areas (OAST 1989):

- Film condensation, flow boiling and two-phase regimes
- Advanced radiators
- Heat pipes
- Heat pumps

LeRC has been investigating liquid sheet radiators (LSRs) which offer the potential advantage of having a lower mass than solid wall radiators and being nearly immune to micrometeroid damage. LeRC has completed a new facility to investigate large sheet flows (Chubb and Calfo 1989).

A number of capillary pumped loops (CPLs) have been developed at the Goddard Space Flight Center (GSFC) for the purpose of transferring large heat loads in space applications and they have a demonstrated heat transfer capability of 25 kW with no moving parts. GSFC has been working on controlling the speed of the mechanical pump used to complement the evaporator pumps to enhance the pressure rise (Schweickart et al. 1989).

CSTI High-Capacity Power

The Civil Space Technology Initiative (CSTI) is intended to remedy gaps in the U. S. space technology program and to help restore NASA's technical strength. The CSTI program will provide advanced technologies that are focused on three specific areas of near-term, high-priority missions: technologies to support near-term transportation needs, technologies to enhance operations in Earth orbit, and technologies that support science operations (OAST 1989). The high-capacity power program is one element of CSTI. The objective of the CSTI high-capacity power program is to develop the key technologies that satisfy the needs for long-duration and high-capacity

power for future missions such as outpost habitats and extended bases associated with lunar missions. The program includes work on the following technology areas:

- Conversion systems
- Thermal management
- Power management
- System diagnostics
- Environmental interactions

The CSTI high-capacity power program is a focused technology development to enhance the capability of space power systems using the SP-100 ground engineering system (GES) reactor. The goals are to raise the specific power from 25 W/kg to 80 W/kg and to raise the power from 100 kWe (baseline SP-100 thermoelectric system) to 800 kWe. Two advanced energy conversion technologies are being pursued: free piston Stirling engines and advanced thermoelectrics. Both the Stirling work and the advanced thermoelectric work build upon the foundations laid in the R&T Base program. Under CSTI a 25-kWe/cylinder Stirling space engine is being built to operate at a heater temperature of 1050 K (which is the first step toward the goal of operating an engine at 1500 K) and a cooler temperature of 525 K (Winter 1989).

An important part of both the R&T Base and CSTI is the work on environmental interactions including experimentally and theoretically studying such phenomena as spacecraft charging and atomic oxygen attack.

Pathfinder

The Pathfinder program, which was initiated in FY 1989, is designed to provide the advanced technologies in space exploration, space operations, humans-in-space and transfer vehicles to enable a broad set of future piloted or robotic solar system exploration missions (OAST 1989). There are two power-related program elements in the Pathfinder program: surface power and the SP-100 space nuclear reactor program.

Surface Power

The objectives of the surface power program are to

- Develop solar-based power technology to a level of readiness sufficient to enable or enhance extraterrestrial surface missions
- Demonstrate critical components for a 300 W/kg AM0 solar array
- Demonstrate critical components for a 500 to 1000 W-h/kg regenerative fuel cell with high efficiency and >5000 h reliable operation

- Complete the feasibility assessment of a 55-kW/kg electric power management system

The principal technology areas of this program will be power generation (e.g., advanced photovoltaics and arrays) and advanced energy storage (e.g., fuel cells).

Space Nuclear Power (SP-100)

The objective of the SP-100 space nuclear reactor program is to develop and validate the technology for space nuclear reactor power systems that can produce tens to hundreds of kilowatts of electric power and be capable of seven years of operational life at full power. The technology areas include

- Refractory metal reactor
- Fuel pins
- High-temperature control system
- Liquid-metal thermoelectric magnetic pump
- Thermal-to-electric conversion
- Heat-pipe heat-rejection systems

The SP-100 program is a joint endeavor of NASA, the Department of Energy (DOE) and the Strategic Defense Initiative Organization (SDIO). Under the SP-100 program a generic 100-kWe space reactor power system is being designed. The reactor concept will be scalable from 10 kWe to 1000 kWe. SP-100 provides a technology base for nuclear electric propulsion (NEP) missions to the outer planets, surface power and spacecraft power. Nuclear fuel development and manufacture is under way at DOE's Los Alamos National Laboratory. Fuel tests are being conducted in DOE's reactors at the Hanford Engineering Development Laboratory (HEDL) and the Idaho National Engineering Laboratory. Radiation hardened electronics tests are under way at DOE's Sandia National Laboratories and high-temperature materials development is being conducted at DOE's Oak Ridge National Laboratory, LeRC, General Electric (GE) and Westinghouse Electric (Pluta et al. 1989).

Major components will be tested on the ground in a simulated space environment to demonstrate compliance with safety, reliability and performance requirements. Preparations have begun for reactor testing in an existing containment building at HEDL. Other major modules of the power system, including the thermoelectric power conversion are planned for testing in a vacuum chamber at GE (Pluta et al. 1989).

Directions in Space Energy Conversion R&T

The following sections tabulate the directions being pursued in OAST's space power program as derived from OAST 1989.

Photovoltaic Energy Conversion

- 300 W/kg; 300 W/m^2; radiation hard
- Efficiencies from 20% to 35% (depending on hardness)
- Array technology for near-Sun and far-Sun applications

Chemical Energy Conversion

- 100 W-h/kg secondary batteries capable of 1000 cycles
- 50 W-h/kg bipolar NiH_2 battery capable of 40,000 cycles at 50% DOD
- Advanced regenerative fuel cells for GEO applications with specific energies >200 W-h/kg
- Advanced energy storage systems with 1000 W-h/kg

Thermal Energy Conversion

- High-efficiency fixed and deployable concentrator concepts with surface accuracies of 1 to 2 milliradians and concentration ratios of 2000 to 5000
- Long-life concentrator substrates, optical surfaces and thermal energy storage materials
- Long-life, high-power density (>0.5 W/m^2) electrode technology applicable to high-efficiency (20%) AMTEC
- High-efficiency (>10%) thermoelectric conversion

Power Management

- High-power (100 kWe), high-temperature (673 K), radiation- resistant (100 Mrad) components and circuits
- Fault-tolerant PMAD systems
- Increased efficiency (>10%) laser power transmission
- Advanced packing/thermal/electrical devices (power integrated circuits)

Thermal Management

- High-capacity heat pipes, pumped loops, thermal buses
- Advanced radiators, thermal storage, fluid management

Conclusion

The OAST space power program covers a broad range of important technologies that will enable or enhance future U. S. space missions. The program is well under way and is providing the kind of experimental and analytical information needed for spacecraft designers to make intelligent decisions about future power system options.

References

Chubb, D. L. and F. D. Calfo (1989) "Scaling Results for the Liquid Sheet Radiator", paper number 899163 in *Proceedings of the 24th Intersociety Energy Conversion Engineering Conference (IECEC)* held in Crystal City, VA, 6-11 August 1989.

Cull, R. and K. A. Faymon (1989) "Orbit to Surface Beamed Power for Mars Bases Expansion", paper 899139 in *Proceedings of the 24th IECEC.*

Dochat, G. R. and M. Dhar (1989) "Free Piston Space Stirling Technology Program" , paper 899603 in *Proceedings of the 24th IECEC.*

Faymon, K. A., G. R. Sundberg, R. W. Bercaw, and D. J. Weeks "LeRC Power System Autonomy Program 1990 Demonstration", paper number 879106 in *Proceedings of the 22nd Intersociety Energy Conversion Engineering Conference (IECEC)* held in Philadelphia, PA, 10-14 August 1987.

Fleurial, J-P, C. B. Vining, and A. Borshchevsky (1989) " Multiple Doping of Silicon-Germanium Alloys for Thermoelectric Applications ", in *Proceedings of the 24th IECEC.*

Flood, D. J., M. Piszczor, Jr., P. M. Stella, and G. L. Bennett (1989) "NASA Advanced Space Photovoltaic Technology - Status, Potential and Future Mission Applications", NASA Technical Memorandum 102093 prepared for the European Space Power Conference held in Madrid, Spain, 2-6 October 1989. (Also available in European Space Agency publication SP-294, *Proceedings of the European Space Power Conference.*)

Heidenreich, G. R., R. S. Downing, and D. E. Lacy (1989) "Brayton Advanced Heat Receiver Development Program", paper number 899007 in *Proceedings of the 24th IECEC.*

Kesseli, J. B. and D. E. Lacy (1989) "The Cavity Heat Pipe Stirling Receiver for Space Solar Dynamics", paper number 899187 in *Proceedings of the 24th IECEC.*

Klein, J. W. and P. C. Theisinger (1987) "The Role of Power Integrated Circuits in Lightweight Spacecraft", paper presented at the AIAA/DARPA Joint Conference on Lightweight Spacecraft, Monterey, CA, August 1987.

Kwon, J. H. and J. H. Lee (1989) "Far Field Beam Pattern of One MW Combined Beam of Laser Diode Array Amplifiers for Space Power Transmission", paper number 899592 in *Proceedings of the 24th IECEC.*

Lim, H. S. and S. A. Verzwyvelt (1987) "KOH Concentration Effect on Cycle Life of Nickel-Hydrogen Cells" in *Proceedings of the Space Electrochemical Research and Technology (SERT) Conference*, NASA Conference Publication 2484, held at the NASA Lewis Research Center, Cleveland, Ohio, 14-16 April 1987.

Martin, R. E. and M. A. Manzo (1988) "Alkaline Fuel Cell Performance Investigation", paper number 889498 in *Proceedings of the 23rd Intersociety Energy Conversion Engineering Conference (IECEC)* held in Denver, CO, 31 July - 5 August 1988.

Naujokas, G. J. and J. M. Savino (1989) "A Program for Advancing the Technology of Space Concentrators", paper number 899366 in *Proceedings of the 24th IECEC.*

OAST (1989) *Office of Aeronautics and Space Technology Space Research and Technology Program, Program and Specific Objectives Document*, Fiscal Year 1990, 9 August 1989.

Pluta, P. R., M. A. Smith, and D. N. Matteo (1989) "SP-100, A Flexible Technology for Space Power from 10s to 100s of kWe", paper number 899287 in *Proceedings of the 24th IECEC.*

Rippel, W. R. (1987) "A High Performance, Integrable Current Sensor", paper presented at the Power Conversion and Intelligent Motion (PCIM) 87/Conference, Long Beach, CA, September 1987.

Rippel, W. R. (1989a) "MCT/FET Composite Switch Achieves High Silicon Utilization and High Switching Performance", PCIM 89/Conference, Long Beach, CA, October 1989.

Rippel, W. R. (1989b) "GTO/FET Cascode Three-Terminal High Performance Switch ", PCIM 89/Conference, Long Beach, CA, October 1989.

Schweickart, R., L. Ottenstein, B. Cullimore, C. Egan, and D. Wolf (1989) "Testing of a Controller for a Hybrid Capillary Pumped Loop Thermal Control System", paper number 899476 in *Proceedings of the 24th IECEC.*

Subbarao, S., D. H. Shen, F. Deligiannis, C-K. Huang, and G. Halpert (1989) "Ambient Temperature Secondary Lithium Batteries for Space Applications", *Proceedings of the Fourth Annual Battery Conference on Applications and Advances*, held at California State University, Long Beach, CA, 17-19 January 1989.

Underwood, M. L., R. K. Sievers, D. O'Connor, R. M. Williams, B. Jeffries-Nakamura, and C. P. Bankston (1989) "AMTEC Recirculating Test Cell Component Testing and Operation", paper number 899501 in *Proceedings of the 24th IECEC.*

Vandersande, J., C. Wood, and S. Draper (1987) "Effect of High Temperature Annealing on the Thermoelectric Properties of GaP-Doped SiGe," *Proceedings of the Material Research Society Symposium*, Vol. 97, pp. 347-352, Spring Meeting held at Anaheim, CA.

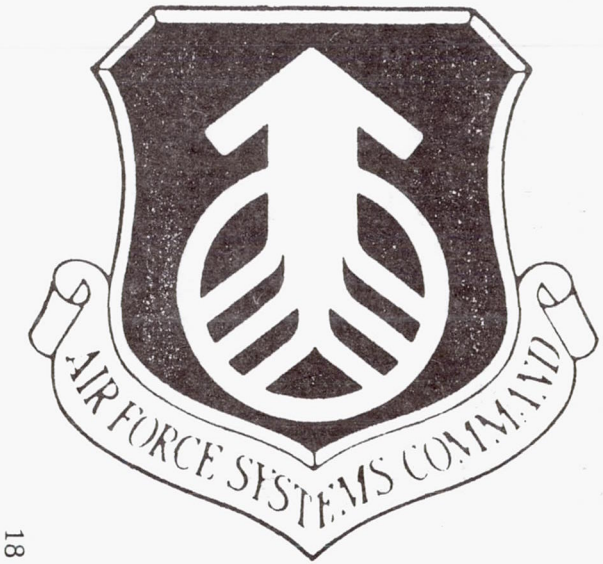

AIR FORCE PHOTOVOLTAICS TECHNOLOGY

JAMES S. CLOYD

STATIC ENERGY CONVERSION
TECH AREA (WRDC/POOC-2)
WPAFB, OH 45433-6563

PHOTOVOLTAICS

OBJECTIVES / GOALS

- **HIGH EFFICIENCY PHOTOVOLTAIC CELLS**
  - GREATER THAN 25 % EFFICIENCY (BOL)
  - LESS THAN 15 % DEGRADATION AT 10^{15} 1 MeV e/SQ CM
  - PLANAR AND CONCENTRATOR ARRAY USE
  - MANUFACTURABILITY
- **LIGHTWEIGHT, HARDENED ARRAYS**
  - 100 WATTS/KG, 250 - 300 WATT/SQ M
  - 10 YEAR OPERATIONAL LIFE, POWER LEVELS TO 250 KW
- **FLIGHT EXPERIMENTS**
  - DEMONSTRATE PERFORMANCE
  - ENGINEERING DATA CORRELATED WITH ACTUAL EXPOSURE
- **SURVIVABILITY**

PHOTOVOLTAICS

WHY HIGH EFFICIENCY ?

EXAMPLE : 5 KILOWATT, GEOSYNCHRONOUS (CELLS ONLY)

PARAMETER	CURRENT 18 %	25 %	30 %
WEIGHT (KG)	76	55	46
AREA (SQ M)	36	26	21
COST ($M)	5.6	4.1	3.3

PHOTOVOLTAICS

HIGH EFFICIENCY CELL PROGRAM

PROGRAM	GOAL	FY 89 STATUS
PLANAR MULTIBANDGAP	27 % AlGaAs/Ge (22 % TOP CELL)	DEMONSTRATED GRADED BANDGAP, 19 % TOP CELL
CONCENTRATOR MULTIBANDGAP	30 % EFF. GaAs/Ge (2 JUNCTION)	RECORD 24.5 % EFF., AM0 100 SUNS, NO PRIS COVER
	AlGaAs/GaAs/X (3 JUNCTION)	FIRST SPACE CELLS FABRICATED (2 JUNCTION) - 18.5% EFF.
	Ge : Si ALLOY BOTTOM CELL	MATERIAL GROWTH VERIFIED
HIGH TEMPERATURE METALLIZATION AND CONTACTS (IN - HOUSE)	550 - 600 DEGREES C SURVIVABILITY	METALS DEPOSITION EQUIPMENT RECEIVED BINARY/TERNARY PHASE DIAGRAMS NEARING COMPLETION

MANUFACTURING TECHNOLOGY
RUGGED THIN GaAs SOLAR CELLS

OBJECTIVE PROCESS TECHNOLOGY FOR:

- 3 MIL THICKNESS, 18 % EFFICIENCY
- 4 CM X 4 CM AND 6 CM X 6 CM CELLS
- TOTAL OF 50,000 SQ CMS, QUALIFIED CELLS FOR DEMONSTRATION
- HIGH TEMPERATURE (550 DEG C) CONTACTS / METALLIZATION

PAYOFF

- SO FAR, 45 % COST REDUCTION IN SUBSTRATE COST
- 35 % REDUCTION IN MATERIAL COST (BULK PURCHASES)

FY 89 STATUS

- CONTRACT MODIFICATION IN JUNE 89 (SDI ADD-ON)
- 3.5 MIL, 18.5 % EFFICIENCY, 4 CM X 4 CM CELL DEMONSTRATED

PHOTOVOLTAICS

LIGHTWEIGHT, HARDENED ARRAYS

PROGRAM	GOAL	FY 89 STATUS
ADVANCED HARDENED ARRAY (AHA)	AGILE, 40 W/KG SURVIVABLE UNINTERRUPTED POWER	CONTRACT AWARDED MAY 89 MINERAL QUARRY SAMPLES SEP 89
ENHANCED SURVIVABLE SOLAR ARRAY (ESSA)	1.5 X SMATH 2 10 X JCS CELL STACK, POWER HINGE, POWER SUBSTRATE	PHASE IA COMPLETED COMPONENT DEV, BRASSBOARD INITIATED
SURVIVABLE CONCENTRATING PHOTOVOLTAIC ARRAY (SCOPA)	15 W/KG, SMATH 2, 10 X JCS CONCENTRATOR	TRW: DIRECT TRANSITION TO SUPER BOEING: TERMINATED

PHOTOVOLTAICS

FLIGHT EXPERIMENTS

PROGRAM	GOAL	FY 89 STATUS
HIGH EFFICIENCY SOLAR PANEL (HESP) ON CRRES	PROVIDE SCIENTIFIC AND ENGINEERING DATA ON RADIATION EFFECTS	FLIGHT PANELS INTEGRATED ON VEHICLE, TESTING IN PROCESS LAUNCH PLANNED JUNE 1990
PHOTOVOLTAIC ARRAY SPACE POWER PLUS DIAGNOSTICS (PASP +)	ASSESS ARRAY ARCING AS A FUNCTION OF BIAS VOLTAGE AND PLASMA ENVIRONMENT	BRASSBOARD COMPLETED FLIGHT VEHICLE NOT YET IDENTIFIED

PHOTOVOLTAICS

ANTICIPATED FY90 "GOOD NEWS"

- AHA PHASE 1 GO/NO GO DECISION - APRIL 90
- LAUNCH OF CRRES - JUNE 90
- 27% EFFICIENT MULTIBANDGAP CONCENTRATOR CELL GO/NO GO DECISION - AUGUST 90
- IN-HOUSE CLEAN ROOM INSTALLED, PROCESS DEMONSTRATED, HIGH TEMPERATURE METALLIZATION OPTIMIZED - SEPTEMBER 90

PHOTOVOLTAICS

SUMMARY

THIS PROGRAM IS :

- BREAKING RECORDS IN MULTIBANDGAP SPACE CELL EFFICIENCIES
- PROVIDING TECHNOLOGY FOR DOUBLING WEIGHT PERFORMANCE OVER NEAR-TERM SURVIVABLE ARRAYS
- ESTABLISHING REAL ENGINEERING DATA TO OUR USERS VIA FLIGHT EXPERIMENTATION

Session 1
Multi-Junction Cell Technology

Preceding Page Blank

Progress Toward the Development of Dual Junction GaAs/Ge Solar Cells

D.R. Lillington, D.D. Krut and B.T. Cavicchi
Spectrolab, Inc.
Sylmar, CA

E. Ralph
Hughes Aircraft Company
Los Angeles, CA

Lt. M. Chung
AFWAL/POOC-2, Wright Research and Development Center
Wright Patterson Air Force Base
Dayton, OH

Introduction

Space photovoltaic cell technology has seen substantial improvements to cell efficiency, size, and weight and cost reduction since the first cells were flown in the early '60s.

Improvements to material and process technology together with a better understanding of device physics has resulted in planar space silicon solar cell efficiencies of up to approximately 15% AM0 in sizes up to 8 cm x 8 cm. Although terrestrial solar cell designs have shown substantially higher conversion efficiencies at beginning of life (BOL) [ref. 1,2] the susceptibility of these designs to radiation damage has made them unsuitable for space use at this time. It is generally accepted therefore that current silicon efficiencies of 15% represent the plateau in space silicon cell technology until more advanced qualified designs evolve.

In contrast, GaAs and related III-V material based solar cells are in their infancy of development and offer substantial increases in efficiency and radiation hardness compared to silicon. Single junction GaAs cell efficiencies of 18.5% have already been demonstrated in production [ref. 3] and efficiencies up to 32% have been reported on prototype two junction cells [refs. 4-6].

A significant impediment to the widespread use of GaAs cells is the cost and fragility of the wafer. Although 5 mil GaAs cells up to 2 cm x 4 cm have been demonstrated [ref. 3], the manufacture of larger area, thinner GaAs/GaAs cells is virtually impossible given their poor mechanical strength. Both Si and Ge have been considered as alternative substrates on which to grow GaAs layers. The problems associated with the GaAs/Si system, while not unsolvable, are formidable, and large area solar cells based on this system are somewhat distant in the future. Ge on the other hand is well suited for GaAs epitaxy both in terms of thermal expansion coefficient and lattice match and Spectrolab has been actively developing this cell

for several years. Furthermore, with appropriately focussed development on 4 inch diameter Ge wafer growth and high volume MOCVD reactor systems it will become possible to manufacture cells up to 8 cm x 8 cm in size with thicknesses down to 3 mils thus providing the aerospace industry with a "plug in" high power replacement technology for many silicon solar arrays.

Cell Construction

The cross-section of the GaAs cell is shown in Figure 1. It consists of an N^+ GaAs buffer (2.0 microns),N-GaAs base (3.0 microns), P-GaAs emitter (0.4-0.5 microns) and a P-$Al_{0.87}Ga_{0.13}As$ window (0.05-0.1 microns). An P^+ GaAs cap separates the front contact from the window allowing very low contact resistance to be achieved while at the same time preventing the diffusion of metal into the sensitive junction region during interconnect attachment. Contact to the cap is made using a stable Ti/Pd/Ag metallization, proven to be stable at 300°C for 500 hours. Further addition of diffusion barriers to the metallization system also shows promise of increasing thermal stability to 550°C or more. The thin window also allows high efficiency, both by minimizing the absorption of short wavelengths and by improving the optical performance of the antireflection (AR) coating. This is important at short wavelengths where optical interference effects in the window are high.

Modeling of GaAs/Ge Cell Performance

Spectrolab has developed computer codes to predict the performance of GaAs/Ge cells. These models determine the cell characteristics as a function of optical coupling into the cell and material parameters for each layer such as thickness of each region, minority carrier diffusion length, diffusion coefficient, doping concentration and recombination velocity.

Our model assumes that the top GaAs cell is electrically joined to a bottom Ge cell by an N^+ GaAs/P^+ Ge tunnel junction. This junction may be formed by the diffusion of Ga into the Ge and out-diffusion of Ge into the GaAs during growth. A full description of this cell and the model is given elsewhere [refs. 7,8].

Our analysis performed to date shows that in order to achieve high efficiencies in the dual junction configuration it is important that certain boundary conditions are met. These are:

1. A low recombination velocity at the Ge back surface.
2. A low recombination velocity at the Ge emitter surface.
3. A thin Ge emitter.
4. Good optical coupling of infra red wavelengths into the Ge cell.

5. Long diffusion length in the Ge bulk.

6. A highly reflecting back contact to the Ge cell.

Each of these boundary conditions results from the need to maximize the current generation in the Ge cell since current matching between the GaAs and Ge cells is required in order to achieve monolithic (i.e. two terminal) device performance. The problem is further exacerbated by the weakly absorbing nature of Ge beyond 1.4 microns wavelength and the thinness of the substrate (typically 4 mils).

Effect of Ge Wafer Diffusion Length on Cell Performance

The importance of material quality on Ge cell performance is shown in Figure 2 where we have plotted the internal Q.E. as a function of Ge base diffusion length. The calculated short circuit current generation in both the GaAs and Ge cells is also shown in the figure. Current generation in the GaAs cell at wavelengths below 0.35 microns is assumed to be negligible since the cell will ultimately be covered by a filter which is either absorbing below 0.35 microns wavelength (e.g. cerium oxide doped borosilicate glass) or is coated with a UV rejecting filter. Other parameters used in the calculation are shown in Table 1. The value for Ge emitter diffusion length was obtained from data on experimental discrete Ge cells recently made at Spectrolab. A base diffusion length of 80 microns was also measured on these cells. The GaAs cell parameters are those known to give good agreement between experiment and theory for high efficiency MOCVD and LPE homojunction cells. The window and emitter thickness of 0.05 and 0.5 microns respectively are chosen to give the highest efficiency and best radiation hardness and are well established. The thin window thickness of 500 Å also forms a fourth component of the multilayer a.r. coating described later.

In Table 2 we also show the computed effect of Ge base diffusion length on cell efficiency. Other parameters used were again those shown in Table 1. Provided good quality GaAs layers may be grown on the Ge substrate, the model conservatively predicts an AM0 conversion efficiency of 20.29% for the GaAs cell with a short circuit current density of 32.57 mA cm^{-2}. In order to achieve equal current generation in the Ge cell, good quality base material is obviously required. For a base diffusion length of 100 microns the Ge short circuit current density is 31.57 mA cm^{-2} indicating that current matching is indeed possible. The Ge cell efficiency is then 4.12% giving a total GaAs/Ge cell efficiency of approximately 24.3%.

Back Surface Reflector/Back Surface Field

The use of a BSR and BSF is also important in maximizing current generation in the Ge cell. In Figure 3 we show the computed reflectance, (based on literature values of the optical constants) from the interface between various metals and Ge. It is clear that the reflectance for the Ge/Ti interface is only 17% whereas it is greater than 95% for Al or Au making the use of the latter desirable as a back contacting

material. In Figure 4 we also show the corresponding effect of these various back contacting metals on the Ge cell internal Q.E. We note a substantial improvement in QE at long wavelengths due to the use of Al or Au as a BSR. The effect of a BSF in the Ge cell is also shown. If an 80 micron Ge base diffusion length is assumed and other parameters shown in Table 1 are used we calculate a Ge short circuit current density of 31.04 mA cm^{-2} for an Al BSR/BSF contact, 30.36 mA cm^{-2} for a Ti/BSF contact and 29.35 mA cm^{-2} for the case of a Ti contact with no BSF. The use of an Al (or Au) BSR *and* BSF is therefore clearly desirable.

Experimental Performance Data

GaAs/Ge dual junction cells, 2 cm x 2 cm in size have been fabricated on 8 mil thick polished Ge substrates. No attempt was made to improve the boundary conditions such as incorporating a BSF or BSR, optimizing the Ge emitter or enhancing the red performance of the AR coating. Measurements were made under an XT10 solar simulator at 28°C. An average efficiency of 18.7% was measured. A full description of the cells is given elsewhere [ref. 9].

In order to evaluate the performance of the GaAs and Ge cell components we measured the temperature coefficient of efficiency of several cells. Typical data on a 19.1% (28°C) cell is shown in Figures 5 and 6. Our computer model predicts that the Ge cell efficiency falls to zero at approximately 120°C due to the extremely high first diode saturation current. Hence extrapolation of the high temperature portion of the curve predicts a 28°C GaAs AM0 cell efficiency of 16.6% and a Ge AM0 cell efficiency of 2.5%. Improvements to GaAs cell efficiency will be made by improvements to GaAs MOCVD growth quality while the Ge cell may be improved by the use of a BSF/BSR and by better IR optical coupling as mentioned earlier.

In Figure 6 we also show the temperature coefficient of open circuit voltage of the same cell. At lower temperatures the temperature coefficient is equal to -3.94 mV/°C due to the series connection of both GaAs and Ge cells. At higher temperatures the coefficient of -2.33 mV/°C approaches that of GaAs for reasons previously mentioned. Both temperature coefficients of voltage and power are in broad agreement with our model.

Improved A.R. Coating Design

Most GaAs/Ge cells reported to date have utilized a dual antireflection coating of TiO_2/Al_2O_3 optimized for GaAs homojunction cells. In Figure 7 we show the measured reflectance from such a cell. A passive thermal absorptance of 0.88 was measured. This is high compared to GaAs alone due to the absorbing nature of the Ge substrate out to 1.85 microns. It is also evident that the DAR coating does not provide a good bandpass filter at long wavelengths for high Ge cell performance in a dual junction configuration.

In contrast we also show in Figure 7 the effect of a third layer of MgF_2 in the optical stack to form a triple layer AR (TAR) coating. There is a significant reduction in red reflectance beyond 0.87 microns wavelength, thus allowing more light to reach the Ge cell.

In order to evaluate the efficacy of this third coating on cell performance under "true" AM0 illumination, two GaAs/Ge cells were flown on the NASA LeRC Lear jet. This technique has proven to be extremely valuable in providing rapid access to "true" AM0 measurements and has shown good correlation with high altitude balloon and shuttle flight data.

In Figures 8 and 9 we show data on a DAR and TAR coated cell as measured on the Lear jet flight at approximately AM0.22. Since it was the purpose to make relative measurements between AR coatings rather than obtain absolute data, no corrections for ozone, Earth-Sun distance or air mass were made. The kink seen on the DAR coated cell is caused by current starvation in the Ge cell causing it to become reverse biased as the GaAs/Ge cell approaches short circuit conditions. Similar effects have been observed by others [ref. 7]. In contrast the cell with the TAR has a substantially improved fill factor due to increased Ge cell current generation although further improvements to achieve current matching are obviously needed.

We have continued to identify superior a.r. coatings to ensure that the increase in Ge cell performance still persists after glassing, since MgF_2 becomes ineffective when an adhesive of refractive index n=1.43 is applied.

In Figure 10 we show the computed normal reflectance from the filtered optical stack comprising the 0.05 μm AlGaAs window plus an additional proprietary three layer a.r. coating. An adhesive of n=1.43 was assumed to cover the cell. The tolerance on the thicknesses of the individual layers of this stack is high making it a viable production coating. In addition all of the materials are space qualified. This a.r. coating will shortly be used on experimental GaAs/Ge cells and should minimize reflection losses from GaAs in the IR region.

Conclusions

Large area GaAs/Ge cells offer substantial promise for increasing the power output from existing silicon solar array designs and for providing an enabling technology for missions hitherto impossible using silicon. Single junction GaAs/Ge cells offer substantial advantages in both size, weight, and cost compared to GaAs cells but the efficiency is limited to approximately 19.5%-20% AM0. The thermal absorptance of GaAs/Ge cells is also worse than GaAs/GaAs cells (0.88 vs 0.81 typ.) due to the absorption in the Ge substrate.

On the other hand dual junction GaAs/Ge cells offer efficiencies up to ultimately 24% AM0 in sizes up to 8 cm × 8 cm but there are still technological issues remaining

to achieve current matching in the GaAs and Ge cells. This can be achieved through tuned AR coatings, improved quality of the GaAs growth, improved quality Ge wafers and the use of a BSF/BSR in the Ge cell.

Although the temperature coefficients of efficiency and voltage are higher for dual junction GaAs/Ge cells it has been shown elsewhere [ref. 9] that for typical 28°C cell efficiencies of 22% (dual junction) vs 18.5% (single junction) there is a positive power trade-off up to temperatures as high as 120°C. Due to the potential ease of fabrication of GaAs/Ge dual junction cells there is likely to be only a small cost differential compared to single junction cells.

Acknowledgements

The authors wish to thank Russ Hart and Dave Brinker of NASA LeRC for their continued interest in GaAs/Ge cell development and for making the Lear jet flight measurements. Part of this work was performed under USAF Contract No. F33615-89-C-2900.

References

[1.] R. A. Sinton and R. M. Swanson Proc. *19th IEEE PVSC*, 1201 (1987).

[2.] M. A. Green, S. R. Wenham, and A. W. Blakers *Proc. 19th IEEE PVSC*, 6 (1987).

[3.] D. R. Lillington, M. Gillanders, G. F. J. Garlick, B. T. Cavicchi, G. S. Glenn, and S. Tobin, *Proc. 9th SPRAT*, 299 (1988).

[4.] L. D. Partain, M. S. Kuryla, R. E. Weiss, J. G. Werthen, G. F. Virshup, H. F. MacMillan, H. C. Hamaker, and D. L. King,,*Proc 19th IEEE PVSC*, 1504 (1987).

[5.] G. H. Negley, J. B. McNeely, P. G. Lasswell, E. A. Gartley, and A. M. Barnett, *Proc 8th SPRAT*, 55 (1986).

[6.] L. Fraas, J. Avery, J. Martin, V. Sundaram, G. Girard, V. Dinh, N. Mansoori, and J. Yerkes, *Proc 24th IECEC*, 815 (1989).

[7.] S. P. Tobin, S. M. Vernon, C. Bajgar, V. E. Haven, L. M. Geoffrey, M. M. Sanfancon, D. R. Lillington, and R. E. Hart, *Proc 20th IEEE PVSC*, (1988), To be published.

[8.] B .T. Cavicchi, D. R. Lillington, G. F. J. Garlick, G. S. Glenn and S.P. Tobin, *Proc 20th IEEE PVSC*, (1988), To be published.

[9.] D.R. Lillington, B. T. Cavicchi, M. S. Gillanders, G. T. Crotty and D. D. Krut, *Proc 24th IECEC*, 773 (1989).

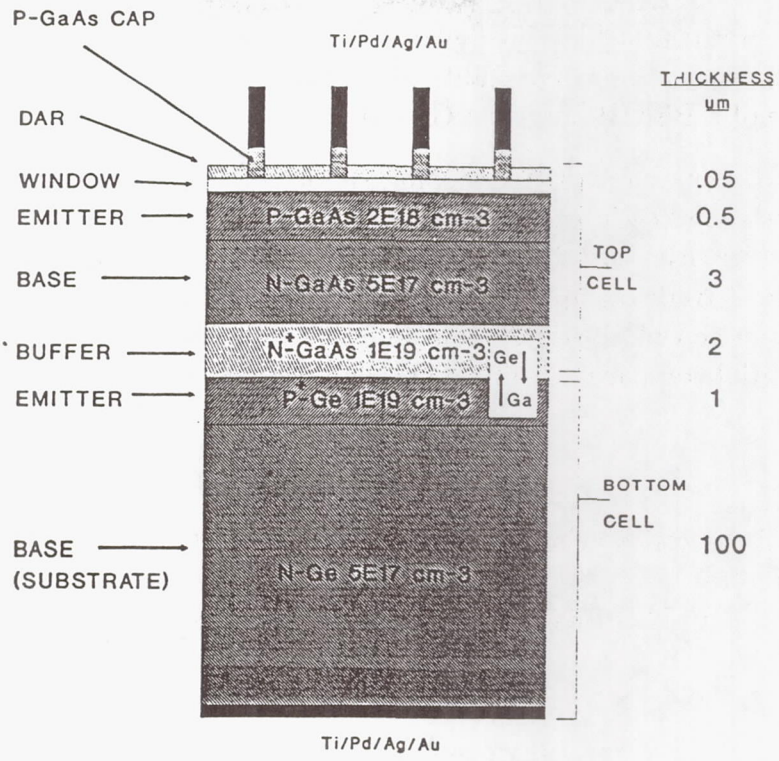

Figure 1 CROSS SECTION OF GaAs/Ge CELL

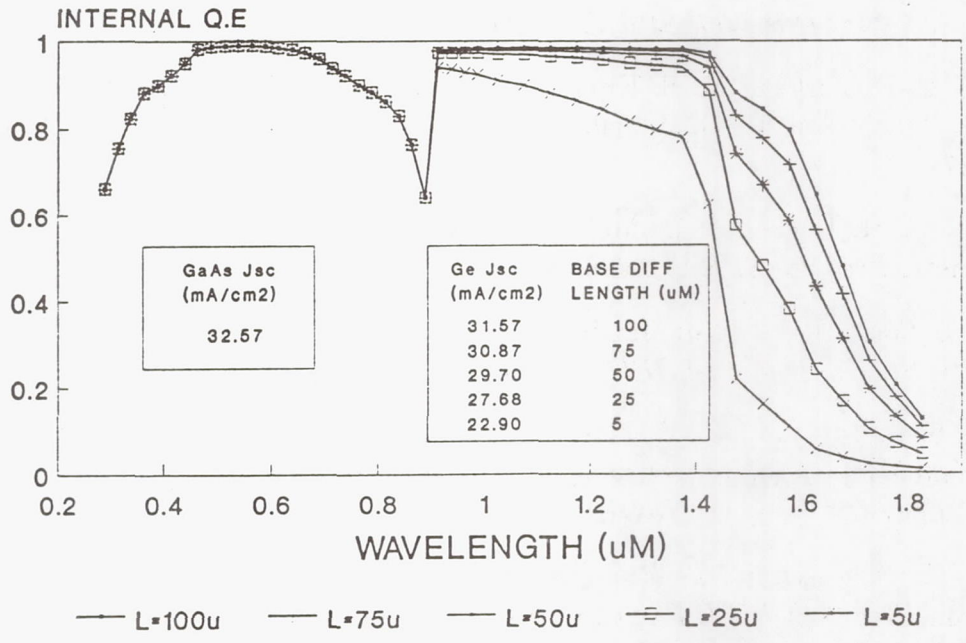

Figure 2 EFFECT OF Ge BASE DIFFUSION LENGTH ON INTERNAL Q.E.

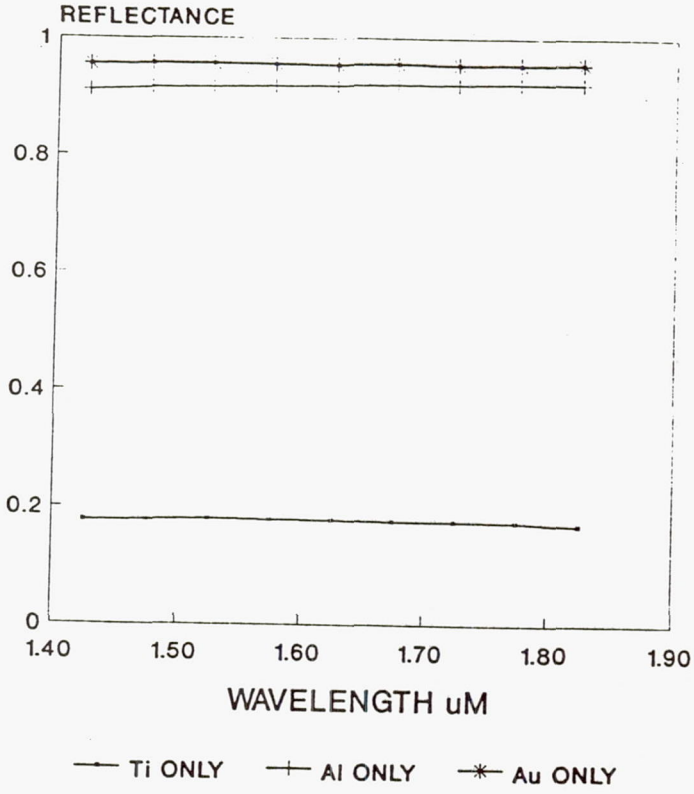

Figure 3 COMPUTED REFLECTANCE FROM THE INTERFACE BETWEEN Ge AND Ti, Al AND Au

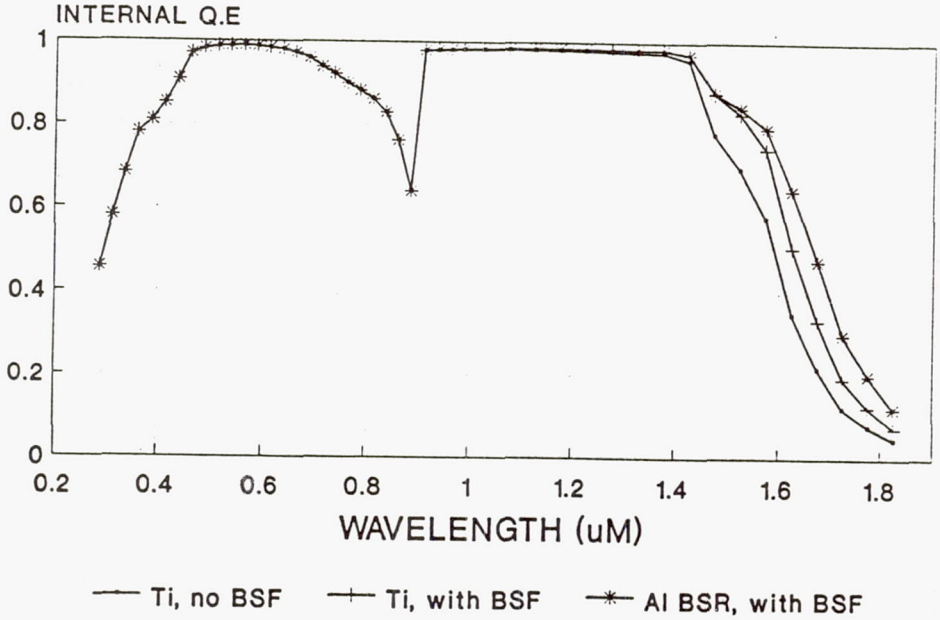

Figure 4 EFFECT OF VARIOUS BACK METALLIZATIONS AND BACK SURFACE FIELD ON INTERNAL Q.E.

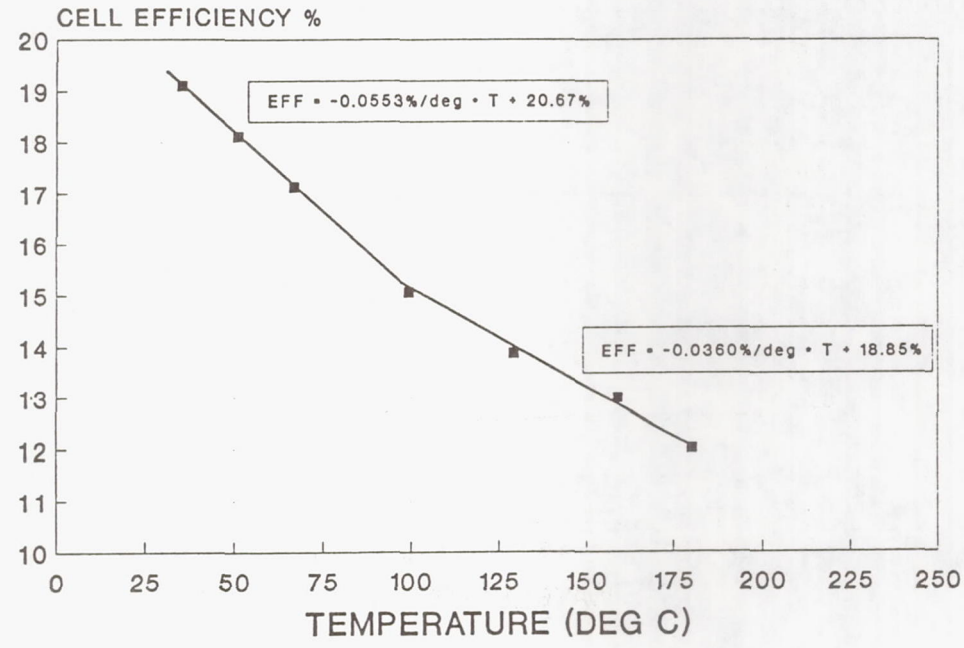

Figure 5 EXPERIMENTALLY MEASURED TEMPERATURE COEFFICIENT OF EFFICIENCY OF DUAL JUNCTION GaA/Ge CELL

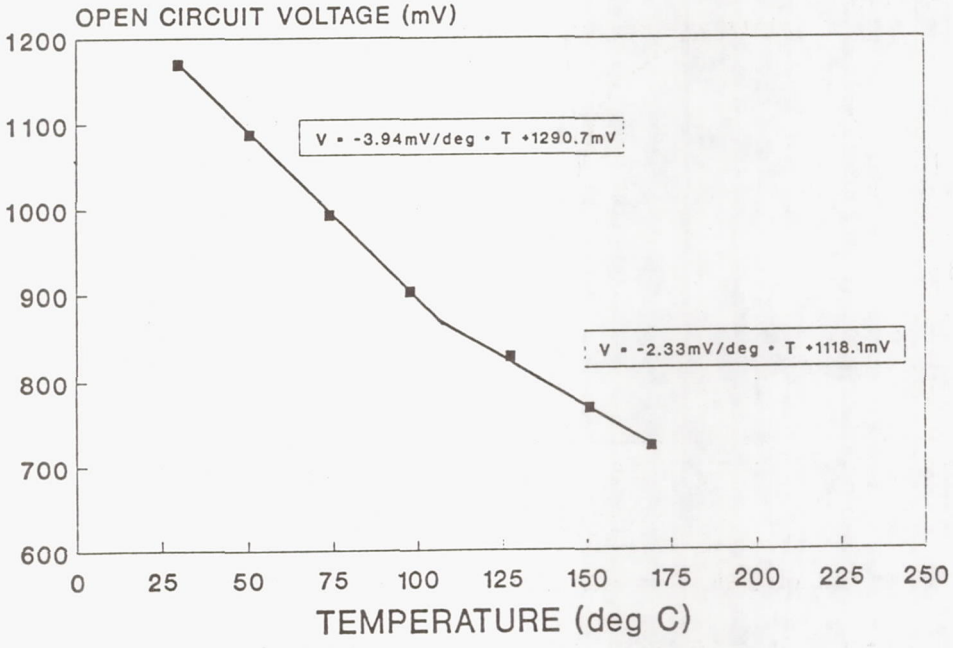

Figure 6 EXPERIMENTALLY MEASURED TEMPERATURE COEFFICIENT OF OPEN CIRCUIT VOLTAGE OF DUAL JUNCTION GaAs/Ge CELL

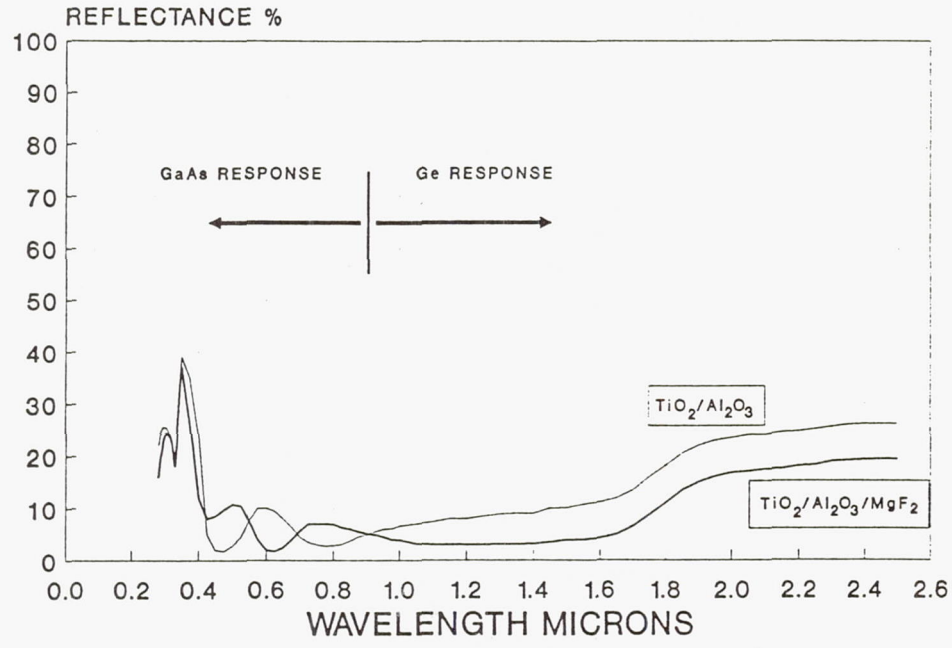

Figure 7 EXPERIMENTLALY MEASURED REFLECTANCE FROM DUAL JUNCTION CELLS WITH TiO_2/Al_2O_3 AND $TiO_2/Al_2O_3/MgF_2$ A.R. COATING

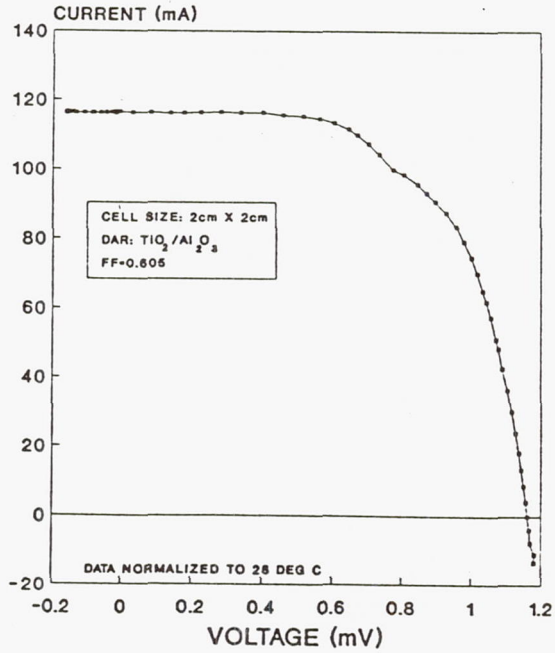

Figure 8 MEASURED AM0.22 I-V CURVE OF GaAs/Ge CELL WITH TiO_2/Al_2O_3 DUAL A.R. COATING. (COURTESY OF NASA LeRC)

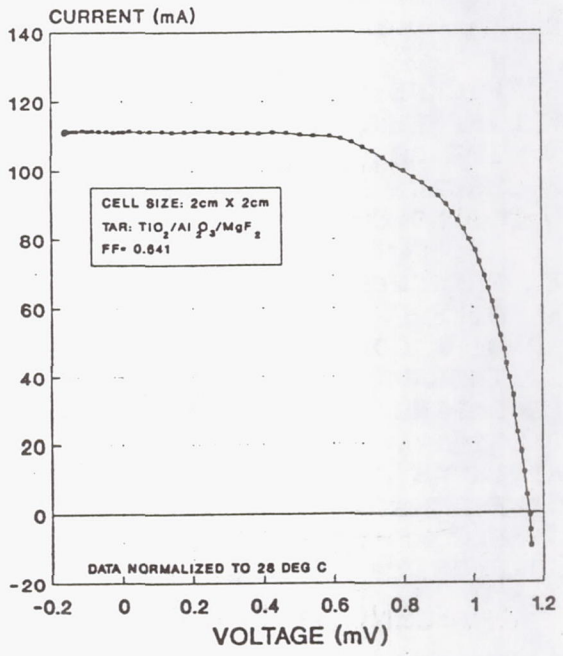

Figure 9 MEASURED AM0.22 I-V CURVE OF GaAs/Ge CELL WITH $TiO_2/Al_2O_3/MgF_2$ TRIPLE LAYER A.R. COATING (COURTESY OF NASA LeRC)

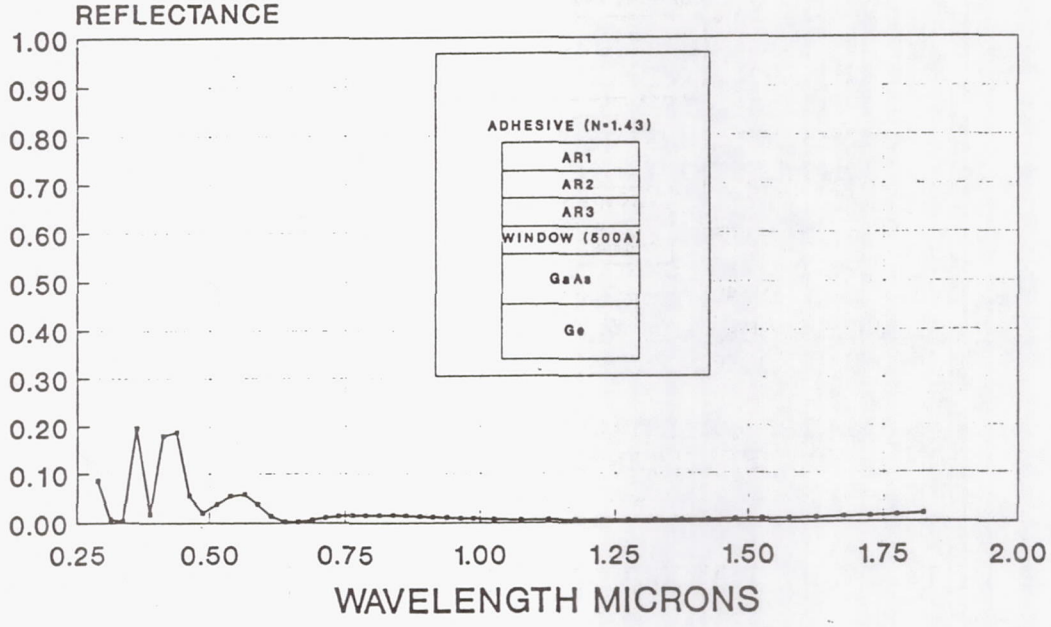

Figure 10 CALCULATED REFLECTANCE OF FILTERED OPTIMIZED GaAs/Ge CELL WITH TRIPLE LAYER A.R. COATING

GaAs CELL PARAMETERS

WINDOW THICKNESS uM	0.05
WINDOW DIFF LENGTH uM	0.2
WINDOW DIFF COEFFT cm2/S	0.27
WINDOW SURFACE REC VELOCITY cm/S	1000000
WINDOW DOPING CM-3	1.0E+18
EMITTER THICKNESS uM	0.5
EMITTER DIFF LENGTH uM	5
EMITTER DIFF COEFFT cm2/S	90
EMITTER INTERFACE REC VELOCITY cm/S	10000
EMITTER DOPING CM-3	2.0E+18
BASE WIDTH uM	3
BASE DIFF LENGTH uM	2
BASE DIFF COEFFT cm2/S	5
BACK SURFACE REC VELY cm/S	100
BASE DOPING CM-3	2.0E+17
SERIES RESISTANCE OHMS	0.2
SHUNT RESISTANCE OHMS	10000
GRID OBSCURATION %	5
TEMP DEG C	28
NO OF SUNS CONC	1

Ge CELL PARAMETERS

EMITTER THICKNESS uM	0.2
EMITTER DIFF LENGTH uM	1
EMITTER DIFF COEFFT cm2/S	24
EMITTER SURFACE REC VELOCITY cm/S	10000
EMITTER DOPING CM-3	1.0E+19
BASE WIDTH uM	100
BASE DIFF LENGTH uM	80
BASE DIFF COEFFT cm2/S	15
BACK SURFACE REC VELY cm/S	100
BASE DOPING CM-3	5.0E+17
SERIES RESISTANCE OHMS	0.2
SHUNT RESISTANCE OHMS	10000

Table 1 GaAs AND Ge CELL PARAMETERS USED IN CALCULATIONS

	GaAs CELL	Ge CELL				
		L=100μ	L=75μ	L=50μ	L=25μ	
Voc (V)	1.023	0.269	0.264	0.255	0.237	0.179
Jsc ($mAcm^{-2}$)	32.57	31.57	30.87	29.7	27.68	22.9
FF	0.821	0.655	0.646	0.630	0.597	0.500
Pmax ($mWcm^{-2}$)	27.37	5.57	5.27	4.78	3.93	2.05
Effy (%)	20.23	4.12	3.89	3.53	2.90	1.52

Table 2 EFFICIENCY PREDICTIONS FOR GaAs/Ge CELL WITH Ge BASE DIFFUSION LENGTH AS A VARIABLE

Status of GaAs/Ge Solar Cells*

P. A. Iles, F. Ho and Y. C. M. Yeh
Applied Solar Energy Corporation
City of Industry, CA

This is a brief status report on GaAs/Ge solar cell work at ASEC.

Substrates

Germanium has good lattice and thermal match to GaAs, allowing epitaxial growth of high quality GaAs and AlGaAs layers. The higher mechanical strength of Ge provides thinner (lighter) cells of useable areas. The combination of higher power/unit area and power/unit mass available from thin GaAs/Ge cells is of interest to many satellite missions using lightweight arrays, and in some cases requiring high survivability.

Present Ge substrates cost less than GaAs substrates. Additional significant cost reductions are emerging from the greater ease of growing good quality, large area crystals from an element rather than a compound, and as a result of the increasing production volume of GaAs/Ge cells.

Cell Design

Figure 1 shows a cross-section of a generic GaAs/Ge cell. All of the high efficiency structures developed for GaAs/GaAs cells (thin base, BSF, thin emitter and windows) have been demonstrated successfully for GaAs/Ge cells.

The GaAs/Ge interface can be photovoltaically active, providing additional voltage. However, to facilitate immediate acceptance for production quantities of GaAs/Ge cells, ASEC has ensured that the GaAs/Ge interface is inactive. The inactive-Ge cell retains the performance of the best GaAs/GaAs cells, namely high efficiency, low temperature coefficients, and good radiation resistance. The inactive-Ge structure is not sensitive to enhanced solar simulator output in the near infrared. Under true AM0 illumination, the inactive-Ge cells do not show kinked curves when the current collected near the GaAs/Ge interface is not matched to the current collected at the GaAs PN junction.

An additional advantage of the inactive Ge structure is the ability to relax the specified properties of the Ge substrate, and this also leads to significant cost reduction.

*Some of the work reported was supported by a USAF MANTECH Contract, F33615-88-C-5415

Performance of GaAs/Ge Cells

The results quoted below are for GaAs/Ge cells grown and processed under typical production conditions. The GaAs layers were grown in high throughput MOCVD reactors (750-900cm^2 substrates per run).

AM0 Efficiency

The best efficiency measured for GaAs/Ge cells was 20.5% for a 2 x 2 cm^2 cell, 200μm thick (Figure 2). In production, 2 x 4 cm^2 cells, 200μm thick typically have 18.5% efficiency. 4 x 4 cm^2 cells have exceeded 19%. For this size, efficiencies up to 20.5% can be confidently projected from measurements on four 2 x 2 cm^2 cells formed on a single Ge substrate 4.5 x 4.5 cm^2 in size, because all four cells exceeded 20.3%.

In the MANTECH program, 4 x 4 cm^2 cells less than 90μm thick averaged 18.5%, and further increases are possible when the cell structure is optimized.

6 x 6 cm^2 cells, 90μm thick are being developed, in some cases with coplanar back contacts.

Bond Strength

Under bonding conditions which caused less than 2% change in cell output, both soldering and welding gave good adhesion (Tables 1, 2).

Cover-interconnected cells (CIC's), using both welded and soldered interconnects, have been supplied with typical output as shown in Table 3.

Radiation

GaAs/Ge cells show the same radiation performance as GaAs/GaAs cells with equivalent GaAs layer properties. Figure 3 shows output power versus 1 Mev electron fluence. The values shown are consistent with the GaAs PN junction depth (0.5μm). Further increase in radiation resistance will result from incorporation of shallower emitters.

Other Properties

Under temperature cycling, temperature - humidity exposure and photonexposure, GaAs/Ge cells have performed well (same as GaAs/GaAs cells). The performance for both substrates under high temperature exposure (long term or bursts) is determined by the contact metallization used. Even with the alloyed-Au metallization presently used, good stability to 400°C was obtained. To withstand higher

temperatures, the metallization stack is being changed, to withstand exposure to temperatures around 600°C.

GaAs/Ge cells have shown high stability under application of high reverse-bias currents ($< I_{sc}$) for long times at high temperature, indicating good performance under array shadowing conditions. This enhanced stability over GaAs/GaAs cells is attributed to the presence of shunting paths resulting from the heteroepitaxy. These shunting paths do not limit achievement of high voltages and fill factors when the cell is forward biassed, in normal operation.

The solar absorptivity of GaAs/Ge cells is higher than that of GaAs/GaAs cells, because some wavelengths beyond the GaAs bandedge are absorbed in the Ge. Alpha values as low as 0.82 have been achieved.

Summary

With experience at increasing production levels, GaAs/Ge cells are proving their effectiveness for some demanding missions.

The experience in producing inactive-Ge structures should benefit parallel work on forming monolithic cascade cells using AlGaAs or GaAs top cell layers grown on Ge or other bottom cell materials. The adjustments needed to ensure that the GaAs/Ge interface is inactive are more likely to preserve the properties of a separately optimized bottom cell.

Table 1. GaAs/Ge CELL - SOLDERING TEST - PULL STRENGTHS

	Front Side		Back Side	
Cell No.	Force (Gr)	Failure Mode	Force (Gr)	Failure Mode
3	950	Cell Broke	1325	Divot
	1300	Cell Broke	875	Cell Broke
8	525	Cell Broke	1700	Divot
	1050	Cell Broke	750	Cell Broke
12	1350	Cell Broke	1150	Cell Broke
	1000	Cell Broke	1075	Cell Broke
15	775	Cell Broke	500	Cell Broke
	850	Cell Broke	525	Cell Broke
20	650	Divot	1075	Cell Broke
	650	Cell Broke	1325	Cell Broke
29	700	Cell Broke	975	Cell Broke
	1700	Cell Broke		Could Not Test
31	775	Divot	625	Cell Broke
	1450	Cell Broke	1400	Cell Broke
37	950	Cell Broke	975	Divot
	1300	Cell Broke	1450	Cell Broke
48	500	Cell Broke	1850	Cell Broke
	500	Divot		Could Not Test
58	675	Solder Separated	1425	Cell Broke
	725	Cell Broke		Could Not Test

Table 2. GaAs/Ge CELL - WELDING TEST - PULL STRENGTHS

	Front Side		Back Side	
Cell No.	Force (Gr)	Failure Mode	Force (Gr)	Failure Mode
21	300	Divot	425	Divot
	225	Divot	775	Divot
25	300	Divot	475	Cell Broke
	375	Divot	600	Cell Broke
33	150	Divot	800	Divot
	275	Divot	700	Divot
34	200	Divot	875	Divot
	540	Divot	800	Divot
51	250	Divot	600	Divot
	250	Cell Broke	900	Divot
53	575	Divot	680	Divot
	300	Divot	900	Divot
54	275	Divot	625	Divot
	275	Divot	900	Cell Broke
55	150	Divot	400	Cell Broke
	150	Divot	980	Divot
65	375	Cell Broke	450	Divot
	450	Cell Broke	250	Divot
67	150	Divot	725	Cell Broke
	275	Divot	900	Tab Broke

Table 3. **Photovoltaic Characterisitics (AMO) for CIC's (2x2cm^2 cells)**

Cell #	Voc mV	Isc mA	CFF %	EFF %
1	1005	128.0	80.5	19.1
2	1000	128.2	79.2	18.8
3	998	128.1	79.6	18.8
4	1000	128.0	79.6	18.8
5	1001	128.8	80.2	19.1
6	1003	127.3	79.8	18.8
7	994	127.1	74.0	17.3
8	998	128.2	78.5	18.6
9	1002	128.4	79.5	18.9
10	994	128.4	77.2	18.2
11	1005	127.5	78.1	18.5
12	1003	128.1	79.7	18.9
13	997	127.0	80.5	18.9

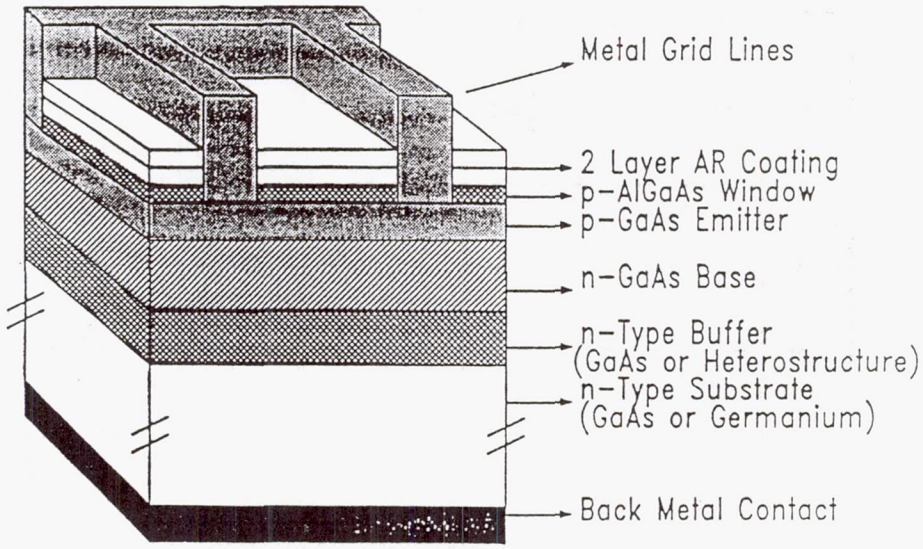

Figure 1. Structure of GaAs/GaAs or GaAs/Ge Solar Cell

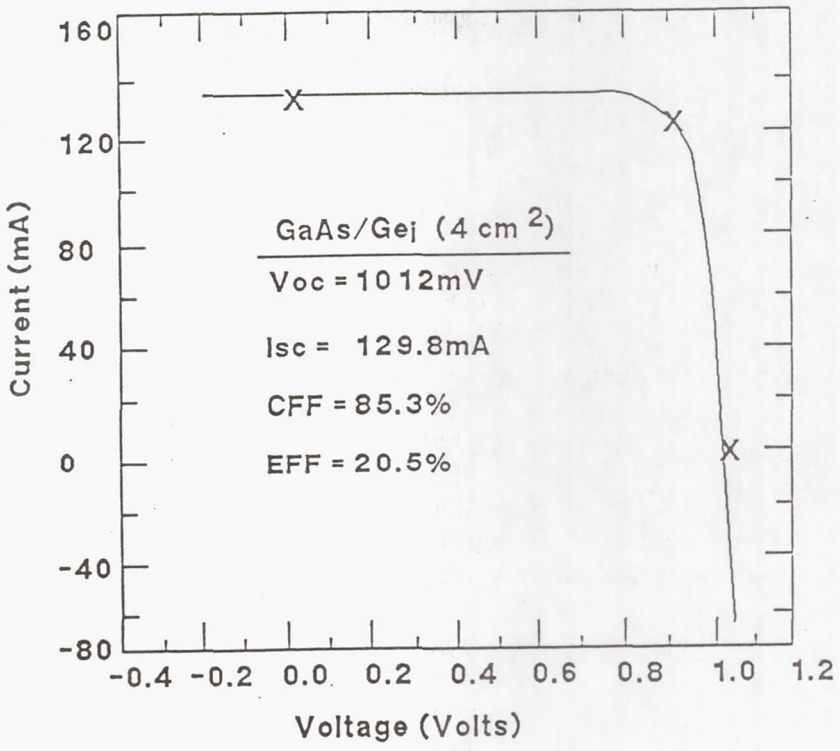

Figure 2. Photovoltaic characteristics (AMO) for GaAs/Ge (inactive) solar cell

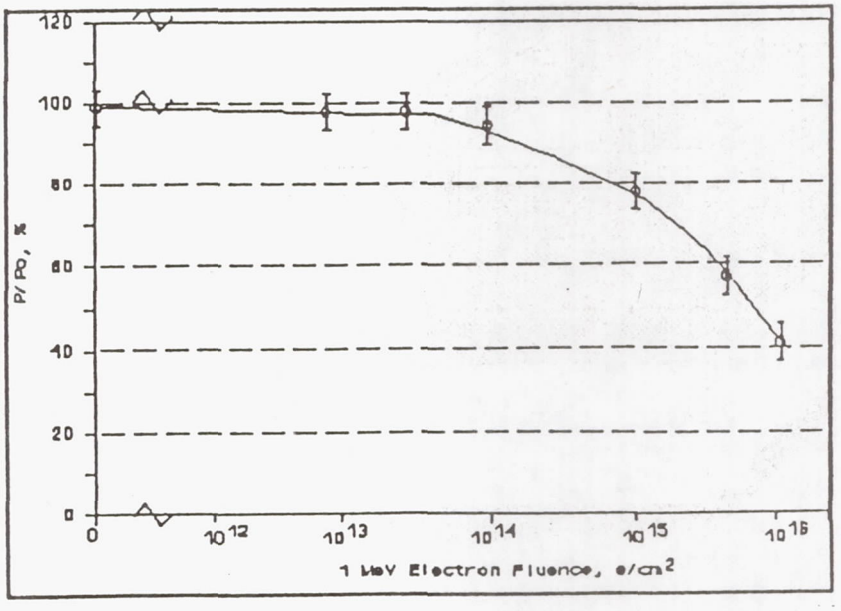

Figure 3. Relative maximum power versus 1 MeV electron fluence

Graded-Bandgap AlGaAs Solar Cells for AlGaAs/Ge Cascade Cells*

M.L. Timmons, R. Venkatasubramanian, T.S. Colpitts, J.S. Hills and J.A. Hutchby
Research Triangle Institute
Research Triangle Park, NC

P.A. Iles and C.L. Chu
Applied Solar Energy Corporation
City of Industry, CA

P/N graded-bandgap $Al_xGa_{(1-x)}As$ solar cells have been fabricated and show AM0 conversion efficiencies in excess of 15 percent without AR coatings. The emitters of these cells are graded between $0.08 \leq x \leq 0.20$ during growth of 0.25- to 0.30-μm-thick layers. The keys to achieving this performance have been careful selection of organometallic sources and scrubbing oxygen and water vapor from the AsH_3 source. Source selection and growth has been optimized using time-resolved photoluminescence. Preliminary radiation-resistance measurements show AlGaAs cells degraded less than GaAs cells at high 1-MeV electron fluences, and AlGaAs cells grown on GaAs and Ge substrates degrade comparably.

Introduction

Bandgap grading in the emitters of AlGaAs/GaAs solar cells is an attractive method for improving minority-carrier collection. The bandgap gradient creates an electric field that, according to the modeling of Hutchby and Fudurich [ref. 1], allows 80- and 97-percent reductions in bulk and surface hole recombinations, respectively. Reducing these losses substantially increases the "blue" response of cells. Compositional grading of emitters is also thought to increase radiation resistance, an important factor for cells intended for use in space. Experimentally, though, the predicted benefits of bandgap grading have not been fully realized. For example, Wagner and Shealy reported almost identical performance for graded-bandgap and a heteroface cells with neither outperforming homojunctions [ref. 2]. Reports on the radiation resistance of graded-bandgap AlGaAs cells are very sparse, if they exist at all.

In this paper, we present results for the growth, fabrication, and characterization of graded-emitter AlGaAs cells grown on $Al_{0.08}Ga_{0.92}As$ base layers. This structure is a candidate component (along with $Al_{0.08}Ga_{0.92}As$ homojunctions or $Al_xGa_{(1-x)}As$-$Al_{0.08}Ga_{0.92}As$ heteroface cells) of an AlGaAs/Ge cascade cell that offers close current matching between the top and bottom cells under AM0 conditions. Radiation-resistance measurements have been made on nonoptimized AlGaAs graded-bandgap cells, and these data are also included.

* This work funded by the U.S. Air Force under Contract No. F33615-87-C-2804. Contents of this paper have been cleared for release at this meeting.

Material Growth and Cell Fabrication

The AlGaAs growth was carried out at atmospheric pressure by organometallic vapor phase epitaxy (OMVPE). Trimethylgallium (TMG), trimethylaluminum (TMA), and arsine (AsH_3) in a 10-percent mixture diluted with H_2, were the Ga, Al, and As sources, respectively. Zinc (Zn) from diethylzinc (DEZ) and selenium (Se) from hydrogen selenide (H_2Se) were the p- and n-type dopants, respectively. During the growths the V/III ratio was kept between 30 and 40, and growth rates of about 0.1 μm/min were used. When graded layers were required, the H_2 flows through both the TMG and TMA bubblers were controlled by a computer to keep the growth rates approximately constant, yielding reproducible linear grading.

Material quality is the cornerstone of any good solar cell, and $Al_xGa_{(1-x)}As$ is particularly difficult to grow even at compositions as low as x=0.10. In earlier work, we showed that minority-carrier lifetimes, determined from time-resolved photoluminescence (TPL), can decrease relative to GaAs by factors of 3 and 10 in $Al_{0.1}Ga_{0.9}As$ and $Al_{0.2}Ga_{0.8}As$, respectively, even for moderately high growth temperatures (750 to 770°C) [ref. 3]. Therefore, optimizing the AlGaAs growth has been a key factor in achieving good cell results. Optimization has relied upon TPL lifetime measurements, performed under the direction of Dr. R.K. Ahrenkiel of the Solar Energy Research Institute, and cell performance. Using these techniques, we have been able to screen TMA and TMG sources and select ones that yield long minority-carrier lifetimes. The current TMA and TMG sources were provided by American Cyanamid and Eagle-Picher, respectively.

The quality of the AsH_3 is the second factor that needed scrutiny. During this work, an oxygen and water-vapor scavenger, marketed by Millipore Corp., was evaluated for the AsH_3. This unit resulted immediately in significant increases in the PL intensity from $Al_{0.08}Ga_{0.92}As$ double heterojunctions when the growth temperature was 780°C. At lower temperatures, the increases are even greater. The minority-carrier lifetimes in $Al_{0.08}Ga_{0.92}As$ grown with this oxygen and water-vapor scrubber have been as much as 50 percent greater (~67 versus ~42 ns) for growth at 780°C compared to growth without scrubber use.

At the device level, these factors–good quality TMA and TMG sources and AsH_3 scrubbing–have permitted us to grow $Al_{0.08}Ga_{0.92}As$ homojunction cells recently at 725 °C that perform almost as well as those grown previously at 780°C. This will be discussed in more detail below.

All the cells fabricated during this program have used standard processing. A typical device structure is shown in Figure 1. Hall measurements and C-V analyses, using individually grown layers on semi-insulating GaAs substrates, have yield the following data:

1. the base carrier concentrations are about 3 X 10^{17} cm^{-3},

2. the emitter carrier concentrations are 1-3 X 10^{18} cm^{-3}, and

3. carrier concentrations in the GaAs caps are about 8-10 X 10^{18} cm^{-3}.

Carrier concentrations in $Al_{0.88}Ga_{0.12}As$ window layers are low ($\sim 10^{17}$ cm^{-3}) when grown at 780°C with Zn doping, but by lowering growth temperatures for the windows to 700°C, values above 10^{18} cm^{-3} have been achieved. Reducing the growth temperature for the window and cap layers improved cell fill factors.

The interface recombination velocity S between the $Al_{0.88}Ga_{0.12}As$ window layer and the AlGaAs emitter is high. Using TPL to examine $Al_{0.88}Ga_{0.12}As/Al_{0.08}Ga_{0.92}As$, we have estimated values for S as large as 3×10^4 cm/s in spite of high growth temperatures ($\sim$780°C) [ref. 4]. Values of S of this magnitude have recently been reported by Ahrenkiel et al. for AlGaAs/GaAs interfaces grown at 700°C [ref. 5]. Our data indicate higher S values for AlGaAs/AlGaAs interfaces that may require additional passivation. This will be addressed in future work.

Cell Characterization

The graded emitter has been characterized and optimized in grown structures based on cell performance. At the beginning of the program, the intent was to compositionally grade the $Al_xGa_{(1-x)}As$ in the emitter from x=0.08 to x=0.30 while growing a 0.5-μm-thick layer. Emitters with values of x greater than x$\simeq$0.3 have also been examined. The spectral responses from several cells are shown in Figure 2. The compositions at the end of the emitter grading are x=0.3, 0.45, and 0.6 for these cells, and emitter thicknesses are about 0.35 μm, except for one (Sample No. 447) that has a 0.5-μm-thick layer. The short-wavelength response decreases as the Al concentration increases even for the thin, 0.35-μm emitters. This shows that the reduction in minority-carrier lifetime that accompanies the increasing Al content outweighs the field-induced advantages that come from grading, and many carriers generated in the surface region are not being collected. Even with limiting the endpoint of the graded composition to $Al_{0.3}Ga_{0.7}As$, graded-emitter cells show only marginal improvement relative to homojunction $Al_{0.08}Ga_{0.92}As$ cells with comparable emitter thicknesses. This is illustrated in Figure 3 where the dark and illuminated I-V characteristics of a homojunction cell and a cell graded to x=0.3 are displayed. The graded-cell efficiency (11.9 percent) was the best during the early phase of program but has only a 1-percent efficiency advantage over a shallow homojunction that is typical of the homojunction cells (best homojunction cell grown during this period has a 13.6-percent conversion efficiency with no AR coating).

Since the homojunctions continued to outperform the graded-emitter junctions with x=0.3 at the end of the grading, reduced minority-carrier lifetimes, coupled

with possible large interface recombination velocities, appeared to negate the advantages that were hoped for the graded emitters. Grading an $Al_xGa_{(1-x)}As$ layer from $0.08 \leq x \leq 0.3$ over 0.5 μm produces an electric field of about 5300 V/cm, and a layer graded from $0.08 \leq x \leq 0.18$ over 0.30 μm contains a field of about 4700 V/cm. This latter layer, though, will have a minority-carrier lifetime that is between 3 and 10 times longer than in the former while sacrificing only about 25 percent of the desired field. Therefore, the emitter-grading limits and thicknesses were reduced to $0.08 \leq x \leq 0.18$ and 0.25 to 0.3 μm, respectively. These values have become the guidelines for current cell growth.

As the quality of the AlGaAs has improved, cell efficiencies have also increased. The scrubbing described above for the AsH_3 resulted in step-like increases in cell efficiencies. The I-V characteristic of one of the first graded-bandgap cells (Sample No. 492) grown using the scrubber-and the reduced grading composition-is shown in Figure 4; this cell has a power conversion efficiency of 15.3 percent without an AR coating. The $Al_xGa_{(1-x)}As$ emitter composition varied from $0.08 \leq x \leq 0.18$ over 0.25 μm of emitter material. In Figure 5, the spectral response of Sample No. 492 is compared to a cell (Sample No. 482) with a $Al_{0.08}Ga_{0.92}As$ homojunction (0.2-μm-thick emitter) that was grown without use of the AsH_3 scrubber, and a cell (Sample No.494) graded from $0.08 \leq x \leq 0.18$ during growth of a 0.6-μm-thick emitter. The short-wavelength response of Sample No. 492 is significantly improved compared to either of the other two samples. The response difference between 492 and 494 is somewhat surprising and shows that many of the carriers generated at the surface in sample 494 are still not being collected. With a good AR coating, cell 492 projects a efficiency between 18.5 and 19.5 percent, which is very close to our maximum modeled value for this composition .

Graded-bandgap cells have also been compared to two kinds of heteroface cells. Sample No. 563, whose I-V characteristic is shown in Figure 6, contains a 0.4-μm-thick, $Al_{0.18}Ga_{0.82}As$ emitter. For this sample V_{oc} equals 1.081 V, J_{sc} equals 28.03 mA/cm^2 (active-area), and the fill factor is 0.82 yielding an active-area efficiency of 17.9% (cell has a single-layer Si_3N_4 AR coating). Comparison has also been made with a cell (Sample No. 564) containing an emitter consisting of three different $Al_xGa_{(1-x)}As$ layers, 0.10 μm of$Al_{0.08}Ga_{0.92}As$,As, 0.10 μm of $Al_{0.13}Ga_{0.87}As$, and 0.1 μm of $Al_{0.18}Ga_{0.82}As$. The I-V characteristic for this cell is also shown in Figure 6, and J_{sc}, V_{oc}, and fill factor are 24.2 mA/cm^2, 1.056 V, and 0.78, respectively, for an active-area efficiency of 14.7% (no AR coating). The efficiency of this cell projects to about 18.5 percent with a coating and, based on the results of our study of AlGaAs/AlGaAs interfaces [ref. 4], may be benefiting from a reduction in S.

The cells described above were grown at 780 to 800°C. One of the most encouraging recent developments is the growth of AlGaAs cells at 725°C. The I-V characteristic of two of these cells (Sample Nos. 566 and 567) are shown in Figure 7 and are comparable to cells grown at 780°C; sample 566 is an $Al_{0.08}Ga_{0.92}As$ homojunction, and

sample 567 contains a graded emitter ($0.08 \leq x \leq 0.18$). Both emitters are about 0.25 μm thick, and cell performances of the two devices are almost identical–$J_{sc} \simeq 26$ mA/cm^2, $V_{oc} \simeq 1.02$ V and fill factor $\simeq 0.78$–with active-area efficiencies of about 15.2 percent (no AR coating). The spectral responses from the two cells are also very comparable to each other and to cells grown at higher temperatures.

Considering all of the cell data, it appears that, as long as the AlGaAs quality is very high and limited to $x \leq 0.2$ and that the emitter is thin (~ 0.3), the details of emitter growth are not as critical as we originally suspected. The similar performances of the different structures described above support this conclusion. Therefore, it will likely be other factors, radiation resistance, for example, that will determine the optimum top-cell structure in the AlGaAs/Ge cascade cell.

Radiation Resistance

AlGaAs cells with different types of emitters were exposed to l-MeV electrons at fluences of 5×10^{14}, 1×10^{15}, and 5×10^{15} cm^{-2} to begin determining the radiation-resistance properties of the cells. Cells with the following six types of emitters have been irradiated at the JPL facility:

1. homojunction $Al_{0.08}Ga_{0.92}As$ cells with ~ 0.5-μm-thick emitters,

2. cells with 0.5-μm-thick emitters graded from $0.08 \leq x \leq 0.30$ (emitters have a 0.1-μm thick $Al_{0.08}Ga_{0.92}As$ spacer before the grading was initiated),

3. heteroface cells with $Al_{0.08}Ga_{0.92}As$ bases and $Al_{0.3}Ga_{0.7}As$ emitters (0.5 μm thick),

4. cells with thick $Al_{0.08}Ga_{0.92}As$ emitters (3-4 μm),

5. GaAs cells, and

6. $Al_{0.08}Ga_{0.92}As$ homojunction cells grown on Ge substrates.

Beginning efficiencies for the cells of the first group ($Al_{0.08}Ga_{0.92}As$ homojunctions) ranged from 14 to 16 percent, the graded-emitter-cell efficiencies of the second group ranged from about 7 to 10 percent, GaAs efficiencies (group 5) were about 17 to 18 percent, and the AlGaAs-on-Ge-cell efficiencies (group 6) were about 14 percent. The remaining two types had lower efficiencies of about 3 and 7 percent for the thick-emitter and heteroface cells, groups 4 and 3, respectively.

In Table 1, data for the fraction of V_{oc}, I_{sc} (2 cm $\times$ 2 cm cells), and the V_{oc}–I_{sc} product remaining after exposure of the six cell types to the three fluence levels are presented. Disregarding the data for the thick-emitter cells, which are especially sensitive to diffusion-length reductions, the fraction of the V_{oc}–I_{sc} product remaining for the lower two fluences, 5×10^{14} and 1×10^{15}cm^{-2}, are about the same for the AlGaAs

and GaAs cells, but at the $5 \times 10^{15} cm^{-2}$ level, the AlGaAs cells show less degradation than the GaAs. The efficiency of the GaAs cells, however, was initially higher, and it is commonly accepted that lower efficiency cells usually show lower damage. Therefore, the differences may not be as significant as the data would suggest. Also encouraging is the performance of the AlGaAs-on-Ge cells; these devices are no worse than AlGaAs-on-GaAs junctions regarding performance degradation. Finally, at the highest fluence, the data suggest that the graded-emitter structure, although not optimized, outperforms homojunction cells, but initial efficiency differences keep this observation from being more definitive at the present time.

In Table 2, quantum efficiencies (QE) at two wavelengths, 0.5 and 0.8 μm, are presented before and after irradiation at the three fluences. Remaining QE fractions are also indicated. Considering the 5×10^{15} cm^{-2} fluence and disregarding the data for thick-emitter cells (group 4), the long-wavelength QE degradation, as expected, is greater than the shortwavelength degradation. The AlGaAs-on-Ge cells perform comparably to AlGaAs-on-GaAs cells (groups 1 and 6) at the short wavelength and is slightly better at 0.8 μm, and both have higher QEs than the GaAs cell. The graded-emitter cells (and the heteroface cell) show less short-wavelength degradation and more long-wavelength degradation than either the AlGaAs or GaAs homojunctions.

These data, although not considered definitive, clearly suggest that grading may enhance the radiation resistance of the emitters. These experiments will be repeated using optimum graded-emitter cells that have higher initial efficiencies and will be coupled with deep-level-transient-spectroscopy measurements and TPL determinations of minority-carrier lifetimes.

Conclusions

In this paper, we have described the growth and characterization of high-quality AlGaAs solar cells that are intended for use as the top cell in the AlGaAs/Ge monolithic cascade cell. Several different emitter structures – homojunction, graded, and heteroface – have been grown. Performances of the best of these cells are approaching practical theoretical limits. Improved material quality is thought to be the key to increased efficiencies. Material growth has been optimized with TPL measurements of minority-carrier lifetime. Graded-bandgap cells ($0.08 \leq x \leq 0.20$) using 0.25- to 0.3-μm-thick emitters have yielded power conversion efficiencies greater than 15 percent without AR coatings.

Preliminary radiation-resistance measurement with 1-MeV electron fluences as great as 5×10^{15} cm^{-2} have shown AlGaAs cells on GaAs and Ge substrates may degrade less than GaAs cells, and graded emitters (or heteroface cells) may be advantageous for preserving short-wavelength QE response, which is, in fact, a demonstration of one major program goals.

References

[1.] J. A. Hutchby and R. L. Fudurich, J. Appl. Phys. **47**, 3140 (1976).

[2.] D. K. Wagner and J. R. Shealy, Appl. Phys. Lett. **45**, 162, (1984).

[3.] M. L. Timmons, J. A. Hutchby, R. K. Ahrenkiel and D. J. Dunlavy, *Proceedings of the 15th International Symposium on GaAs and Related Compounds*, 289, Inst. Phys. Conf. Ser. No. 96, Inst. Phys., Bristol (1989).

[4.] M. L. Timmons, T. S. Colpitts, R. Venkatasubramanian, B. M. Keyes, D. J. Dunlavy, and R. K. Ahrenkiel, "Measurement of AlGaAs/AlGaAs Interface Recombination Velocities", (submitted for publication).

[5.] R. K. Ahrenkiel, D. J. Dunlavy, B. M. Keyes, S. M. Vernon, T. M. Dixon, S. P. Tobin, K. L. Miller and R. E. Hayes, Appl. Phys. Lett. **55** 1088 (1989).

Table 1. Fraction Of Initial V_{oc}, I_{sc}, And V_{oc}–I_{sc} Product Remaining After Irradiation By 1-MeV Electrons.

Cell Group	$5x10^{14}$ cm^{-2} F (V_{oc})	F (I_{sc})	F ($V_{oc}xI_{sc}$)	$1x10^{15}$ cm^{-2} F (V_{oc})	F (I_{sc})	F ($V_{oc}xI_{sc}$)	$5x10^{15}$ cm^{-2} F (V_{oc})	F (I_{sc})	F ($V_{oc}xI_{sc}$)
1. Homojunction (8% E,B on GaAs)	0.93-0.96	0.91-0.92	0.85-0.89	0.92-0.95	0.88-0.89	0.81-0.84	0.87-0.88	0.63-0.69	0.57-0.61
2. Graded Emitter (8-30% E,8% B)	0.95-0.97	0.88-0.91	0.85-0.88	0.91-0.95	0.85-0.88	0.80-0.82	0.87-0.94	0.68-0.76	0.64-0.70
3. Heteroface (30% E, 8% B)	0.94-0.97	0.90-0.91	0.86-0.88	0.88, 0.93	0.85-0.87	0.77-0.79	0.85-0.87	0.74-0.75	0.65-0.66
4. Homojunction (8% Thick-E,B)	0.94-0.95	0.62-0.65	0.59-0.61	0.91-0.93	0.42-0.44	0.39-0.40	0.63	0.09	0.06
5. GaAs	---	---	---	0.91	0.85	0.77	0.83	0.54	0.44
6. Homojunction (8% E,B on Ge)	0.95	0.92	0.88	0.94	0.90	0.84	0.89	0.69	0.61

Table 2. Quantum Efficiencies Of AlGaAs Solar Cells At Wavelengths Of 0.5 And 0.8 μm After Irradiation.

Cell Group	Before Irradiation QE0.5	QE0.8	1-MeV Electron Fluence 5×10^{14} cm^{-2} QE0.5	QE0.8	10^{15} cm^{-2} QE0.5	QE0.8	5×10^{15} cm^{-2} QE0.5	QE0.8
1. Homojunction (8% E,B on GaAs)	0.88	0.61	0.81 (0.92)	0.47 (0.77)	0.835 (0.95)	0.445 (0.73)	0.635 (0.72)	0.32 (0.52)
2. Graded Emitter (8-30% E,8% B)	0.80	0.70	0.745 (0.93)	0.355 (0.51)	0.76 (0.95)	0.32 (0.46)	0.73 (0.91)	0.19 (0.27)
3. Heteroface (30% E,8% B)	0.70	0.445	0.69 (0.98)	0.30 (0.62)	0.68 (0.97)	0.21 (0.44)	0.62 (0.88)	0.15 (0.31)
4. Homojunction (8% thick-E,B)	0.165	0.30	0.09 (0.54)	0.19 (0.64)	0.75 (0.46)	0.185 (0.62)	0.01 (0.06)	0.055 (0.18)
5. GaAs	0.77	0.895	--	--	0.63 (0.82)	0.66 (0.74)	0.43 (0.56)	0.445 (0.50)
6. Homojunction (8% E,B on Ge)	0.895	0.625	--	--	--	--	0.65 (0.72)	0.375 (0.60)

Note: Values in parentheses are fractions of QE remaining after irradiation.

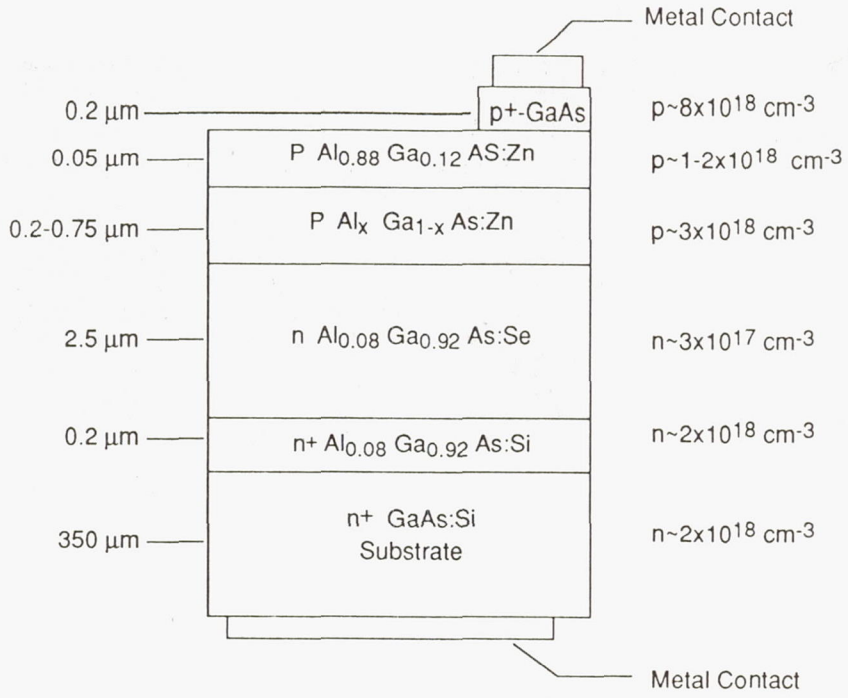

Figure 1. Schematic diagram of AlGaAs cells being developed for this program. Emitter compositions and thicknesses vary to optimize the structure.

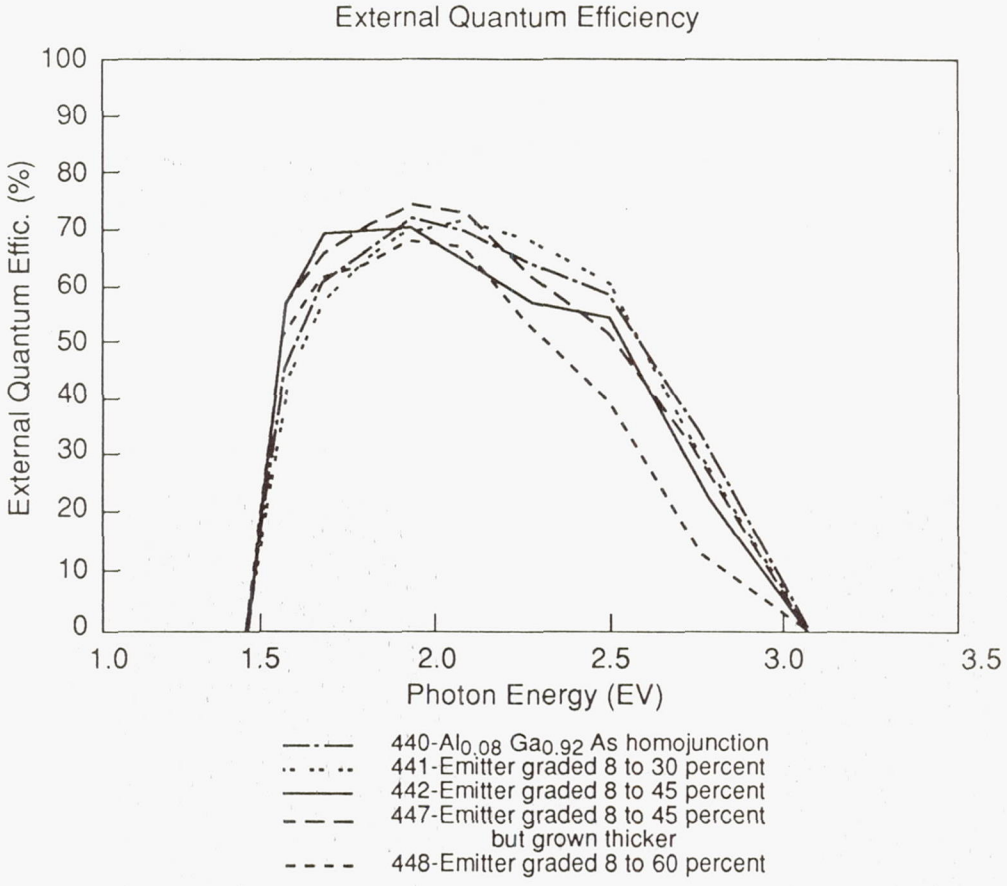

Figure 2. Spectral responses of five AlGaAs solar cells.

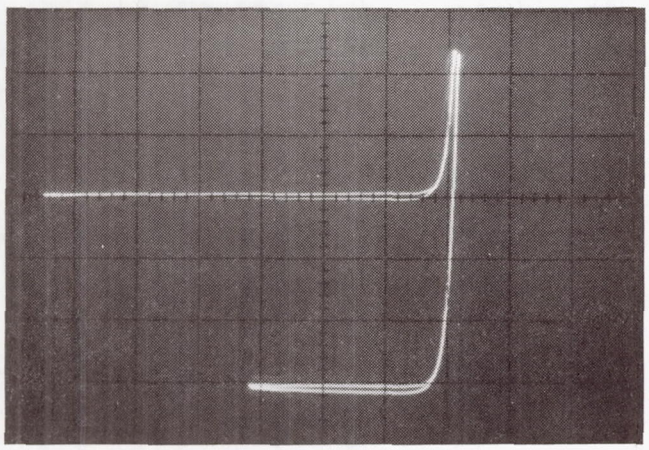

a) Sample 440 — $Al_{0.08}Ga_{0.92}As$
emitter: $V_{oc} \sim 1.030$ V
$J_{sc} \sim 17.0$ mA/cm^2
FF ~ 0.83
$\eta \sim 10.7\%$

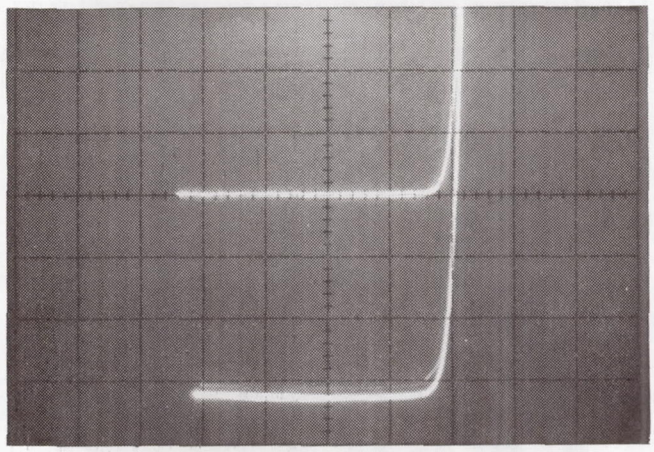

b) Sample 441 — Graded Bandgap
emitter: $V_{oc} \sim 1.055$ V
$J_{sc} \sim 18.6$ mA/cm^2
FF ~ 0.82
$\eta \sim 11.9\%$

Figure 3. Dark and illuminated I-V characteristics of good $Al_{0.08}Ga_{0.92}As$-homojunction and best graded-bandgap cell fabricated during early part of program. Horizontal and vertical scales are 0.5 V and 1 mA, respectively. Efficiencies calculated from active areas of devices (no AR coatings).

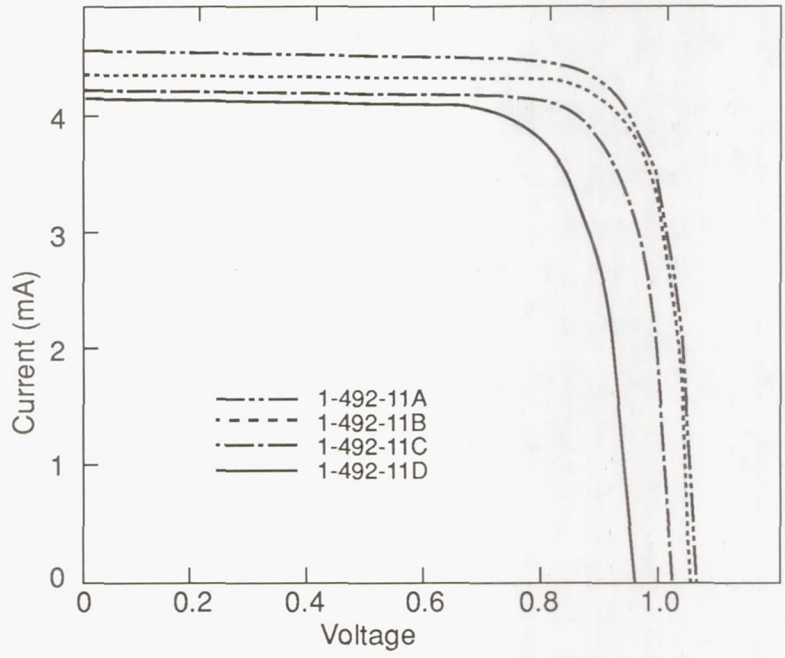

Figure 4. Illuminated I-V characteristics of graded-bandgap AlGaAs solar cells (4 cells fabricated on wafer 1-492). Emitter graded from $Al_{0.08}Ga_{0.92}As$ to $Al_{0.2}Ga_{0.8}As$ over 0.27 μm. Best cell: V_{OC} = 1.061 V, J_{SC} = 24.4 mA/cm^2, FF = 0.81, n = 15.3% (no AR coating).

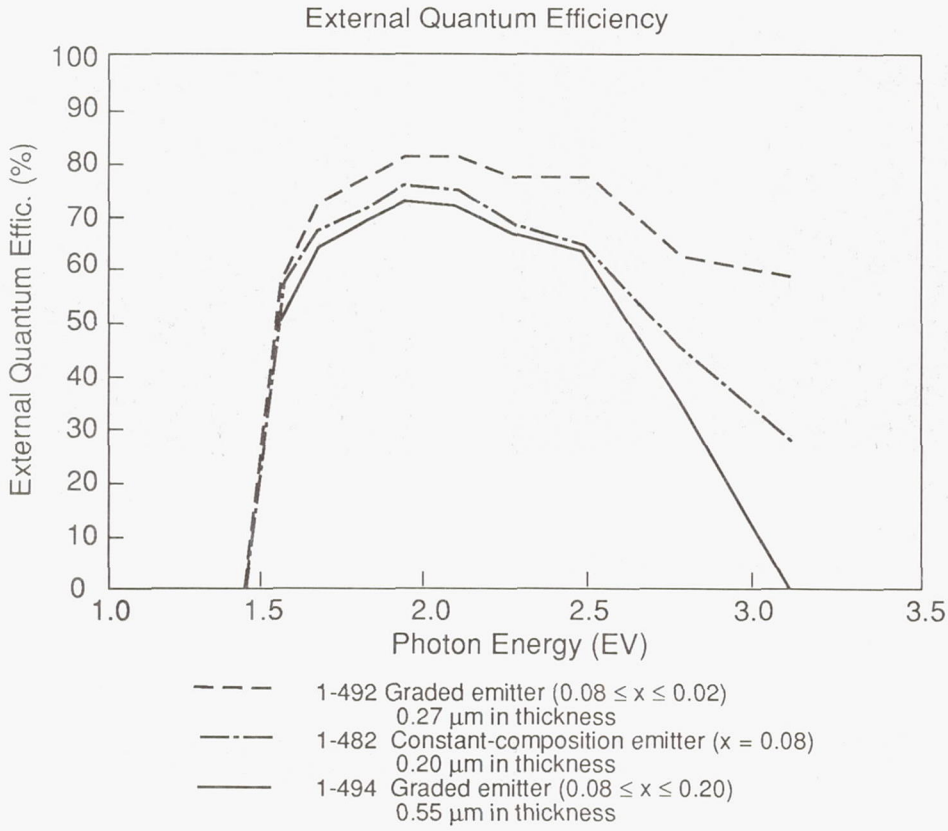

Figure 5. Spectral responses from several Al_x-$Ga_{(1-x)}As$ solar cells (no AR coatings).

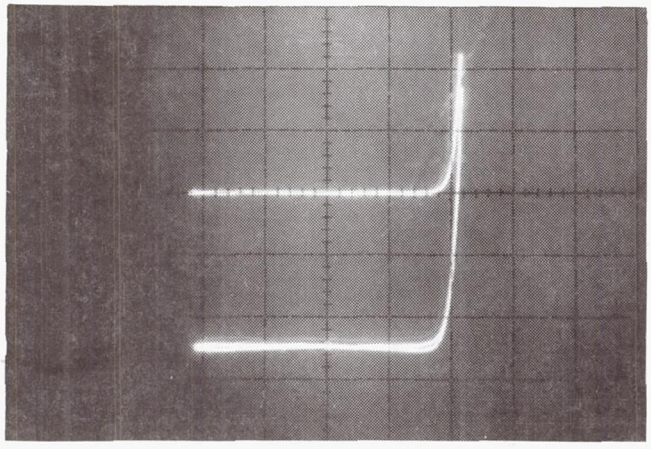

a) Sample 563 — Heteroface cell with 0.4-μm thick $Al_{0.18}Ga_{0.82}As$ emitter:

V_{oc} ~ 1.081 V (0.5 V/div)
J_{sc} ~ 28.03 mA/cm^2 (2 mA/div)
FF ~ 0.80
η ~ 17.92%

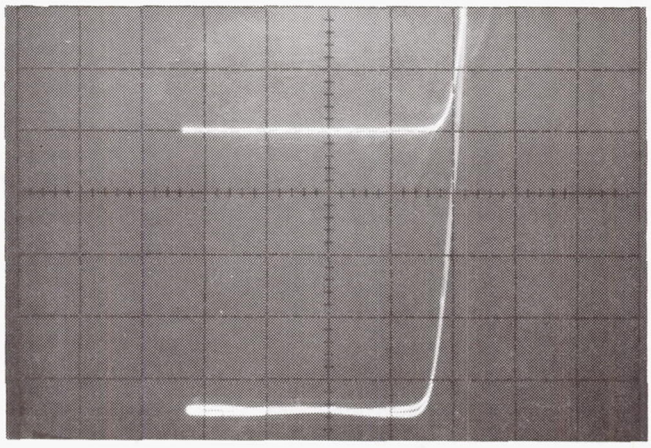

b) Sample 564 — AlGaAs cell with emitter containing 3 Al-concentration step changes:

V_{oc} ~ 1.056 V (0.5 V/div)
J_{sc} ~ 24.2 mA/cm^2 (1 mA/div)
FF ~ 0.78
η ~ 14.73%

Figure 6. Dark and illuminated characteristics of AlGaAs cells with step changes in emitter Al concentration: a) single step to $Al_{0.18}GA_{0.82}As$; b) Al concentration changes from $Al_{0.08}Ga_{0.92}As$ to $Al_{0.13}Ga_{0.87}As$ to $Al_{0.18}Ga_{0.82}As$. Sample 563 has a single layer of Si_3N_4 for an AR coating; sample 564 is uncoated.

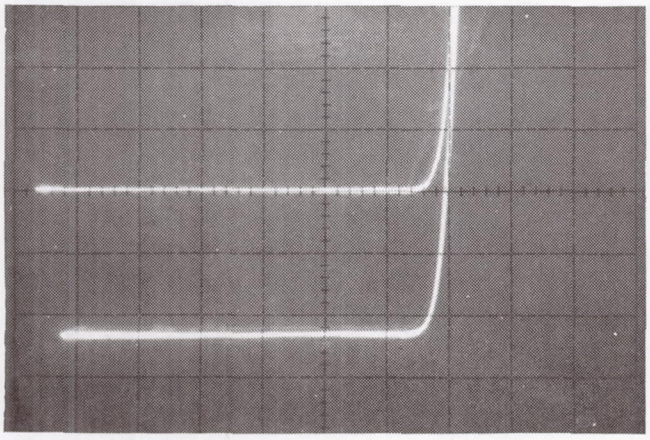

a) Sample 566 — $Al_{0.08}Ga_{0.92}As$
emitter: V_{oc} ~ 1.02 V (0.5 V/div)
J_{sc} ~ 25.8 mA/cm^2 (2 mA/div)
FF ~ 0.78
η ~ 15.2 %

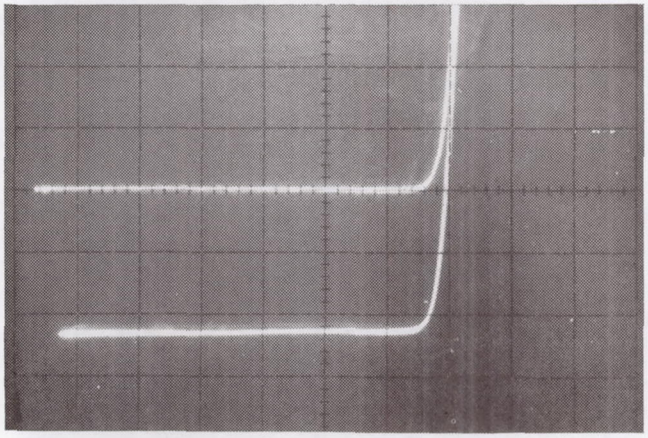

b) Sample 567 — Graded Bandgap AlGaAs
emitter: V_{oc} ~ 1.018 V
(0.5 V/div)
J_{sc} ~ 25.7 mA/cm^2 (2 mA/div)
FF ~ 0.78
η ~ 15.1%

Figure 7. Dark and illuminated I-V characteristic of graded-bandgap and $Al_{0.08}Ga_{0.92}As$-homojunction solar cells grown at 725 °C.

AlGaAs Top Solar Cell for Mechanical Attachment in a Multi-Junction Tandem Concentrator Solar Cell Stack*

L.C. DiNetta, M.H. Hannon, and J.B. McNeely
AstroPower, Inc.
Newark, DE
A.M. Barnett
University of Delaware
Newark, DE

Introduction

The theoretical limits for the AlGaAs/Si tandem stack were determined using a solar cell model by Nell [ref. 1] based on tabulated standard spectra, the fit of experimentally achieved open-circuit voltages, and the assumption of unit quantum efficiency. More recent work [ref. 2] indicates that Nell's model underestimates open-circuit voltages. Incorporating this change, a theoretical AM0 efficiency of 42.9% at 100 suns is predicted for the tandem stack. The 100× values were calculated by assuming a linear increase in short-circuit current values and scaling the remainder of the cell operating parameters in accord with the diode equation. The result of device modeling shown in Table I assumes a subbandgap transparency of 100%.

Shown in Figure 1 are iso-efficiency curves for various bandgap combinations. The curves indicate that there are a wide range of acceptable bandgap combinations within a given performance window.

A value of 95% transparency to sub-bandgap photons was used in the prediction of the "best case" performance. For direct-bandgap materials, predictions were determined by reducing the open-circuit voltage, short-circuit current, and fill factor to 96%, 91%, and 96%, respectively, of their theoretical limits. Indirect bandgap material reductions are correspondingly 91%, 96%, and 96%, respectively [ref. 3]. This permits stack performance predictions for the various combinations of top and bottom solar cell bandgaps. Performance of the "best case" AlGaAs top solar cells with 1.93 and 1.80 eV bandgaps on silicon bottom solar cells are listed in Table II. The "best case" performance of the individual solar cells assumes no reflective losses or grid obscuration. However, the current generated by the bottom solar cell is limited by the bandgap of the top solar cell and reduced further by the transparency of the top solar cell to sub-bandgap photons.

*The work was supported in part by NASA Lewis Research Center under contract NAS3-25570.

Four-terminal MSMJ tandem stack assemblies appear to be the best short term method to a 30% commercially available solar cell as demonstrated by recent results at AstroPower and elsewhere. Modeling of a four terminal stack of AlGaAs on InGaAsP indicates that it will be possible to achieve efficiencies of greater than 35%. InGaAsP also has the added advantage of greater radiation hardness when compared to silicon. Predictions of this stack appear in Table III.

The next logical step in the development of high efficiency solar converter systems is the goal of 40% overall conversion efficiency. Table IV demonstrates the results of our modeling utilizing materials which are being developed at this facility. The predicted efficiencies include losses and are "best case" examples, not theoretical maximum values.

Results

The top solar cell is fabricated on a thick AlGaAs substrate that is i) highly transparent, ii) sufficiently rugged so as not to require additional support during subsequent processing, and iii) utilizes existing process technology. Liquid phase epitaxial growth techniques are employed for materials fabrication. When compared to MBE and MOCVD, the LPE technique has demonstrated higher quality AlGaAs material. Li [ref. 4] has reported that AlGaAs layers prepared by LPE have lower defect density than those prepared by other techniques. Minority carrier lifetimes of AlGaAs for LPE grown material are larger than for MOCVD grown material as reported by Ahrenkiel and Dunlavy [ref. 5]. Both Saletes [ref. 6] and Mayet [ref. 7] have reported material problems with compositions near the 1.93 eV direct-indirect energy bandgap cross-over region. Lewis and coworkers [ref. 8], on the other hand, have reported excellent devices at this bandgap. Regardless, our modeling indicates that the tandem stack efficiency is virtually unchanged with a top solar cell bandgap between 1.93 and 1.80 eV.

Utilizing an AlGaAs substrate that has a bandgap equal to or greater than the active device region of the solar cell provides the required high transparency. The reflection plus transmission curves of the substrate layer with a wider bandgap than the active layer and the active layer grown on the substrate layer appear in Figure 2.

The base and emitter can be tuned to any desirable energy bandgap between 1.43 eV and 1.93 eV, the direct-indirect crossover point for the Al-Ga-As mixed crystal system. Typically, a 10-micron base and a 0.1 micron emitter are used with a graded bandgap window layer to reduce surface recombination. The graded window layer also improves the current collection since i) a field exists to attract the minority carriers to the junction, and ii) a gradual change in index of refraction minimizes reflection at the AlGaAs window/emitter interface [ref. 7].

The devices fabricated are p/n structures. The solar cell is a 4 mm diameter active area design based on a 5 mm × 5 mm die. Ohmic contacts are accomplished

through the deposition of conducting alloys to the top and bottom surfaces. Presently, the contact scheme consists of Au-Ge compounds for the n+ contacts and Au-Zn compounds for the p+ contacts.

An "AlGaAs filter" was fabricated to study the transparency of the material to sub-bandgap photons. The filter consisted of a 1.9 eV active layer on a self-supporting $Al_{0.7}Ga_{0.3}As$ layer of approximately 120 microns thickness. Quantum efficiency curves of a silicon solar cell with and without the filter in place are shown in Figure 3. Calculating the transparency of the "AlGaAs filter" is straight forward. First, a ratio of the filtered bottom cell light generated current to the unfiltered light generated current is calculated.

$$\text{Ratio}_{\text{Jl}} = \text{Jl}_{\text{filtered}}/\text{Jl}_{\text{unfiltered}}$$

Then, the same rationale is applied to the photon flux assuming unit quantum efficiency of the bottom cell.

$$\text{Ratio}_{\Phi} = \Phi_{\text{sub-bandgap}}/\Phi_{\text{Silicon}}$$

The transparency is calculated as:

$$\text{Transparency} = \text{Ratio}_{\text{Jl}}/\text{Ratio}_{\Phi}$$

Results of this calculation yield a sub-bandgap transparency of 91% for the AM0 solar spectrum.

Detailed analysis of the R+T measurement of the AlGaAs filter revealed that free-carrier absorption in the AlGaAs substrate was less than 2%, and the remaining loss was purely reflective.

Quantum efficiency and current-voltage curves were employed to evaluate the quality of the AlGaAs solar cells. Growth conditions were changed to optimize the operation of the solar cell based on the results of these measurements. Parameters included junction depth and emitter doping, window thickness, base layer thickness and doping, and contact alloy time and temperature.

Characteristics of a wide bandgap solar cell are presented in Figures 4 and 5. As can be seen from the external quantum efficiency measurement, there is a sharp band-edge demonstrating excellent material quality. This is supported further by the high fill factors yielded by this device.

A decrease in the quantum efficiency corresponding to an increase in aluminum content of the Al-Ga-As mixed crystal system has been reported [ref. 8]. With greater than 32% Al, there is a dramatic reduction in quantum efficiency and therefore a decrease in the solar cell performance. The operating characteristics of the 1.80 eV AlGaAs concentrator solar cell are presented in Figures 6 and 7.

The internal quantum efficiency of the device is over 90% for much of the absorbed spectrum when allowance is made for the grid obscuration.

Results of the two best AstroPower AlGaAs solar cells to date and the predicted stack efficiencies are demonstrated in Table V. Silicon performance is projected based on 95% top solar cell transparency.

Performance of this stack configuration would be enhanced with a few basic refinements in fabrication. Substitution of an anti-obscuration, prismatic cover with a matched grid structure will reduce contact shading to zero. With these improvements the AlGaAs concentrator solar cells will yield the predicted efficiencies shown in Table VI.

The approach used to fabricate a free-standing AlGaAs top concentrator cell, useful for concentrator systems, was to grow a 50 micron thick graded base layer on the GaAs substrate. After contacts are made to the AlGaAs device on the GaAs substrate, the GaAs is etched away under the illuminated region of the AlGaAs device. This device structure is shown in Figure 8.

The method for substrate removal used to fabricate the above devices is an etch bath consisting of H_2O_2, NH_4OH, and EDTA added as a complexing agent. This etch exhibits a temperature dependent rate as can be seen in Figure 9. Excellent control can be exercised over the rate of etching by controlling the temperature: making it possible to remove the GaAs substrate quickly and at the same time continuing to maintain the selectivity of the etch.

A family of current-voltage curves was measured during each step in the fabrication process. No degradation of the solar cell operating characteristics, exhibited by device G-156 #2, was observed during the processing of the device. Most AlGaAs solar cells possess excellent process survivability as shown in Figure 10. After this particular device was processed, the glass slide onto which it had been bonded with RTV silicone was found to have cracked and consequently the device was removed. During the removal the lead attachment which had been made to the front and back of the solar cell was inadvertently removed. The solar cell was retested and no cell degradation was exhibited by this device even after the abusive handling.

Conclusion

The AstroPower self-supporting, transparent AlGaAs top solar cell can be stacked upon any well-developed bottom solar cell for improved system performance. This is a unique approach to improve the performance and scale of space photovoltaic power systems. Mechanically stacked tandem solar cell concentrator systems based on the AlGaAs top concentrator solar cell can provide near term efficiencies of 36% (AM0, 100×). Possible tandem stack efficiencies greater than 38% (100×, AM0) are feasible with a careful selection of materials. In a three solar cell stack, system efficiencies

exceed 41% (100×, AM0) . These device results demonstrate a practical solution for a state-of-the-art top solar cell for attachment to an existing, well-developed solar cell.

References

[1.] M. E. Nell, and A. M. Barnett, IEEE Trans. Electron Devices, bf ED-34, 257.

[2.] P. H. Mauk, N. E. Terranova, and A. M. Barnett, To be published.

[3.] A. M. Barnett, and J. S. Culik, *19th IEEE Photovoltaic Specialists Conference*, 931, 1987.

[4.] Sheng S. Li, *15th IEEE Photovoltaic Specialists Conference*, 1283, 1981.

[5.] R. K. Ahrenkiel, and D. J. Dunlavy, Journal of Vacuum Science and Technology, **7**, 822, 1989.

[6.] A. Saletes, A. Rudra, P. Basmaji, J. F. Carlin, M. Leroux, J. P. Contour, P. Gibard and C. Verie, *19th IEEE Photovoltaic Specialists Conference*, 124, 1987.

[7.] L. Mayet, M. Gavand, B. Montegu, and A. Laugier, *20th IEEE Photovoltaic Specialists Conference*, 597, 1988.

[8.] C. R. Lewis, H. C. Hamaker and R. T. Green, Journal of Electronic Materials, **16**, 1987.

[9.] A. W. Blakers, A. Wang, A. M. Milne, J. Zhao, X. Dai and M. A. Green, *4th International Photovoltaic Science & Engineering Conference*, Sydney, Australia, 1989.

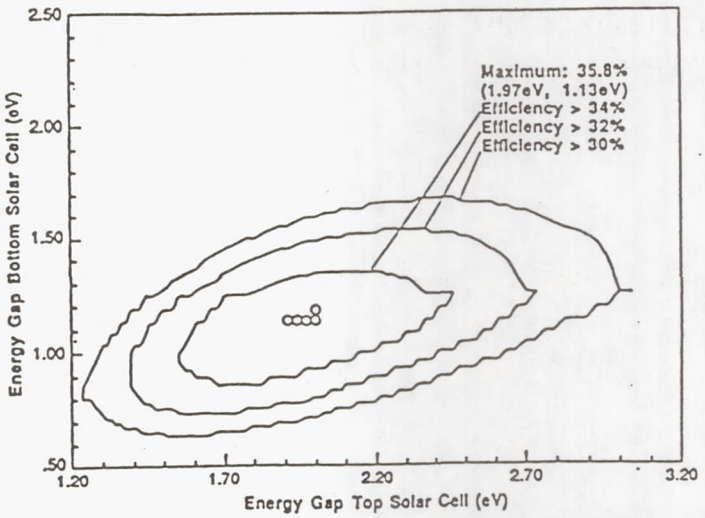

Figure 1. Iso-efficiency curves for various bandgap combinations (AM0,1X) [2].

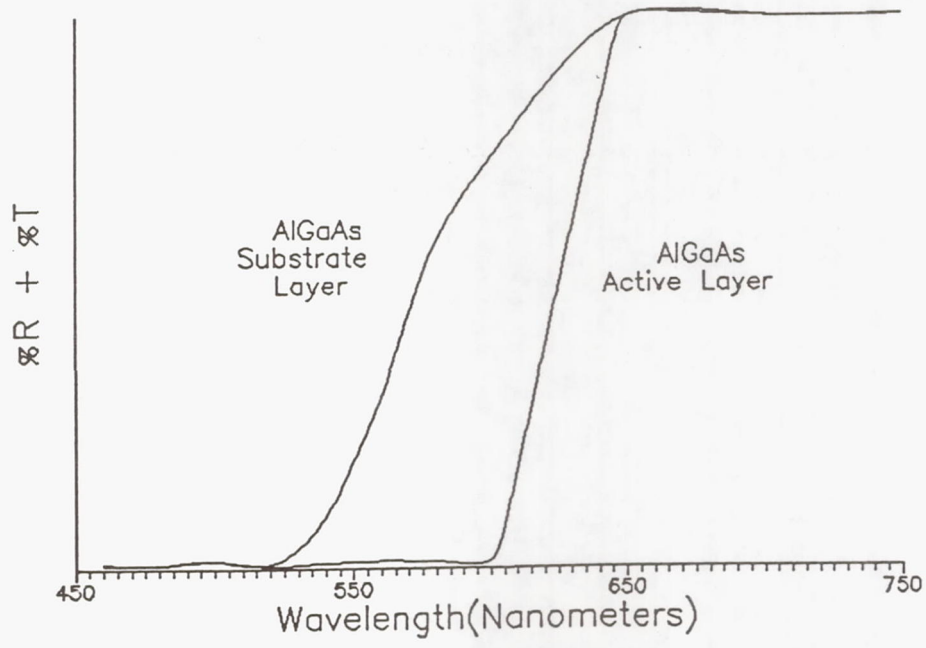

Figure 2. Reflection + transmission of active layer on substrate layer.

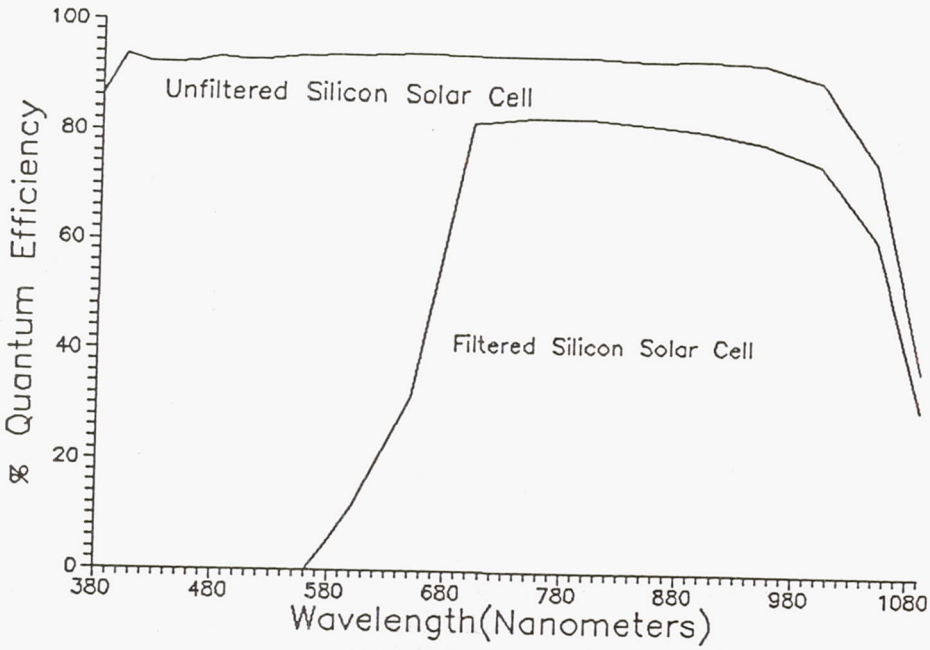

Figure 3. AlGaAs top solar cell transparency demonstrated by placement over an existing cell.

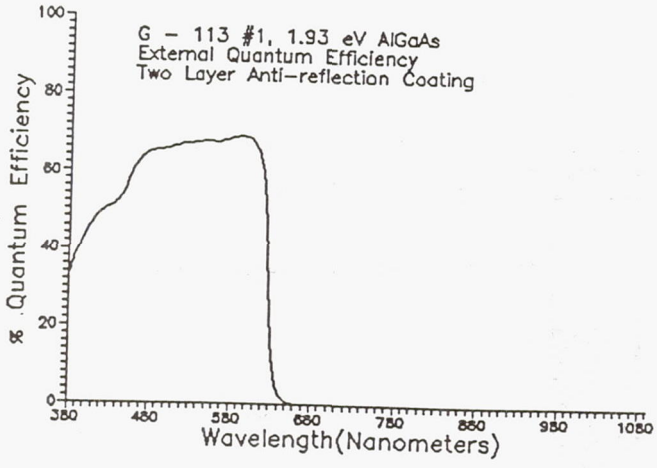

Figure 4. External quantum efficiency of 1.93 eV AlGaAs solar cell with grid obscuration.

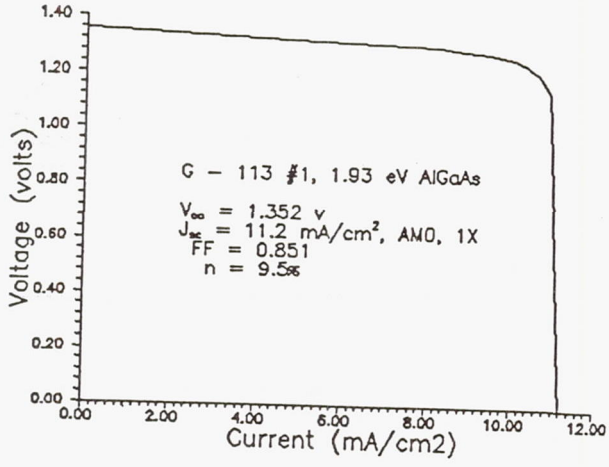

Figure 5. Operating characteristics of 1.93 eV AlGaAs solar cell with grid obscuration.

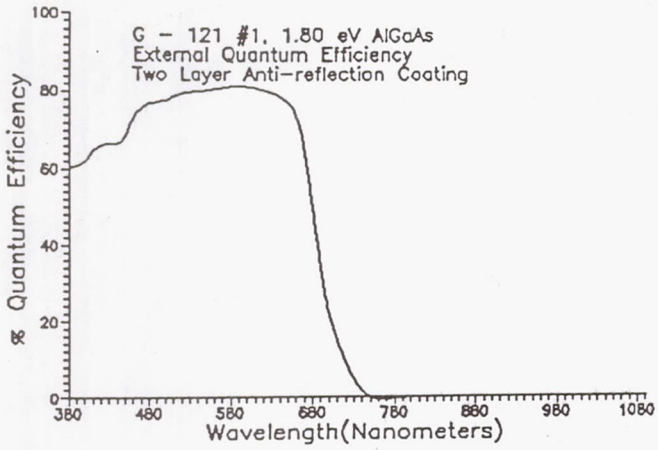

Figure 6. External quantum efficiency of a 1.80 eV AlGaAs solar cell with grid obscuration.

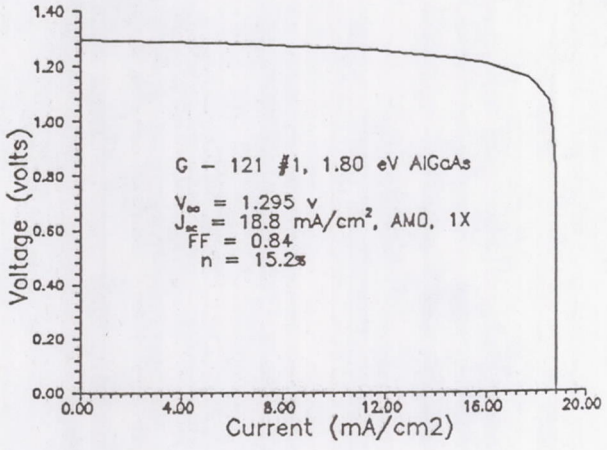

Figure 7.Operating characteristics of a 1.80 eV AlGaAs solar cell with grid obscuration.

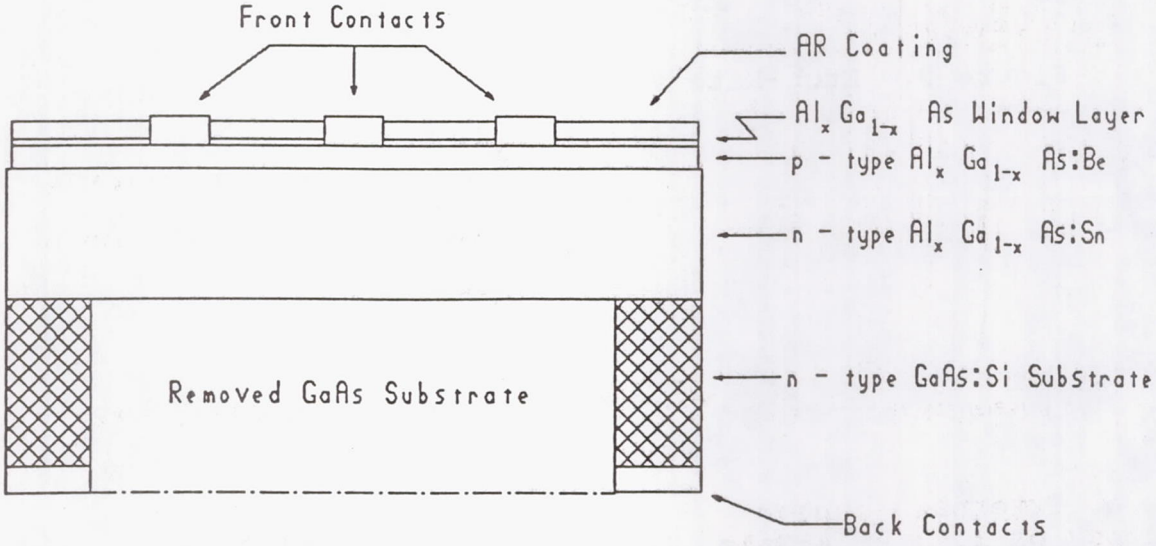

Figure 8. AlGaAs/AlGaAs on GaAs contact for concentrator systems.

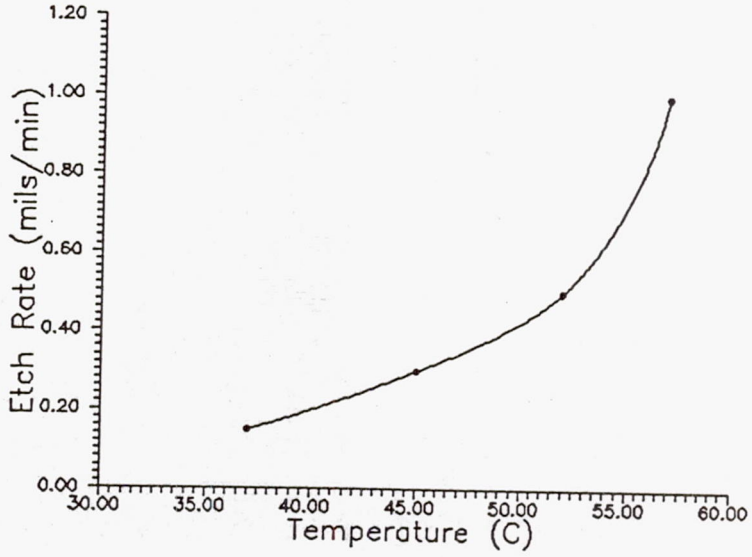

Figure 9. Etch-Rate vs. Temperature for a selective GaAs etch.

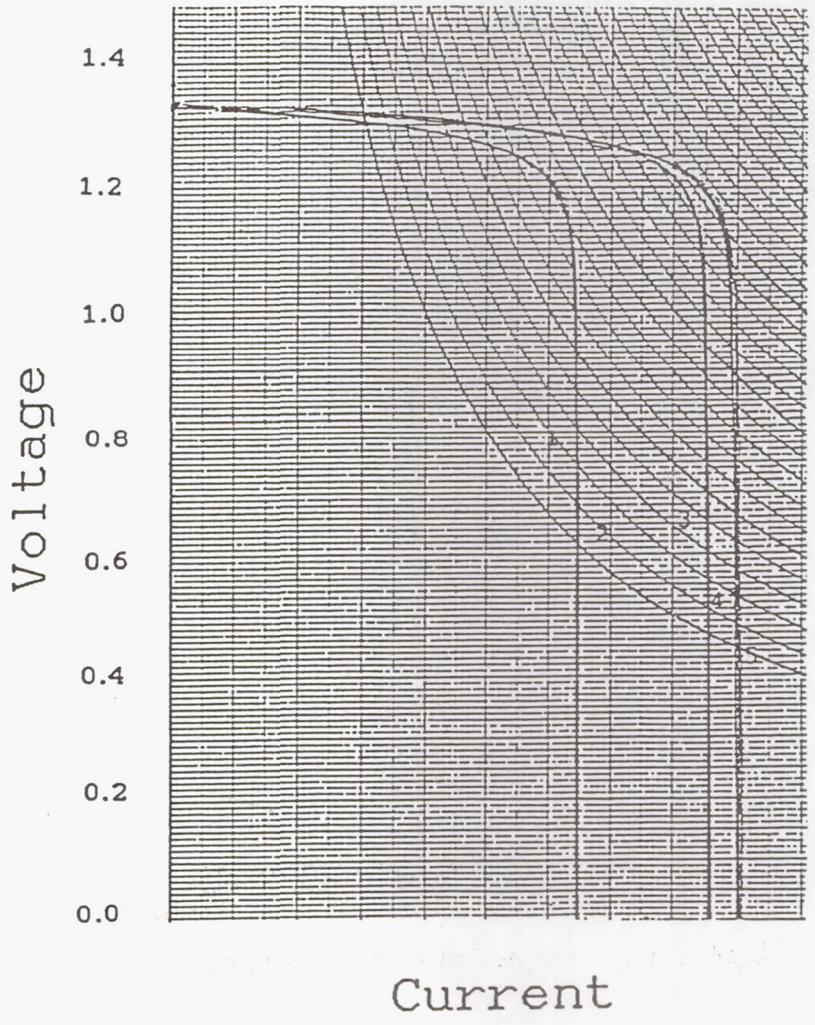

CURVE #	V_{oc} (volts)	J_{sc} (mA/cm^2)	FF	Effi (%)	COMMENT
1	1.331	6.93	0.85	5.81	Initial
2	1.329	6.93	0.85	5.81	Front lead attach
3	1.341	9.08	0.85	7.67	AR coating & RTV bond to glass superstrate
4	1.333	10.03	0.85	8.41	GaAs substrate removed & back lead attach
5	1.333	10.03	0.85	8.41	removal of RTV and lead attachment

Figure 10. Operating characteristics of AlGaAs top solar cell during processing.

Table I

Predicted Theoretical Maximum Efficiency for a Four-Terminal AlGaAs/Si Mechanical Stack (AM0, 135 mW/cm^2)

Material	E_g (eV)	Voc (volts)	Jsc (mA/cm^2)	FF	Eff(1X) (%)	Eff(100X) (%)
AlGaAs	1.93	1.588	21.55	0.91	23.0	24.7
Silicon	1.13	0.788	31.88	0.85	15.8	18.2
Four Terminal Stack Efficiency --->					38.8	42.9

Table II

"Best Case" Prediction for Four-Terminal Configuration of AlGaAs/Si Mechanical Stack (AM0, 135 mW/cm^2)

Material	E_g (eV)	Voc (volts)	Jsc (mA/cm^2)	FF	Eff(1X) (%)	Eff(100X) (%)
AlGaAs	1.93	1.52	19.6	0.87	19.2	20.7
Silicon	1.13	0.71	29.0	0.82	12.6	14.7
Four Terminal Stack Efficiency --->					31.8	35.4

Material	E_g (eV)	Voc (volts)	Jsc (mA/cm^2)	FF	Eff(1X) (%)	Eff(100X) (%)
AlGaAs	1.80	1.45	23.1	0.87	21.6	23.4
Silicon	1.13	0.71	25.5	0.82	11.0	12.9
Four Terminal Stack Efficiency --->					32.6	36.3

Table III

"Best Case" Prediction for Four-Terminal Configuration of AlGaAs/InGaAsP Mechanical Stack (AM0, 135 mW/cm^2)

Material	E_g (eV)	Voc (volts)	Jsc (mA/cm^2)	FF	Eff(1X) (%)	Eff(100X) (%)
AlGaAs	1.80	1.450	23.1	0.87	21.6	23.4
InGaAsP	1.08	0.763	27.7	0.81	12.7	14.7
Four Terminal Stack Efficiency --->					34.3	38.1

Table IV

"Best Case" Prediction for Six-Terminal Configuration of AlGaAs/InP/InGaAsP Mechanical Stack (AM0, 135 mW/cm^2)

Material	E_g (eV)	Voc (volts)	Jsc (mA/cm^2)	FF	Eff(1X) (%)	Eff(100X) (%)
AlGaAs	1.93	1.520	19.6	0.87	19.2	20.7
InP	1.35	1.009	18.2	0.84	11.4	12.8
InGaAsP	0.89	0.519	22.4	0.77	6.6	8.1
Six Terminal Stack Efficiency --->					37.2	41.6

Table V
AstroPower AlGaAs Top Solar Cell Data
with 95% Transparency on State of the Art Bottom Solar Cell
(AM0, 100X)

Material	E_g (eV)	Voc (volts)	Jsc (A/cm^2)	FF	Eff (%)
AlGaAs	1.93	1.47	1.12	0.85	10.4
Silicon[9]	1.13	0.813	2.90	0.814	14.2
		Four Terminal Stack Efficiency --->			24.6

Material	E_g (eV)	Voc (volts)	Jsc (A/cm^2)	FF	Eff (%)
AlGaAs	1.80	1.414	1.88	0.84	16.5
Silicon[9]	1.13	0.813	2.59	0.814	12.7
		Four Terminal Stack Efficiency --->			29.2

Table VI
AstroPower AlGaAs Solar Cell Data Used for
Predicted Performance of AlGaAs/Si Mechanical Stack
with Anti-Obscuration Prismatic Cover and 95% Transparency
(AM0, 100X)

Material	E_g (eV)	Voc (volts)	Jsc (A/cm^2)	FF	Eff (%)
AlGaAs	1.93	1.47	1.27	0.85	11.8
Silicon[9]	1.13	0.813	2.90	0.814	14.2
		Four Terminal Stack Efficiency --->			26.0

Material	E_g (eV)	Voc (volts)	Jsc (A/cm^2)	FF	Eff (%)
AlGaAs	1.80	1.414	2.14	0.84	18.8
Silicon[9]	1.13	0.813	2.59	0.814	12.7
		Four Terminal Stack Efficiency --->			31.5

Progress Toward a 30%-Efficient, Monolithic, Three-Junction, Two-Terminal Concentrator Solar Cell for Space Applications

L. D. Partain, B-C. Chung, G. F. Virshup, J. C. Schultz, H. F. MacMillan,
M. Ladle Ristow, M. S. Kuryla and K. A. Bertness
Varian Research Center
Palo Alto, CA

Component efficiencies of 0.2-cm^2 cells at $\sim$ 100× AM0 light concentration and 80°C temperatures are now at 15.3% for a 1.9-eV AlGaAs top cell, 9.9% for a 1.4-eV GaAs middle cell under a 1.9-eV AlGaAs filter, and 2.4% for a bottom 1.0-eV InGaAs cell under a GaAs substrate. The goal is to continue improvement in these performance levels and to sequentially grow these devices on a single substrate to give 30%-efficient, monolithic, two-terminal, three-junction space concentrator cells.

The broad objective is a 30%-efficient monolithic two-terminal cell that can operate under 25 to 100× AM0 light concentrations and at 75 to 100°C cell temperatures. Detailed modeling predicts that this requires three junctions. Two options are being pursued, and both use a 1.9-eV AlGaAs top junction and a 1.4-eV GaAs middle junction grown by 1-atm OMVPE on a lattice matched substrate. Option 1 uses a low-doped GaAs substrate with a lattice-mismatched 1.0-eV InGaAs cell formed on the back of the substrate. Option 2 uses a Ge substrate to which the AlGaAs and GaAs top junctions are lattice matched, with a bottom 0.7-eV Ge junction formed near the substrate interface with the GaAs growth. The projected efficiency contributions are 16%, 11% and 3%, respectively, from the top, middle and bottom junctions.

The best component cell efficiencies so far are 15.4% for the top AlGaAs, 10.8% for the middle GaAs under a 1.9-eV AlGaAs filter layer, and 3.0% for the bottom 1.0-eV InGaAs under a GaAs substrate. All of these are for $\sim$ 100× concentration and 25°C measurements in a flash simulator. At 80°C and $\sim$ 100×, these efficiencies decrease a small amount to 15.3%, 9.9% and 2.4%, respectively. Figure 1 shows the 80°C AlGaAs cell I-V data measured in Sandia's elaborate and expensive flash simulator. The simpler and less expensive Varian simulator gave the 80°C I-V data for the GaAs and InGaAs cells shown in Figs. 2 and 3. The comparisons show the Varian measurements approach the more accurate Sandia results to within 10 relative percent or less.

The one-sun short circuit current densities of these best component cells at 25°C are 15.5, 15.1 and 10.0 mA/cm^2, respectively, indicating that the current from the bottom InGaAs junction needs to be increased by about 50% to match the top two for two-terminal operation. The peak external quantum yield of this InGaAs cell of

This work was supported in part by Wright-Patterson Air Force Base under Contract F33615-88-C-2845.

50% indicates that it has the potential for this improvement when compared to the 80-85% peak external quantum yields of the AlGaAs and GaAs component cells. Such improvement requires that a better accommodation be made for the lattice mismatch between the GaAs substrate and the InGaAs junction. The best Ge device so far was obtained by growing n-GaAs onto an n-Ge substrate. The resulting Ge junction had a peak quantum yield of 53% and a 25°C short-circuit current at one sun of 15.1 mA/cm^2. This is sufficient for current matching. However, the remaining challenges for the Ge cell are to obtain high enough V_{oc} and FF values for 3% efficiency performance, and to maintain this efficiency while both the AlGaAs and GaAs junctions are grown on top of it.

The AlGaAs and GaAs junctions have been grown on GaAs substrates and processed into two-terminal, two-junction cells. A metal busbar was deposited into an etched groove to interconnect the junctions. At 100× and 25°C, the best measured V_{oc} was 2.64V that compares well with the V_{oc} values of 1.54V and 1.12V from the best component AlGaAs and GaAs cells, respectively. This same two-junction cell had a two-terminal short circuit current density at one sun of 14.7 mA/cm^2 after application of a prismatic cover glass to remove the obscuration of the metal interconnect. Further improvements in multijunction current are expected as the growth techniques are perfected.

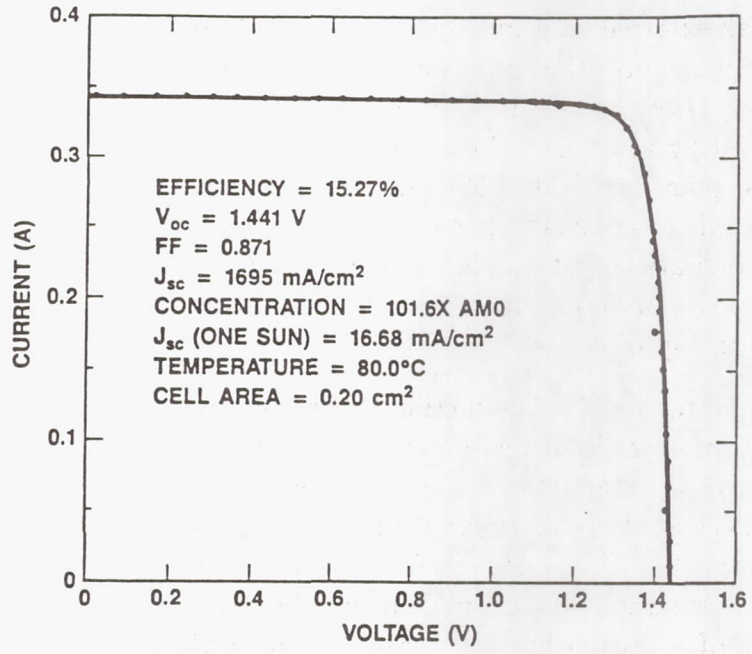

Fig. 1 A top 1.9-eV AlGaAs cell with 15.3% AM0 efficiency at 80°C and 102X concentration as measured in Sandia's flash simulator.

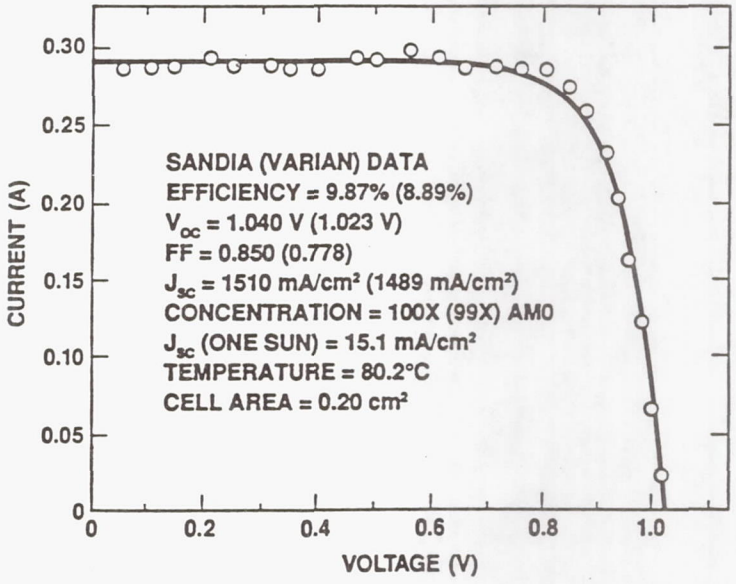

Fig. 2 A GaAs middle cell under an 1.9-eV AlGaAs filter at 80°C as measured in Varian's flash simulator. For comparison, the Sandia-determined 9.9% AM0 efficiency, V_{oc}, FF and X values are shown for the specified J_{sc}.

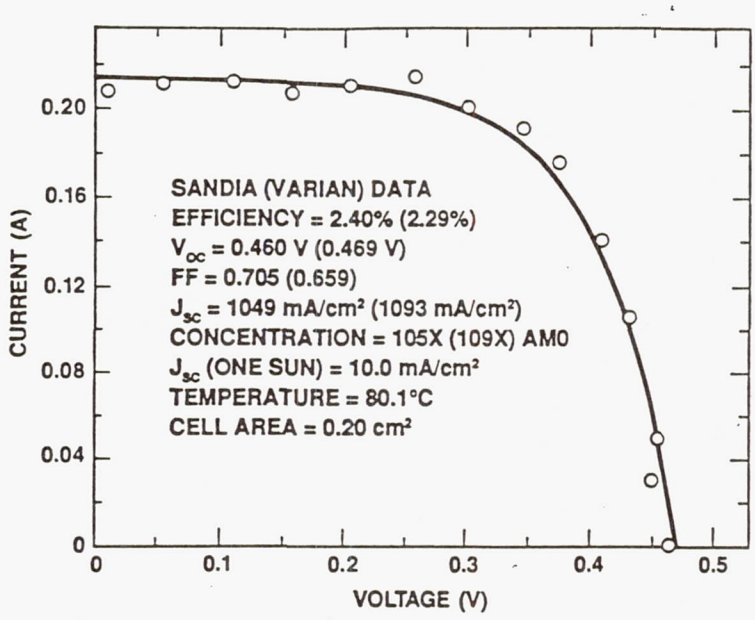

Fig. 3 A bottom 1.0-eV InGaAs cell under a GaAs substrate at 80°C as measured in Varian's flash simulator. For comparison, the Sandia-determined 2.4% AM0 efficiency, V_{oc}, FF and X values are shown for the specified J_{sc}.

Tandem Concentrator Solar Cells with 30% (AM0) Power Conversion Efficiency

J.E. Avery, L.M. Fraas and V.S. Sundaram
Boeing High Technology Center
Seattle WA

D.J. Brinker
NASA Lewis Research Center
Cleveland OH

J.M. Gee
Sandia National Laboratories
Albuquerque NM

M.J. O'Neill
Entech, Inc.
DFW Airport TX

Introduction

Very high efficiency concentrator solar panels are envisioned as economical and reliable electrical power subsystems for space based platforms of the future. Single junction GaAs solar cell efficiencies as high as 25% have been reported at concentrated light levels of 300 suns AM0 [ref. 1]. However, this material precludes the collection of about 40% of the solar energy spectrum below the GaAs bandgap energy of 1.42 eV since this energy cannot be absorbed by the GaAs. Enhanced efficiencies may be realized by stacking GaAs either monolithically or mechanically on top of such lower bandgap materials as Ge, Si, CIS or InGaAs which do convert at least some portion of the longer wavelength light [refs. 2-5].

Gallium Antimonide (GaSb) was selected as a preferred low bandgap candidate material [ref. 6] because it has an appropriate bandgap energy of 0.72 eV and is a direct gap material with a high absorption coefficient. It is a binary compound that can be formed into high quality single crystal ingots using the liquid-encapsulated Czochralski technique (LEC) and then shaped, wafered and polished. Solar cell junctions can be diffused into GaSb so wafers can be processed directly without any epi growth. With all of these desirable features GaSb cells are likely to reach theoretical performance limits.

Mechanical stacking permits independent processing of the two wafer materials allowing process variables like temperature to be optimized for a lesser set of materials interfaces [ref. 7]. Also, separate stacked cells can be interconnected in a voltage matched configuration to achieve 2 terminal operation.

Entech solar cell covers [ref. 8] were applied to both the GaAs and GaSb cells to enhance the collected current and efficiency. These covers have molded optical

elements that divert incoming light away from obscuring grid lines onto active cell area.

Transparent GaAs and GaSb Booster Cell Development

Both types of cells are processed at the wafer level starting with single crystal wafers and using fairly conventional equipment and procedures. Dozens of individual concentrator cell dies are then scribed out of each wafer. Figure 1 shows a processed wafer and a waffle pack of dies ready for assembly, along with a mounted die and a finished test article which are described later.

The GaAs active layers are deposited by MOCVD epi growth. Subsequent steps include patterned metallizations, cap etching and AR coating. Transparent GaAs cells for tandem stacks differ from their single junction counterparts in several ways. The back metal must be opened to let sub-bandgap radiation pass through. Back surface gridlines are not necessary for small cells which have low back surface sheet resistance. The doping level of the bulk wafer is selected to minimize absorption below the bandedge of the GaAs, without increasing series resistance loss through the wafer or at the back contact interface. Good results are obtained in the $1-3\times10^{17}$ range for N-type substrates. Absorption losses for standard wafer thicknesses of 450 microns are normally less than 10% in the range of interest, from the bandedge of the GaAs at 0.9 microns to the bandedge of GaSb at 1.72 microns. Further reductions in absorption loss would be gained by thinning the wafer or using less bulk doping. However, the electrical performance or mechanical yield might suffer.

The transparent GaAs cell is AR coated on both the front and back surface to maximize the transmission of long wavelength energy through to the GaSb booster cell. Figure 2 shows schematically a GaAs filter that consists of a GaAs wafer with solar cell epi layers and front and back surface multilayer AR coatings. The figure also shows measured transmission and reflectance characteristics of the real filter. Note the broadband peak transmission rising from the GaAs bandedge to 95%, and the very low total reflectance over the entire solar spectral range.

Figure 3 shows the IV performance curve of a transparent GaAs solar cell fabricated at Boeing and measured at NASA/Lewis. The 23.8% efficiency of this transparent GaAs cell compares very favorably with the best non-transparent cell values measured in the same lab, and is equivalent to non-transparent cells from the same Boeing epi run.

GaSb cell processing [ref. 9] is accomplished using conventional semiconductor processing equipment and procedures. After applying a nitride diffusion mask , a planar patterned emitter is formed by zinc diffusion in an open tube. The back surface is fully metallized. Patterned front metal is deposited using standard lift-off techniques. Only gridlines touch the semiconductor surface. Bonding pads are on top of the dielectric layer away from the junction.The junction is etched back and

AR coated to maximize photocurrent, while leaving a deeper junction under the grid metal. This configuration helps to prevent shunting of the junction during bonding and assembly.

The very first GaSb solar cells were over 5% efficient behind a GaAs filter. Table 1 shows this filtered efficiency increasing with time to a recent high value of 8.7%. Further increases are expected. The improvements in current, voltage and fill factor shown in the table are the result of basic improvements in specific recipes for each process step. Also, with better cells the efficiency peak versus intensity moves out to higher light levels as the voltage and fill factor continue to climb. As with GaAs, the currents and efficiencies of GaSb cells increase over 10% with Entech covers. Notice how "covered" efficiencies in the table track the baseline filtered measurements. Stacked efficiencies, measured behind a transparent GaAs cell, will also follow the upward trend.

Figure 4 shows the IV characteristics of a covered and filtered GaSb cell from the Sep-89 group of table 1, measured at Sandia on a pulsed xenon lamp simulator using a NASA flown GaAs AM0 reference standard. The voltage, fill factor and current are consistent with Boeing measured values.

Mechanically Stacked GaAs/GaSb Test Article Assembly

Figure 5 illustrates how one front cell and one back cell are assembled together into a test article for illuminated performance testing. Cells are first bonded to thin metal disks with silver epoxy. The disks have center holes slightly larger than the cell active areas so that light can pass through. Entech covers are applied to both cells at this point. Front and back disks are then positioned as shown in the figure and clamped between insulators and terminals to the heat sink. The locator provides for alignment of the disks. The back contact of the back cell is either pressed against the block or wire bonded to the bottom terminal. The front contact of the back cell and the back contact of the front cell share a common terminal pressed against both disks. The front contact of the front cell is preferably wire bonded to the top terminal, otherwise this contact can be probed. In this configuration each of the stacked cells is tested individually and an added total efficiency is reported.

The metal disks provide for heat spreading from the cells through the conductive epoxy, distributing excess thermal energy over a larger area path to the block. This particular configuration, when held by vacuum to a temperature controlled chuck, holds the junction temperature of both cells to within a few degrees of the chuck during testing with light beam intensities on the cells up to 200 suns.

The test articles described above are useful for monitoring cell performance during process development and for verification testing between labs. However, they do not allow for testing both cells together in a 2 terminal configuration because the maximum power currents and voltages of the different bandgap cells are not matched.

In fact typical max power voltages for the GaSb cells are about 1/3 of the GaAs. 3 to 1 voltage matched circuits have been fabricated and tested [ref. 10] using double sided printed circuit boards. 2 terminal operation has been demonstrated up to a 3×3 matrix level with a total efficiency equal to the sum of the front and back circuits measured separately.

Concentrated Light Performance Testing

Figure 6 shows the concentrated light IV test station constructed and used at Boeing to measure front and back cells during processing and after assembly. The station provides up to 200 suns AM0. A standard wafer prober allows for automatic step and repeat testing at the wafer level. The one inch beam from a 300 watt xenon spotlight is focused through microscope optics onto a temperature controlled test plane. Selectable objective lenses and adjustable irises in the optical path provide for a continuous range of light levels up to the 200× maximum. At the highest light level with a 10× final objective, the beam size is about 3 millimeter diameter with a power density of 25 watts/cm^2. An electronic shutter in the lamp housing is synchronized with the testing to prevent overheating the optics.

I-V data pairs are collected by the control computer and reduced to summary values. The cycle time per cell test is 500 milliseconds. During the test cycle good thermal contact to the chuck holds the cells near a standard block temperature of 25 degrees C.

At NASA and Sandia, assembled cells were tested on pulsed-xenon flashlamp simulators using fresnel lenses to concentrate the light. Very short pulse times minimize thermal loading of the test structure for constant temperature measurements. These simulators are also capable of producing high test-beam intensities and may be suitable for testing larger area samples and minimodules with multiple lenses.

Boeing, Sandia and NASA share a common procedure for calibrating the concentrated light beam intensity using 1 sun reference standards and assuming a linear relationship between the I_{sc} of a solar cell and the beam intensity. This procedure is fairly well developed for GaAs, but since GaSb is a new solar cell material it will require additional calibration testing. Additional test articles are being assembled for upcoming NASA high altitude plane flight calibrations to the AM0 spectrum [ref. 11].

Table 2 presents the performance data summary of a mechanically stacked GaAs/GaSb tandem cell. It compares values measured at Boeing and NASA/Lewis. Note that combined efficiencies greater than 30% at light levels up to 100x AM0 were recorded at both locations. V_{oc}, FF, V_{max} and 1 sun current (I_{sc}/C_{onx}) values are all quite consistent. Recent improvements in GaSb cell performance are expected to raise the total efficiency by another 1 to 2 percentage points.

Conclusions

GaAs concentrator cells with very high efficiencies and good sub-bandgap transmissions can be fabricated on standard wafers. GaSb booster cell development is progressing very well; performance characteristics are still improving dramatically. Consistent GaAs/GaSb stacked cell AM0 efficiencies greater than 30% are expected.

References

[1.] H. C. Hamaker, M. Grounner, N. R. Kaminar, M. S. Kuryla, M. J. Ladle, D. D. Liu, H. F. MacMillan, L. D. Partain, G. F. Virshup, J. G. Werthen and J. M. Gee, *Space Photovoltaic Research and Technology 1988*, NASA Conference Publication 3030, 292 (1988).

[2.] S. P. Tobin, S. M. Vernon, C. Bajgar, V. E. Haven, L. M. Geoffroy and D. R. Lillington, IEEE Electron Device Letters, **9**, 256 (1988).

[3.] J. M. Gee, C. J. Chiang, D. L. King, *4th International Photovoltaics Science and Engineering Conference*, Sydney Australia, Feb 14-17, 1988.

[4.] B. J. Stanbery, J. E. Avery, R. M. Burgess, W. S. Chen, W. E. Devaney, D. H. Doyle, R. A. Mickelson, R. W. McClelland, B. D. King, R. P. Gale and John C. C. Fan, *Conference Record 19th IEEE Photovoltaic Specialists Conference*, 280, (1987).

[5.] M. W. Wanlass, K. A. Emery, T. A. Gessert, G. S. Horner, C. R. Osterwald and T. J. Couts, to be published in Solar Cells.

[6.] L. M. Fraas, L. D. Partain, P. S. McLeod and J. A. Cape, Solar Cells, **19**, 73 (1986-1987).

[7.] L. D. Partain, L. M. Fraas, P. S. McLeod, J. A. Cape, and M. S. Kuryla,J. Appl. Phys. **62**, 694 (1987).

[8.] M. J. O'Neill, US Patent # 4,711,972, Dec 1987.

[9.] L. M. Fraas, G. R. Girard, J. E. Avery, B. A. Arau, V. S. Sundaram, A.G. Thompson, J.M. Gee, J.Appl.Phys. (1989).

[10.] L. M. Fraas, J. E. Avery, V. Sundaram, V. Dinh, T. Davenport, M. J. O'Neill, to be published in IEEE Aerospace and Electronic Systems, Nov 1989.

[11.] R. E. Hart Jr., D. J. Brinker and K. A. Emery, *Conference Record 20th IEEE Photovoltaic Specialists Conference*, 764 (1988).

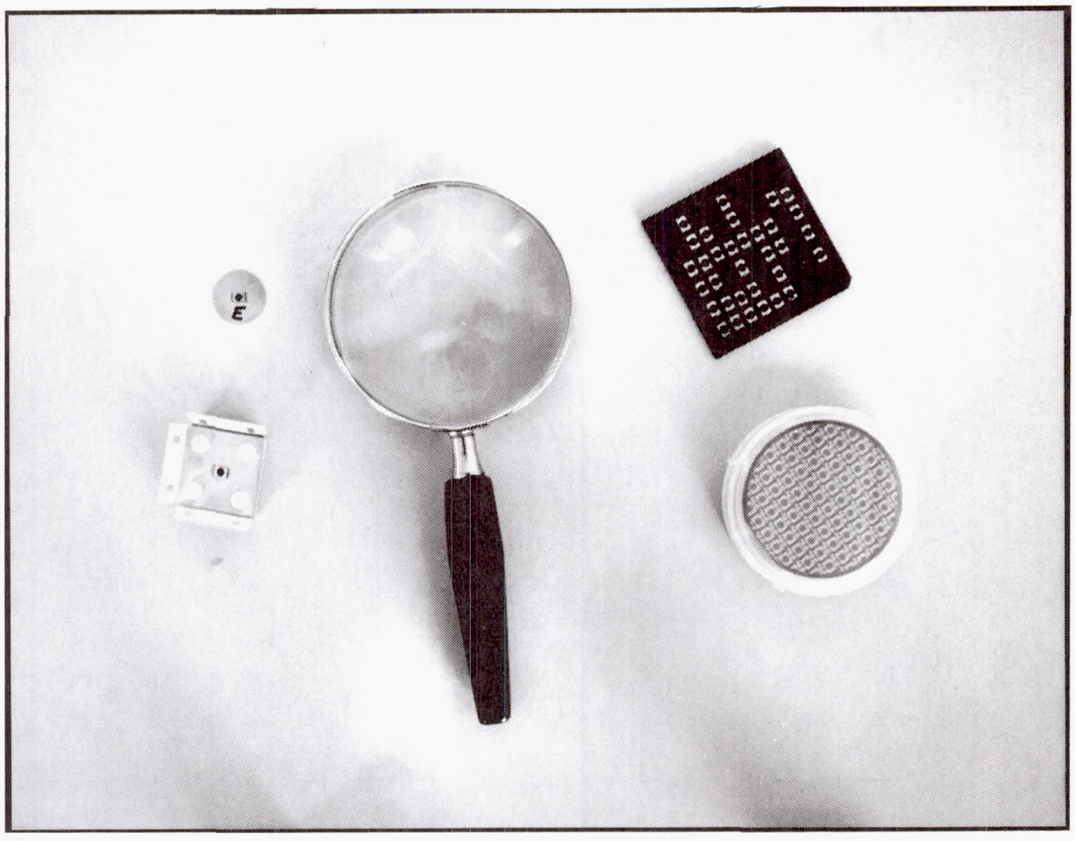

Figure 1. Boeing Processed Wafer, Diced Concentrator Cells and Mounted Concentrator Cells

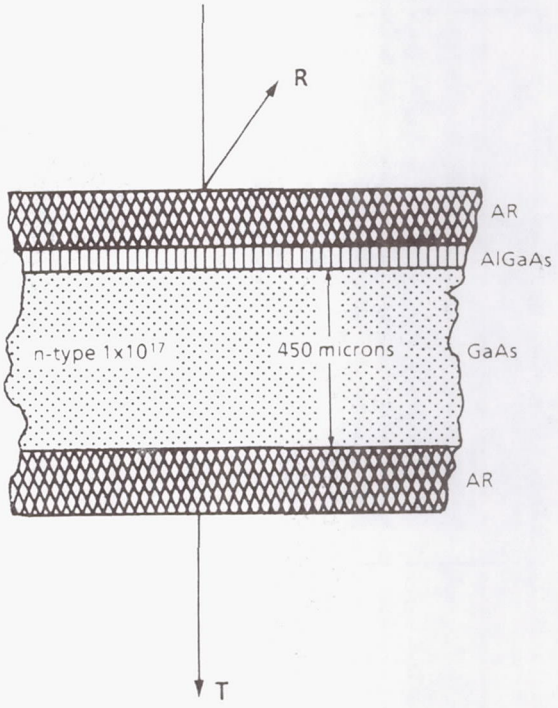

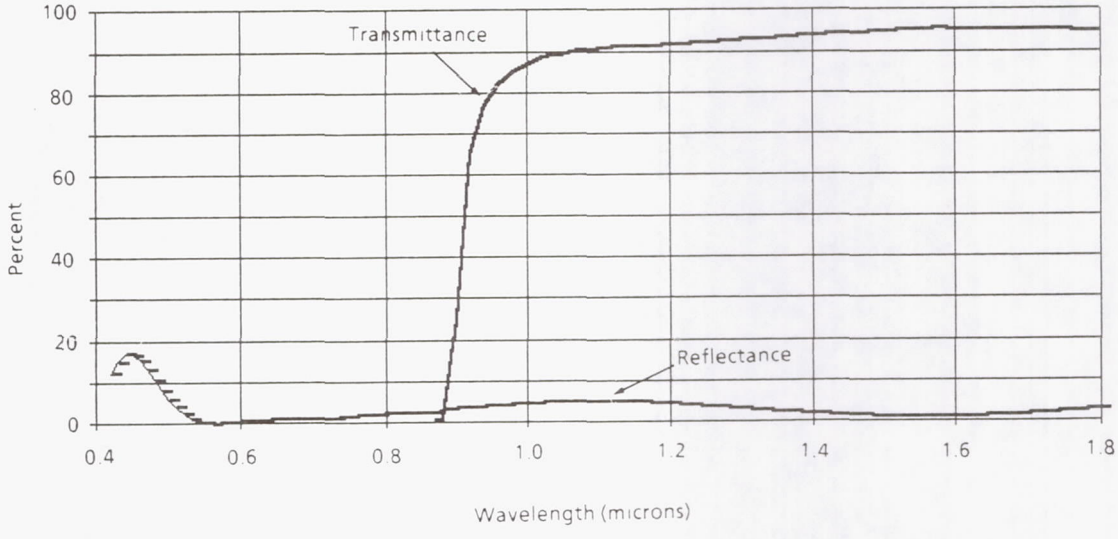

Figure 2. Transparent GaAs Filter

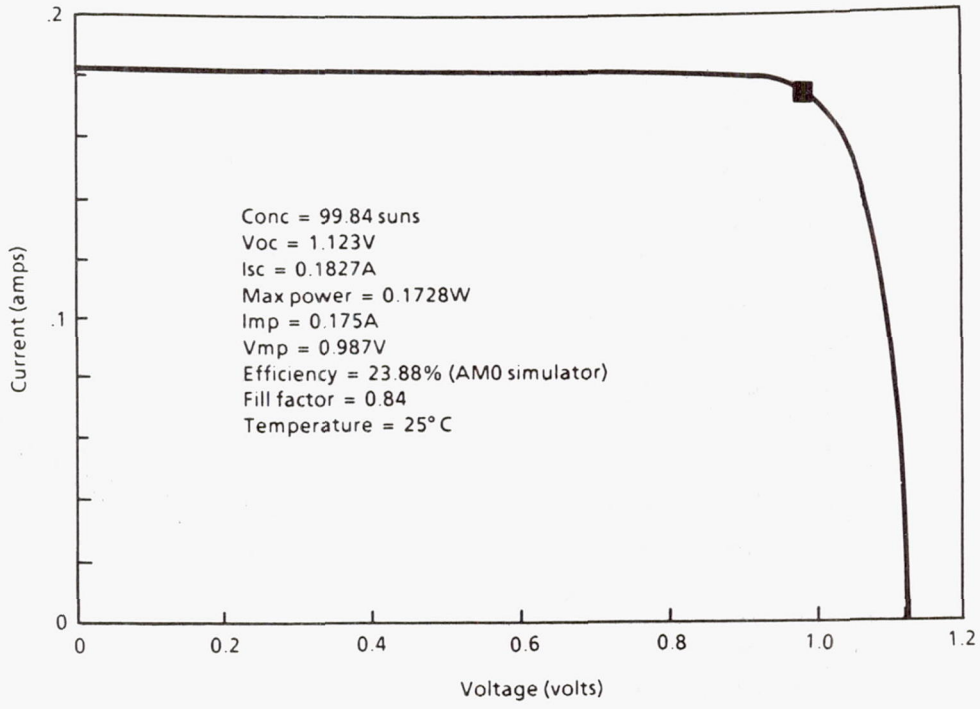

Figure 3. Boeing GaAs Cell, NASA Test AM0

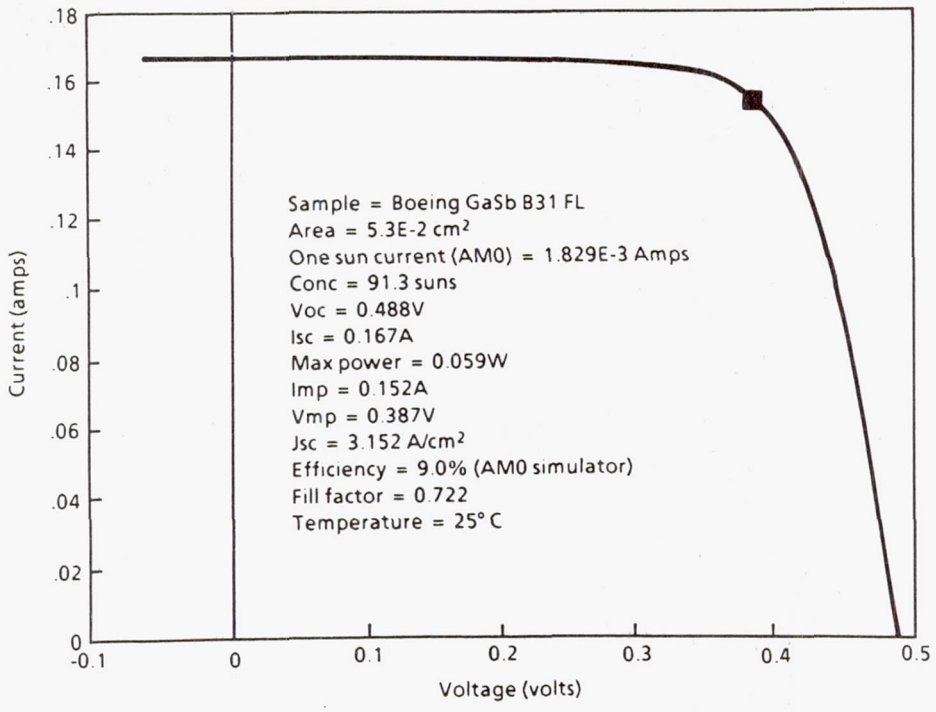

Figure 4. Boeing GaSb Cell, Sandia Test AM0

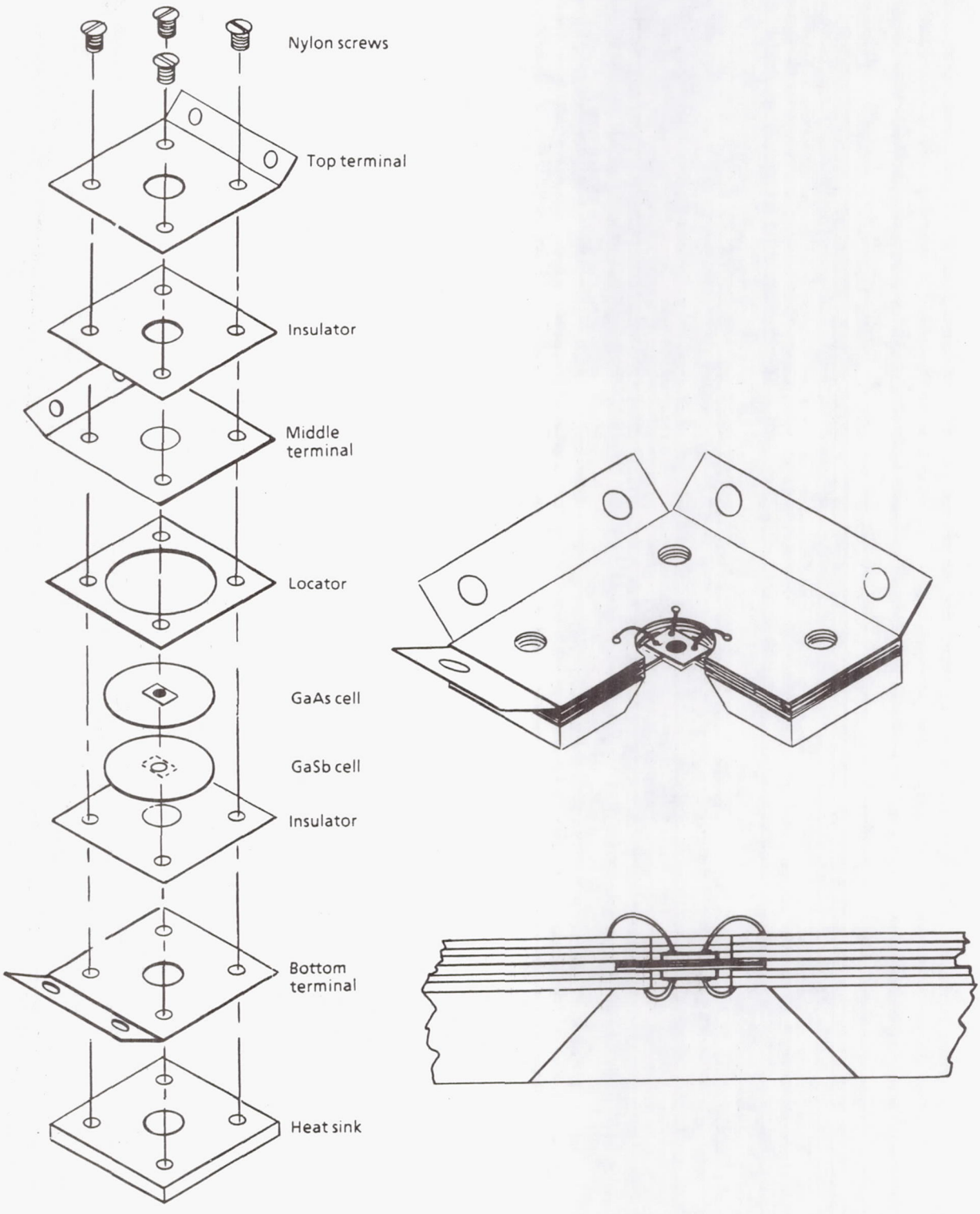

Figure 5. . Tandem Cell Test Article

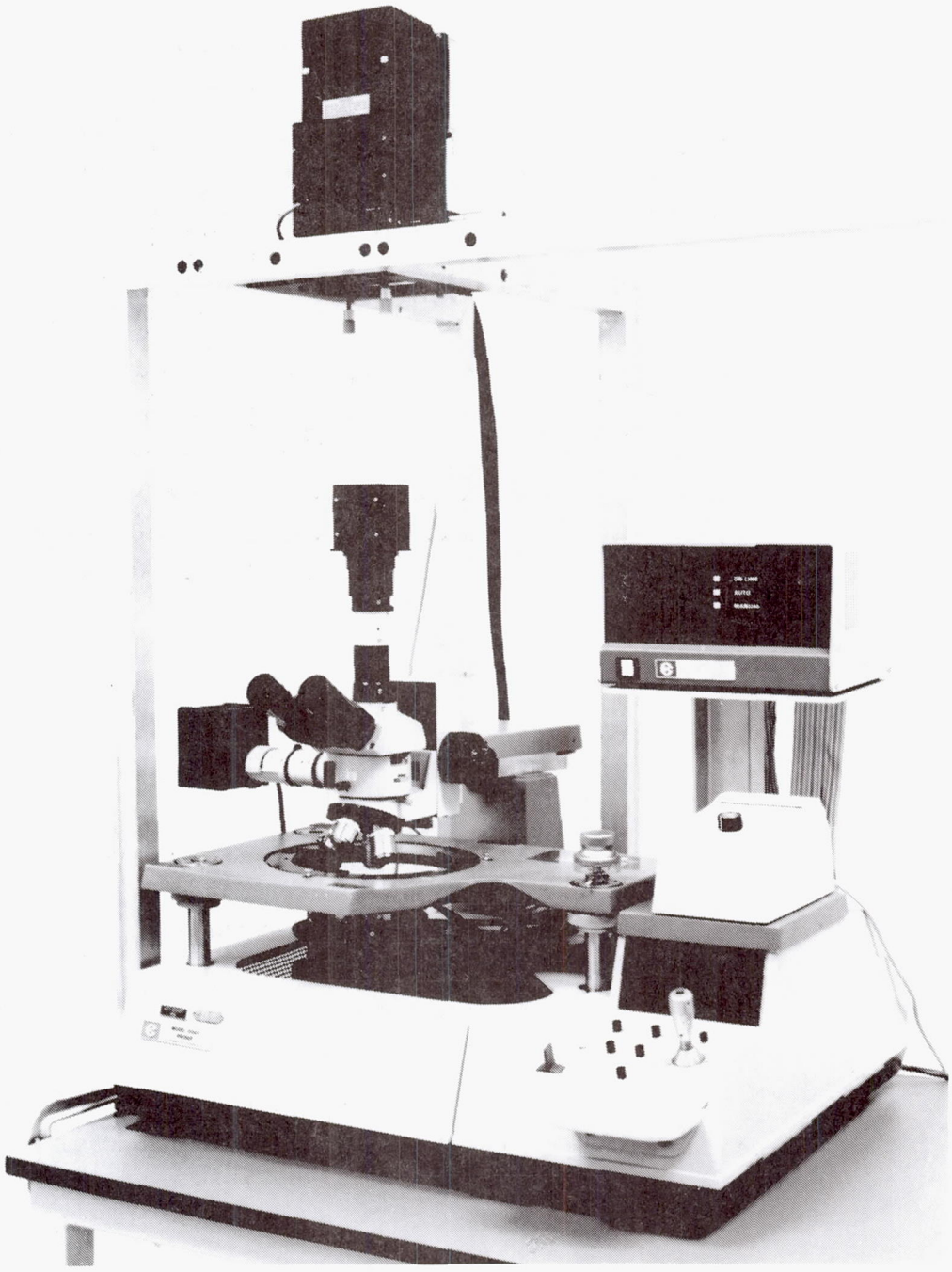

Figure 6. Concentrated Light Solar Cell Test Station

Table 1. GaSb Cell Performance Progress

	Jun-1988	Mar-1989	May-1989	Sept-1989	Oct-1989
Isc (mA)	37	50	101	210	317
Voc (volts)	0.442	0.446	0.462	0.482	0.491
FF	0.66	0.7	0.72	0.69	0.745
Vmax (volts)	0.33	0.353	0.37	0.37	0.401
Imax (mA)	33	44	92	189	289
1 sun Isc (mA)	1.35	1.37	1.37	1.64	1.64
Concentration ratio	27.4	37	73	128	193
Filtered efficiency (%)	5.7	6.18	6.7	7.9	8.7
Covered efficiency (%)			8.2	9.1	9.6
Stacked efficiency (%)			7		

Table 2. Stacked GaAs/GaSb Test Article Performance Verification

Air Mass Zero Simulation

	Isc (mA)	Voc (volts)	FF	Vmax (volts)	Conx	Eff (%)
Boeing						
GaAs	70	1.100	0.84	0.984	38.2	23.7
GaSb	106	0.462	0.72	0.370	85	7.0
				Efficiency total		30.7
NASA						
GaAs	183	1.120	0.84	0.987	100	23.9
GaSb	125	0.469	0.71	0.367	100	6.9
				Efficiency total		30.8

Progress in GaAs/$CuInSe_2$ Tandem Junction Solar Cells

N. P. Kim, R. M. Burgess, R. A. Mickelsen and B. J. Stanbery
Boeing Aerospace & Electronics
Seattle, WA

R. W. McClelland, B. D. King and R. P. Gale
Kopin Corporation
Taunton, MA

Introduction

Much more power is required for spacecraft of the future than current vehicles. To meet this increased demand for power while simultaneously meeting other requirements for launch, deployment, and maneuverability, the development of higher-efficiency, lighter-weight, and more radiation resistant photovoltaic cells is essential. Mechanically stacked tandem junction solar cells based on (AlGaAs)GaAs thin film CLEFT (Cleavage of Lateral Epitaxial Film for Transfer) top cells and $CuInSe_2$ (CIS) thin film bottom cells are being developed to meet these power needs.

The mechanically stacked tandem configuration is chosen due to its interconnect flexibility allowing more efficient array level performance. It also eliminates cell fabrication processing constraints associated with monolithically integrated multi-junction approaches [refs. 1-2], thus producing higher cell fabrication yields. The GaAs cell is used as the top cell due to its demonstrated high efficiency [ref. 3], and good radiation resistance [ref. 4]. Furthermore, it offers a future potential for bandgap tuning using AlGaAs as the absorber to maximize cell performance [ref. 5]. The $CuInSe_2$ cell is used as the bottom cell due to superb radiation resistance [ref. 4], stability, and optimal bandgap value in combination with an AlGaAs top cell. Since both cells are incorporated as thin films, this approach provides a potential for very high specific power. This high specific power (W/kg), combined with high power density (W/m^2) resulting from the high efficiency of this approach, makes these cells ideally suited for various space applications.

Cell Fabrication and Characterization

The schematic of the (AlGaAs)GaAs/$CuInSe_2$ tandem cells is shown in Figure 1. It consisted of a double-heterostructure (AlGaAs)GaAs CLEFT thin-film top cell and a polycrystalline $CuInSe_2$ thin-film heterojunction lower cell. All tandem cells were fabricated with a 4 cm^2 cell design.

The bottom $CuInSe_2$ cell was fabricated on a glass substrate whose thermal expansion coefficient is the same as or very similar to that of a coverglass. Fabrication of the CIS cell included sequential deposition of Mo back electrode, $CuInSe_2$ absorber

layer, and CdZnS window layer, and photolithographic patterning followed by etching to form a solar cell device. Grid metal deposition and anti-reflection coating were added to complete fabrication of the n-on-p CIS cell. A schematic of this cell is shown in Figure 2 and details of the fabrication process are found in prior publications [refs. 6-8]. Contact pads used for the interconnect of the top cell electrodes and the sub-array string were formed during the lower cell fabrication when the contact pads for the lower cell electrode were formed.

The top (AlGaAs)GaAs thin-film cell was fabricated by the CLEFT process described elsewhere [refs. 9-10]. The schematic of the cell and the fabrication process are shown in Figure 3. A thin film layer was grown on a bulk GaAs substrate through seed lines using a vapor phase epitaxy method. The double-heterostructure n-on-p cell was formed by sequential growth of p-GaAs buffer, p+-AlGaAs BSF, p-GaAS base, n-GaAs emitter, n+-AlGaAs window and n+-GaAs cap layer. Further details on growth parameters are found in other publications [refs.10-11]. The thin-film was cleaved from the substrate after front grid metallization and support mounting. The structure was bonded to the $CuInSe_2$ cell using a space qualified adhesive after a gridded back metallization and transmission enhancement coating were applied. A single layer of SiN was normally used as the front side anti-reflection coating, although a double layer of SiN/Al_2O_3 was used on some cells to enhance light transmission to the bottom cell.

Interconnection from the top cell bonding pads to substrate bonding pads was made using a gold ribbon. A MgF_2 coated coverglass was mounted on the top of the tandem stack using a space qualified optically transparent adhesive.

Electrical measurements were conducted in the four terminal configuration at one sun and 28°C with an AM0 power normalization of 137.2 mW/cm^2. The GaAs I-V characteristics were measured at Kopin. An ORC 1000 solar simulator was used with a NASA calibrated AM0 GaAs reference cell. These measurements were found to be in good agreement with SERI and NASA measurements. The $CuInSe_2$ I-V characteristics were measured at Boeing using an AM0 filter-equiped Spectrolab XT-10 simulator. A JPL balloon flight calibrated solar cell consisting of a $CuInSe_2$ solar cell under an intimately contacted GaAs filter was used as the reference cell. Some GaAs cells were also measured at Boeing using the XT-10 simulator and adjusted following the procedure of the spectral mismatch calculation described elsewhere [ref.12]. The results also showed good agreement with Kopin's measurements. Some tandem cells were measured at Boeing using a recently acquired JPL balloon flight $GaAs/CuInSe_2$ tandem cell as the reference cell. When the same cells were measured at NASA, good agreement was also achieved.

Experimental Results

Cell Efficiency and Cell Weight

The best performance result achieved so far with 4 cm^2 tandem cells was 23.1% one sun AM0. This is the highest efficiency ever-reported for a thin film photovoltaic cell.

The I-V characteristics of this cell are shown in Figure 4. The subcell efficiencies of 20.6% and 2.5% were achieved for the GaAs top and the CIS bottom cells respectively, when the cell was measured at NASA Lewis Research Center. (The NASA measurements were conducted by Dr. D.J. Brinker.) Also included in the figure are the results of Boeing measurements that are indicated in the parentheses. This confirmed good agreement between the measurents by the two laboratories. The external spectral response curves of the same cell are shown in Figure 5 and indicate a significant improvement in IR response over the previously reported results [ref.7].

Among the completed tandem cells, the highest efficiency for the GaAs CLEFT cell was 20.6%. The highest efficiency for the $CuInSe_2$ cell under the GaAs CLEFT cell was improved to 3.0% using a double layer front AR coating on the GaAs CLEFT cell. The I-V characteristics and the external spectral response curves are shown in Figure 6. These cells demonstrate that a total efficiency over 23.5% can be readily achieved using this approach without significant process or structure changes. Further improvement up to 26% is projected when AlGaAs is incorporated as the absorber in the top cell.

Among the 4 cm^2 tandem cells on 2-mil glass, the highest efficiency achieved thus far was 20.8% one sun AM0. The subcell efficiencies of 18.2% and 2.6% were measured for the GaAs top and the $CuInSe_2$ bottom cells respectively. The I-V characteristics and the external spectral response curves of this cell are shown in Figure 7 and Figure 8. This cell weighed 188 mg without optimal substrate trimming before coverglass mounting, and provided a cell power output of 113 mW. After mounting a 1-mil thick coverglass using a space qualified adhesive, the cell weighed 258 mg, and provided an power ouput of 114 mW, yielding a cell-coverglass specific power of 442 W/kg. Cell-coverglass specific power up to 630 W/kg is projected with a 2-mil thick coverglass when optimal substrate and adhesive thicknesses are incorporated. Further improvement in specific power up to 750 W/kg is expected when the projected efficiency of 26% is achieved.

Environmental Effects

The radiation resistance of this tandem cell structure is expected to be excellent. Results of radiation experiments conducted with bare cells confirmed that the $CuInSe_2$ cells have superior radiation resistance compared to Si or GaAs cells, and that the

thin-film double-heterostructure GaAs cells are as resistant as bulk GaAs cells to 1 MeV protons and more resistant to 0.2 MeV protons and 1 MeV electrons. Details of this experiment have been reported elsewhere [ref.4].

An experiment was conducted to confirm the stability of the $CuInSe_2$ cell in a vacuum environment. The experiment consisted of exposure of the $CuInSe_2$ cells to pressure as low as 1×10^{-7} torr at various temperatures from 25°C to 110°C. No cell performance degradation was observed during this experiment. A thermal cycling experiment was also conducted to confirm survivability of tandem cell structure and ribbon interconnects by subjecting interconnected 4 cm^2 tandem cells to thermal cycling from 80°C to −130°C for up to 850 cycles. No significant difference in electrical characteristics was observed between the experimental samples and the control samples stored at room temperature.

Potential Applications

A voltage-matched module circuit based on three GaAs cells in parallel and three $CuInSe_2$ cells in series is proposed as a possible circuit unit. The schematic of this module string is shown in Figure 9. Even though this highly automatable interconnect method is sufficiently flexible to permit any circuit configuration, the present approach is based on a voltage-matched string. Since the temperature dependence of the tandem cell power and voltage at maximum power are important parameters for array and power system design, the temperature dependence of this tandem cell was characterized and the results plotted in Figure 10. As the $CuInSe_2$ cell power output is much less sensitive to voltage in the neighborhood of the maximum power point voltage, this voltage-matched two terminal configuration achieves over 98% of the four terminal circuit output over a broad operating temperature range as shown in Figure 11.

Correlation of on-orbit array level circuit performance in space to cell performance at the standard test conditions in the labaratory is complex, especially for the tandem cell, and difficult due to the application-specific nature of array performance optimization methods. Three generic orbits were chosen with two array structures, rigid and flexible, to compare the impacts of different cell technologies on the array level performance. Optimization of shielding thickness was conducted to minimize the array weight for the fixed end-of-life power output. Data available in the literature (refs. 4 and 13) were used for calculation of radiation and temperature effects on cell performance. The advanced photovoltaic solar array (APSA) design developed for JPL [ref. 14] was used as the base for the flexible array in the analysis. As shown in Table 1 and Table 2, this tandem cell approach provides significant array level weight and area savings over other cell technologies.

Program Status

We have recently increased our tandem cell throughput and fabricated quantities of cells that produce tens of watts of power in total. A significant increase in cell throughput and a 2 cm x 4 cm cell design with high active area utilization, and further performance improvement using AlGaAs instead of GaAs as absorber are currently being investigated to make GaAs(AlGaAs)/$CuInSe_2$ tandem cells more viable for near-term space power applications.

Conclusions

The efficiency of GaAs/$CuInSe_2$ thin-film tandem cells improved to 23.1%, one sun, AM0. This is the highest efficiency ever-reported for a thin-film photovoltaic cell. Further improvement up to 26% is projected when an AlGaAs absorber layer is incorporated in the top cell.

Lightweight GaAs/$CuInSe_2$ tandem cells (2-mil thick) were demonstrated with efficiencies as high as 20.8%. The cell with a 1-mil thick coverglass weighed 258 mg even without optimal substrate trimming. This provides a cell-coverglass specific power of 442 W/kg, and offers a potential for specific powers up to 750 W/kg with an AlGaAs top cell.

Environmental tests including radiation test, vacuum experiment and thermal cycling test were conducted and provided favorable results. On-array level performance was analyzed for three generic orbit levels to compare the impact of different cell technologies, and results indicated that a significant array weight and area savings can be achieved with these tandem cells. A voltage-matched module circuit is proposed and its projected performance is discussed. The current status of the program and the near term plan is also summarized.

References

[1.] H. F. MacMillan, H. C. Hamaker, G. F. Virshup and J. G. Werthen, *Conference Record 20th IEEE Photovoltaic Specialist Conference*, 48, 1988.

[2.] S. P. Tobin, S. M. Vernon, C. Bajgar, V. E. Haven, L. M. Geoffroy, M. M. Sanfacon, D. R. Lillington, R. E. Hart, K. A. Emery and R. J. Matson, *Conference Record 20th IEEE Photovoltaic Specialist Conference*, 405, 1988.

[3.] N. Ogasawara, S. Ochi, N. Hayafuji, M. Kado, K. Mitsui, K. Yamanaka, and T. Murotani, *Technical Digest of the International PVSEC-3*, 477, Tokyo, Japan, 1987.

[4.] R. M. Burgess, W. S. Chen, W. E. Devaney, D. H. Doyle, N. P. Kim, and B. J. Stanbery, *Conference Record 20th IEEE Photovoltaic Specialist Conference*, 909, 1988.

[5.] J. C. C. Fan and B. J. Palm, Solar Cells **12**, 401, 1984.

[6.] B. J. Stanbery, J. E. Avery, R. M. Burgess, W. S. Chen, W. E. Devaney, D. H. Doyle, R. A. Mickelsen, R. W. McClelland, B. D. King, R. P. Gale and J. C. C. Fan, *Conference Record 19th IEEE Photovoltaic Specialist Conference*, 280,1987.

[7.] N. P. Kim, R. M. Burgess, B. J. Stanbery, R. A. Mickelsen, J. E. Avery, R. W. McClelland, B. D. King, M. J. Boden and R. P. Gale, *Conference Record 20th IEEE Photovoltaic Specialist Conference*, 457, 1988.

[8.] R. A. Mickelsen, and W. S. Chen, *Conference Record 16th IEEE Photovoltaic Specialist Conference*, 781, 1982.

[9.] R. W.McClelland, C. O. Bozler and J. C. C. Fan, Appl. Phys. Lett. **37**, 560, 1980.

[10.] R. P. Gale, R. W. McClelland, B. D. King and J. V. Gormley, *Conference Record 20th IEEE Photovoltaic Specialist Conference*, 446, 1988.

[11.] R. P. Gale, J. C. C. Fan, G. W. Turner, and R. L. Chapman, *Conference Record 18th IEEE Photovoltaic Specialist Conference*, 296, 1985.

[12.] K. A. Emery, C. R. Osterwald, T. W. Cannon, D. R. Myers, J. Burdick, T. Glastfelter, W. Czubatyj and J. Yang, *Conference Record 20th IEEE Photovoltaic Specialist Conference*, 1246, 1988.

[13.] C. R. Osterwald, T. Glatfelter, and J. Burdick, *Conference Record 19th IEEE Photovoltaic Specialist Conference*, 188, 1987.

[14.] R. M. Kurland and P. Stella, *Proceedings of 9th Space Photovoltaic Research and Technology Conference*, 122, 1988, and also see *Advanced Photovoltaic Solar Array Prototype Fabrication*, Final Review Data Package, TRW Report No. 51760-6002-UT-00, JPL Contract No. 957990.

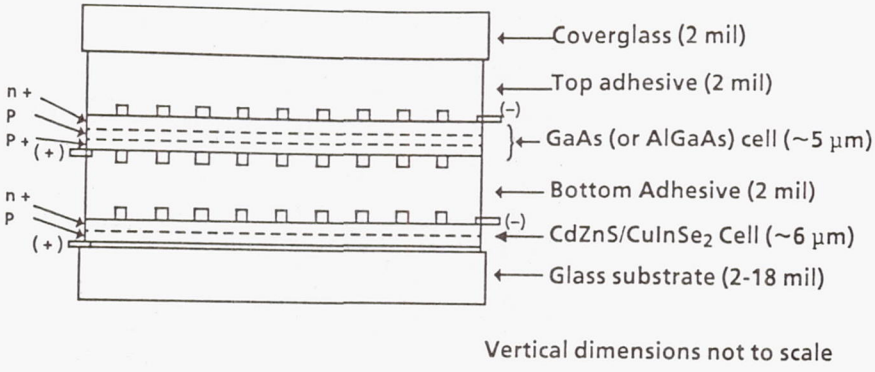

Figure 1. Schematic of Tandem Cell Structure

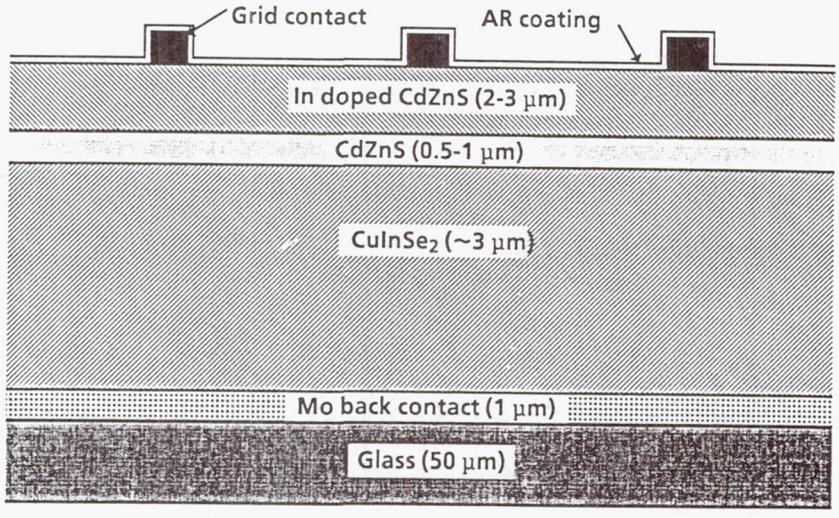

Figure 2. Cross Sectional View of $CuInSe_2$ Cell

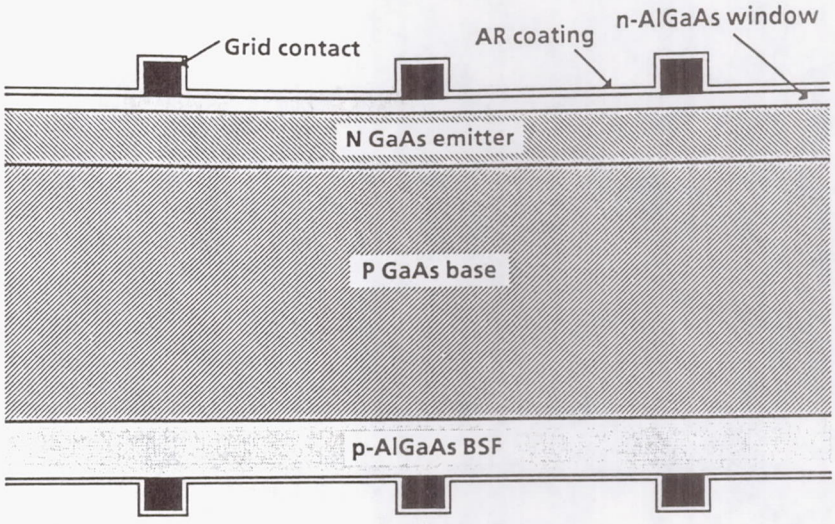

(a) Cross Sectional View of GaAs Thin-film Cell

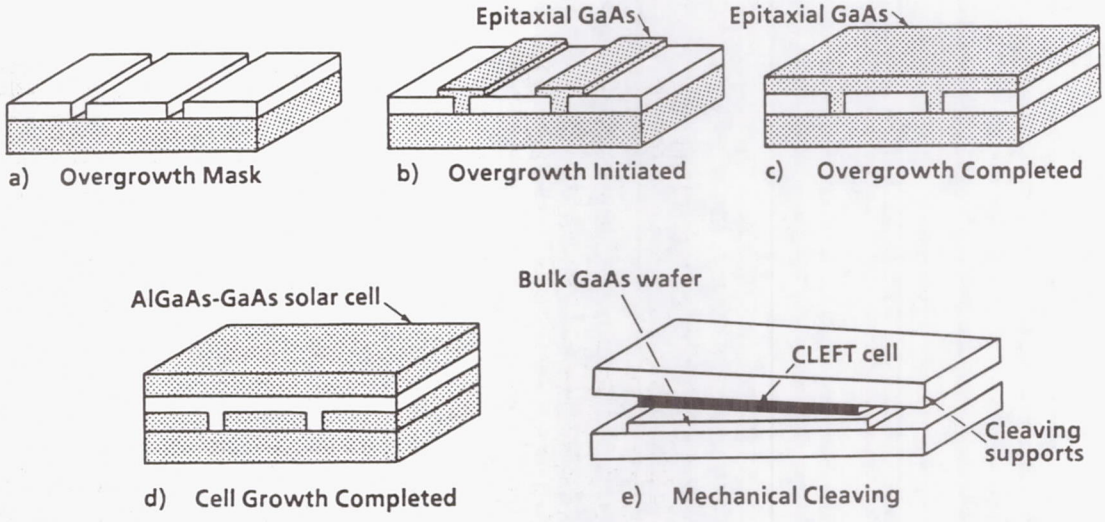

(b) Sequence of GaAs CLEFT Process (Solar cell device processing steps are not included)

Figure 3. Structure and Process Sequence of GaAs CLEFT Cell

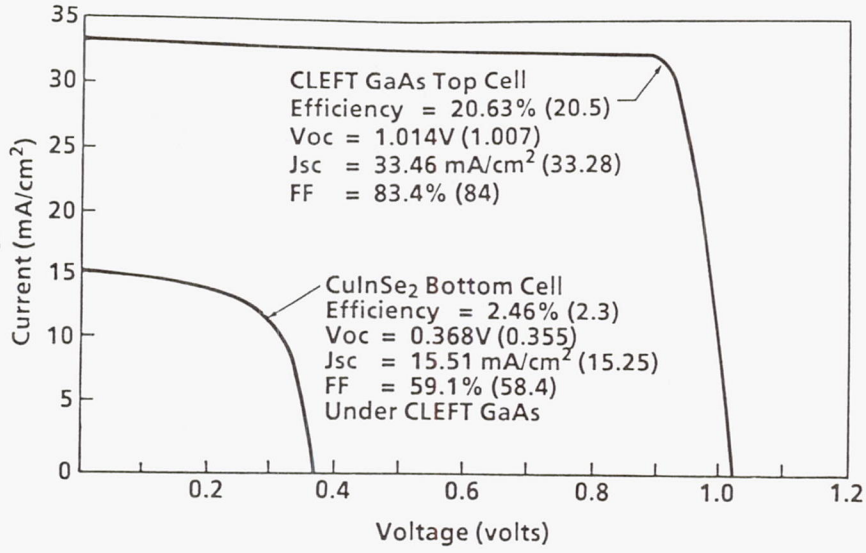

( ) Boeing measurements

- Total efficiency: 23.1% (22.8)
- Cell area: 4 cm^2

Figure 4. I-V Data on NASA Measured GaAs/$CuInSe_2$ Tandem Cell

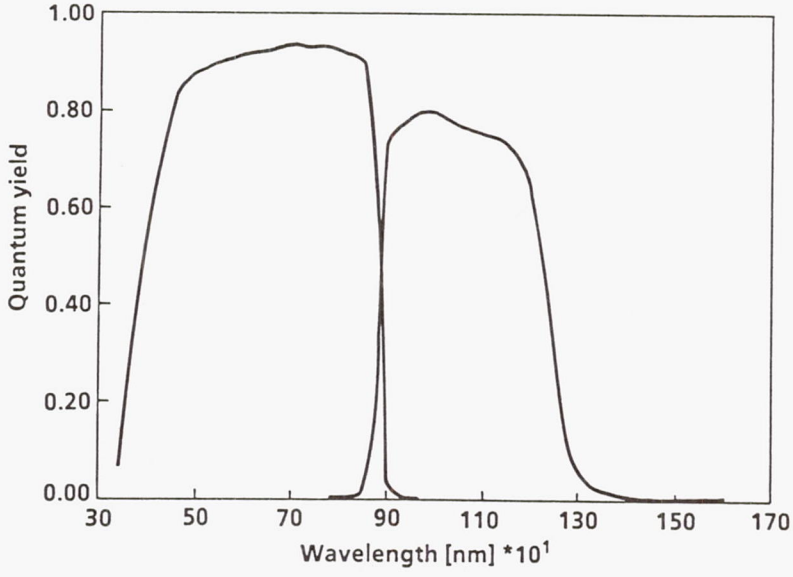

Figure 5. Spectral Response of A Tandem Cell

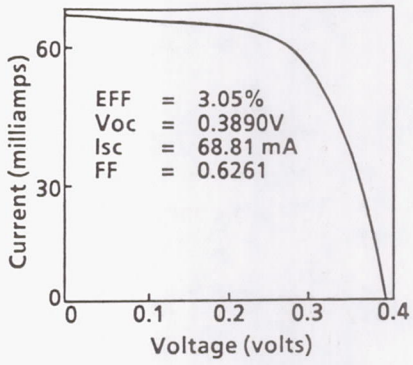

a) I-V Curves From a $CuInSe_2$ Cell Under the GaAs CLEFT

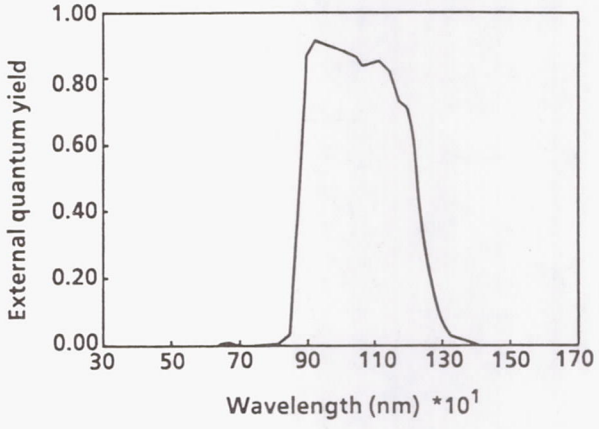

b) Spectral Response Curves From a $CuInSe_2$ Under the GaAs CLEFT

Figure 6. I-V and Spectral Response Curves From a $CuInSe_2$ Cell under the GaAs CLEFT Cell

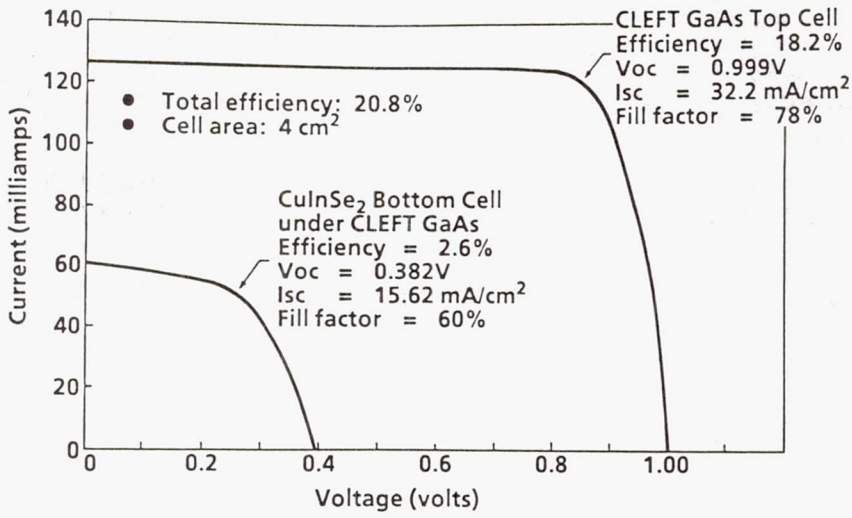

Figure 7. I-V Curves From a Lightweight Tandem Cell on 2-mil Substrate

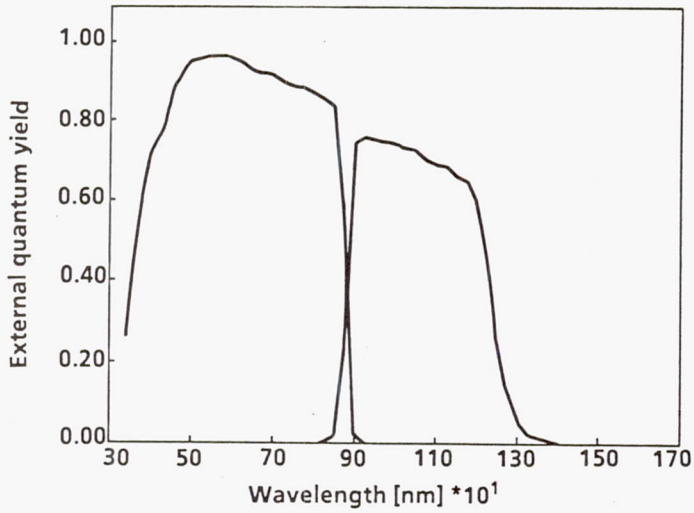

Figure 8. Spectral Response Curves From a Lightweight Tandem Cell on 2-mil Substrate

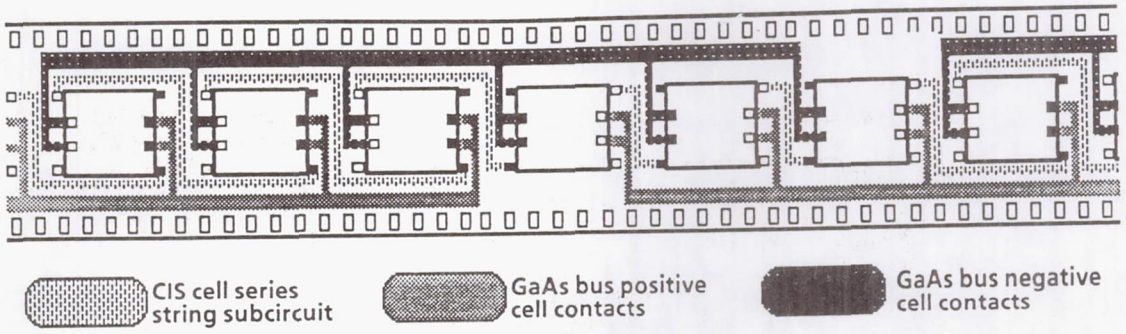

Figure 9. Schematic of Buss Interconnection for a Voltage-Matched String (The figure is not meant to illustrate the actual conductor pattern layout.)

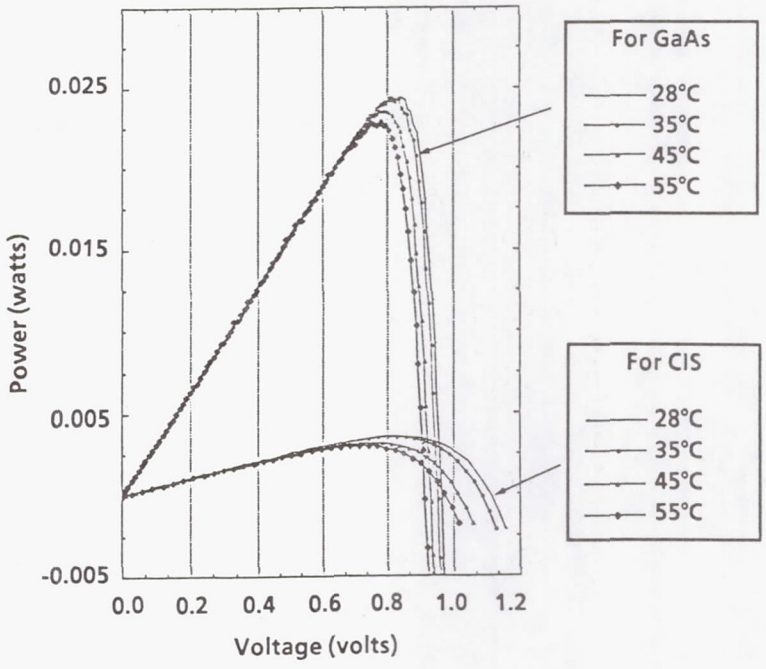

Figure 10. Power vs. Voltage Curves At Various Temperatures (Four terminal measurement, Plotted CIS voltages are three times of the actual CIS voltages.)

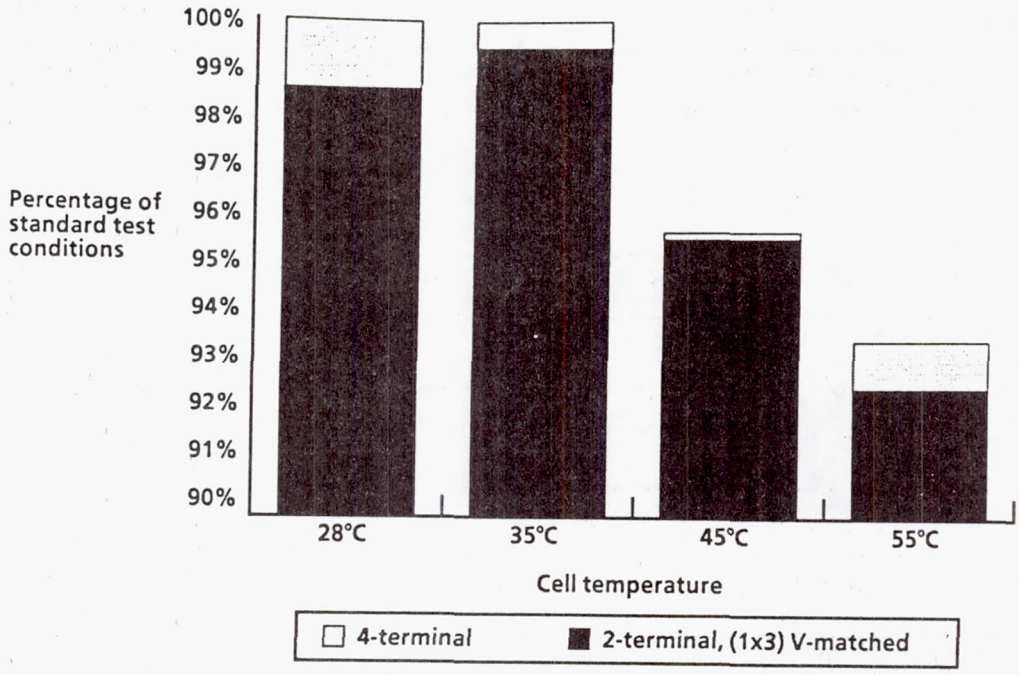

Figure 11. Relative Performance of a Voltage-Matched Two-Terminal String

Cell Technology (Thickness, BOL Efficiency at 28° C) / Orbital Environment	Silicon (8 mil, 14%)		Silicon (2 mil, 13.5%)		GaAs (8 mil, 19%)		GaAs/Ge (3 mil, 19%)		CLEFT GaAs (Thin, 2 mil substrate, 19%)		CLEFT GaAs/CIS Tandem (Thin, 2 mil substrate, 22%)	
	Array Weight (Kg)	Array Area (m^2)	Array Weight (Kg)	Array Area (m^2)	Array Weight (Kg)	Array Area (m^2)	Array Weight (Kg)	Array Area (m^2)	Array Weight (Kg)	Array Area (m^2)	Array Weight (Kg)	Array Area (m^2)
Low-Earth Orbit (LEO) • 270 N.M. Circular, 53° inclination • 5 year lifetime	89	19	78	18	182	13	65	14	60	13	53	12
Optional shielding thickness	All cases contain minimum shieldings of 2 mil thick coverglass and 5 mil thick Al facesheets											
Mid-Earth Orbit (MEO) • 5700 N.M., circular, 63° inclinaton • 7 year lifetime	157	24	147	24	229	15	100	17	102	16	85	16
Optional shielding thickness	F:27 mil, B:19 mil		F:25 mil, B:22 mil		F:27 mil, B:10 mil		F:22 mil, B:10 mil		F:22 mil, B:22 mil		F:18 mil, B:10 mil	
Geosynchronous Earth Orbit (GEO) • 19,700 N.M., circular, 0° inclination • 10 year lifetime	95	21	82	20	191	14	68	15	62	14	55	12
Optional shielding thickness	All cases contain minimum shieldings of 2 mil thick coverglass and 5 mil thick Al facesheets											

Table 1. Array Level Performance Comparison (For 2.5 KW EOL Rigid Array)

Cell Technology (Thickness, BOL Efficiency at 28° C) / Orbital environment	Silicon (4 mil, 14%)		Silicon (2 mil, 13.5%)		GaAs/Ge (3 mil, 19%)		CLEFT GaAs (Thin, 2 mil substrate, 19%)		CLEFT GaAs/CIS Tandem (Thin, 2 mil substrate, 22%)	
	Array Weight (Kg)	Array Area (m^2)	Array Weight (Kg)	Array Area (m^2)	Array Weight (Kg)	Array Area (m^2)	Array Weight (Kg)	Array Area (m^2)	Array Weight (Kg)	Array Area (m^2)
Low-Earth Orbit (LEO) • 270 N.M. Circular, 53° inclination • 5 year lifetime	47	41	41	39	41	30	35	27	34	25
Optional shielding thickness	All cases contain minimum shielding of 2 mil thick coverglass									
Mid-Earth Orbit (MEO) • 5700 N.M., circular, 63° inclinaton • 7 year lifetime	188	60	186	59	112	42	112	39	95	37
Optional shielding thickness	F:22 mil, B:20 mil		F:21 mil, B:20 mil		F:18 mil, B:10 mil		F:18 mil, B:4 mil		F:17 mil, B:12 mil	
Geosynchronous Earth Orbit (GEO) • 19,700 N.M., circular, 0° inclination • 10 year lifetime	56	53	48	51	43	31	36	29	35	27
Optional shielding thickness	All cases contain minimum shielding of 2 mil thick coverglass									

Table 2. Array Level Performance Comparison (For 5 KW EDL Flexible Array)

InP/$Ga_{0.47}In_{0.53}As$ Monolithic, Two-Junction, Three-Terminal Tandem Solar Cells

M.W. Wanlass, T.A. Gessert, G.S. Horner, K.A Emery and T.J. Coutts
Solar Energy Research Institute
Golden, CO

Summary

The work presented in this paper has focussed on increasing the efficiency of InP-based solar cells through the development of a novel, high-performance InP/$Ga_{0.47}In_{0.53}As$ two-junction, three-terminal monolithic tandem cell. Such a tandem is particularly suited to space applications where a radiation-hard top cell (i.e., InP) is required. Furthermore, the InP/$Ga_{0.47}In_{0.53}As$ materials system is lattice matched and offers a top cell/bottom cell bandgap differential (0.60 eV at 300K) suitable for high tandem cell efficiencies under AM0 illumination. A three-terminal configuration has been chosen since it allows for independent power collection from each subcell in the monolithic stack, thus minimizing the adverse impact of radiation damage on the overall tandem efficiency. Realistic computer modeling calculations predict an efficiency boost of 7-11% from the $Ga_{0.47}In_{0.53}As$ bottom cell under AM0 illumination (25°C) for concentration ratios in the 1-1000 range. Thus, practical AM0 efficiencies of 25-32% appear possible with the InP/$Ga_{0.47}In_{0.53}As$ tandem cell.

Prototype n/p/n InP/$Ga_{0.47}In_{0.53}As$ monolithic tandem cells have been fabricated and tested successfully. Using an aperture to define the illuminated area, efficiency measurements performed on a non-optimized device under standard global illumination conditions (25°C) with no antireflection coating (ARC) give 12.2% for the InP top cell and 3.2% for the $Ga_{0.47}In_{0.53}As$ bottom cell, yielding an overall tandem efficiency of 15.4%. With an ARC, the tandem efficiency could reach ~22% global and ~20% AM0. Additional details regarding the performance of individual InP and $Ga_{0.47}In_{0.53}As$ component cells, fabrication and operation of complete tandem cells and methods for improving the tandem cell performance, are also discussed.

Introduction

Current strategies for increasing the power-to-mass ratio and end-of-life efficiency of space cells include the development of tandem cells, both monolithic and mechanically stacked (e.g., GaAs/Ge [ref. 1] and GaAs/$CuInSe_2$ [ref. 2], respectively), concentrator cells [ref. 3] and radiation-hard InP cells [ref. 4]. The work presented in this report is based on an approach which merges the above strategies into a single monolithic, three-terminal tandem device by combining an InP top cell with a lattice

matched, infrared-sensitive $Ga_{0.47}In_{0.53}As$ (hereafter GaInAs) bottom cell. Monolithic, two-junction, three-terminal tandem cells have been fabricated previously in the $Al_xGa_{1-x}As/GaAs$ [ref. 5] and $GaAs_xP_{1-x}/GaAs_ySb_{1-y}$ [ref. 6] materials systems. However, to our knowledge the present work constitutes the first report of monolithic tandems demonstrated in the lattice matched, InP-based $InP/Ga_xIn_{1-x}/As_yP_{1-y}$ materials system. In the remaining sections, the techniques used and progress made in the early development of this new tandem space cell are reviewed.

Device Concept

A schematic illustration of the InP/GaInAs three-terminal tandem cell structure is given in figure 1. In its simplest form, the device consists of four lattice matched epitaxial layers grown on a single-crystal InP substrate. The n^+/p InP top cell and p^+/n GaInAs bottom cell junctions are of opposite polarity in order to provide a common intermediate p-type region for placement of the middle contact, resulting in a transistor-like n/p/n overall doping configuration. In practical tandems, the middle contact is placed below the photoactive region of the InP top cell so as to avoid enhanced carrier recombination (i.e., the p-InP base layer is grown thicker than that necessary to provide complete optical absorption - this is described in more detail in following sections). Top and back contacts are placed on the front surface of the InP cell emitter and the back surface of the n^+-InP substrate, respectively. The three-terminal design offers special advantages with respect to both characterization of the component subcells and operation in space. Quantum efficiency and current-voltage measurements can be made on each subcell individually and independently due to the common middle terminal. Furthermore, through proper design of the middle contact (i.e., by minimizing the associated series resistance) the subcells can operate as if independently connected, thus minimizing the deleterious impact of radiation damage on the combined tandem efficiency.

An n^+/p shallow-homojunction design (~30nm deep) identical to that used for high-efficiency InP single-junction cells [ref. 4] is employed for the top cell, whereas the GaInAs bottom cell utilizes a p^+/n deep-junction design (0.25-0.50μm deep) which takes advantage of the natural minority carrier confinement provided by the InP layers on the back surface of the GaInAs base layer and the front surface of the GaInAs emitter. The InP top cell responds to photons with energies above 1.35eV, while the GaInAs bottom cell responds to photon energies in the 0.75-1.35eV range. Thus, the tandem exhibits an extremely wide response range which extends from the ultraviolet to well into the infrared (out to 1.65μm). The tandem offers the additional advantage of employing a radiation-resistant InP top cell which should result in higher end-of-life/beginning-of-life (EOL/BOL) efficiency ratios as compared to AlGaAs/GaAs or GaAs/Ge tandem cells, for example.

Tandem Performance Modeling

Computer modeling studies have been used to evaluate the performance potential of the tandem under different operating conditions. The results shown in table 1 were calculated assuming unity absolute extemal quantum efficiency (AEQE) when computing the short-circuit current density (J_{sc}). However, realistic parameters characterizing the junction behavior were employed, including an ideality factor (n) of 1.03, along with the following form for the reverse-saturation current density (J_0)

$$J_0 = \beta(E_g)T^3\exp(-E_g/kT) \qquad [1]$$

where

$$\beta(E_g) = 3.85 * 10^{(0.24E_g)}\text{mA cm}^{-2}\text{K}^{-3} \qquad [2]$$

In these expressions, E_g is the bandgap (in eV) at absolute temperature T and k is Boltzmann's constant. $\beta(E_g)$ was determined by fitting to open-circuit voltage/short-circuit current density (V_{oc}/J_{sc}) data for actual state-of-the-art cells measured at SERI covering a wide bandgap range (0.75-1.93eV) and employing the usual expression for J_0 as a function of V_{oc} and J_{sc} given by

$$J_0 = J_{sc}/\{\exp[qV_{oc}/nkT] - 1\} \qquad [3]$$

Spectral and total irradiance values used for the AM0 spectrum were those recommended by the World Radiation Research Laboratory (1365.3 Wm^{-2}) [ref. 7]. Owing to the three-terminal tandem configuration, the top and bottom subcells were considered as being independently connected such that the computed tandem efficiency is equal to the sum of the individual subcell efficiencies in the stacked configuration. The bandgaps for InP and GaInAs at 25°C and 80°C were taken as 1.35 eV and 1.33 eV, and 0.75 eV and 0.73 eV, respectively. Additional details regarding the tandem cell model have been outlined in a previous paper [ref. 8]. The present modeling method represents a similar, but improved, procedure for calculating potential cell performance.

Although the bandgap combination offered by the InP/GaInAs tandem system is not the optimum for AM0 operation at 1 sun [ref. 8], the modeled efficiencies are quite respectable and represent 90-97% of the achievable maximum depending upon the operating temperature. The data in table 1 indicate that efficiencies of 26.9-33.0% are possible for operating temperatures in the 25-80°C range. As the concentration ratio is increased, the optimum-bandgap-pair values decrease due to the direct logarithmic dependence of V_{oc} and the fill factor (FF) on the ratio J_{sc}/J_0. As

a consequence, the InP/GaInAs bandgap combination is nearly optimum for concentration ratios in the 100-1000 range. The tandem efficiency increases substantially with increased concentration, particularly the contribution from the GaInAs bottom cell, and efficiencies of 34.7-42.7% are predicted for operation at 100-1000 suns. The concentration effect is especially pronounced and important for operation at higher temperatures. Note that the InP top cell is responsible for 73.5-83.6% of the total tandem efficiency under the range of conditions considered, thus emphasizing the need to develop high-performance InP cells in order to realize high tandem cell efficiencies. Nevertheless, the GaInAs bottom cell provides an impressive efficiency boost under all conditions due to the abundance of infrared radiation in the AM0 spectrum to which the InP cell is transparent. Using an arbitrary reduction factor of 0.75 to account for practical cell losses, it is concluded that practical AM0 efficiencies of 25-32% should be possible with the InP/GaInAs three-terminal tandem cell.

Performance of Component Subcells

Individual top and bottom cells have been fabricated and tested as a means of establishing a basis for assessing the highest achievable three-terminal tandem efficiency using current cell technologies. Figure 2 gives illuminated current/voltage (LIV) data under the AM0 spectrum, 25°C for a typical high-performance n/p InP shallow-homojunction (SHJ) cell without an ARC. The cell exhibits an efficiency of 12.4%, which would increase to ~17.5-18% with an optimally designed two-layer ARC. In a previous report [ref. 9], it was shown that the maximum efficiency of InP SHJ cells is limited by the relatively low values of the short-wavelength response and V_{oc}, both of which can be attributed to excessive surface recombination in the emitter layer. Effective passivation of the emitter surface will be necessary in order to realize InP cells with efficiencies approaching the theoretical limit. Moreover, the development of passivation techniques will allow deep-junction InP cells to be fabricated which will result in several advantages, including: i) a more robust cell design due to the deeper junction, ii) reduced performance sensitivity to junction depth variations and iii) reduced emitter sheet resistance, thus allowing the production of efficient InP concentrator cells, a key to achieving ultra-high efficiencies with the InP/GaInAs tandem cell.

LIV data for a p/n GaInAs cell with a 5μm-thick p-InP capping/window layer tested under similar conditions are shown in figure 3. The thick InP capping layer has been included on the GaInAs cell to simulate the optical filtering effected by an overlying InP top cell in the tandem configuration. An efficiency of 4.2% is observed for the low-bandgap GaInAs cell thus illustrating that the bottom cell offers a substantial efficiency gain over an InP cell alone, a result which is consistent with the modeling calculations for the InP/GaInAs tandem. It should be noted that large spectral mismatch corrections [ref. 10] (e.g., minus 20-30%) are typically necessary when measuring such low-bandgap devices using a Si reference cell to set the intensity

of a standard simulator (e.g., a Spectrolab X25) since most simulators are red-rich compared to the standard AM0 spectrum and, therefore, tend to give inflated J_{sc} values for cells with bandgaps below 1.0 eV. Another interesting characteristic of GaInAs cells with thick overlying InP filters is that their AM0 efficiency is actually higher than their global efficiency due to the absence of atmospheric absorption bands in the AM0 spectrum.

AEQE data for the same GaInAs cell, given in figure 4, show a high, "boxcar"-like response over the entire wavelength range (930-1650 nm) and sharp cutoffs at the bandgaps of both InP and GaInAs which indicate: i) complete optical filtering and effective surface passivation by the InP cap and ii) high-quality n-GaInAs base material and back surface minority carrier confinement by the n-InP buffer layer, respectively. From these results, it appears that the GaInAs junctions are at an advanced stage of development.

Using the results obtained for each of the component subcells, a combined tandem AM0 efficiency of 16.6% at 1 sun (25°C, no ARC) appears possible which would increase to 23-24% with an ARC. Additionally, the large increase in efficiency anticipated for operation at high solar concentration has been verified, at least partially, through flash-test concentrator LIV measurements performed at Sandia National Laboratories on SERI-grown GaInAs concentrator cells. For these cells, values of V_{oc} as high as 530mV have been observed at a concentration ratio of 471 suns. The above results demonstrate that the performance potential for the InP/GaInAs tandem cell is very high.

Epilayer Growth Procedures and Tandem Device Processing

The InP/$Ga_{0.47}In_{0.53}As$ heteroepitaxial device structures were grown by atmospheric-pressure metalorganic vapor phase epitaxy (APMOVPE) in a specially designed, homebuilt reactor system using trimethylindium, trimethylgallium, phosphine and arsine as the primary reactants with hydrogen sulfide and diethylzinc as the n- and p-type dopant sources, respectively. Growth was carried out on (100)-oriented, single-crystal InP substrates in a hydrogen ambient using a high-purity graphite susceptor inductively heated to 650°C. The structures were grown in a continuous manner without employing stopgrowth techniques at the heterointerfaces. Transmission electron microscopic (TEM) examination of InP/GaInAs multiple-quantum-well test structures grown in the same reactor has verified that extremely abrupt InP/GaInAs heterointerfaces (1-2 monolayers wide) are achieved using the current reactor design in the continuous growth mode. Additional characterization of the InP/GaInAs structures, using techniques such as photoluminescence (PL), electron probe microanalysis (EPMA), electron-beam-induced current (EBIC) and selective wet-chemical etching, has shown that the epitaxial growth process is under a level of control sufficient to produce high-performance tandem devices.

Prototype n/p/n InP/GaInAs tandems were successfully fabricated using the epitaxial device structure illustrated in figure 5. The structures were grown on n^+-InP substrates (S-doped) and consisted of the following sequence of layers: (i) an n-InP buffer layer, 0.5μm thick, which forms a minority carrier mirror for the back surface of the n-GaInAs base layer, (ii) an n-GaInAs base layer, 6μm thick, (iii) a p^+-GaInAs emitter layer, 200nm thick, (iv) a p^+-InP non-photoactive intermediate layer, 6μm thick, which serves to passivate the p^+-GaInAs emitter layer and also provides a conductive pathway for lateral current flow to the middle contact from both junctions, thus lowering the sheet resistance sufficiently to allow the use of a single middle contact gridline as explained in following sections, (v) a p^+-GaInAs stop-etch layer, 18nm thick, which facilitates correct placement of the middle contact, (vi) a p^+-InP back-surface field layer, 1μm thick, to enhance minority carrier confinement in the p-InP base layer, (vii) a p-InP base layer, 5μm thick and (viii) an n^+-InP emitter layer, 30nm thick.

Ohmic contacts to the back surface of the n^+-InP substrate (back contact) and the surface of the InP cell emitter layer (top contact) were formed by electroplating pure Au without annealing. The middle contact to the GaInAs stop-etch layer was formed by electroplating a three-layer metallization of Au/Zn/Au which was then annealed at 395°C for 1 minute in forming gas ($10\%H_2/N_2$). Wet chemical etching of the middle contact trough and the mesa isolation troughs was accomplished using the $10H_2SO_4$:$1H_2O_2$: $1H_2O$/Concentrated HCl system (both at room temperature) which etches the InP/GaInAs materials system selectively. $10H_2SO_4$:$1H_2O_2$:$1H_2O$ etches GaInAs at approximately 0.8 μm min^{-1}, whereas it attacks InP at an extremely slow rate (about 10 nm $min.^{-1}$). In contrast, concentrated HCl etches InP at about 8 μm $min.^{-1}$ and attacks GaInAs at only 25 nm $min.^{-1}$. The use of a thin GaInAs stop-etch layer in combination with the selective etching system makes correct placement of the middle contact in the structure a relatively straightforward procedure, and still allows for high transmission of sub-InP-bandgap photons to the GaInAs junction. The prototype tandem devices were tested without ARC's.

A long, narrow device geometry (1 cm x 0.165 cm overall dimensions) was used for the prototype devices in a "unit-cell" approach to testing the tandem concept as a precursor to developing three-terminal devices with fully interdigitated top/middle grids and square mesa geometries. This approach allowed for an array of five electrically isolated tandem cells from each growth run. The top/middle contact metallization scheme for the prototype consists of a middle contact pad at one end of the device with an associated single gridline, both of which are recessed (as described above) and interdigitated with a four-finger grid top contact facing the opposite direction with a contact pad at the other end. Details of the metallization and device mesas are shown in figure 6. The grid line parameters, including the width, height and spacing, were optimized for both the top and middle contacts using a computer model, with the sheet resistance, contact resistance and bulk metal resistivity as input parameters. The area required for the middle contact pad on the GaInAs stop-etch layer results

in a significant reduction of the top cell total area (0.140 cm^2 compared to 0.165 cm^2 for the bottom cell), thus, in practice, an aperture is used to illuminate selectively the intermediate region between the top and middle contact pads when performing LIV measurements.

Prototype Tandem Cell Performance

Completed tandem cells were characterized using AEQE and LIV techniques to assess current performance and also to identify areas for improvement. Composite AEQE data for one of the better tandems are shown in figure 7. Each component cell exhibits AEQE spectra which are essentially identical to those observed for high-performance top and bottom cells fabricated individually, which demonstrates that the integrity of the individual cells is maintained during the tandem growth and fabrication procedures. Note that the peak AEQE for the GaInAs cell (~81%) is substantially higher than for the InP cell (~66%) which is probably due to optical interference provided by the GaInAs stop-etch layer resulting in a mild antireflection effect for the GaInAs bottom cell.

Figure 8 shows composite LIV data for one of the better tandems measured under the global spectrum using an aperture to define the illuminated area (0.0822 cm^2), which corresponded to approximately one-half of the total junction area (0.165 cm^2). During these measurements, the cell not being tested was not connected to a load (i.e., it was left as an open circuit). The combined top cell/bottom cell efficiency is 15.4% global (roughly equivalent to 14% AM0) which would increase to ~22% global (~20 AM0) with a two-layer ARC.

Although the initial tandem efficiencies are encouraging, they fall short of the expected performance based on the results obtained with the individual top and bottom subcells. However, several possibilities for improving the tandem cell performance exist which should be relatively straightforward to implement. The present tandem device design suffers from several loss mechanisms which can be delineated as follows: i) the top/middle contact metallization results in excessive obscuration of the bottom cell, while the middle contact trough leads to a substantial loss of top cell area, ii) use of an aperture during LIV measurements results in a decreased value of J_{sc}/J_0 which lowers the V_{oc} and FF of both the top and bottom cells, iii) the InP top cell performance is limited by surface recombination and iv) optical reflection is high.

Solutions to the above-mentioned problems, in the order listed, include: i) application of Entech prismatic covers to reduce optical losses due to grid obscuration and to redirect light away from the middle contact troughs back into the InP top cell, ii) development of improved fully interdigitated grids with reduced bus-bar (contact pad) areas, thus eliminating the need to use apertures when performing LIV measurements, iii) development of emitter surface passivation techniques for InP cells.

Methods under current investigation include the use of lattice matched $Al_{0.48}In_{0.52}As$ pseudomorphic $Ga_xIn_{1-x}P$ window layers and iv) development of optimally designed ARC's. This task will require a detailed knowledge of the optical constants $n(\lambda)$ and $k(\lambda)$ of doped InP and GaInAs in order to model correctly the optical characteristics of the tandem stack. These data are currently unavailable, however, methods for determining such information are presently under development at SERI.

Conclusion

The InP/GaInAs three-terminal tandem cell is a promising photovoltaic device for achieving ultra-high efficiencies, high power-to-mass ratios and high EOL/BOL efficiency ratios in space power applications. Early experimental results regarding the fabrication and performance of this novel tandem cell have demonstrated its potential in these areas. Methods for improving the tandem cell efficiency have been identified and efforts to realize the full practical potential of the device are currently underway.

References

[1.] S. M. Vernon, S. P. Tobin, C. Bajgar, V. E. Haven, L. M. Geoffroy, D. R. Lillington and R. E. Hart, *Proc. NASA Conf. Space Photovoltaic Research and Technology*, 167, 1988.

[2.] N. P Kim, B. J. Stanbery, R. P. Gale and R. W. McClelland, *Proc. NASA Conf. Space Photovoltaic Research and Technology*, 138, 1988.

[3.] H. C. Hamaker, M. Grounner, N. R. Kaminar, M. S. Kuryla, M. J. Ladle, D. D. Liu, H. F. MacMillan, L. D. Partain, G. F. Virshup, J. G. Werthen and J. M. Gee, *Proc. NASA Conf. Space Photovoltaic Research and Technology*, 292, 1988.

[4.] M. W. Wanlass, T. A. Gessert, K. A. Emery and T. J. Coutts, *Proc. 20th IEEE PVSC*, 491, 1988.

[5.] L. Mayet, M. Gavand, B. Montegu and A. Laugier, *Proc. 20th IEEE PVSC*, 597, 1988.

[6.] L. M. Fraas, B. K. Shin, J. A. Cape, R. A. Ransom and D. E. Sawyer, *Proc. 16th IEEE PVSC*, 655, 1982.

[7.] C. Wehrli, *Physical Meteorological Observatory and World Radiation Center, tech. rep. 615*, Davos-Dorf, Switzerland, 1985.

[8.] M. W. Wanlass, K. A. Emery, T. A. Gessert, G. S. Horner, C. R. Osterwald and T. J. Coutts, *Proc. 9th PVAR&D Meeting*, 1989. To be published in Solar Cells.

[9.] M. W. Wanlass, G. S. Horner, T. A. Gessert and T. J. Coutts, *Proc. 1st Intemational Conference on Indium Phosphide and Related Materials for Advanced Electronic and Optical Devices*, 1989. To be published by SPIE.

[10.] C. R. Osterwald, Solar Cells **18**, 269, 1986.

Table 1. Computer modeling summary of the performance of an InP/$Ga_{0.47}In_{0.53}As$ independently connected tandem solar cell under AM0 illumination as a function of the operating temperature and solar concentration ratio.

Temperature (°C)	Concentration Ratio	InP Top Cell Efficiency (%)	$Ga_{0.47}In_{0.53}As$ Bottom Cell Efficiency(%)	Tandem Cell Efficiency (%)
25	1	25.9	7.1	33.0
	10	27.8	8.5	36.3
	100	29.6	9.9	39.5
	1000	31.4	11.3	42.7
80	1	22.5	4.5	26.9
	10	24.7	6.1	30.8
	100	26.9	7.8	34.7
	1000	29.1	9.4	38.5

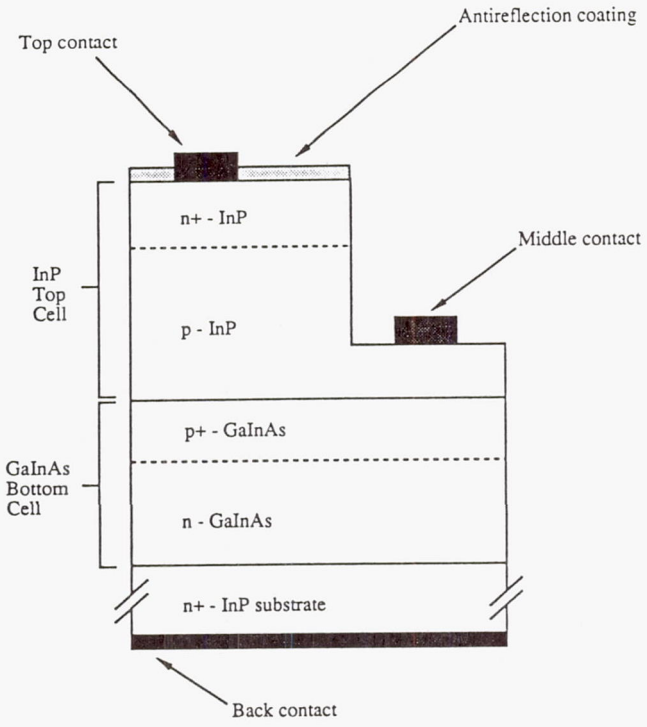

Figure 1. Schematic cross sectional diagram of the InP/$Ga_{0.47}In_{0.53}As$ three-terminal tandem solar cell.

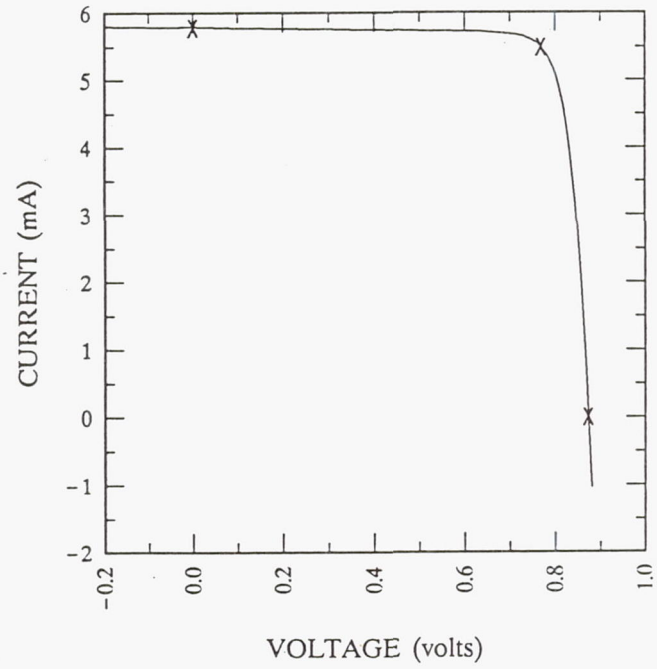

V_{oc} = 0.8735 volts
I_{sc} = 5.782 mA
J_{sc} = 23.13 mA/cm²
P_{max} = 4.224 mW
Fill factor = 83.64 %
I_{max} = 5.496 mA
Efficiency = 12.4 %
V_{max} = 0.7686 V

Figure 2. LIV data for a high-performance n/p InP shallow-homojunction solar cell (AM0, 25°C, no ARC).

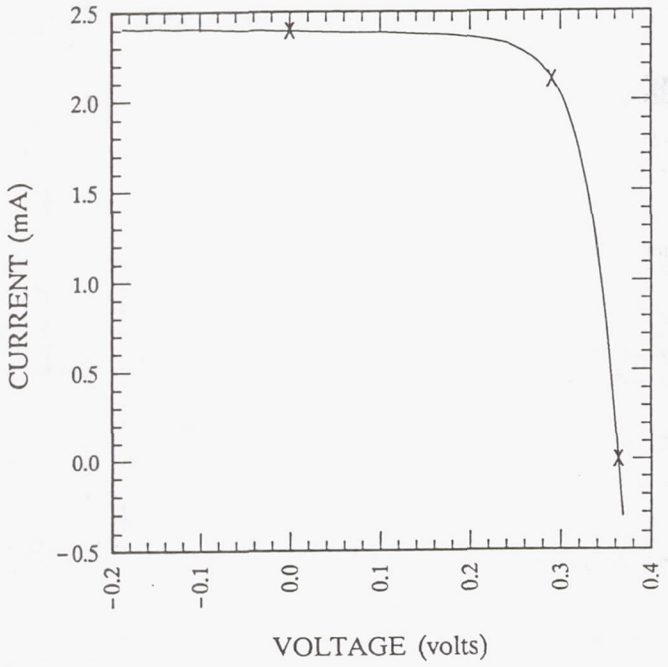

V_{oc} = 0.3635 volts
I_{sc} = 2.397 mA
J_{sc} = 22.19 mA/cm²
P_{max} = 0.615 mW
Fill factor = 70.62 %
I_{max} = 2.119 mA
Efficiency = 4.2 %
V_{max} = 0.2904 V

Figure 3. LIV data for a high-performance p/n $Ga_{0.47}In_{0.53}As$ solar cell with a 5μm-thick InP capping layer (AM0, 25°C, no ARC).

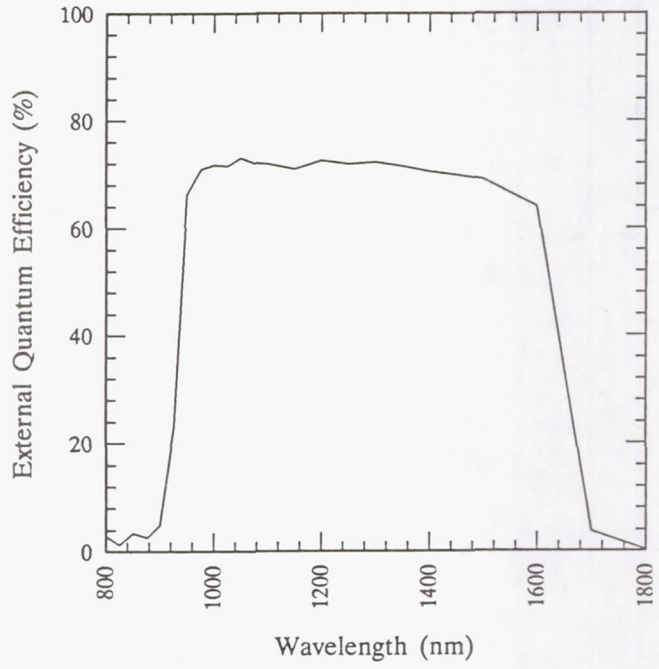

Figure 4. AEQE data (no ARC) for the $Ga_{0.47}In_{0.53}As$ cell with LIV data given in figure 3.

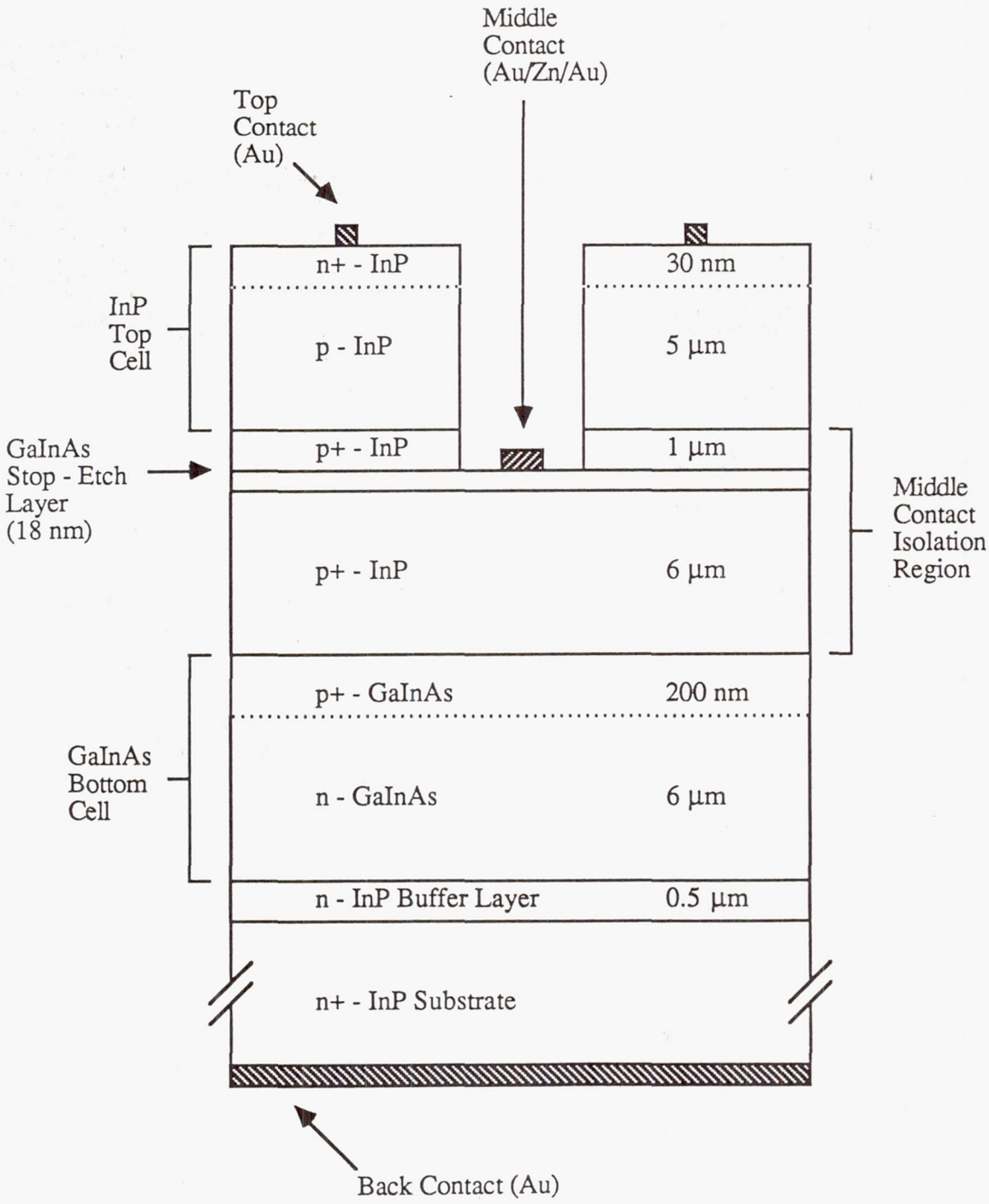

Figure 5. Cross sectional diagram of the prototype InP/$Ga_{0.47}In_{0.53}As$ three-terminal tandem solar cell structure.

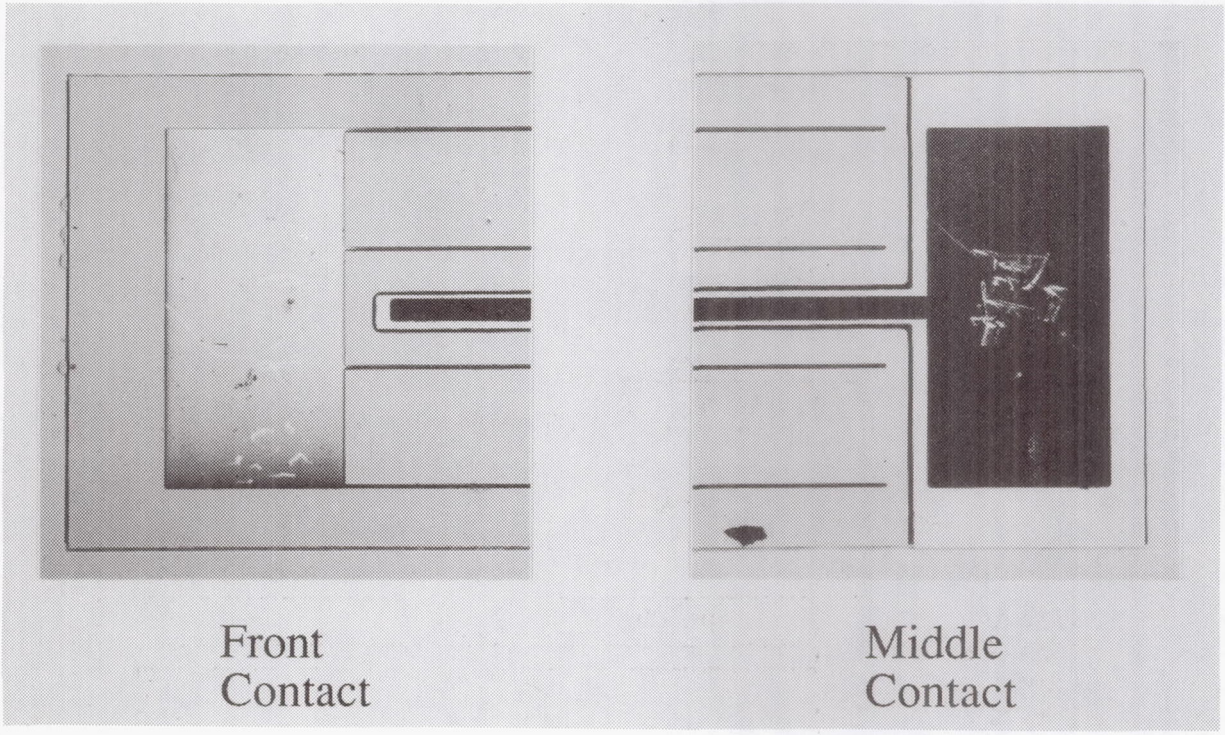

Figure 6. Optical micrographs showing details of the front and middle contact areas (plan view, 40X) on an actual prototype InP/$Ga_{0.47}In_{0.53}As$ three-terminal tandem cell.

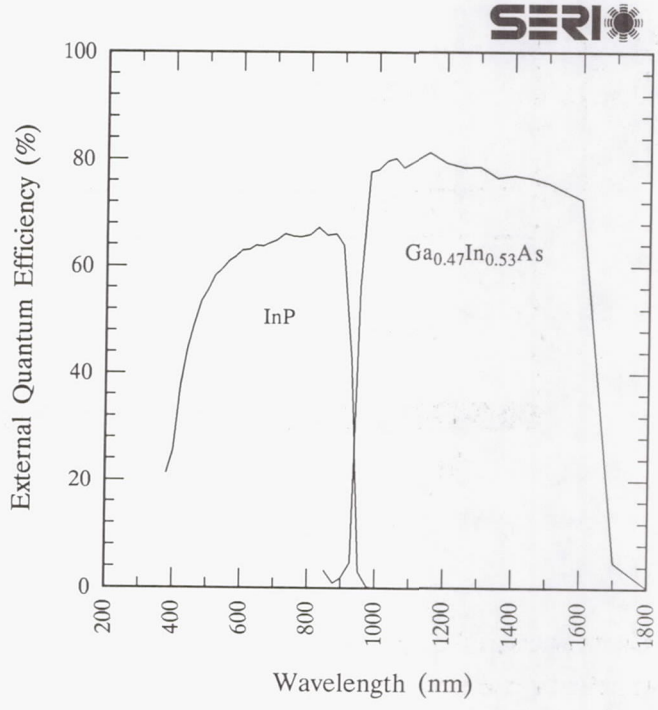

Figure 7. Composite AEQE data (no ARC) for an n/p/n InP/$Ga_{0.47}In_{0.53}As$ tandem cell.

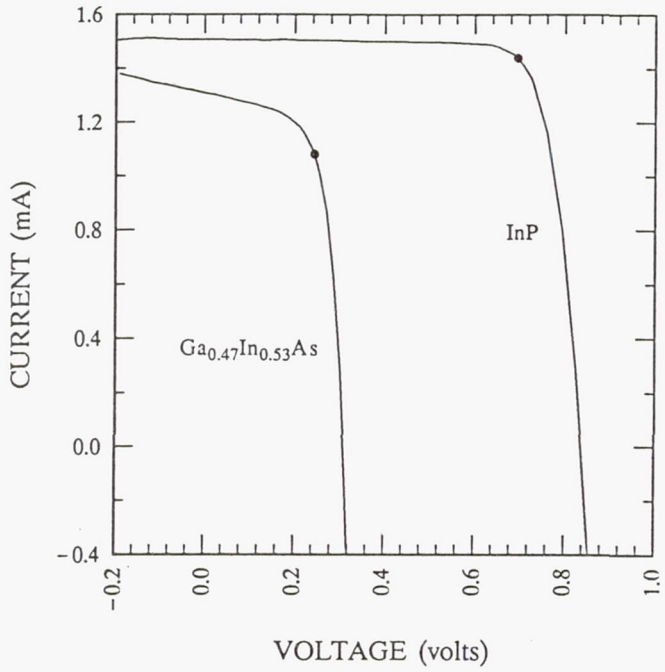

InP Top Cell	$Ga_{0.47}In_{0.53}As$ Bottom Cell
V_{oc} = 0.838 V	V_{oc} = 0.310 V
J_{sc} = 18.4 mAcm^{-2}	J_{sc} = 15.9 mAcm^{-2}
FF = 0.794	FF = 0.647
Eff. = 12.2 %	Eff. = 3.2 %

Figure 8. Composite LIV data (Global, 25°C, no ARC) for an InP/ $Ga_{0.47}In_{0.53}As$ three-terminal tandem cell using an aperture to define the illuminated area.

Session 2
GaAs Cells

Preceding Page Blank

Phase Equilibrium Modeling for High Temperature Metallization on GaAs Solar Cells*

M. A. Chung
Wright Research and Development Center
Wright-Patterson AFB, OH

J. E. Davison and S. R. Smith
University of Dayton Research Institute (UDRI)
Dayton, OH

Recent trends in performance specifications and functional requirements have brought about the need for high temperature metallization technology to be developed for survivable DOD space systems and to enhance solar cell reliability. The temperature constitution phase diagrams of selected binary and ternary systems have been reviewed to determine the temperature and type of phase transformation present in the alloy systems. Of paramount interest are the liquid-solid and solid-solid transformations. This data is being utilized to aid in the selection of electrical contact materials to gallium arsenide solar cells. Published data on the phase diagrams for binary systems is readily available [refs. 1-5]. However, information for ternary systems is limited. A computer model is being developed which will enable the phase equilibrium predictions for ternary systems where experimental data is lacking.

Introduction

The challenge to obtaining high temperature contacts to solar cells is to control the diffusion properties of the contact metals. Commonly used contact metals such as Ag and Au diffuse considerable distances in GaAs and if allowed to reach the junction (≤ 0.5 μm for space cells) considerable performance degradation will result. Diffusion barriers developed by Varian [ref. 6] and Spire Corporation [ref. 7] have demonstrated stability up to 500°C and 550°C, respectively for 5 minutes. At higher temperatures, dissociation of GaAs occurs and puddling of liquid Ga becomes the chief failure mechanism. A second problem at high temperatures (> 500°C) is the direct reaction between the GaAs compound and other elements to form ternary or more complex compounds or alloys.

GaAs decomposes into an arsenic vapor phase and an elemental liquid Ga phase which readily reacts with electrical conductor materials such as Au, Ag, Cu, or Al. The GaAs decomposition is resolved by applying an AlGaAs capping layer (see figure 1) to prevent losing arsenic via the vapor phase. The direct metallurgical reaction between GaAs and another element/metal is best addressed by choosing metals which prevent or limit the reaction.

* UDRI is being supported by the Aero Propulsion and Power Laboratory, Wright Research and Development Center under Contract F33615-86-C-2722, Task 13.

Approach

Our approach for selecting contact materials is to use the equilibrium temperature constitution phase diagrams. These phase diagrams show the metallurgical phases occurring in the alloy system of interest. Of particular interest are those ternaries containing gallium, arsenic, and one of the electrical contact metals. Extensive compilations exist for binary systems [refs 1, 2, and 3] but a limited number of phase diagrams for ternary systems are available [refs. 8 and 9]. Using the data in the binary diagrams to determine the necessary thermodynamic data, we can construct the appropriate ternary phase diagram. Computational methods are being developed and utilized to predict/calculate the ternary boundaries. These calculated ternary phase boundaries are performed using thermodynamic models of the free energy of the ternary phases and where necessary, the calculations supplemented with experimental data. These experimental measurements are utilized in an iterative manner with the computations to improve the reliability of the phase diagrams. The projections of the ternary phase diagrams are compared to known experimental results at selected alloy compositions to verify the projections from the binary diagrams.

Phase Diagram Calculations

A FORTRAN IV code for calculating the equilibrium phase diagrams of binary systems containing intermediate compound phases has been developed. The computations of the phase boundaries for this particular class of phase diagrams requires, as input, the following data:

1. The melting temperatures and heats of fusion of the elements.
2. The composition, melting temperature, and heat of fusion of the compound.
3. The binary quasi-chemical interaction parameter for the liquid and solid phase.

A phase diagram calculated with this model is shown in figure 2. Since the primary purpose of this model is to utilize the phase diagram to determine the liquid-solid transformation temperatures, only those phase boundaries involved in a liquid-solid reaction are calculated. Those boundaries are shown as solid lines in figure 2. The solid-solid transformations are shown as dotted lines. Two eutectic transformations occur in this type of phase diagram and are shown as e1 and e2. The temperatures of these eutectic reactions are the temperatures at which liquid-solid transformations will occur on heating in this type of system. In all instances, these temperatures occur below the melting point of either the compound or the elements.

Before the model for figure 2 could be developed, a code had to be written to calculate the binary eutectic phases. This requires that the code calculates the liquidus, solidus, and solvus phase boundaries as well as the temperature and composition of the eutectic transformation. The binary eutectic is one of the basic building blocks of

our modeling. By combining it with the phase diagram of binary systems with intermediate binary phases, ternary gallium arsenide phase diagrams can be calculated.

Figure 3 is a simple binary eutectic phase diagram. There are three single-phase regions, the liquid phase and two solid phases, which are labeled as the α and β phases. In addition, three two-phase regions exist, the α+liquid region, the β+liquid region, and the $\alpha + \beta$ region. The intersection of the two liquidus boundaries, e1, locates the eutectic temperature and composition. The temperature and type of transformation for a combination of materials can be determined by analyzing the phase diagram.

Preliminary Model Verifications

The results of the calculation for the Ga-Zn binary eutectic system are shown in figure 4. Because of the large difference between the melting points of Ga and Zn, the eutectic point (e1) is displaced toward the lower melting element, Ga. In comparing figures 3 and 4, it is seen that the liquidus 1 and solidus 1 boundaries are almost completely lost and the solidus 2 boundaries differ. The behavior of the solidus boundary is referred to as exhibiting retrograde solubility [ref. 3]. This means that the solubility of gallium in solid zinc increases as the temperature decreases from the melting point of zinc. At a temperature between the melting point and the eutectic temperature, the solubility reaches a maximum value and then decreases as the temperature continues to decrease.

Figure 5 is previously published experimental data for the Ga-Zn binary eutectic. Comparing this diagram to the one generated by our model (figure 4) shows almost identical results and thereby indicating that our model is accurate.

Discussion and Conclusion

Verification of the accuracy of our model for binary systems with intermediate compound phases is necessary before proceeding to the ternary systems. This will be done by comparing diagrams from our model to published experimental data. Results to date indicate that our model should be accurate and will therefore be an invaluable tool in theoretically determining the thermal stability of ternary systems prior to any experimental activity. Presently, an Edisonian approach is the way that high temperature metallization for GaAs solar cells is being developed.

References

[1.] M. Hansen, *Constitution of Binary Alloys, McGraw-Hill Book Co.*, New York, (1958).

[2.] R. Elliott, *Constitution of Binary Alloys, 1st Supplement*, McGraw-Hill Book Co., New York, (1965).

[3.] F. Shunk, *Constitution of Binary Alloys, 2nd Supplement*, McGraw-Hill Book Co., New York, (1969).

[4.] M. Panish, Journal of the Electrochemical Society: Solid State Science, 516 (1967).

[5.] C. Cooke and W. Hume-Rothery, Journal of the Less Common Metals, 10942 (1966).

[6.] W. E. Horne et al., *High Temperature Contact Metallizations For Advanced Solar Cells*, AFWAL-TR-84-2044 (1984).

[7.] Stephen P. Tobin, *Highly Temperature Stable, Low Shadow Loss Metallization for Superior Space Solar Cells*, AFWAL-TR-88-2058 (1988).

[8.] Rainer Schmid-Fetzer, J. Electron. Mat. **17** (1988).

[9.] Stanley R. Williams, *Proc. Int'l. Conf. on Semiconductor and Integrated Circuit Technology*, World Scientific Publishing Co. (1986).

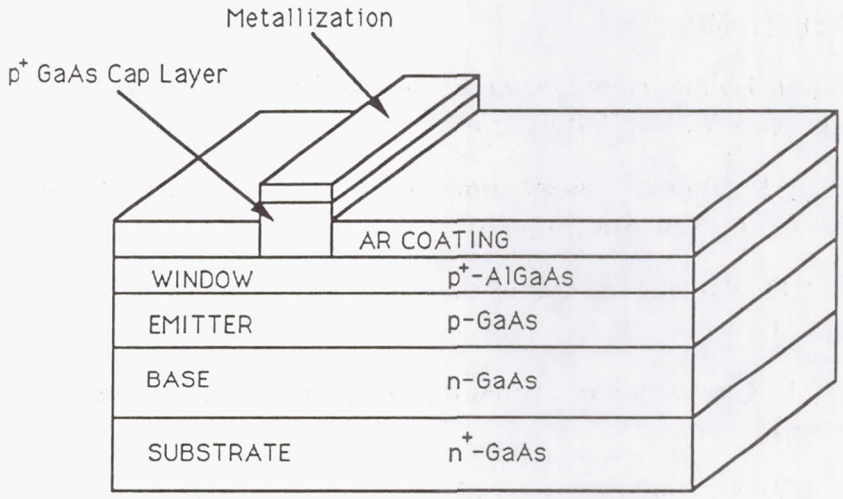

Figure 1 - Schematic of a typical GaAs solar cell with grid contact.

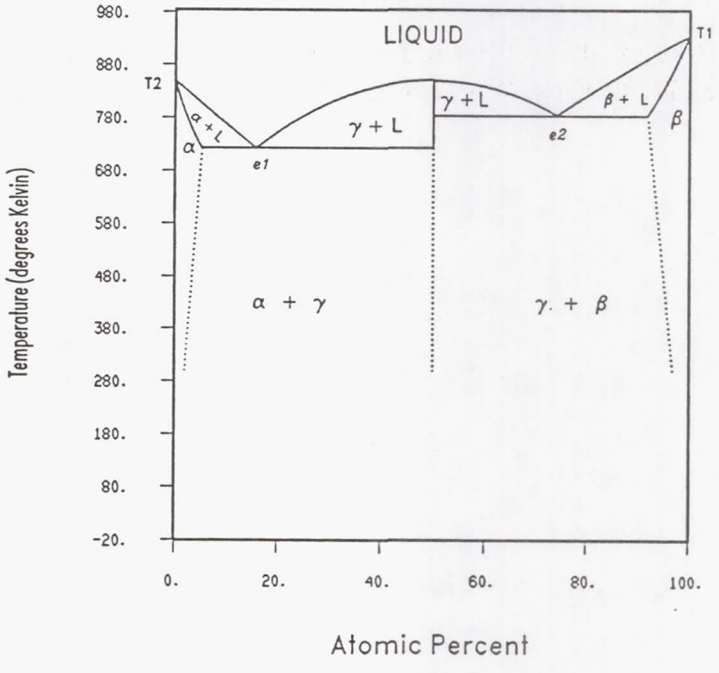

Figure 2. - Phase diagram for a binary system containing an intermediate melting compound phase.

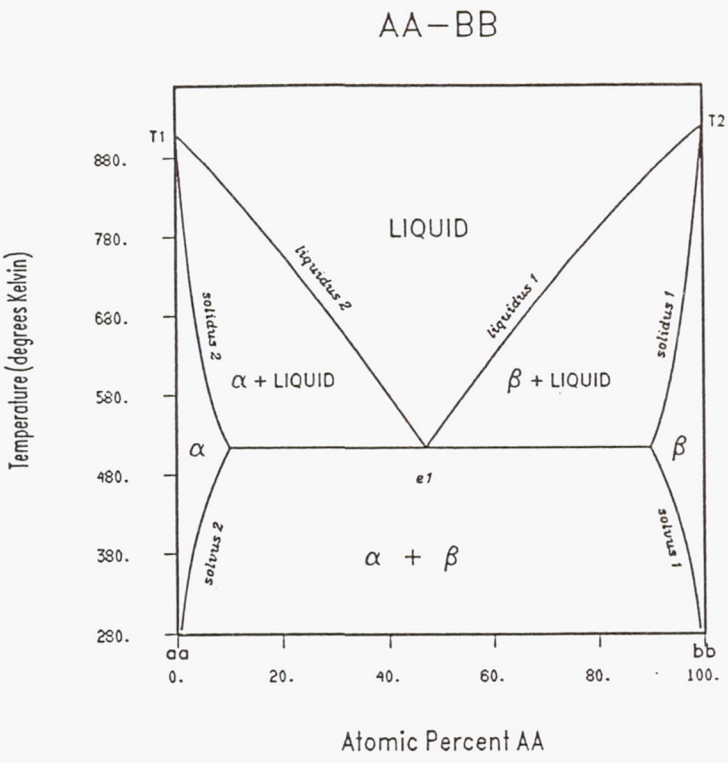

Figure 3. - Binary eutectic phase diagram.

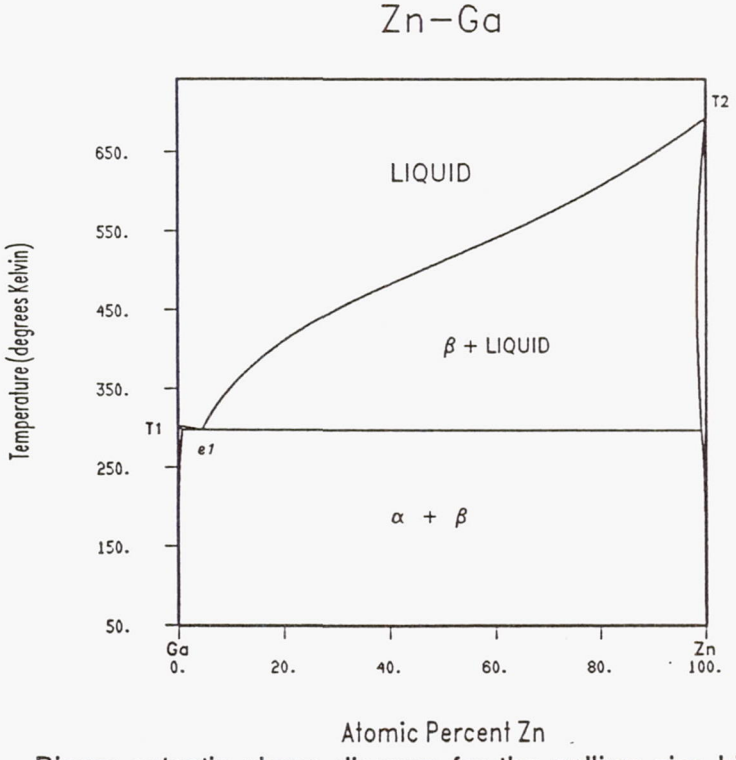

Figure 4. - Binary eutectic phase diagram for the gallium-zinc binary system.

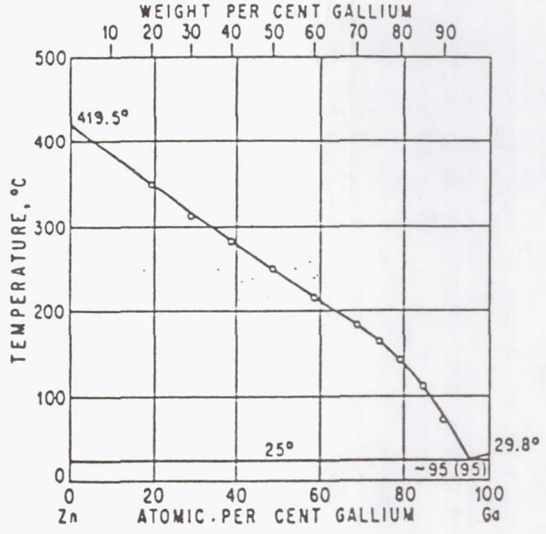

Figure 5. - Experimental phase diagram for gallium-zinc (ref. 3).

GaAs Solar Cell Photoresponse Modeling Using PC-1D V2.1

D.A. Huber, L.C. Olsen, G. Dunham and F.W. Addis
Washington State University/Tri-Cities
Richland, WA

Introduction

In this study, photoresponse data of high efficiency GaAs solar cells have been analyzed using PC-1D V2.1. This paper discusses the approach required to use PC-1D for photoresponse data analysis, and the physical insights gained from performing the analysis. In particular, the effect of $Al_xGa_{(1-x)}As$ heteroface quality has been modeled. Photoresponse or spectral quantum efficiency is an important tool in characterizing material quality and predicting cell performance [ref. 1]. The strength of the photoresponse measurement lies in the ability to precisely fit the experimental data with a physical model. PC-1D provides a flexible platform for calculations based on these physical models.

Cell Fabrication and Performance

GaAs cell structures studied in this work were P/N homojunctions with $Al_xGa_{(1-x)}As$ heteroface layers for front and back minority carrier reflectors. All cells were 1.5 cm × 1.5 cm and fabricated from films grown on horizontal Bridgman wafers by MOCVD. The cells were fabricated from epi-structures supplied by SPIRE Corp., as well as grown in WSU/TC's SPI-MO CVD 500XT reactor. The SPIRE epitaxial layers were grown at atmospheric pressure using trimethylgallium, trimethylaluminum and 10% arsine in H_2. The WSU/TC cells were grown at low pressure using pure arsine. N-type doping was accomplished using silane and the p-type doping with dimethylzinc in H_2 in both cases. The basic structure described in Figure 1 was constant for these cells which facilitated side-by-side comparison of performance and material quality. Contacts for the devices were made by electroplating Au for the front contact and Au/Sn for the back contact. After sintering, the GaAs cap was removed between the contact fingers and a mesa was etched around the perimeter. The individual cells selected for this study correspond to varying growth conditions which affect the cell's performance [ref. 2]. These conditions include growth temperature of GaAs and $Al_xGa_{(1-x)}As$ as well as dopant flows and change of temperature at the heteroface. Efficiencies for these cells range from 18% to 22% for one-sun AM1.5 illumination. Cell performance is listed in Table 1.

Modeling Photoresponse Data with PC-1D V2.1

The Iowa State code PC-1D utilizes a finite element numerical approach to solve the semiconductor equations [ref. 3]. Version 2.1 allows significant improvements in the complexity of the problems that can be solved, compared to earlier versions [ref. 4]. Several key additions have proven especially applicable to the modeling of GaAs solar cells. The program permits modeling of minority carrier confinement due to the $Al_xGa_{(1-x)}As$ heteroface with recombination at the interface. PC-1D is equipped with an internal model for the absorption of $Al_xGa_{(1-x)}As$ as a function of x and permits the use of an external model or absorption data. Up to three regions of different material parameters can be used to define the device, each with its own doping profiles and electronic and optical properties. The ability to model the grading of material properties at the interface between each region increases the usefulness of the program to model realistic structures. Recombination of the electron hole pairs can be defined in each region by S-R-H band to band transitions or through user-defined deep level transitions. The recombination model can also account for Auger recombination, surface recombination at the interfaces within the device or saturation current terms.

The first approach at modeling heteroface GaAs solar cells divided the device into two materials an $Al_xGa_{(1-x)}As$ region in front of the GaAs homojunction region. The grading between these two materials was set at the minimum value of 10 Å, an abrupt interface. This generated photoresponse which was independent of surface recombination due to the high drift fields produced. Reasonable values for the grading thickness always led to the same result since the ΔE_G is large. The response of the cells, however, showed definite signs of front surface recombination. Incorporating our previously reported "dead layer" model allowed for an additional interface and recombination current [ref. 2].

For the cells studied, modeling studies with PC-1D predict the necessity of a thin defective GaAs region located between the emitter and the front $Al_xGa_{(1-x)}As$ layer where defect states result in current loss due to recombination within the region. This approach models the $Al_xGa_{(1-x)}As$ window region, a two-region emitter consisting of the defective layer and a high quality region, and an n-type base region. This is accomplished using three material parameter files - a wide bandgap $Al_xGa_{(1-x)}As$ material, a defective low-lifetime GaAs material, and a high quality GaAs material. Figure 2 shows a bandgap diagram illustrating the modeled regions. The effect of the back $Al_xGa_{(1-x)}As$ reflector was modeled only by a surface recombination velocity in this study since absorption of photons is inconsequential. This allows more flexiblity in the modeling of the front interface .

Results and Discussion

The model was used to produce a very close fit to the unique photoresponse of several cells. Figures 3 through Figure 7 show the experimental data for several cells as well as the modeled curves for comparison. The values modeled for individual cells are given in Table 2. The defective region size increases with $Al_xGa_{(1-x)}As$ growth temperature, which correlated with the length of transition time between GaAs growth and $Al_xGa_{(1-x)}As$ growth. Defective layer thickness varied from less than 30 Å to greater than 100 Å. Front surface recombination velocities ranged from 1×10^4 cm/s to approximately 2×10^5 cm/s. As shown previously, both a surface recombination and a finite "dead layer" thickness are needed to fit some devices due to the absorption in the thin defective region [ref. 4]. The modeled structures corresponded well with the layer thicknesses derived from electrochemical C-V profiling. Earlier cells could only be modeled using window Al concentrations lower than the $Al_{0.85}Ga_{0.15}As$ specified. $Al_xGa_{(1-x)}As$ concentrations were confirmed using surface photovoltage measurements and reflectance modeling. This was remedied in later growth runs which produced higher response. The internal model for photon absorption in $Al_xGa_{(1-x)}As$ included in PC-1D gives good magnitudes for the absorption coefficients but produces a rather jagged appearing curve compared with the smooth experimental curves. Our previous model based on Mazier's approach [ref. 5] and reported elsewhere gave somewhat lower but smoother coefficients [ref. 6].

Both defect layer thickness and surface recombination velocity were functions of growth conditions. Table 3 lists growth conditions for some of the cells studied. These studies lead to the conclusion that interrupted growth for a change of $Al_xGa_{(1-x)}As$ composition or temperature leads to the introduction of defect states which allow recombination in the vicinity of the heteroface. The cells grown at WSU/TC incorporated the results of the studies on earlier cells which produced devices with high internal photoresponse.

Acknowledgement

The authors wish to thank the Air Force Office of Scientific Research for support to investigate solar cells based on III-V compounds under Grant AFOSR-89-0182.

References

[1.] L. C. Olsen, et al., *Space Photovoltaic Research and Technology Conference*, NASA (1986).

[2.] L. C. Olsen, et al., *Proceedings of the Nineteenth IEEE Photovoltaic Specialists Conf.* (1987).

[3.] P. A. Basore, et al., *Proceedings of the Eighteenth IEEE Photovoltaic Specialists Conf.* (1988).

[4.] P. A. Basore, et al., *Proceedings of the Twentieth IEEE Photovoltaic Specialists Conf.* (1988).

[5.] C. Maziar, Subcontract Report - SERI/STR-211-2512, DE 85000501 (1984).

[6.] L. C. Olsen, et al., *Space Photovoltaic Research and Technology Conference*, NASA (1988).

TABLE 1
AM1.5 EFFICIENCIES

Cell	V_{oc} (V)	J_{sc} mA/cm^2	Fill Factor	Efficiency (%)
1	.954	22.6	.803	17.3
2	1.02	23.2	.82	19.3
3	1.02	24.91	.851	21.5
4	NA	22.1*	NA	NA
5	NA	25.4*	NA	NA

* Active Area Before Antireflection Layer

TABLE 2
MODELED PARAMETERS

Cell	S(F) cm/s	L(E) microns	L(B) microns	S(B) cm/s	X(DL) Å	X(WH) Å	Al (conc) %
1	2×10^5	3.0	2.0	1×10^4	100	500	65
2	2×10^4	5.0	0.2	1×10^7	50	500	70
3	1×10^4	5.0	4.0	1×10^4	30	500	75
4	1×10^4	>6.0	3.0	1×10^4	0	500	80
5	1×10^4	>6.0	4.0	1×10^4	0	500	80

TABLE 3
GROWTH PARAMETERS

Cell	NA(E) cm^{-3}	T(E) °C	T(BR) °C	ND(B) cm^{-3}	T(BASE) °C	T(AlGaAs) °C	X(AlGaAs) %
1	1×10^{18}	700	800	1×10^{17}	650	800	65
2	1×10^{18}	700	750	1×10^{18}	750	700	70
3	1×10^{18}	700	750	3×10^{17}	700	750	75
4 LP	1×10^{18}	720	720	1×10^{18}	720	720	80
5 LP	1×10^{18}	720	720	3×10^{17}	720	720	80

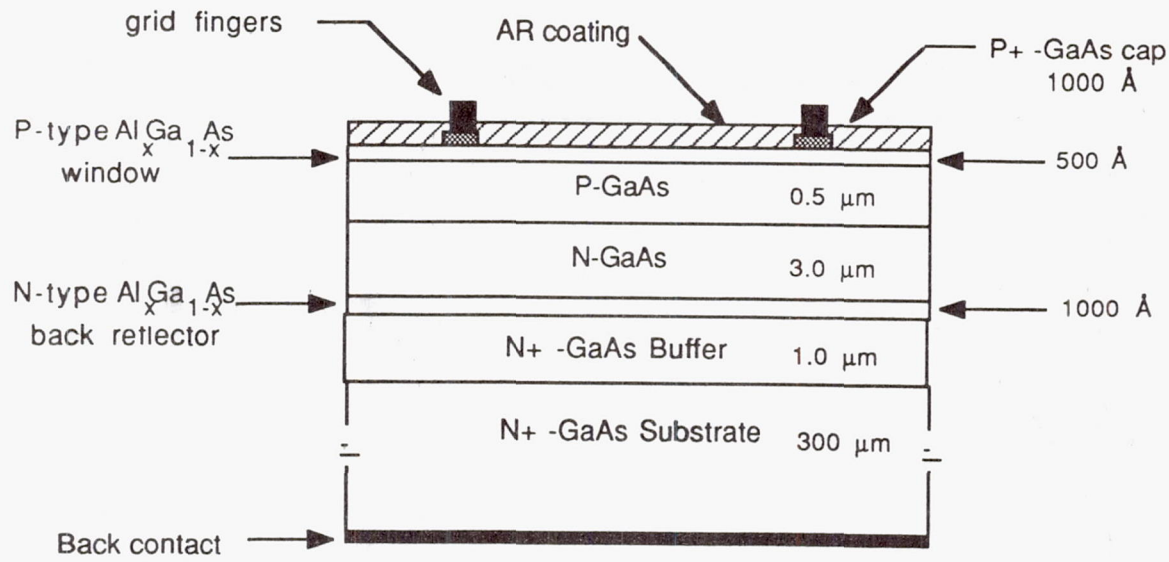

Figure 1 The basic structure for the high efficiency GaAs solar cells modeled.

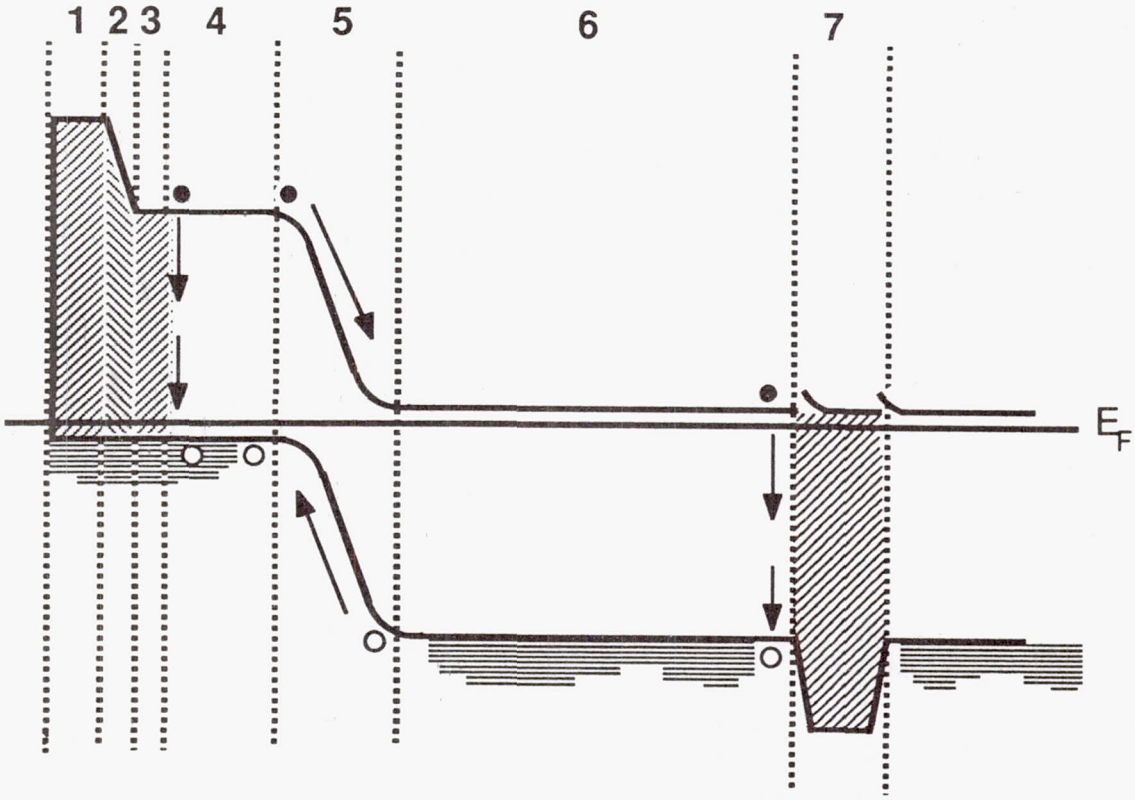

Figure 2 Energy bandgap diagram showing regions modeled using PC-1D.

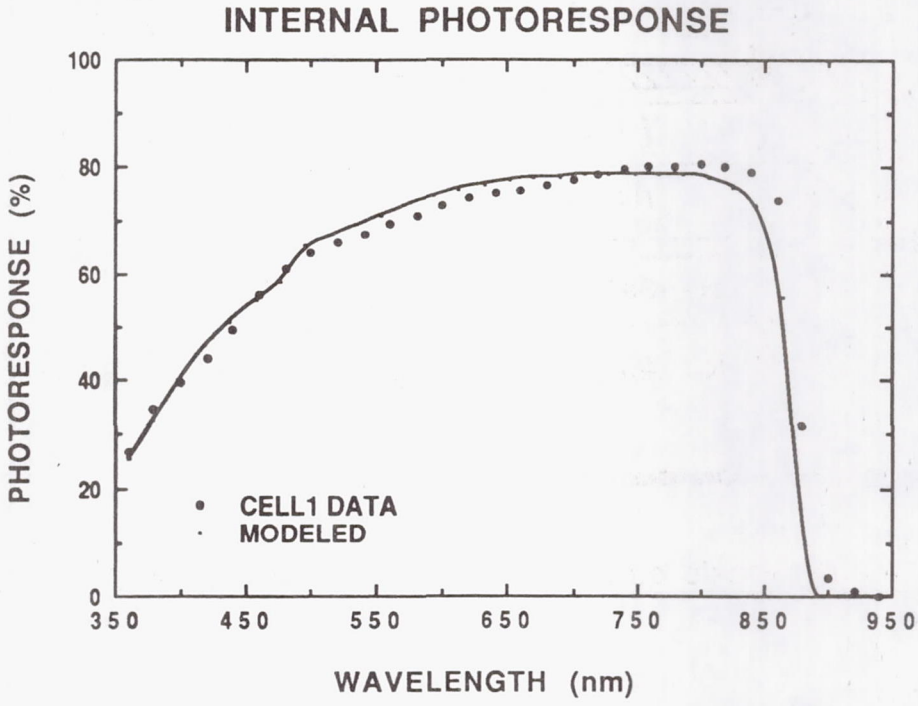

Figure 3 Photoresponse data and PC-1D model for CELL1

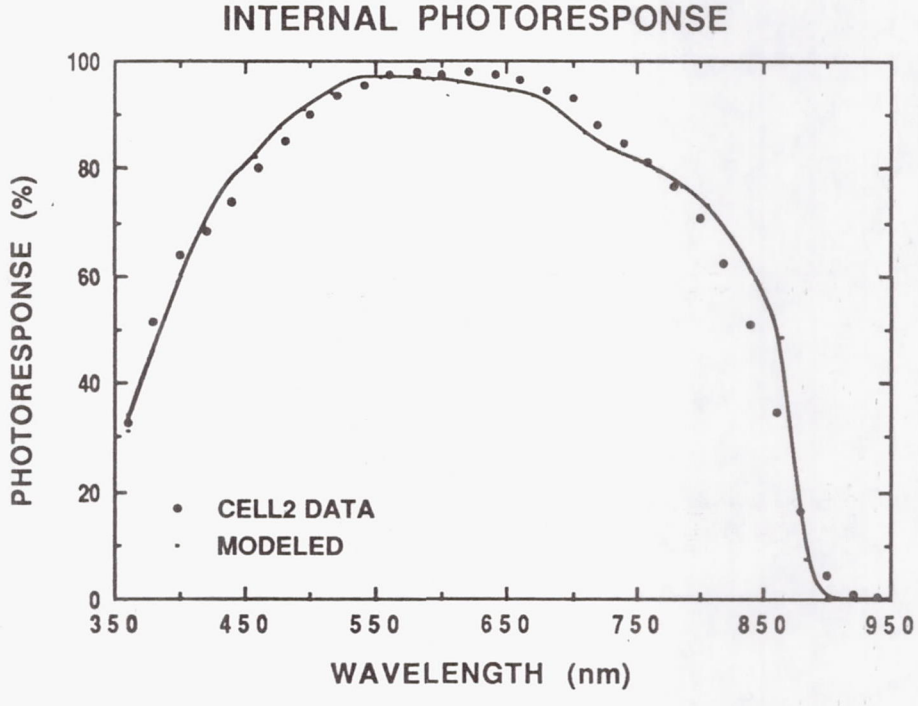

Figure 4 Photoresponse data and PC-1D model for CELL2

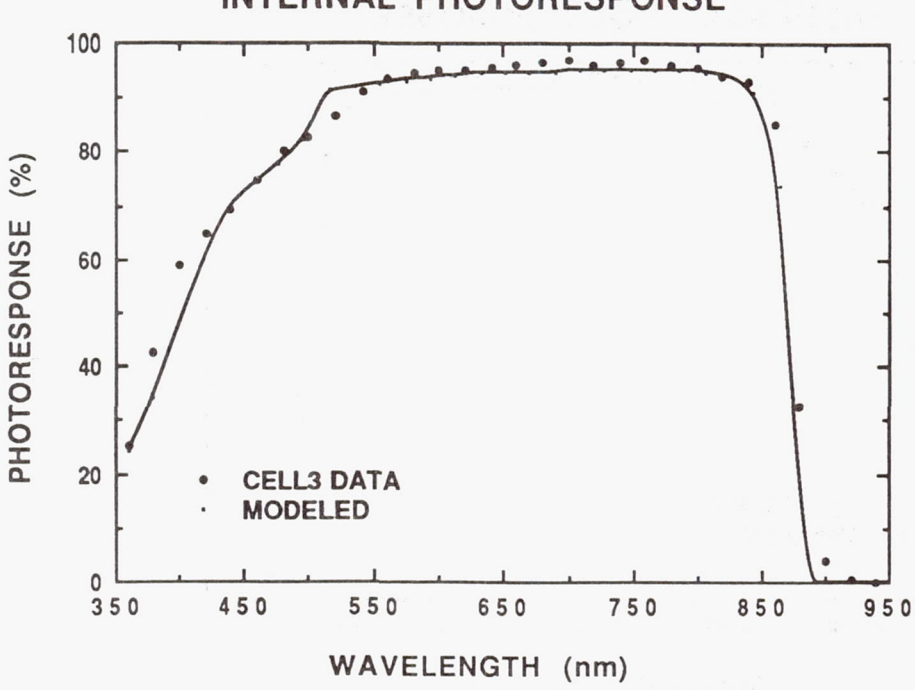

Figure 5 Photoresponse data and PC-1D model for CELL3

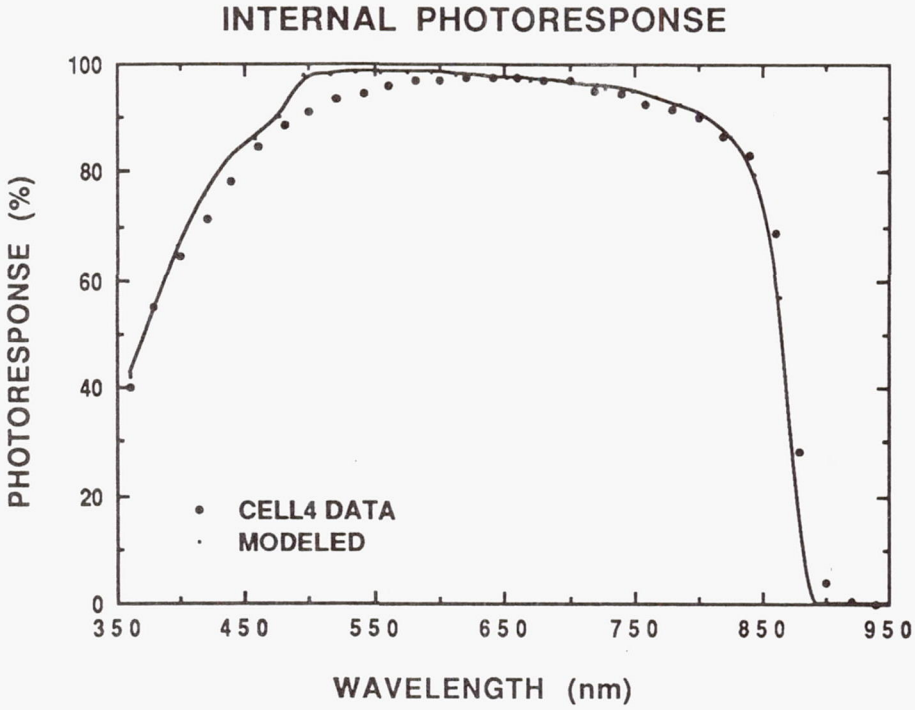

Figure 6 Photoresponse data and PC-1D model for CELL4

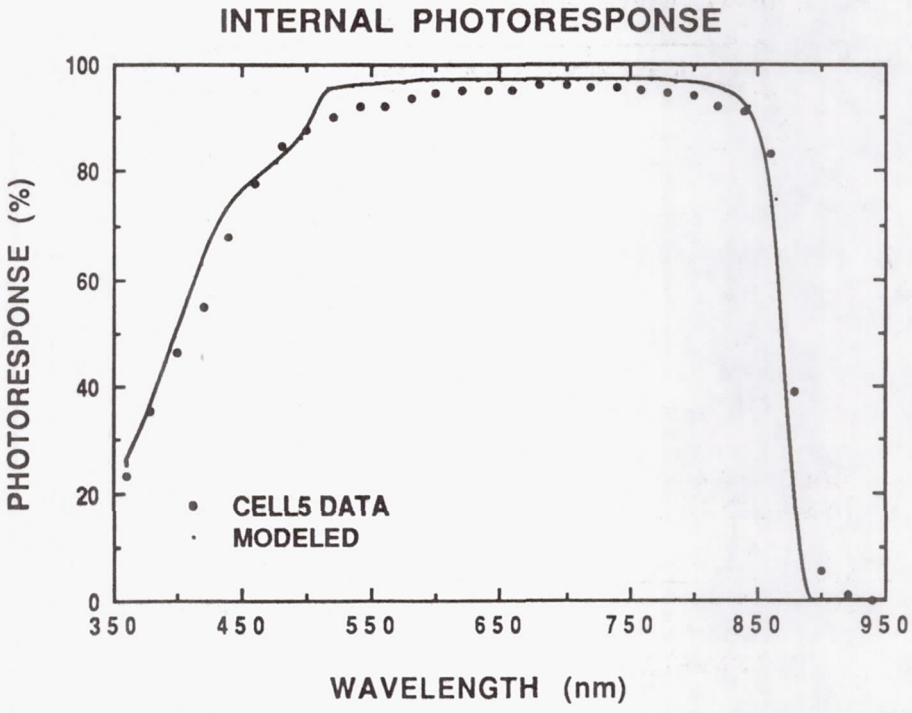

Figure 7 Photoresponse data and PC-1D model for CELL5

High-Efficiency, Radiation-Resistant GaAs Space Cells

K. A. Bertness, M. Ladle Ristow, M. Grounner, M. S. Kuryla and J. G. Werthen
Varian Research Center
Palo Alto, CA

Although many GaAs solar cells are intended for space applications, few measurements of cell degradation after radiation are available, particularly for cells with efficiencies exceeding 20% (one-sun, AM0). Often the cell performance is optimized for the highest beginning-of-life (BOL) efficiency, despite the unknown effect of such design on end-of-life (EOL) efficiencies. In this paper, the results of a study of the radiation effects on p-n GaAs cells are presented.

The large-area (4-cm^2) cells were processed in the Varian pilot line facility after growth in a multiwafer organometallic vapor phase epitaxy (OMVPE) reactor. The effects of varying the (1)emitter thickness and (2) base doping in a p-n structure were investigated. A typical Varian space cell has an emitter thickness of 0.6μm and a base doping level of 3×10^{17} cm^{-2}. In separate growths, the thickness was reduced and the doping level decreased. As shown in Figure 1, the median efficiency of the cells prior to irradiation is 21.2%. Furthermore, the cell efficiencies were not significantly affected by emitter thickness, although improvement from lowering the base doping was apparent.

Eight cells representative of the original group were exposed to 1-MeV electron radiation for a total fluence of 10^{15} cm^{-2}. The cell efficiencies after radiation have a significantly wider distribution, as shown in Figure 2. A combination of high BOL efficiency and radiation resistance for the cell with lower base doping resulted in an EOL efficiency of 15.9% (one-sun, AM0)–the best EOL efficiency reported to date.

More details of the radiation losses in efficiency and other cell performance parameters are given in Figure 3. Those cells grown with thick emitters or with high base doping suffered the largest efficiency loss, resulting in EOL/BOL ratios of about 69%. Cells with thinner emitters only dropped to 76% of their BOL efficiency. For all cells, most of the efficiency loss results from decreases in the open-circuit voltage (V_{oc}) and short-circuit current density (J_{sc}). The cells with the largest decreases in efficiency differ from the more radiation resistant ones in that they also suffer from a significant loss in fill factor.

Although all cells with emitter thicknesses of 0.5μm or less performed equally well after irradiation, the quantum efficiency of those cells differed dramatically, as shown in Figure 4. The tradeoff between blue response and red response is explained by the fact that as the emitter thickness is increased, the p-n junction moves deeper into the material. A deeper junction increases the distance which minority carriers generated near the surface (by blue light) must travel to be collected while decreasing the distance to be traveled by carriers generated deep in the material (by red light).

The differences only become apparent when radiation has decreased the minority carrier diffusion lengths to the same dimensions as the emitter layer thickness. When calibration cells with a better spectral match to the irradiated cells are obtained, it may well be found that thinner emitter cells have a better actual efficiency because of their higher blue responsivity.

In summary, the end-of-life (EOL) efficiency of GaAs space cells can be increased by adjusting materials growth parameters, resulting in a demonstration of 16% EOL efficiency at one-sun, AM0. Reducing base doping levels to below 3×10^{17} cm^{-3} and decreasing emitter thickness to 0.3 to 0.5μm for p-n cells led to significant improvements in radiation hardness as measured by EOL/BOL efficiency ratios for irradiation of 10^{15} cm^{-2} electrons at 1MeV. BOL efficiency was not affected by changes in emitter thickness but did improve with lower base doping.

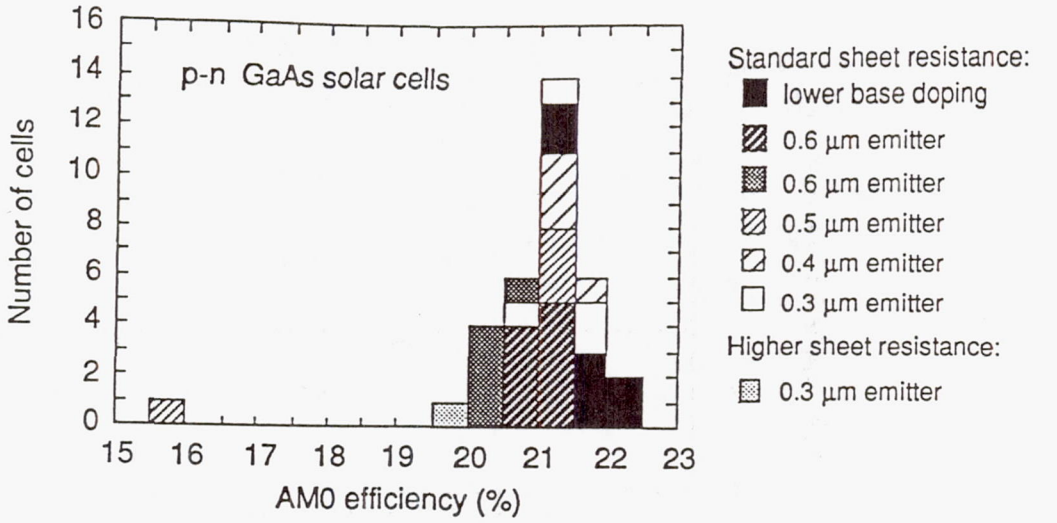

Figure 1. One-sun, AM0 efficiency histogram of 2x2-cm^2 GaAs solar cells grown for radiation tests prior to irradiation.

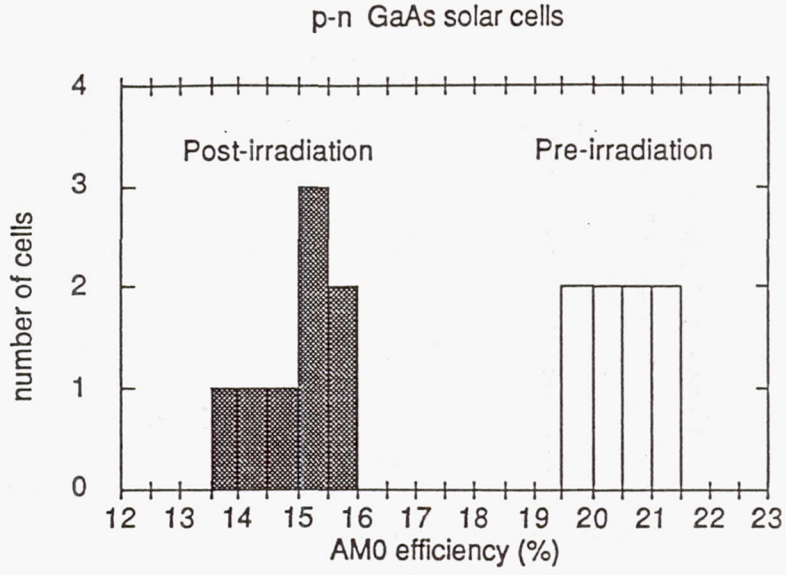

Figure 2. Cell efficiencies before and after irradiation with 1-MeV electrons for a total fluence of 10^{15} cm^{-2}.

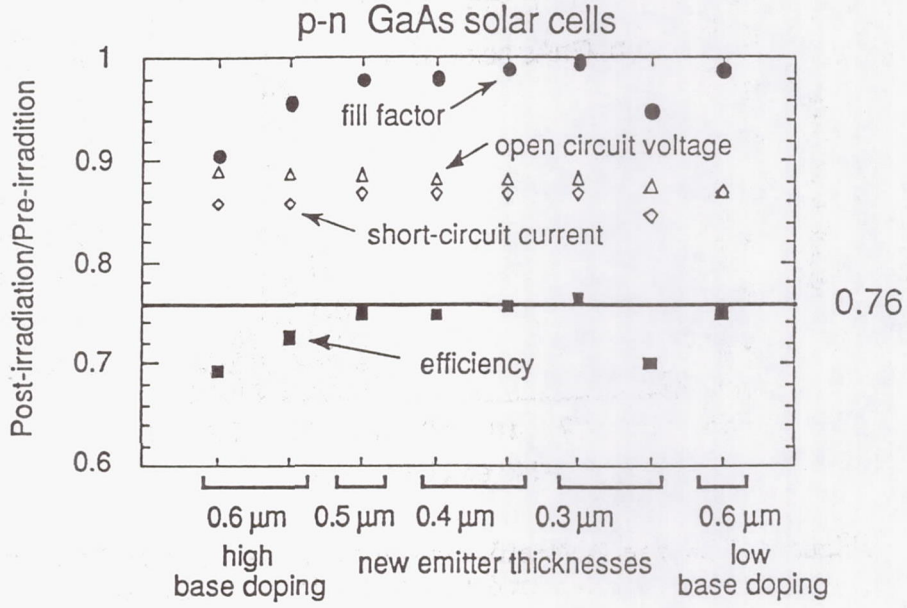

Figure 3. Ratio of cell electrical parameters before and after irradiation with 1-MeV electrons for a total fluence of 10^{15} cm^{-2}.

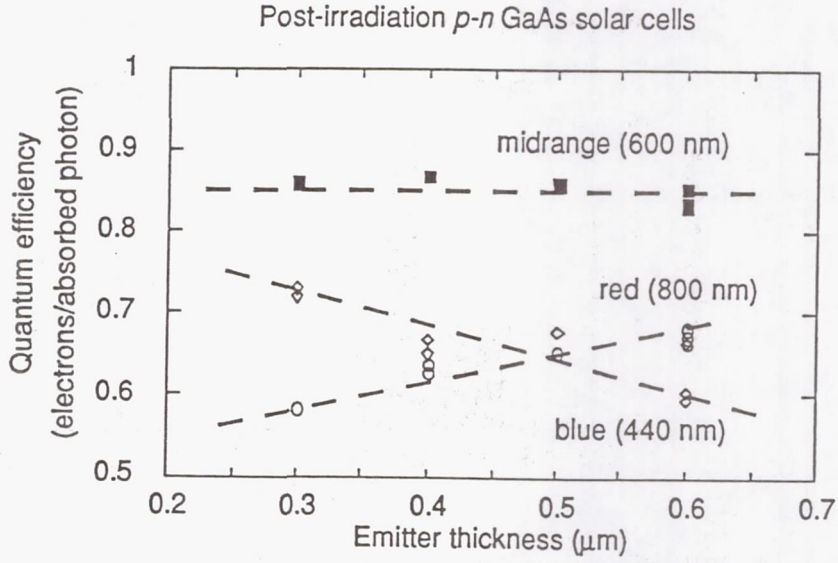

Figure 4. Spectral dependence of post-irradiation quantum efficiency as a function of emitter thickness.

Thermal Annealing of GaAs Concentrator Solar Cells

H. B. Curtis and D. J. Brinker
NASA Lewis Research Center
Cleveland, OH

Introduction

The use of concentrators for space photovoltaic power generation has been under consideration for several years. There are several reasons for the use of concentrator cells. Among them are a higher operating efficiency; a more efficient utilization of higher cost advanced solar cells, i.e., multi-junction cells; and a built in shielding for hostile environments, both natural and man-made. Along with the advantages of concentrators there are some drawbacks such as a higher operating cell temperature and the optical losses of the concentrator itself. These are obviously very dependent on the concentrator design and they usually can be minimized.

There are several solar cell types which can be used for concentrators with GaAs being the general first choice. The GaAs bandgap of 1.43 eV is very near the optimum bandgap for solar cells in AM0 sunlight. GaAs also exhibits a fairly low decrease in power with increasing temperature. There is some data on the radiation resistance of GaAs concentrator cells under both electron and proton irradiations [refs. 1-4]. Results include measurements at concentrated sunlight levels and typical operating temperatures (100× AM0-80C), as well as temperature coefficients for current and voltage of irradiated cells.

Since cells have a tendency to run hotter in a concentrator, the possibility of annealing the damage caused by particle irradiation becomes appealing. Thermal annealing of GaAs planar cells has been shown to be effective at temperatures as low as 150C [ref. 5]. Earlier work has suggested that continuous annealing, such as continuously operating GaAs cells at temperatures around 150C, could greatly reduce radiation degradation [ref. 6]. Recent work at Wright Aeronautical Labs [ref. 7] involved annealing GaAs cells at 250C and 300C for one hour periods after successive 1 MeV irradiations of 1×10^{16} e/cm^2. Roughly half the output was still available after 1×10^{17} e/cm^2 and 10 annealing periods. This piecemeal annealing, although not continuous, gives some experimental backing to continuous annealing. In other work at JPL, a set of 30 minute isochronal anneals on GaAs cells indicated that proton damage is annealed less than electron damage [ref. 8].

All the previous work on annealing of GaAs has been done on cells designed for one sun operation, with all performance data taken at AM0. Concentrator cells have somewhat different designs and are usually much smaller. Our earlier work [refs. 1-4] indicated there are some moderate (10%) differences in measured degradation between data at AM0 and at 100×. Since we had several GaAs concentrator cells

which had been irradiated with various energy electrons, we decided to initiate an annealing program with GaAs concentrator cells at Lewis. For this paper, cells which had been irradiated with electrons with energies from 0.7 to 2.3 MeV were annealed with 20 minute isochronal anneals to 350C, and isothermally annealed at 150C, 200C, and 250C. The isothermal anneals were carried out until recovery ceased. In the case of the 150C annealing, this amounted to months of time. Future work will include radiation with protons of various energies and subsequent annealing studies.

Cell Description

The GaAs concentrator cells used in this work were obtained from three suppliers, ASEC, Hughes, and Varian. The cells are all small (5×5 mm with a 4 mm dia. active area) and designed to operate near 100× AM0. They all have AlGaAs windows and junction depths of near 0.5 microns. Some of the Varian cells are n/p while all the others are p/n. The Varian and Hughes cells were supplied to NASA/Lewis as part of research contracts, while the ASEC cells were directly purchased. The Varian and ASEC cells are OM-CVD grown while the Hughes cells are LPE grown. There were a total of 24 cells which were annealed in this work. Table I shows their average electrical performance values *before* electron irradiation. The average efficiency of over 21% at 25C and 100× AM0 indicates a quality group of GaAs cells.

Experimental Description

The GaAs concentrator cells had been irradiated with electrons in earlier work [refs. 1,4]. Varian cells, both n/p and p/n, were irradiated with electrons with energies of 0.4, 0.7, 1.0, and 2.3 MeV to 3×10^{15} e/cm^2. ASEC, Hughes, and other Varian cells, all p/n, were irradiated with 1 MeV electrons to 1×10^{16} e/cm^2. There were no cover glasses on the cells during electron irradiations. During cell performance measurements, the small area concentrator cells were individually mounted in separate cell holders. The holders consisted of a small metal base and a washer-like metal top with a beveled hole slightly larger than the illuminated area of the cell. These two pieces supply both a support for the cell and an area for the four wire electrical attachment. There was no soldering or welding of any contact to the cell.

There were two types of annealing done for this work, isochronal and isothermal. The isochronal annealing consisted of 20 minute anneals at temperatures starting at 100C and increasing to 350C in 50C intervals. Performance measurements were made at each temperature level. The isothermal annealing consisted of constant temperature anneals at temperature levels of 150C, 200C, and 250C. Performance measurements were made at increasingly longer time intervals. Total annealing time was in the thousands of hours for the 150C case.

During annealing the bare cells were in a quartz tube in a furnace with dry nitrogen flowing through the tube to prevent any oxidation of the cells. The temperature in

the tube was monitored with a thermocouple and power to the furnace was adjusted for constant temperature. Performance measurements consisted of the following:

1. I-V data at 25C and one sun AM0 using an X-25 xenon solar simulator and an appropriate standard cell.

2. I-V data at 25C and 100× AM0 using a pulsed xenon lamp solar simulator and the linear assumption between irradiance and short-circuit current.

Results and Discussion

Isochronal Annealing

Six different cells were used for the isochronal annealing study. Three n/p and three p/n Varian cells. In each polarity, one cell had been irradiated with 0.7 MeV, 1.0 MeV, and 2.3 MeV electrons respectively. The total fluence was 3×10^{15} e/cm^2 for all six cells. In the original irradiation work some cells were irradiated with 0.4 MeV electrons, but their degradation was so small they were not included in the annealing studies. Figures 1 and 2 show the results of the 20 minute isochronal annealing out to 350C for the n/p cells and the p/n cells respectively. There are several items to note in the two figures. First, the 20 minute annealing period does not produce any recovery until about 250C. Also, the recovery is fairly complete after the 300C anneal. Further annealing at 350C for 20 minutes has no effect. This *may* be as far as the cells can be annealed with 20 minute isochronal annealing, but it says nothing about longer annealing periods or continuous annealing.

The data for the p/n cell irradiated with 2.3 MeV electrons is not complete. This cell shunted during the test sequence and data was not available. Three of the 24 cells annealed during this work shunted somewhere during the test sequence. Four other cells had small partial shunts which lowered fillfactor (and hence P_{max}) but left I_{sc} and V_{oc} unaffected. It appears clear that the source of the cell shunting is the numerous times the cell was mounted and de-mounted in its measurement holder. The top part of the holder is held down on the cell by a small pressure but GaAs cells are known to have some problems in being repeatedly handled. For the three cells which completely shunted, the data ceases, however for the four cells with small shunts, the I_{sc} and V_{oc} data is still available. Figure 3 shows the isochronal anneal data for I_{sc}, V_{oc}, Fill, and P_{max} for the n/p cell irradiated with 2.3 MeV electrons. This is typical of all the cells during this work. Note that most of the degradation is in the current with a corresponding major portion of the annealed recovery also in the current. This allows us to discuss annealing results using the current recovery on those cells which are partly shunted.

A tabular version of the results of the isochronal annealing is given in table II. (The three figures in each column are 1) I/I_o, V/V_o, or P/P_o after irradiation; 2) the same

data after isochronal annealing; and 3) the un-annealed fraction). The most notable feature of the data is the trend for less annealing as the electron energy increases. Most of the damage caused by the 0.7 MeV electrons can be annealed compared to about half for the 2.3 MeV electrons. There appears to be no major difference in the results of isochronal annealing between the n/p cells and the p/n cells. Even though the current degradation is much larger than the voltage degradation, the un-annealed fractions after isochronal annealing are in most cases about the same. Future work is planned using DLTS to investigate the trap levels and help explain these trends.

Isothermal Annealing

Based on the results of the isochronal annealing, we decided to do isothermal annealing at three temperatures, 150C, 200C, and 250C. At each temperature, a set of six cells was annealed. Each set consisted of three Varian cells, either p/n or n/p, irradiated to 3×10^{15} e/cm^2 with 0.7, 1.0, or 2.3 MeV electrons, similar to those used in the isochronal annealing. Each set also contained three other cells, irradiated with 1.0 MeV electrons to a fluence of 1×10^{16} e/cm^2. These three were made by Varian, ASEC, and Hughes. This gave us some additional annealing data on cells irradiated to a higher fluence. At each temperature, the cells would be removed for performance measurements at increasing time intervals. Measurements were made after total annealing times of: 20 min, 80 min, 3 hr, 9 hr, 27 hr, 81 hr, 243 hr, 729 hr, 1326 hr (200C only), and 2174 hr. For the 250C case, annealing was finished at 81 hours, and no further annealing was done. At 200C, the cells are finished after 2174 hours. At 150C, a data point was taken at 5533 hours and the experiment is continuing.

The results of the isothermal annealing are summarized in tables III and IV. Table III has data for the Varian cells irradiated with 0.7, 1.0, or 2.3 MeV electrons out to 3×10^{15} e/cm^2, while table IV is for the cells irradiated with just the 1.0 MeV electrons out to 1×10^{16} e/cm^2. (As in table II the three figures in each column are 1) I/I_o, V/V_o, or P/P_o after irradiation; 2) the same data after *isothermal* annealing; and 3) the un-annealed fraction).

By comparing the un-annealed fractions for the cells annealed at 250C or 200C with the isochronal anneal data, we note that the cells have about the same amount of recovery. For example, consider the cells irradiated with 0.7 MeV electrons. For the isochronal annealing, the un-annealed fractions for P_{max} were about 14% and 23% (table II), while for the isothermal annealing, they were 11% and 25% (table III). Similar comparisons can be made for the cells irradiated with 1.0 and 2.3 MeV electrons. This implies that there may be a limit to how much recovery can be obtained with post-irradiation annealing.

For the data in table IV, all the cells were irradiated with 1 MeV electrons to a larger fluence of 1×10^{16} e/cm^2. However, even though they started recovery at

a deeper degradation than the isochronal annealed cells (3×10^{15} e/cm^2), the un-annealed fractions, both for I_{sc} and P_{max}, are very similar. For example the I_{sc} un-annealed fractions for the isochronal annealed 1 MeV (3×10^{15} e/cm^2) cells are approximately 27% and 28%, while for the isothermal annealed 1 MeV cells (1×10^{16} e/cm^2) they are 17%, 25%, 25%, 26%, 27% and 30%. This implies that any limit to post-irradiation annealing recovery may be independent of fluence level.

Isothermal annealing was done at three temperatures, 250C, 200C, and 150C. It is reasonable to assume that annealing at higher temperatures will bring on recovery quicker. This is indeed the case. Figure 4 shows P_{max} recovery for three cells annealed at 250C. Since some of the cells in the 250C portion of the experiment had shunting problems, the data in figure 4 is for cells irradiated to different fluences. The lower two curves are for cells irradiated with 1 MeV electrons to 1×10^{16} e/cm^2 while the upper curve is for a cell irradiated with 0.7 MeV electrons to 3×10^{15} e/cm^2. Note that the annealing is essentially complete after the 27 hour point, and further annealing to 81 hours has little effect.

For the 200C annealing, more time is required to obtain recovery. Figure 5 shows normalized P_{max} as a function of annealing time at 200C for the Varian cells irradiated with three different electron energies. Most of the recovery occurs between about 10 and 200 hours. However there is more annealing even out to 2174 hours, which is the last data point.

At 150C, it appears that quite a bit of time is required for annealing to take place. Figures 6 and 7 both show annealing results at 150C. Figure 6 shows normalized P_{max} vs. annealing time for the three cells irradiated to 1×10^{16} e/cm^2 with 1 MeV electrons. At the last data point, 5533 hours, there is some significant annealing. The cells have recovered about one third of their degraded power and the trend appears to indicate much more recovery. Figure 7 shows the normalized I_{sc} ratio for three Varian cells irradiated to 3×10^{15} e/cm^2 with different energy electrons. Again, we are starting to see some annealing, especially in the cell irradiated with 0.7 MeV electrons. This cell has recovered over half its degraded current, while the cells irradiated with 1.0 and 2.3 MeV electrons have only regained about one third of their original value. This agrees with the isochronal data and the isothermal data at 250C and 200C which seem to indicate less annealing for cells irradiated with higher energy electrons. A comparison of the annealing at each of the three temperatures is given in figure 8. The P_{max} ratio is plotted for three similar Varian cells irradiated with 1 MeV electrons to 1×10^{16} e/cm^2. The annealing at longer times for lower temperatures is quite evident.

If we do get significant annealing at 150C, the annealing time will be too long to be practical. There are no spacecraft which can wait months to anneal their arrays. What could be very beneficial is real time continuous annealing as described in ref. 6. In this case, the cells are operated from the very beginning at their lowest annealing temperature such as 150C, and a continuous annealing occurs side-by-side with the

radiation induced degradation. What we have shown in this paper is the ability of GaAs concentrator cells to recover most of the electron induced degradation by a post-irradiation annealing at 200C and perhaps at 150C in a time period of months. The time required to reach the degradation levels involved in this work in space is several years, depending on the orbit. This slow degradation rate of cells in space is at the heart of the argument for continuous annealing. Even though the annealing is slow, it happens as fast as the induced degradation, hence complete or near complete annealing occurs. Operating temperatures of near 150C can readily be achieved in concentrator arrays, and continuous annealing may be possible.

For continuous annealing to be proven successful, several questions must be answered. Among them are:

1) The annealing characteristics of proton induced damage.

2) The annealing effects of irradiating cells in the lab at the annealing temperature.

3) The annealing effects when the cells are irradiated at temperature with a flux similar to those encountered in space (typically several orders of magnitude slower than lab experiments).

We intend to look at the first two items in future work. Due to the long term nature of the third item, there are no practical experiments which can be performed using particle accelerators. A final answer to the feasibility of continuous annealing may require a flight test, probably in the radiation belts.

Summary

We have performed isochronal and isothermal annealing tests on GaAs concentrator cells which had been irradiated with electrons of various energies to fluences up to 1×10^{16} e/cm^2. The results include:

1) For cells irradiated with electrons from 0.7 to 2.3 MeV, recovery decreases with increasing electron energy.

2) As determined by the un-annealed fractions, isothermal and isochronal annealing produce the same recovery. Also, cells irradiated to 3×10^{15} or 1×10^{16} e/cm^2 recover to similar un-annealed fractions.

3) We are starting to see some significant annealing at 150C although very long times are required.

References

[1.] H. B. Curtis and C. K. Swartz, *18th PVSC*, 356, 1985.

[2.] H. B. Curtis and C. K. Swartz, *19th PVSC*, 664, 1987.

[3.] H. B. Curtis and R. E. Hart Jr., *23rd IECEC*, **3**,85, 1988.

[4.] H. B. Curtis and R. E. Hart Jr., *20th PVSC*, **2**, 1020, 1988.

[5.] R. Loo, R. C. Knechtli, and G. S. Kamath, *15th PVSC*, 33, 1981.

[6.] J. H. Heinbockel, E. J. Conway, and G. H. Walker, *14th PVSC*, 1085, 1980.

[7.] M. A. Chung et al, *20th PVSC*, 924, 1988.

[8.] B. E. Anspaugh and R. G. Downing, *15th PVSC*, 499, 1981.

Table I PRE-IRRADIATED ELECTRICAL CHARACTERISTICS
(25C and 100X AMO)

	Isc (mA)	Voc (V)	Fill	Eff. (%)
Maximum	400	1.146	.869	22.14
Minimum	348	1.085	.774	19.48
Average	379	1.126	.844	21.03

Table II RESULTS OF ISOCHRONAL ANNEALING

n/p cells

0.7 MeV			1.0 MeV			2.3 MeV		
Isc	Voc	Pmax	Isc	Voc	Pmax	Isc	Voc	Pmax
.762	.901	.656	.725	.889	.605	.669	.889	.557
.981	.975	.921	.925	.966	.853	.848	.952	.764
8.0%	25.9%	23.0%	27.1%	30.4%	37.2%	45.8%	43.7%	53.3%

p/n cells

0.7 MeV			1.0 MeV			2.3 MeV		
Isc	Voc	Pmax	Isc	Voc	Pmax	Isc	Voc	Pmax
.729	.903	.637	.674	.892	.585	.668	.854	.553
.976	.988	.948	.910	.978	.879	---	---	---
8.8%	11.9%	14.2%	27.8%	20.7%	29.1%	---	---	---

in each column, the three data points are:
1) I/Io, V/Vo, or P/Po after irradiation
2) The same data after annealing
3) The un-annealed fraction

Table III RESULTS OF ISOTHERMAL ANNEALING
(Varian n/p and p/n cells)

250C --- p/n cells

0.7 MeV			1.0 MeV			2.3 MeV		
Isc	Voc	Pmax	Isc	Voc	Pmax	Isc	Voc	Pmax
.806	.882	.690	.755	.859	.632	.539	.872	.448
.987	.985	.922	---	---	---	---	---	---
6.8%	12.8%	25.2%	---	---	---	---	---	---

(Annealing complete after 81 hours)

200C --- n/p cells

0.7 MeV			1.0 MeV			2.3 MeV		
Isc	Voc	Pmax	Isc	Voc	Pmax	Isc	Voc	Pmax
.782	.890	.659	.735	.875	.598	.661	.861	.523
1.003	.987	.964	.963	.963	.864	.853	.937	.752
-1.2%	12.0%	10.5%	14.0%	29.6%	33.8%	43.3%	45.3%	52.0%

(Annealing complete after 2174 hours)

150C --- n/p cells

0.7 MeV			1.0 MeV			2.3 MeV		
Isc	Voc	Pmax	Isc	Voc	Pmax	Isc	Voc	Pmax
.778	.904	.661	.706	.885	.601	.666	.875	.536
.899	.917	---	.802	.905	.685	.794	.900	.650
45.2%	86.1%	---	67.6%	82.3%	79.0%	61.7%	80.1%	75.5%

(Annealing well underway after 5533 hours)

in each column, the three data points are:
1) I/Io, V/Vo, or P/Po after irradiation
2) The same data after annealing
3) The un-annealed fraction

Table IV RESULTS OF ISOTHERMAL ANNEALING
(Varian, ASEC, and Hughes p/n cells)

250C

Varian			ASEC			Hughes		
Isc	Voc	Pmax	Isc	Voc	Pmax	Isc	Voc	Pmax
.525	.781	.427	.288	.831	.224	.414	.806	.305
.883	.924	.836	.814	.935	---	.823	.926	.706
24.7%	34.7%	28.7%	26.1%	38.4%	---	30.3%	37.9%	42.3%

(Annealing complete after 81 hours)

200C

Varian			ASEC			Hughes		
Isc	Voc	Pmax	Isc	Voc	Pmax	Isc	Voc	Pmax
.483	.785	.381	.268	.820	.209	.411	.807	.307
.913	.934	.833	.818	.946	---	.841	.911	---
16.9%	30.6%	27.0%	24.9%	29.8%	---	26.9%	45.9%	---

(Annealing complete after 2174 hours)

150C

Varian			ASEC			Hughes		
Isc	Voc	Pmax	Isc	Voc	Pmax	Isc	Voc	Pmax
.514	.785	.415	.385	.839	.307	.440	.813	.320
.734	.818	.599	.673	.881	.552	.664	.852	.528
54.6%	84.6%	68.5%	53.2%	73.7%	64.7%	60.0%	79.4%	69.4%

(Annealing well underway after 5533 hours)

in each column, the three data points are:
1) I/Io, V/Vo, or P/Po after irradiation
2) The same data after annealing
3) The un-annealed fraction

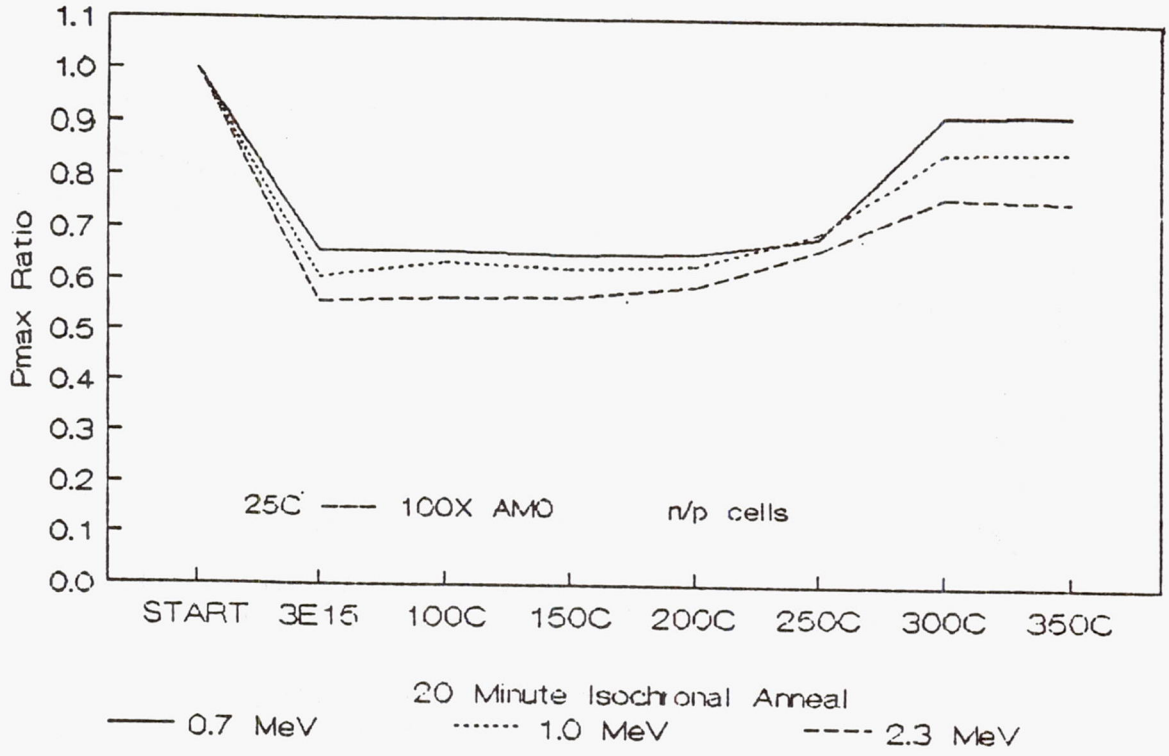

Figure 1 Results of 20 minute isochronal annealing on Varian n/p cells irradiated with 0.7, 1.0, and 2.3 MeV electrons to 3E15.

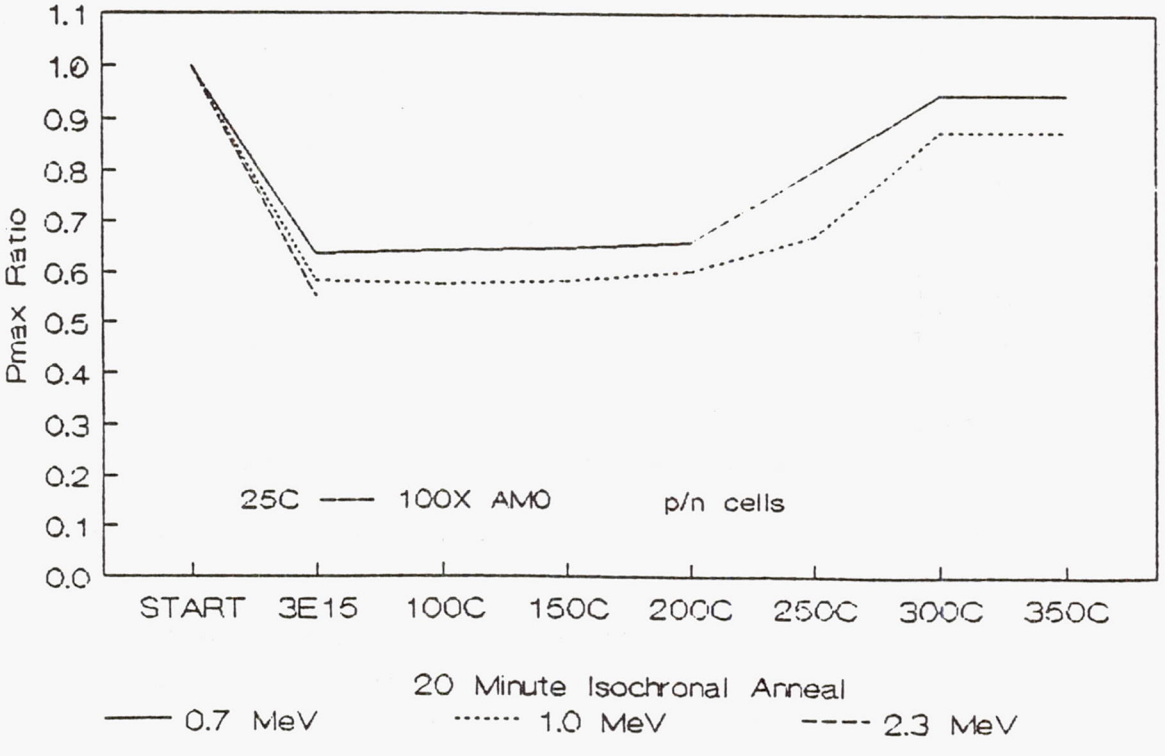

Figure 2 Results of 20 minute isochronal annealing on Varian p/n cells irradiated with 0.7, 1.0, and 2.3 MeV electrons to 3E15.

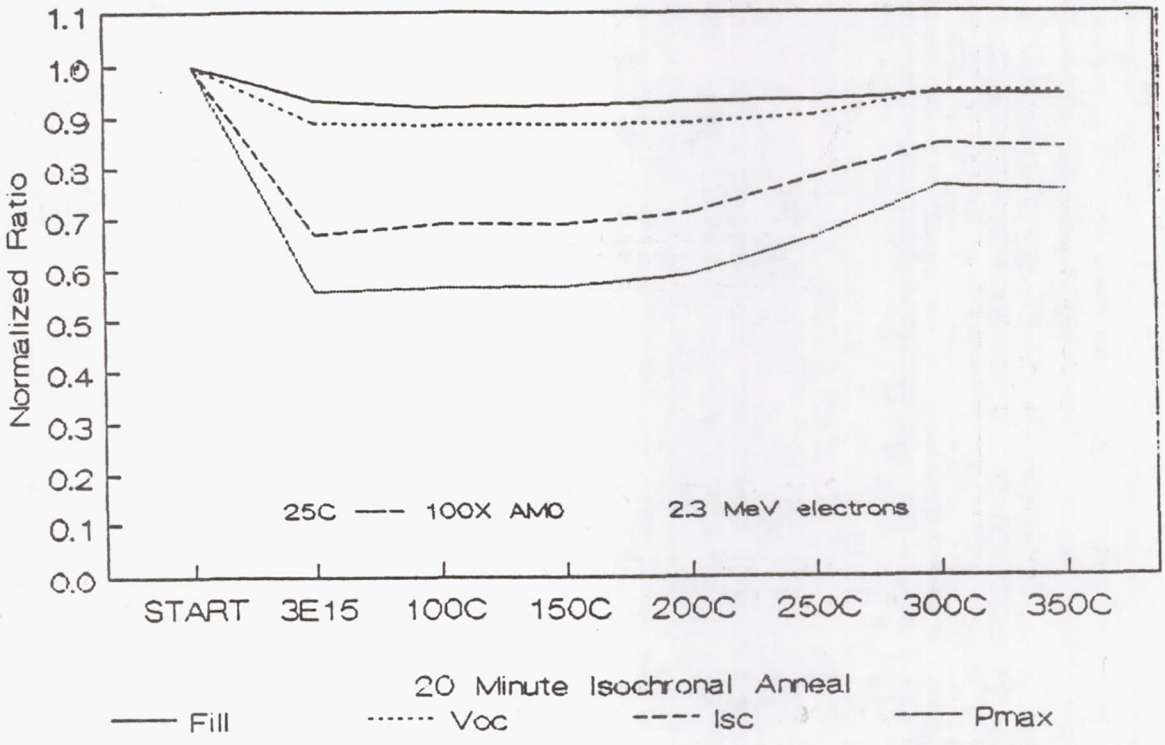

Figure 3 Results of 20 minute isochronal annealing on one Varian n/p cell irradiated with 2.3 MeV electrons to 3E15.

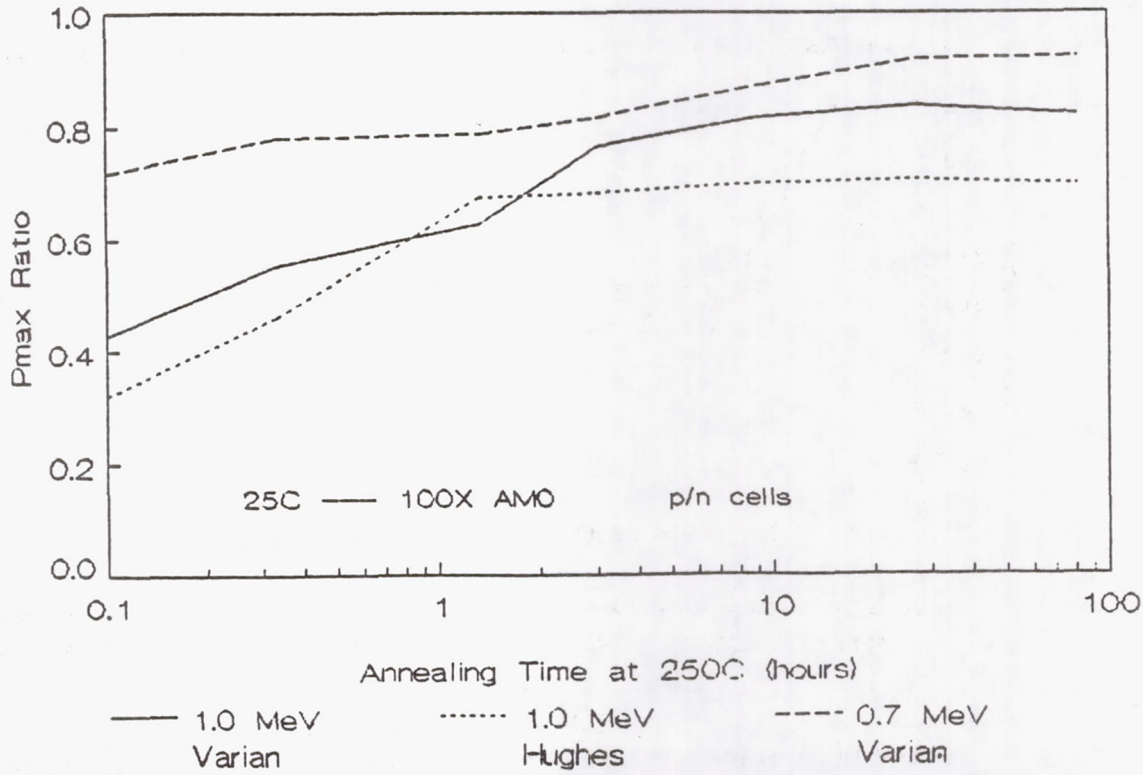

Figure 4 Results of 250C isothermal annealing on two cells irradiated with 1 MeV electrons to 1E16 and one cell irradiated with 0.7 MeV electrons to 3E15.

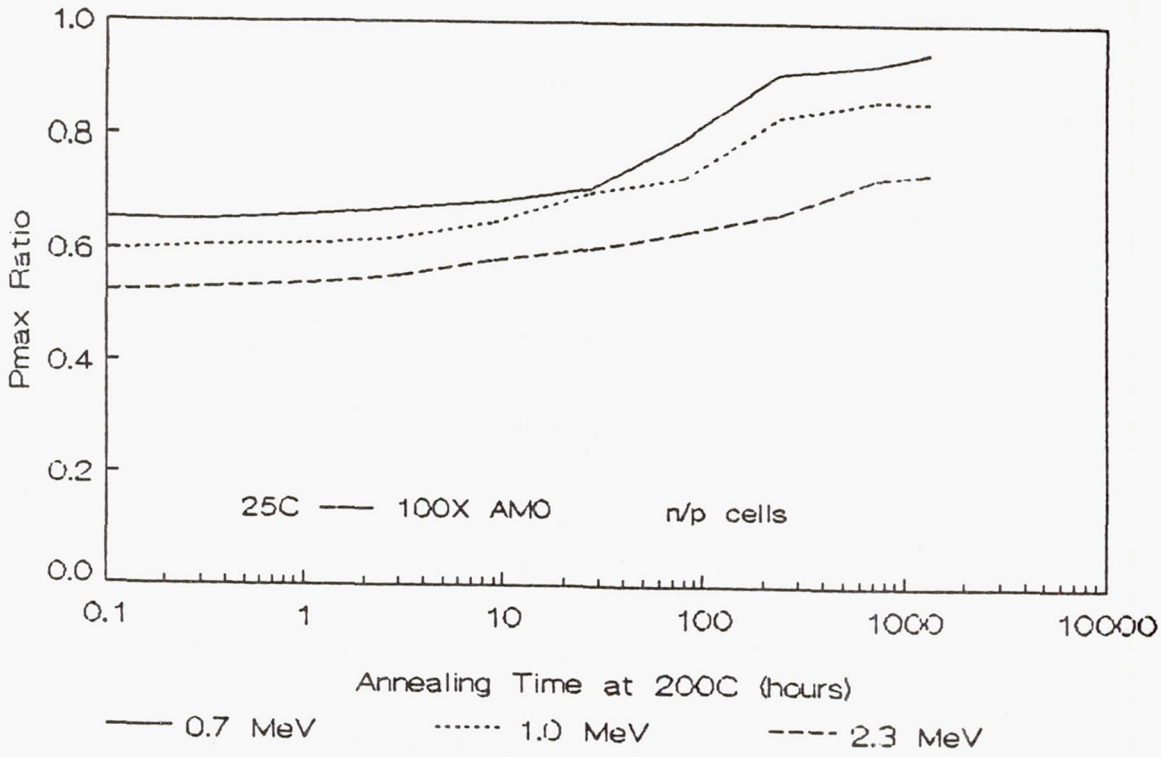

Figure 5 Results of 200C isothermal annealing on Varian n/p cells irradiated with 0.7, 1.0, and 2.3 MeV electrons to 3E15.

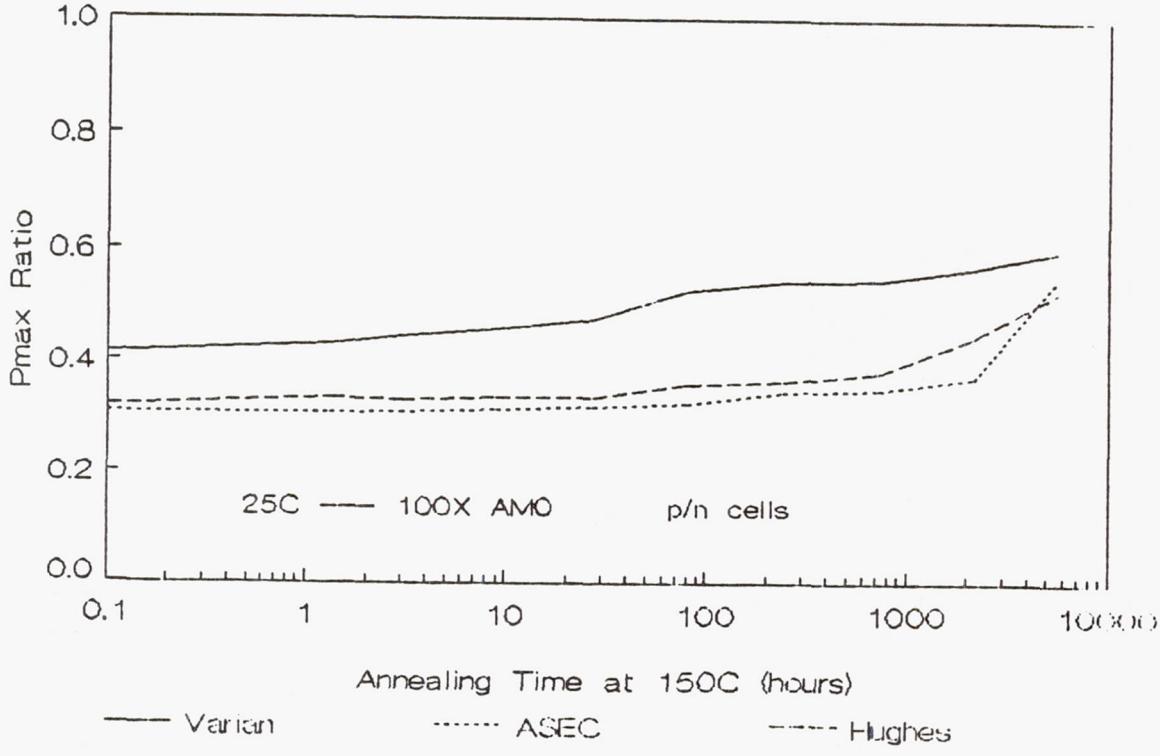

Figure 6 Results of 150C isothermal annealing on three p/n cells irradiated with 1 MeV electrons to 1E15.

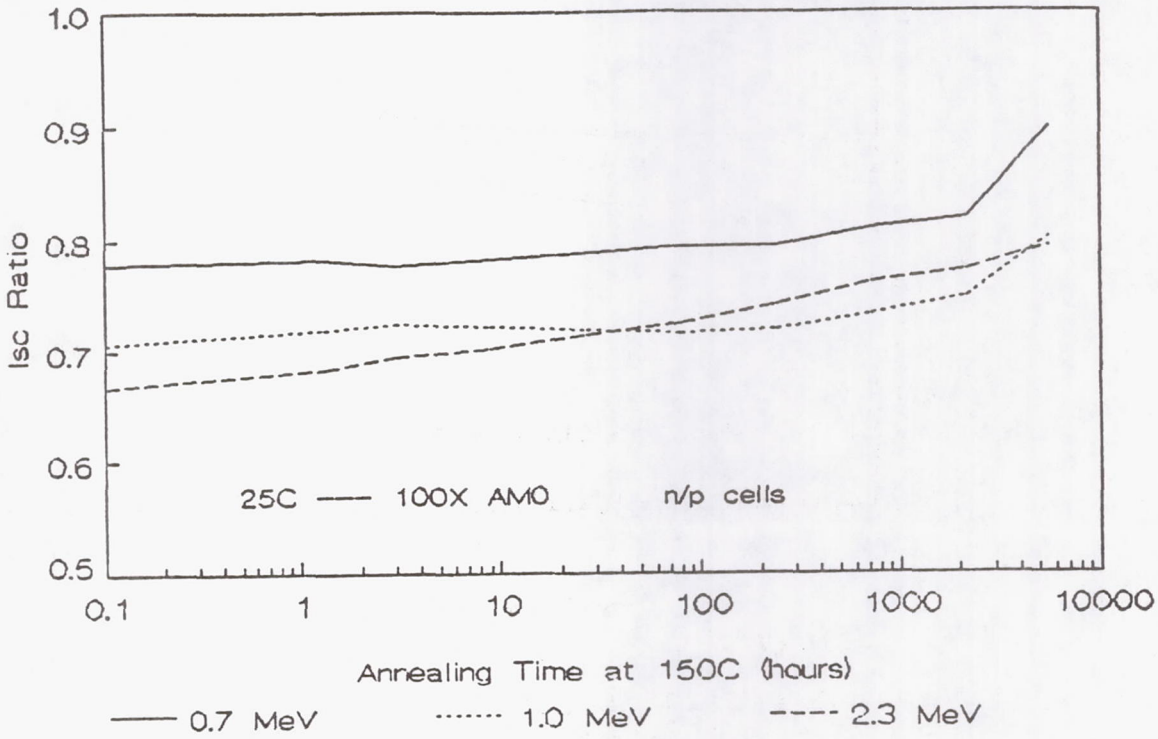

Figure 7 Isc ratios for Varian n/p cells irradiated with 0.7, 1.0, and 2.3 MeV electrons to 3E15 annealed at 150C.

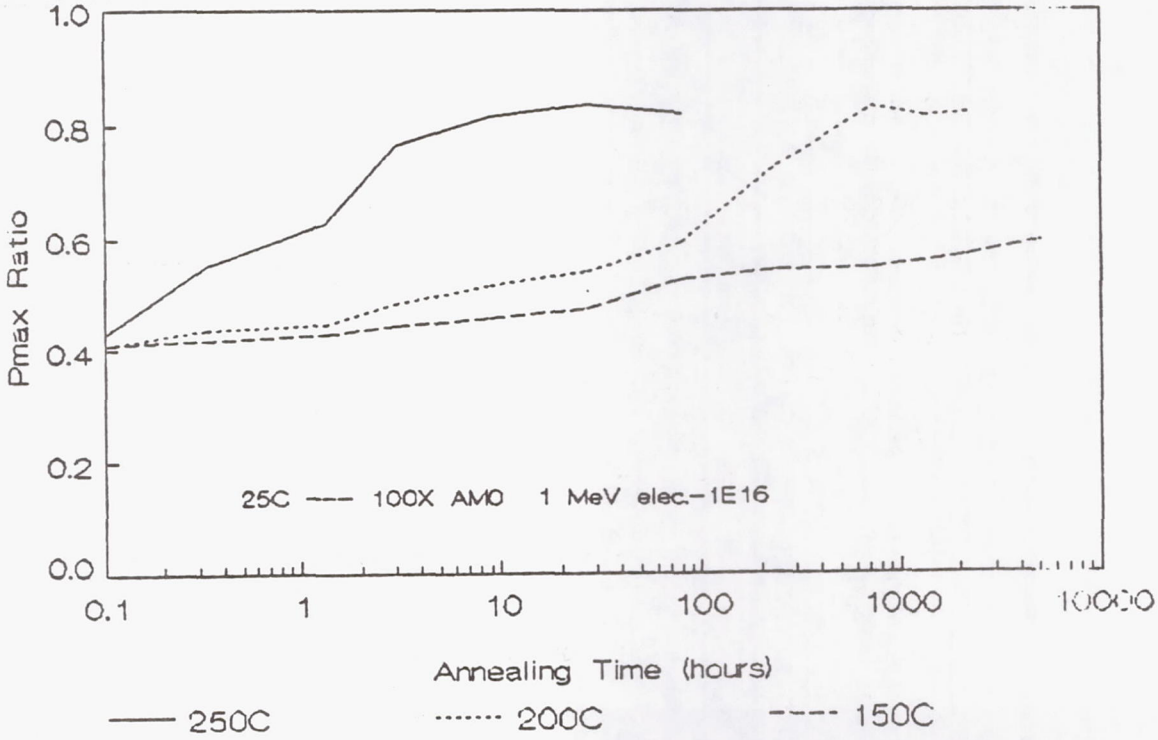

Figure 8 Comparison of Pmax annealing for three cells irradiated with 1 MeV electrons to 1E16 at 250C, 200C, and 150C.

Burst Annealing of High Temperature GaAs Solar Cells

P.R. Brothers and W.E. Horne
Boeing
Seattle, WA

Introduction

One of the major limitations of solar cells in space power systems is their vulnerability to radiation damage. One solution to this problem is to periodically heat the cells to anneal the radiation damage. Annealing has been demonstrated with silicon cells [ref. 1]. The obstacle to annealing of GaAs cells has been their susceptibility to thermal damage at the temperatures required to completely anneal the radiation damage. GaAs cells with high temperature contacts and encapsulation have been developed under a joint effort by Boeing and the Kopin Corp [ref. 2]. The cells tested are designed for concentrator use at 30 suns AM0. The circular active area is 2.5 mm in diameter for an area of 0.05 cm^2. Typical one sun AM0 efficiency of these cells is over 18%. They have been demonstrated to be resistant to damage after thermal excursions in excess of 600°C. This high temperature tolerance should allow these cells to survive the annealing of radiation damage. A limited set of experiments were devised to investigate the feasibility of annealing these high temperature cells. The effect of repeated cycles of electron and proton irradiation was tested. The damage mechanisms were analyzed. Limitations in annealing recovery suggested improvements in cell design for more complete recovery. These preliminary experiments also indicate the need for further study to isolate damage mechanisms.

The primary objective of the experiments was to demonstrate and quantify the annealing behavior of high temperature GaAs cells. Secondary objectives were to measure the radiation degradation and to determine the effect of repeated irradiation and anneal cycles.

Test Conditions

The test plan illustrated in figure 1 was developed to guide the use of a limited number of cells available for testing in a limited period of time. The GaAs cells were divided into three groups of four cells each. There was a control group, a thermal control group, and an irradiation test group. The control group was used to verify the performance of the measurement equipment and to factor out slight changes in the behavior of the solar simulator. A Spectrolab XT10 solar simulator was used in conjunction with a custom built load bank to make IV curve measurements. The irradiation test group was exposed to electrons, annealed, exposed to protons, and annealed a second time. The thermal control group was annealed at the same time

as the irradiation group but not exposed to irradiation. In this way any degradation from thermal exposure could be evaluated as a factor separate from the radiation effects.

The Boeing Physical Sciences Research Center linear accelerator was used as a source of electrons for the electron irradiation. The cells were exposed to 1×10^{15} 10 Mev e^-/cm^2. After steps to measure and anneal the cells, they were then exposed to 2×10^{11} 1.7 Mev p^+/cm^2 using a Van De Graff accelerator at the University of Washington as a source. Electron dose was measured using thermal luminescence dosimetry. At the University of Washington, a solid state detector was used in conjunction with a Faraday cup to measure proton dose. For each type of radiation the exposure was in two steps with an intermediate step to check cell degradation by measuring short circuit current in ambient room lighting. The target degradation for demonstrating thermal annealing was a 20% loss in maximum power.

The annealing test fixture is shown in figure 2. The fixture was mounted in a high vacuum chamber which was evacuated to less than 5×10^{-5} torr during the annealing cycles. Heating was accomplished by passing a current through a graphite bar. The bar had a slot machined in it to accommodate the solar cells. Since the cells were recessed completely in the slot, they were tightly coupled thermally to the heater bar. The temperature was monitored by two thermocouples. Only the center third of the heater bar was used in order to maintain a uniform temperature. A typical annealing thermal profile curve is shown in figure 3. The temperature rises from room ambient to the target temperature within 10 to 15 seconds. The cool down was relatively slower due to limited radiative cooling, but still dropped below 100°C within two minutes.

Results

Light IV curves were measured for the 12 GaAs cells before the first irradiation. After the electron and again after the proton irradiations, the four control cells and the four irradiated cells were measured. After each anneal cycle all 12 cells were measured. Meter measurements of V_{oc} (open circuit voltage) and I_{sc} (short circuit current) were made at the same time. Figure 4 charts the results for V_{oc} for a typical irradiated cell showing the changes at each step in the experiment. V_{oc} shows a definite degradation after the electron irradiation, with only partial recovery after the first anneal cycle. This lead to the expansion of the anneal schedule from one minute at 500°C to five minutes at 500°C. In order to attempt further improvement, a third anneal was implemented at 600°C for five minutes. As is shown in figure 4, each anneal cycle resulted in an improvement in V_{oc} so that it recovered to within 95% of its original value. The proton irradiation caused another drop which was almost completely recovered in the subsequent anneal cycle. The V_{oc} measurements for the irradiated cells were corrected for the changes in the thermal controls. A typical example of the thermal control cells is shown in figure 5. There was little

change in V_{oc} for the thermal controls as they were subjected to the annealing cycles. The slight improvement has been noted in previous thermal cycle experiments to test high temperature tolerance and has been attributed to annealing of surface damage caused by application of the antireflection coating.

I_{sc} measurements for typical irradiated and thermal control cells are shown in figures 6 and 7 respectively. Figure 7 shows some degradation in I_{sc} as the cell was annealed. It is possible that this is due to the use of a new annealing fixture which may have deposited small quantities of contaminants on the cells during the anneal cycles. This would tend to affect the I_{sc} performance more than the V_{oc} since I_{sc} is more sensitive to light intensity. The irradiated cell in figure 6 shows almost complete recovery after the electron irradiation and partial recovery after the proton irradiation.

After the proton irradiation and again after the final annealing, dark IV curves were measured in an attempt to discover the thermal and radiation damage mechanisms. These measurements were made with a Keithley 236 source-measure instrument forcing currents from 0.1na to 10 ma and measuring voltage. Typical dark IV curves for one of the irradiated cells are shown in figure 8. The pretest curve is from one of the control cells. The curves labeled "post proton" and "post anneal 4" are from one of the irradiated cells. The control cell is used to show typical pretest characteristics because dark IV measurements were not made prior to the proton irradiation. These curves were modeled by two diodes, a series resistance, and a shunt resistance:

$$I = I_1(e^{q(V-IR_{series})/n_1kT} - 1) + I_2(e^{q(V-IR_{series})/n_2kT} - 1) + \frac{V}{R_{shunt}}$$

The slope of the dark IV curve for the control cell (pretest) corresponds to a value of n = 2 in the higher current portion (between 1μa and 1ma). This indicates a recombination region of the cell. The higher n value (2 - 3) in the lower currents from 1pa to 1μa indicates tunneling. The folding over of the curve above 1ma indicates a series resistance of about 25Ω for the control cell. The electron, proton radiation, and first three anneal cycles apparently had little effect on any of the dark IV parameters for this cell except series resistance, although this was not consistent from cell to cell. After the fourth anneal cycle, the folding over of the lower current portion of the curve indicates a decrease in the shunt resistance.

Similar dark IV curves are shown for one of the thermal control cells in figure 9. The trend for this cell is apparently an increase in the tunneling effect and a decrease in shunt resistance with additional time at high temperatures, although again this is not consistent from cell to cell. In some of the cells, the series resistance decreased with increasing time at high temperature. The parameters derived from the dark IV measurements are listed in table 1. Since dark IV curves were not measured in the earlier steps of the test program, the trends with increasing radiation and time at

temperature are not obvious. It is likely that these results are showing an intermixing of thermal and radiation effects.

Conclusions

The results of this experiment indicate that annealing of electron and proton induced radiation damage was taking place. It is apparent from the results that GaAs cell lifetimes in space applications can be extended by periodic thermal annealing of radiation damage. Complete recovery from radiation degradation may be possible with slight changes in cell design or careful design of annealing temperature profiles. Further study of the radiation and thermal damage mechanisms will be required to upgrade the cell design and determine optimum anneal profiles. These studies should include measurement of dark IV curves at varying temperatures before and after irradiation and thermal exposure in order to identify specific tunneling mechanisms. More thorough examination and modeling of the light IV curves may indicate additional damage mechanisms. Experiments with isochronal and isothermal annealing are then required in order to identify the most beneficial thermal profile. Again, measurement of dark IV curves at varying temperatures as well as light IV curves will help in detecting the intermediate stages of cell damage. Analysis of these will be important in determining the most effective thermal profile for annealing radiation damage.

References

[1.] A. C. Day, W. E. Horne and I. Arimura, IEEE Transactions on Nuclear Science NS-27, 1665 (1980).

[2.] M. B. Spitzer, J. Dingle, R. P. Gale, P. Zavracky, M. Boden and D. H. Doyle,*IEEE Photovoltaic Specialists Conference*, 930 (1988).

Cell	Type	Phase (post)	R_{shunt} (MΩ)	I_{01} (pa)	n_1	I_{02} (pa)	n_2	R_{series} (Ω)
17	thermal	anneal 3	505	62	2.39	14.2	2.15	238
18	thermal	anneal 3	9	5991	5.02	15.9	2.08	26
19	thermal	anneal 3		80	2.32	15.9	2.08	31
20	thermal	anneal 3	410	89	2.51	10.1	2.05	37
22	irradiated	p+	17	1308	3.30	75.6	2.25	126
23	irradiated	p+	124	174	2.48	18.1	2.02	
24	irradiated	p+		86	2.24	29.8	2.15	769
13	control	anneal 4		226	2.90	7.9	2.00	25
14	control	anneal 4	107	299	2.87	23.4	2.12	49
15	control	anneal 4	119	204	2.87	7.5	2.01	30
16	control	anneal 4	115	230	2.83	8.9	1.99	24
17	thermal	anneal 4		76	2.56	4.9	1.99	25
18	thermal	anneal 4	486	173000	8.45	37.6	2.20	29
19	thermal	anneal 4	72	469	3.04	14.4	2.07	26
20	thermal	anneal 4	286		2.62		2.01	25
22	irradiated	anneal 4						
23	irradiated	anneal 4	4	21560	8.26	0.5	1.74	30
24	irradiated	anneal 4	10	6075	5.68	1.4	1.84	27

Table 1. Dark IV Curve Parameters.

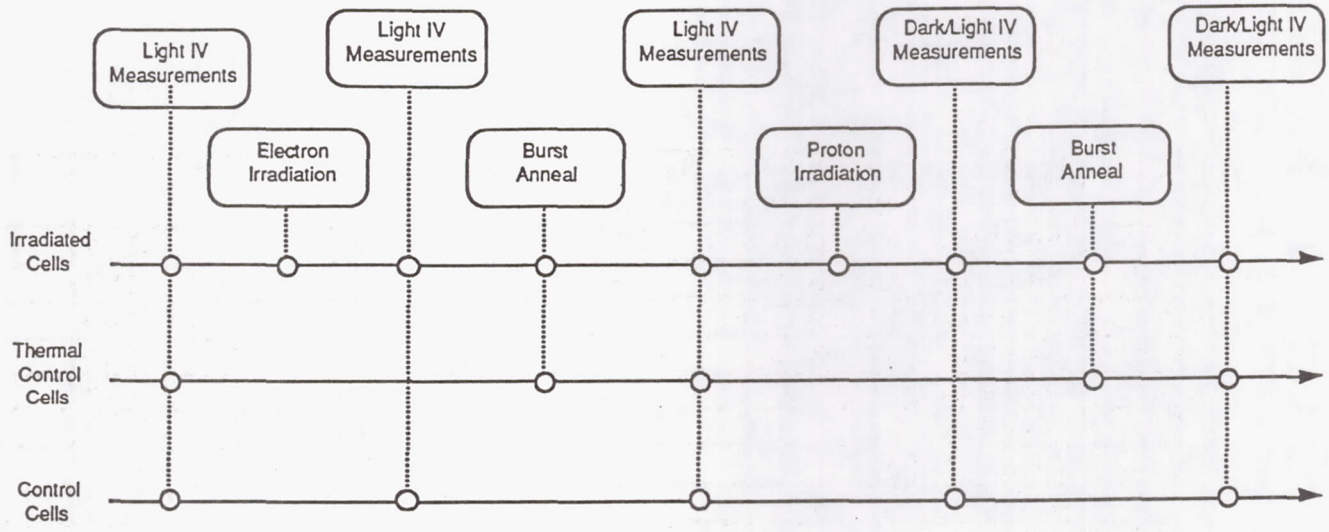

Figure 1. Burst Anneal Experiment Test Plan.

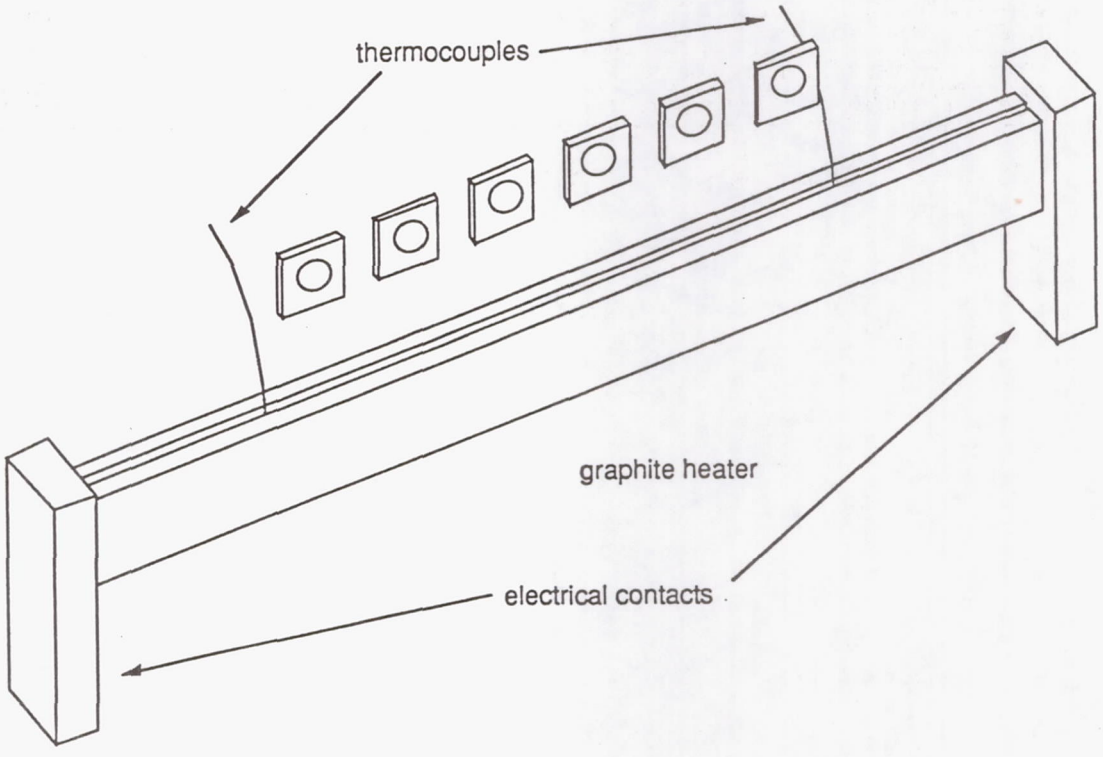

Figure 2. Annealing Test Fixture.

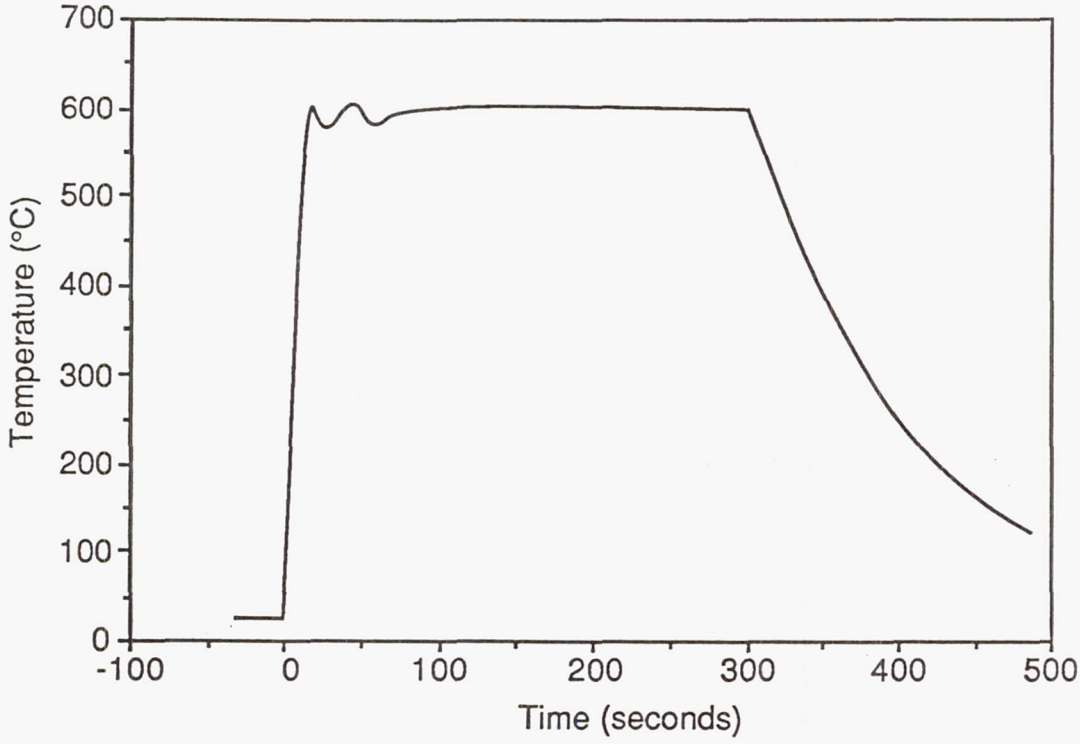

Figure 3. Typical Annealing Temperature Profile.

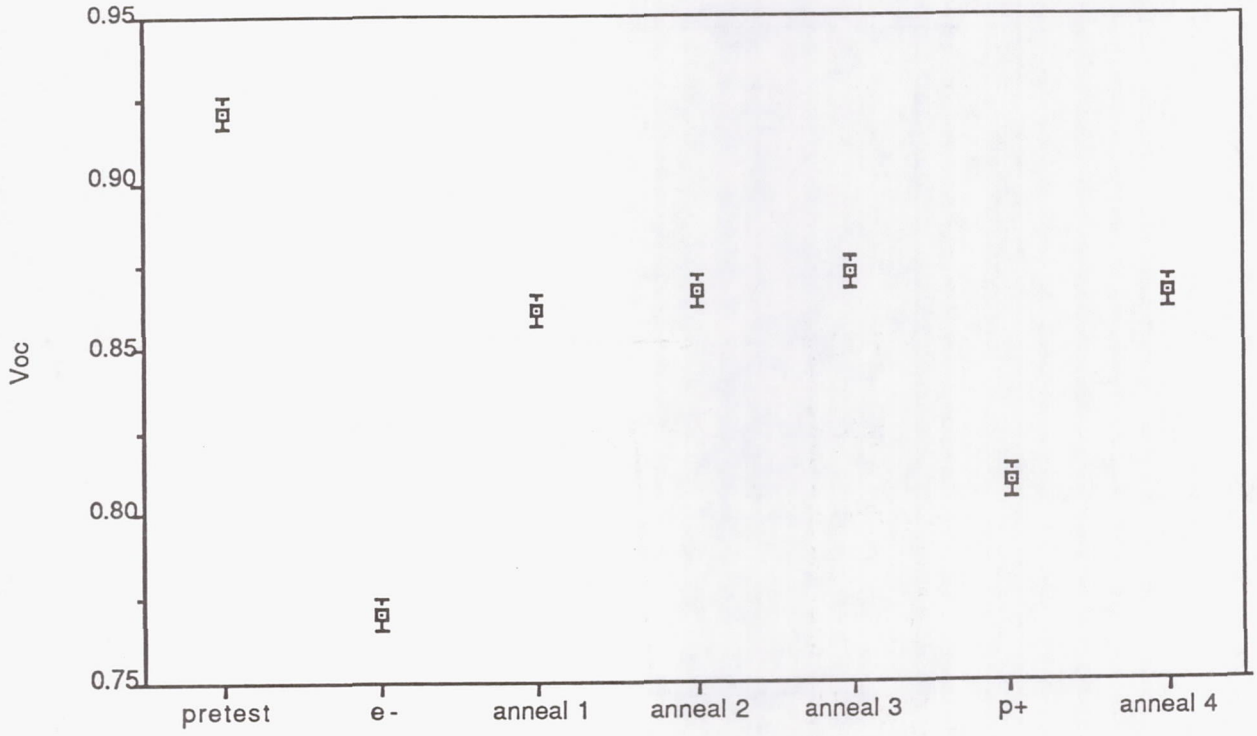

Figure 4. Irradiated Cell V_{OC} Changes.

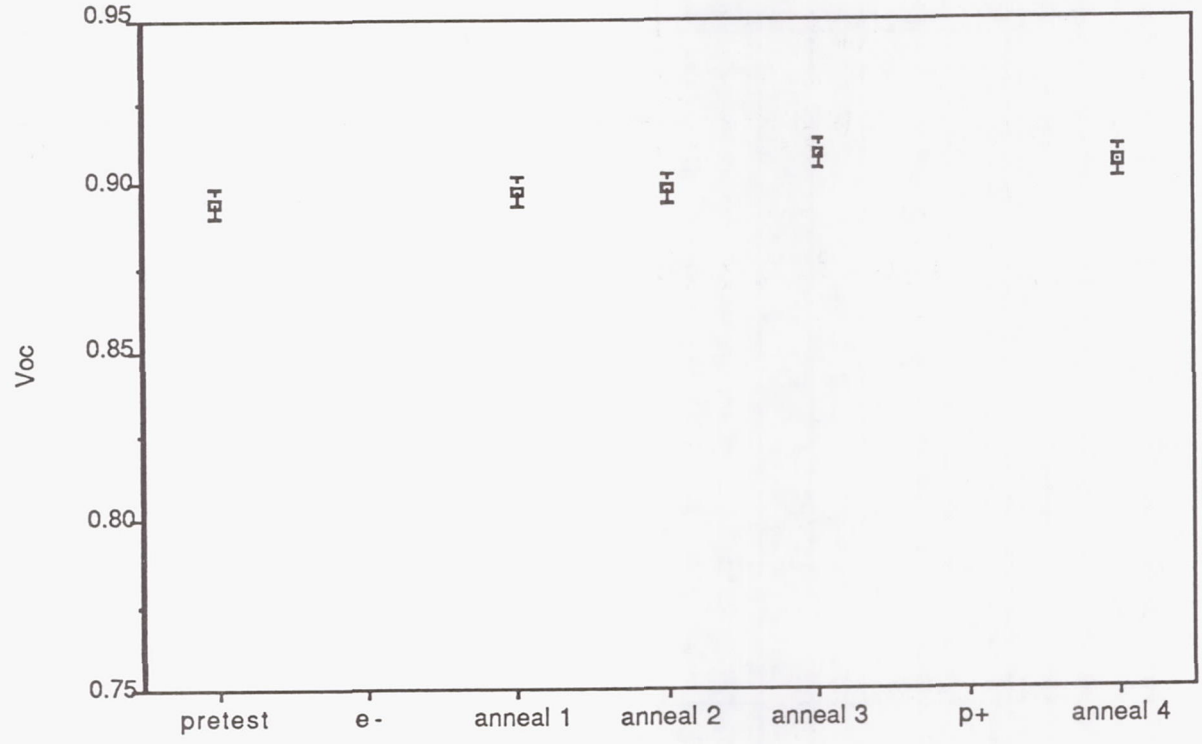

Figure 5. Thermal Control Cell V_{OC} Changes.

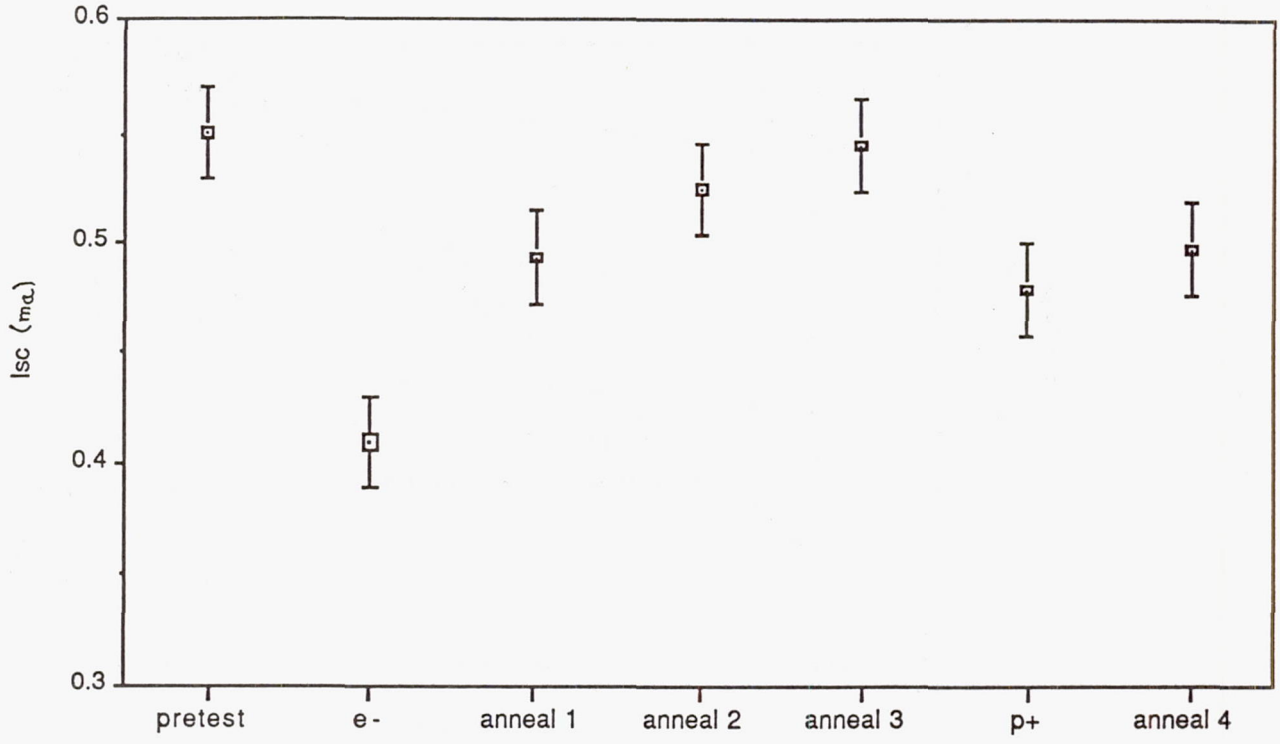

Figure 6. Irradiated Cell I_{SC} Changes.

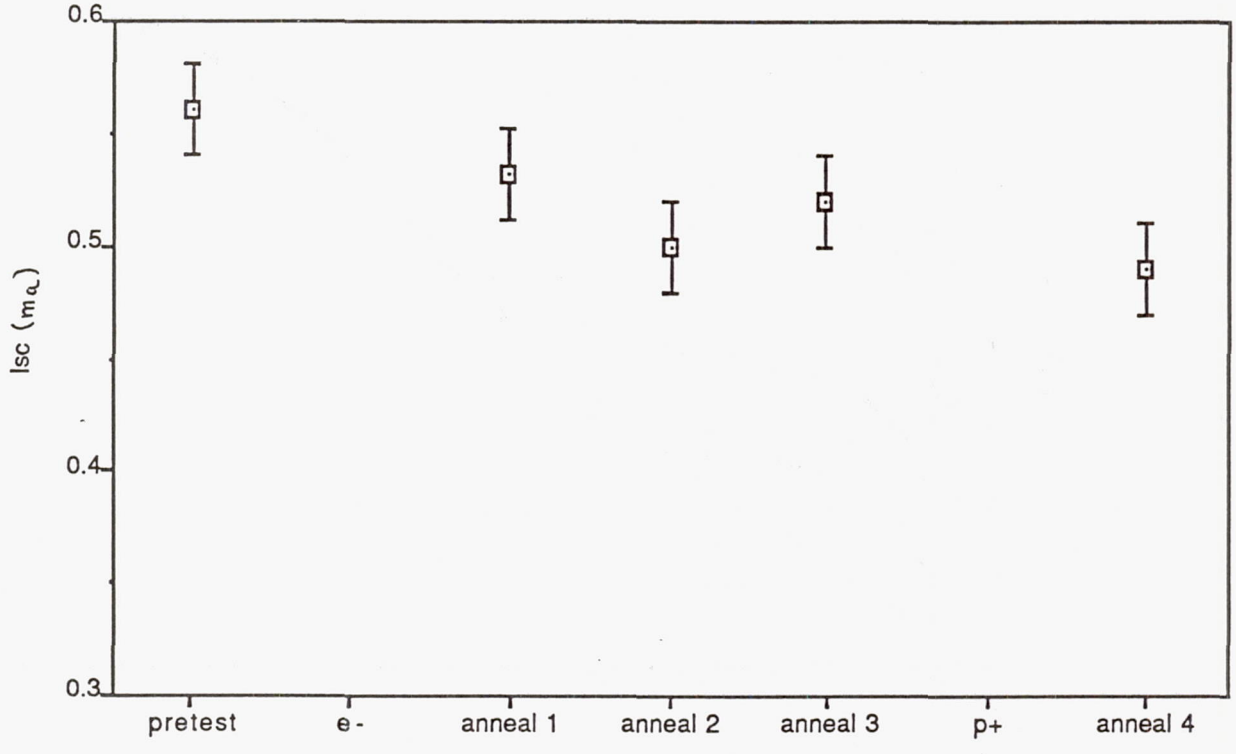

Figure 7. Thermal Control Cell I_{SC} Changes.

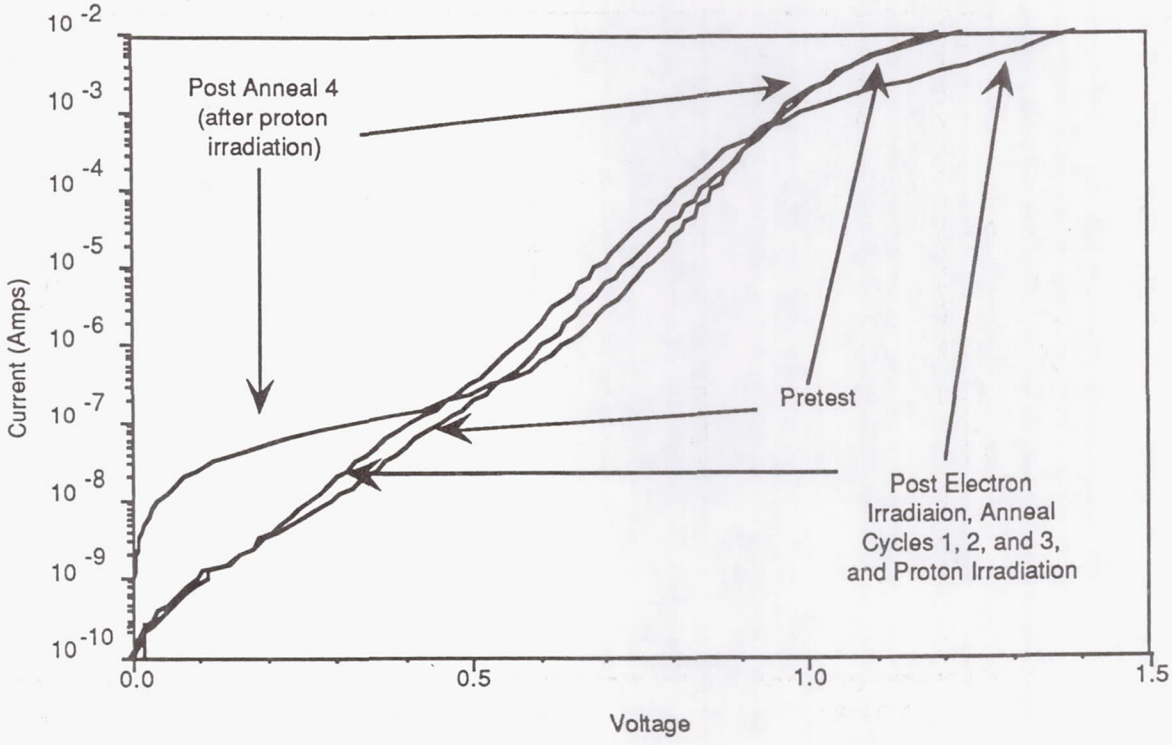

Figure 8. Irradiated Cell Dark IV Curve.

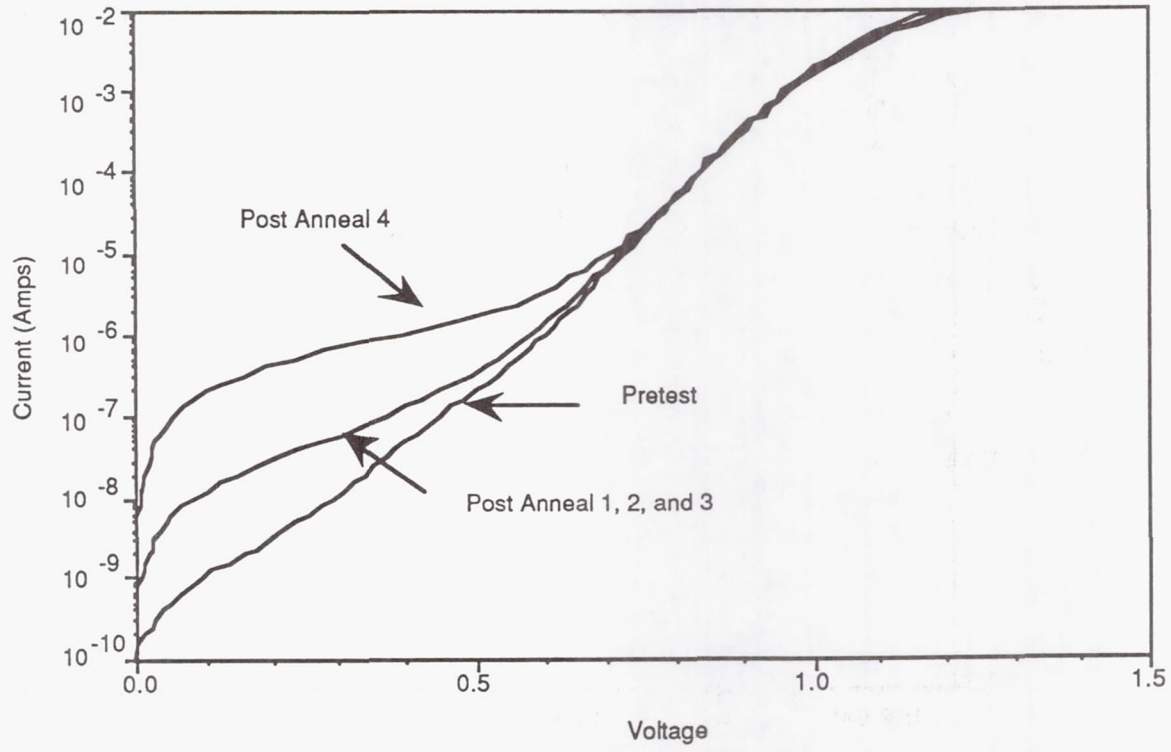

Figure 9. Thermal Control Cell Dark IV Curve.

Session 3
System Studies

Preceding Page Blank

An Approach for Configuring Space Photovoltaic Tandem Arrays Based on Cell Layer Peformance

C. S. Flora and P. A. Dillard
Boeing Aerospace & Electronics
Seattle, WA

Introduction

Meeting solar array performance goals of 300 W/Kg requires use of solar cells with orbital efficiencies greater than 20% [ref. 1]. Only multijunction cells and cell layers operating in tandem produce this required efficiency. An approach for defining solar array design concepts that use tandem cell layers involve the following:

1. Transforming cell layer performance at standard test conditions to on-orbit performance
2. Optimizing circuit configuration with tandem cell layers
3. Evaluating circuit sensitivity to cell current mismatch
4. Developing array electrical design around selected circuit
5. Predicting array orbital performance including seasonal variations

Advanced Cell Performance Data Requirements

The accuracy of predicting on-orbit array performance is governed by the accuracy and completeness of cell layer performance data. Although acceptable performance predictions are made for Si and GaAs single layer arrays from existing data, additional cell layer performance data is required for accurate predictions of arrays with tandem cell layers. This includes spectral response and transmission as a function of environment since changes to these properties on one cell layer modify performance of other cell layers. Like Si and GaAs cells, response of tandem cell layers to radiation and other environmental conditions must be known. However, the 1 MeV electron radiation damage equivalent for Si and GaAs may be inadequate for other cell types used as a tandem cell layer, such as the electron insensitive CIS [ref. 3]. For these cell layers, another radiation methodology, such as a 1 MeV proton damage equivalent, may be needed to accurately characterize their performance.

Orbital Operating Efficiency Predictions

An early step in array design is to transform cell layer performance data reported at standard test conditions (STC) to operating performance expected at a particular orbit after a given lifetime. Performance change from STC to operating condition

Preceding Page Blank

is particularly significant for tandem cell layers because their use of a broader solar spectrum range results in higher solar absorptance (solar alpha) creating higher operating temperatures than single layer cells.

Single and tandem cell layers (mechanically stacked) are evaluated with performance parameters obtained from current production cells, advanced near-term cells, and future cells. Because of uncertainty and changes in reported cell performance parameters, particularly in emerging cell technologies, the analysis was conducted parametrically with respect to cell efficiency and solar absorptance. In this manner, the scope of a particular cell technology is bound between the lower capability associated with current production cells and higher capability possible with future designs.

Specific solar cells and their performance values used are listed in table 1. Additional thermal analysis parameters considered include mean solar condition (1353 W/m^2), no albedo or earth thermal load (GEO), and a 0.85 front emissivity and 0.80 rear emissivity.

By calculating operating temperatures and using temperature coefficients listed in table 1, beginning-of-life (BOL) operating efficiencies are calculated and illustrated in figure 1. In figure 1, performance boxes are shown for each cell type where the highest efficiency (upper right corner of each box) corresponds to the highest standard condition efficiency and lowest operating temperature (lowest solar absorptance). Although figure 1 shows that the on-orbit performance of most tandem cells produce higher efficiencies than single cells, the challenge to the array designer is to translate these performances into array circuits which maintain these high efficiencies.

Tandem Cell Circuit Configuration

Design analysis of tandem cell circuits will use cell layer performance data from tandem cell modules being developed jointly by Boeing and Kopin [refs. 2-5]. The tandem cell module consists of a CLEFT GaAs top cell mechanically attached to a CIS bottom cell of equal area. The mechanically stacked cell module with external interconnection to both cell layers permits a range of circuit options to be constructed. For a particular application (orbit, temperature, radiation, etc), a circuit arrangement can be selected that maximizes circuit performance by allowing full benefit of each cell type to be obtained without restricting performance of the other cell type. This is obtained in a voltage matched circuit by series connecting each cell layer type up to a common voltage compliment at which point the cell types can then be added in parallel. To evaluate performance sensitivity of circuitry options and to select the best configuration, a 10 year GEO orbit point design case is assumed.

For this case, circuit arrangements with 2 to 4 CIS cells in series for each series GaAs cell are evaluated. Table 2 lists the cell layers electrical parameters at standard test conditions (AM0, 28°C), solar alpha and temperature coefficients [ref. 6]

considered. An estimate of end-of-life (EOL) performance was obtained by examining radiation test data of these cells [ref. 3] with a 10 year radiation fluence. The fluence consists of trapped electrons and solar flare protons shielded by 2 mil CMX coverslides on the front and rear of the module. The quantity of trapped electrons was derived from ref. 7 while refs. 8 and 9 were used to obtain the solar flare proton fluence. Calculated EOL radiation degradation factors are contained in table 2.

Figure 2 illustrates the basic analysis flow used to determine the composite current vs voltage (IV) curve of the circuit from which the maximum power of the circuit is obtained.

Figure 3 illustrates the BOL and EOL circuit efficiency of each circuitry option. The horizontal lines in this figure corresponds to the sum of the peak power of the 2 cell layers. This is the maximum possible combined circuit output. The circuit arrangements produce less power because maximum power voltage (V_{mp}) of the cell layers do not match. For the 3:1 series ratio, this voltage mismatch is very slight and circuit power approaches that of the combined individual layers.

From figure 3, it can be seen that a 3 to 1 CIS to GaAs series ratio provides the highest BOL and EOL efficiency of the circuitry options. The relative softness of the series ratio sensitivity (above 2.5:1) is due to the low CIS fill factor (50%-60%) that causes a relatively flat power response over a large voltage range around its maximum power voltage point (V_{mp}). However, dropping below 2.5:1 causes a sharp drop in circuit output as the circuit V_{mp} nears the open circuit voltage (V_{oc}) of the CIS group and is no longer contributing significant power to the circuit.

Although these results show the 3:1 arrangement provides highest performance for the 10 year GEO mission, other mission environments will produce different maximum power series ratios. Because GaAs cells degrade faster than CIS [ref. 2], in a high radiation environment the series ratio shifts toward a lower number of CIS to GaAs. Whereas, larger temperature coefficients of CIS to GaAs shifts the maximum power series ratio toward a higher number of CIS to GaAs for higher operating temperature applications, such as low earth orbit (LEO). With the mechanically stacked cell assembly arrangement, near optimum series ratios can always be constructed for a given environment. However, application of this tandem cell technology to missions which experience a range of environments (such as LEO to GEO), need to shift the circuit series ratio to remain optimum or accept a performance loss during portions of its mission as the circuit remains fixed at a nonoptimum series ratio.

To examine the degree of series ratio shift in different environments, two alternative mission orbits were considered:

LEO (500 KM, 55° inclination, 5 year life),

MEO (2000 KM, 63° inclination, 5 year life)

A series ratio analysis, similar to that conducted for the GEO case, was performed for these cases with results illustrated in figures 4 and 5 (BOL and EOL respectively). From figure 4, it can be seen the optimum BOL series ratio shifts from 3:1 at GEO to 4:1 for LEO and MEO. From figure 5, the best EOL series ratio for LEO remains 4:1 because the low radiation environment has only slightly degraded the cells, while the series ratio of the high radiation MEO case has shifted from 4:1 to 3:1 as the GaAs cells have degraded significantly more than the CIS.

Cell Mismatch Impacts on Circuit Performance

With a 3:1 series ratio circuit configuration selected for the GEO application, influence individual cell layer current mismatching has on the circuit performance is evaluated. Mismatch considerations are especially a concern with high fill factor cells such as GaAs which can be forced into their reverse bias mode with only modest amount of current mismatch in the circuit.

The analysis considers an electrical circuit composed of 27 substrings in series. Each substring contains 3 GaAs cell layers in parallel and 3 CIS cell layers in series. All cell layers in the circuit were divided into 3 current categories: average, high, and low. For a given current mismatch level, current of a high cell layer equals the average current level plus the degree of mismatch, similarly for a low current cell layer. For example, with a 5% mismatch case the average, high, and low cell layers produce 1.00, 1.05, and 0.95 of the average cell layer current, respectively. These mismatched cell layers were then statistically distributed throughout the circuit.

Using BOL cell layer properties discussed previously, the composite current vs voltage (IV) curve for the circuit was calculated with the analysis flow illustrated in figure 6.

Figure 7 illustrates the circuit IV curves for mismatch cases from 0 to 5% (Si cells are typically matched to within 1.5 to 2%). Note the current range of the graph is enlarged for improved clarity. In this figure, notching of the IV curves occur as some substring elements move toward their reverse bias mode to satisfy circuit current demand. The 'x's in this figure denote voltage positions where the lowest current substring 'LLL' (containing only low cells) shifts from reverse to forward voltage bias mode. Operating this circuit at voltages below this voltage point (at a higher current level) cause this substring and its internal cells into their reverse voltage mode. Similarly, '*'s denote the position where the second lowest current substring shifts from reverse to forward voltage bias mode. To better illustrate the circuit response to mismatching, figure 8 illustrates only the 5% mismatch case and contains some of the IV curves of its substring elements.

From figure 7, power at three voltage points (V_{mp}, 87.5% V_{mp}, and 75% V_{mp}) relative to the 0% mismatch case was calculated and is illustrated in figure 9. From this figure, a 5% mismatch causes 1% loss at V_{mp} rising to 3% at 75% V_{mp}.

To prevent excessive cell layer heating caused by reverse voltage bias operation, bypass diode circuitry can be used. By limiting voltage drop in reverse voltage bias substrings to the diode voltage drop (0.9V), heating and curve notching illustrated in figures 7 and 8 are reduced. Figure 10 illustrates IV curves for the above circuit with bypass diode circuitry. Figure 11 illustrates the 5% mismatch case with some of its substrings.

Analysis of circuit sensitivity to mismatched cells, based on statistical cell layer performance, indicates the array designer must accommodate power loss and reverse bias operation of lower current cell layers during lower operating voltages if significant mismatching is present. Corrective measures include: maintaining operating voltage above critical voltage points, incorporating bypass diodes, use of cells with long term reverse bias capability, or ensuring very low mismatching occurs.

10 KW Array Electrical Design and Performance

To illustrate array performance using tandem cell layers, a BOL 10 KW (at 160V) electrical design is sized around the 3:1 circuit arrangement selected previously. Array performance was calculated from the circuit performance coupled to various array performance factors (harness loss, blocking diode voltage drop, etc) under the incident solar flux. For this study, a solar array containing a single axis tracking system in a 10° inclination orbit at GEO was assumed. These assumptions create a seasonal incident solar flux variation as illustrated in figure 12. Figure 12 also contains incident solar flux with other array assumptions (two axis tracking, etc). The varying incident solar flux modifies cell layer performance directly by changes in solar intensity and by changes in cell layer operating temperature as illustrated in figure 13. Analysis of array output at lowest solar incidence (summer solstice) determined that 123966 4 cm^2 tandem cell modules are required to supply 10 KW. To satisfy the operating voltage requirement of 160 volts, the modules are divided into 213 strings each with 194 substrings in series. Seasonal performance of this array is illustrated in figure 14 with IV curves for maximum and minimum solar cases illustrated in figure 15. From these figures it can been seen the 10 KW at 160V requirement is achieved.

Summary

It has been shown that advanced cell layers in tandem offer significant efficiency improvements compared to single cells in a GEO environment. An approach has been shown that combines tandem cell layers into a configuration that maximizes circuit and array performance tailored to specific mission requirements. For a 10 year GEO case, maximum circuit performance is obtained with a series ratio of 3 CIS in series for each series GaAs. Circuit current mismatch sensitivities revealed modest power loss with mild current mismatch (2-3%) and some substrings with their cell layers shifting into potentially damaging reverse voltage bias mode at lower circuit

voltages. On going efforts include near term testing of GaAs/CIS tandem cell modules in individual and circuit elements to provide additional data for refinement of array performance predictions.

References

[1.] R. W. Francis, W. A. Somerville and D. J. Flood, *Conference Record 20th IEEE Photovoltaic Specialist Conference* (1988).

[2.] N. P. Kim, B. J. Stanbery, R. M. Burgess and R. A. Mickelsen, *Conference Record 24th IECEC Conference* (1989).

[3.] R. M. Burgess, W. S. Chen, W. E. Devaney, D. H. Doyle, N. P. Kim and B. J. Stanbery, *Conference Record 20th IEEE Photovoltaic Specialist Conference* (1988).

[4.] N. P. Kim, B. J. Stanbery, R. P. Gale and R. W. McClelland, *Conference Record Ninth Space Photovoltaic Research and Technology Conference* (1988).

[5.] N. P. Kim, R. M. Burgess, B. J. Stanbery, R. A. Mickelsen, J. E. Avery, R. W. McClelland, B. D. King, M. J. Boden and R. P. Gale, *Conference Record 20th IEEE Photovoltaic Specialist Conference* (1988).

[6.] C. R. Osterwald, T. Glatfelter and J. Burdick, *Conference Record 19th IEEE Photovoltaic Specialist Conference* (1987).

[7.] *Solar Cell Radiation Handbook, 3rd Ed.*, JPL Pub. 82-69 (1982).

[8.] R. G. Pruett, A Solar Proton Model for the 21st Solar Cycle (1977-1983), The Aerospace Corp. Report ATM-74(4624-01)-5 (1974).

[9.] B. E. Anspaugh and R. G. Downing, *Radiation Effects in Silicon and Gallium Arsenic Solar Cells Using Isotropic and Normally Incident Radiation*, JPL Pub. 84-61 (1984).

Table 1. Solar Cell Parameters

CELL TYPE	TEMP COEF (%/°C)	SOLAR ALPHA			TOP CELL EFFICIENCY			BOTTOM CELL EFFICIENCY UNDER		
		A	B	C	A	B	C	AlGaAs	GaAs	Si
AlGaAs	0.155	0.50	0.50	0.65	18%	17%	16%	n/a	n/a	n/a
GaAs	0.23	0.63	0.70	0.81	21%	19%	17%	4.4%	n/a	n/a
Si	0.45	0.65	0.65	0.70	16%	15%	14%	7%	2%	n/a
CIS	0.69	0.80	0.83	0.85	n/a	n/a	n/a	8%	3%	2.1%
GaSb	0.309	0.90	0.90	0.95	n/a	n/a	n/a	9.5%	4.5%	3.1%

A : POTENTIAL (FUTURE)
B: STATE-OF-THE- ART (NEAR TERM)
C: TYPICAL PRODUCTION (DEMOSTRATED OR ESTIMATED)

Table 2. Cell Layer Parameters
($1cm^2$ 1988 balloon flight standards)

PARAMETER		SOLAR CELL TYPE		UNITS
		GaAs	CIS	
Isc		0.02993	0.01506	A
Voc		0.9818	0.3637	V
Imp		0.02885	0.01209	A
Vmp		0.8526	0.2835	V
Temp Coeff:	Isc	615	260	PPM/°C
	Voc	-2100	-4580	PPM/°C
	Imp	615	260	PPM/°C
	Vmp	-2300	-5670	PPM/°C
SOLAR ALPHA		0.78	0.83	
EOL FACTOR:	Isc	0.90	1	
	Voc	0.93	1	
	Imp	0.885	1	
	Vmp	0.885	1	

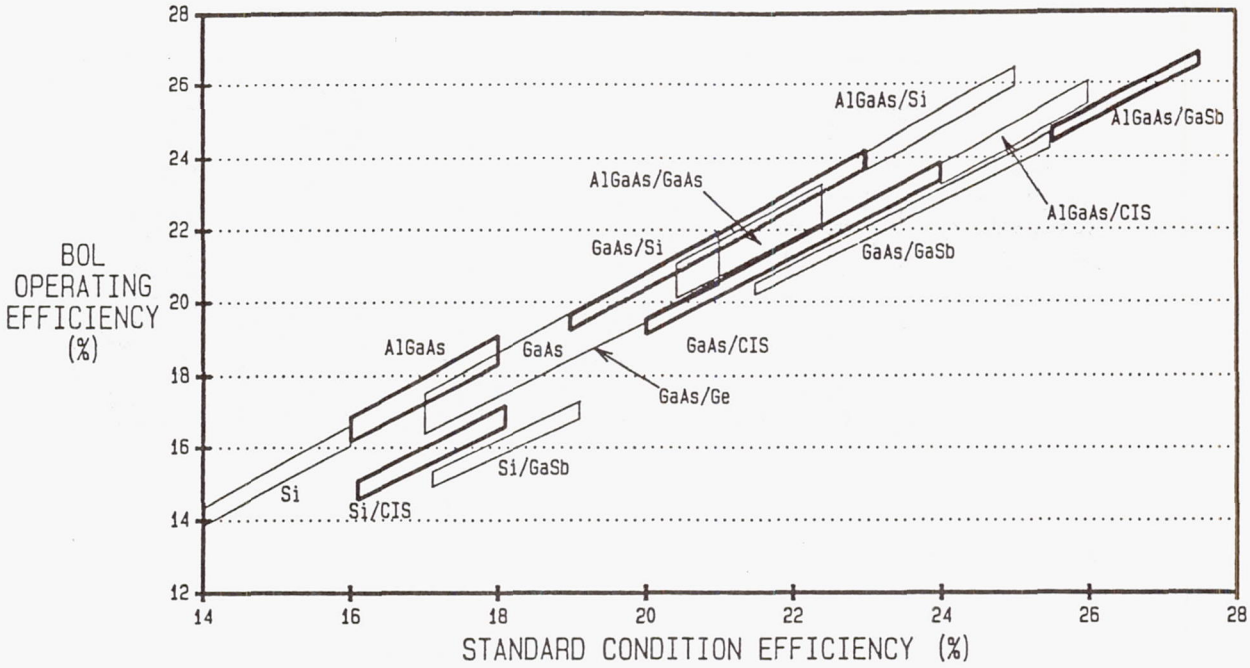

Figure 1. BOL Operating Efficiency at GEO vs Standard Test Condition Efficiency

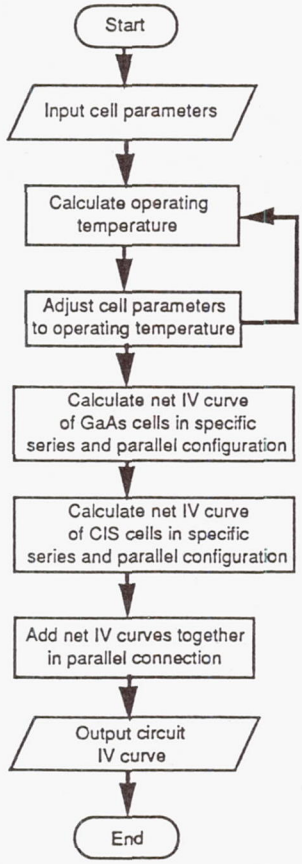

Figure 2. Algorithm Flow for Circuit Analysis Model 'IV.FOR'

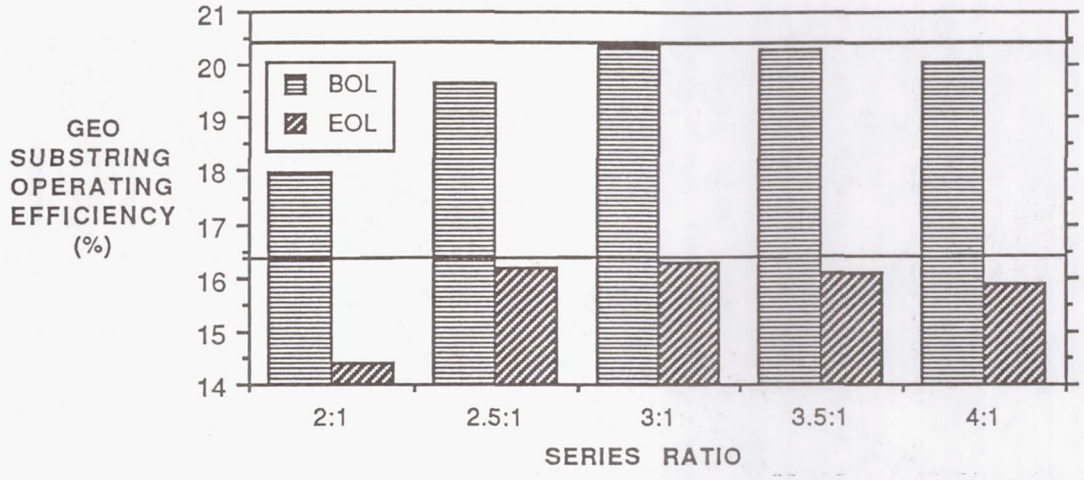

Figure 3. GEO On-orbit Circuit Sensitivity to Series Ratio

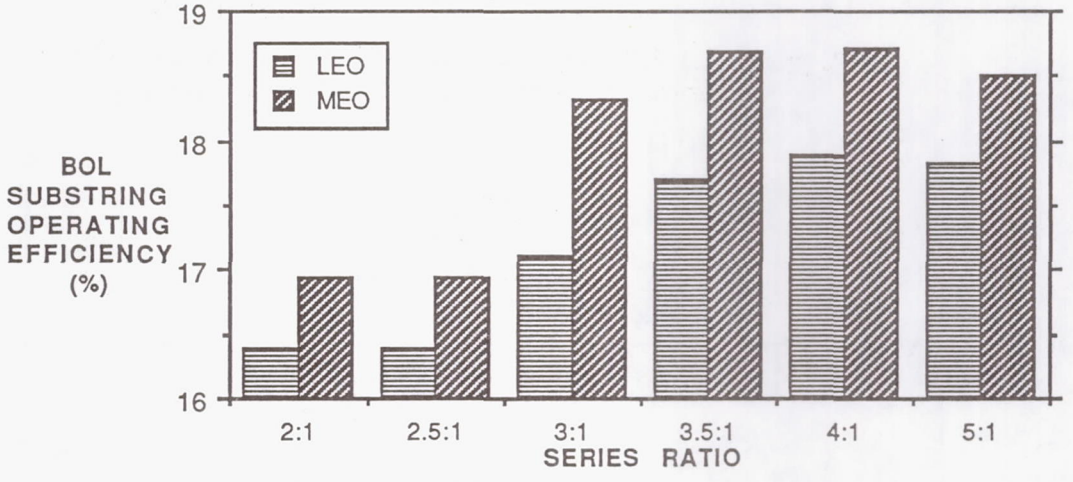

Figure 4. BOL On-orbit Circuit Sensitivity to Series Ratio

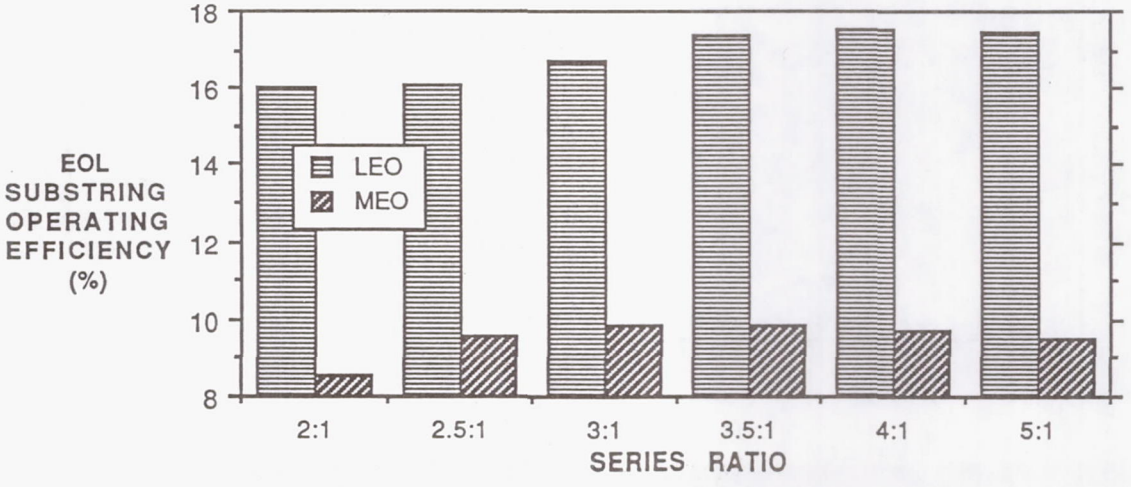

Figure 5. EOL On-orbit Circuit Sensitivity to Series Ratio

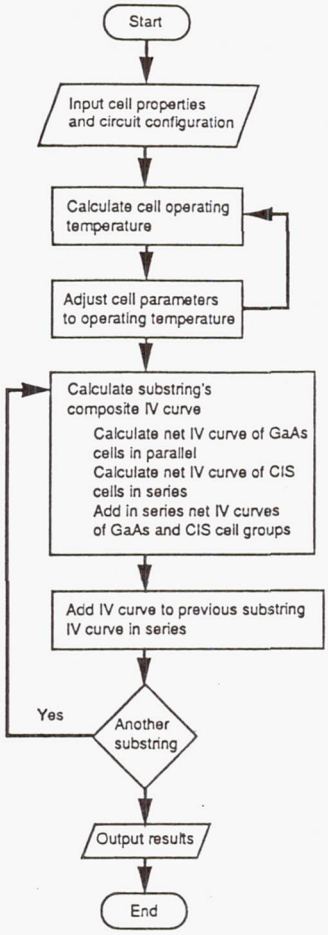

Figure 6. Algorithm Flow for Mismatch Model 'CKT.FOR'

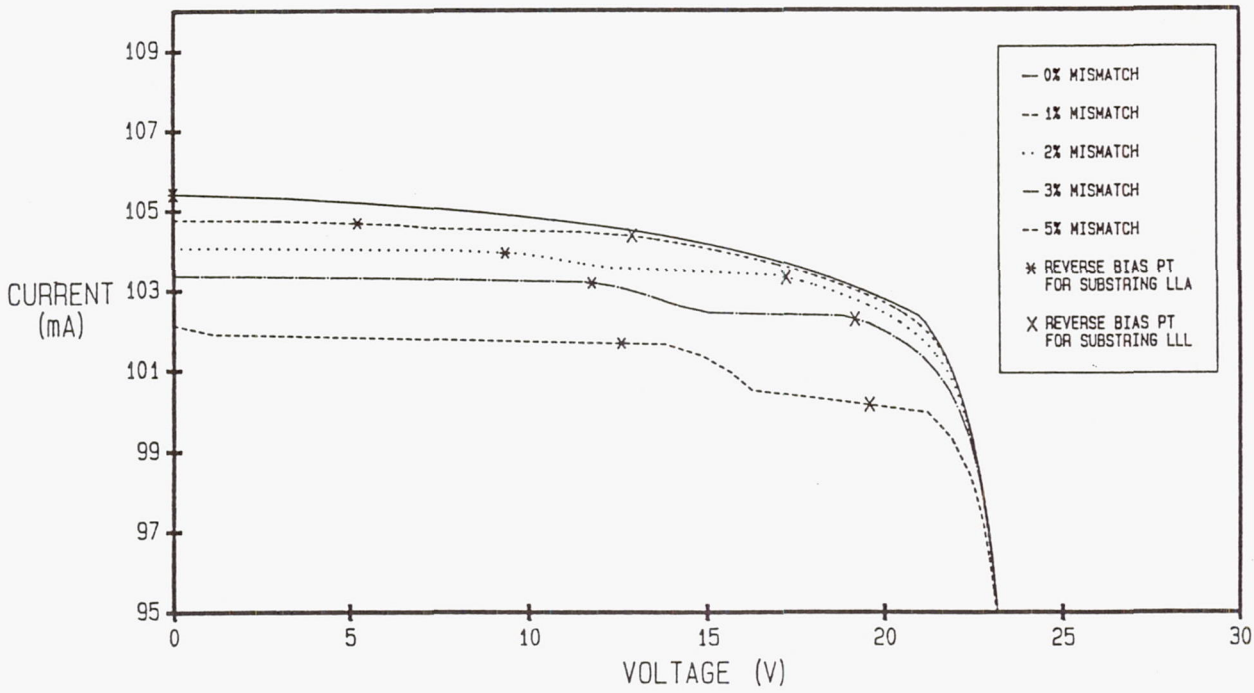

Figure 7. Circuit Sensitivity to Cell Mismatching

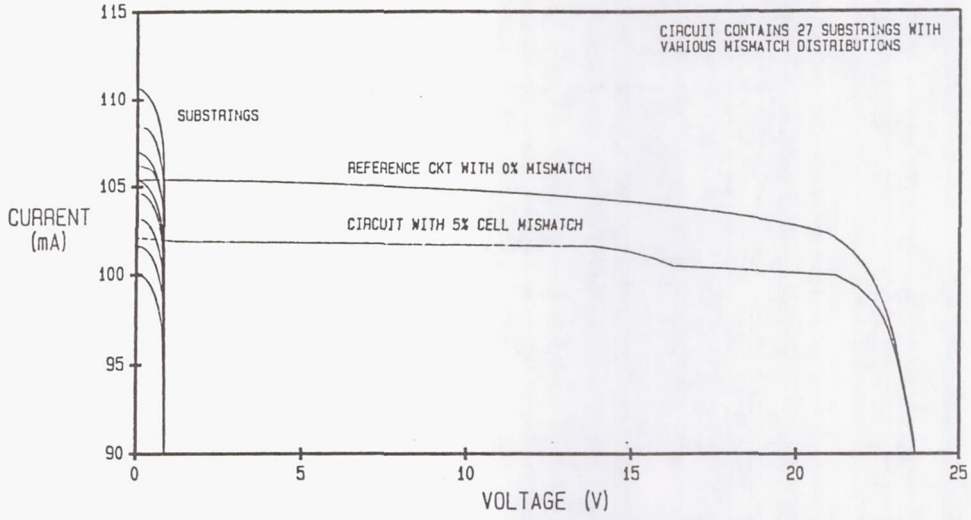

Figure 8. Circuit Sensitivity to Cell Mismatching

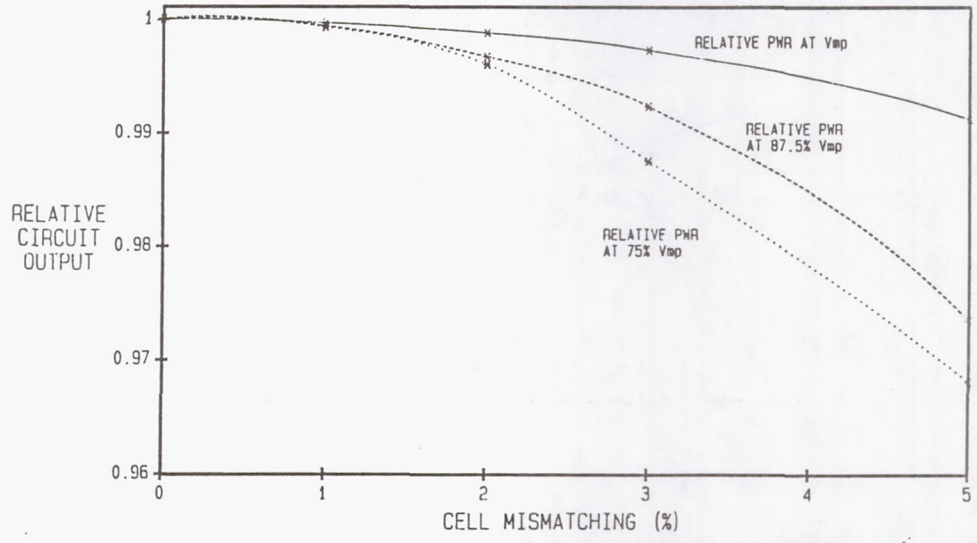

Figure 9. Relative Circuit Performance to Cell Mismatching

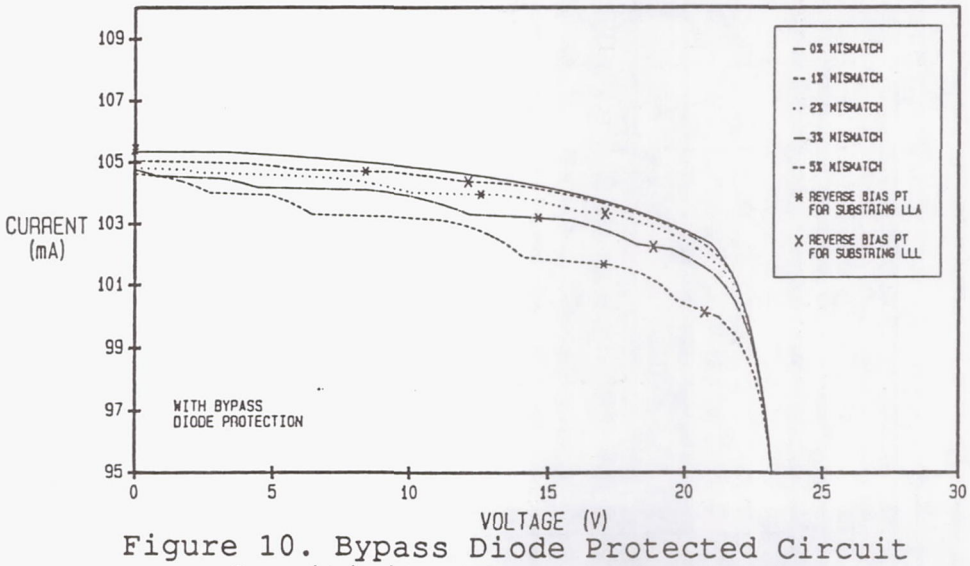

Figure 10. Bypass Diode Protected Circuit Sensitivity to Cell Mismatching

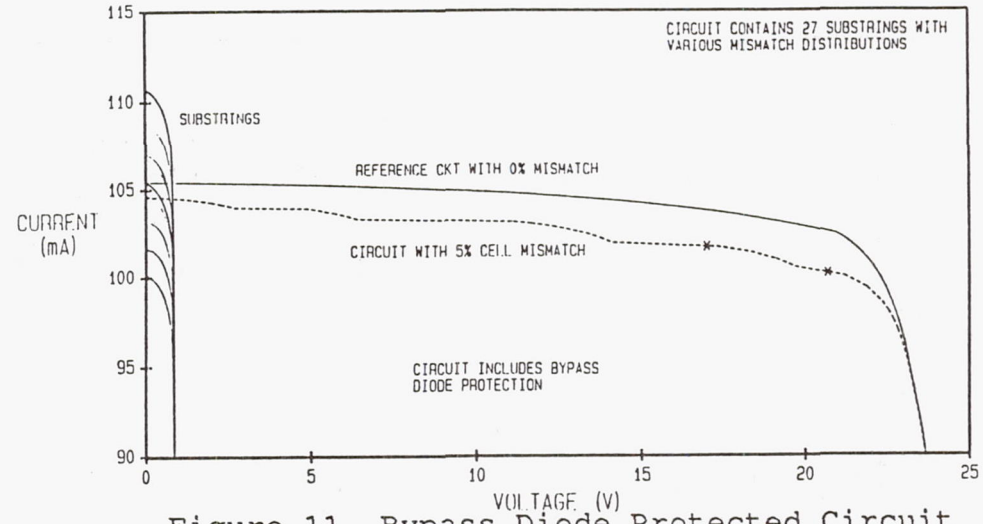

Figure 11. Bypass Diode Protected Circuit Sensitivity to Cell Mismatching

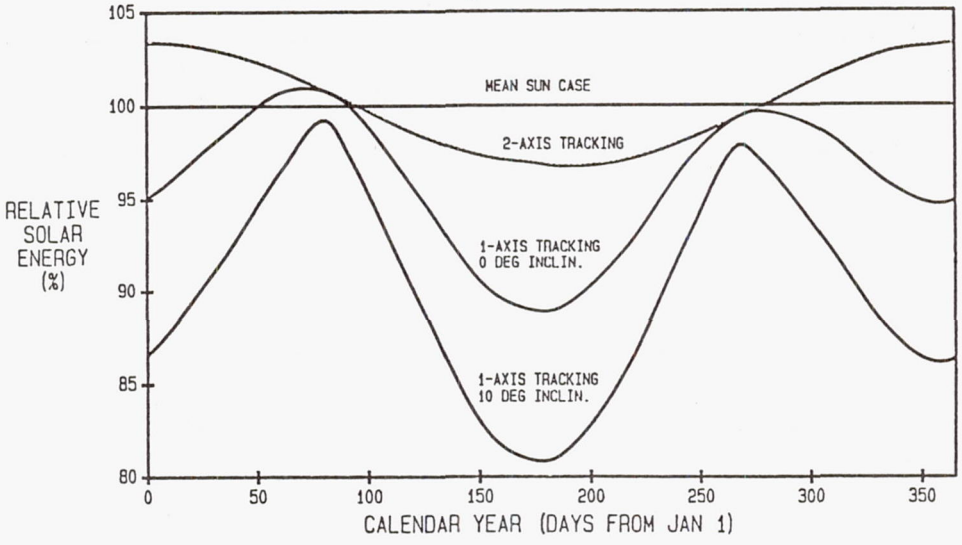

Figure 12. Seasonal Incident Solar Flux

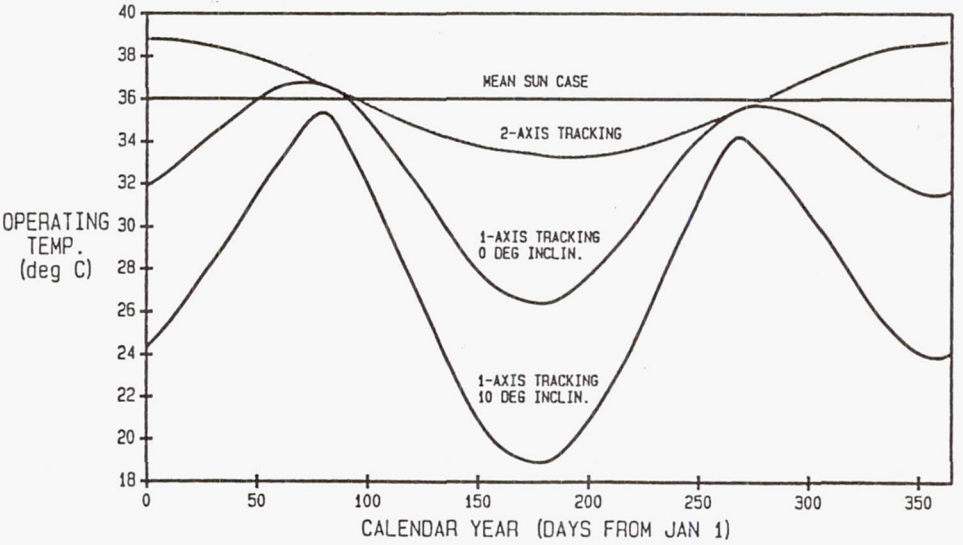

Figure 13. Seasonal Cell Module Operating Temperature

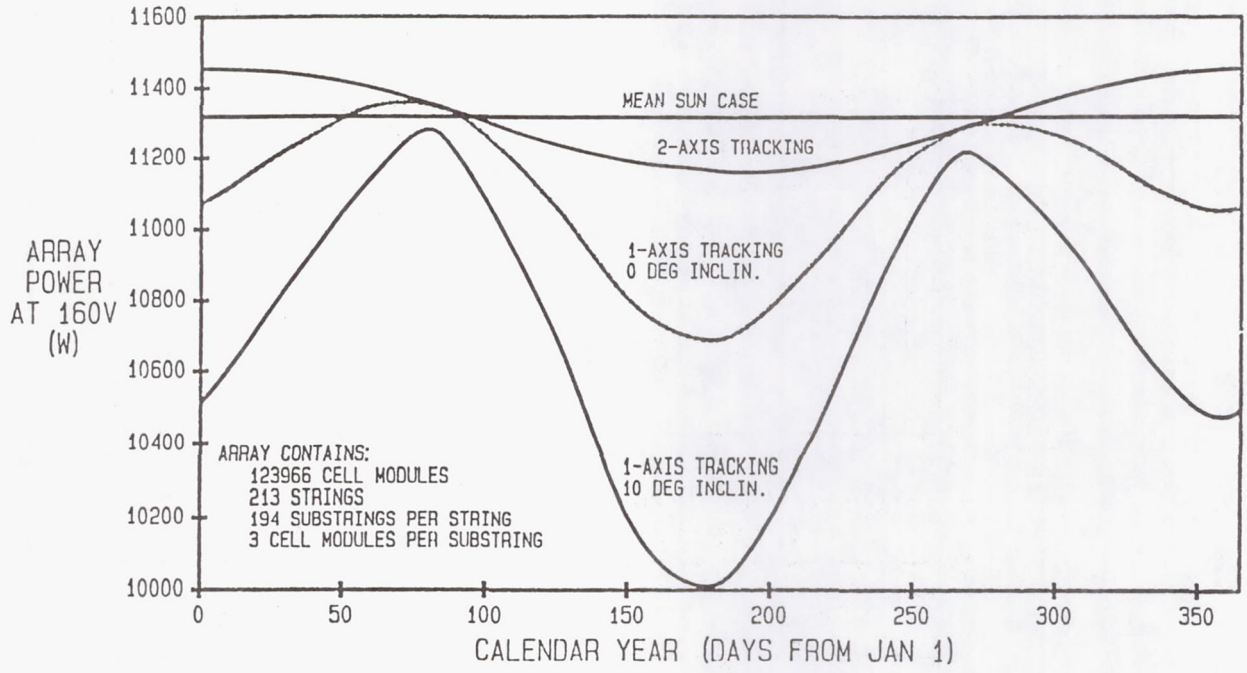

Figure 14. Seasonal Array Performance at Rated Voltage

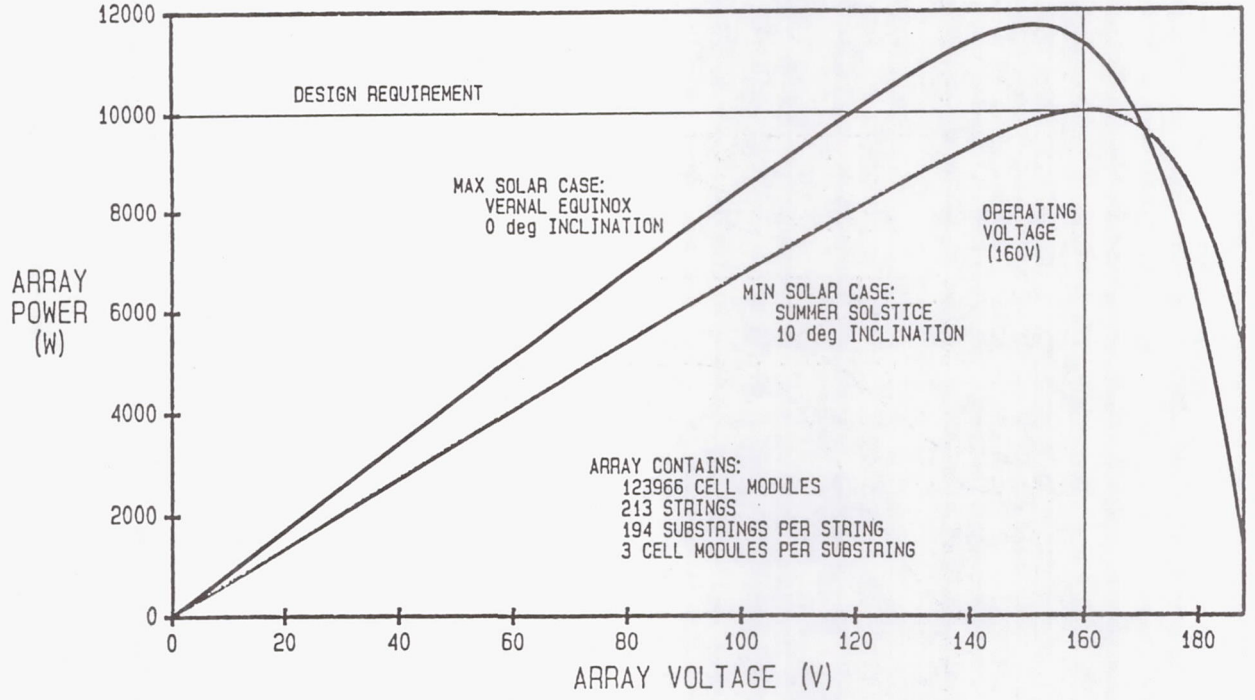

Figure 15. Minimum and Maximum BOL Array Performance

Review of Thin Film Solar Cell Technology and Applications for Ultra-Light Spacecraft Solar Arrays

Geoffrey A. Landis*
NASA Lewis Research Center
Cleveland, OH

*National Research Council Resident Research Associate at NASA Lewis

Introduction

In this paper developments in thin-film amorphous and polycrystalline photovoltaic cells are reviewed and discussed with a view to potential applications in space. Two important figures of merit are discussed: efficiency (i.e., what fraction of the incident solar energy is converted to electricity), and specific power (power to weight ratio).

Current Generation Technology

Solar cells currently used in space are single-crystal silicon and gallium arsenide cells [ref. 1]. Silicon solar cell performance has recently had major gains, and the previous estimates for the "limits" to performance have had to be revised upwards. New estimates taking into account new technologies such as light trapping and surface passivation suggest achievable efficiencies of up to 22%, with the best cells to date having already achieved efficiency of 20%.

The best GaAs cells are roughly 21.4% efficient under space (AM0) conditions [ref. 2]. Cells manufactured using current production technology have a somewhat lower efficiency. LSI in Japan has demonstrated production runs of 120 cells with an average efficiency of 20% AM0 [ref. 3]. For GaAs on Ge, an efficiency of 21.7% has been measured under the simulated AM0 spectrum [ref. 4,5]. Unfortunately, high altitude tests have shown that the actual space solar spectrum does not contain as much long wavelength irradiance as simulations, and the actual efficiency is lower than the tested values [ref. 6]. This problem can potentially be eliminated either by improving the Ge subcell or by adding Al to the GaAs to let through more light. Tobin et al. calculate a limit efficiency for this cell design of 35.7%, compared to 27.5% for GaAs alone [ref. 5].

Next generation technology will likely improve these efficiency values. For ultrathin silicon cells with light trapping and surface passivation, the optimum thickness decreases and the efficiency increases. For highest end-of-life efficiency, the optimum thickness of silicon cells may be as low as 2 microns, leading to potentially very high specific power. The radiation tolerance of such ultrathin cells may be extremely good,

since the thickness is less than the diffusion length even after radiation damage. Calculations predict that such ultrathin Si cells have efficiency and radiation tolerance as good as that of III-V solar cells [ref. 7].

Considerable interest has recently been focussed on indium phosphide (InP) as a new high efficiency solar cell material. Cells with efficiencies as high as 18.8% AM0 [ref. 8] have been produced [ref. 9]. A major reason for the interest in the material is that InP is considerably more resistant to radiation damage than silicon or GaAs.

Finally, it should be noted that efficiency can be increased by concentrating the incident sunlight, either by means of a mirror or a lens. This approach will not be discussed in detail here.

Thin-Film Solar Cells

An alternative to the conventional single crystal solar cell is the thin-film solar cell. Thin-film solar cells are made from thin (1 to 5 micron) polycrystalline or amorphous semiconductor layers deposited on an inert substrate or superstrate material. The materials used are high absorption direct bandgap semiconductors; the high absorption constant allows essentially complete absorption of the light within the first micron or so of the material. Recently thin film solar cells have been the topic of intense research for low-cost terrestrial electricity production, since the low materials usage and potential for high throughput, automated deposition allows the production cost to be extremely low. Initial research efforts focussed on amorphous silicon; recently copper indium selenide and cadmium telluride have shown extremely good experimental results. For space applications, however, little work has been done. The potential use of thin film solar cells for space will be a topic of research under the surface power task of the NASA "Pathfinder" program to develop enabling technology for future NASA missions.

Thin-film solar cells can be made from a wide variety of materials including ternaries and quaternaries; many of these have not been extensively studied. The achievable efficiency of a solar cell material will depend on the characteristic energy bandgap of the material. An idealized calculation of achievable efficiency versus bandgap is shown in figure 1, with the bandgaps of some of the important solar cell materials indicated (after Loferski, [ref. 10]). For the technologically well-developed materials, such as silicon and GaAs, the efficiencies on this chart are very close to the achieved efficiencies (*e.g.*, 21.4% for GaAs, 20% for Si). For thin film materials, achieved efficiencies as yet fall well below these values. This is for two reasons. First, Si and GaAs have received the benefit of extensive materials development research done for the electronics industry, and are technologically very well understood materials, while thin film materials are relatively new and have been comparatively little researched. Second, because the thin film materials are polycrystalline or amorphous, there are additional sources of efficiency loss due to grain boundary effects and the effects of

structural disorder. It is as yet unknown whether the ultimate efficiencies of these materials will approach those of the single crystal materials.

Since the absorption coefficients of all of the materials discussed is very high, the cells can be made extremely thin, typically a few microns, compared to several hundred microns thickness required for conventional silicon solar cells. This means that the technology could potentially be extremely low weight, if the cells can be deposited on low mass substrates (or superstrates). However, the urrent technology development programs are directed at terrestrial use, for which the preferred substrate is typically 1/4 inch thick glass; cheap and rugged but not light. There is little or no research on alternative, lightweight substrates

Advantages of thin-film solar cells are:

–high radiation tolerance

–high specific power; potentially in the kilowatt/kilogram range.

–large area solar cells with integral series interconnections.

–flexible blankets

–large (by spacecraft standards) body of array manufacturing experience.

–low cost.

The disadvantages of thin-film solar cells are:

–lower efficiency

–lack of spacecraft experience

–not currently produced on lightweight substrates.

Experimental measurements on thin film solar cells are almost always quoted for a solar spectrum filtered by passage through the atmosphere (Air Mass 1.5, or AM1.5 spectrum). Almost no measurements have been made of cells under the space (Air Mass Zero, or AM0) spectrum. Efficiency measured under space sunlight is lower than that under terrestrial sunlight because most of the added energy available in space is in the infrared and ultraviolet regions, to which solar cells are generally not very responsive. The conversion from AM1.5 to AM0 efficiency typically involves an efficiency decrease of about 20 percent for cells with bandgaps in the range of 1 to 1.5 eV, varying slightly with the spectral response of the solar cell in question. For example, for one amorphous silicon cell discussed in the literature [ref. 11], conversion of AM1.5 efficiency to AM0 is by a multiplicative factor of 0.80. In this paper efficiency figures quoted at AM1.5 have all been converted to AM0 efficiency using an assumed conversion factor of 0.80.

While thin-film technologies have not yet been demonstrated in space, there is a very large (by space standards) manufacturing base on the Earth: tens of megawatts per year for a-Si, a rapidly increasing capability of perhaps one megawatt per year for $CuInSe_2$, and around a hundred kilowatts per year for CdTe.

Very little actual flight experience is available on thin-film cells. $CuInSe_2$ and a-Si cells are both now flying on the LIPS-III satellite [ref. 12].

Table 1 summarizes the historical and projected efficiency of some of the most important solar cell types.

CdS/Cu_2S

The first thin-film solar cell developed was the heterojunction cadmium sulfide/copper sulfide cell [ref. 13,14]. The best achieved efficiency on these cells is about 7% [ref. 15], with very high radiation tolerance. These cells were made obsolete by the development of more stable and higher-efficiency thin-film materials.

Copper Indium Selenide

Currently the leading technology for thin film photovoltaics is copper indium selenide [ref. 16]. As of 1989, an efficiency of 10.4% AM0 has been achieved by Arco Solar (again using the factor of 0.8 to convert from values measured at AM1.5 of 13% [total area] 14.1% [active area]). 12% efficiency can be confidently predicted in the near term [ref. 17]. Figure 2 (courtesy ARCO Solar) shows the electrical characteristics of the best $CuInSe_2$ cell. Modules can be made with integral interconnection of the deposited thin-film cells. ARCO Solar, for example, produces large area (4000 cm^2) modules [ref. 18] with multiple cells series interconnected on a single substrate.

The bandgap of copper indium selenide is 1.0 eV. This is on the low side of the efficiency maximum shown in figure 1, but still reasonable. It is, as discussed below, nearly ideal for the bottom cell of a cascade.

The absorption constant of $CuInSe_2$ is extremely high, allowing the possibility of cells as thin as one micron. Existing cells consist of a layer of the active copper indium selenide, typically about 3 microns in thickness; a front contact and heterojunction window of either cadmium/zinc sulfide or zinc oxide plus cadmium sulfide, thickness typically about one micron; and a back contact of molybdenum, typically several thousand angstroms thick. Thus the material has inherently low weight, and the primary mass is that of the substrate onto which the film is deposited.

A wide variety of manufacturing methods have produced ¿8% efficiency, including vacuum evaporation, reactive sputtering, and electroplating of the base material onto the substrate. In general, all of these techniques either involve high temperature deposition, or a high temperature post-deposition anneal step. This could be a problem for space applications, where it would be desirable to be able to deposit the cell onto

a thin plastic (e.g., Kapton) substrate. Deposition onto a thin substrate has not been demonstrated to date.

Copper indium selenide has the highest measured tolerance to electron irradiation of any solar-cell material known to date.

Other I-III-VI_2 Compounds

Related I-III-VI_2 semiconductors have also been studied for solar cell use, although not as extensively as $CuInSe_2$. The goal of investigations has been to identify related semiconductors which have the same ease of manufacturing into thin-film solar cells, but have wider bandgaps and thus presumably higher ultimate efficiency.

Copper gallium selenide is a major candidate for the proposed higher efficiency sucessor to copper indium selenide. The advantage of $CuGaSe_2$ is the wider bandgap, 1.67 eV, which is much closer to the optimum for the solar spectrum (see figure 1), and nearly ideal for a cascade upper cell.

While the best experimental results to date are only 4.6% efficiency, the material has not been extensively developed. One known problem is that the CdS heterojunction used for $CuInSe_2$ absorbs light in the short wavelength end of the spectrum. Since this is more important for the wider bandgap material, a different (wider bandgap) heterojunction material needs to be developed to reach maximum efficiency for $CuGaSe_2$ [ref. 19,20]. Unless $CuGaSe_2$ differs electronically from $CuInSe_2$ in some yet-unknown way, ultimate efficiency for $CuGaSe_2$ cells should be about 18% better than for $CuInSe_2$.

$Cu(InGa)Se_2$ quaternary compounds can be produced with bandgaps intermediate between copper indium selenide and copper gallium selenide. This allows a bandgap variable from 1.0 to 1.67 eV. Such materials can be tailored for a good match to the AM0 spectrum, yet be easier to work with than the wide bandgap $CuGaSe_2$. Cells made with the In/Ga ternary show performance as good or better than that achieved with $CuInSe_2$. Boeing has reported efficiencies of 10.5% measured as AM0 results with $CuIn_{(1-x)}Ga_xSe_2$ cells where x is on the order of 25% [ref. 21]. Arco Solar and SERI have also reported good results [ref. 22].

Another proposed wide bandgap candidate is copper indium sulfide. $CuInS_2$ has a bandgap of 1.55 eV, very close to the optimum. It is not a very well studied material, and until recently no good semiconductor properties had been made with the material. The results on $CuInSe_2$ cells have restimulated interest in the material, and recently thin-film cells have been made with an efficiency of 5.8% AM0 [ref. 23].

Many other I-III-VI_2 ternaries exist; only a minimum amount of research has been done

Cadmium Telluride

A second material which is being extensively studied for thin film solar cells is cadmium telluride. The bandgap of CdTe is 1.5 eV, which is very well matched to spectrum. It is produced in thin-film form by a wide variety of deposition methods. Best solar cell results to date have an AM0 efficiency of about 9.8% [ref. 24].

Like $CuInSe_2$, it is currently not produced on thin substrates. However, unlike $CuInSe_2$, most CdTe deposition methods are "superstrate" technologies, where the cell is deposited inverted upon transparent glass, which is used as the front cover. This glass can easily be produced in 50 micron (two mil) sheets. It is also possible that a transparent plastic could be used.

Mixed alloys are also possible in the II-VI_2 system. Ternary alloys of cadmium zinc telluride and cadmium manganese telluride [ref. 25] can be made with a higher bandgap than CdTe; ternary alloys of mercury cadmium telluride can be made with lower bandgap. Mercury cadmium telluride (HgCdTe) ternary cells have been made with efficiency as high as 8.5% AM1.5 [ref. 26]. HgCdTe with high mercury content (low bandgap) is a material which has been well developed for infrared sensors. Transfer of the technology to solar cells should be straightforward. One advantage of HgCdTe is that it is easier to contact than CdTe, and, in fact, the best CdTe cells utilize HgCdTe for the electrical contacts.

Another II-VI_2 compounds which may be useful for thin-film solar cells is cadmium selenide (CdSe) [ref. 27]. The bandgap of CdSe is 1.7 eV, slightly high for a single junction cell, but excellent for the top element of a cascade.

Amorphous silicon

The material referred to as amorphous silicon is actually a mixed alloy of silicon and hydrogen, where the hydrogen incorporation is necessary for good electronic properties and can range from a few percent to as much as 15%.

The material differs from the thin film materials described above in that the crystal is unstructured. The effective bandgap of amorphous silicon can be varied depending on the deposition parameters within a range of about 1.6-1.7 eV. This is well matched to the solar spectrum. The bandgap can be tailored further by addition of carbon to raise the bandgap, and germanium or tin to reduce it, but so far such amorphous silicon alloy cells have not shown as high performance as pure amorphous silicon.

Amorphous silicon solar cells for terrestrial use are the subject of a very large and active research program, currently funded at several million dollars per year. Much of this research will likely be applicable to space. The manufacturing technology base for a-Si is very large by space standards. Amorphous silicon solar cell modules are currently in production by a number of companies at the ten million watts/year

level. This yearly production level is considerably larger than the entire amount of conventional solar cells flown in space.

The best measured efficiency of an amorphous cells under space conditions is currently about 9% AMO for single junction cells. Some better efficiencies have been reported, but not independently verified. Efficiencies of 5% are more typical of what we measure.

A difficulty with amorphous silicon solar cell technology is the light-induced degradation, or Staebler-Wronski effect. First generation a-Si modules experienced about 20% degradation in peak power over two years of exposure to light. The best current a-Si solar cells are more stable, but still experience a 10 to 15% loss of performance. It is believed that future improvements and better understanding of the physics will reduce this degradation still further.

Technology to manufacture amorphous silicon solar cells on lightweight thin substrates has been demonstrated, on thin polymer and metals by ECD [ref. 11], on thin polyimide by 3M [ref. 28], and on thin polyethylene terepthalate by Teijin Ltd [ref. 29]. There is some interest in lightweight, high specific power amorphous Si arrays for space [ref. 11, 30]. The best reported amorphous silicon module manufactured on a thin substrate is that of Hanak *et al.* [11], who reported an efficiency of 4.2% AM0 on a 60 by 30 cm module. Despite the modest efficiency, they nevertheless note that the unencapsulated specific power is 2.4 kW/kg, a value which is very impressive by conventional spacecraft standards.

Thin Polycrystalline silicon

A final thin film technology which should be mentioned is thin polycrystalline silicon. Recently results of up to 12.6% AM0 have been reported by a proprietary technique developed by Astropower [ref. 31]. Crystalline silicon is an indirect bandgap material and does not have the extremely high absorption constant typical of the other thin-film materials; consequently, a "thin" polycrystalline silicon cell is considerably thicker and heavier than other thin film technologies. The silicon is deposited on a ceramic substrate; due to the high-temperatures typical of most silicon deposition processes it is not clear if it will ever be possible to produce the material on lightweight substrates. Nevertheless, future developments in this technology may make it of interest, especially for the bottom element of a cascade.

Radiation Tolerance of Thin-Film Solar Cells

In general, all of the thin-film solar cell types have exceptionally high radiation tolerance compared to conventional single-crystal cells. A review of radiation damage effects in thin film cells will be published [32].

Thin-film CdS/Cu_2S solar cells showed excellent radiation tolerance, with no degradation in power on exposure to up to 10^{17} 1-MeV electrons/cm^2 [ref. 33], as well as high tolerance to proton irradiation [ref. 34]. This led to the hope that thin-film cells in general would have high radiation tolerance, an expectation which has for the most part been proven correct.

Thin-film copper indium selenide solar cells have the highest radiation tolerance of any solar cell measured to date. Existing experimental data show no noticible degradation in performance at 1-MeV electron fluences of up to 10^{16} electrons/cm^2, a dose equivalent to about 200 years of exposure at geosynchronous orbit if standard coverglass protection is assumed. (In fact, the measured efficiencies actually improved slightly) [ref. 35].

Under 1 MeV proton irradiation, the cells do show some loss of power; to about 90% after 10^{12} protons/cm^2, as shown in Figure 3 (courtesy Boeing [ref. 36]). This represents about 50 times greater resistance to 1-MeV proton radiation than either Si or GaAs.

The damage from the proton irradiation could be almost completely recovered by a low-temperature anneal. The cells exhibited 95% recovery of initial power after 6 minutes at 225 C.

While it remains to be seen whether the high radiation tolerance will remain for future high-performance versions of the cell technology, this radiation tolerance is so extrordinary that the end of life (EOL) efficiency of even present-day $CuInSe_2$ cells may outperform conventional cell technologies in some high radiation orbits.

Thin-film cadmium telluride cells have not, to date, been extensively tested for radiation tolerance. Preliminary results of 1-MeV electron irradiation, quoted by Zweibel [ref. 37], show moderately high radiation tolerance with some loss of short circuit current but negligible loss of voltage or fill factor. All of the degradation they saw could be attributed to darkening of the glass superstrates used for the cells, which could be avoided by using radiation tolerant glass. Bernard et al. [ref. 38] also noticed little change in CdTe cell performance at 1-MeV electron fluence of up to $3{\cdot}10^{16}$/cm^2.

Amorphous silicon cells from Arco Solar exposed to 1-MeV electrons degraded from 8.57% AM0 to 8% at 10^{15} electrons/cm^2 [ref. 35]. The efficiency dropped to 5.95% at 10^{16} electrons/cm^2. The damage could be almost completely removed

with a low temperature anneal; the cells showed 97% recovery after a fifteen minute treatment at 175 °C.

Somewhat worse degradation was found on nip a-Si cells by NASA Langley [ref. 39]; they also found recovery with a 2-hr, 200 °C anneal.

Thin-Film Cascades

Introduction

An important technology for the production of high-efficiency thin film arrays is the ability of thin films to be produced in multibandgap "cascade" structures [ref. 40].

In the cascade structure, short wavelength (high energy) photons are absorbed in a high bandgap material on the top of the solar cell. The high bandgap material is transparent to longer wavelength (low energy) photons, which pass through and are absorbed by a second layer consisting of a photovoltaic material with lower bandgap.

In principle, cascades could consist of an arbitrary number of elements, which would approach complete utilization of the solar spectrum. The largest jump in photon utilization comes from the increase from one bandgap to two. In practice, it is unlikely that thin film materials will be made with more than two cascaded elements, at least in the reasonable future.

In an optimum current-matched two-element cascade, the efficiency can be approximately calculated as equal to the top cell efficiency plus half the bottom cell efficiency. If current matching is not required, the efficiency is approximately equal to the top cell efficiency plus $(1\text{-}J_{sc\ (top)}/J_{sc\ (bottom)})$ times the bottom cell efficiency.

The optimum bandgap combination depends slightly on the materials properties; for the air mass zero spectrum, using ideal materials, maximum efficiency of a two element series- connected cascade occurs at bandgaps of 1.75 for the top cell and 1.05 for the bottom cell [ref. 41]. For the efficiencies of figure 1, this results in a maximum efficiency of 33%, about 50% higher than the efficiency of 24.4% calculated for a single bandgap cell.

Cascades can be configured as monolithic, in which the top cell is integrally deposited on the bottom cell (or vice-versa), or mechanically stacked, in which the two sets of cells are formed separately. Electrical interconnections can be set up as two terminal, three terminal, or four terminal configurations. In general, monolithic modules must be two terminal or possibly three terminal devices; while mechanically stacked modules can be configured as four-terminal devices as well. For a two-terminal current-matched cascade, the current through the top cell must equal that through

the bottom. This means that once the bandap of one component has been chosen, the bandgap of the other is determined.

Four terminal cascades allow separate connection to the top and bottom cells. If the power is taken separately from each set of sub-cells, this connection requires no matching of current. Four terminals also allow monolithic connection in the voltage-matched configuration, with bottom cells connected in series.

The maximum efficiency is almost the same for all configurations. However, the current-matched configuration is very sensitive to the bandgaps, and loses efficiency very rapidly when the matching condition is not exactly met. The four-terminal system is relatively insensitive to the exact bandgap, while voltage-matched configurations are intermediate in sensitivity.

Figure 4A and B show efficiencies calculated by Fan [ref. 41] for cascade solar cells at AM0 in both the series connected and in the independent operation mode. The maximum efficiency is about the same for both, but the independent operation allows a much wider rnge of bandgaps.

An important element in a monolithic cascade is a shorting junction to connect the base of the top cell to the emitter (or window layer) of the bottom cell to allow current to flow from the first to the second.

The main question about monolithic cascades is whether technology can be developed to deposit the second cell and interconnections without degrading the first cell, either by thermal effects during deposition causing decomposition or interdiffusion of the first cell, or due to material incompatability, such as might happen if some component of one cell reduces minority carrier lifetime in the other

For cascades where the top cell bandgap is lower than the optimum bandgap for current matching, it is possible to create a current-matched cascade if the top cell is made to pass through some of the light that would normally be absorbed. This is discussed in [ref. 40].

There is a wide range of possible thin-film semiconductors for a two-cell cascade. Only a few, however, have to date shown potential for producing good thin-film solar cells.

Experimental Results

The best currently demonstrated thin-film cascade, reported by ARCO Solar [ref. 42], uses an amorphous silicon top cell on a $CuInSe_2$ bottom cell. The achieved efficiency is 12.5% AM0. In this cell the two elements were deposited separately, the a-Si on a glass superstrate and the $CuInSe_2$ on a metal-coated glass substrate, and the two elements optically coupled with a transparent encapsulant. This module configuration is shown in figure 5 (courtesy ARCO Solar). For higher specific power,

it would be desirable to eliminate the intermediate layer by depositing the a-Si cell directly on the $CuInSe_2$.

An alternative technology, CdTe on $CuInSe_2$, has shown about 8% AM0 efficiency for a mechanically stacked prototype [ref. 43].

A problem with existing $CuInSe_2$ technology is that the current solar-cell structures use a heterojunction window layer which may not withstand the temperatures needed to directly deposit a second cell on top. Thus, either a technology must be developed to deposit the $CuInSe_2$ after the top cell deposition, a low temperature top cell must be used, or a more robust window layer found.

Cascade cells with amorphous silicon alloys for both top and bottom elements have also been demonstrated. Energy Conversion Devices (ECD), has reported an efficiency of 10% measured at Air Mass Zero for a three junction, two bandgap cell [ref. 30].

Future

Bottom Cell Materials

$CuInSe_2$ is nearly ideal for the bottom cell for a cascade. The bandgap of $CuInSe_2$ can be modified by alloying with related I-III-VI_2 materials; for example, $CuInTe_xSe_{(2-x)}$, will have a lower bandgap, with x selected to form the bandgap required; a higher bandgap material can be formed in $CuGa_xIn_{(1-x)}Se_2$. This may be important for monolithic cascades requiring current-matched cells.

Mercury-Cadmium Telluride, with a bandgap continuously variable from 0 to 1.5 eV, is also a good candidate for a bottom cell.

Other materials for bottom cells are polycrystalline silicon and crystalline silicon.

Top Cell Materials

The optimum material for the top cell of a two element cascade would have a bandgap near 1.75 eV. Of the wide-bandgap thin-film solar cell materials, CdTe is the most well developed. The bandgap of CdTe, 1.5 eV, is slightly low for an optimum cascade. For a current-matched cascade this could be remedied by use of a "perforated" cell; alternatively, a bottom cell (for example, HgCdTe) with correspondingly lower bandgap could be used and the small penalty for off-optimum performance accepted.

The related ternary alloys with Mn, $Cd_xMn_{(1-x)}Te$; Zn, $Cd_xZn_{(1-x)}Te$; or Se, $CdTe_xSe_{(2-x)}$, could be used to increase the bandgap to closer to optimum [ref. 25]. A related wide bandgap material is cadmium selenide, CdSe [ref. 44]. Electronic

properties and performance of solar cells made from these materials are still comparatively uninvestigated.

$CuGaSe_2$, with a bandgap of 1.7 eV, and $CuInS_2$, with bandgap 1.5 ev, are also promising choices, as discussed in the previous section.

Amorphous silicon, with an effective bandgap of around 1.6 to 1.7 eV, may also make a good choice. Alloys with Ge, Sn, SiC and SiN can tailor the bandgap as necessary. Amorphous materials have the advantage that tunnel junctions are relatively easily formed. The efficiency and lifetime of these materials require improvements to allow them to be used for efficient elements in cascades, however, it should be noted that intensive research into amorphous silicon alloys is in progress.

While mechanically stacked modules will likely be simpler to build, high specific power arrays will probably require monolithic construction.

Applications

Future thin-film solar cells are likely to have greatly increased specific power at the solar cell level compared to conventional technology solar cells.

Table 2 compares existing and projected efficiency for the best single crystal and thin-film cells (where "current" means for the best cells achieved in the lab, not for cells currently manufactured into space arrays). Table 3 shows these figures converted into specific power at the cell level. These specific powers are for the cell only, not including the radiation shielding, interconnections, support layers, array structure, etc., all of which are major contributors to the actual mass. It must be noted that cell mass is only a small component of the array mass, and thus of array specific power.

Achieved specific power is typically about a tenth of the cell-level specific power. In a well designed structure, the structural mass should be able to be decreased roughly proportionately to the cell mass. As a rule of thumb, the array structural mass is generally roughly equal to the (covered) cell mass. (The rest of the power system–batteries, power conditioners and controllers, etc–contributes an additional mass element which is nearly independent of the array.)

Specific power is not only concern in solar array design. Other criteria include high array stiffness (i.e., resistance to bending during acceleration), high resonant frequency, and low moment of inertia in order to minimize force required for orientation. For all of these parameters higher specific power, by reducing the mass of the solar cells, increases the relevant performance; while lower efficiency, by increasing the size, decreases it. In general, for these parameters the relevant figure of merit scales as product of the specific power and the efficiency.

Low Earth orbit provides a special case, where the drag area is a criterion. For these orbits, efficiency takes on increased importance.

However, for many, and perhaps even most missions, these concerns are secondary compared to the array mass. In this case achieving maximum specific power is the dominant factor in the choice of technology.

System Applications and Missions

The important applications for thin film solar cells are to missions where specific power is a concern or where significant radiation exposure occurs during the course of the mission. While most spacecraft can benefit from increased specific power and radiation tolerance, specific missions for which thin-film photovoltaic arrays may be an enabling technology are solar electric propulsion, a manned Mars mission, and lunar exploration and manufacturing.

For solar electric propulsion, the system performance is directly proportional to the specific power. Accurate pointing is not important during the thrust. One proposed mission for solar electric propulsion is for a low-thrust vehicle to transfer satellites from low Earth orbit to geosynchronous orbit, or from low Earth orbit to lunar transfer. In both cases the orbit is a slowly rising spiral which spends a long time in the radiation belts, and for these missions the potential radiation hardness of thin film cells may be very important. For a Mars unmanned cargo ship, required power levels could be very high (Megawatts), and specific power very important.

A manned Mars mission would require up to 1 MW of power, both for the spacecraft during the journey, and to power the surface base [ref. 45]. For the baseline mission, the transportation cost is extremely high, and specific power becomes the dominant concern, with efficiency of little importance. This makes thin film cells a very attractive option. Figure 6 shows an artist's conception of astronaut unrolling a thin-film solar array to provide power for a manned base on the surface of Mars.

For a long-term manned lunar base, transportation costs are moderately high. However, the mass of the solar array for a lunar base is negligible compared to the storage capacity required for the 14 day lunar night, so specific power of the array is not an issue. Important uses for thin film cells may be for intermediate (14 day) stay-time missions where the array is brought with the spacecraft, and for manufacturing power, *e.g.*, lunar oxygen extraction, that require large amounts of power but could be run only during the sunlit periods.

Another option is a base at or near the lunar poles, which may be able to place a solar array to receive continuous sunlight [ref. 46]. For such a base the high specific power of thin-film cells could be very important.

In the long term, it may be economically feasable to manufacture solar cells on the moon from available lunar materials. In this case, the only practical cell material

is silicon, and the much smaller materials requirement for amorphous cells makes this the preferred technology. This is discussed in more detail by Landis and Perino [ref. 47].

Finally, it should be noted that in general, thin-film materials are tested at room temperature. Operating temperatures for surface power use, however, will vary considerably. On the moon, for example, peak operating temperatures may be as high as 90°C [ref. 48]; while on Mars, the operating temperatures may be as low as −100°C. Thermal cycling stresses are also likely to be considerably greater in many space applications, including both greater temperature changes and more rapid rates of heating and cooling. These issues will have to be addressed and cells and arrays will have to be designed and tested to function in the appropriate space environment.

Conclusions

Thin-film solar cells show a potential for making extremely lightweight solar arrays. Research programs for terrestrial photovoltaic power have resulted in dramatic improvements in the state of the art performance for thin-film photovoltaic materials. These improvements necessitate a reassessment of the potential for thin-film materials to be used for space power applications. Cells which have demonstrated over 9% efficiency $CuInSe_2$ and $Cu(In,Ga)Se_2$, CdTe, and amorphous silicon. While the efficiencies are low compared to current technology space cells, the projected specific power levels are still extremely good. Development of multibandgap cascades raises the possibility that the efficiencies can be considerably improved.

Ultra lightweight space arrays will require that the materials can be deposited on thin, space-qualified materials. This issue is not being addressed in current research progras.

Data gathered to date [32] indicates that the radiation tolerance of such thin-film materials is equal to or better than any other known photovoltaic materials. While much of the radiation data is preliminary or incomplete, it appears that in some high radiation orbits, thin film materials may be the prefered technology even at present efficiency and specific power levels.

Data on the behavior of these devices in space is scanty. Even the efficiency information is extrapolated from terrestrial measurements, and needs to be verified in a rigorous manner using a spectrum calibrated for the specific material.

For several missions, including solar-electric propulsion, a manned Mars mission, and lunar exploration and manufacturing, thin film photovoltaic arrays may be a mission-enabling technology.

In order to take advantage of advances produced by existing terrestrial research programs, it is important that space power research programs focus attention on the issues not being addressed by research programs aimed at terrestrial power: weight,

radiation tolerance, AM0 calibration and measurement, space qualification of cells and arrays, and design of lightweight arrays for space and surface power use. Specific recommendations are:

(1) Thin film solar cells are inherently flexible and light weight. However, existing research programs are focussed on low cost (but not low weight) rigid substrates. *It is of critical importance that we stimulate interest in deposition on light-weight, space-qualifiable materials.* If this is not done, the entire thin-film research program is useless for space.

(2) Thin-film materials appear to be inherently highly radiation tolerant. However, preliminary results on radiation tolerance must be verified and continuing tests made that radiation tolerance remains high on new cell designs and emerging technologies and materials.

(3) Thin-film solar cells are currently tested almost exclusively under terrestrial (AM1.5) conditions. Calibration standards for space (AM0) measurement do not currently exist.

(4) The road to full space qualification is long and slow. It is important that we continually verify performance in space on each emerging technology in order for us to have sufficient confidence in the materials to rely on them when critical space and surface power requirements come on line in the early decades of the next century. Required tests include not only space demonstrations, but tests of the cells under thermal extremes and thermal cycling conditions characteristic of the environments they will be needed in.

(5) Thin-film cells for space and surface power use will require unique light-weight array designs with structural mass reduction comparable to the reductions in mass per unit area of thin-film cells. It may not be too early to begin considering how such arrays should be designed.

Acknowledgement

I would like to thank Ken Zweibel of SERI (whose review article on the use of thin-film cells for space [ref. 37] is recommended) for helpful discussions, and Kim Mitchell of ARCO Solar for providing several of the figures used here. This paper is based in part on an earlier review of thin film solar cell technology for space presented at the IAF International Conference on Space Power, Cleveland, Ohio, in June 1989.

References

[1.] D. J. Flood and H. Brandhorst Jr., Current Topics in Photovoltaics, **2**, 1988.

[2.] S. P. Tobin *et al.*, *4th International Photovoltaic Science and Engineering Converence*, Sydney Australia, 14, 1989.

[3.] S. Ochi *et al.*, Tech Digest of the International PVSEC-3, Tokyo, Japan 755, 1987.

[4.] S. P. Tobin *et al.*, IEEE Electron Dev. Lett, EDL-9(5) 256.

[5.] S. P. Tobin *et al.*, *20th IEEE Photovoltaic Specialists Conference*, 405, 1988.

[6.] R. E. Hart, Jr., D. J. Brinker, and K. A. Emery, *20th IEEE Photovoltaic Specialists Conference*, 764, 1988.

[7.] G. A. Landis, *20th IEEE Photovoltaic Specialists Conference*, 708, 1988.

[8.] C. J. Keavney and M. B. Spitzer, Appl. Phys. Lett. bf 52, 1439, 1988.

[9.] I. Weinberg, C. K. Schwartz, and R.E. Hart Jr., *Space Photovoltaic Research and Technology Conference*, NASA Lewis Research Center, 17, 1988.

[10.] J. J. Loferski, J. Appl. Phys. **27**, 777, 1956; reprinted in Solar Cells, C.E. Backus, ed, 89, IEEE Press, NY 1976.

[11.] J. J. Hanek *et al.*, *1986 Space Photovoltaic Research and Technology*, NASA CP 2475, 99.

[12.] J. Severns *et al.*, *20th IEEE Photovoltaic Specialists Conference*, 801, 1988.

[13.] R. Hill and J. D. Meakin, in Current Topics In Photovoltaics, Volume 1, (T.J. Coutts and J.D. Meakin, eds), 223, Academic Press, Inc., 1985.

[14.] A. L. Fahrenbruch and R. H. Bube, Fundamentals of Solar Cells, 418, Academic Press, NY, 1983.

[15.] A. M. Barnett, *2nd EC Photovoltaic Solar Energy Conference*, 328, 1979.

[16.] L. L Kazmerski and S. Wagner, in Current Topics In Photovoltaics, Volume 1, (T. J. Coutts and J. D. Meakin, eds), 41, Academic Press, Inc., 1985.

[17.] K. W. Mitchell *et al.*, *20th IEEE Photovoltaic Specialists Conference*, 1384, 1988.

[18.] K. W. Mitchell *et al.*, *4th International Photovoltaic Science and Engineering Converence*, Sydney Australia, 1989.

[19.] W. S. Chen *et al.*, *19th IEEE Photovoltaic Specialists Conference*, 1445, 1987.

[20.] R. Noufi *et al.*, Solar Cells, **17**, 303, 1987.

[21.] W.E. Devaney *et al.*, *IEEE Trans. Electron Dev.*, **37**:2, 428-433, 1990.

[22.] K. Zweibel, H.S. Ullal, and R.L. Mitchell, *20th IEEE Photovoltaic Specialists Conference*, 1469, 1988.

[23.] K. W. Mitchell, G.A. Pollock, and A.V. Mason, *20th IEEE Photovoltaic Specialists Conference*, 1542, 1988.

[24.] P. V. Meyers, *7th European PV Conference.*

[25.] A. Rohatgi *et al.*, *20th IEEE Photovoltaic Specialists Conference*, 1477, 1988.

[26.] B. M. Basol and E.S. Tseng, Appl. Phys. Lett **48**, 946, 1986.

[27.] H. Richter, *20th IEEE Photovoltaic Specialists Conference*, 1537, 1988.

[28.] W. Wallace *et al.*, *19th IEEE Photovoltaic Specialists Conference*, 593, 1987.

[29.] N. Nakatani *et al.*, *4th International Photovoltaic Science and Engineering Conference*, Sydney, NSW Australia, Vol. 2, 639, 1989.

[30.] J. H. Hanak *et al.*, *Space Photovoltaic Research and Technology*, 176, 1988..

[31.] A. M. Barnett *et al.*, *4th International Photovoltaic Science and Engineering Conference*, Sydney, NSW Australia, Vol. 1, 151, 1989.

[32.] J. Woodyard and G.A. Landis, "Radiation Tolerance of Thin Film Solar Cells," (to be published) *Solar Cells*, 1990.

[33.] H.W. Brandhorst, Jr. and R.E. Hart, *4th Photovoltaic Specialists Conference, Volume II,* A7-1, 1964.

[34.] D.J. Curtin, *7th Photovoltaic Specialists Conference,* 206, 1968.

[35.] C. F. Gay *et al.*, *17th IEEE Photovoltaic Specialists Conference*, 151,1984.

[36.] R. M. Burgess *et al.*, *20th IEEE Photovoltaic Specialists Conference*, 909,1988.

[37.] K. Zweibel, *23rd Intersociety Energy Conversion Engineering Conference*, July 31-August 5 1988, Denver, CO.

[38.] J. Bernard *et al.*, *Cellules Solaires,* Gordan and Breach, 229, July 1970.

[39.] C. E. Byvik *et al.*, *17th IEEE Photovoltaic Specialists Conference*, 155, 1984.

[40.] G. A. Landis, Solar Cells **15**, 203, 1988.

[41.] J. C. C. Fan, B-Y Tsaur, and B. J. Palm, *16th IEEE Photovoltaic Specialists Conference*, 692, 1982.

[42.] K. Mitchell, C. Eberspacher, J. Ermer and D. Pier, *20th IEEE Photovoltaic Specialists Conference* 1384, 1988.

[43.] P. V. Meyers *et al.*, *20th IEEE Photovoltaic Specialists Conference*, 1448, 1988.

[44.] H. Richter, *20th IEEE Photovoltaic Specialists Conference*, 1537, 1988.

[45.] R. W. Francis, D. J. Flood, and W. A. Somerville, *20th IEEE Photovoltaic Specialists Conference*, 8, 1988.

[46.] J. D. Burke, in *Lunar Bases and Space Activities of the 21st Century*, W. W. Mendell, ed., 77, Lunar and Planetary Institute 1985.

[47.] G. A. Landis and M.A. Perino, 9th Biennial Princeton/SSI Conf. Space Industrialization, 1989; printed in *Space Manufacturing* **7**, 144, AIAA, 1989.

[48.] G.A. Landis, S.G. Bailey, D.J. Brinker, and D.J. Flood, *40th IAF Congress,* Malaga, Spain, Oct. 1989. To be published, *Acta Astronautica,* **22**, 1990.

[49.] J. Appelbaum and G.A. Landis, *10th Space Photovoltaic Research and Technology Conference,* Cleveland, OH, Nov. 1989.

TABLE I. - HISTORICAL PROGRESS OF THIN-FILM SOLAR CELL EFFICIENCY

[Experimentally achieved efficiencies (at Air Mass Zero, in percent) as of 1978, 1983, 1988, and projected values for future performance.]

Material	1978	1982	1988	1990's
CdS/Cu_2S	7.3	8.2	9.	10.0
$CuInSe_2$	5.3	8.5	11.2	12
$CuGaSe_2$	---	---	4.6	12.5
$CuInS_2$	2.9	2.9	6.1	12.5
CdTe	4.1	8.4	8.6	12.5
a-Si	4.4	8.1	9.0	11.5

note added in proof: CdTe cells developed by Photon Energy Co. have since reached efficiency of 9.8 % AM0.

TABLE II. - PROJECTIONS FOR FUTURE EFFICIENCY

[In percent.]

Material	Current	Future	
		Conservative	Optimistic
Si	18	19.5	22
GaAs	21.4	22	25
$CuInSe_2$	11.2	12	13
Opt. thin-film	8.6	12.5	15
Thin-film Cascade	12.5	18	20

TABLE III. - PROJECTIONS FOR SPECIFIC POWER

[Does not include coverglass.]

Material	Thickness, μm	Substrate, μm	Current, kW/kg	Future	
				Conservative, kW/kg	Optimistic, kW/kg
Si	60	–	1.8	1.9	2.2
GaAs	60	–	0.9	0.9	1.0
$CuInSe_2$	3	6	7.0	7.5	8.1
Opt. thin-film	3	6	5.3	7.8	9.4
Thin-film cascade	6	6	3.9	5.6	6.2

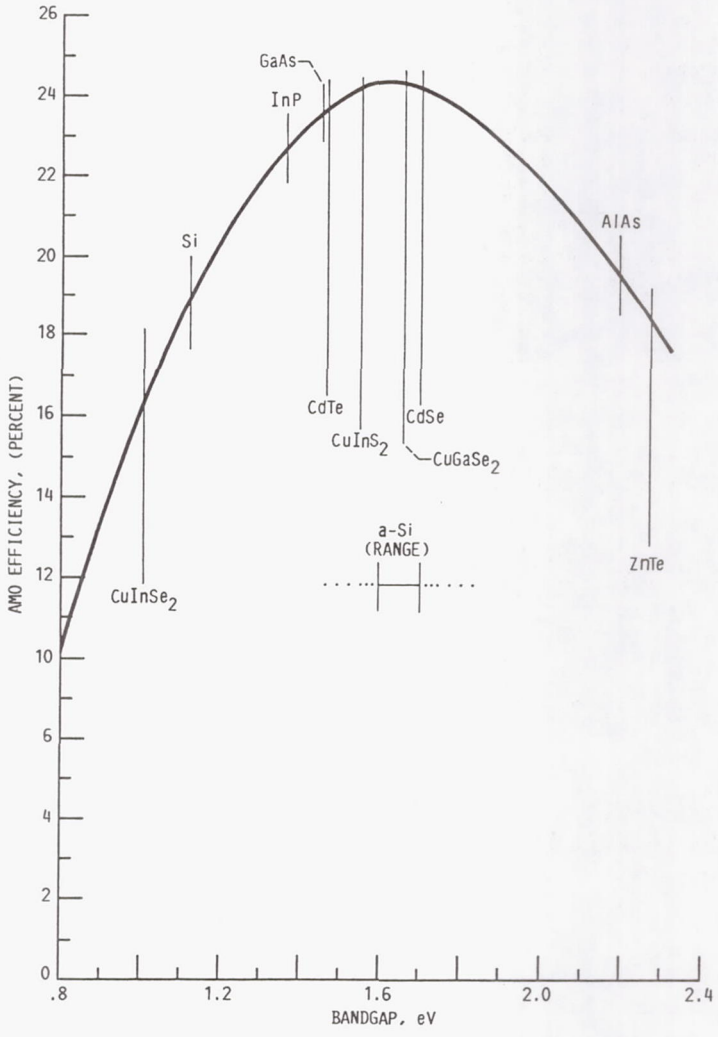

1. Achievable Efficiency for a Single Junction Solar Cell as a Function of the Bandgap of the Material.

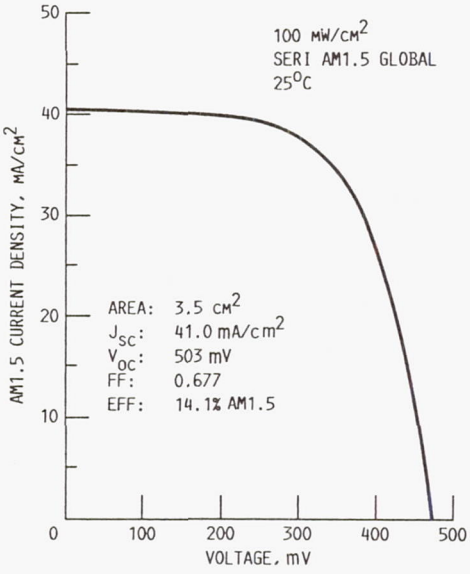

(a) CURRENT VERSUS VOLTAGE MEASURED AT AIR MASS 1.5.

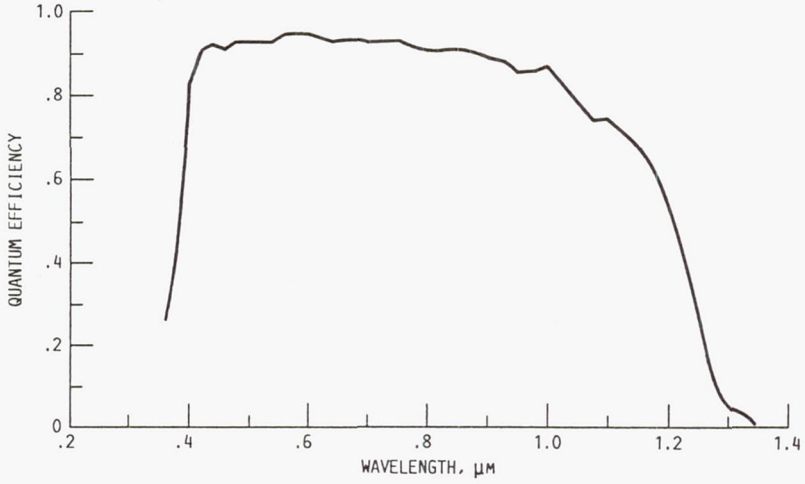

(b) QUANTUM EFFICIENCY VERSUS WAVELENGTH.

2. Electrical Characteristis of ARCO-Solar High-efficiency ZnO/CdS/Copper Indium Selenide Solar Cell.

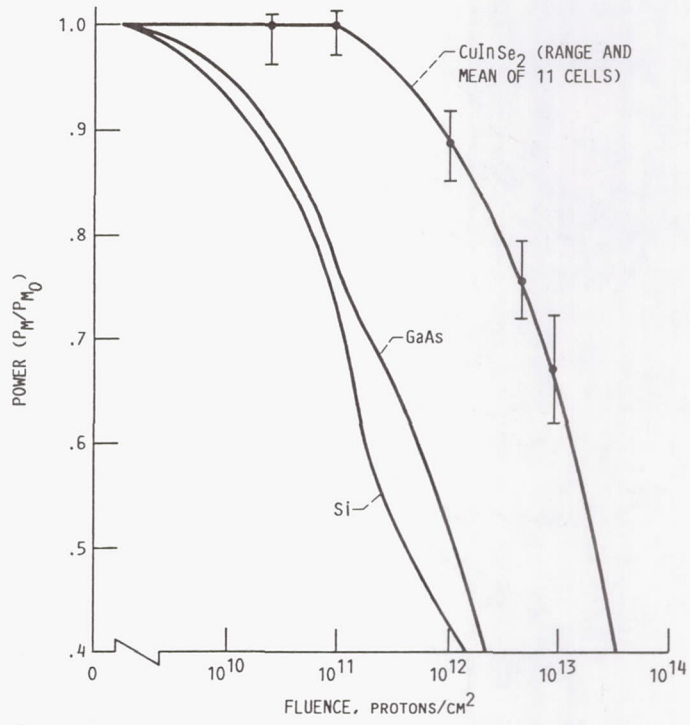

3. Effect of 1-Me Proton Irradiation on the Maximum Power of Silicon, Gallium Arsenid, and Copper Indium Selenide Solar Cells.

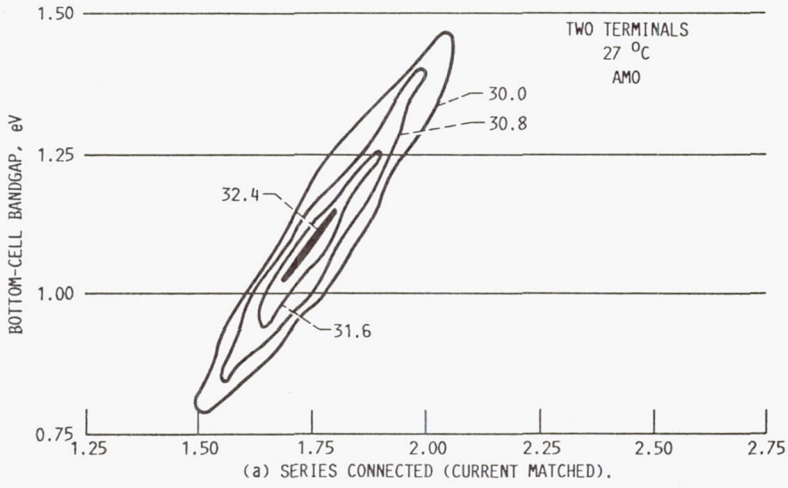

(a) SERIES CONNECTED (CURRENT MATCHED).

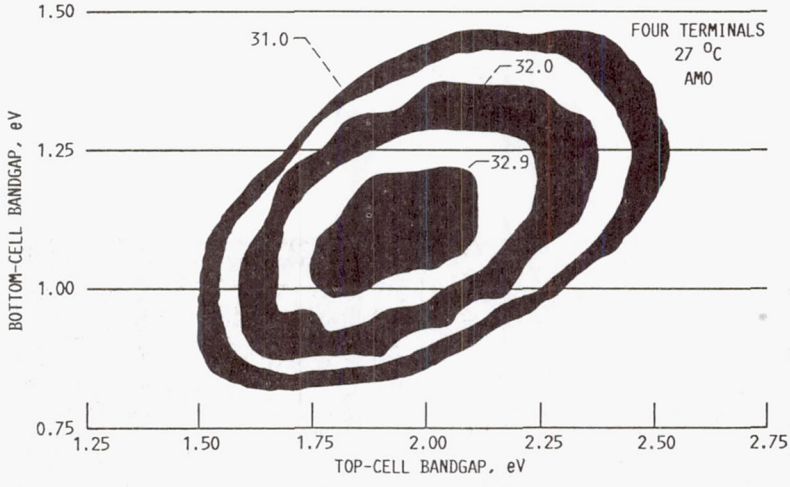

(b) INDEPENDENT ELEMENTS.

4. Maximum Theoretical Efficieny of a Solar Cell Cascade as a Function of the Bandgaps of the Top and Bottom Cell Material

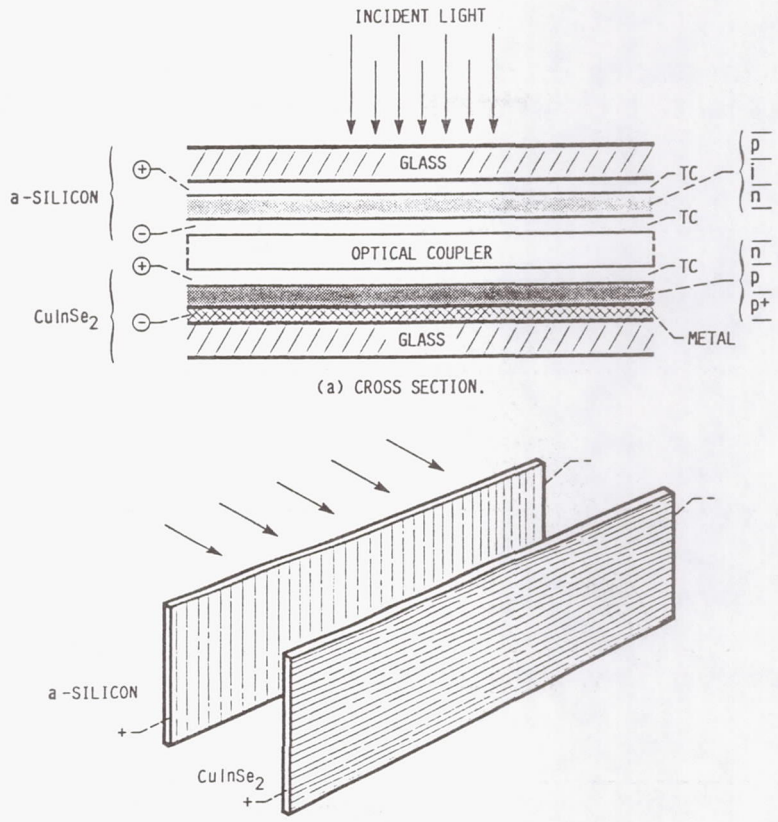

5. ARCO Soar Tandem module

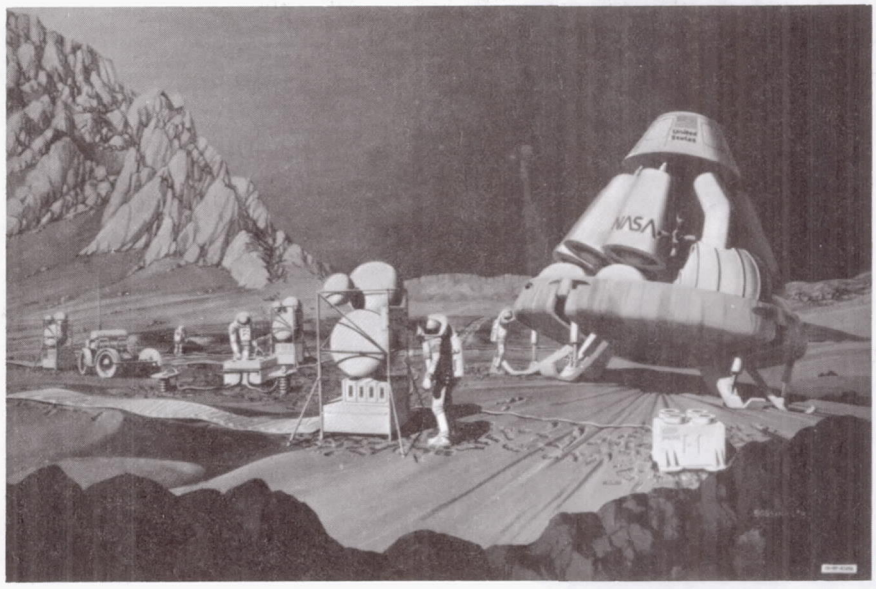

Artist's Conception of Power System for a Manned Mars Base.

Performance, Size, Mass and Cost Estimates for Projected 1KW EOL Si, InP and GaAs Arrays

Luther W. Slifer, Jr.
Consultant to Solarex Aerospace Division
Rockville, Maryland

Introduction

One method of evaluating the potential of emerging solar cell and array technologies is to compare their projected capabilities in space flight applications to those of established Si solar cells and arrays. Such an application-oriented comparison provides an integrated view of the elemental comparisons of efficiency, radiation resistance, temperature sensitivity, size, mass and cost in combination. In addition, the assumptions necessary to make the comparisons provide insights helpful toward determining necessary areas of development or evaluation. Finally, as developments and evaluations progress, the results can be used in more precisely defining the overall potential of the new technologies in comparison to existing technologies. This paper compares the projected capabilities of Si, InP and GaAs cells and arrays.

Cell Characteristics

Si, InP and GaAs cell efficiencies are compared in Table I. A small range is given for the theoretical limit and for typical production since various sources give slightly different values. The projected efficiencies are those used for the calculations in this paper. It was assumed that there will be more near-term improvement in the InP cells than in the others because it is a less mature technology.

Radiation effects on current cells are shown in Table II. The results are calculated from Reference 1 for the proton irradiation and for the 1×10^{15} electron irradiation. The 3×10^{15} electron irradiation data are from Reference 2.

Table III shows the projected EOL efficiencies for radiation of 3×10^{15} e/cm^2 (1 Mev equivalent) calculated from Tables I and II. This assumes that relative damage coefficients are similar for the three cell types. This fluence level was selected to take advantage of the radiation resistance characteristics of the InP and GaAs cells.

The variation of peak power (P) with temperature (T) for the cells is shown in Table IV. The calculations were based on data from Reference 2. The InP and GaAs cells show less sensitivity to temperature than the Si cells primarily because their open circuit voltages are significantly higher while their temperature coefficients are similar.

The mass for 2 × 4 cm cells is shown in Table V. The cell thickness used for the cells is different because of differences in fragility. As a result the mass of the cells

reflects both the differences in material density and the differences in cell thickness. As can be seen, the cell mass for InP and GaAs cells is projected to be significantly higher than for Si cells.

Cell costs for 2 × 4 cm cells in quantities necessary to produce 1 kw EOL power were estimated using typical, proprietary production cost estimating procedures, including effects of mechanical and electrical yield. The results are shown in Table VI. As shown, the wafer or substrate price for InP and GaAs cells is a significant fraction of the cell cost.

Array Characteristics

The projected cell characteristics were used to estimate the size, weight and cost for Si, InP and GaAs solar arrays with a 1 kw EOL power capability. Details are shown in Table VII. It was assumed that the arrays were oriented and that the degraded Si array temperature was 60°C. The temperatures of the InP and GaAs arrays were then calculated according to the equation:

$$[1] \qquad (T_1/T_2)^4 = (\alpha_1 - F_1\eta_1)/(\alpha_2 - F_2\eta_2).$$

where
T is the absolute operating temperature
α is the absorptivity
F is the packing factor (assumed to be 0.9)
η is the operating (EOL) efficiency
and subscripts 1 and 2 refer to the two cell types.

For these calculations the absorptivity was taken as 0.75 for Si and 0.78 for GaAs as given in Reference 3. The absorptivity for InP was assumed to be 0.78, the same as for GaAs. Array temperatures of 55°C and 58°C were calculated for the InP and GaAs arrays respectively as shown in Table VII.

The estimate of orbital degradation included radiation degradation due to 3×10^{15} e/cm^2 (1 Mev equivalent), ten year ultraviolet degradation of 4% and thermal cycle losses, expected to increase with cell fragility. Assembly losses of 3%, 2% for cell mismatch and 1% for interconnection, were also included. Glassing losses were assumed to be negligible.

From these, the beginning of life (BOL) power requirements were calculated and the cell requirements were determined. The array area was determined for an assumed packing factor of 0.9. Array mass was then calculated for flexible arrays assuming a mass of 1.0 kg/m^2 excluding cells, and for a rigid array assuming a mass of 2.5 kg/m^2 excluding cells.

Finally, array costs were estimated for the rigid arrays using typical proprietary production cost estimating procedures. Again, effects of mechanical and electrical yield were included. Cost estimates were not made for the flexible arrays because of the paucity of available background data. The cost estimates for the rigid arrays are shown as relative costs in Table VIII to protect their proprietary nature.

Discussion and Conclusion

The overall results are summarized in Table VIII. It is projected that array area requirements will be significantly lower, by almost a factor of 2, for InP and GaAs arrays compared to Si arrays. This could result in significant reductions in requirements for spacecraft orientation and station keeping propulsion systems. The savings in array mass due to the smaller area; however, is largely lost for lightweight flexible arrays because of the higher cell mass of InP and GaAs cells compared to Si cells. Nevertheless, there is some savings, about 15%, anticipated for InP arrays. For rigid arrays, where the cell mass is a smaller fraction of the array mass, the savings become more significant, about 30% for InP and 20% for GaAs compared to Si. These factors are important to launch capability and cost, or, alternatively, the savings can be passed on to spacecraft instruments.

The cost per EOL watt is estimated to be higher by a factor of 6 for the InP array and by a factor of 3 for the GaAs array than for the Si array. These are major considerations since cost is a driving factor in most solar array procurements. Justification for these costs would have to come at the spacecraft and mission level which is beyond the scope of this paper.

In the process of developing these estimates, the need for several areas of technology development and evaluation became apparent. These include:

1. Development of cells to meet projected performance levels,
2. Increase in strength and reduction of mass of InP and GaAs cells by using alternative substrates such as GaAs on Ge as is underway,
3. Reduction of wafer cost, especially for InP,
4. Broad radiation damage studies for InP and GaAs cells to permit accurate engineering calculations of in-flight degradation,
5. Experimental determination of InP and GaAs solar cell temperature characteristics for both new and degraded cells,
6. Development and characterization of stable contacts and coatings, especially for InP cells,
7. Determination of absorptivity and emissivity of InP cells.

References

[1.] I. Weinberg, C.K. Swartz, and R.E. Hart, *Conference Record of the 18th IEEE Photovoltaic Specialists Conference*, 1722, IEEE, New York (1985).

[2.] I. Weinberg, C.K. Swartz, R.E. Hart, and R.L. Statler, *Record of the 19th Photovoltaic Specialists Conference*, 548, IEEE, New York (1987).

[3.] Michael W. Mills and Richard M. Kurland, *Proc. Space Photovoltaic Research and Technology Conference*, 117 (1988).

TABLE I. CELL EFFICIENCY (% AT AMO, 25° C)

Cell Type	Theoretical Limit	Typical Production	Projected Production
Si	18-21	15-15.5	15.5
InP	21-22	16-17	19.0
GaAs	23-25	19-20	20.0

TABLE II. RADIATION EFFECTS ON CURRENT CELLS
(Eff./Initial Eff. at AMO, 25° C)

Cell Type	After 10^{12}p/cm^2	After 10^{15}e/cm^2	After $3x10^{15}$e/cm^2
Si	.593	.673	.57
InP	.922	.939	.85
GaAs	.805	.779	.68

Note: Protons (p) 10 Mev
Electrons (e) 1 Mev

TABLE III. PROJECTED END OF LIFE EFFICIENCY
(% AT AMO, 25° C)

Cell Type	Initial Efficiency	EOL After $3x10^{15}$e/cm^{2}eq.
Si	15.5	8.8
InP	19.0	16.2
GaAs	20.0	13.6

Note: Assumes similar 1 Mev electron equivalencies.

TABLE IV. VARIATION OF PEAK POWER WITH TEMPERATURE

Cell Type	Efficiency (%)	P/A (mw/cm^2)	dP/AdT ($mw/cm^2 °C$)	dP/PdT (%/°C)
Si	15.5	21.0	- 0.092	- 0.438
InP	19.0	25.7	- 0.053	- 0.206
GaAs	20.0	27.1	- 0.044	- 0.162

TABLE V. MASS OF TYPICAL 2 CM X 4 CM CELLS

Wafer Material	Density (gm/cm^3)	Thickness (cm)	Substrate Mass (gm)	Cell Mass(gm)[1]
Si	2.328	0.0203	0.378	0.438
InP	4.787	0.0356	1.363	1.423
GaAs	5.316	0.0305	1.297	1.357

[1] Metallization and coating = 0.060 gm/cell.

TABLE VI. ESTIMATE OF 2 CM X 4 CM CELL COST

Cell Type	Wafer Size(mm)	Wafer Price($)	Substrates Per Wafer	Price per Substrate($)	Cost per Cell ($)
Si	100(d.)	5.50	6	0.92	12
InP	60(d.)	256.00	2	128.00	440
GaAs	45(sq.)	60.00	2	30.00	155

TABLE VII. PERFORMANCE, SIZE AND MASS ESTIMATES FOR 1KW EOL ARRAYS

	Si	InP	GaAs
EOL Power (w)	1000	1000	1000
EOL Temperature (°C)	60	55	58
EOL Power at 25° C (w)	1181	1066	1056
Orbital Losses (%)			
Radiation Damage	43	15	32
UV Degradation	4	4	4
Thermal Cycle Effects	2	5	4
Total	49	24	40
BOL Power at 25° C(w)	2316	1403	1760
Assembly Losses (%)	3	3	3
Total Cell Power (w)	2388	1446	1814
Cell Efficiency (%)	15.5	19.0	20.0
Cell Output (mw)	167.8	205.6	216.4
Cells Required	14231	7033	8383
Array Area (m^2)	12.65	6.25	7.45
Cell Mass (kg)	6.233	10.008	11.375
Flexible Array Mass (kg)	18.88	16.26	18.83
Rigid Array Mass (kg)	37.86	25.63	30.00

TABLE VIII. SUMMARY OF RESULTS

	Si	InP	GaAs
EOL Power at T (w)	1000	1000	1000
BOL Power at 25° C (w)	2316	1403	1760
Array Area (m^2)	12.65	6.25	7.45
EOL Power Density (w/m^2)	79	160	134
BOL Power Density (w/m^2)	183	224	236
Flexible Array:			
Mass (kg)	18.88	16.26	18.83
EOL Specific Power (w/kg)	53	62	53
BOL Specific Power (w/kg)	123	86	93
Rigid Array:			
Mass (kg)	37.86	25.63	30.00
EOL Specific Power (w/kg)	26	39	33
BOL Specific Power (w/kg)	61	54	59
Relative Cost Per Watt EOL	1.00	6.14	2.88
Relative Cost Per Watt BOL	1.00	10.14	3.79

Dual-Purpose Self-Deliverable Lunar Surface PV Electrical Power System

Jack H. Arnold, David W. Harris and Eldon R. Cross
Rockwell International, Rocketdyne Division
Canoga Park, CA

Dennis Flood
NASA Lewis Research Center
Cleveland, OH

Introduction

A safe haven and work support PV power system on the lunar surface will likely be required by NASA in support of the manned outpost scheduled for the post-2000 lunar/Mars exploration and colonization initiative. For purposes of this paper, a lunar surface outpost power was baselined for a daylight power level of 50-kW, and 25-kW during the night, although no critical limitations were discovered to prevent the implementation of higher power levels.

The concept presented in this paper provides the means of delivering a moderately large power system to the moon by employing the PV array to power an electrical propulsion module to take the system from LEO to the Moon. The vehicle is then placed in lunar orbit and descends to the lunar surface using conventional chemical rockets.

In order to support a 50-kW load on the lunar surface, a raw EOL array power of about 100-kW is required. As can be seen in the ensuing LTV (Lunar Transit Vehicle) power degradation modeling, the LTV BOL array size must be increased because of the transit time the system spends as it exits the Earth's atmosphere, and the attendant Van Allen radiation. This period is somewhat variable, but will be in the neighborhood of 140-days, or the approximate equivalent of a radiation fluence of 1×10^{15} electrons per cm^2 if 20-mil thick solar cell coverglass shielding is employed.

After landing on the lunar surface, the electrical power system will reconfigure itself so that during daylight hours the array bus will not only support the safe haven load, but will also operate a water electrolyzer. The resulting hydrogen and oxygen will be stored in insulated storage tanks. During the lunar night, these gases will operate fuel cell modules to support the loads, the resulting water returned to the water storage system for recirculation.

For the system modeled in the paper, a high-pressure electrolyzer was employed based on technology the Navy is developing for undersea applications. Water stored under ambient pressure is delivered to the electrolyzer using a high-pressure pump at about 3000 psi. From the electrolyzer, the resulting gases are stored in insulated flasks. During the lunar night, the gases are regulated down to between 60 and 100 psi

and delivered to a fuel cell stack sized to the required night bus loads, remembering that by nature fuel cells are capable of handling highly variable transient loads.

Single-Axis Solar Array Tracking

The study revealed that the solar array should be provided with a single axis of tracking for maximizing the solar electric conversion process both during the in-transit phase, and during lunar surface operation; this shows that one-axis tracking reduces the array size by 50%, and substantially lowers the mass and volume of other system components, including electrolyzer and fuel cell.

Initial On-Orbit Configuration and Mass Analysis

The following section includes an initial configuration of the LTV as it launches from Space Station Freedom and begins its journey to the Moon, including the electric propulsion module which can be subsequently jettisoned when lunar orbit is achieved.

It should be noted that the electric propulsion "truck"can be designed to be reusable and recoverable, a substantial incentive when the concept is compared with conventional delivery systems.

This section also provides the configuration and preliminary analysis of the lunar surface power system when it switches over to the electrolyzer and fuel cell mode, remembering that during the in-transit flight the array will directly feed the electric propulsion bus, and will convert to the surface mode after landing.

Up and down link telecommunications for performance monitoring and control, plus fault detection and correction are in the preliminary planning stages.

Orbital Trajectory Preliminary Analysis

This section presents the initial orbit and trajectory analyses and the initial assumptions used for the preliminary computer codes. Naturally, it was necessary to assume certain system characteristics associated with the power system, various masses, and the array power (see Table 1). As new iterations and second generation design models are generated, they will be fed back into the codes for reiterative system upgrading. Figure 2 shows the results of the orbital trajectory analysis.

Earth Magnetosphere Radiation Analysis and Preliminary LTV Power System Model (Including Initial Assumptions)

This section presents the initial radiation and array degradation analysis based on the first iteration orbit and trajectory models developed. Clearly, this must be continually upgraded as the system model changes.

Figure 3 is a plot of the Yearly Radiation Fluence versus Altitude for varying orbital inclinations. From this figure it can be seen that as the inclination increases the total yearly fluence decreases. Also, 7000 nmi is the altitude with the highest level of radiation flux. The flight path inclination for this analysis was assumed to be at the Space Station Freedom inclination of about 30°. Figure 4 shows the effect coverglass thickness has on the yearly fluence at this inclination. To relate the flight time to the radiation data in the JPL Radiation Handbook the flight time was broken into discreet time periods relating to the altitude found in the handbook. Figure 5 is a plot of the time spent at each altitude. Due to the lack of data for the region from GEO to a lunar orbit, the flight time remaining after the LTV has reached 18000 nmi was lumped together and assumed to be at GEO altitude, hence the jump in the curve near 19000 nmi. The total fluence for the complete flight to the moon as a function of coverglass thickness is shown in Figure 6. Figure 7 shows the accumulative fluence seen by a cell as the LTV position increases in altitude along the flight path. It can be seen that by time the LTV has reached 9000 nmi it has received most, if not all of the total fluence. Figures 9, 10 and 11 show the effect of the fluence on maximum power for Si, GaAs/Ge and InP cells respectively. How radiation degradation effects the array mass is shown in figure 11. This mass is for an array that is capable of delivering the assumed 247 kW at a post-lunar transfer/pre-lunar descent condition. Once on the lunar surface the array power will degrade due to the increase in cell operating temperature. Finally, Figure 12 shows the cost of launching different propulsion types of LTV's to LEO. It can be seen that at today's STS costs and at Shuttle-C launch costs the use of a Solar Electric-Ion can provide a significant cost savings.

Also, it should be remembered that the initial analysis was based on remaining on the Space Station Freedom inclination after leaving Freedom and exiting the magnetosphere, which does not appear to be the most benign course through the Van Allen belts. If more benign inclinations are discovered during subsequent analysis, plane change scenarios will be evaluated and new array degradation and shielding requirements will be integrated into the modeling process.

Conclusions and General Observations

1. Initial system modeling and computer analysis shows that the concept is workable and contains no major high risk technology issues which cannot be resolved in the circa 2000-2025 timeframe.

A specific selection of the best suited type of electric thruster has not been done; the initial modeling was done using an ion thruster, but Rocketdyne must also evaluate arc and resisto jets before a final design can formulated.

2. As a general observation, it appears that such a system can deliver itself to the Moon using many system elements that must be transported as dead payload mass in more conventional delivery modes.

3. It further appears that a larger power system providing a much higher safe haven power level is feasible if this delivery system is implemented, perhaps even sufficient to permit resource prospecting and/or lab experimentation.

4. The concept permits growth and can be expanded to include cargo transport such as habitat and working modules. In short, the combined payload could be manned soon after landing and checkout.

5. NASA has expended substantial resources in the development of electric propulsion concepts and hardware that can be applied to a lunar transport system such as described herein. In short, the paper may represent a viable mission on which previous investments play an invaluable role.

6. A more comprehensive technical paper which embodies second generation analysis and system size will be prepared for near-term presentation.

TABLE 1. GROUND RULES AND ASSUMPTIONS

- SOLAR POWER SYSTEM SIZED FOR 50/25 KW DAY/NIGHT
- POWER AVAILABLE FOR PROPULSION = 247 KW
- SOLAR POWER SYSTEM WEIGHT = 16894 LB
- LUNAR ORBIT INSERTION AND LANDING PERFORMED WITH CHEMICAL PROPULSION
- LO2 AND LH2 TANKS ARE INITIALLY FILLED AND USED FOR PROPULSION (CAPACITY = 7333 LB)
- TOTAL O2/H2 REQUIRED IS 13130 LB
- WEIGHT LANDED ON MOON = 17704 LB (INCLUDING 810 LB OF PROPULSION SYSTEM INERTS)
- WEIGHT IN LUNAR ORBIT AFTER SEPARATION FROM TRANSFER STAGE = 30834 LB
- BURN TIMES INCREASED APPROXIMATELY 5% TO ACCOUNT FOR TIME SPENT IN EARTH'S SHADOW
- TANKAGE FOR ELECTRIC PROPULSION = .144 X PROPELLANT WEIGHT

TABLE 2. PROPULSION SYSTEM CHARACTERISTICS

	ION ENGINE	ARCJET	CHEMICAL
THRUST LEVEL, LB	2.227	4.026	15K
SPECIFIC IMPULSE, SEC	3000	1000	482.8
ENGINE WEIGHT, LB	4169	2062	342
DELTA V, FT/SEC	21400	21400	12150
WEIGHT IN LEO, LB	45311	74057	77647
PROPELLANT WEIGHT, LB	9010	35977	42130
TANK AND STAGE WEIGHT, LB	1297	5181	4681
BURN TIME, DAYS,(MINUTES)	137	103	(23)
APPROX. TRIP TIME, DAYS	144	109	3-5

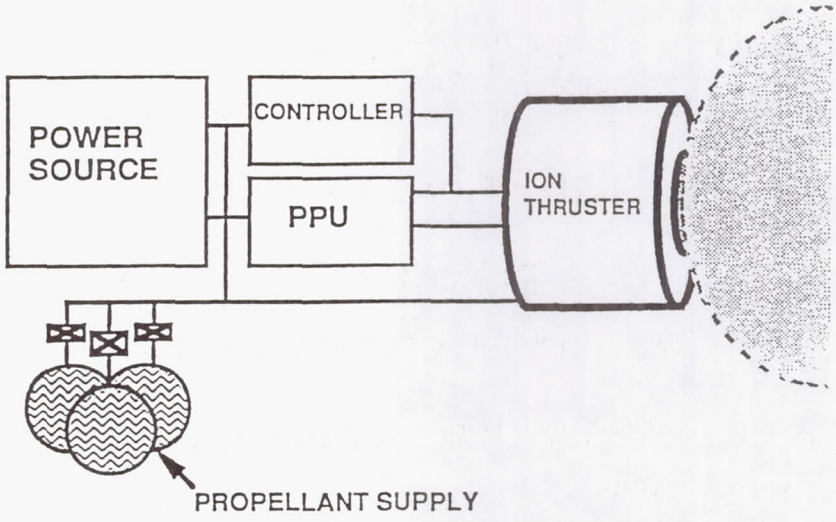

Figure 1: Ion Propulsion System Block Diagram

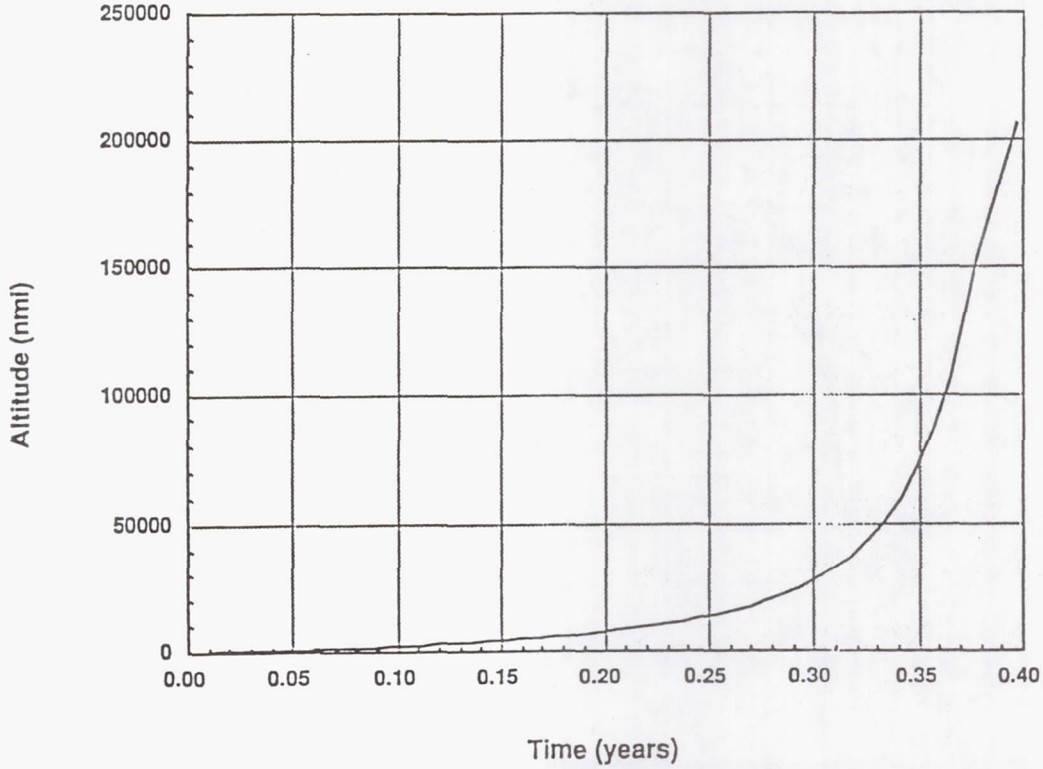

Figure 2: Photovoltaic LTV Flight Profile

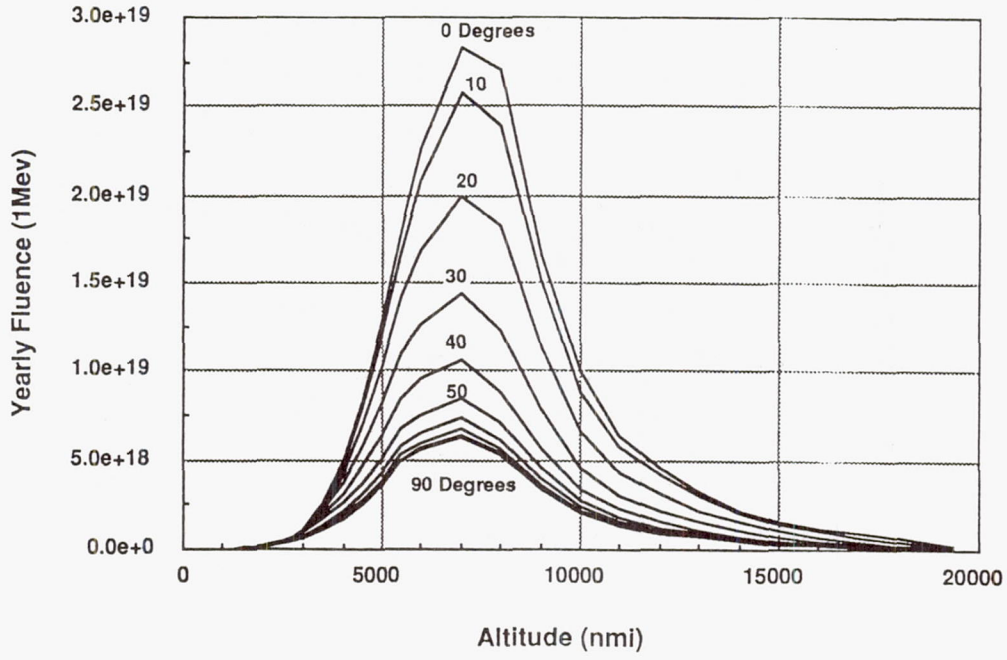

Figure 3: Yearly Fluence vs Altitude
for Various Inclinations

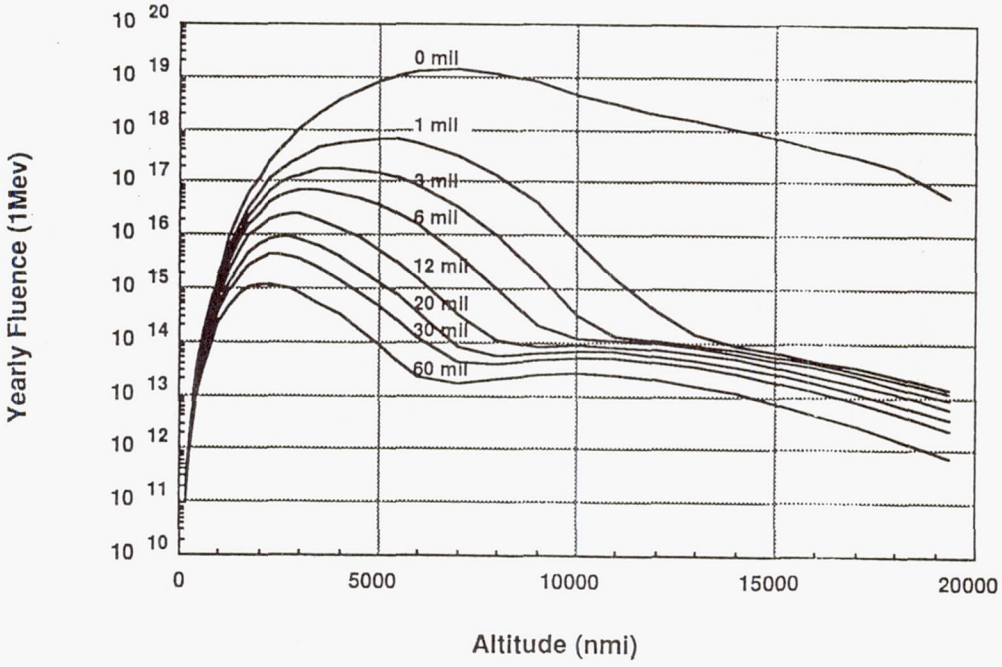

Figure 4: Yearly Fluence vs Altitude
for Various Cover Glass Thickness
at 30 Degrees Inclination

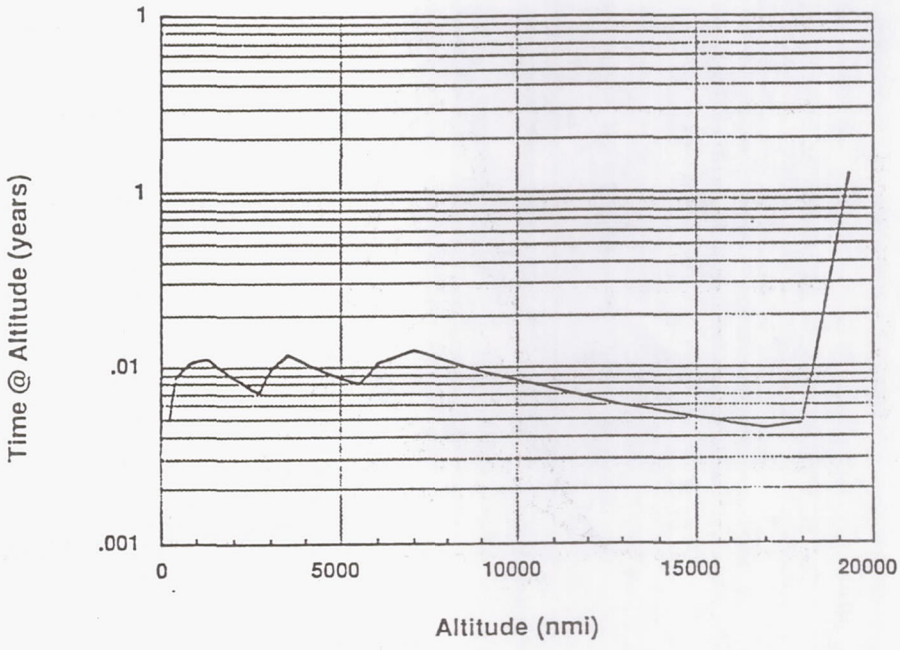

Figure 5: Time at Altitude Flight Profile

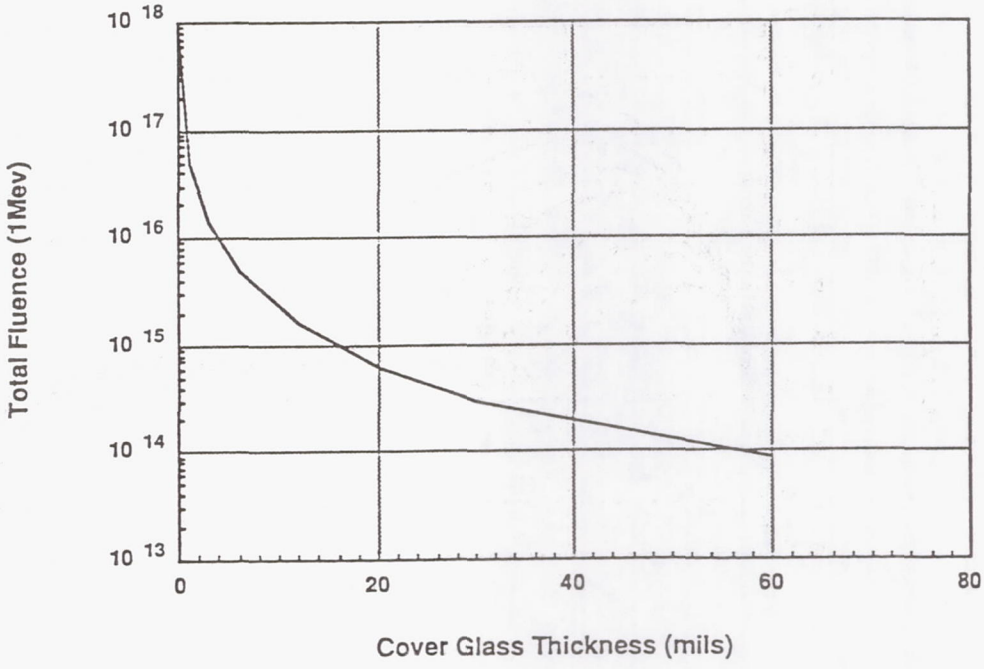

Figure 6: Total Fluence vs Cover Glass Thickness

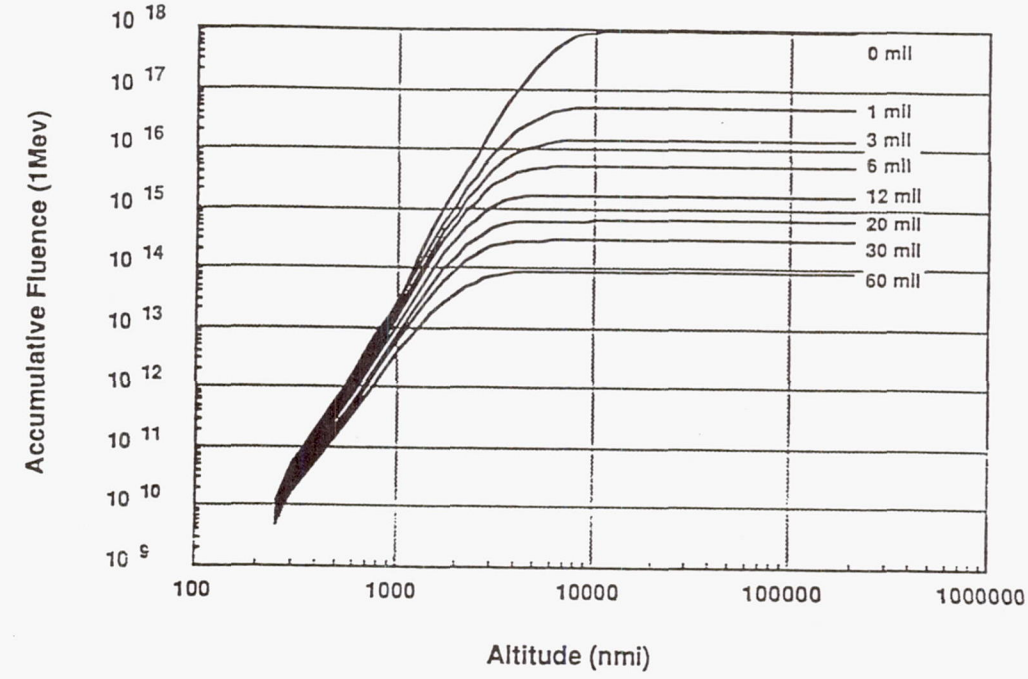

Figure 7: Accumulative Fluence vs Altitude
for Various Cover Glass Thickness
and 30 Degree Inclination

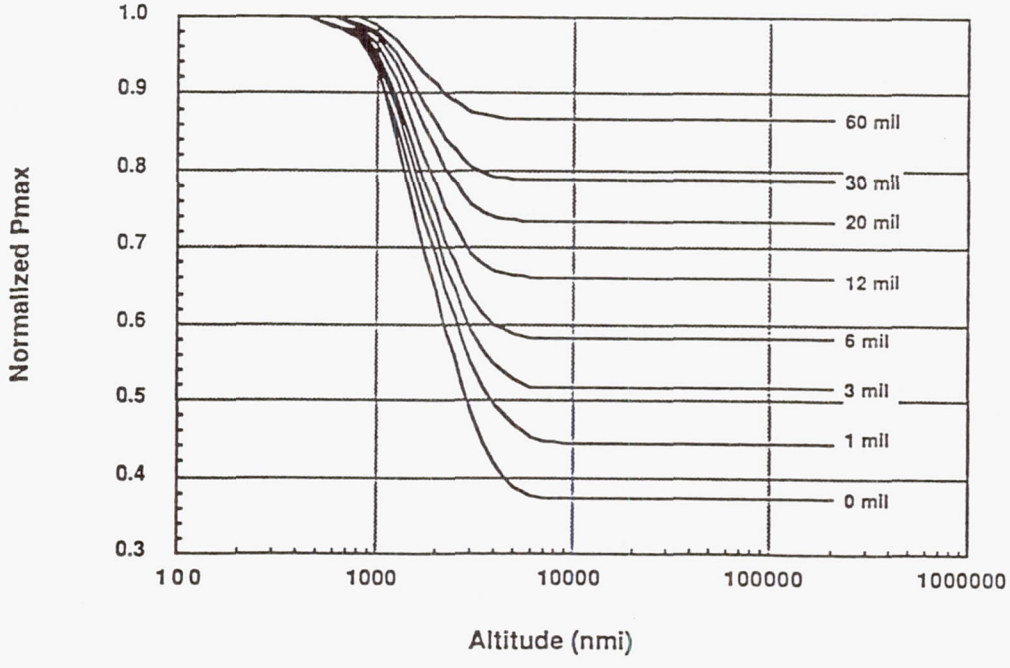

Figure 8: Cell Performance vs Altitude
for Si at 30 Degree Inclination
Infinite Back Shield

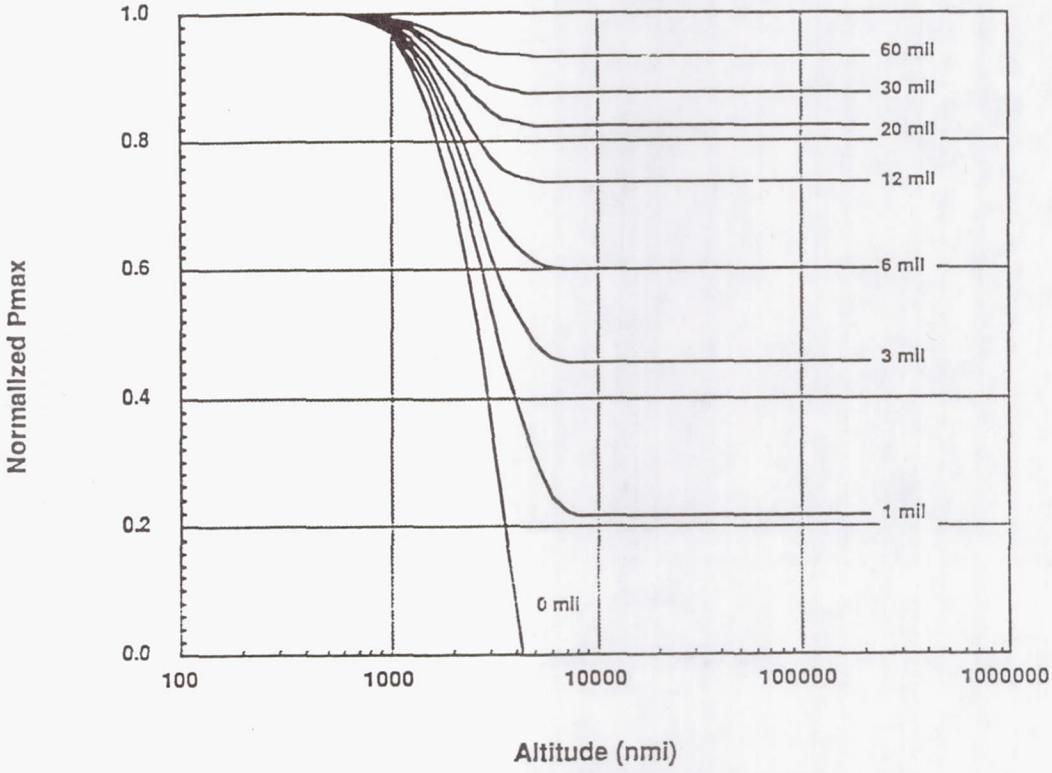

Figure 9: Cell Performance vs Altitude
for GaAs/Ge at 30 Degree Inclination
Infinite Back Shield

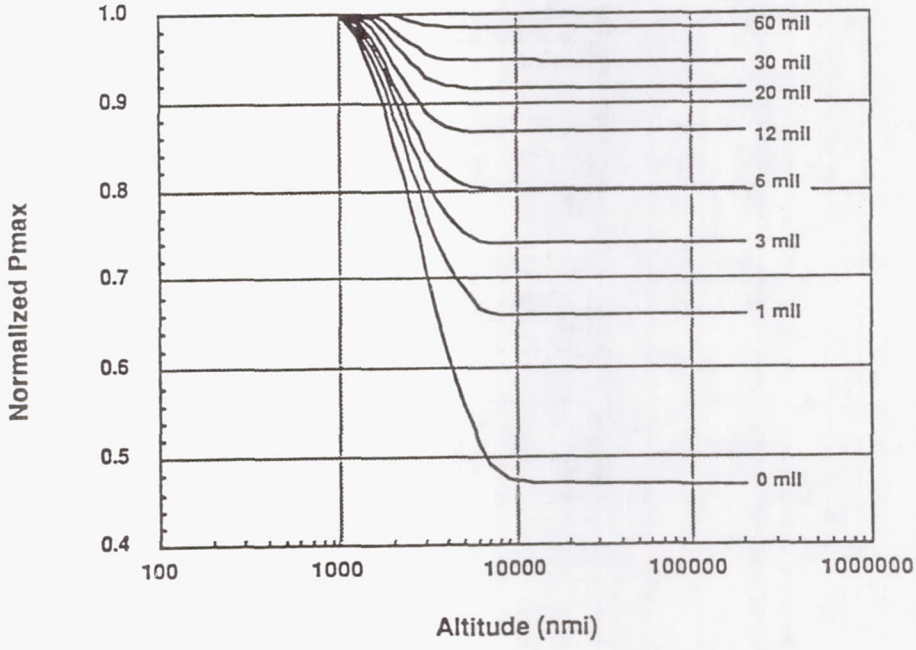

Figure 10: Cell Performance vs Altitude
for InP at 30 Degree Inclination
Infinite Back Shield

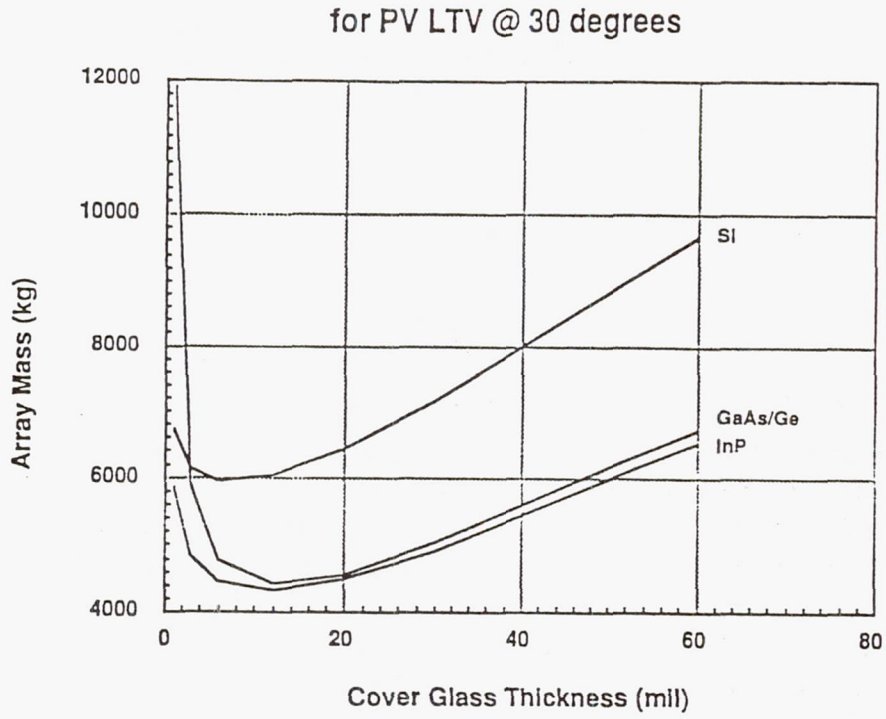

Figure 11: Array Mass vs Cover Glass Thickness

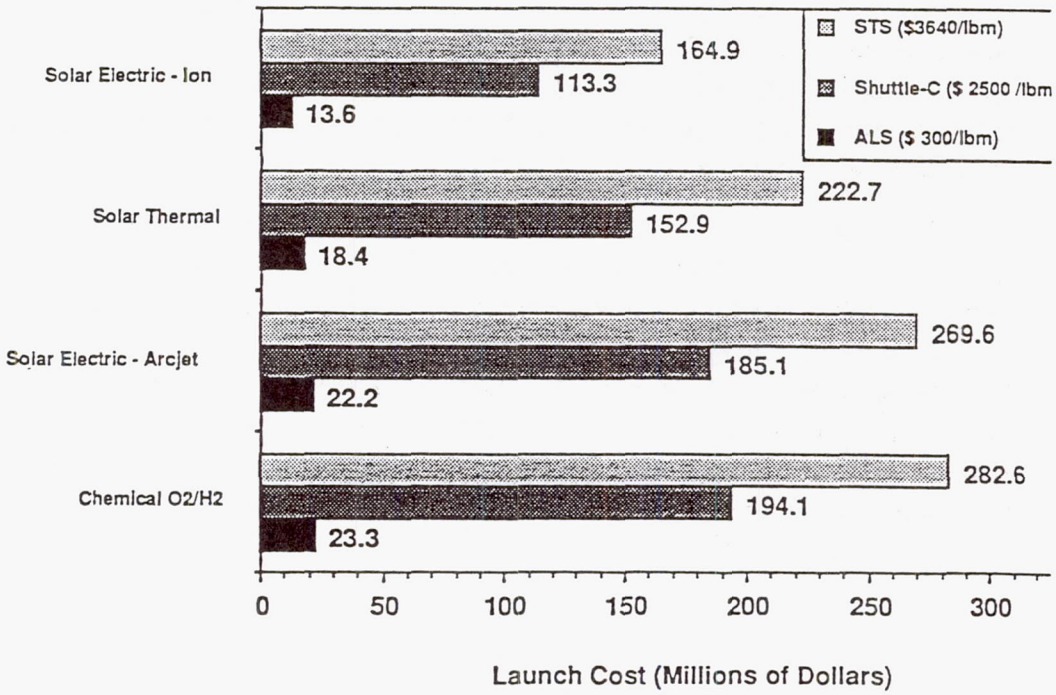

Figure 12: Launch Cost Comparison
for Representative LTV's

Feasibility of Solar Power for Mars

Joseph Appelbaum and Geoffrey A. Landis
NASA Lewis Research Center
Cleveland, OH

Introduction

NASA, through Project Pathfinder, has put in place an advanced technology program to address future needs of manned space exploration. Included in the missions under study is the establishment of outposts on the surface of Mars. The Surface Power program in Pathfinder is aimed at providing photovoltaic array technology for such an application (as well as for the lunar surface). Figure 1 shows an artist's conception of one such array being deployed by astronauts on the surface of Mars. Another important application is for unmanned precurson missions, such as the photovoltaic-powered airplane shown in figure 2, which will scout landing sites and investigate Mars geology for a 1-2 year mission without landing on the surface (ref. 1).

Detailed information on solar radiation data and the climatic conditions on the Martian surface is necessary to allow accurate estimates of photovoltaic power system size and mass, and as input in system analysis and trade-off studies of technology options. Important information includes the distribution of solar insolation, ambient temperature, albedo, and wind speeds and directions on the surface; all as functions of surface position, season, and time of the day.

Of major concern are the dust storms, which have been observed to occur on local as well as on global scales, and their effect on solar array output. In general, the assumption has been that global storms would reduce solar array output essentially to zero, because the opacity of the atmosphere may rise to values ranging from 3 to 9, depending on the severity of the storm. These high values of opacity may persist for long periods of time such that the requirement for energy storage quickly becomes much too large to be practical. However, as shown in Refs. 2 and 3, there is still an appreciable large diffuse illumination, even at high opacitites, so that solar array operation is still possible.

*This work was done while the authors were National Research Council - NASA Lewis Research Associates.

Calculation of solar radiation incident on the top of Martian atmosphere and on the Martian surface has been previously published (Refs. 4 to 6) taking into account the direct beam component only of the solar radiation. The introduction of the diffuse component in this paper became possible with the normalized net flux. This is described in more detail in reference 2.

As on the planet Earth, the solar radiation on the surface of Mars is composed of two components: the direct ("beam") component and the diffuse component. The direct beam is reduced by scattering and absorption along the path from the top of the Martian atmosphere to the Martian surface. Measurement of the optical depth (Refs. 7 and 8) of the Martian atmosphere allows an estimate of the absorption and scattering out of the beam. These estimates were derived from images taken of the Sun and Phobos with a special diode on the Viking lander cameras.

Earth-terrestrial insolation data are accumulated over many years at different locations around the world and are given as long term average values. The optical depth data for Mars, however, are derived from less than two Mars years. Consequently, the calculated insolation, in the present paper, corresponds to short term data. Furthermore, the measured opacities (optical depth) and the calculated insolation pertain to just two locations on the planet: the Viking lander 1 site, (VL1), located at 22.3° N latitude and 47.9° W longitude; and the Viking lander 2 site, (VL2), located at 47.7° N latitude and 225.7°W longitude. However, the similarity in the properties of the dust suspended above the two landing sites suggests that the sites are representative of ones at other locations, at least, at latitudes not too far from the lander's sites. Data from lander VL1 may be used for latitudes 40°N to 40°S and data from lander VL2 for higher latitudes.

Absorption and scattering by the Martian atmosphere stems mainly from suspended dust particles, the amounts of which vary daily, seasonally, and annually, depending on local and global storm intensities and their duration. Large values of optical depth correspond to global storms, i.e., days with low insolation (dark days).

The albedo of the Martian surface varies in the range of about 0.1 to 0.4. The irradiances derived in the section entitled Solar Radiation correspond to 0.1 albedo, but can be also used for other values of albedo, to the first approximation. In this paper a normalized net solar flux function is introduced from which, together with the variation of the opacities, characteristics of the solar radiation on the Martian surface are calculated. This includes, among others, the diurnal and hourly variation of the global, beam and diffuse radiation on the horizontal surface. The results are presented in a series of figures and tables. The solar radiation data and the procedure presented in this paper can be used for the calculation of any desired solar radiation quantity in engineering design. New information about Mars may be forthcoming in the future from new analysis of previously collected data, from new Earth-based observation, or from future flight missions. The Mars solar radiation data will thus be updated accordingly.

Nomenclature

Radiation values:
G solar irradiance
H daily insolation
I hourly insolation
f(z,τ) diffuse scattering function as a function of sun angle and optical depth
H Mars hour (1/24 sol), equal to 24.65/24 of an actual (terrestrial) hour
hr actual (terrestrial) hour

Subscripts:
b beam (i.e., direct insolation) values
d diffuse values
h values for a fixed horizontal surface
o values on top of Mars atmosphere

Other values:
e orbital eccentricity = 0.093377
Ls areocentric longitude (position of Mars in orbit)
m(z) air mass as a function of solar zenith angle
r instantaneous Sun-Mars distance in astronomical units (AU).
S solar constant = 1371 W/m^2 at the mean Sun-Earth distance of 1 AU.
T Mars solar time
T_d Mars daylight hours
z zenith angle of the sun
δ declination angle
δ_o axial tilt of Mars = 24.936°
τ optical depth (opacity) of the atmosphere
ϕ latitude
ω hour angle, measured at 15° per (Mars) hour from solar noon.

Optical Depth

The most direct and probably most reliable estimates of opacity are those derived from Viking lander imaging of the Sun. Figures 3 and 4 show the seasonal variation of the normal-incidence of the optical depth at the Viking lander locations VL1 and VL2, respectively. The season is indicated by the the value of Ls, areocentric longitude of the Sun, measured in the orbital plane of the planet from its vernal equinox (Ls = 0°). The optical depth values were derived from references by Pollack (Refs. 7 and 8) and Zurek (Ref. 9) and discretized for each 5° of Ls value. The optical depth is assumed to remain constant throughout the day. Opacities are minimum during the northern spring (Ls = 0° to 90°) and summer (Ls = 90° to 180°), and maximum during southern spring (Ls = 180° to 270°) and summer (Ls = 270° to 360°), the seasons during which most local and major dust storms occur. When dust storms

are not present, the optical depth is typically about 0.5, corresponding to a direct-beam solar intensity (at zenith angle of 90°) of exp(-0.5) = 61% of I_o. Two global dust storms occurred during the periods of each observation as indicated by the high values of the optical depth (they are lower bound values).

Mars has seasons comparable to those of Earth. However, the seasons are on the average about twice as long as on the Earth, corresponding to the greater length of the Martian year (Table I). Furthermore, they are distinctly unequal in duration as a result of the appreciable eccentricity of the Martian orbit. For that reason, the Martian year is not divided into months. Table I gives the duration of the Martian seasons in terrestrial and Martian days (a Martian day, or "sol", = 24.65 hr). Areocentric longitudes Ls = 0° and 180° correspond to the spring and fall equinox for the northern hemisphere, respectively, and Ls = 90° and 270° correspond to northern and southern summer solstices, respectively.

Global and Local Dust Storms

The intensity of Martian global and local dust storms is defined in terms of the atmospheric opacity created by the dust raised. Global dust storms obscure planetary-scale sections of the Martian surface for many martian days (sols). Local dust srorms are less intense, and form and dissipate in a few days or less. From a photovoltaic system design point of view, the intensity, frequency, and duration of these storms may be viewed as "partially cloudy" and "cloudy" days, for which additional capacity and possibly energy storage may be required. Characeristics of global and local dust storms are listed below.

Global Dust Storms

(1) One, or occasionally two, global dust storms of planetary scale may occur each Martian year. The duration may vary from 35 to 70 days or more. Although global dust storms may not occur every year, their occurrance is fairly frequent.

(2) The global dust storms occur near perihelion, i.e., southern hemisphere spring and summer, when insolation is maximum in the southern mid-latitudes where such storms typically originate.

(3) The first global dust storm observed by Viking (1977) spread from a latitude of 40°S to a latitude of 48°N in about 5 to 6 days.

(4) The atmospheric opacity during a global dust story is typically greater than 1.

Local Dust Storms

(1) Local dust storms occur at almost all latitudes and throughout the year. However, they have been observed to occur most frequently in the latitude 10° to

20°N and 20° to 40°S, with more dust clouds seen in the south than in the north, the majority of which occurred during the southern spring.

(2) Based on Viking orbiter observations, it is estimated that approximately 100 local storms occur in a given Martian year.

(3) Local dust storms last a few days.

(4) Atmospheric opacity during a local dust storm may be assumed to be about 1.

Solar Radiation at the Top of the Mars Atmosphere

The variation of the solar radiation at the top of the Mars atmosphere is governed by the location of Mars in its orbit and by the solar zenith angle. The sun-Mars distance is (ref. 10):

$$r = a \frac{(1-e^2)}{[1+e\ cos(Ls-248°)]} \tag{1}$$

where 248° is the areocentric longitude of the perihelion of the orbit. The sun-Mars mean distance a is 1.52369 AU (Astronomical units), thus, the mean irradiance at the top of the Martian atmosphere is $1371/1.52369^2 = 590$ W/m^2. The irradiance thus varies with orbital position as:

$$G_{ob} = 590 \frac{[1+e\ cos(Ls-248°)]^2}{(1-e^2)} \text{ W/m}^2 \tag{2}.$$

This is the solar intensity which would be received, for example, by a Mars orbiter.

The solar zenith angle is a function of the solar declination angle, given by:

$$Cos(z) = sin\phi\ sin\delta + cos\phi\ cos\delta\ cos\omega \tag{3}$$

where the solar declination angle is:

$$sin(\delta) = sin\delta_o sinLs \tag{4}$$

The four seasons pertain here to the northern hemisphere; the seasons are reversed for the southern hemisphere.

The ratio of Mars to Earth length of day is 24.65/24. It is convenient, for calculation purposes, to define a Mars hour, H, 2.7% longer than a terrestrial hour, by dividing the Martian day (sol) into 24 Martian hours. The final solar radiation results expressed in terms of Mars hours can then be multiplied by 1.027 to give results in actual (terrestrial) time.

Examples of the solar radiation calculation procedure and results shown pertain to five example days at Viking Lander location VL1 at $\phi = 22.3°$N. Areocentric longitude Ls=69° corresponds to aphelion, the lowest exoatmospheric irradiance; Ls=249° to perihelion, the highest exoatmospheric irradiance; Ls=153° to the mean radiation of 590 W/m^2; Ls=120° corresponds to the lowest observed atmospheric opacity of 0.4, and Ls=299° to the highest opacity of 3.25.

For a given Ls and latitude ϕ, one can calculate the zenith angle z as a function of time using equations (3) and (4). The direct beam irradiance on a horizontal surface is then determined by multiplying the direct irradiance from equation (2) by the cosine of the zenith angle. The number of daylight hours is (from ref. 11):

$$T_d = 1.027 \cdot \frac{12}{15}\, cos^{-1}(-tan\ \phi\ tan\ \delta) \qquad (5).$$

Table II gives the hourly beam insolation I_{obh} and the daily beam insolation H_{obh} on a horizontal surface at the top of the atmosphere. To obtain terrestrial watt-hours, one needs to multiply the values in Table II by 1.027.

Solar Radiation on the Surface of Mars

The variation of the solar radiation on the Martian surface is governed by three factors: (1) the Mars-sun distance, (2) the solar zenith angle, and (3) the opacity of the atmosphere. The global solar radiance is composed of direct beam and the diffuse components. The direct beam irradiance normal to the incident rays, G_b, is related to the optical depth of the intervening suspended dust by (Beer's law):

$$G_b = G_{ob} exp[-\tau\ m(z)] \qquad (6)$$

where m(z) is the air mass determined by the zenith angle z, and can be approximated, for zenith angles up to about 80°, by:

$$m(z) \approx \frac{1}{cos(z)} \qquad (7).$$

The net solar flux integrated over the solar spectrum on the Martian surface was calculated by Pollack (Ref. 12) based on multiple wavelength and multiple scattering of the solar radiation. Derived data from this calculation are shown in Table III by the normalized net flux function $f(z, \tau)$ where the parameters are the zenith angle z and the optical depth τ. This table pertains to an albedo of 0.1. Using this data we calculated the global solar irradiance. We assumed that the diffuse irradiance is obtained by subtracting the direct beam from the global irradiance. The solar irradiance components, on a horizontal Martian surface, is the sum of the direct beam and the diffuse components:

$$G_h = G_{bh} + G_{dh} \tag{8}.$$

The diffuse irradiance of the Martian atmosphere may be a result of a different mechanism than that for the Earth atmosphere, nevertheless, we can apply Eq. (7) as for Earth-terrestrial calculations. The global irradiance G_h on a horizontal surface is given by:

$$G_h = G_{ob} cos(z) \frac{f(z,\tau)}{0.9} \tag{9}.$$

The factor 0.9 comes from the expression (1-albedo) in the denominator assuming albedo of 0.1. This accounts for sunlight reflected from the ground and backscattered by atmospheric dust back to the solar array. An albedo value of 0.1 is conservative. The actual Mars albedo can be as high as 0.4. To first order, higher surface albedo can be taken into account by replacing the 0.9 in (9) by (1-albedo).

The direct beam irradiance G_{bh} on a horizontal surface is obtained by:

$$G_{bh} = G_{ob}\ cos(z)\ exp[\frac{-\tau}{cos(z)}] \tag{10}.$$

The diffuse irradiance on a horizontal surfaces is obtained from Eqs. (7) to (9). The irradiances were calculated based on Table III data and the mean irradiance of 590 W/m^2. The variation of the global irradiance on a horizontal Martian surface, G_h, Eq. (8), is shown in Fig. 6 as a function of the optical depth τ and zenith angle z.. The direct beam irradiance on a horizontal surface G_{bh} is obtained using Eq. (9) and is shown in Fig. 7. The direct beam irradiance shows a sharp decrease with increasing optical depth, and a relatively moderate decrease with increasing zenith angle. The diffuse irradiance on a horizontal surface G_{dh} is shown in fig. 8. The diffuse irradiance shows a sliding maximum with the variation of the zenith angle.

The solar radiation (global, direct beam and diffuse) variation (diurnal, hourly and daily) can be calculated based on the preceeding equations and the $f(z,\tau)$ data of Table III. The following examples pertain again to the Viking lander VL1 location and the five example days at areocentric longitudes Ls = 69°, 120°, 153°, 249°, and 299°, representative of the the range of martian conditions. Daily solar insolation are also given for Ls = 0°, 30°, 60°, 90°, 150°, 180°, 210°, 240°, 300°, and 330°. For a given Ls and ϕ, one can calculate the variation of the zenith angle z as function of the Mars solar time T using Eqs. (3) and (4). Referring to Fig. 3 for the given Ls, the optical depth τ is determined; with Table III and Eqs. (6) to (10) one can calculate the solar radiation variation for the given day. The results are shown in Figs. 9 to 11. (Because of symmetry around solar noon, the graphs show the forenoon or afternoon

variation.) The figures show clearly that for higher opacities, the diffuse component dominates the solar radiation.

The total (global, direct beam and diffuse) energy on a horizontal surface can be calculated based on Figs. 9 to 11 by integrating hourly areas. The direct beam insolation, for a desired period of time, can be also calculated by:

$$I_{bh} = \frac{12^*}{\pi} G_{ob} \int_{\omega_1}^{\omega_2} [sin\phi\ sin\delta + cos\phi\ cos\delta\ cos\omega]\ exp[\frac{-\tau}{(sin\phi sin\delta + cos\phi cos\delta cos\omega)}]\ d\omega \quad (11).$$

*Replace the 12 by 12.325 in Eq. (11) to get the insolation with reference to actual (terrestrial) time.

Tables IV to VI give the hourly global I_h, direct beam I_{bh} and diffuse I_{dh} insolation as well as the daily global H_h, direct beam H_{bh} and diffuse H_{dh} insolation. Included in the tables are also the number of Martian daylight hours and the daily mean irradiance. For a day with a relative high opacity (Ls = 299°), the daily mean global irradiance is still appreciable and is about 30 percent of that in a clear day. The percentage of diffuse and direct beam insolation for the five analyzed Ls days is shown in Fig. 12. The daily global insolation on a horizontal surface on Mars is shown in Fig. 13 for twelve areocentric longitudes covering a Martian year. Using the procedure outlined, one can calculate the variation of the solar radiation for any desired day to use for any engineering system design.

Temperature

The ambient air temperature at the Viking lander's locations was measured for more than two Martian years at the height of 1.6 m above the ground. The ambient temperature sensors consists of chromel-constantan thermocouples. Again, these are short term data and pertain to the two Viking locations. While the array operating temperature will not, in general, be the same as the local air temperature, measured air temperature is needed as one factor needed to compute the array operating temperature

Mars temperature data was information was supplied to us by Tillman (ref. 13). Figure 14 shows the variation of the ambient temperature at Viking lander VL1 for part of the first year after landing. The top time coordinate (abscissa) has units of sol number, the number of Martian solar days from touchdown on sol 0 (1 sol = 24.65 hr). The bottom abscissa is the seasonal date Ls. The temperature variation over the course of a day is shown in more detail for sols 191 and 192 (autumn) in figure 15. The figure shows a quite significant large diurnal ambient temperature variation. Figure 16 shows the ambient temperature at Viking lander VL2 for the first year after landing. During dust storm events, the Martian atmosphere is strongly

heated up by absorption of solar radiation due to the suspended dust. As a result, the maximum ambient temperature at the surface decreases significantly while the minimum increases, especially during the more intense 1977 B storm. The diurnal ambient temperature variation for sols 285 and 286 at the time of 1977 B global storm is shown in Fig. 17. The variation in temperature, 16°C, is rather small. For the less intense 1977 A global storm, the diurnal temperature variation was larger (28°C), and for a local storm, the diurnal ambient temperature variation is still larger (38°C).

Wind

An array deployed on Mars will have to withstand wind loads. Surface wind velocities were measured at the VL-2 site. The average windspeed is about 2 m/sec. 90% of the time the wind was below 5 m/sec; 99% of the time below about 15 m/sec. For some applications it may be a viable design strategy to retract the array if windspeeds reach higher values. Less than 0.01% of the time the winds reached 25-30 m/sec. During dust storms up to 32 m/sec has been observed.

Due to the very low air density, the actual pressures produced by the wind are not very high. The effect is roughly that of a terrestrial wind of 1/7th the velocity.

Atmospheric pressure varies with season and temperature. At a typical pressure of 8 mb and temperature of 200°K, the maximum wind velocity of 30 m/sec produces a dynamic pressure of 10 nt/m^2, similar to that of a 4 m/sec (9 MPH) wind on Earth.

The array surface will have to resist abrasion by wind-blown sand and dust. Since the atmospheric density is so low, sand should not be lifted more than a few centimeters above the surface. Dust can be blown quite high in the atmosphere; however, since typical dust seems to consist of silicate particles with mean radius of 1 to 2 micron, abrasion due to dust is not expected to be a significant difficulty. The question of whether the array can be designed so that settling dust will be cleared from the array surface by wind is currently being addressed in wind tunnel studies (ref. 14); preliminary results seem to indicate that this will be the case if the array surface is tilted from the horizontal.

Conclusions

Effective design and utilization of solar energy depend to a large extent on adequate knowledge of solar radiation characteristics in the region of solar energy system operation. The two major climatic components needed for photovoltaic system design are the distributions of solar insolation and ambient temperature. These distributions for the Martian climate are given in the paper at the two Viking lander locations but can also be used, to the first approximation, for other latitudes. One of the most important results of this study is that there is a large diffuse component of the insolation, even at high optical depth, so that solar energy system operation is still

possible. If the power system is to continue to generate power even on high optical opacity (i.e., dusty atmosphere) days, it is thus important that the photovoltaic system be designed to collect diffuse irradiance as well as direct. In absence of long term insolation and temperature data for Mars, the data presented in this paper can be used until updated data are available. The ambient temperature data are given as measured directly by the temperature sensor; the insolation data (global, direct beam, and diffuse) are calculated from optical depth measurements of the atmosphere. Additional insolation data, such as daily insolations, can be further derived based on Table 1 and the expressions above and in reference 3.

Acknowledgement

We are very grateful to James B. Pollack from the Space Science Division, NASA Ames Research Center for supplying us with the f(z,τ) table; to James E. Tillman from the Department of Atmospheric Sciences, University of Washington for supplying the ambient temperature distribution graphs; and for their informative discussions.

References

[1.] A.J. Colozza, *to be published, 26th AIAA/SAE/ASME/ASEE Joint Propulsion Conf.,* Orlando, FL, 16-18 July 1990.

[2.] J. Appelbaum and D. J. Flood, Space Power, **8**, No. 3, 307, 1989.

[3.] J. Appelbaum and D. J. Flood, NASA Technical Memorandum TM-102299, 1989 (to be published, Solar Energy, 1990).

[4.] J. S. Levine, D. R. Kramer and W. R. Kuhn, ICARUS, **31**, 136, 1977.

[5.] E. Van Hemelrijk, Earth, Moon, and Planets, **33**, 157, 1985.

[6.] E. Van Hemelrijk, Earth, Moon, and Planets, **38**, 209, 1987.

[7.] J. B. Pollack, et al., Journal of Geophysical Research, **82**, 4479, 1977.

[8.] J. B. Pollack, et al., Journal of Geophysical Research, **84 B6**, 2929, 1979.

[9.] R. W. Zurek, ICARUS, **50**, 288, 1982.

[10.] E. V. P. Smith and K. C. Jacobs, *Introductory Astronomy and Astrophysics*, W.B. Saunders Co., 1973.

[11.] J. A. Duffie, W. A. Beckman, Solar Engineering of Thermal Processes, Wiley, 1980.

[12.] J. B. Pollack, R. M. Harberle, J. Schaeffer, H. Lee, Journal of Geophysical Research (in press).

[13.] J. E. Tillman, Director and N. C. Johnson, Viking Computer Facility, Department of Atmospheric Sciences, University of Washington, Seattle, Washington, private communication.

[14.] J.R. Gaier, M.E. Perez-Davis, and M. Marabito, NASA Technical Memorandum TM-102507, Feb. 1990 (in press).

TABLE I. - MARS SEASONAL DURATION

Areocentric longitude of the sun, L_S	Season		Duration of the season Mars	
	Northern hemisphere	Southern hemisphere	Martian days	Terrestrial days
0 to 90°	Spring	Autumn	194	199
90 to 180°	Summer	Winter	178	183
180 to 270°	Autumn	Spring	143	147
270 to 360° or 0°	Winter	Summer	154	158
			669	687

TABLE II. - HOURLY AND DAILY BEAM INSOLATION ON A HORIZONTAL SURFACE AT TOP OF MARS ATMOSPHERE

[VL1: ϕ = 22.3°N]

Hourly* I_{obh} (Whr/m^2-hr) for hours ending at:								Daily* H_{obh}, Whr/m^2-day
Day-L_S	13:00	14:00	15:00	16:00	17:00	18:00	19:00	
69°	488	460	405	328	234	128	25	4136
120°	528	497	437	353	249	134	23	4442
153°	572	536	467	368	247	113	7	4620
249°	496	455	376	263	126	8	--	3449
299°	478	439	364	257	127	10	--	3350

*Multiply by 24.65/24 to obtain actual (terrestrial) Whr/m^2

TABLE III. - NORMALIZED NET FLUX FUNCTION $f(z,\tau)$ AT THE MARTIAN SURFACE

Optical depth	Zenith angle Z, deg									
τ	0	10	20	30	40	50	60	70	80	85
0.1	0.885	0.883	0.882	0.880	0.876	0.870	0.857	0.830	0.755	0.635
0.2	.866	.865	.860	.858	.851	.836	.813	.758	.640	.470
0.3	.847	.846	.841	.836	.826	.806	.774	.708	.562	.412
0.4	.828	.827	.821	.815	.802	.778	.740	.667	.502	.373
0.5	.810	.810	.802	.796	.778	.752	.708	.628	.452	.342
0.6	.793	.791	.785	.775	.755	.725	.677	.593	.414	.318
0.7	.776	.773	.766	.755	.733	.700	.646	.555	.383	.298
0.8	.760	.756	.750	.736	.710	.675	.616	.520	.360	.280
0.9	.745	.740	.733	.717	.690	.650	.587	.487	.336	.264
1.0	.732	.725	.717	.700	.670	.628	.560	.455	.317	.252
1.1	.713	.709	.700	.682	.651	.604	.539	.433	.300	.239
1.2	.697	.692	.683	.662	.632	.585	.518	.413	.288	.230
1.3	.682	.677	.667	.646	.613	.567	.498	.394	.273	.220
1.4	.666	.661	.650	.629	.596	.546	.478	.379	.262	.210
1.5	.651	.646	.633	.612	.580	.530	.460	.362	.251	.202
1.6	.637	.630	.618	.597	.563	.512	.441	.348	.240	.195
1.7	.622	.615	.601	.581	.546	.494	.424	.332	.232	.188
1.8	.609	.600	.586	.568	.531	.480	.408	.318	.224	.181
1.9	.596	.587	.571	.551	.514	.464	.393	.304	.217	.176
2.0	.582	.573	.558	.537	.500	.448	.378	.293	.208	.170
2.25	.552	.542	.522	.501	.462	.410	.343	.265	.190	.156
2.50	.518	.509	.492	.469	.430	.378	.316	.242	.174	.145
2.75	.486	.478	.462	.440	.401	.353	.293	.224	.158	.136
3.00	.460	.450	.434	.414	.376	.330	.273	.206	.150	.128
3.25	.434	.424	.410	.390	.354	.308	.254	.193	.140	.120
3.50	.411	.400	.387	.367	.333	.290	.240	.180	.132	.110
4.00	.370	.360	.347	.330	.296	.258	.212	.160	.118	.100
5.00	.294	.286	.275	.258	.230	.203	.166	.130	.094	.080
6.00	.228	.223	.215	.200	.178	.153	.130	.103	.080	.068

TABLE IV. - HOURLY AND DAILY GLOBAL INSOLATION ON A HORIZONTAL SURFACE AT MARS SURFACE

[VL1: ϕ = 22.3°N]

Hourly global insolation* I_h (Whr/m^2-hr) for hours ending at:									Daily global insolation,* H_h, Whr/m^{2}day	Daylight hours* T_d, hr	Daily mean global irradiance, W/m^2
Day-L_s	τ	13:00	14:00	15:00	16:00	17:00	18:00	19:00			
69°	0.65	420	390	338	263	170	78	11	3340	13.34	250
120°	.40	477	446	387	306	201	98	15	3860	13.24	292
153°	.50	508	471	399	302	185	73	3	3882	12.62	308
249°	1.40	307	270	204	122	45	2	--	1900	10.66	178
299°	3.25	170	149	107	61	24	1	--	1024	10.75	95

*Multiply by 24.65/24 to obtain actual (terrestrial) Whr/m^2 or hours

TABLE V. - HOURLY AND DAILY BEAM INSOLATION ON A HORIZONTAL SURFACE AT MARS SURFACE

[VL1: ϕ = 22.3°N]

Hourly beam insolation* I_{bh} (Whr/m^2-hr) for hours ending at:									Daily beam insolation*, H_{bh}, Whr/m^{2}day	Daylight hours* T_d, hr	Daily mean beam irradiance, W/m^2
Day-L_s	τ	13:00	14:00	15:00	16:00	17:00	18:00	19:00			
69°	0.65	252	230	186	128	67	20	3	1768	13.34	133
120°	.40	352	322	265	190	103	33	2	2534	13.24	191
153°	.50	345	310	244	163	77	15	--	2308	12.62	183
249°	1.40	69	50	26	10	2	--	--	314	10.66	29
299°	3.25	3	2	1	---	--	--	--	12	10.75	1

*Multiply by 24.65/24 to obtain actual (terrestrial) Whr/m^2 or hours

TABLE VI. - HOURLY AND DAILY DIFFUSE INSOLATION ON A HORIZONTAL SURFACE AT MARS SURFACE

[VL1: = 22.3°N]

Hourly diffuse insolation* I_{dh} (Whr/m^2-hr) for hours ending at:									Daily diffuse insolation,* H_{dh}, Whr/m^{2}day	Daylight hours* T_d, hr	Daily mean diffuse irradiance, W/m^2
Day-L_s	τ	13:00	14:00	15:00	16:00	17:00	18:00	19:00			
69°	0.65	168	160	152	135	103	58	10	1572	13.34	118
120°	.40	125	124	122	116	98	65	13	1326	13.24	100
153°	.50	163	161	155	139	108	58	3	1574	12.62	125
249°	1.40	238	220	178	112	43	2	--	1586	10.66	149
299°	3.25	167	147	106	61	24	1	--	1012	10.75	94

*Multiply by 24.65/24 to obtain actual (terrestrial) Whr/m^2 or hours

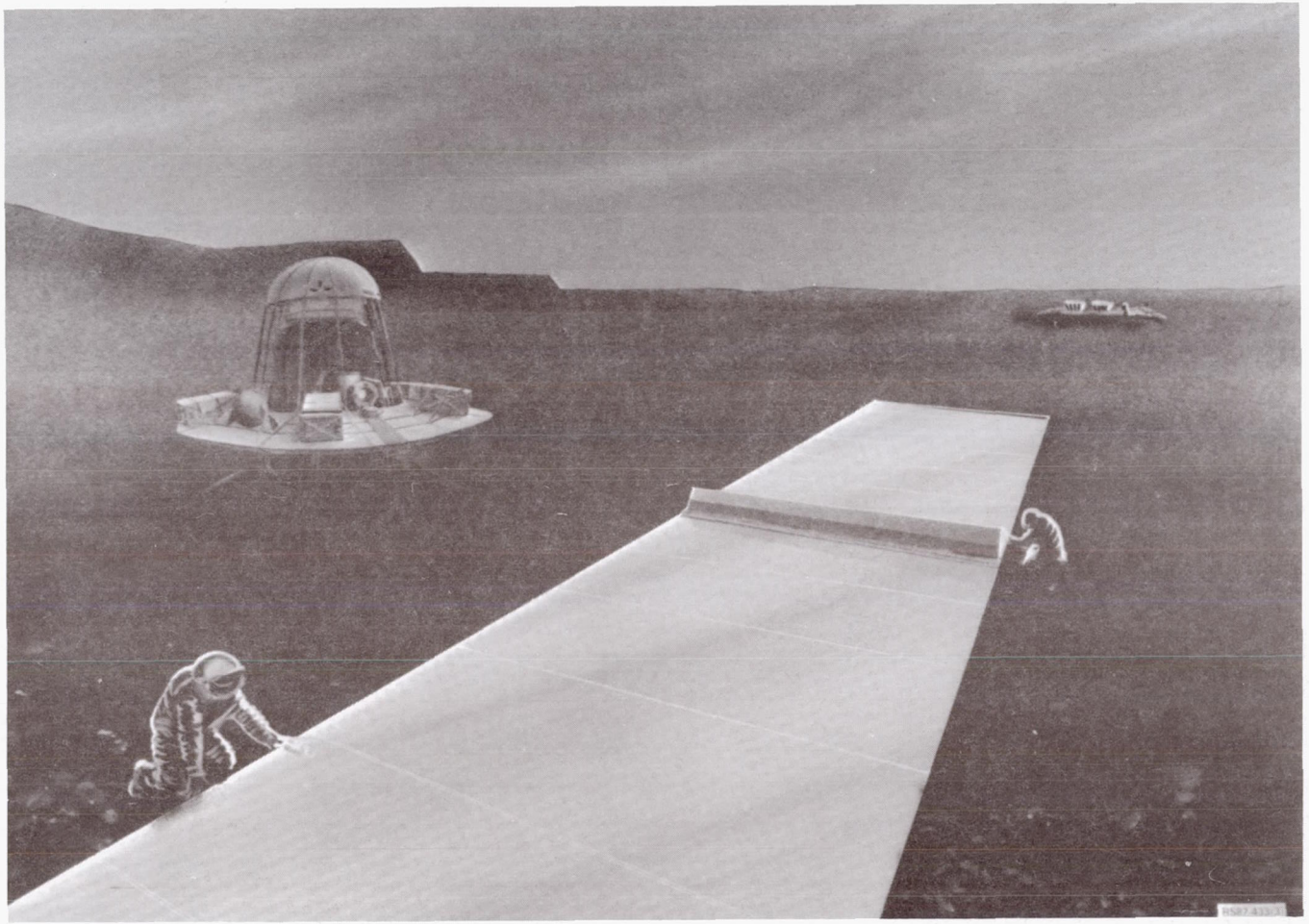

Figure 1: artist's conception of a roll-out solar array being deployed by astronauts on Mars.

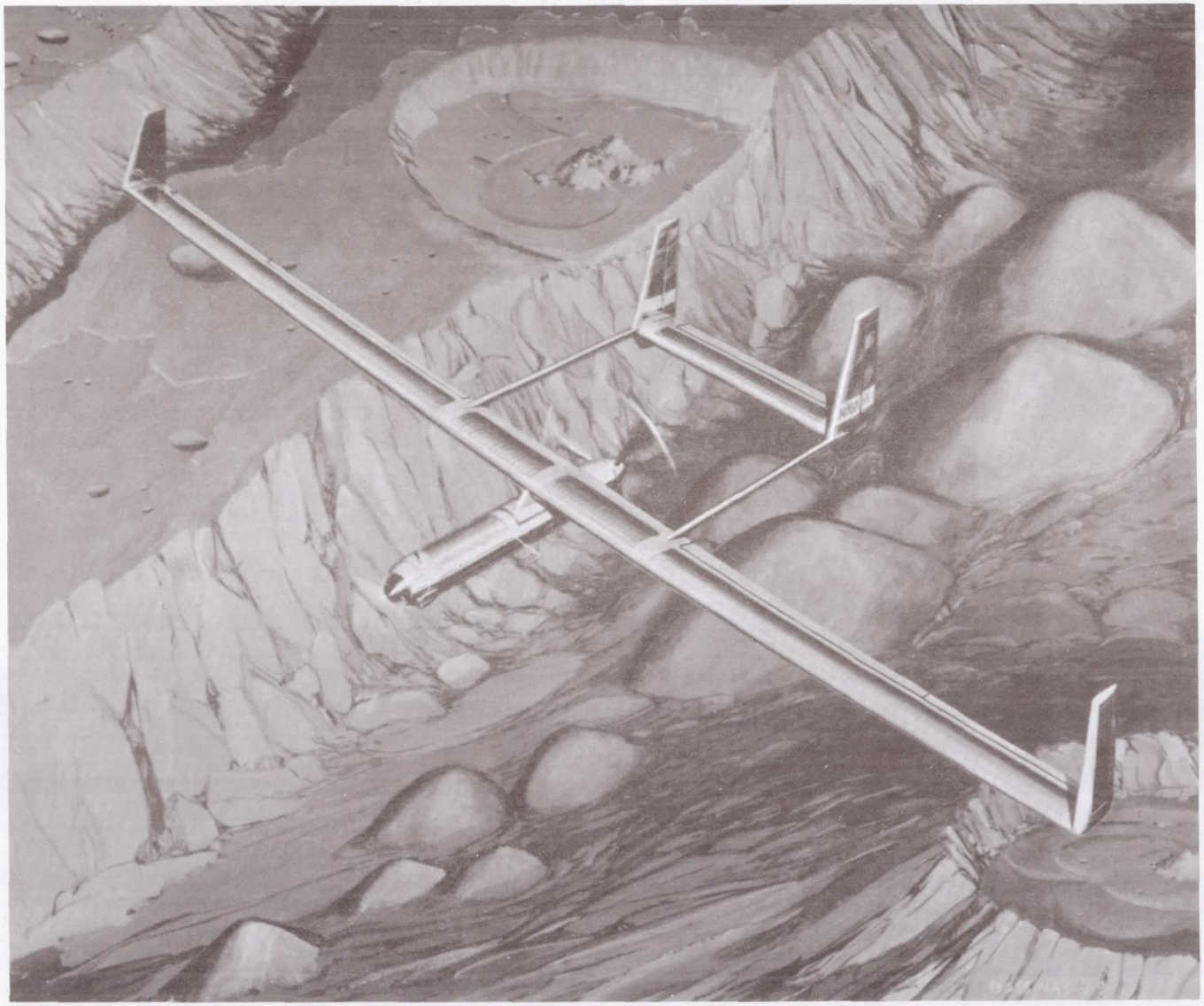

Figure 2: artist's conception of a photovoltaic-powered unmanned Mars airplane.

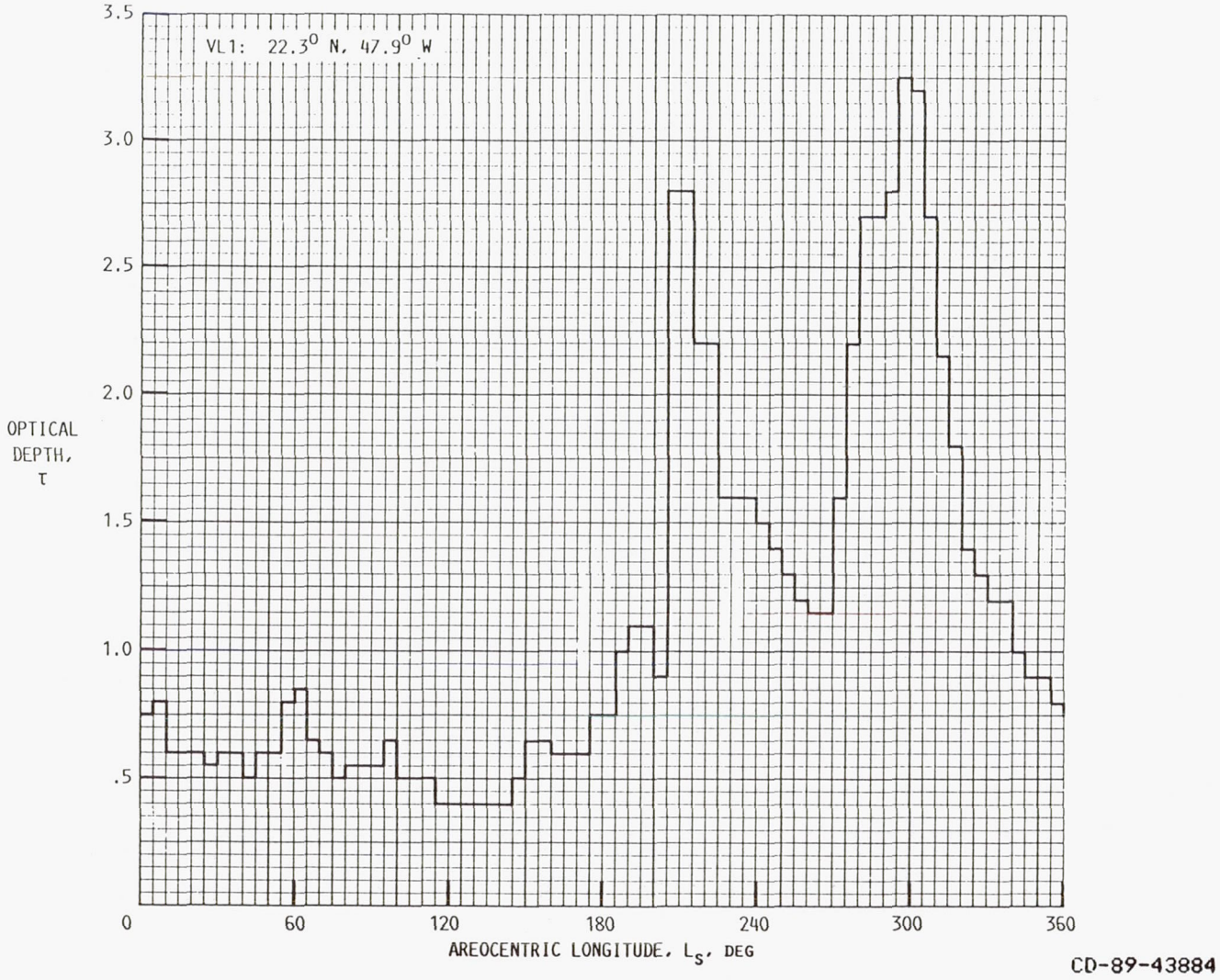

Figure 3: seasonal variation of the normal-incidence of the optical depth at the Viking lander location VL1 [From Pollack (Refs. 7 and 8) and Zurek (Ref. 9)].

Figures 4: seasonal variation of the normal-incidence of the optical depth at the Viking lander location VL2 [From Pollack (Refs. 7 and 8) and Zurek (Ref. 9)].

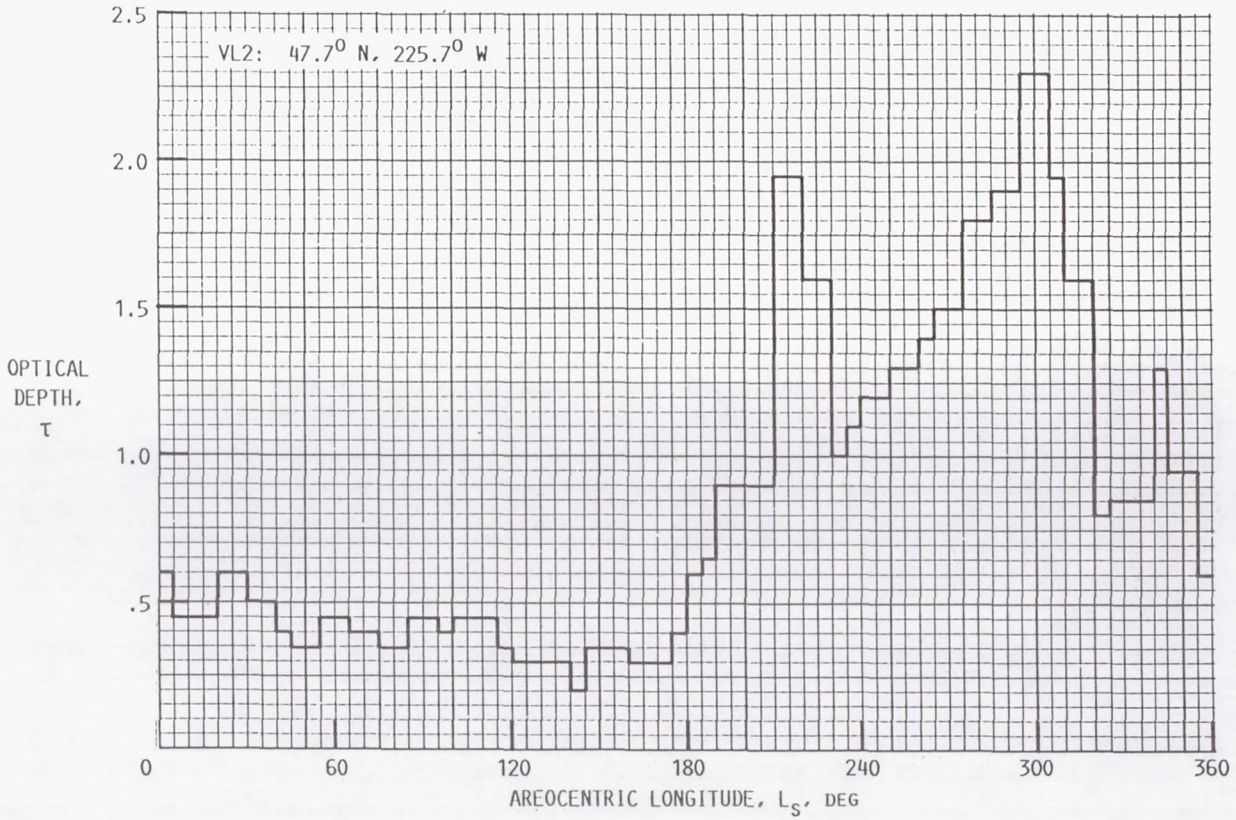

CD-89-43885

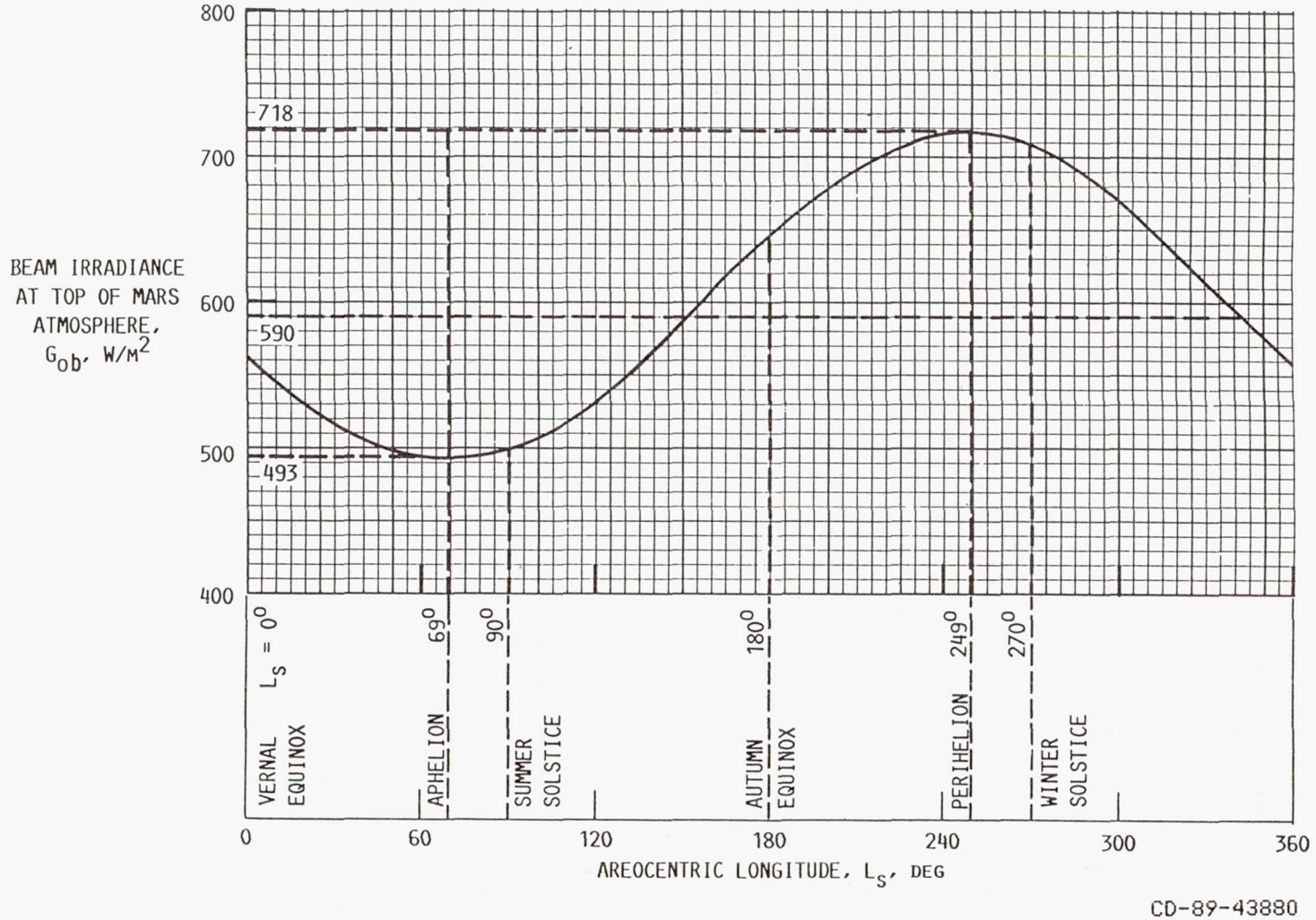

Figure 5: Solar irradiance above the Mars atmosphere as a function of position of Mars in orbit.

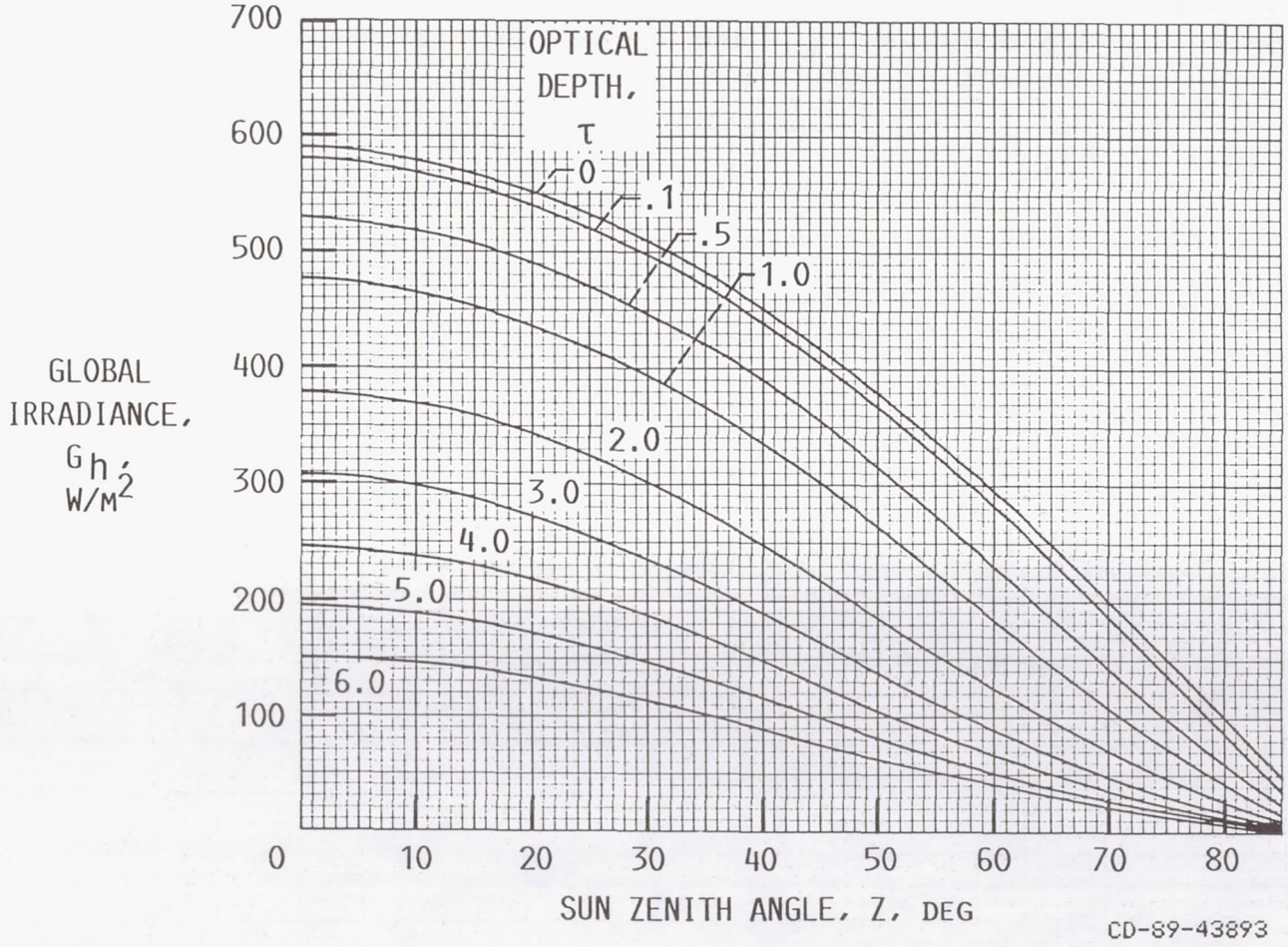

Figure 6: the variation of the global irradiance G_h on a horizontal Martian surface as a function of the optical depth τ and zenith angle z.

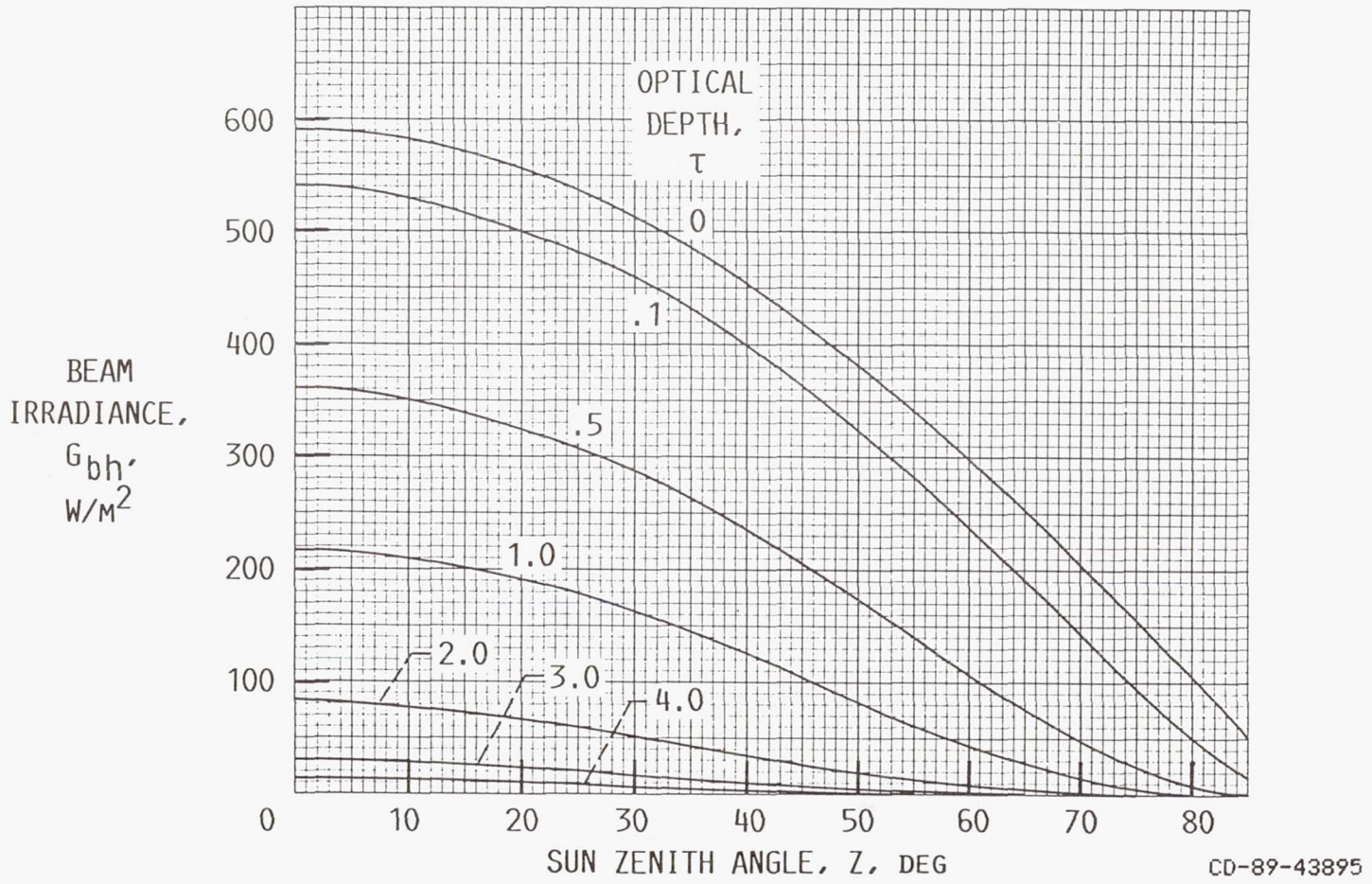

Figure 7: the direct beam irradiance G_{bh} on a horizontal Martian surface as a function of the optical depth τ and zenith angle z.

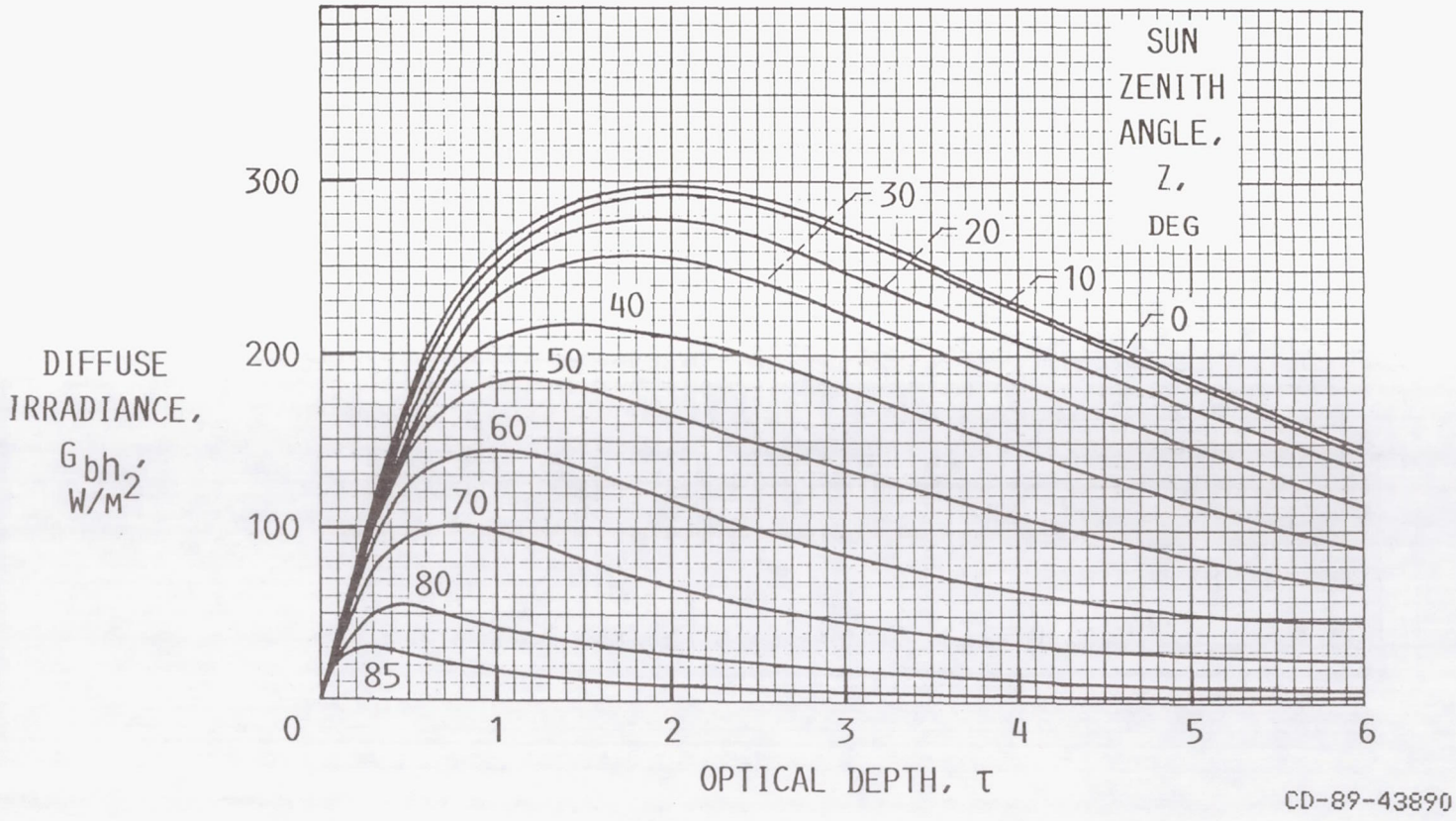

Figure 8: the diffuse irradiance G_{dh} on a horizontal Martian surface as a function of the optical depth τ and zenith angle z.

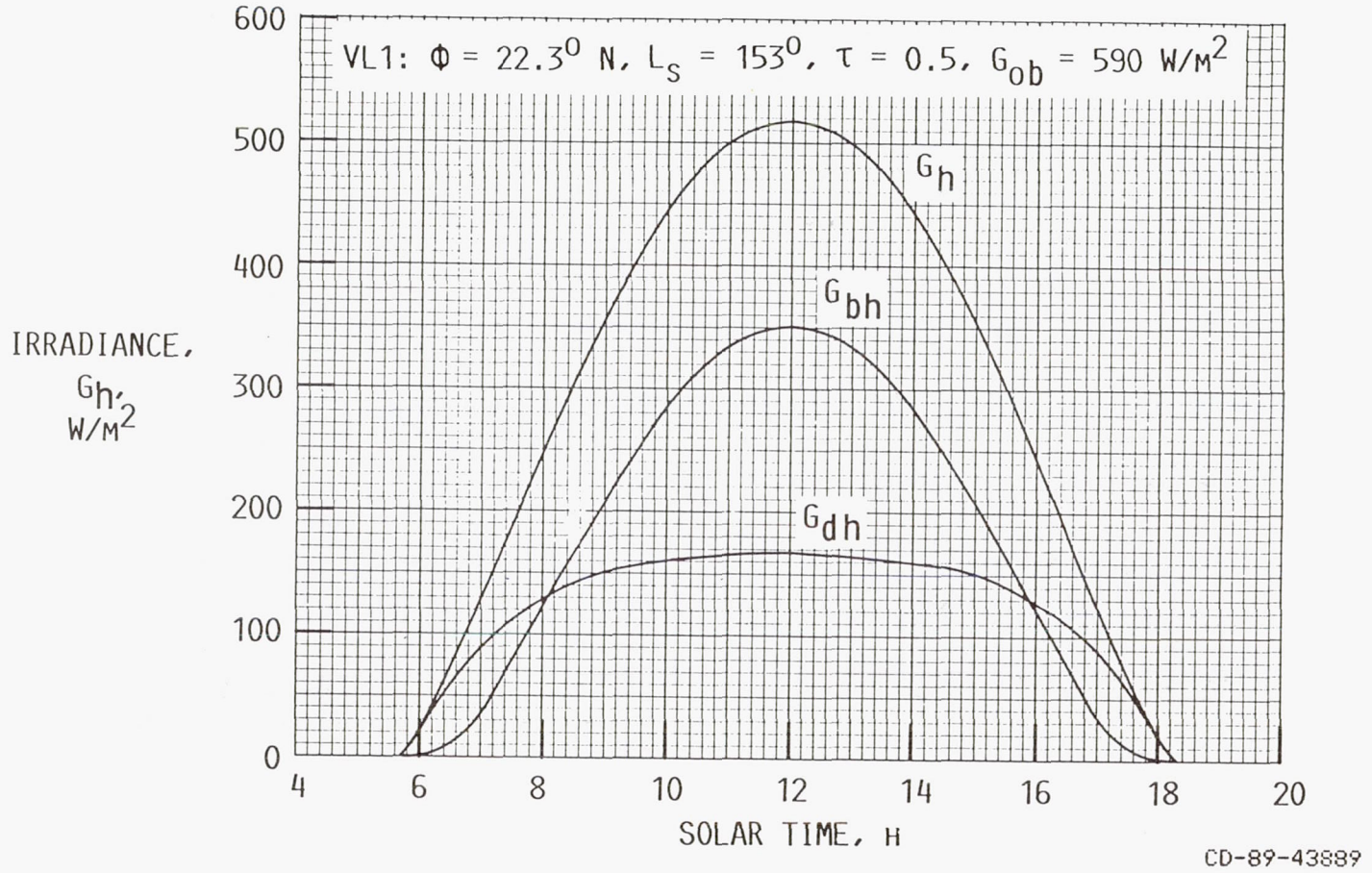

Figures 9-11: the solar radiation variation for several particular days.

Figure 9

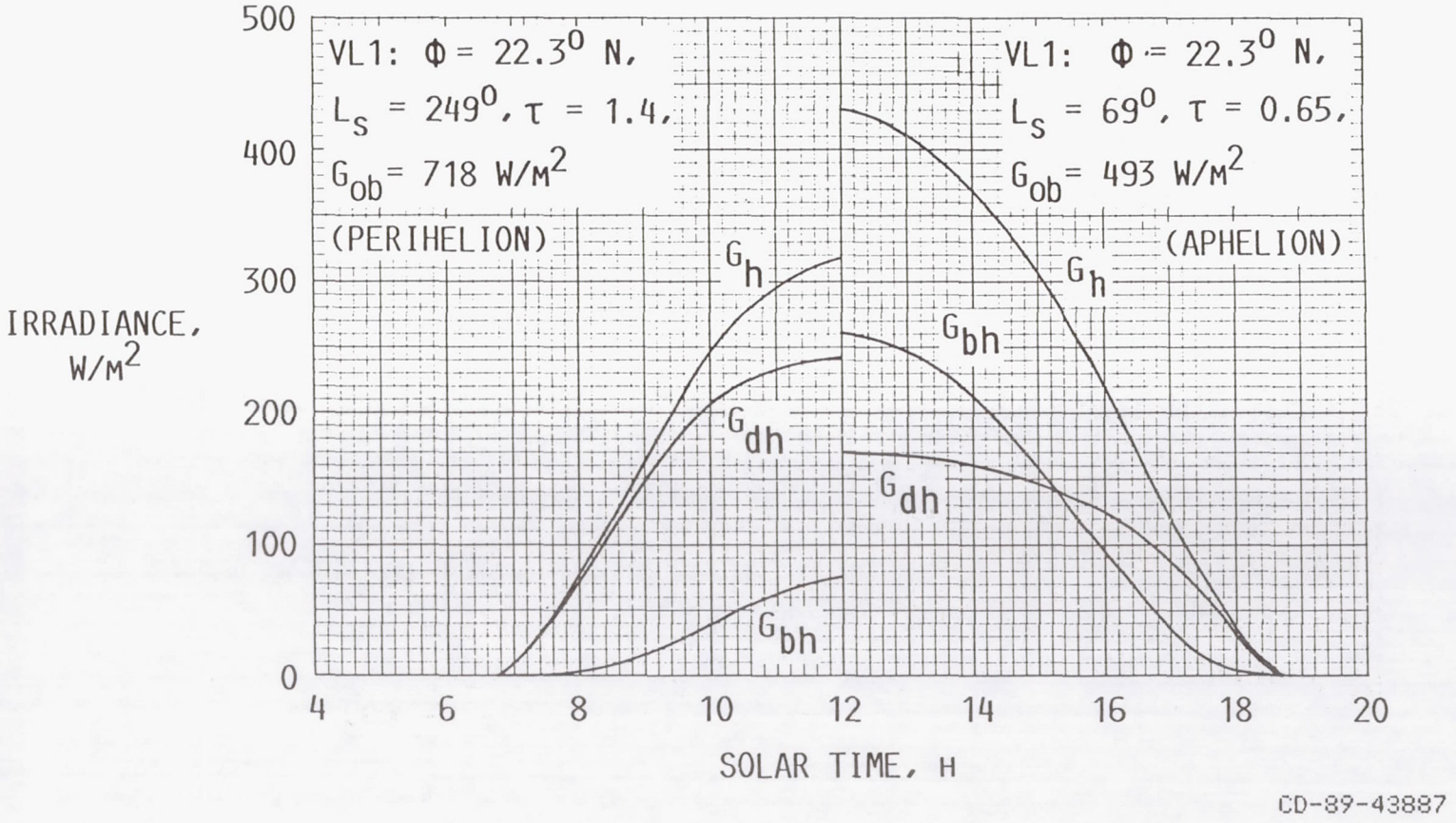
VL1: Φ = 22.3° N,
Ls = 249°, τ = 1.4,
Gob = 718 W/m2
(PERIHELION)
VL1: Φ = 22.3° N,
Ls = 69°, τ = 0.65,
Gob = 493 W/m2
(APHELION)
Gh
Gdh
Gbh
IRRADIANCE, W/m2
SOLAR TIME, H
CD-89-43887

Figure 10

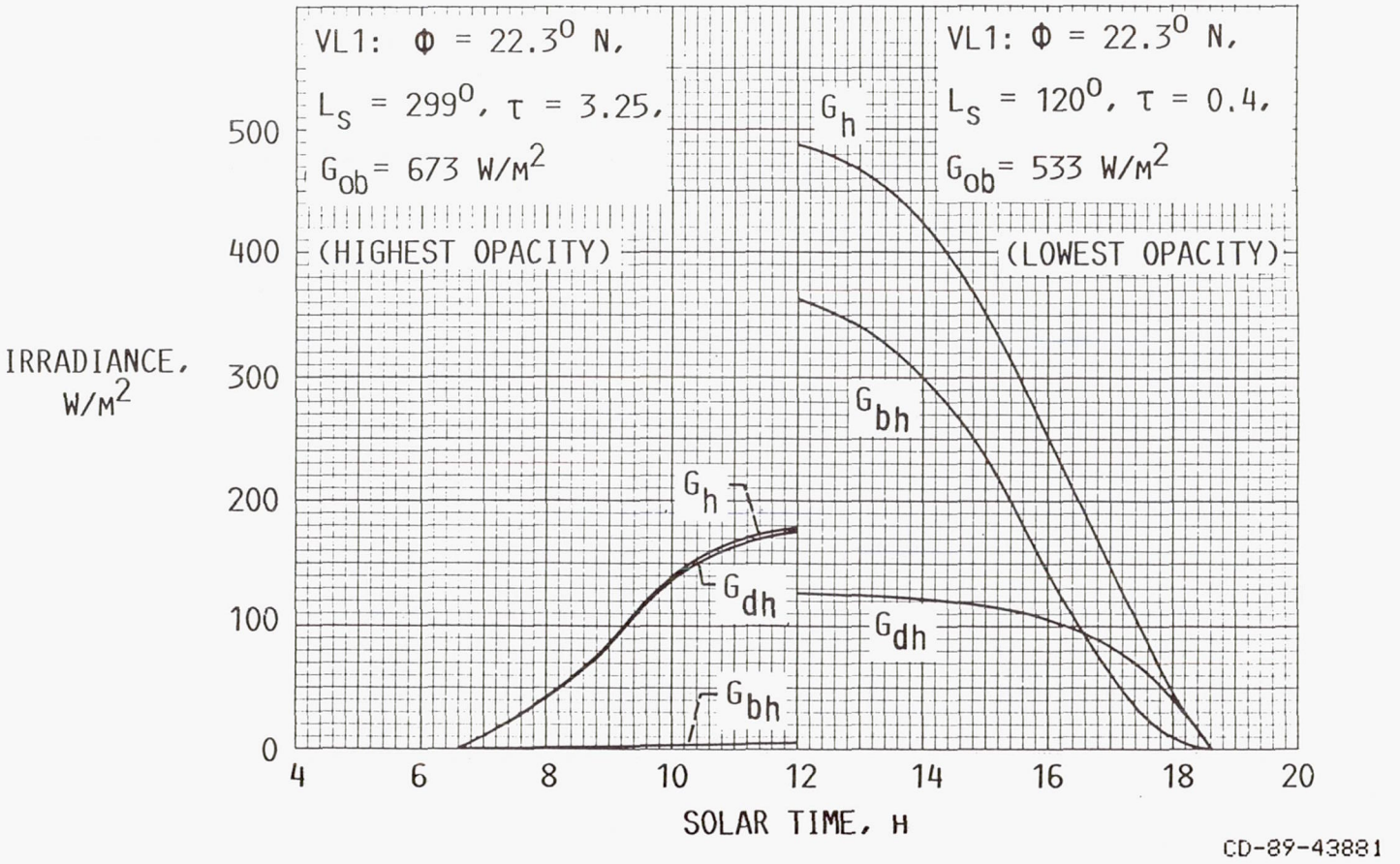
VL1: Φ = 22.3° N,
Ls = 299°, τ = 3.25,
Gob = 673 W/m2
(HIGHEST OPACITY)
VL1: Φ = 22.3° N,
Ls = 120°, τ = 0.4,
Gob = 533 W/m2
(LOWEST OPACITY)
Gh
Gbh
Gh
Gdh
Gdh
Gbh
IRRADIANCE, W/m2
0
100
200
300
400
500
4
6
8
10
12
14
16
18
20
SOLAR TIME, H
CD-89-43881

Figure 11

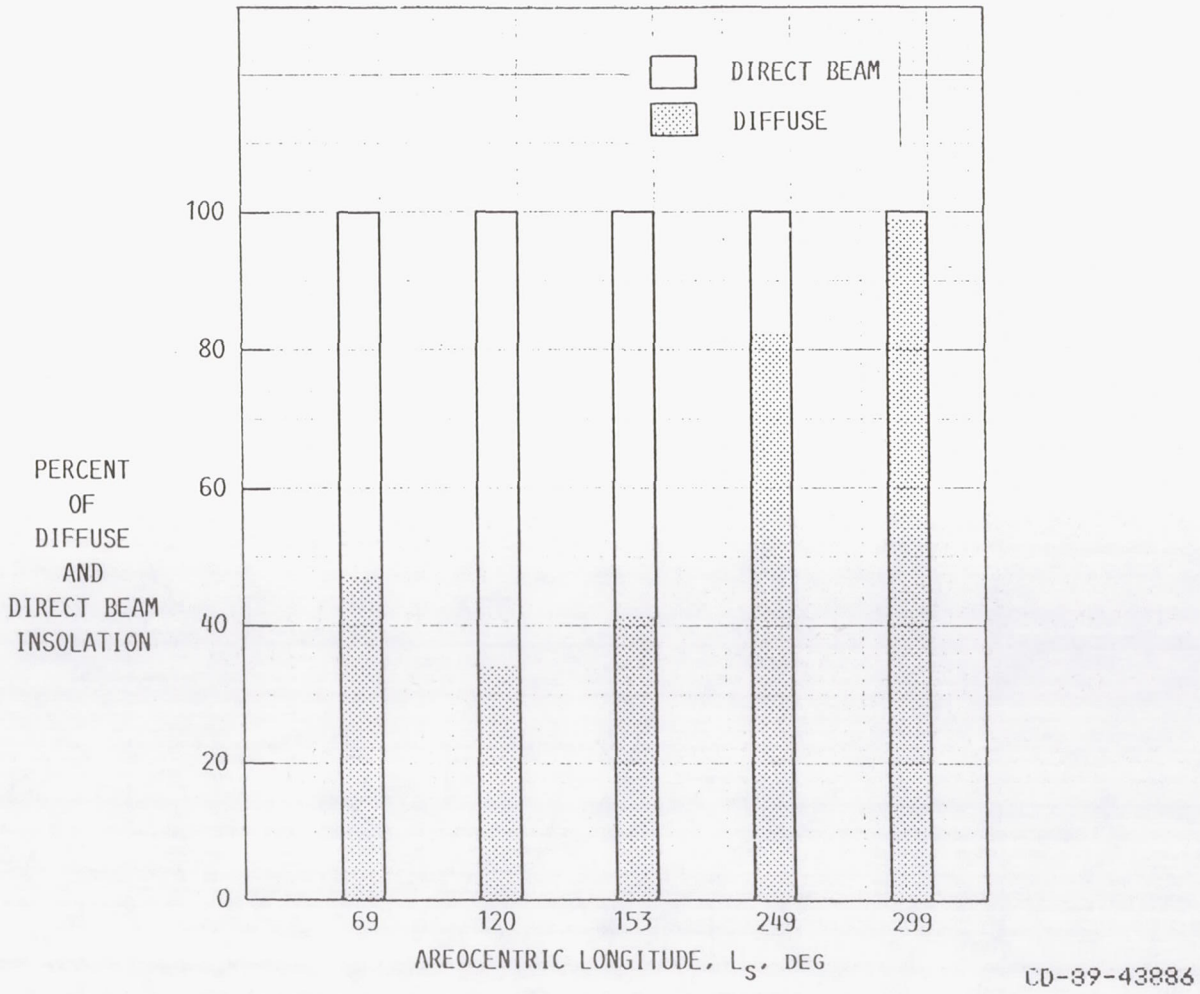

Figure 12: the percentage of diffuse and direct beam insolation for the five analyzed Ls days.

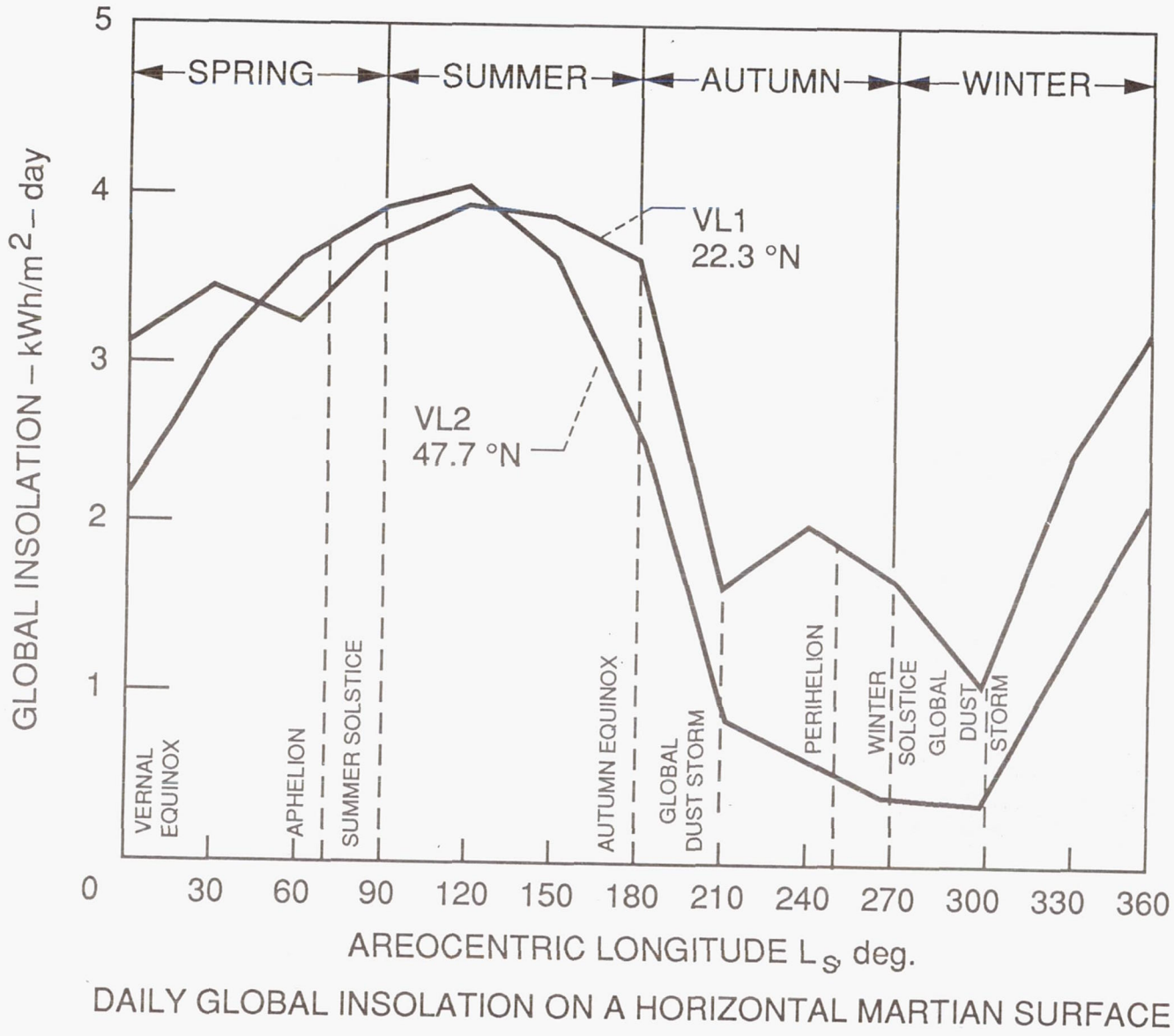

Figure 13: the daily global insolation on a horizontal surface on Mars for twelve areocentric longitudes covering a Martian year.

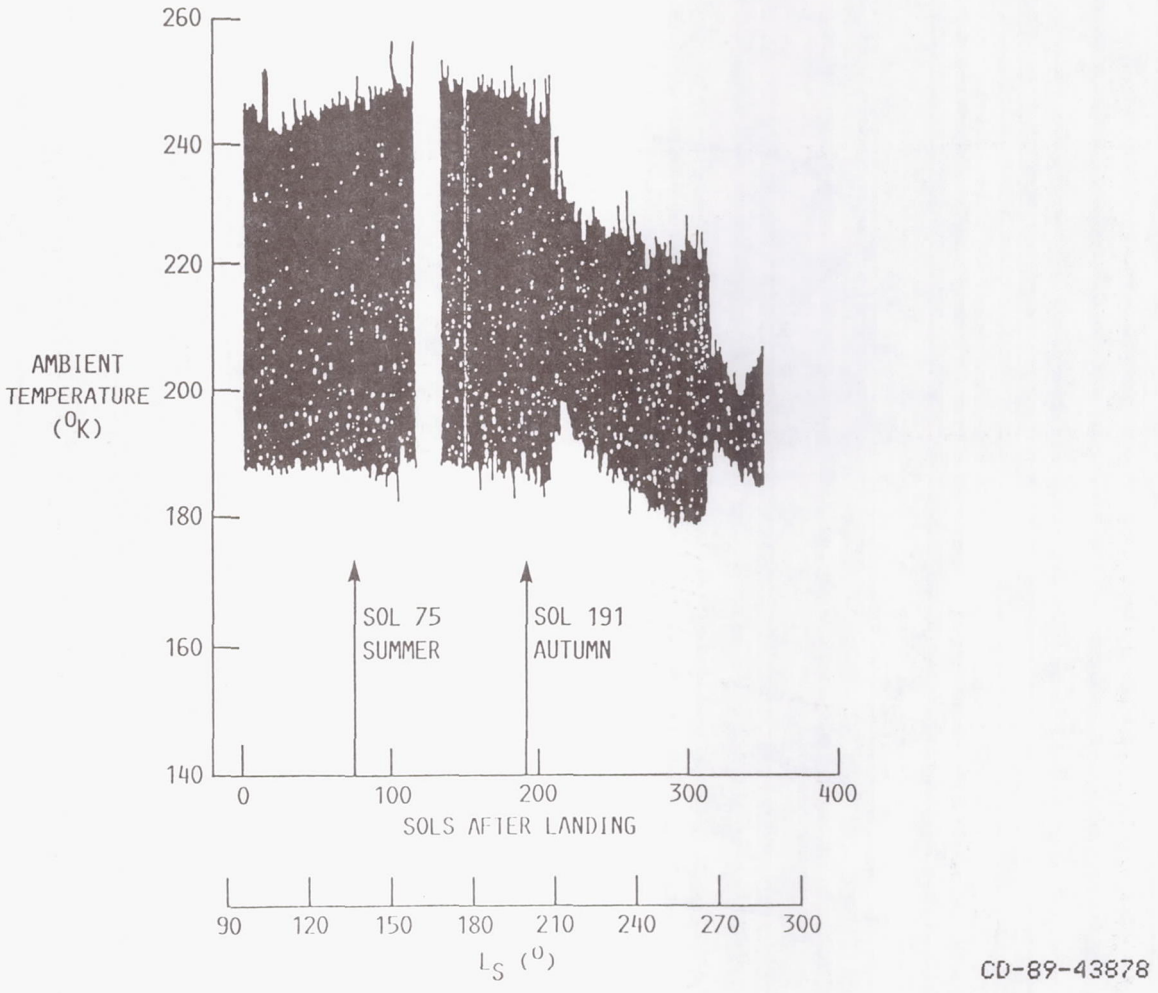

Figure 14: the variation of the ambient temperature at Viking lander VL1 for part of the first year after landing. The top time coordinate is the number of Martian solar days from touchdown; the bottom the seasonal date Ls.

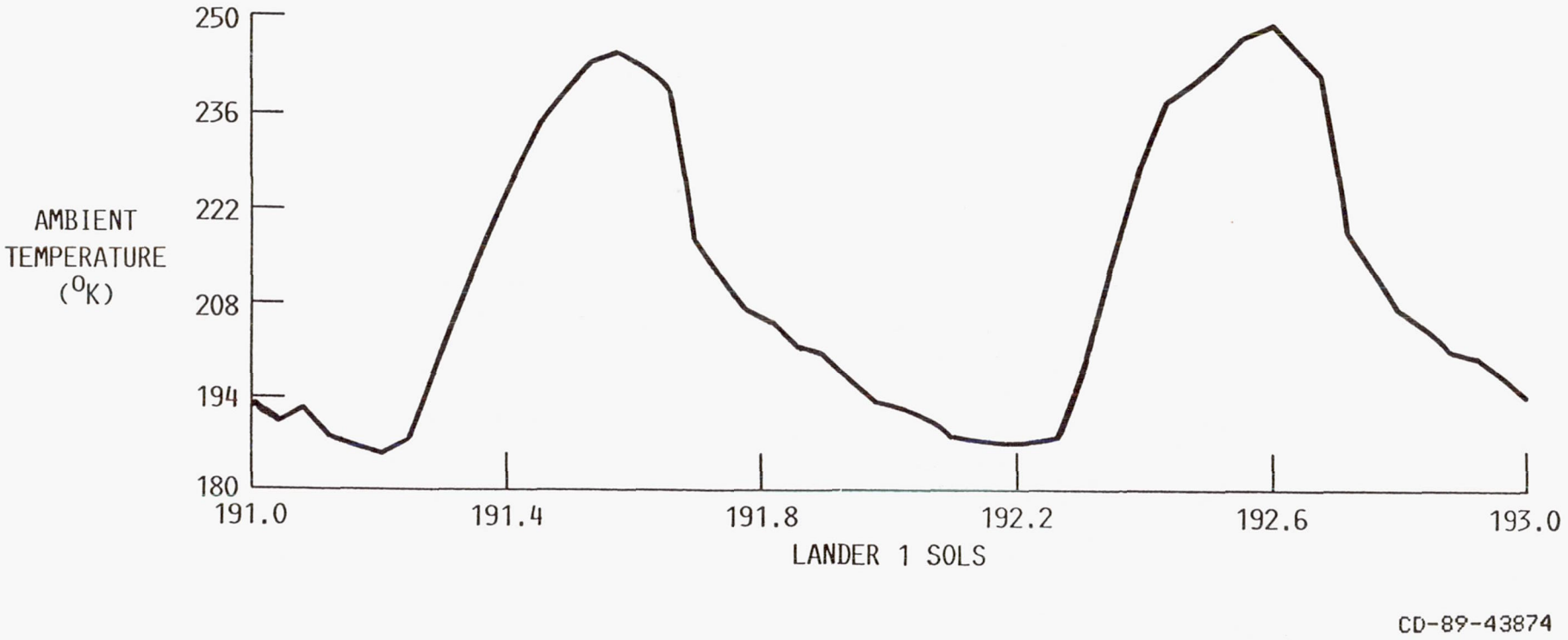

Fig 15: diurnal ambient temperature variation at VL1 for sols 191 and 192 (autumn).

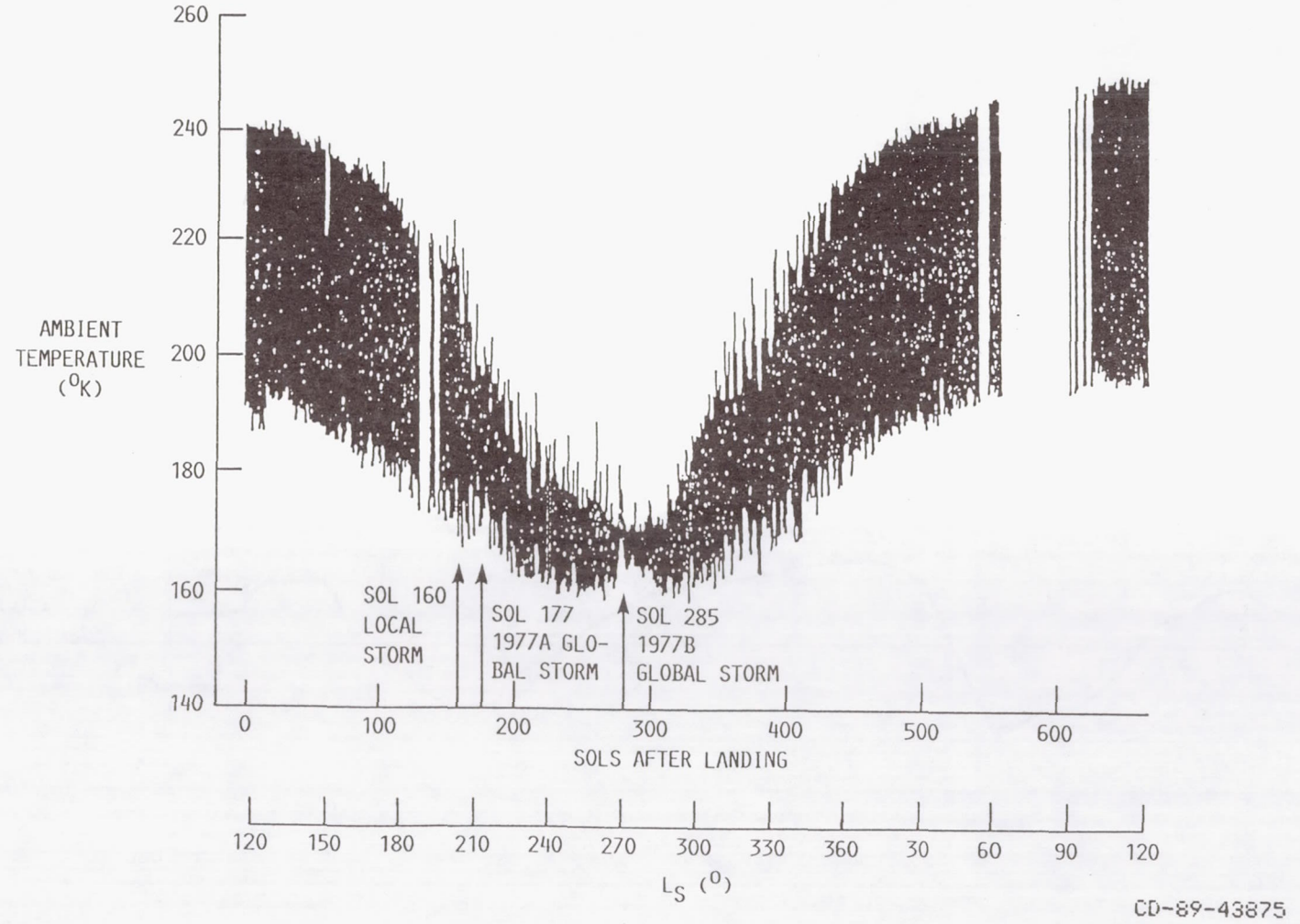

Figure 16: the variation of the ambient temperature at Viking lander VL2 for the first year after landing.

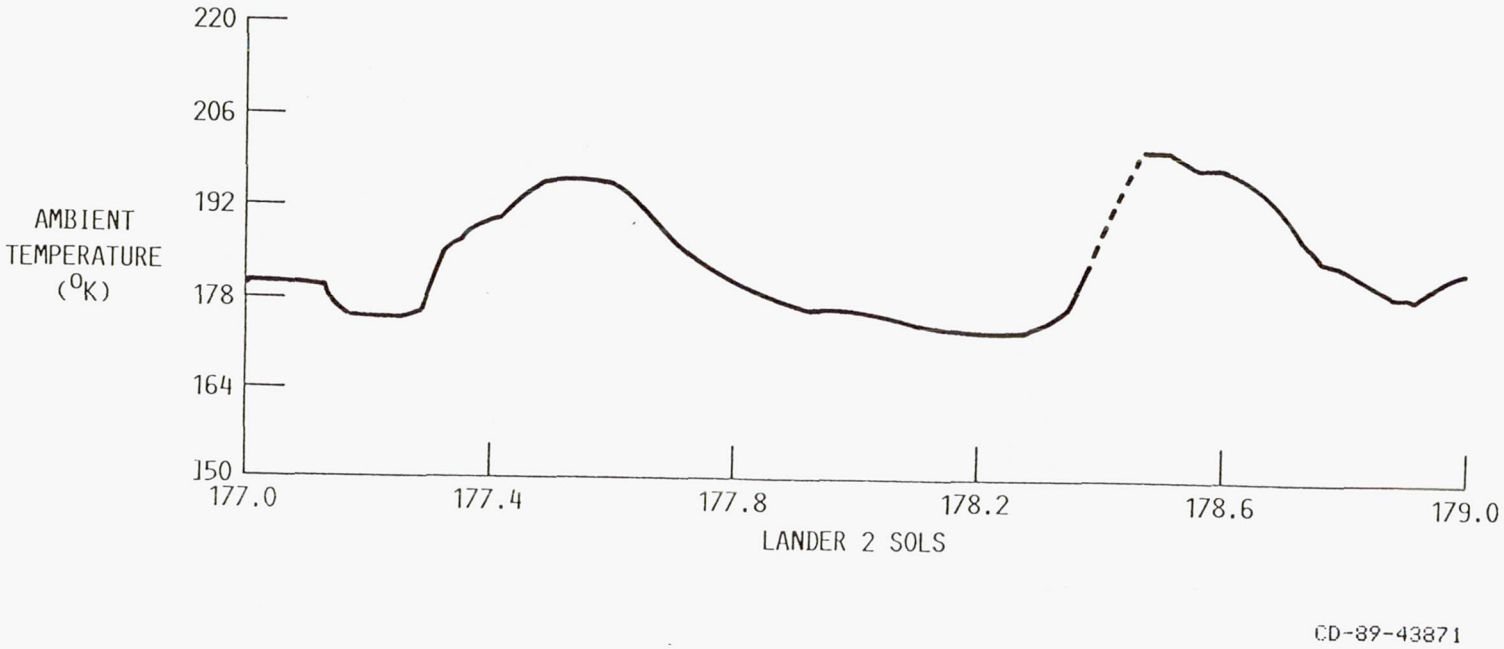

Figure 17: diurnal ambient temperature variation for sols 285 and 286 (1977 B global storm).

Session 4
InP Cells

Preceding Page Blank

Recent Advances in the ITO/InP Solar Cell*

T.A. Gessert, X. Li, M.W. Wanlass and T.J. Coutts
Solar Energy Research Institute
Golden, CO

Introduction

InP based solar cells have become important for space applications in recent years due to their combination of radiation resistance and high efficiency [refs. 1-2]. Although the highest efficiencies (> 18% AM0) have been achieved through epitaxial growth of homojunction cells, remarkable performance of 17.0% AM0 and radiation hardness have been achieved with indium tin oxide (ITO)/InP cells [refs. 3-4] In this later cells design, the ITO is sputter deposited, onto a crystalline InP p^- base substrate, at room temperature, using either RF or DC magnetron sputtering of an In_2O_3/SnO_2 composite target. In addition to its relative simplicity, this technique can be easily scaled to produce the 4 cm^2 cells necessary for flight experiments.

During past studies, several noteworthy observations have been made which have led to either improved device performance, or a greater understanding of the device operating principles. Some of these observations are: [refs. 4-6] 1) The top surface of the p^- InP is type converted during the ITO sputter deposition process resulting in a junction which demonstrates homojunction behavior, 2) The device characteristics (notably the open circuit voltage [V_{oc}]) can be increased through the use of an epitaxially grown p^- base layer (i.e., "hybrid" cells), 3) The type conversion and device performance is enhanced further through the incorporation of H_2 into the sputtering gas mixture and, 4) After the deposition process, Sn is observed to have diffused into the InP bulk. Although all these observations are still valid, several more can now be added to the list as will be described.

The first of these new observations involves the choice of substrate. As stated above in observation 2, efficiency improvements were realized when the bulk p^- InP substrate was replaced with a p^+ substrate which had been specially prepared with an epitaxially grown p^- base layer (hybrid cells). Although this technique resulted in very efficient cells and also enabled optimum base doping level studies, the epitaxial growth step complicated an otherwise simple junction formation procedure. Thus, efforts have continued to take what was learned with this hybrid cell study and use it to improve the simpler ITO/InP cell design utilizing bulk p^- InP substrates. Currently, although the best ITO/InP cell made to date is still a hybrid structure, cells can now be made on bulk material which are of virtually identical quality.

*This work was supported by NASA Lewis Research Center under Interagency Order No. C-3000-K and by the Department of Energy under Contract No. DE-ACH02-83CH10093.

The second continuing area of study involves the more fundamental question of what actually happens during the ITO sputtering process. Although, at present, this area is viewed more as pure science rather than solar cell technology, it is believed that only by thoroughly understanding this aspect of junction formation will insight to future cell improvements be acquired. Thus far, attempts to identify the mechanism of type conversion unambiguously have met with only limited success. The most recent example of this involves the above observation 4 in that, for a considerable time, it was believed that indiffusion of Sn was the most probable cause of type conversion. With this in mind, a series of experiments involving the sputter deposition of (Sn free) In_2O_3 (IO) was performed. The (unexpected) result of this experiment has made it necessary to question whether Sn is the cause of type conversion, and to consider more seriously the possibility that "sputter damage" may instead be the dominant mechanism.

The final area of recent studies involves measuring the stability of the ITO/InP cells over a period of about a year. This study was enabled by the development of a highly durable top contact grid metallization, necessary for long term grid integrity. The new contact procedure replaces the plated Au contacts with a metallization stack composed of Cr, Pd and Au which provided the necessary components of adhesion, diffusion barrier and conduction layers respectively. This contact proved so durable that the previous difficulties with contact adhesion loss have been completely eliminated.

Experimental

As mentioned in the past, one of the single most important elements of producing high efficiency ITO/InP solar cells is the preparation of the InP substrate before ITO deposition. Since this cell is formed by the sputter deposition interacting with the near surface ($< 0.1\ \mu m$) of the InP substrate, all techniques we have used to prepare the InP have one goal in mind: to produce InP surfaces with are of both reproducible and high quality. Although these goals are difficult in themselves, they are further complicated by the fact that, due to the high temperature necessary to form the ohmic back contact, this contact must be made before junction formation, thereby subjecting the untreated front surface to, possibly damaging, thermal effects. In an effort to satisfy these conflicting criteria, three main approaches to cell fabrication have been (historically) developed: These are: 1) Using p^- bulk substrates and chemo-mechanically repolishing the front surface after back contact formation thereby polishing away any suspected thermal damage. 2) Using p^+ substrates with an epitaxially grown p^- base layer. Although this structure is rather complicated, it has the combined benefits of lower bulk resistance, lower back contact formation temperature and a very high quality and controllable base layer. 3) Using high quality p^- bulk substrates, but forming the back contact at the lowest possible temperature thereby avoiding the need for chemo-mechanical repolishing of the front surface. It

is this final technique which has been used extensively for the cells described in this paper.

The p^- InP bulk substrates, from Nippon Mining Co. Ltd., are of carrier concentration $1.6 - 2.5 \times 10^{16}$ cm^{-3}, Zn doped and of (100) orientation. Before back contacting, they are typically cleaved to size on which either about eight - 0.1 cm^2 cells or one - 4.0 cm^2 cell (2 cm x 2 cm) can be fabricated. Back contacting is a two-step process involving first the resistive vacuum evaporation of Au/Be (1 w% Be, available from Metron Inc.), sintering on a graphite strip heater at $375 - 395°C$ for approximately 30 sec. in forming gas (10% H_2:90% N_2), etching in a concentrated H_2O:NaOH solution and plating with high purity Au. The specific details are explained elsewhere [ref. 7].

For sputter deposition of the ITO and IO (and thus the junction formation), a 2 inch planar US Gun is used in DC magnetron mode in a sputter-up orientation. In order to improve junction quality, the initial ~5 nm of ITO or IO is deposited in a H_2 rich atmosphere, while the remaining ~50 nm is deposited in a more conventional oxygen rich environment (leading to improved transmittance) [ref. 4]. The operating parameters are typically 300-400 Volts and 0.05-0.15 Amps, resulting in a deposition rate of ~0.01 nm sec^{-1}, for H_2 rich material and ~0.05 nm sec^{-1} for oxygen rich material, at ~14 cm in front of the target. The targets (purchased from KEMA, Fallbrook, CA) are made from 99.99% pure In_2O_3 and 99.9% pure SnO_2, the ITO mixture being 91:9 molar percent respectively. Predeposition is normally done for ~3 min. with the substrate shuttered. The InP substrate is not heated or cooled during deposition.

Although the deposition is primarily done in Ar ($\sim 5 \times 10^{-3}$ Torr), both O_2 and H_2 are added to predetermined partial pressures of $\sim 2 \times 10^{-5}$ Torr and $1 - 8 \times 10^{-4}$ Torr respectively. All gases are UHP grade and the flow is controlled with needle valves. The O_2 and H_2 pressures are set with an ion gauge, while the Ar pressure is set with a Convectron gauge. The vacuum system is a Perkin Elmer ULTEK ACRS equipped with both a cryogenic and a turbomolecular/mechanical pump. Although base pressures in the range of $\sim 1 \times 10^{-7}$ Torr are attainable with the cryo pump, the turbomolecular/mechanical pump configuration, having a base pressure of $\sim 1 \times 10^{-5}$ Torr, is normally used during sputter deposition.

After ITO deposition, individual cells are formed. Two different photolithographic patterns of different nominal areas as mentioned above are used. Top contact metallization was performed via a two step process involving first the E-beam deposition and photolithographic lift-off of 80 nm of Cr and 40 nm of Pd (adhesion layer and diffusion barrier respectively) and, second, the over-plating with ~6 um of high purity Au (conduction layer) [ref. 7]. Electrical isolation of the cells was done by photolithographically defined mesa etching using HCl. After the cells were formed, a nominally 77 nm thick MgF_2 coating was applied, thereby creating an optimized two layer MgF_2/ITO antireflection coating [ref. 8].

The electrical characterization of the cells consisted of both light and dark current-voltage measurements, quantum efficiency measurements and capacitance-voltage measurements. For the light current-voltage measurements, two different solar simulators were used. For primary measurements (Figures 1, 4& 6), standard solar cell efficiency measurement procedures were employed [ref. 9], while, for the variational analysis of the short circuit current (J_{sc}) and V_{oc} (Figure 7), a different simulator was used. Although the output of this second simulator was adjusted to simulate currents as near as possible to those obtained on the primary simulator, these values should not be considered absolute. Additionally, for the variational analysis of J_{sc}, a correction for the effect of ITO and IO thickness variations was done using a computer simulation which, by incorporation of the quantum efficiency of the cell, the necessary optical parameters of the layers in the antireflection coating stack and the appropriate solar spectrum, resulted in a normalization of the J_{sc} to a constant (50 nm) ITO thickness [ref. 8]. Depth profiling of the electrical characteristics of the type converted region was performed using a spreading resistance technique (Point Contact Current Voltage [PCIV] method) provided through collaboration with Solid State Measurements, Pittsburgh, PA [ref. 10].

Optical measurements (thickness and refractive index) were performed with a Rudolph Research Ellipsometer operating with a HeNe laser.

Results and Discussion

Bulk ITO/InP Cells

As mentioned above, the best efficiency ITO/InP devices have been produced using the hybrid structure in which, the ITO is deposited onto a high quality epitaxially grown p^- base layer. Although these cells resulted in 17.0% AM0 efficiency, they lacked the simplicity of earlier structures in which the ITO was deposited directly onto bulk p^- InP substrates (i.e., InP which did not have an epi layer base). Recently, however, results from cells made with bulk substrates have indicated that, if cell fabrication and processing are carefully controlled, bulk cells of essentially identical efficiencies to their hybrid counterparts can be made (See Figure 1).

There are several reasons for the recent success in using bulk InP which are not immediately obvious. First, it has been determined, if sufficient temperature control is achieved, then the back Au/Be ohmic contact can be formed without damage to the front InP surface. This, in turn, makes repolishing of the front InP surface unnecessary and subsequently increases the reproducibility of the surface quality before deposition. Specifically, the contact will form between $\sim$ 365°C and $\sim$ 375°C, yet surface damage is not detected until $\sim$ 405°C [ref. 7]. Secondly, if InP substrate material is acquired from a select group of vendors, then the as-received surface quality appears to be only slightly worse than that which can be made with APMOVPE growth. Additionally, although it is true that the series resistance will be increased if

the p^+ substrate is replaced by p^- material, measurable reductions in the fill factor (FF) due to the p^- substrates have not been observed. Indeed, the fill factors of the bulk cells are often slightly higher than those measured for the hybrid cells. This artifact may, however, be due to the higher quality of the Cr/Pd/Au top grid metallization, which had not been developed at the time of the hybrid cell study. Finally, it appears that the addition of H_2 to the sputtering gas is of even greater benefit to the bulk cells than it was found to be for the hybrid cells. Since this process appears to passivate both deep and shallow acceptors to a significant depth, it not only improves the dark characteristics (and thus the V_{oc} and FF), but also, in the case of the bulk cells, significantly improves current collection in the base. Specifically, the V_{oc} is increased by ~50 -60 mV and the FF is increased by ~5-7% (apparent increase in shunt resistance). Although the J_{sc} should increase due to the improved long wavelength collection (See Figure 2), since the H_2 rich ITO layer is of such poor optical quality, the gains due to increases in quantum efficiency (QE) are presently being offset by increased absorption losses in the ITO. Presently, work is proceeding to minimize or eliminate this absorption loss.

There are several fundamental observations which can be drawn from comparisons of the bulk vs hybrid ITO/InP cells. The first is that it appears once type conversion has been effected, then the minority carrier lifetime in the hybrid cells is slightly better than in the bulk cells. Evidence of this is the slightly higher V_{oc} of the hybrid cells (15-20 mV). Unfortunately, this difference in V_{oc} is so small that comparisons of dark I-V measurements are not conclusive. Additionally, capacitance-voltage (C-V) measurements indicate further that this V_{oc} difference is not due simply to the higher value of N_A in the hybrid cells (See Figure 3). On the contrary, analysis of hybrid cells indicates a trend of higher V_{oc} as N_A decreases. Although this observation is not yet fully understood, it may be due to increases in the minority carrier diffusion length in the base as N_A decreases. Also, although this general trend of higher V_{oc} with lower N_A may be equally true for bulk material, the measured V_{oc} of the bulk cells ($N_A \approx 5 \times 10^{16} cm^{-3}$) are much lower than would be extrapolated from base doping studies done with the hybrid cells. Thus, there appears to be an added degree of quality in the epitaxially grown material which leads to slightly higher V_{oc}. Although, if the parameters leading to this difference could be understood, further improvements in V_{oc} would possibly follow, it should nevertheless be stressed that the bulk and hybrid cells are very similar, indicating that the passivation/compensation effects of sputtering in H_2 do indeed create very similar type converted regions.

Large Area ITO/InP Cells

Another aspect of bulk vs hybrid comparisons is that the sputtering / hydrogenation process appears relatively insensitive to surface irregularities of the bulk substrates. This is noted by observing that if several cells are made on a single p^- bulk InP substrate, the V_{oc} does not vary greatly between cells located at different

parts of the substrate (the J_{sc} will vary slightly, however, due to ITO thickness variations). This can be compared to hybrid cells where, if an epitaxial growth-related defect is present, then the characteristics of the particular cell containing this defect often would be very poor. Thus, it is the degree of spatial uniformity of the epitaxial growth which limits the performance of large area hybrid ITO/InP cells. However, with the combined observations that high-efficiency cells could be made directly from as-received bulk InP substrates, and the inherent spatial uniformity of the sputter-formed homojunction, the opportunity to fabricate large area ITO/InP cells was immediately presented. Using the same technology explained above, cells with a total area of 4 cm^2 were fabricated. Although these cells lacked an optimum grid design, they demonstrated nearly 17% (Global) efficiency (see Figure 4), thereby not only supporting the above observation concerning the spatial uniformity of the type conversion process, but also greatly supporting earlier speculation about the ease of scaling this technique for production purposes. Furthermore, examinations of the V_{oc} and the QE of these first large area cells indicates that, once these cells are optimized, the resultant efficiency should be very near to that which has been (thus far) achieved with smaller cells (~17% AM0).

IO/InP vs ITO/InP Cells

As mentioned above, it was believed for several years that the Sn played an active role in the type conversion of the InP surface during sputtering, thereby forming the InP homojunction of the ITO/InP cell. This was supported primarily by secondary ion mass spectroscopy (SIMS) analysis which showed Sn penetration to about 100 nm into the InP after the ITO deposition [ref. 5], and by a spreading resistance technique (PCIV) which showed electrical type conversion to roughly the same depth (see Figure 5). Furthermore, experiments to assess the role of "sputter damage" suggested that this mechanism alone did not produce strong type conversion or good quality cells. With these observations in mind, it seemed probable that if Sn free IO/InP cells were made, than they would demonstrate very poor device quality (low V_{oc} and J_{sc}), thereby further proving the crucial role of the Sn species. However, this was not the observed result.

As shown in Figure 6, the IO/InP cells demonstrated remarkably good performance of nearly 17% (Global) with V_{oc} within a few millivolts of their ITO/InP counterparts. Additionally, since the same sputter conditions were used for the IO as those used for the ITO, the IO optical quality is dubious and, as can be inferred from Figure 7, it is likely that if the IO transmittance were improved, the J_{sc} of these cells may indeed be equivalent to that of the ITO cells.

The fact that the IO cells demonstrated such similar quality to the ITO cells strongly suggests that the Sn in the ITO is not the essential part of type conversion as it was previously believed to be. The IO result also indicates that the previous conclusion about the limited effect of "sputter damage" is probably in error, and that

deposition-related (and not Sn-related) effects are very important to the type conversion process. Currently, work is proceeding to determine whether "sputter damage" may manifest itself by causing the InP to lose P from the bulk (these vacancies might then act as donor states, assisting type conversion).

Initial Stability Studies

Finally, since the Cr/Pd/Au contact is very adherent and durable, initial stability studies have been conducted during the past year. Although it should be stressed that, thus far, data has been collected on only two cells (two - 0.1 cm^2, bulk ITO/InP cells on a single substrate), the results are very encouraging. In Figure 8 are shown results indicating that, within experimental uncertainty, the J_{sc} and the FF are stable. The V_{oc} is shown to decrease linearly at a rate of about 8 mV per year. However, this reduction occurred while the cells were stored under dim light conditions and, as shown in Figure 9, the original V_{oc} is quickly restored when the cells are light-soaked at V_{oc} for several hours (for example, in an XT-10 solar simulator set at ~AM1.5). From these observations, it is believed that, if the cells had been securely mounted in a durable test structure and if they had been continuously operated between successive measurements, no V_{oc} reduction would have been observed and the efficiency would have been stable.

Conclusions

It has been demonstrated that ITO/InP solar cells can now be made on as-received p^- bulk substrates which are of nearly equal quality to those which could previously only be made on epitaxially grown p^- InP base layers. Although this advancement is due in part to both increases in substrate quality and a better understanding of back contact formation, it appears that the passivation/compensation effects resulting from having H_2 in the sputtering gas tends to reduce significantly the performance differences previously observed between these two substrates.

It is shown that since high efficiency ITO/InP cells can be made from as-received substrates, and since the type conversion process is not highly spatially dependent, large area ITO/InP cells (4 cm^2) with efficiencies approaching 17% (Global) can be made. Furthermore, the measured V_{oc}'s and QE's from these large cells suggest that, when they are processed using optimum grid designs, the efficiencies will be nearly equal to that of the smaller cells thus far produced (i.e., ~17% AM0).

It has been shown, through comparative experiments involving ITO/InP and IO/InP cells, that Sn may not be the major cause of type conversion of the InP surface and thus further implies that the ITO may not be an essential element in this type of device. Specifically, very efficient photovoltaic solar cells have been made by sputtering (Sn free) In_2O_3 showing that type conversion and subsequent junction formation will occur even in the absence of the sputtered Sn species. This result

suggests that "sputter damage" (P depletion and/or H_2 incorporation) may indeed be the important mechanism(s) of type conversion.

Finally, an initial study of the stability of the ITO/InP cell done over the course of about one year has indicated that the J_{sc} and the FF are measurably stable within experimental uncertainty. Also, although the V_{oc} does decrease linearly at a rate of about 8 mV per year if the cell is kept in the dark, the original V_{oc} of the cell is quickly restored if the cell is light soaked. It is therefore believed that, if the cells were continuously operated between successive measurements, this V_{oc} reduction would not be observed and the overall efficiency of the cells would be stable.

References

[1.] C. J. Keavney and M. B. Spitzer, Appl. Phys. Lett. **52**, 1439, 1988.

[2.] M. Yamaguchi, A. Yamamoto, Y. Itoh and C. Uemura, *Proc. of the 2nd Int. Photovoltaic Science and Engineering Conf.*, 573, 1986.

[3.] I. Weinberg, C. K. Swartz, R. E. Hart Jr., and T. J. Coutts, *Proc. 20th IEEE Photovoltaics Specialists Conf.*, 893, 1988.

[4.] X. Li, M. W. Wanlass, T. A. Gessert, K. A. Emery, and T. J. Coutts, Appl. Phys. Lett. **54**, 2674, 1989.

[5.] X. Li, T. E. Furtak, T. A. Gessert, M. W. Wanlass, and T. J. Coutts, *Proc. 1989 Industry-University Advanced Materials Conf.*, 1988. (To be published).

[6.] T. J. Coutts, X. Wu, T. A. Gessert, and X. Li, JVST-A, **6**, 1722, 1988.

[7.] T. A. Gessert, X. Li, T. J. Coutts, M. W. Wanlass, and A. B. Franz, Proc. Optical Engineering (SPIE Proceedings), Vol. 1144, 1989.

[8.] T. J. Coutts and J. D. Meakin, eds., *Current Topics in Photovoltaics, Vol. 3*, 184 (1988).

[9.] K. A. Emery and C. R. Osterwald, Solar Cells **17**, 253, 1986.

[10.] R. J. Hillard, H. L. Berkowitz, R. G. Mazur and P. Rai-Choudhury, Solid State Technol. **32**, 119, 1989.

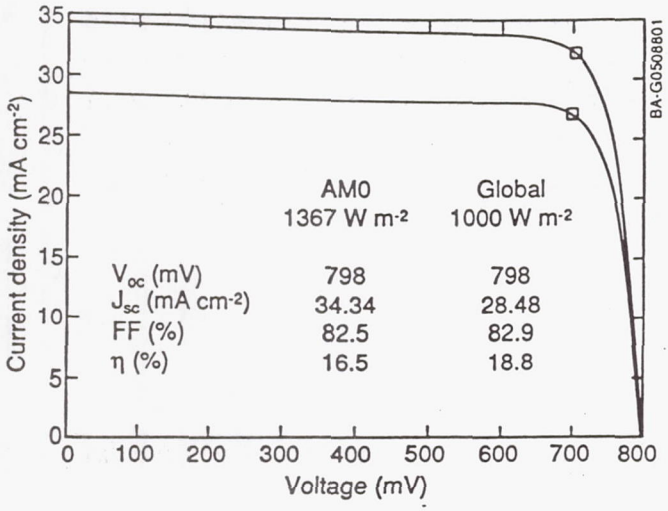

Figure 1

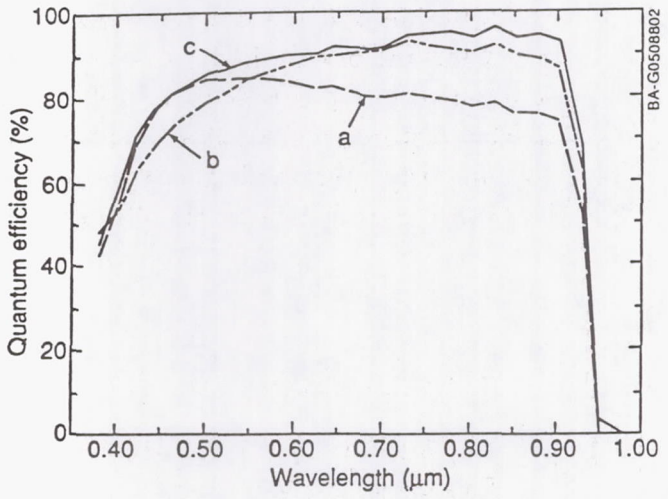

Figure 2

Figure 1. Current-voltage characteristics of the best ITO/InP cell made to date from bulk InP p^- material (i.e., the ITO is sputter deposited directly onto as-received InP substrates, no epitaxially grown base layers). These characteristics are measured under standard Global and AM0 reporting conditions (however, the AM0 measurement is not confirmed at NASA). Cell temperature = 25°C, total area = 0.108 cm^2.

Figure 2: External/Internal quantum efficiencies (QE's) for the device in Figure 5. (a) External QE for cell with 50.7 nm of ITO only, (b) with additional 75.0 nm of MgF_2 coating and (c) internal QE of the same device. Note this device demonstrates an internal QE of >90% over a substantial portion of the spectral range. Note particularly the high collection at long wavelengths indicating the passivation effect of the H_2 in the sputtering gas.

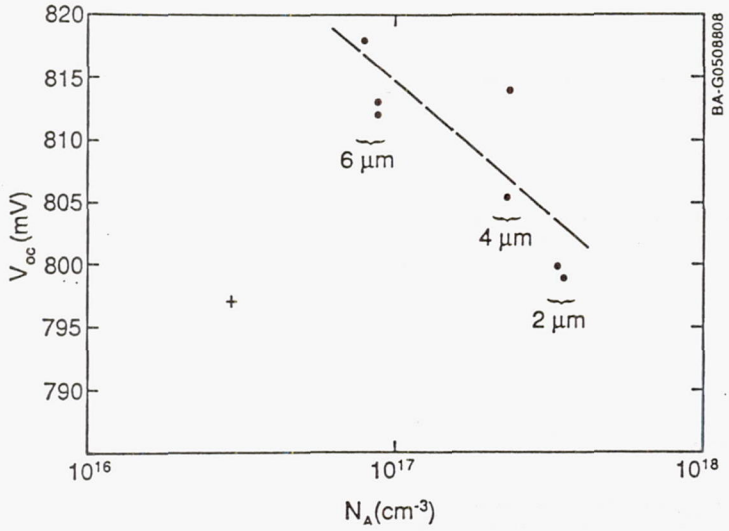

Figure 3

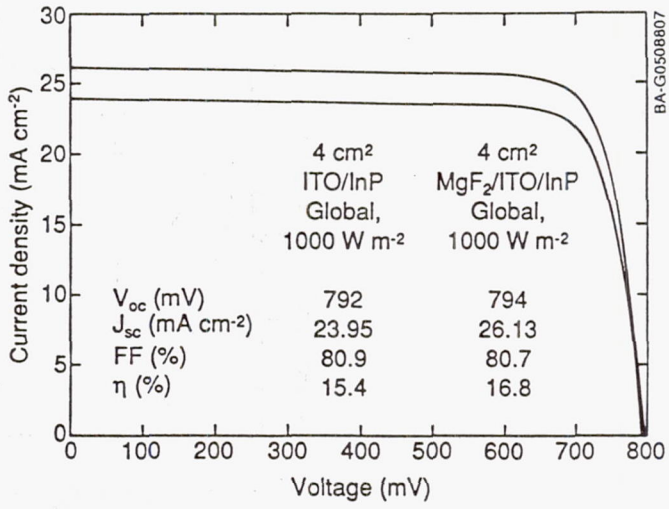

Figure 4

Figure 3: Plot of data from capacitance-voltage measurements. The circles indicate the values of N_A for a series of hybrid cells made with three nominally different values of (epitaxial) base doping (base thickness noted next to corresponding data). The dashed line indicates trend of increasing V_{OC} with decreasing N_A. Note also that the V_{OC} of the bulk cell (as indicated by the cross) does not fall on the same trend as the hybrid cells.

Figure 4: Current-voltage characteristics of a 4 cm^2 ITO/InP cell (a) before and (b) after MgF_2 deposition. These measurements are performed under standard Global reporting conditions. Although this cell lacked an optimized grid design, it demonstrated performance attesting that this technique can be easily scaled.

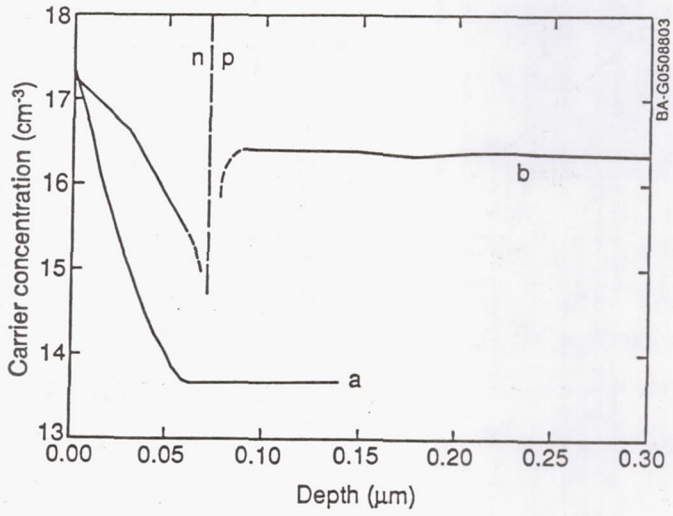

Figure 5

Figure 5: Carrier concentration vs depth profile resulting from a Point Contact Current Voltage (PCIV) Spreading Resistance technique. (a) Illustrates the type conversion of a semi-insulating (Fe doped) InP substrate due to the sputter deposition (in H_2) of 5 nm of ITO. Note that in this case, 8 x 10^{13} cm-3 is the lower limit of the PCIV technique. (b) Illustrates the same profiling technique applied to an actual bulk ITO/InP solar cell in which the ITO was sputter deposited (H_2 partial pressure ~ 2 x 10^{-4} torr) onto a p- (Zn: 2 x 10^{16} cm^{-3}) InP substrate. In both cases, the ITO was removed by chemical etching in 1000 H_2O:HF before PCIV profiling. The vertical dashed line at about 70 nm indicates the approximate depth of type conversion. These data were fitted by assuming Hall mobilities for the n and p regions of 100 and 120 cm^2 V^{-1} sec^{-1} respectively.

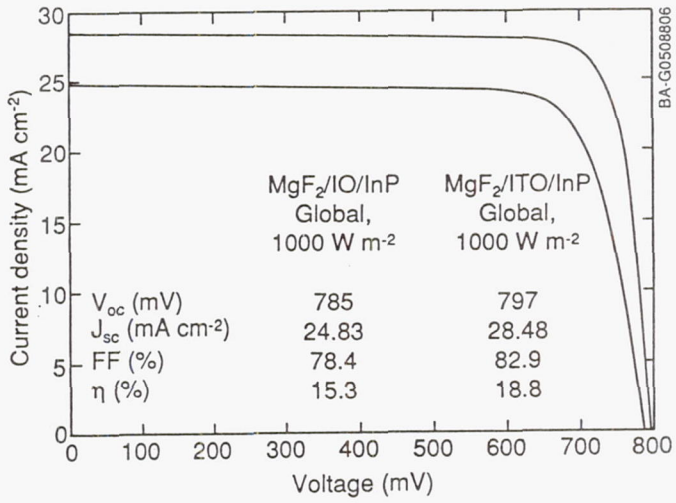

Figure 6

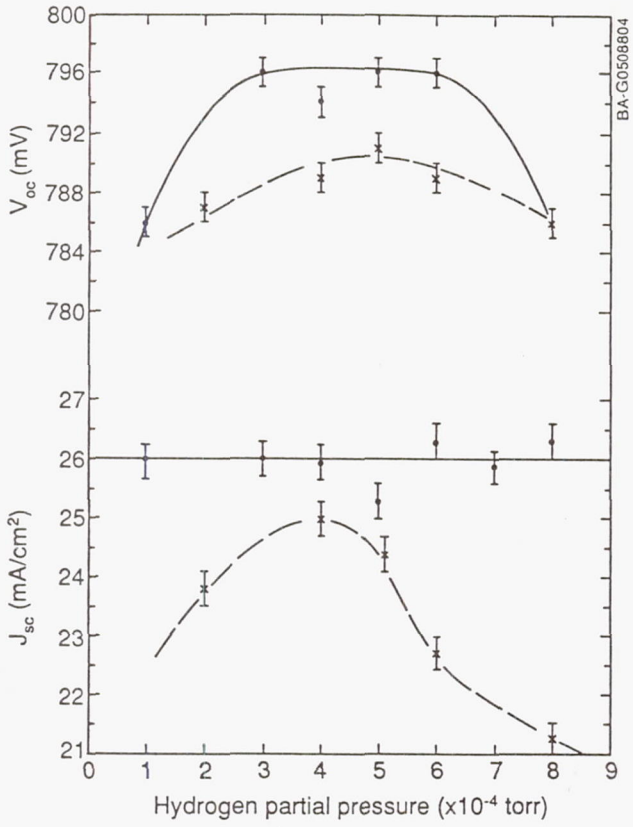

Figure 7

Figure 6: Comparison of the current-voltage characteristics of an IO/InP and an ITO/InP cell. Note that, even though only a few IO/InP cells were made, and thus the junction fabrication was not optimized, these cells are remarkably similar. This strongly suggests that, contrary to earlier speculation, Sn incorporation into the InP is not the main cause of type conversion. Note also that, although at the time of fabrication the efficiency of these IO/InP cells was 16% - 17% (Global), the above measurement, taken under standard reporting conditions, was not performed until over six months later, during which time the V_{OC} and the fill factor had each degraded slightly, resulting in lower measured efficiencies. Cell temperature = 25°C, cell area = 0.108 cm^2. IO (and ITO) and MgF_2 thicknesses are ~50 nm and ~70 nm respectively.

Figure 7: Illustration of the dependence of V_{OC} and J_{SC} on hydrogen partial pressure for both ITO (solid line) and IO (dashed line) solar cells made on bulk substrates. Although the main feature of this comparison is that the Sn (present only in the ITO/InP cells) is not necessary to produce homojunction like behavior, one notes that both the V_{OC} and the J_{SC} are lower in the IO/InP cells. Furthermore, unlike the J_{SC} in the ITO/InP cells which is seemingly insensitive to hydrogen partial pressure, the J_{SC} of the IO/InP cells demonstrate considerable sensitivity to this parameter. These data were collected for 0.108 cm^2 cells using an XT-10 solar simulator referenced to a Global (1000 W m^{-2}) reference spectrum using a Si reference cell. The error bars on the J_{SC} represent the changes in J_{SC} which would be expected from a ± 2.5 nm variation in ITO thickness.

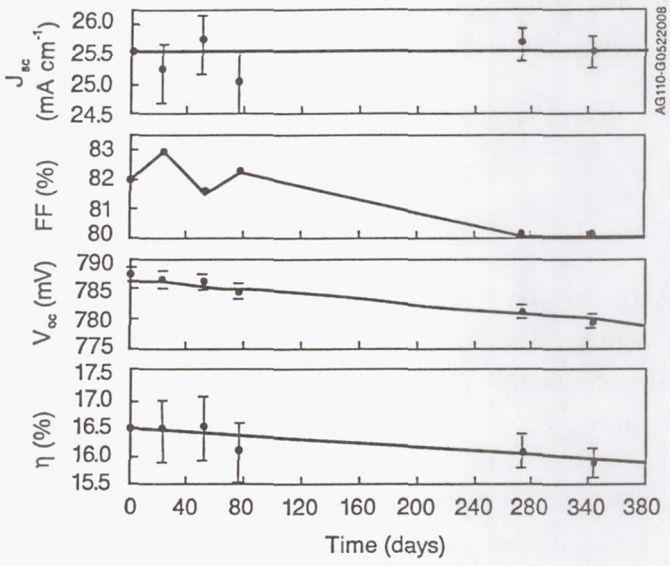

Figure 8

Figure 8. Diagram illustrating successive measurements of the light I-V characteristics of an ITO/InP cell during the year after fabrication. Note that, within experimental uncertainty, the J_{SC} is stable. It is also believed that the slight reduction in fill factor is an artifact of a progressively dirty back contact rather than a junction effect. The apparent reduction in V_{OC} is, however, a real effect (and equates into a reduction in efficiency). This reduction however appears to be only an artifact of the cell being kept in a dark location between measurements, the original V_{OC} being restored when the cell is operated (see Fig. 9).

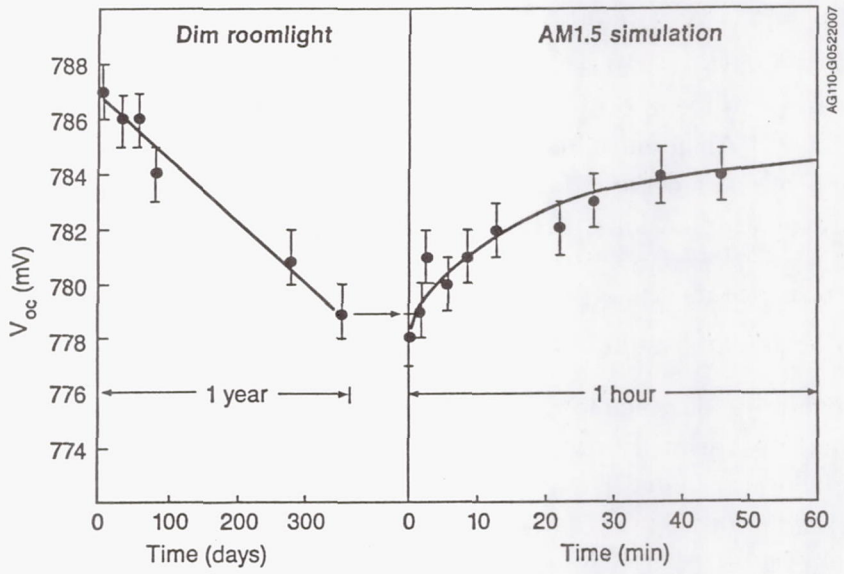

Figure 9

Figure 9. Diagram illustrates the improvement of the V_{OC} as the ITO/InP cell.shown in Fig. 8 is light soaked at ~AM1.5. Note the two different time scales on the horizontal axis.

Semiconductor Structural Damage Attendant to Contact Formation in III-V Solar Cells

Navid S. Fatemi* and Victor G. Weizer
NASA Lewis Research Center
Cleveland, OH

In order to keep the resistive losses in solar cells to a minimum, it is often necessary for the ohmic contacts to be heat treated to lower the metal- semiconductor contact resistivity to acceptable values. Sintering of the contacts, however can result in extensive mechanical damage of the semiconductor surface under the metallization. An investigation of the detailed mechanisms involved in the process of contact formation during heat treatment may enable us to control the structural damage incurred by the semiconductor surface to acceptable levels, while achieving the desired values of contact resistivity for the ohmic contacts. In this work, we have determined the reaction kinetics of sintered gold contacts to InP. We have found that the Au-InP interaction involves three consecutive stages marked by distinct color changes observed on the surface of the Au, and that each stage is governed by a different mechanism. A detailed description of these mechanisms and options to control them are presented.

Introduction

Gold and gold-based contact systems are extensively used as metallization materials for III-V solar cells. In some cases, acceptably low metal-semiconductor contact resistivity is achieved to highly doped emitters by as-deposited contacts. For instance, as-deposited Au contacts on InP and Au-Zn contacts on GaAs heavily doped substrates can produce specific contact resistivity (R_c) values in the 10^{-4} ohm-cm^2 range [refs. 1-2]. Although this contact resistivity range may be adequate for one sun operation of solar cells, it falls short of the 10^{-6} ohm-cm^2 values often required for concentrator applications. There are also concerns about the stability of these contacts with aging, for no stable compounds are present at the metal-semiconductor interface. The most prominent advantage of the as-deposited contacts is that virtually no structural damage is suffered by the semiconductor under the metallization.

On the other hand, much lower R_c values are readily obtained by heat treating Au-based contacts to variously doped III-V semiconductors. R_c values in the $10^{-6}$and 10^{-7} ohm-cm^2 range have been measured by Au-based systems to InP and GaAs substrates [refs. 2-6]. Heat treated contacts also tend to be more stable with aging [ref. 6]. The greatest disadvantage of the heat treating process is the appearance of severe pitting at the metal-semiconductor interface during contact formation. The electrical and mechanical changes which occur during the heat treatment process

*Sverdrup Technology Inc., Lewis Research Center Group.

however, may not necessarily be related. For example, encapsulation of Au-Ge-Ni and Au-Zn contacts with SiO_2 prior to heat treatment can not only slightly reduce the metal-GaAs interaction rate but at the same time produce lower R_c values [refs. 7-9].

The purpose of our research program is to understand contact formation in III-V semiconductor materials, and use that knowledge, to devise a contact system and/or a processing scheme by which desired R_c values are achieved with minimal structural damage to the semiconductor. In this paper, our focus has been on the investigation of the mechanisms involved in contact formation in the Au-InP system.

The Kinetics of the Au-InP Interaction

The Au-InP interaction consists of three consecutive stages of reaction, each governed by a different rate limiting mechanism. The three stages are: 1. Au-to-Au(In) (saturated solid solution), 2. Au(In)-to-Au_3In, and 3. Au_3In-to-$AuIn_2$ transitions. In addition, spreading of Au contacts occurs concurrent with the third stage of the reaction. In what follows, a discussion of the mechanisms operating in each stage, as well as in the Au spreading phenomenon, and means to control them are presented.

STAGE I. At this early stage of the reaction In is dissolved into the Au lattice via a dissociative diffusion mechanism until the saturation limit of 10% atomic is reached. Rapid interstitial diffusion of In from the InP lattice toward the surface of the Au is controlled by the rate of vacancy generation at the free surface of the metallization. Consequently, the condition of the Au surface can dictate the reaction rate at the Au-InP interface. The reaction suppressing effect of the capping of the contacts with SiO_2 before heat treatment is due to the suppression of vacancy generation rate at that surface. Conversely, surface abrasion of the Au tends to enhance the reaction rate at the metal-semiconductor interface due to the fact that regions of lattice disorder in the metallization are a greater source of vacancies than the undisturbed regions. We have previously demonstrated the effect of surface damage and capping of the contacts on the metal-semiconductor reaction rates in both the Au-GaAs and Au-InP systems [refs. 10-11].

STAGE II. The conversion of Au(In) into Au_3In occurs via nucleation and grain growth. The reaction proceeds via an exchange or kickout mechanism by which the substitutional Au atoms are displaced by interstitial In atoms, forcing the Au atoms to become interstitial. These interstitial Au atoms, in turn diffuse to the Au-InP interface, filling the vacancies left there by the out-diffusing In atoms. There they form the compound Au_2P_3 with the unbound P. Au_2P_3 and Au_3In are formed simultaneously with the phosphide located directly underneath the Au_3In nucleation sites.

Since stage II is governed by the kickout mechanism, it was expected that capping of the contacts would have no effect on the reaction rate. To verify this, we deposited a

saturated solid solution of In in Au (10% atomic) on a number of (100) oriented p-type InP substrates doped to about 2.5×10^{16} cm^{-3} and capped half of each sample with 600 Å layer of SiO_2. Indeed after heat treating these samples at various temperatures, no difference in the reaction rates of capped vs. uncapped areas could be detected. It should be noted that much structural damage is done to the InP surface during this stage of the interaction.

Since the compound Au_3In is pink in color, its nucleation and grain growth is easily distinguished in the gold colored Au(In) matrix. Upon isothermal annealing of the Au contacts, after an initial incubation period, the growth (i.e., the area) of the Au_3In grains increases linearly with time. Repeating such isothermal annealing experiments at different temperatures and measuring the time required (in the linear region) for the metallization to convert to 100% Au_3In, allows us to measure the activation energy (E_a) for stage II. The results, shown in figure 1, indicate an activation energy of about 2.6 eV.

It should be mentioned that because the Au_3In grain growth is linear with time all the way to completion, and not proportional to the circumference of the grains as they grow in size, the rate limiting mechanism with an E_a of 2.6 eV is not the activation energy for the localized kickout mechanism. In fact, the rate limiting mechanism in this case is the rate of In release from the InP substrate, which also would have to have a slower rate than the kickout mechanism.

Although for the data points of figure 1, we had used Au(In) contacts, repeating the same experiment for samples with pure Au as the contacting metal, we essentially obtained the same activation energy (2.8 eV) for stage II. Also since the capping of the pure Au contacts suppresses the reaction rate for stage I, and therefore delays the emergence of stage II, repeating the same isothermal annealing experiments with half-capped Au samples enabled us to extract the activation energy for stage I. Using the delay times caused by capping of the contacts in the growth of Au_3In grains and plotting them as a function of temperature, we obtained the data points in figure 2. Although there is much scatter in the data points, the least square fit to the points renders an E_a value of about 1.1 eV. This is slightly lower than the gold self-diffusion activation energy of 1.8 eV expected for the reaction rate for Stage I. But our calculations based on the In concentration profiles at and near the Au surface obtained by Auger electron Spectroscopy (AES) show that surface effects can lower this activation energy to the vicinity of 1 eV. A thorough discussion of the kinetics of stage I and stage II is presented in an upcoming publication [ref. 12].

STAGE III. Much like the reaction in stage II, the conversion of Au_3In to $AuIn_2$ occurs via nucleation and grain growth. We believe that similar to stage II, the reaction rate in this stage is also governed by the kickout mechanism, given the localized nature of the interaction. One marked difference here is that the compound Au_2P_3 which was created at the Au-InP interface in stage II, does not form in stage III. In other words, no Au_2P_3 was observed to grow under the $AuIn_2$ nucleation sites when

a layer of Au-In alloy with slightly lower In concentration than the Au_3In compound was deposited on InP and heat treated to stage III nucleation. However, if the Au_2P_3 compound is already present at the metal-InP interface (leftover from stage II), it is observed to grow further under the $AuIn_2$ nucleation sites at temperatures below approximately 431°C . At temperatures above 431°C, the phosphide layer seems to remain unchanged from its original form when created during stage II.

As with the marked color change from gold to pink occurring during stage II, the $AuIn_2$ grains are silver in color and are easily distinguished from the pink Au_3In background matrix. Using the same procedure described for measuring the activation energy for stage II, we find that there are two distinct activation energies present for stage III with their intersection point at about 431°C.

As shown in figure 3, for temperatures above 431°C , E_a has a value of 12.1 eV, and for temperatures below 431°C, E_a increases to 28.5 eV. The measurement of such abnormally high activation energies is perhaps the result of a multi-step reaction process, with each step having a much lower activation energy. Similarly a high activation energy of 8.6 ± 3 eV has been reported by Elias, et al [ref. 13] while investigating a phenomenon known as gold spreading in the Au-InP system. The results of our findings on this spreading phenomenon and its relationship with stage III are presented in the following section.

Lateral Spreading of Au Contacts

The lateral spreading of Au dots beyond the metallization boundaries on the surface of InP upon heat treatment was first observed by Keramidas, et al [ref. 14]. Silver colored spread regions were observed to grow faster in certain crystallographic directions. Later, Elias, et al [ref. 13], reported on the characteristics of the spreading phenomenon and determined the activation energy of the process. In our investigations, we have observed that the lateral spreading of the contacts occurs concurrent with stage III of the Au-InP interaction. In other words, the region on the Au dot adjacent to the spread area has to be transformed to $AuIn_2$ before the spreading can start.

Lateral spreading of a Au dot (2000 Å) heat treated at 434°C for 2.5 hours is shown in figure 4a. An analysis of the rate of the growth front indicates that the rapid rate of spreading is about four orders of magnitude faster than what would be expected for a common vacancy dependent diffusion process. The only diffusion mechanism capable of reconciling such a high growth rate is the interstitial transport of Au to, and In from, the spread front. EDAX analysis has revealed the presence of significant amounts of both In and Au in the spread region.

The activation energy that Elias, et al [ref. 13], measured for the spreading of the Au contacts (8.6 ± 3 eV) is close to the E_a of 12.1 eV that we measured for stage

III for temperatures greater than 431°C . This is an indication that perhaps similar mechanisms operate in both processes.

The Au dot of figure 4a is shown in figure 4b after removing the metallization by a thiourea based chemical etchant. As shown in the figure, the gold phosphide (Au_2P_3) is present only in the dot region and not in the spread area. Also apparent from the enlarged view of figure 4b in figure 4c is the large amount of InP which has disappeared from the growth area. This volume loss along with the absence of the phosphide layer in the spread area suggest that the P atoms made available after In interstitial transport toward the Au dot, had to volitalize before having an opportunity to form the compound Au_2P_3 with the interstitial Au atoms.

From the above argument, it becomes clear that in order to prevent the spreading process, the loss of P should be inhibited. To test this, we capped a few Au dots and their adjacent InP surface with a 600Å layer of SiO_2 and heat treated them along with a few uncapped samples. Indeed, capping prevented the spreading of the contacts. It was observed that the spread front is able to move under the cap for a distance of about one micron before stopping. This one micron represents the P escape length. The effect of capping on suppressing the spreading process is shown in figure 5.

Another method to prevent spreading is to deposit, instead of pure Au, Au-In alloys having In concentrations in excess of 25% (i.e., Au_3In) on InP. Such alloys will not only inhibit the spreading process, but they will also suppress the interaction rate of the metal-InP to a large degree. As mentioned earlier, no Au_2P_3 compound is formed during the interaction of these alloys with InP, for the formation of the phosphide is strictly a stage II phenomenon. The presence of Au_2P_3 at the Au-InP interface slows down the reaction to such an extent that it is easier for the reaction to proceed to a phosphide free location (i.e., outside of the Au dot on the InP surface) where the reaction rate is much faster. But in the absence of the phosphide layer the reaction can continue underneath the Au dot, and there is no need for the reaction to move outside of the metallization region.

Figures 6a and 6b are comparisons of the structural damage incurred by the semiconductor by heat treating a pure Au and a Au-In alloy with nearly 25% In concentration samples on InP at 434°C for 2.5 hours with all the reaction products removed. As shown in these figures, the Au-In alloy sample has reduced the pitting of the InP surface to a great extent compared to the pure Au sample.

Summary and Conclusions

The purpose of our research program has been to identify the mechanisms involved in the process of contact formation in metal-semiconductor interactions. Fundamental understanding of these mechanisms should enable us to manipulate them in such a way as to satisfy our requirements of a nearly ideal metal-semiconductor contact system (i.e., low R_c values plus minimum structural damage to the semiconductor).

In this paper, we have presented the results of an investigation of the mechanisms involved in the contact formation process in the Au-InP system.

We have shown that the Au-InP interaction entails three consecutive stages of reactions. Stage I of this interaction operates via a dissociative diffusion mechanism, and the vacancy generation rate on the surface of the metallization is rate limiting with an activation energy of about 1 eV. Capping of the metal surface or deposition of a Au(In) layer instead of pure Au suppresses the reaction rate at this stage.

Stage II operates via an exchange or kickout mechanism. The reaction is localized, and it is controlled by the rate of In release from the InP substrate with an activation energy of about 2.6 eV. Extensive pitting of the semiconductor surface is observed after this stage goes to completion. Deposition of the alloy Au_3In in place of pure Au inhibits the reaction at this stage.

Stage III reaction is also localized in nature and is likely to operate via the kickout mechanism. There are two activation energies observed for this stage: 12.1 eV for temperatures greater than 431°C, and 28.5 eV for temperatures below 431°C. It is likely that such high activation energy values are the result of many steps involved for the reaction to go to completion, with each step having much lower activation energy. The resultant activation energy would then be a complicated sum of these smaller activation energies.

Also concurrent with stage III, a phenomenon known as spreading of Au is observed. Fast interstitial movements of Au and In control the rate of reaction for this process. We have shown that capping of the InP surface near the spread region inhibits the process by preventing the escape of P from the InP surface. In addition, in contrast to pure Au, it was demonstrated that Au-In alloys (In concentration $\geq$25%) show no sign of spreading.

We have shown that the mechanical damage to the semiconductor incurred by heat treatment can be reduced considerably through deposition of Au-In alloys ($\geq$25% In) on InP in place of pure Au. We have also shown that capping of the contacts suppresses the reaction rate. Our future thrust is to compare the electrical characteristics of Au-In alloys with that of pure Au, and also to correlate the electrical behavior of heat treated contacts (unary, binary, and ternary systems) with their metallurgical behavior.

References

[1.] M. Faur, M. Faur, C. Goradia, M. Goradia, N. S. Fatemi, D. Brinker, I. Weinberg, *First International Conference on InP and Related Materials for Advanced Electronic & Optical Devices Proc.*, 1989.

[2.] N. S. Fatemi, "Study of Ohmic Contacts to GaAs for Solar Cell Applications," MS Thesis, Cleveland State University, 1987.

[3.] E. Kuphal, Solid State Electronics, **24**, 69, 1981.

[4.] A. Piotrowska, A. Guivarc'h, G. Pelous, Solid State Electronics, **26**,179, 1983.

[5.] C. Dubon-Chevallier, M. Gauneau, J. F. Bresse, A. Izrael, D. Ankri, J. Appl. Phys. **59**, 3783, 1986.

[6.] N. S. Fatemi, *Proc. Ninth Space Photovoltaic Research and Technology (SPRAT) Conference*, 1988; Also as NASA Contractor Report No. 182146, 1988.

[7.] A. J. Barcz, E. Kaminska, A. Piotrowska, Thin Solid Films, **149**, 251, 1987.

[8.] F. Vidimari, Electron. Lett. **15**, 674, 1979.

[9.] A. A. Lakhani, L. C. Oliver, E. F. Dvorsky, E. U. Hempfling, IEEE Elect. Dev. Lett., V. EDL-6, No. 11, 1985.

[10.] V. G. Weizer, N. S. Fatemi, J. Appl. Phys. **64**, 4618, 1988.

[11.] N. S. Fatemi, V. G. Weizer, J. Appl. Phys. **65**, 2111, 1989.

[12.] N. S. Fatemi, V. G. Weizer, J. Appl. Phys. **15**, 1989 (to be published).

[13.] K. R. Elias, S. Mahajan, C. L. Bauer, A. G. Milnes, J. Appl. Phys. **62** 1245, 1987.

[14.] V. G. Keramidas, H. Temkin, S. Mahajan, Inst. Phys. Conf. Ser. No. 56: Chapter 5, 293.

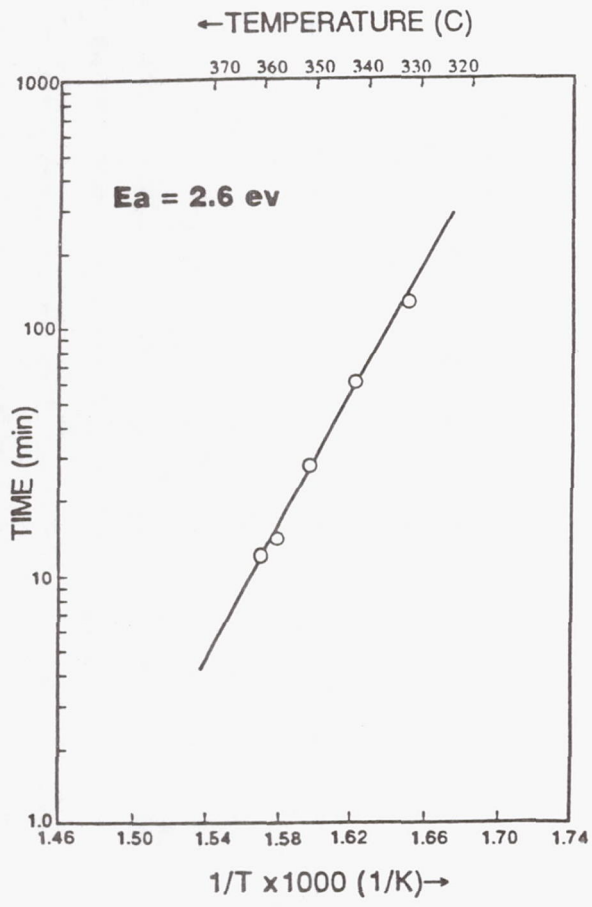

Fig. 1 Activation energy plot for stage II.

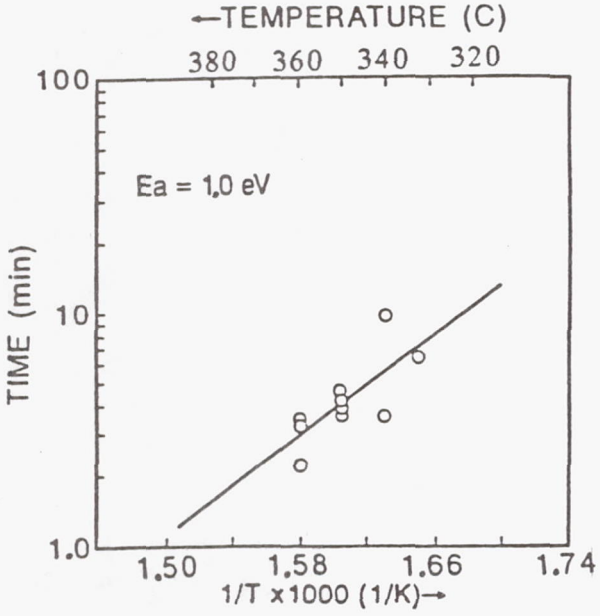

Fig. 2 Activation energy plot for stage I.

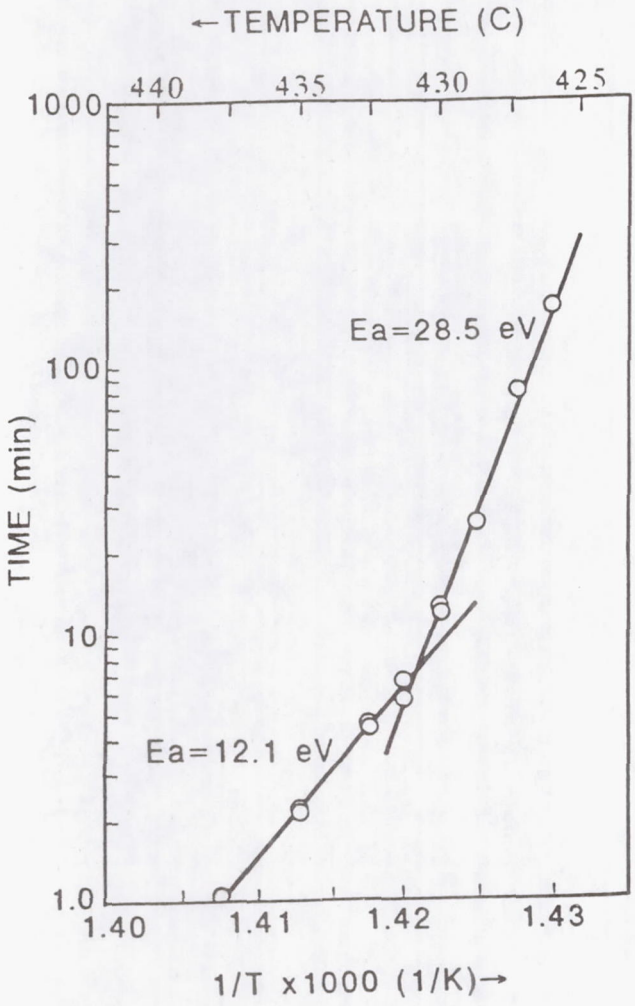

Fig. 3 Activation energy plot for stage III.

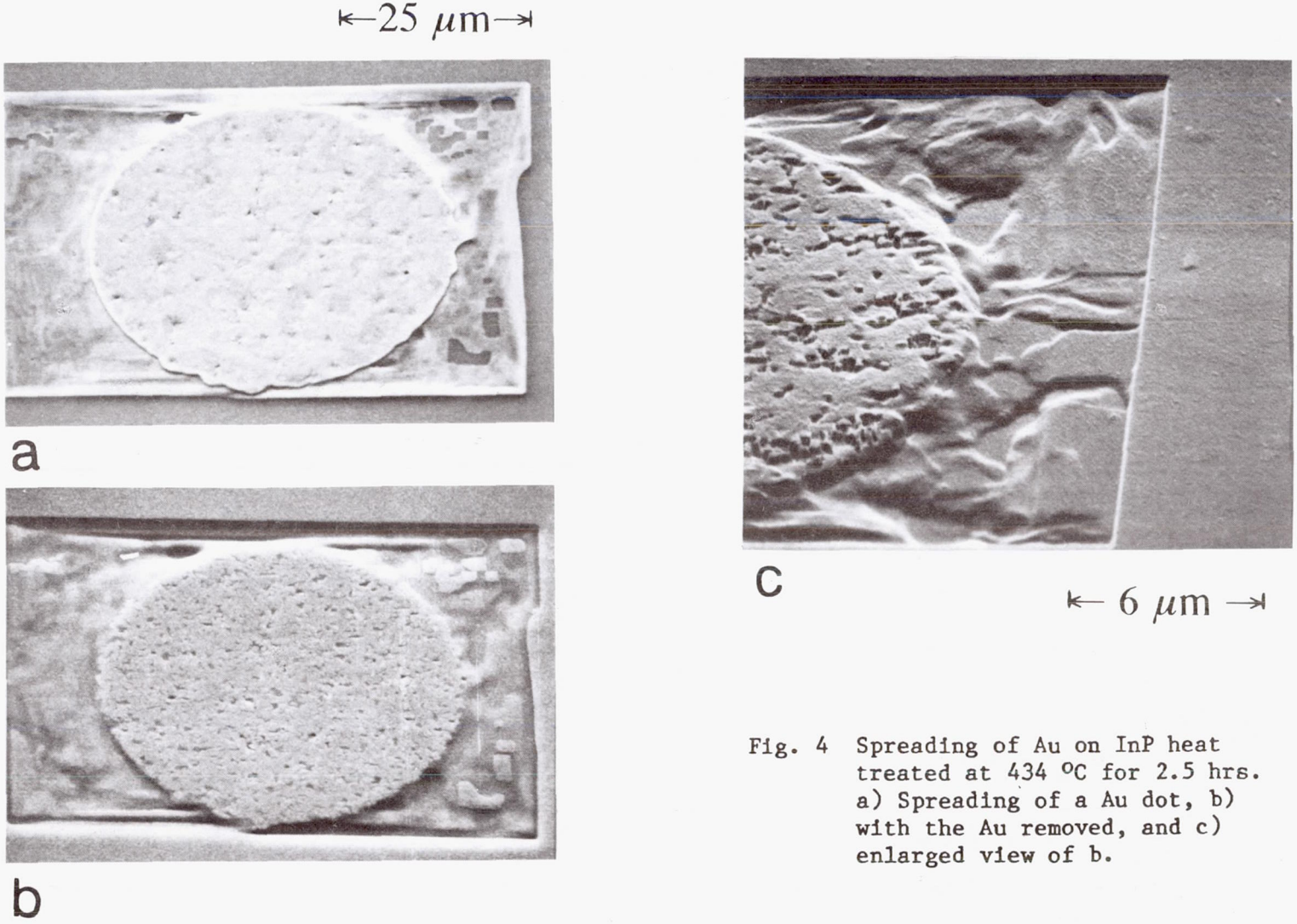

Fig. 4 Spreading of Au on InP heat treated at 434 °C for 2.5 hrs. a) Spreading of a Au dot, b) with the Au removed, and c) enlarged view of b.

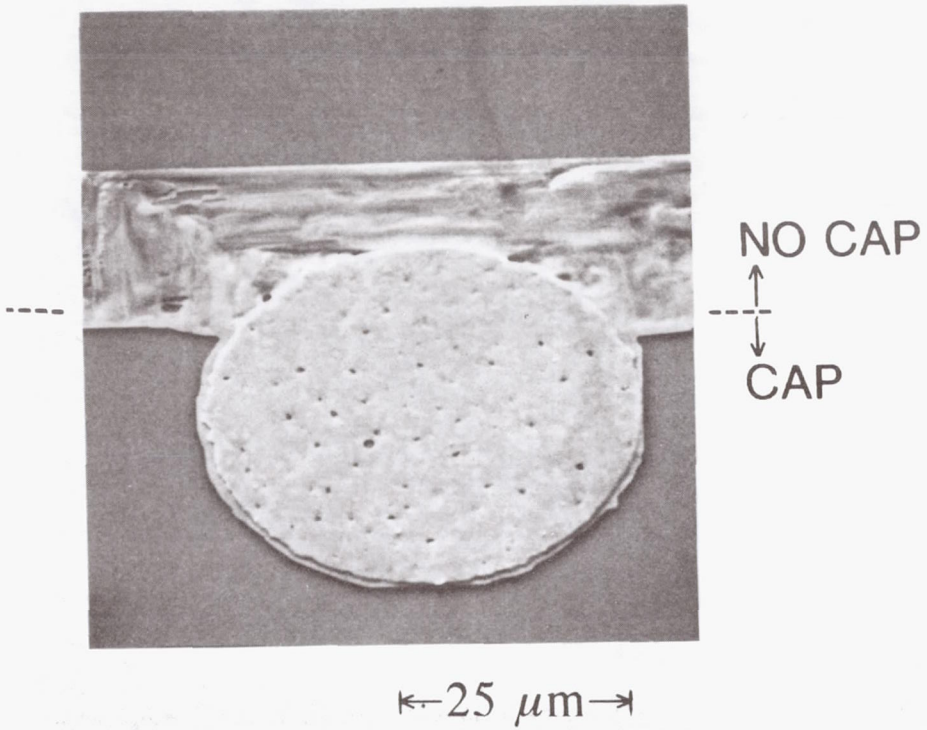

Fig. 5 The effect of SiO_2 capping on the spreading of Au heat-treated at 434 °C for 2.5 hrs.

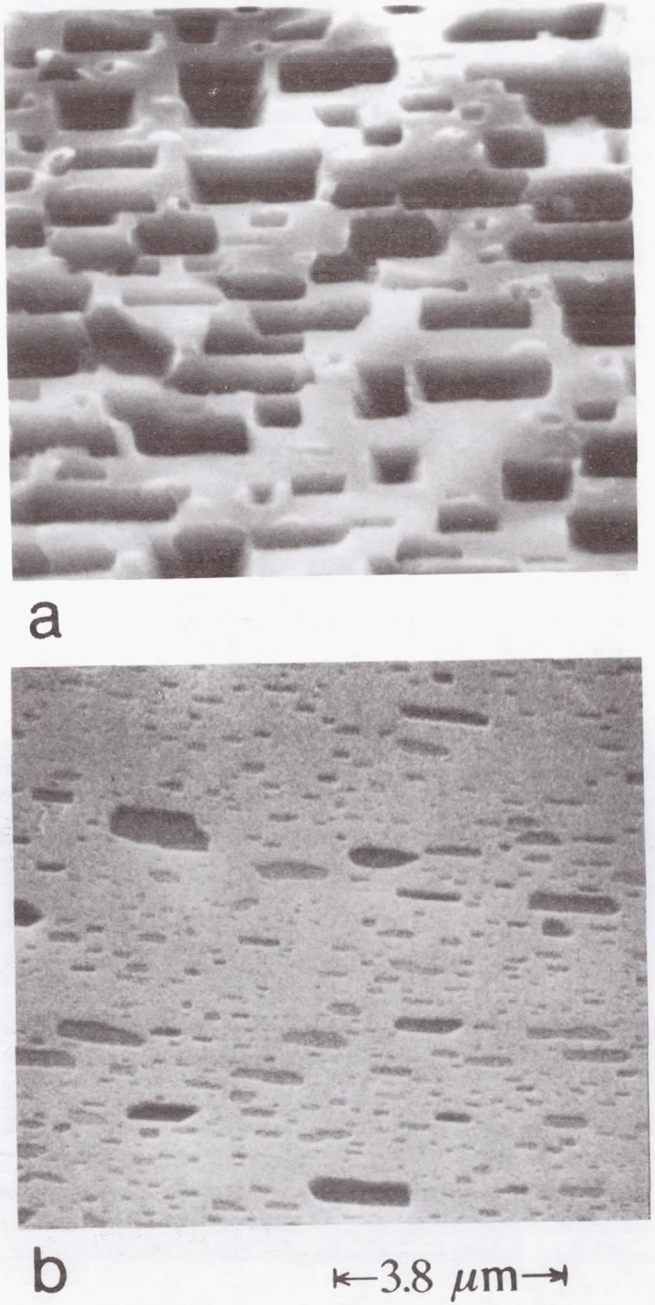

Fig. 6 Pitting on the InP surface under the metallization heat-treated at 434 °C for 2.5 hrs. a) Au removed, b) Au_3In removed.

The Effect of Process Conditions on the Performance of Epitaxial InP Solar Cells*

J. M. Borrego and S. K. Ghandi
Rensselaer Polytechnic Institute
Troy, NY

Introduction

Indium phosphide solar cells have a higher resistance to electron irradiation than Si or GaAs cells of comparable junction depths [ref. 1, 2]. As a result, there is much interest in the use of this material for space applications. Cells of this material have been made in bulk InP by a number of techniques, including ion implantation [ref. 3], direct diffusion in sealed ampoules [ref. 4] and by open tube diffusion methods [ref. 5]. However, it is generally considered that the epitaxial approach will be superior to all of these techniques.

The epitaxy of Indium Phosphide is considerably more difficult than that of gallium arsenide, for a number of reasons. Perhaps the most important is the fact that the native oxides of In are extremely difficult to remove, as compared to that of Ga. In addition, thermal treatments for the desorption of these oxides often result in the formation of phosphorus vacancies and free indium on the surface. Thus, inadequate sample preparation before epitaxy, poor reactor cleaning procedures, or poor transition procedures between the growth of successive layers, all give rise to trap phenomena and to high interface recombination velocities. Moreover, the lifetime of the grown material is dominated by the occurrence of native defects, so that it is a strong function of growth parameters.

These problems are of special interest to the fabrication of solar cells, where long lifetime, combined with the absence of traps, is highly desirable. This paper describes a study of this problem, using a non-invasive diagnostic technique which we have developed.

Technical

InP layers were grown at atmospheric pressure in a horizontal reactor with an r.f. heated susceptor. The reactor tube was 50 mm in diameter, and all flows were set by mass flow controllers. Semi-insulating (100) InP substrates, misoriented $2^{o} \rightarrow (110)$ were used for this study.

*Supported by NASA Lewis Research Center under Grant NAG 3-604.

Growth was carried out by the simultaneous pyrolysis of trimethylindium (TMIn) and phosphine gas, with a TMIn partial pressure of 0.042 Torr. The partial pressure ratio of PH_3/TMIn, referred to as the V/III ratio, was varied from 70 to 210 for this study. For these conditions, the growth rate was 1.5 μm/hr.

Lifetime and trapping phenomena were studied by analysis of photoconductive decay transients. In this method, excess carriers are generated by irradiating the sample with light of short wavelength, so as to produce hole-electron pairs. Since the conductivity of the sample is proportional to the total number of carriers, monitoring the conductivity decay after the light is turned off allows the determination of the lifetime.

We have developed a non-destructive method for performing this function, using time domain microwave reflectance spectrometry. Details of this system have been described elsewhere [ref. 6]. In summary, the block diagram of Fig. 1 shows that it consists of four subsystems: a microwave bridge, a pulsed light source for creating the excess hole-electron pairs, a mechanical stage for positioning the sample with respect to the incident RF wave and a data acquisition system. The main components of each subsystem are now described.

The microwave bridge operates at K_a-band (26-40 GHz) and consists of a Gunn oscillator, isolator, attenuators, directional couplers, magic-T, precision sliding short and attenuator, detectors and a few sections of K_a-band waveguide to assemble the bridge. The RF wave is directed to the sample by using a parallel plate antenna which confines and directs the RF wave to a small region of the sample.

The light source for generating the excess carriers is a pulsed GaAs or AlGaAs laser diode with an optical fiber attached to it. This source is used with a generator with a fast decay time to allow measurement of lifetimes as low as 3 nsec.

The mechanical stage is used for positioning the sample with respect to the light beam or the RF wave. The probed region of the sample is defined by the optical fiber which is 0.1 mm in diameter. By using micropositioners, it is possible to do spatial probing of the sample.

The data acquisition system allows saving and analyzing the photoconductivity decay transients for determining excess carrier lifetime. The main components are a digital oscilloscope with at least 100 MHz bandwidth and a low noise wide band amplifier. A computerized analysis of the data is used to extract the appropriate lifetime values.

Figure 2 shows a detailed plot of a typical transient measurement made with this system, averaged over 256 traces to extract the signal from the noise. This characteristic did not change under flood illumination, indicating that the layer is trap free. Computer analysis of this transient resulted in a bulk lifetime of 30 nsec, and a surface recombination velocity (SRV) of 3000-5000 cm/sec.

Results

Effect of HCl Cleaning of the Reactor:

Our reactor cleaning procedure involves a HCl clean of the reactor prior to each growth. This is done by flowing HCl through the reactor with the susceptor held at 1050°C, followed by a bakeout at 1100°C in H_2 gas for two hours. The substrate is loaded after reactor cool down to room temperature, and growth started shortly thereafter.

Figure 4 shows the microwave reflectance transient in the absence of this susceptor clean step. For this sample, strong evidence of traps is observed in the change of transient decay behavior upon flood illumination. From analysis of the transient, the trap lifetime was 1.19 μsec. Trapping phenomena were greatly reduced (but not eliminated) in layers grown after the HCl clean step, as seen from Fig. 5. Here, the trap lifetime, as obtained from an analysis of the transient, was 0.98 μsec.

Effect of an HCl Dip Prior to Growth:

Our cleaning procedure prior to epitaxy is as follows: the substrate is washed in hot organic solvents, followed by a soak in concentrated H_2SO_4. Next, it is rinsed in deionized water and then in methanol. This is followed by a Br-methanol etch step, and a rinse in hot methanol. Additionally, the InP substrate is given a 30 sec. dip in 5% HCl, just prior to loading into the reactor.

Results for two InP layers, grown side by side, are given in Table I, to illustrate the effect of this pre-growth step. The use of this step is seen to greatly improve the minority carrier lifetime, and to completely eliminate traps in the growing layer. The signal amplitude also increased as a result of the lifetime improvement.

Effect of Changing the V/III Ratio:

A series of runs were made at 625°C, with V/III ratios of 70, 140 and 210. In all cases, a pre-cleaned reactor was used, together with a substrate dip in HCl prior to epitaxy. Microwave reflection measurements indicated a bulk lifetime of approximately 30 nsec for all of these layers. We conclude, therefore, that the lifetime is relatively independent of the V/III ratio.

Effect of Growth Temperature:

A number of runs were made with a V/III ratio of 210, and growth temperatures from 600 – 650°C. All samples were treated with the HCl dip before loading in a pre-cleaned reactor, and all were grown with a TMIn partial pressure of 0.042 Torr.

Results of this experiment are presented in Table II. No traps were seen in any of the samples. However, the lifetime was seen to be a strong function of growth temperature, and peaked at 625°C. It should be emphasized that this temperature is machine specific, i.e., it is related to our system configuration and thermocouple placement.

Table II also shows the long wavelength (800 nm) internal quantum efficiency (IQE) of solar cells made at these growth temperatures. All cells were 0.25 cm × 0.25 cm, and were grown on p^+-doped InP substrates. The cell structure consisted of a 0.5 μm p^+-buffer, followed by 3.5 μm p-base and a 500 Å n^+-emitter. In all cases, the reactor was HCl cleaned, and samples were given a short HCl dip, prior to epi-growth. As seen, the IQE peaks for cells grown at 625°C.

Discussion

The effects of process conditions described here can be explained by noting that the electronic properties of InP, grown by organometallic vapor phase epitaxy (OMVPE) are dominated by its defect structure. The starting chemicals, in contrast, are relatively pure except in isolated cases.

DLTS studies made on material grown by OMVPE [ref. 7] show four electron traps, at E1 (0.23 ± 0.03), E2 (0.29 ± 0.03), E3 (0.38 ± 0.04) and E4 (0.61 ± 0.04) eV respectively. Of these, the last has been attributed to iron, which is present in bulk material as well as in semi-insulating substrates which are intentionally Fe-doped. The precise nature of the other three is not known, but is generally associated with phosphorus vacancies and V_p-complexes. They are also observed in MBE-grown material [ref. 8]. All of these defects are of comparable concentration and capture cross section, and reduce the minority carrier lifetime in InP.

As observed earlier, the surface of InP, even after an etch procedure, is covered with a thin film of native oxide. This surface oxide is non-stoichiometric, and is not fully understood at the present time [ref. 9]. Its removal, by thermal treatment prior to epi-growth is not complete; additionally, there is preferential loss of phosphorus during this process. The presence of these residues initiates the formation of defects which propagate through the growing layer.

The HCl dip prior to growth leaves the surface with a strongly adsorbed chlorine layer. The HCl reactor clean step, by the same time, results in adsorbed chlorine on the reactor walls. We propose that, at growth temperatures this reacts with these surface residues, and facilitates their removal via halide formation.

The behavior of El, E2 and E3 each exhibits a pronounced maximum with increasing growth temperature, and then rises sharply. This, in turn, results in a minority carrier lifetime which peaks at some specific growth temperature.

The relative independence of the lifetime with V/III ratio, as well as the sharp maximum with growth temperature, can probably be explained if we assume that these defects are due to V_p and V_p-complexes. Two effects are present with increasing temperature. First, PH_3 is extremely stable, and is not fully cracked until 700°C. Thus, we can expect the pressure of phosphorus over InP to increase exponentially with temperature resulting in a correspondingly rapid *fall* in the native defect concentration. On the other hand, the thermally generated $[V_p]$ can be expected to *increase* exponentially (for constant phosphorus pressure). The presence of these competing effects can explain the observed temperature behavior of lifetime.

In our experiments we have used V/III ratios from 70 to 210, i.e., a relatively small 1:3 range. From equilibrium thermodynamics, this represents a change in $[V_p]$ by a factor of 1.73 assuming P_2 species, and 1.32 assuming P_4 species. These relatively small changes are within the accuracy of lifetime measurement. As a result, the lifetime is relatively independent of V/III ratios for this study.

Conclusion

We have used time domain reflectometry to study the effect of process conditions on lifetime in epitaxial InP. The importance of HCl clean steps, and of reactor temperature have been identified by this technique and verified by measurements of the quantum efficiency of solar cells. A theory, based on the role of V_p and V_p-complexes, has been proposed to explain these results.

References

[1.] A. Yamamoto, M. Yamaguchi and C. Uemura, Appl. Phys. Lett. **44**, 611 (1984).

[2.] I. Weinberg, C. K. Swartz, R. E. Hart, Jr., S. K. Ghandhi, J. M. Borrego, K. K. Parat and M. Yamaguchi, Solar Cells **22**, 113 (1987).

[3.] L. Gouskov et al., Solar Cells **11**, 343 (1984).

[4.] A. Yamamoto, M. Yamaguchi and C. Uemura, IEEE Trans. Electron Dev., ED-32, 2780 (1985).

[5.] K. K. Parat, S. Bothra, J. M. Borrego and S. K. Ghandhi, Solid State Electron. **30**, 283 (1987) .

[6.] R. Venkatasubramanian, S. Bothra, S. K. Ghandhi and J. M. Borrego, *12th IEEE Photovoltaic Spec. Conf.*, 689 (1988).

[7.] M. A. A. Pudensi, K. Mohammed, J. L. Merz, D. Kasemset and K. L. Hess, J. Appl. Phys. **57**, 2788 (1985).

[8.] H. Asahi, Y. Kawamura, M. Ikeda and H. Okamoto, J. Appl. Phys. **52**, 2852 (1981).

[9.] G. Hollinger, E. Bergignat, J. Joseph and Y. Robach, J. Vac. Sci. Technol. **A3**, 2082 (1985).

TABLE I. EFFECT OF HCl DIP BEFORE EPITAXY

Condition	τ (nsec)	Signal mV	Comment
No HCl dip	3.5	46	Traps (0.95 μsec)
HCl dip	6.2	175	No Traps

TABLE II. THE EFFECT OF GROWTH TEMPERATURE

T_{growth}	Lifetime (nsec)	QE % at 800 nm
600°C	19.8	90
625°C	30	97
635°C	18	87

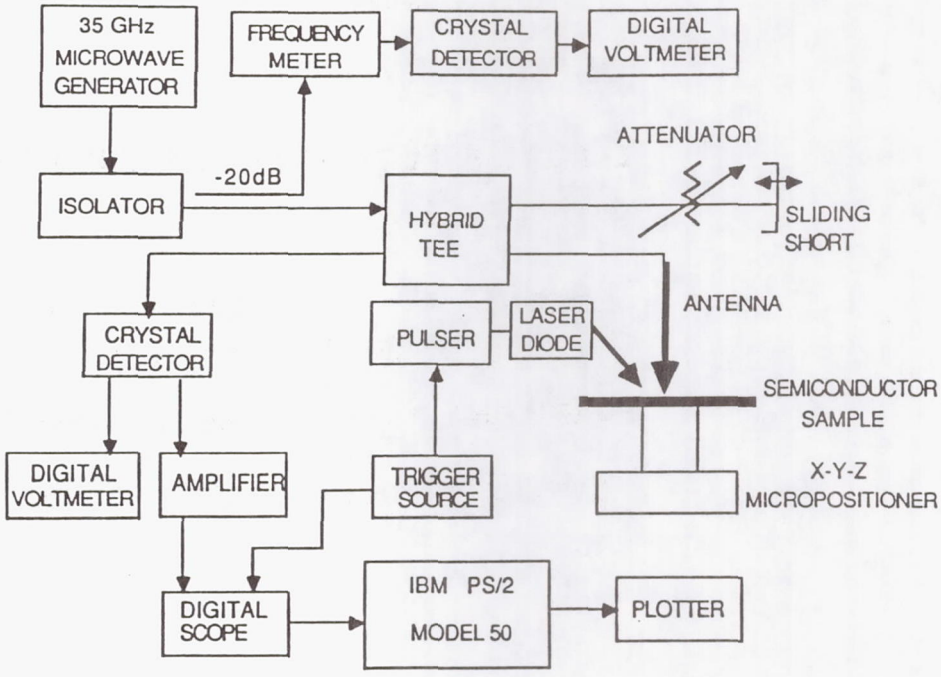

Figure 1. Block Diagram of Microwave Reflectance System.

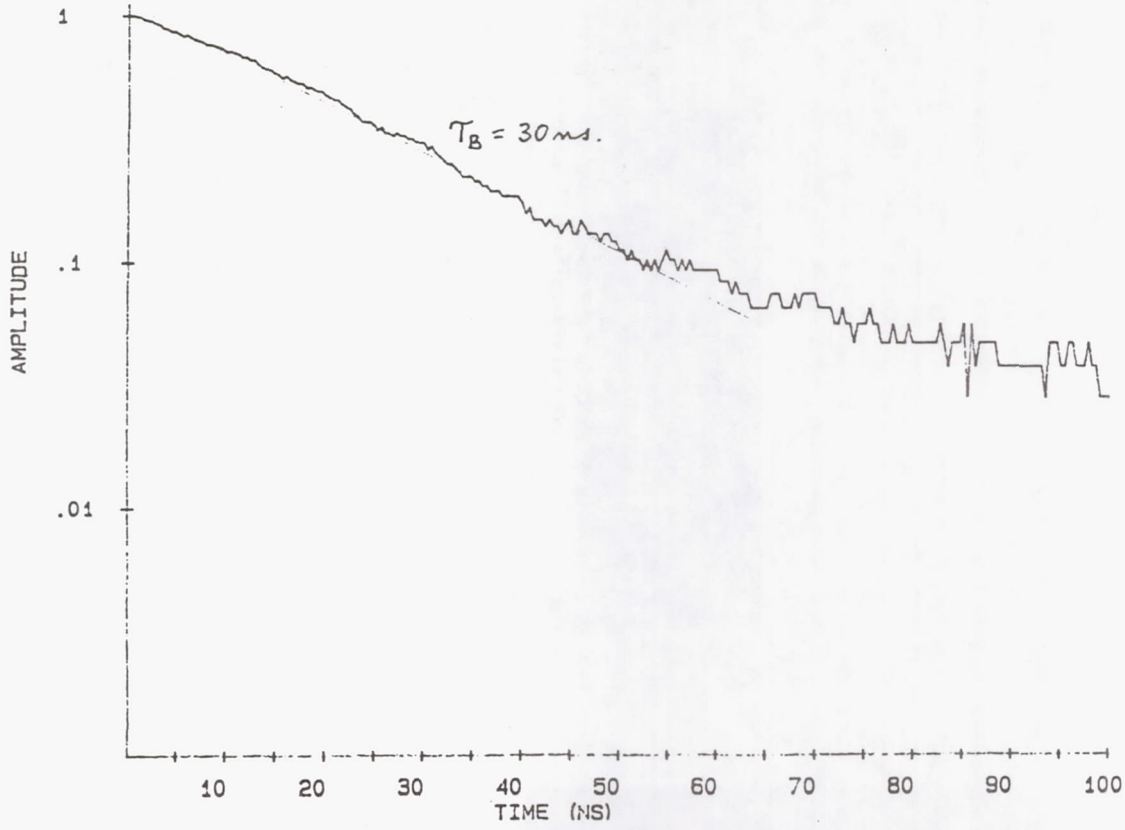

Figure 2. Detail of Transient Response.

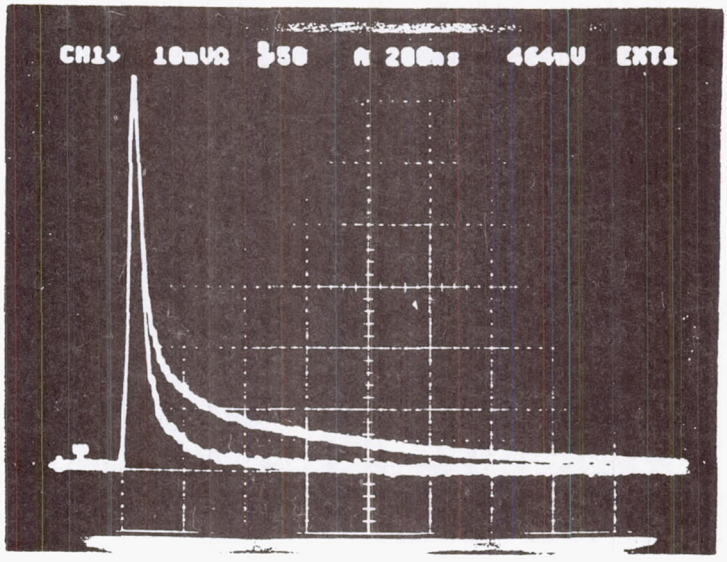

Figure 3. Measurements on a Sample Without Reactor Cleaning (200 nS/div; 10 mV/div).

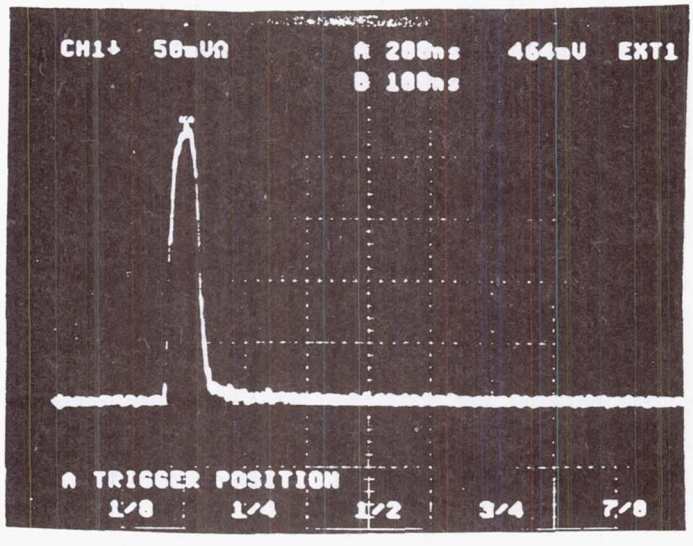

Figure 4. Measurements on a Sample with Reactor Cleaning (200 nS/div; 50 mV/div).

Effects of Proton Irradiation on the Performance of InP/GaAs Solar Cells

I. Weinberg, C. K. Swartz, D. J. Brinker and D. M. Wilt
NASA Lewis Research Center
Cleveland, OH

Introduction

InP solar cells are known to be more radiation resistant than either GaAs or Si [refs. 1-2]. In addition, AM0 total area efficiencies approaching 19% have been attained for InP [ref. 3]. However, the present high substrate cost presents a barrier to the eventual widespread use of InP cells in space. In addition, if cell thinning becomes desirable, their relative fragility presents a problem. For these reasons, the NASA Lewis Research Center has initiated a program, aimed at producing thin InP cells, by heteroepitaxial deposition of InP on cheaper, more durable substrates. To date, a short term feasibility study at Spire has resulted in cells processed from InP heteroepitaxially deposited on Si substrates with an intervening thin GaAs layer (InP/GaAs/Si) and cells produced from InP deposited on GaAs (InP/GaAs) [ref. 4]. As a result of this short study efficiencies of over 7 and 9% were achieved for InP/GaAs/Si and InP/GaAs respectively [ref. 4]. Although these efficiencies are low, they represent a modest and encouraging starting point for a more intensive program. Obviously, when considering economy and mechanical strength, cells processed on silicon substrates are preferred. However, although the InP/GaAs cells are not the final desirable products of this program, their properties serve to highlight several roadblocks to be overcome in producing cells with the more desirable cost and strength properties. Hence, in the present case, we concern ourselves with the properties of the InP/GaAs cells before and after irradiation by 10 MeV protons. A similar study of InP/GaAs/Si cells will be reported on at a later date.

Experimental Details

The InP/GaAs cells were produced at Spire under contract to NASA Lewis. Cell details are shown in figure one. The n^+p InP cells were processed by MOCVD on a relatively thick p-type GaAs substrate. Additional details are contained in reference 4. The cells were irradiated by 10 MeV protons, in the Lewis cyclotron, to a maximum fluence of 1.1×10^{13} cm^{-2}. Performance measurements were accomplished using an X-25 xenon lamp solar simulator and a flight calibrated InP standard cell. Spectral response measurements were performed using a filter wheel. Measurements of I_{sc} and V_{oc} were carried out at varying light intensities in order to determine the diffusion and recombination parameters of cell dark current.

Results and Discussion

Preirradiation performance parameters, averaged over 8 cells, are shown in table one. The measured values for I_{sc}, V_{oc} and efficiency shown in the table are slightly lower than those listed in reference 4. We attribute this to differences in solar simulators and to the fact that a silicon reference cell was used in reference 4 rather than the presently used InP standard. Also shown are predicted values obtained from the modelling calculations of Yamaguchi et al [ref. 5]. These latter calculations list cell parameters as a function of dislocation density. In the present case, the dislocation density of 3×10^8 cm^{-2} was obtained from the x-ray diffraction, ion channeling and cross-sectional TEM study of Pearton et al [refs. 4,6]. Referring to our predicted values, it is noted that figure eight in reference 5 lists parameters for an InP cell without front contact metallization and for a p-layer doping density of 10^{16} cm^{-3}. In the present case, the p-base doping density is 3×10^{16} cm^{-3}. Hence a correction was made to account for a small decrease in cell performance [ref. 7] An additional correction was made for the 5% front contact metallization coverage of the present cells. The low efficiencies attained are attributable to the high dislocation density caused essentially by lattice mismatch between InP and GaAs. It is noted that a reduction in dislocation density by two orders of magnitude is required to attain efficiencies over 18%. A typical preirradiation curve of the present InP/GaAs cells is shown in figure two together with a similar curve for a relatively high efficiency monolithic n^+p InP cell [ref. 8]. From the figure, the greatest difference between the two cells lies in the shunt resistance.

A plot of cell maximum power vs proton fluence is shown in figure three where it is seen that the present cells show relatively little degradation after irradiation to the highest fluence. This is further illustrated by a comparision, on a normalized basis, with similar data for monolithic n^+p cells [ref. 9]. The observed relatively high radiation resistance of the present InP/GaAs cells is attributed to the dominant effects of dislocations. In this connection it is noted that the base minority carrier diffusion length, computed from spectral response, shows a relatively small change at the highest fluence. This indicates that the effects of dislocations dominates over that of the radiation induced defects in determining minority carrier diffusion length. With regard to the remaining cell parameters, it is usually the case that I_{sc} degrades more than V_{oc} [ref. 10]. In the present case, these latter two parameters show approximately the same degradation at the highest fluence (table 2), a result which is considered to be anomalous. A further anomaly is indicated by the normalized long and short wavelength spectral response shown in figure five. It is usually the case that the highest degradation occurs in the long wavelength response, however, the opposite occurs in the present cells. The exact reason for these latter two effects is unclear at present.

The effect of dislocations is also apparent in the values obtained for the diffusion and recombination components of the dark current. These are obtained from the values of I_{sc} and V_{oc} obtained at varying light intensities. Using this data and assuming that the recombination component of dark current can be neglected at high V_{oc}, A_1, the junction ideality factor, is often obtained using the relation;

$$\ln(I_{sc} - (V_{oc}/R_{sh})) = (V_{oc}/A_1V_T) + \ln(I_{01}) \qquad [1]$$

where V_T=kT/q and I_{01} is the diffusion component of the dark reverse saturation current. However, in the present case, using relation one at high V_{oc}, it is found that A_1=1.7. This indicates that it is incorrect to neglect the recombination component at high V_{oc}. Hence to find A_1 we use:

$$\ln(\alpha) = (V_{oc}/A_1V_T) + \ln(I_{01}) \qquad [2]$$

with

$$\alpha = I_{sc} - I_{02}\exp(V_{oc}/A_2V_T) - V_{oc}/R_{sh} \qquad [3]$$

where I_{02} and A_2 correspond to the recombination component of dark current. These latter two quantities are evaluated from the I_{sc}-V_{oc} data at low V_{oc}. A plot of $\ln(\alpha)$ vs V_{oc} should yield a straight line from which A_1 can be evaluated. A typical plot is shown in figure six where, for this particular cell, it is found that A_1=1.3. The preirradiation parameters obtained in the present case are compared, in table three, to similar data obtained for monolithic n^+p InP and ITO/InP cells [ref. 9]. The recombination and diffusion components are noticeably higher for the InP/GaAs cells, the most noticeable difference occuring for the diffusion component. This follows from the fact that the highest concentration of dislocations occurs in the cell base at and near the InP-GaAs interface [ref. 6]. After proton irradiation we found no significant change in the recombination and diffusion components of the InP/GaAs cells. This is consistent with the dominant effect of dislocations in both the cell base and depletion regions.

Conclusion

Although the efficiencies obtained for the present cells are low, they represent a beginning which, with increased effort, should eventually result in cells with reasonably high efficiencies. It should be noted that the initial cells in the previous program which resulted in the best monolithic InP cells yielded efficiencies comparable to those obtained in the present case [refs. 3,11]. Clearly the dislocation density needs to be

drastically reduced. This is evident from both the theory and the dominance of dislocations in the present cells. The challenge here is to obtain increased efficiency while, at the same time, at least, maintaining the radiation resistance exhibited by the present monolithic cells.

References

[1.] M. Yamaguchi, C. Uemura and A. Yamamoto, Japanese Journ of Appl. Physics **23**, 302, 1984.

[2.] I. Weinberg, C. K. Swartz and R. E. Hart Jr., *Proceedings 18th IEEE Photovoltaic Specialists Conf.*, 1722, 1985.

[3.] C. J. Keavney and M. B. Spitzer, Appl. Phys. Lett. **52**, 1439, 1988.

[4.] C. J. Keavney, S. M. Vernon, V. E. Haven, S. J. Wojtczuk and M. M. Al-Jassim, Appl. Phys. Lett., **54**, 1139, 1989.

[5.] M. Yamaguchi, A. Yamamoto, N. Uchida and C. Uemura, Solar Cells **19**, 85, 1986-1987.

[6.] S. J. Pearton, K. T. Short, A. T. Macrander, C. R. Abernathy, V. P. Mazzi, N. M. Haeger, M. M. Al-Jassim, S. M. Vernon and V. E. Haven, J.Appl.Phys. **65**, 1O83, 1989.

[7.] A. Yamamoto, M. Yamaguchi and C. Uemura, IEEE Trans. Electron Devices, **ED12**, 2780, 1985.

[8.] M. B. Spitzer, C. J. Keavney, S. M. Vernon and V. E. Haven, Appl. Phys. Lett. **51**, 364, 1987.

[9.] I. Weinberg, C. K. Swartz, R. E. Hart Jr. and T. J. Coutts, *20th IEEE PVSC*, 893, 1988.

[10.] I. Weinberg, C. K. Swartz, R. E. Hart Jr., S. K. Ghandhi, J. M. Borrego, K. K. Parat and M. Yamaguchi, Solar Cells **22**, 113, 1987.

[11.] M. B. Spitzer, Final Report, *Research on high efficiency radiation resistant indium phosphide solar cells*, NASA Lewis Research Center, Spire FR-60058, 1985.

TABLE I-PREIRRADIATION CELL PARAMETERS

	Jsc	Voc	FF	EFF.
	MA/CM^2	MV	%	%
MEASURED[A]	26.6±.7	667±4	69±1	8.9±.1
PREDICTED[B]	29.6	600	77	9.9

A AVERAGE - 8 CELLS

B $N_{DIS} = 3X10^8/CM^2$, $P = 3X10^{16}/CM^3$

TABLE II-NORMALIZED CELL PARAMETERS AT HIGH FLUENCE

$\phi = 1.1 \times 10^{13}/CM^2$

Jsc(Φ)/Jsc(0)	Voc(Φ)/Voc(0)	FF(Φ)/FF(0)	EFF.(Φ)/EFF.(0)
0.98	0.97	0.96	0.91

TABLE III-DIFFUSION AND RECOMBINATION PARAMETERS

CELL	A_1	A_2	J_{01} A/cm^2	J_{02} A/cm^2
ITO/InP	1.09	1.95	$5.4X10^{-14}$	$4X10^{-9}$
InP (OMCVD)	1.03	2.24	$1.4X10^{-16}$	$4.1X10^{-9}$
InP (DIFFUSED)	1.08	1.94	$1.5X10^{-14}$	$4.1X10^{-9}$
InP (DIFFUSED)	1.02	2.25	$6.9X10^{-16}$	$2.5X10^{-8}$
InP/GaAs	1.27	2.12	$6.6X10^{-11}$	$9.5X10^{-8}$

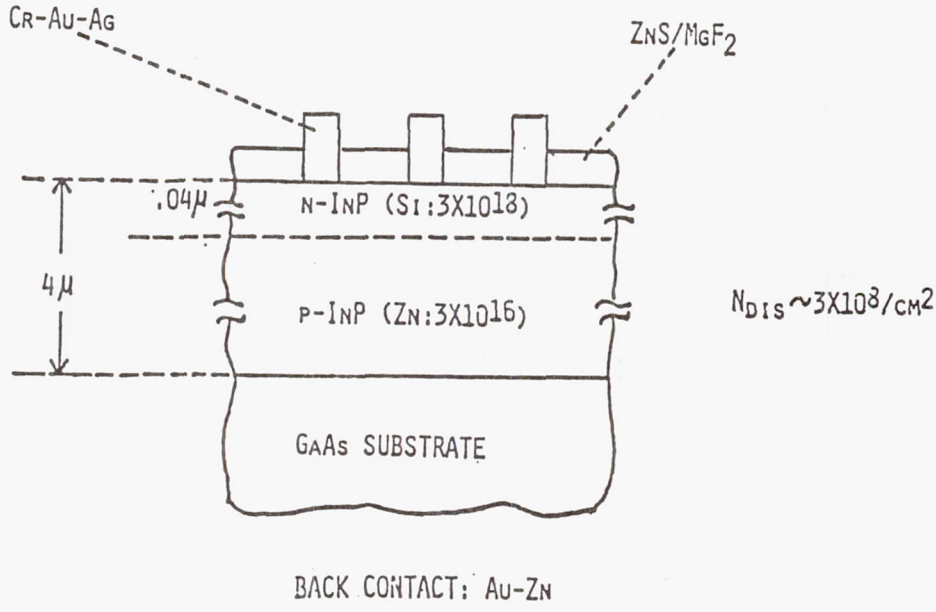

Figure 1. - Cell Details

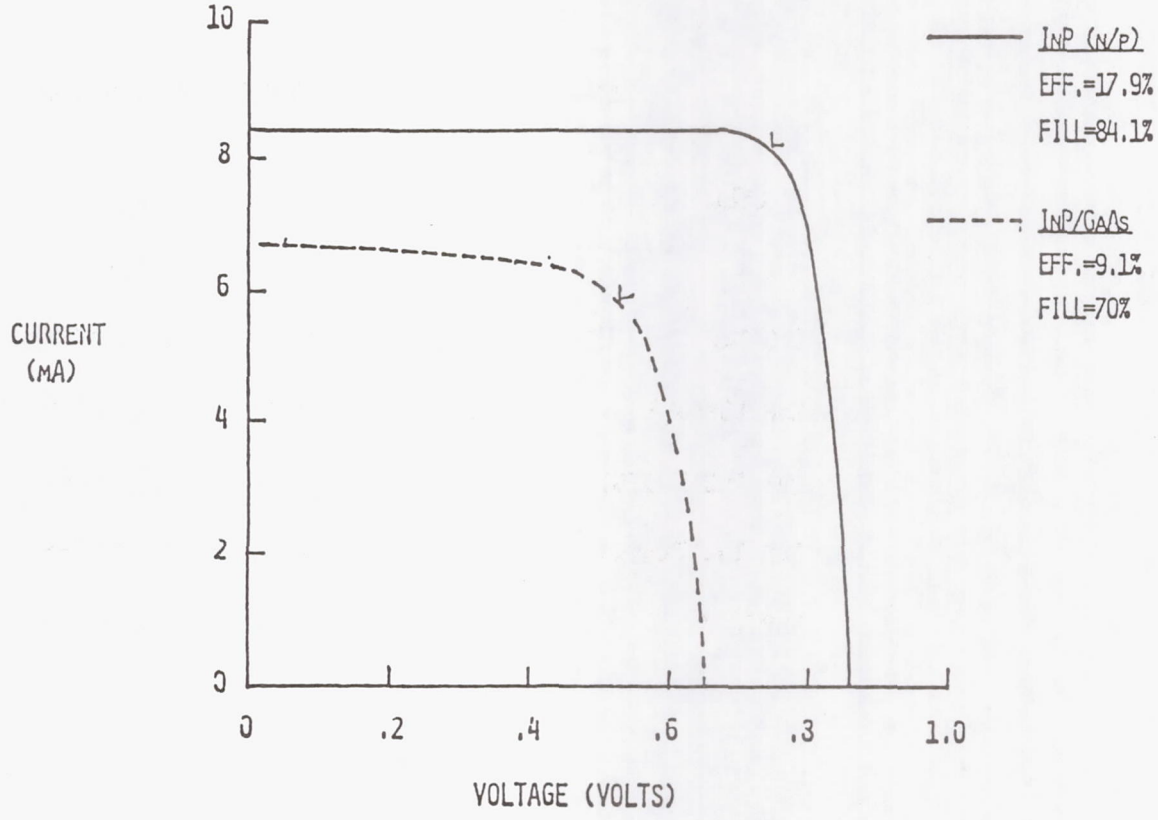

Figure 2 - Preirradiation I-V Curves

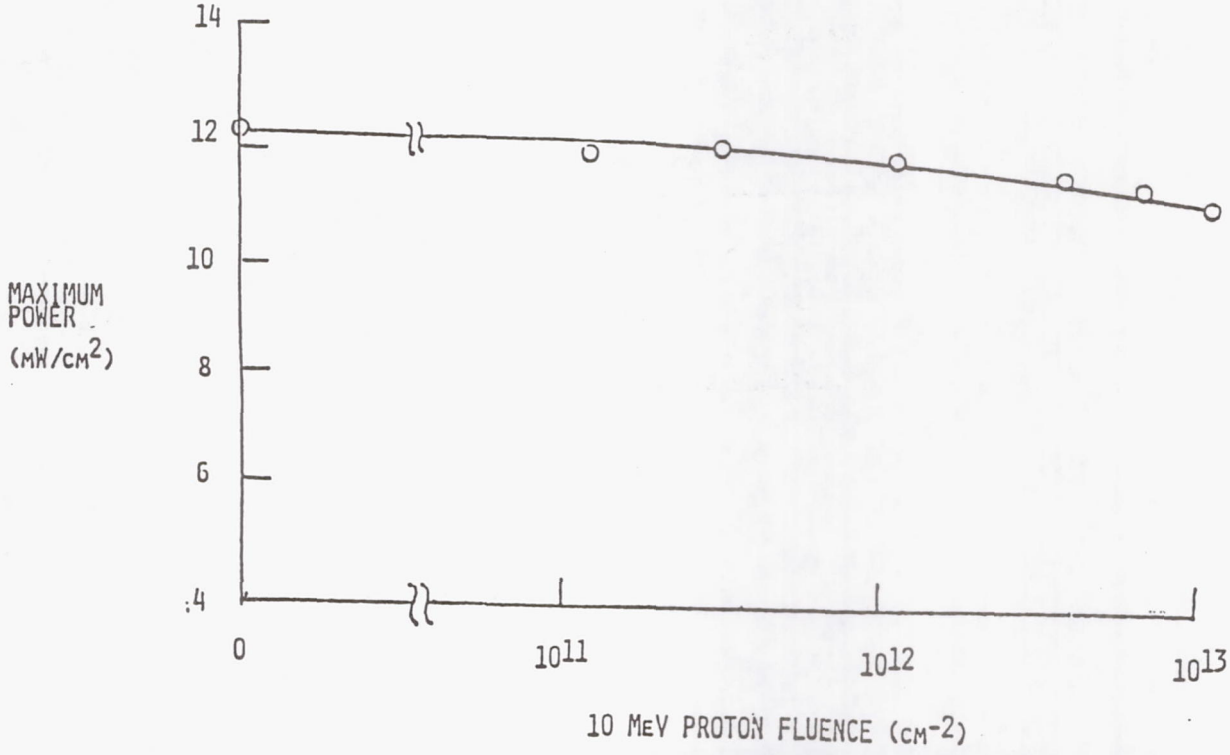

Figure 3 - Pmax After Proton Irradiations - InP/GaAs

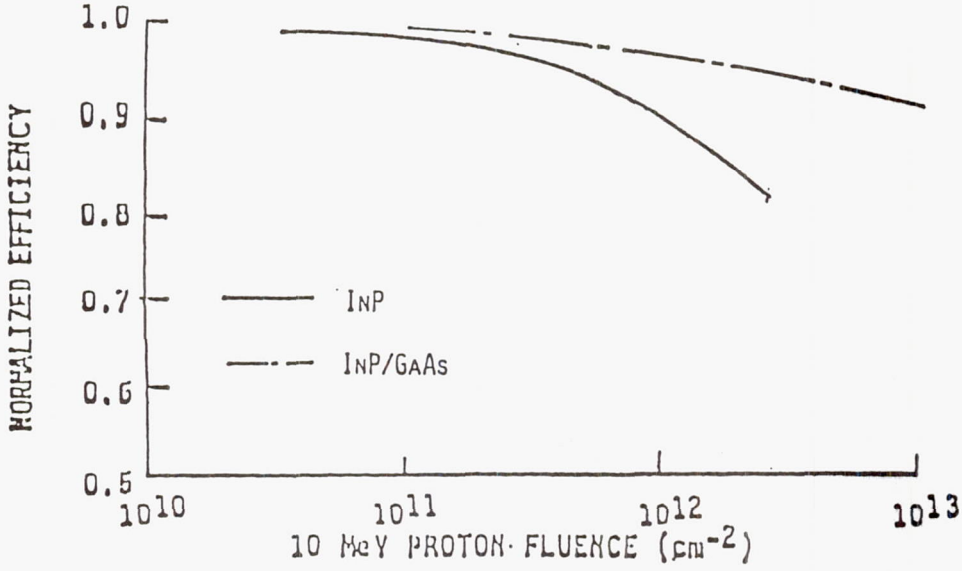

Figure 4 - Normalized Efficiencies After Proton Irradiations

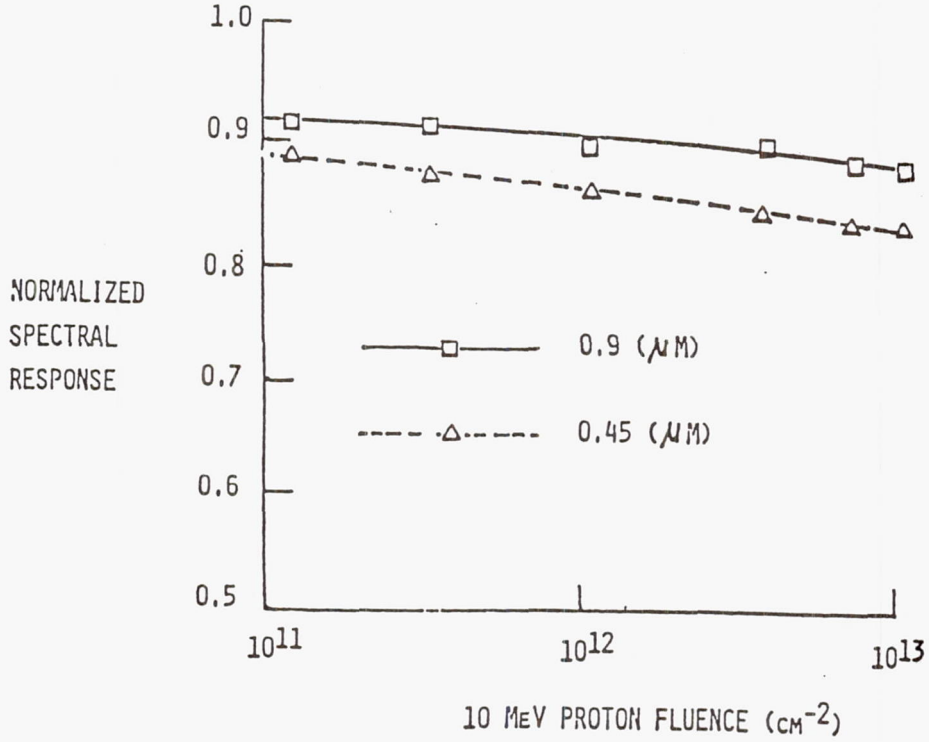

Figure 5 - Normalized Spectral Response After Proton Irradiations-InP/GaAs

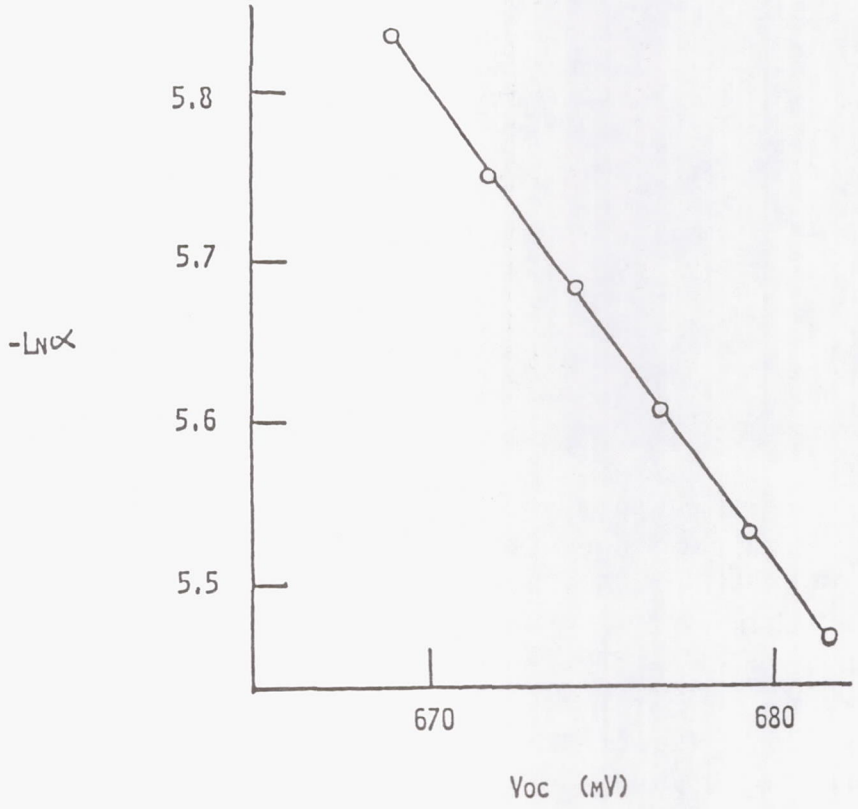

Figure 6 - Plot Used to Obtain A_1 From Variable Intensity Isc-Voc Data

Key Factors Limiting the Open Circuit Voltage of n+pp+ Indium Phosphide Solar Cells

Chandra Goradia and William Thesling
Space Photovoltaic Research Center
Electrical Engineering Department
Cleveland State University
Cleveland, OH

Irving Weinberg
NASA Lewis Research Center
Cleveland OH

Introduction

Solar cells made from gallium arsenide (GaAs), with a room temperature bandgap of $E_g = 1.43$ eV have exhibited the best measured open circuit voltage (V_{oc}) of 1.05 V at 1 AM0, 25C [ref. 1]. The material InP is in many ways similar to GaAs. A simple calculation comparing InP to GaAs then shows that solar cells made from InP, with $E_g = 1.35$ at 300K, should exhibit the best measured V_{oc} of ~950 mV at 1 AM0, 300K. However, to date, the best measured V_{oc} for InP solar cells made by any fabrication method is 899 mV at AM1.5, 25°C [ref. 2], which would translate to 912 mV at 1 AM0, 25°C.

The V_{oc} of an n^+pp^+ InP solar cell is governed by several factors. Of these, some factors, such as the thickness and doping of the emitter and base regions, are easily controlled and can be adjusted to desired values dictated by a good performance-optimizing model. Such factors have not been considered in this investigation. There are other factors which also govern V_{oc}, and their values are not so easily controlled. The primary ones among these are 1) the indirect or Hall-Shockley-Read lifetimes in the various regions of the cell, 2) the low-doping intrinsic carrier concentration n_i of the InP material, 3) the heavy doping factors in the emitter and BSF regions, and 4) the front surface recombination velocity S_F. We have investigated the influence of these latter factors on the V_{oc} of the n^+pp^+ InP solar cell and have used the results to produce a near-optimum design of the n^+pp^+ InP solar cell.

Theoretical Approach

We have developed a fairly comprehensive, one dimensional, closed form solution, computerized model of the shallow homojunction InP space solar cell. This model assumes a cell with three homogeneously doped regions, an n^+ emitter, a p-type base and a p^+ BSF region. Details of the model have been presented elsewhere [ref. 3]. In our earlier near-optimum design of the n^+pp^+ shallow-homojunction InP solar cell using this model [refs. 3,4] no accounting was made of the heavy-doping effects in the

heavily doped emitter and BSF regions. As of this day, to the best of our knowledge, measured heavy doping factors or equivalent bandgap narrowing values as functions of doping for n-type and p-type InP have not been published in the literature, as they have been for GaAs [ref. 5]. This lack of information makes it difficult to take into account heavy doping effects in InP cell modeling. Even so, it is now realized that it is very important to take these into account in order for the modeling to be of much value. Hence, some way must be found to reasonably estimate the heavy doping effects. A prior attempt [ref. 6] at this has been to represent the heavy doping effects, including Fermi-Dirac statistics, by an equivalent effective bandgap narrowing ΔE_g in each heavily doped cell region (emitter, BSF) and to estimate the amount of ΔE_g in these regions by matching the calculated and measured internal spectral response in the short and long wavelength region of the incident light spectrum. We feel that a less roundabout and more accurate method is to lump all the heavy doping effects into an effective intrinsic carrier concentration n_{ie} and to thereby define a heavy doping factor HD in each heavily doped region as, for example in the emitter, by

$$HD_E = \frac{n_{ieE}}{n_{i0}}$$

where n_{ieE} is the the effective value of n_i in the emitter and n_{i0} is the low-doping value of n_i in InP. A similar heavy doping factor HD_{BSF} is defined for the BSF region. The values of HD_E and HD_{BSF} are then estimated by matching the calculated and measured curves of not only the internal spectral response but also the illuminated I-V and log $I_{sc} - V_{oc}$.

The above approach still leaves one major problem. It allows the estimation of HD_E and HD_{BSF}, each for only one value of doping, that of the experimental cell whose measured curves were matched. However, what is needed for general modeling purposes is HD_E and HD_{BSF} as functions of their respective dopings: in other words, curves of HD_E^2 and HD_{BSF}^2 vs. their respective dopings, as are available for GaAs at 300K [ref. 5], as shown in figure 1. In the absence of available measured data on InP, we made the reasonable assumption, as a first approximation, that for both n-type and p-type InP, the nature of the HD^2 versus doping curve is similar to that of GaAs. With this assumption, the curve for InP can be obtained from that of GaAs if one point on the curve could be determined. As stated earlier, this can indeed be done by matching the calculated and measured curves of illuminated I-V, log $I_{sc} - V_{oc}$ and internal spectral response.

Our computer model was designed from the start to correctly take into account heavy doping effects in all three regions of the cell,if necessary, by means of appropriate boundary conditions involving the heavy doping factors in each region. The boundary condition at the emitter-base junction is that of the generalized 'law of the junction', valid at all injection levels, while that at the base-BSF interface is that of the low-injection effective interface recombination velocity S_{pp+} given by

$$S_{pp^+} = \frac{N_{a,base}}{N_{a,BSF}} \cdot \left(\frac{HD_{BSF}}{HD_{base}}\right)^2 \cdot \frac{D_{n,BSF}}{L_{n,BSF}} \cdot \frac{1}{\tanh(\frac{w_{BSF}}{L_{n,BSF}})} \quad [1]$$

where N_a is the doping, HD is the heavy doping factor, as defined earlier (e.g. $HD_{BSF} = n_{ie,BSF}/n_{i0}$), and D, L, w are the minority carrier diffusivity, diffusion length and width of the region, respectively. For a base doping of less than 10^{17} cm^{-3}, $HD_{base} = 1$, and it is seen in equation [1] that the net effect of heavy doping in the BSF region is to increase the effective base-BSF interface recombination velocity S_{pp^+} by a factor of $(HD_{BSF})^2$. As we shall see from the calculated results in the following section, the overall effect of heavy doping in the BSF region is to increase the minority carrier recombination in the base at the base-BSF interface, thereby increasing the dark saturation current in the base and reducing the open circuit voltage of the cell.

As to the task at hand, that of finding HD_E and HD_{BSF} at one doping, we chose to match theoretical and measured curves of illuminated I-V, log $I_{sc} - V_{oc}$ and internal spectral response for a 17.9% efficient n^+pp^+ solar cell labeled Spire 6 [ref. 7], made by the Spire Corporation, for which such measured curves were available. All measurements on this cell were made at the NASA Lewis Research Center in Cleveland, Ohio, and were made available to us by courtesy of Mr. Russell E. Hart.

We obtained excellent matches between the calculated and measured curves of Spire 6 for specific values of $HD_E = 1.4$ for the n-type emitter doping of 1×10^{18} cm^{-3} and $HD_{BSF} = 4.87$ for the p-type BSF doping of 5×10^{18} cm^{-3}. By noting that each of the two HD^2 versus doping curves had to pass through its corresponding specific point indicated above and also that each HD has to become unity at dopings of 10^{17} cm^{-3} and below, we were able to express the general variations of HD_E and HD_{BSF} versus their respective dopings in equation form as:

$$HD^2_{E,n-InP} = 1.92 \cdot [HD^2_{n-GaAs} - 1] + 1 \quad [2]$$

except when HD_{n-GaAs} drops below unity, in which case, for simplicity, we used the approximation

$$HD^2_{E,n-InP} = HD^2_{n-GaAs} \quad [3]$$

Also,

$$HD^2_{BSF,p-InP} = 6.1 \cdot [HD^2_{p-GaAs} - 1] + 1 \quad [4]$$

The +1 on the right-hand side of equations [2] and [4] ensures that HD in InP becomes unity when IID in GaAs becomes unity, at the lower dopings.

The above equations were incorporated into the computer model so that, for any doping concentration in the emitter and BSF, the corresponding heavy doping factor could easily be calculated. This capability to calculate the heavy doping factors HD_E, HD_{BSF} as functions of doping was the only new addition that our computer model required. The computer model was already capable of calculating all other geometrical and material parameters needed to simulate the solar cell, as in the past [refs. 3,4].

Calculated Results and Discussion

In order to see how the V_{oc} varied with each of the individual parameters expected to affect it, we first chose a somewhat modified version of the Spire 6 cell design to serve as a baseline cell. The primary modifications were: a) a reduced grid shadowing from 4.8% of Spire 6 to 4.0% of the baseline design, b) a thinner emitter, from 400Å of Spire 6 to 200Å of the baseline cell, c) a heavier emitter doping, 5×10^{18} cm^{-3} from 1×10^{18} cm^{-3} of Spire 6, d) a thinner base, 2 μm instead of 3 μm, and e) a lighter BSF doping of 2×10^{18} cm^{-3} for the baseline cell instead of 5×10^{18} cm^{-3} for Spire 6. These modifications reflected current practice in cell design and resulted in an improved cell efficiency of 19.23% from the 17.9% of Spire 6. The baseline design also resulted in a somewhat larger V_{oc} of 873 mV from the 868 mV of Spire 6. Table 1 shows all the geometrical and material parameters of the Spire 6 and the baseline solar cells. Note that the numbers in the baseline cell column are for 300 K as opposed to 298 K for Spire 6. This results in a significantly longer radiative lifetime in the base for the baseline cell, since the base radiative lifetime is extremely sensitive to temperature.

In our model, the indirect or Hall Shockley-Read (HSR) lifetime in any cell region is assumed to be inversely proportional to the doping in that region. This assumption is tantamount to the assumption that indirect recombination in InP occurs via a single dominant recombination level whose density is proportional to doping density. Thus, in any cell region,

$$\tau_{HSR} = \frac{\Gamma_{HSR}}{N} \qquad [5]$$

where Γ_{HSR} is the constant of proportionality between τ_{HSR} and the reciprocal of the doping concentration N. Only two different values of Γ_{HSR} are needed, one for n-type and one for p-type InP. These were obtained from our matching the calculated and measured curves for Spire 6, as were the values of HD_E, HD_{BSF} and S_F. For the baseline value of n_i, we chose the prevalent value of $n_i(300\ K) = 1.2 \times 10^7 cm^{-3}$, which may be on the high side according to current thinking [ref. 2].

Thus, knowing the baseline values of HD_E, HD_{BSF}, $\Gamma_{HSR,p}$, $\Gamma_{HSR,n}$, S_F and n_i, all except n_i being derived from the Spire 6 match, we could calculate the complete performance of the baseline cell at 300 K. The second column of Table 1 gives the

geometrical, material and performance parameters of the baseline cell. Note that the baseline cell has a thinner, more heavily doped emitter, a thinner base and a less heavily doped BSF layer than the Spire 6 cell.

Next, we made a large number of parametric variation runs of our computer model simulating the baseline cell, varying one parameter at a time from among HD_E, HD_{BSF}, $\Gamma_{HSR,p}$ and $\Gamma_{HSR,n}$ (in the form of relative HSR or indirect lifetime τ_i/τ_{i0} in the n-type emitter and p-type base and BSF regions), the low-doping intrinsic carrier concentration n_{i0} and finally the front surface recombination velocity S_F. It should be noted that in our model, S_F is the area-weighted average effective surface recombination velocity over both the part of the front surface which is not in actual physical contact with the front grid metallization and the part which is in such contact [ref. 3].

The results of the parameter variation runs are shown in Figs. 2,3,4 and 5, which show, respectively the variation of V_{oc} versus 1) the HSR relative lifetime τ_i/τ_{i0} in the emitter, base and BSF, 2) the low-doping intrinsic carrier concentration n_{i0}, 3) the BSF heavy doping factor HD_{BSF} and 4) the effective front surface recombination velocity S_F.

We now discuss each of these figures in turn. In Fig. 2, we see that if, by using better material and device processing, we can make the indirect or HSR lifetimes in all regions of the cell to be ten times longer than their current-technology values in Spire 6, then V_{oc} can be improved by slightly over 10 mV, which, while not being a very large gain in V_{oc} still is a significant gain. Fig. 2 also shows that V_{oc} begins to level off as the HSR lifetime is made even longer. This is because when the HSR lifetime becomes very long, the overall lifetime is controlled by the radiative lifetime which, for a given doping and temperature, is an inherent property of the material InP and is independent of the quality of the starting material or of the device processing parameters. Thus, it appears from Fig. 2 that by making the HSR lifetime in each region indefinitely long by using the highest quality starting material and using the cleanest possible device processing, the most to be gained in V_{oc} is about 15 mV or so.

Next considering Fig. 3, we see the variation in V_{oc} as the 300 K, low-doping intrinsic carrier concentration n_{i0} decreases from $1.2\times10^7 cm^{-3}$ to a hypothetical value of 5×10^6 cm^{-3}, to show the nature and extent of variation of V_{oc} with n_{i0}. If n_{i0} were somehow halved from its presently used value of 1.2×10^7 cm^{-3} to 6×10^6 cm^{-3}, then Fig. 3 shows that V_{oc} would increase by ~25 mV. The values of n_{i0} and V_{oc} indicated by the two arrows in Fig. 3 are as follows. The one corresponding to n_{i0} $= 1.2 \times 10^7$ cm^{-3} represents the prevalent value of n_i based on both the density of states functions N_c, N_v, and the bandgap E_g corresponding to InP. The other point is the value of n_{i0} that would be obtained by using the density of states values of GaAs but the bandgap of InP–in other words, the value of n_i that InP would have if its N_cN_v product were the same as that for GaAs. The difference in V_{oc} between the

two points is about 18 mV, and it indicates that, in comparison with GaAs, InP has an 18 mV V_{oc} disadvantage merely because its N_cN_v product is too large compared to that of GaAs.

There is some uncertainty about the value of n_i in InP. Yahia and Coutts have done an extensive investigation of this problem, and believe that n_i in InP at 300 K should be around 8 to 9×10^6 cm^{-3} [ref. 8]. If this is true, then the expected maximum V_{oc} of InP would be higher by about 10 mV.

In Fig. 4, we show the calculated variation of V_{oc} for the baseline InP cell with the BSF heavy doping factor $HD_{BSF} = n_{ie,BSF}/n_{i0}$ The point corresponding to the heavy doping factor calculated using equation (4) is indicated by the arrow. It is seen that the lower the heavy doping factor, the higher the V_{oc}.

If the qualitative behavior of heavy doping factor versus doping in p-type and n-type InP is indeed similar to that for GaAs, as we have assumed, then it would appear at first sight that it would be advantageous to have an n-based cell with n^+ BSF. However, only detailed calculations would show whether that would be the case or not, for the following reasons: First, in a p^+nn^+ InP cell, the p^+ emitter would have to be relatively thick in order for the low hole mobility in it to not cause an excessively large emitter sheet resistance component of series resistance. With a thicker emitter, a significant portion of the total cell photocurrent would now come from the emitter, as would the dark saturation current. In that case, any gain due to a low (lower than one) HD_{BSF} could be more than counteracted by the high HD_E in the p^+ emitter. We are in the process of doing such detailed calculations for the p^+nn^+ cell.

Finally, Fig. 5 shows the variation of V_{oc} versus the effective front surface recombination velocity S_F. Here, it is seen that over its entire range of values from $S_F \ll D_{pE}/L_{pE}$, the diffusion velocity of minority carriers in the emitter, to $S_F \gg D_{pE}/L_{pE}$, V_{oc} degrades by only about 3 mV. The reason why V_{oc} is relatively insensitive to S_F is that in any relatively well-designed InP solar cell, as in the baseline cell, the V_{oc} is controlled primarily by the dark saturation current J_0 in the base, which is several times (~10 or more) larger than the J_0 from the emitter. Thus, the S_F variation, which may affect $J_{0,emitter}$ by a factor of a few, does not affect the overall J_0, and therefore V_{oc}, significantly. It is to be noted, however, that S_F has a significant effect on the short circuit current J_{sc} and on the efficiency; therefore, it is most desirable to reduce S_F to a very low value ($S_F \ll D_{pE}/L_{pE}$) by means of front surface passivation or the use of an appropriate higher bandgap window layer.

Near–Optimum Cell Design

Having investigated the individual variation of V_{oc} with each of the parameters $\Gamma_{HSR,n}$ and $\Gamma_{HSR,p}$, n_{i0}, HD_{BSF} and S_F and some other variations (V_{oc} vs. base thickness, base doping, emitter thickness, emitter doping and HD_E) not shown here,

we next proceeded to design a near-optimum InP n^+pp^+ solar cell for 1 AM0, 300 K operation with a view to maximizing its efficiency (not V_{oc})

Our approach to the near-optimum design was to ignore limitations imposed by current technology on such parameters as $\Gamma_{HSR,p}$, $\Gamma_{HSR,n}$ and S_F. With improved technology, in the near future, $\Gamma_{HSR,p}$ and $\Gamma_{HSR,n}$ could realistically be about ten times the values obtained in the Spire 6 match, while S_F could very likely be $\sim 10^4$ cm/s or less. Thus we have used values for $\Gamma_{HSR,p}$ and $\Gamma_{HSR,n}$ that are ten times the values obtained in the Spire 6 match and used in the baseline cell. This is tantamount to assuming that in the near future, material and processing quality is likely to improve to the extent that at moderate and high dopings, the overall lifetime in InP will be limited by the radiative lifetime. We have also used $S_F = 10^4$ cm/s, again assuming that the significant amount of research on surface passivation and searching for an appropriate window material will result, in the near future, in an effective front SRV of $S_F = 10^4$ cm/s or less. As to the technology-independent parameters, such as HD_E, HD_{BSF} and n_{i0} we have used the same values as used earlier, namely, HD_E and HD_{BSF} based on equations [2], [3] and [4], and $n_{i0} = 1.2 \times 10^7$ cm^{-3} at 300 K.

Table 2 gives the complete geometrical, material and performance parameters of the near optimum cell. Note that this optimized cell has a realistic expected efficiency of 22.61% and a V_{oc} of 901.6 mV. According to our model, higher V_{oc} values are obtainable at some sacrifice in J_{sc} and efficiency.

Because of heavy doping effects, our near-optimum design has relatively lighter dopings in the BSF and base. It may seem at first sight that with a BSF doping only ten times the base doping, the base/BSF interface would not be an effective reflector of minority carriers. However, higher BSF dopings result in the base/BSF interface being an even worse reflector of minority carriers because of heavy doping effects in the BSF.

Concluding Remarks

1. The primary factor limiting the V_{oc} in an n^+pp^+ solar cell is the heavy-doping factor in the p^+ BSF.

2. In a well-designed n^+pp^+ InP solar cell, the effective front SRV S_F has a significant effect on I_{sc} and η but a relatively minor effect on V_{oc}.

3. If the effective front SRV is reduced to $\sim 10^4$ cm/s and the HSR lifetime coefficients $\Gamma_{HSR,p}$, $\Gamma_{HSR,n}$ are increased by a factor of 10, then it is theoretically possible to obtain a V_{oc} of 902 mV and $\eta = 22.6\%$ at 1 AM0, 300 K, for an n^+pp^+ InP solar cell. Even higher V_{oc} values should be obtainable at a sacrifice in I_{sc} and η.

References

[1.] Russell E. Hart, NASA Lewis Research Center (LeRC), private communication.

[2.] Timothy J. Coutts, Solar Energy Research Institute (SERI), private communication.

[3.] C. Goradia, J.V. Geier, I. Weinberg, Solar Cells **25**, 235, 1988.

[4.] C. Goradia, J.V. Geier, I. Weinberg, *Conf. Rec. l9th IEEE Photovoltaic Specialists Conf.*, IEEE Publ. No. 87CH2400-0, 937, 1987,.

[5.] M.E. Klausmeier-Brown, P.D. DeMoulin, H.L. Chuang, M.S. Lundstrom and M.R Melloch, *Conf. Rec. 20th IEEE Photovoltaic Specialists Conf.*, IEEE Publ. No. 88CH2527-0, 503, 1988.

[6.] G. Augustine, A.W. Smith, A. Rohatgi, *Conf. Rec. 20th IEEE Photovoltaic Specialists Conf.*, IEEE Publ. No. 88CH2527-0, 903, 1988.

[7.] C.J. Keavney, M.B. Spitzer, Appl. Phys. Lett. **52**, 1439, 1988.

[8.] A.H. Yahia, T.J. Coutts, "Uncertainties in the Physical Parameters Used in Modelling InP Solar Cells: Part I, Effective Mass/Intrinsic Carrier Concentration", to be published.

Table 1

	Spire 6 Match (298 K)	Baseline Cell (300 K)
Grid Shadow	4.8%	4.0%
* Front SRV (cm/sec)	3.3×10^6	3.3×10^6
w_E, Å	400	200
$N_{D,\text{emitter}}$, cm^{-3}	1.0×10^{18}	5.0×10^{18}
* HD_E	1.4	0.632
* τ_{HSR}, ns	2	0.4
τ_{Rad}, ns	0.979	0.287
τ_p, ns	0.653	0.161
L_{pE}, μm	0.355	0.123
w_{base}, μm	3	2
$N_{A,\text{base}}$, cm^{-3}	2×10^{16}	2×10^{16}
* τ_{HSR}, ns	150	150
τ_{Rad}, ns	49.0	71.7
τ_n, ns	36.9	48.4
$L_{n,\text{base}}$, μm	19.4	22.4
w_{BSF}, μm	0.5	0.5
$N_{A,\text{BSF}}$, cm^{-3}	5×10^{18}	2×10^{18}
* HD_{BSF}	4.87	3.62
* τ_{HSR}, ns	0.6	1.5
τ_{Rad}, ns	0.196	0.717
τ_n, ns	0.143	0.477
$L_{n,\text{BSF}}$, μm	0.95	1.76
V_{oc}, mV	868	873
η	17.9%	19.23%

* Value obtained from Spire 6 match

Table 2

Best Theoretical Cell Design

Grid Shadow	4.0%
Front SRV	1×10^4 cm/sec
w_E	200 Å
$N_{D,\text{emitter}}$	3.0×10^{18} cm^{-3}
* $\text{HD}_E = \frac{n_{iE}}{n_{i0}}$	0.837
* τ_{HSR}	6.667 ns
τ_{Rad}	0.478 ns
τ_p	0.431 ns
L_{pE}	0.227 μm
w_{base}	4 μm
$N_{A,\text{base}}$	8×10^{15} cm^{-3}
HD_{base}	1
* τ_{HSR}	3.75 μs
τ_{Rad}	179 ns
τ_n	171 ns
$L_{n,\text{base}}$	43.7 μm
w_{BSF}	250 μm
$N_{A,\text{BSF}}$	7.5×10^{16} cm^{-3}
HD_{BSF}	1
* τ_{HSR}	400 ns
τ_{Rad}	19.1 ns
τ_n	18.24 ns
$L_{n,\text{BSF}}$	12.57 μm

J_{sc}=39.94	mA/cm^2
V_{oc}=901.6	mV
J_{max}=38.59	mA/cm^2
V_{max}=804.4	mV
FF=86.21	%
η=22.61	%

Figure 1

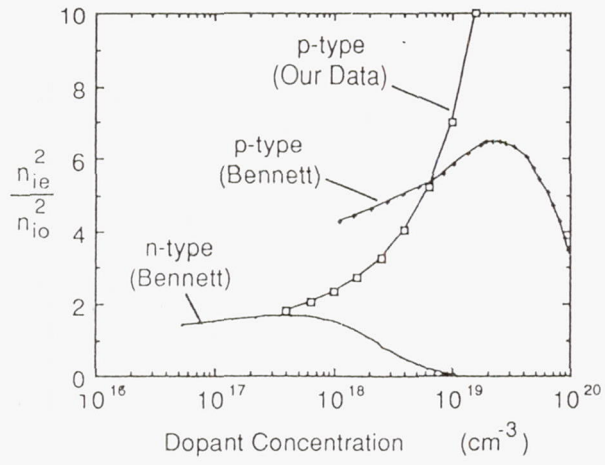

Effective intrinsic carrier concentration in n– and p–type GaAs.
Figure taken form M.E. Klausmeier–Brown et. al. Proc. of the 20th PVSC [5]

Figure 2

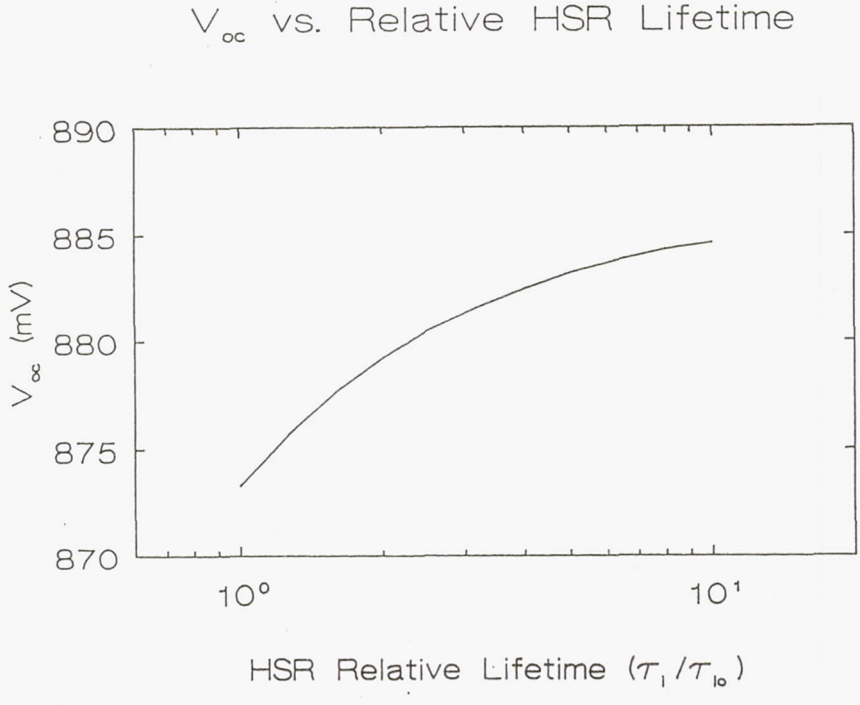

Figure 3

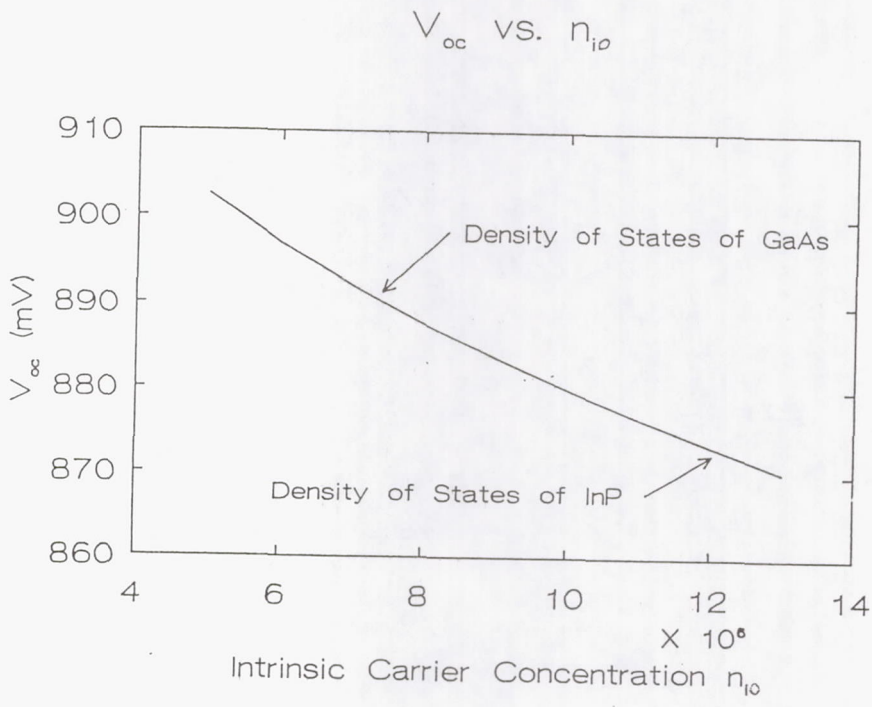

Figure 4

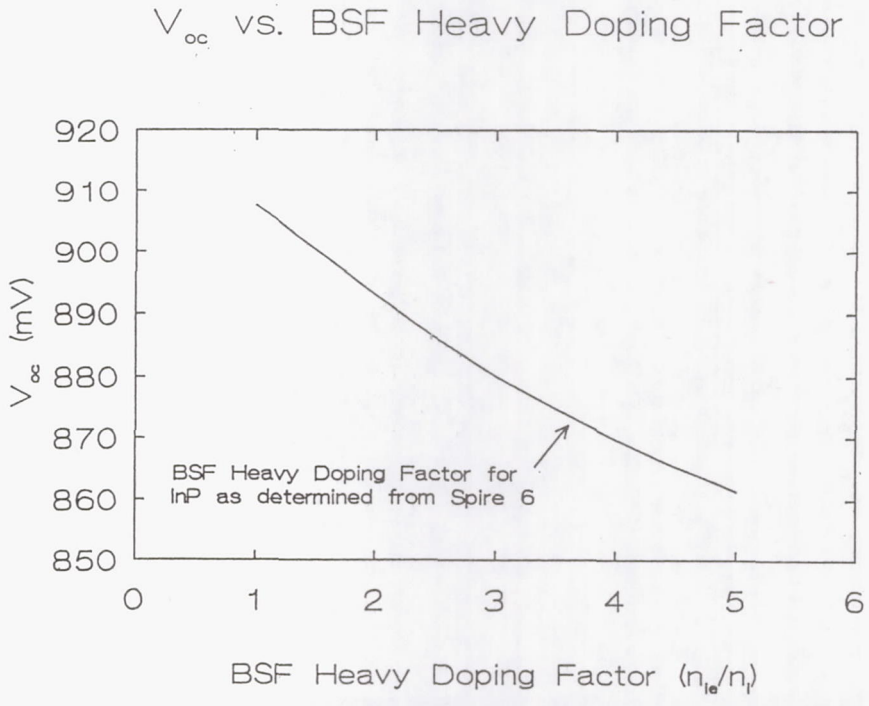

Figure 5

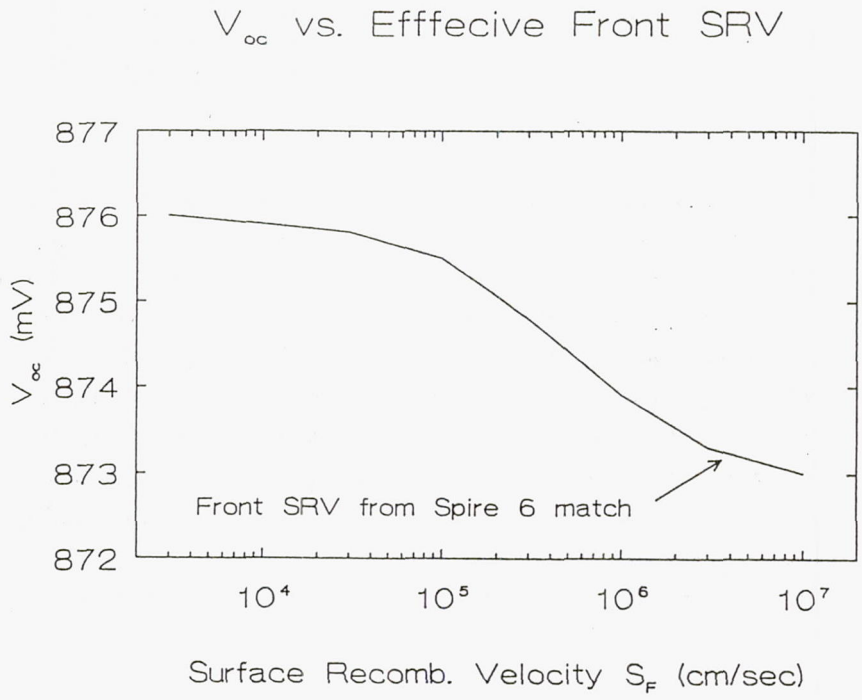
V_{oc} vs. Efffecive Front SRV
877
876
875
874
873
872
V_{oc} (mV)
Front SRV from Spire 6 match
10^4
10^5
10^6
10^7
Surface Recomb. Velocity S_F (cm/sec)

Determination of Series Resistance of Indium Phosphide Solar Cells

R. K. Jain* and I. Weinberg
NASA Lewis Research Center
Cleveland, OH

The series resistance of a solar cell is an important parameter, which must be minimized to achieve high cell efficiencies. The cell series resistance is affected by the starting material, its design and processing. We have used the theoretical approach proposed by Jia, et al, to calculate the series resistance of indium phosphide solar cells. It is observed that the theoretical approach does not predict the series resistance correctly in all cases. We have modified the analysis to include the use of effective junction ideality factor. The calculated results have been compared with the available experimental results on indium phosphide solar cells processed by different techniques. It is found that the use of process dependent junction ideality factor leads to better estimation of series resistance. An accurate comprehensive series resistance model is warranted to give proper feedback for modifying the cell processing from the design state.

Introduction

The series resistance of a solar cell is an important parameter. An accurate knowledge of this parasitic parameter is highly essential for solar cell device processing and modeling. The cell series resistance is affected by the starting material, its design and processing. The series resistance must be minimized to achieve high cell efficiencies. Proper care should be taken to reduce the resistance offered by the front and back metal contacts, diffused and bulk regions of the cell. Though series resistance is an important quantity for solar cells operating at one sun conditions, it becomes very critical for cells working under high intensities of light and for solar cell arrays deployed for space missions near the sun. For these applications series resistance parameter becomes very critical due to large power loss at high currents. With the technological advances made in materials and cell process technologies, it has become possible to minimize the value of solar cell series resistance.

A number of theoretical approaches and experimental techniques are reported in the literature [refs. 1-10] for the determination of series resistance. It would not be possible to discuss the relative merits of various models in the present paper. In the present work we have used the theoretical approach proposed by Jia, et al [ref. 10] to calculate the series resistance of indium phosphide solar cells. Indium phosphide

*This work was done while the author held a National Research Council-NASA LeRC Research Associateship.

solar cells have shown great promise for space use due to their remarkable radiation resistance as compared to silicon and gallium-arsenide cells. A proper understanding of the series resistance of InP solar cells would lead to increased efficiencies.

It is observed that the theoretical approach [ref. 10] does not predict the series resistance correctly in all cases. We have modified the analysis to include the use of effective junction ideality factor. The calculated results have been compared with the available experimental results on indium phosphide solar cells processed by different techniques. It is found tht the use of process dependent junction ideality factor leads to better estimation of series resistance. An accurate comprehensive series resistance model is warranted to give proper feedback for modifying the cell processing from the design state.

Theoretical Approach

Starting with the theoretical I-V relation and under the relevant boundary conditions, the series resistance of a solar cell can be expressed as [ref. 10]:

$$R_s = \frac{V_m(i - I_m)}{I_m(i + I_m)} \qquad [1]$$

where $i = \frac{1}{V_t}(I_{sc} - I_m)[V_{oc} + V_t \ln(1 - I_m/I_{sc})]$
V_t = Thermal Voltage (= kT/q)
V_{oc} = Open – Circuit Voltage
I_{sc} = Short – Circuit Current
V_m = Maximum Power Point Voltage
I_m = Maximum Power Point Current

Calculations and Comparison with Experimental Results

For comparison we have considered the epitaxial base/epitaxial emitter indium phosphide solar cell processed by Spitzer, et al, of Spire Corporation [ref. 11] and measured at NASA Lewis Research Center under simulated AM0 conditions at 25°C. Table I describes the various parameters measured. By substituting the relevant parameter values from Table I into equation [1], the calculated value of the series resistance is 1.715 ohm. This value is in good agreement with the experimentally measured value of 1.748 ohm [ref. 11].

We have tried to calculate the series resistance of a number of solar cells using eq. [1] but it was observed that the calculated results estimate quite high values, which looked unrealistic. For example, we have considered the epitaxial base/ion implanted indium phosphide solar cell processed by Keavney, et al, of Spire Corporation [ref. 12] and measured at NASA Lewis Research Center. This is the best InP cell ever produced in the world to date. Table II describes the various parameters measured.

The eq. [1] gives the value of the series resistance equal to 19.69 ohm. This value is quite high and unrealistic for the best InP solar cell. The measured series resistance value for this cell is 1.06 ohm [ref. 13]. A relook of the Jia, et al's model [ref. 10] showed that the assumption of ideality factor, n equals to unity at V = Voc is not valid for all cases. It is proposed to use effective junction ideality factor, neff in the relation and the i term in eq. [1] modifies to the following

$$i = \frac{1}{V_t}(I_{sc} - I_m)[V_{oc}/n_{eff} + V_t \ln(1 - I_m/I_{sc})] \qquad [2]$$

Now using eq. (1) and modified relation for i as given by eq. [2] it is found that the calculated and measured series resistance values for Table II InP solar cell are in good agreement for n_{eff} equals to 1.46. This value suggests that the effective junction ideality factor is a process dependent parameter. The higher value of neff for the Table II solar cell shows that the ion-implantation for emitter might have generated more damage in the depletion region, as compared to MOCVD grown epitaxial emitter ($n_{eff} = 1$) leading to higher recombination current.

Conclusions

The theoretical approach of Jia, et al, [ref. 10] could determine the value of the solar cell series resistance reasonably well, if proper value of the junction ideality factor at cell open circuit voltage, mentioned in the present work as n_{eff} is known. Inclusion of the effect of recombination in the depletion region would yield a more comprehensive model. Further effort toward a simple and accurate solar cell series resistance modeling are in progress.

References

[1.] M. Wolf and H. Rauschenbach, Adv. Energy Conversion, **3**, 455, 1963.

[2.] R. J. Handy, Solid State Electronics, **10**, 765, 1967.

[3.] W. T. Picciano, Energy Conversion **9**, 1, 1969.

[4.] M. S. Imamura and J. I. Portscheller, *Conf. Record Eighth IEEE PV Specialists Conference*, 102, 1970.

[5.] K. Rajkananj and J. Shewchun, Solid State Electronics, **22**, 193, 1979.

[6.] R. J. Chaffin and G. C. Osburn, Appl. Phys. Lett., **37**, 637, 1980.

[7.] S. K. Agarwal, R. Muralidharan, A. Agarwala, V. K. Tewary and S. C. Jain, J. Phys. D., **14**, 1643, 1981.

[8.] G. L. Araujo and E. Sanchez, IEE Trans. Electron Devices, **ED-29**, 1511, 1982.

[9.] M. A. Hamdy and R. L. Call, Solar Cells, **20**, 119, 1987.

[10.] Q. Jia, W. A. Anderson, E. Liu and S. Zhang, Solar Cells, **25**, 311, 1988.

[11.] M. B. Spitzer, C. J. Keavney, S. M. Vernon and V. E. Haven, Appl. Phys. Lett., **51**, 364, 1987.

[12.] C. J. Keavney and M. B. Spitzer, Appl. Phys. Lett., **52**, 1439, 1988.

[13.] C. J. Keavney, (Private Communication).

Table I. MEASURED PARAMETERS OF EPITAXIAL BASE/EPITAXIAL EMITTER INDIUM PHOSPHIDE SOLAR CELL AT NASA LEWIS RESEARCH CENTER

[AMO, 137.2 mW/cm^2, 25°C, Cell Area 0.25 cm^2]

Short Circuit Current	8.47 mA
Open-Circuit Voltage	868 mV
Maximum Power Point Current	8.19 mA
Maximum Power Point Voltage	751 mV
Maximum Power	6.15 mW
Fill Factor	0.838
Efficiency (Total Area)	17.94%

TABLE II MEASURED PARAMETERS OF EPITAXIAL BASE/IMPLANTED EMITTER INDIUM PHOSPHIDE SOLAR CELL AT NASA LEWIS RESEARCH CENTER

[AMO, 137.2 mW/cm^2, 25°C, Cell Area 0.25 cm^2]

Short Circuit Current	8.93 mA
Open Circuit Voltage	873 mV
Maximum Power Point Current	8.50 mA
Maximum Power Point Voltage	760 mV
Maximum Power	6.46 mW
Fill Factor	0.829
Efficiency (Total Area)	18.84 %

Investigation of Anodic and Chemical Oxides Grown on p-type InP with Applications to Surface Passivation for n^+–p Solar Cell Fabrication

Maria Faur, Mircea Faur, Manju Goradia and Chandra Goradia
*Space Photovoltaic Research Center**
Electrical Engineering Department
Cleveland State University
Cleveland, OH

Phillip Jenkins, Douglas Jayne and Irving Weinberg
NASA Lewis Research Center
Cleveland OH

Introduction

Most of the previously reported InP anodic oxides were grown on n-type InP with applications to fabrication of MISFET structures [refs. 1-3] and have been described as a mixture of In_20_3 and P_20_5 stoichiometric compounds [refs. 4-5] or nonstoichiometric phases which have properties similar to crystalline compounds $In(OH)_3$, $InPO_4$, and $In(P0_3)_3$ [refs. 1,3]. Details of the compositional change of the anodic oxides grown under different anodization conditions have been previously reported [ref. 6]. Here we investigate the use of P-rich oxides grown either by anodic or chemical oxidation for surface passivation of p-type InP and as a protective cap during junction formation by closed-ampoule sulfur diffusion. The investigation is based on but not limited to correlations between PL intensity and XPS chemical composition data.

Experimental

The (100) InP substrates used in this study were p-type Cd-doped to a concentration of 1.7E16cm^{-3}, and Zn-doped to 2.6E16 and 1.2E18cm^{-3}. The as-received 2-inch diameter Crystacomm, Inc. and Nippon Mining, Inc. wafers were cut into suitable size substrates. Prior to anodic or chemical oxidation, the substrates underwent a standard degreasing procedure by sequential light boiling in trichloroethylene, acetone and methanol, followed by the removal of about 10μm from the surface in Br_2-methanol (0.5% Br_2) solution and, finally, native oxide removal in 10% HF solution, just prior to oxidation.

*Funded by NASA Lewis Research Center

Anodic oxides, 15 to 90 nm thick, have been grown in o – H_3P0_4 : H_20 : ACN solutions under no illumination (dark), low intensity (about 40 mW/cm^2), and strong illumination conditions (about 100 mW/cm^2), at room temperature and constant current density (J_c) of 0.1 to 1 mA/cm^2. The oxide thickness was measured via a Dektak profilometer prior to and after oxide dehydration in vacuum or pure hydrogen at temperatures from 150 to 300°C for 10 minutes to 1 hour. Other previously reported electolytes for InP and GaAs oxidation [refs. 2,5,7] were also examined but they proved to be unsatisfactory in terms of oxide uniformity, stability, or contamination level.

Chemical oxides have been grown in 15% $HN0_3$ solution under strong illumination and a bath temperature of about 60°C.

n^+-p junctions have been formed in Cd- and Zn-doped InP substrates by an evacuated closed ampoule diffusion of sulfur through anodic or chemical oxide cap layers. Thermal diffusion was done for 3 hours at several temperatures in the range of 615°C to 675°C.

The composition of the oxide layers was determined prior to and after sulfur diffusion. This was done by XPS analysis of the two parts of the same substrate, one of which was sulfur diffused. XPS spectra were taken and analyzed using VG MKII ESCALAB with VGS 5000 Plus enchanced data processing software. Depth profiles were done using a VG AG60 differentially pumped ion gun with an argon ion beam of 5 mA emission current at 2.5 keV.

PL intensity and its time-dependent behavior data correlated the level of surface passivation to different processing steps (i.e. surface preparation, annealing) and to the oxide composition profiles obtained from the XPS data. The PL intensity data have been measured at room temperature with the 514 nm line of an Ar^+ laser of 1 W/cm^2 power density.

Anodic and Chemical Oxides

Investigation of the oxides grown in various electrolytes at different viscosity, pH, constant current density, and illumination level values have indicated that the depth profiles of the anodic oxides are strongly dependent upon the growth conditions [ref. 6]. The anodic oxide on p-type InP appears complex, and depending on the growth parameters, the presence of $In(OH)_3$, In_20_3, $InPO_4$, $In(P0_3)_3$, $In(P0_3)_4$ and other nonstoichiometric InP_xO_y compounds have been identified.

In general, there is an In-rich oxide at the surface and a P-rich oxide at the interface and their composition varies as a function of anodization conditions. As an example, the effect of variation in current density on the oxide depth profile is shown in Figures 1 and 2. The two oxides were grown under similar conditions in an electrolyte of 0.5% o – H_3P0_4 mixed with acetonitrile (4:6 vol. ratio), under dark,

but the current densities were 0.25 and 0.6 mA/cm^2, respectively. Both oxides were grown while the sample voltage was increasing with time, i.e., in that region where the growth rate is the predominant process as compared to the disolution rate. Although not shown here, the oxide grown at 0.25 mA/cm^2 is made up of a surface layer of $In(OH)_3$ and $InPO_4$, an inner layer of $In_x(PO_3)_y$, and an interfacial layer of $In(PO_3)_4$. The oxide grown at 0.6 mA/cm^2 has a surface layer of $InPO_4$, an inner-layer of In_20_3 and an interfacial layer of a mixture of nonstoichiometric InP_xO_y polyphosphates rich in $In(P0_3)_3$.

P-rich interfacial oxide components are of interest for surface passivation of InP as we are going to see in the next section. Anodization parameters appear to control the thickness and composition of this P-rich interfacial layer, as mentioned. The parameter which seems to control the composition of this layer to the largest extent is the illumination level. Under dark conditions at 0.6 mA/cm^2 current density, a thin $In(P0_3)_3$-rich layer is formed at the interface as mentioned above. Under low illumination, for oxide grown under otherwise identical conditions, the interfacial P-rich oxide layer is made up of $In_x(P0_3)_y$ and $In(PO_3)_4$ compounds as shown in Figures 3a and b.

Under strong illumination the front oxide layer was a mixture of $In(OH)_3$, $InPO_4$ and In_2O_3. The $In3d_{5/2}$ and O1s lines indicated a higher concentration of In_2O_3 in the inner layer as compared to the low illumination case. P-rich interfacial layer, however, was made up of a thinner $In_x(PO_3)_y$ and a thicker $In(PO_3)_4$ layers, as compared to the oxide described above. The $In3d_{5/2}$, $P_{0X}2p$, $P_{bulk}2p$, and O1s depth profiles presented in Figure 4a have been recorded for an anodic oxide grown under strong illumination, after two consecutive oxidation-removal of the front In-rich oxide layer, and finally regrowing the oxide under the above mentioned conditions. As seen in Figure 4b, which represents the P2p spectra, the oxide of about 18nm thick still showed a layered structure with a surface layer consisting of $In(PO_3)_3$, and an interfacial layer of $In(PO_3)_4$. No indication of $In(OH)_3$, In_2O_3, or $InPO_4$ formation could be found from the $In3d_{5/2}$, P2p, and O1s photoelectron binding energies. However, the Auger kinetic energy for In indicated the existence of a very low intensity line of 405.55 eV, which suggests that a low concentration of $In(OH)_3$ still exists at the surface.

The chemical oxide was grown in 15% HNO_3 solution under strong illumination, and a bath temperature of about 60°C. As previously reported for the case of n-type InP oxidation [ref. 1], the chemical oxide is homogeneous in depth and it is an $In(PO_3)_3$-rich polyphosphate. However, in the case of p-type InP which we report on here, the thickness of the oxide layer appear to be limited to less than 40Å , as opposed to n-type substrates, in which case the oxide thickness can be larger than 100 nm.

Surface Passivation

Based on previously reported information on insulators formed on InP (e.g. as gate insulator for MISFET's) [refs. 2,8], the ideal insulator to be used as a cap in view of application to surface passivation and solar cell fabrication, should have the following bulk and interfacial properties:

a) It should have good physical and chemical stability. This means that the cap should adhere well to the substrate, be insensitive to environmental effects such as moisture, and gas absorption, be relatively scratch resistant, and be compatible with semi-conductor processing steps, e.g., masking, etching, diffusion, annealing, AR coating, and metallization.

b) It should act as a preferential diffusion barrier. In this case, it implies that the cap layer should allow in-diffusion but prevent the In and P out-diffusion.

c) It should reduce or eliminate initial surface defects and interface roughness. This means that the oxide growth should occur by the consumption of the underlying InP substrate.

d) It should exhibit a low density of interface states. This means that a minimum of unsaturated bonds should remain at the semiconductor-oxide interface.

e) It should have good dielectric properties, such as a wide energy bandgap, high resistivity, and a low density of defects.

A well established characteristic of the InP surface is that near midgap the density of surface states depends strongly on the surface preparation procedure prior to insulator deposition. Hence, a combination of an appropriate surface chemical treatment and a P-rich oxide layer, should result in low density of states throughout the bandgap.

Different chemical surface treatments have been tried in this study, and a correlation is being made between the PL intensity (PLI) and the XPS chemical composition. Figure 5 shows the time-dependent PLI of ptype substrates after different chemical treatments as compared to the "bare" substrate. A large PLI enhancement is observed for surfaces treated in HF and HNO_3 solutions as compared to the "bare" surface, and the surfaces treated in o – H_3PO_4 and H_2SO_4 solutions. The changes in surface chemistry as a function of dlfferent chemical treatments as revealed by XPS data [ref. 9] have shown that phosphorus enriched surfaces are responsible for the PLI enhancement. The passivating properties of P-rich surfaces is consistent with the prevailing concept that P-enriched surfaces eliminate P vacancies that produce a large density of states near the conduction band edge.

Figure 6 shows steady state PLI before and after annealing in hydrogen of p-type substrates exposed to different chemical treatments, as compared to those with anodic oxides grown under different illumination conditions. The enhancement of

PLI observed in the case of oxidized substrates could indicate that the interface has a low density of surface states due, probably, to the structural compatibility between the oxide layer and InP substrate. We believe that the PLI enhancement as a result of annealing in hydrogen is due to passivation of the intergrain-defects and grain boundary defects in the bulk nonstoichiometric oxide layers and at the oxide-InP interface.

In order to identify the best candidate for the use as a passivating cap layer, we are presently investigating the physical, chemical and optoelectronic properties of the P-rich layers grown under different anodization conditions. As an example, Figure 7 shows the time-dependent PLI for Cd-doped substrates with anodic oxides grown in two different solutions under similar anodization conditions. The XPS compositional data, not shown here, reveal that the anodic oxide in the case of G10 sample, has a thin In-rich outer-layer and the thicker P-rich interfacial layer is mainly made up of $In(PO_3)_3$. In the case of CP series, the oxides have a thicker In-rich surface layer and a thin mixture of $In(PO_3)_3$ and $In(PO_3)_4$ interfacial layer. It is believed that the large enhancement of the PLI in the case of "G10" sample is due to the formation of $In(PO_3)_3$ at the interface, which has a lower bulk defect density and a lower density of interface defects. On the other hand, In-rich surface layers have been previously identified to be the cause of the high density of interface states [refs. 2,10]. From the large enhancement of PLI as a result of removing the In-rich surface oxide layer, as seen in Figure 8, it is apparent that this is the case. It has been assumed [ref. 11] that the donor states which have been found to appear near the InP conduction band minimum as a result of oxidation are associated with indium surface oxides rather than with P vacancies or other native defects.

Junction Formation

As mentioned before, n^+-p junctions have been formed in Cd- and Zn-doped p-type substrates by closed-ampoule diffusion of sulfur through P-rich anodic or chemical cap layers. Thick anodic oxides grown in dark conditions appear to be stable at diffusion temperatures of up to 620°C, except for the In-rich surface oxide layers. An example is shown in Figure 9, which represents the $In3d_{5/2}$, P2p, S2p, and O1s depth profiles after S diffusion at a temperature of 620°C for 3 hours, through the anodic oxide of Fig. 2. It appears that the compounds of the In-O system, i.e. $In(OH)_3$ and In_2O_3, are entirely replaced by compounds of the In-S system, i.e., In_2S_3, InS, or In_6S_7. The front oxide layer appears to be rich in $InPO_4$, and InP_xO_y nonstoichiometric compounds are found at the interface. After a 3 hour diffusion at 650°C, through an oxide similar to that of Fig. 3, the front In-rich oxide decomposed completely, as seen in Figure 10. A thin nP_xO_y oxide layer, less than 60Å thick can still be found at the surface.

Further, closed ampoule diffusion of sulfur was performed through thin (less than 200Å thick) anodic and chemical P-rich oxide cap layers. The P-rich oxides appear

stable even after 3 hours diffusion at 660°C. The surface topography of the S diffused Zn- and Cd-doped substrates through P-rich chemical oxide (about 40Å thick) can be seen in Figure 11. As seen, In_xS_y droplets [ref. 12] accumulate at the oxide-n InP interface at the etch pit areas. In the case of diffusion into Cd-doped substrates the droplets density is about one order of magnitude less than that for Zn-doped ones, indicative of a lower rate of new dislocations introduced by S diffusion in Cd-doped materials [ref. 13].

The histogram in Figure 12 shows the initial and steady state PLI values after S-diffusion into Cd-doped (NPDC) and Zn-doped (NPDZ and FPDZ) substrates for 3 hours at 660°C. The three sets of data in each case were taken after the post-diffusion surface preparation [ref. 11], followed by 5 minutes chemical treatment in 10% HF solution, and finally after annealing in pure H_2 (about 2 atm.), at 275°C for 30 minutes. The differences between the values of PLI in the case of the two structures (NPDZ and NPDC) diffused through a thin P-rich chemical oxide, as compared to the structure diffused through a clean surface (FPDZ), we assumed to be mainly due to recombination centers introduced in the i) front oxide layer and ii) In_xS_y droplets accumulation at the defect areas, rather than V_P or V_{In} vacancies-type defects introduced in the front n^+ layer. This assumption, however, seems to be in disagreement with the differences observed in the PLI values in the case of NPDZ and NPDC structures, since the droplet density in the case of Cd-doped substrates is smaller than that of Zn-doped ones. However, the differences observed in the surface donor density, S diffusion profiles and diffusion depths, in the case of Zn and Cd substrates [ref. 13], should also be taken into account.

Solar Cell Fabrication

Small area (0.48 cm^2) n^+-p InP solar cells have been fabricated on structures diffused through either anodic or chemical oxides, and performance data have been compared with those of solar cells fabricated on structures diffused through clean surfaces. However, no solar cells have been fabricated to date on structures diffused through P-rich oxide cap layers grown under strong illumination (see Fig. 4), which have proven to be stable even at diffusion temperature of 660°C, and which are expected to perform better. Furthermore, the design and fabrication of contacts and AR coating have not been optimized in this work. These aspects are vital to optimal cell performance and good design is essential if unambiguous analytical information is to be obtained from the performance parameters. Therefore, for now, only qualitative information is given from an analysis of these solar cell parameters.

The best overall solar cell parameters were obtained in the case of cells fabricated on structures diffused for 3 hours at 640 to 660°C, through 150 to 250Å thick anodic oxides grown in dark or low illumination. In these cases, the In-rich surface components have been removed prior to diffusion. For these cells AM0, 25°C efficiencies of over 12.5% have been obtained as compared to solar cells fabricated on structures

diffused through as-grown oxides which showed efficiencies of 9 to 11%. The limiting parameter here was Voc, i.e., a maximum value of 760 mV, as compared to values of up to 812 mV for the former cells.

Solar cells fabricated on structures diffused for 3 hours at 660°C through chemical oxide cap layers (about 40Å thick) gave a best AM0 efficiency of 12.6%.

Efficiencies of solar cells fabricated under similar conditions on structures diffused through clean surfaces, gave a best efficiency of 12.1%. In general, cells fabricated on structures diffused through thin oxide layers, gave a slightly higher V_{oc}, higher I_{sc}, and a slightly smaller FF, associated with higher series resistance, as compared to those fabricated on substrates diffused through clean surfaces.

Suggestions for Further Research and Conclusions

Thin P-rich anodic and chemical oxide cap layers have proven to be stable during the close-ampoule diffusion of sulfur at temperatures of up to 660°C. An experiment was done to see if these cap layers can be used for the formation of n^+-p or p^+-n InP structures in an open tube system. In-rich oxide (about 900Å thick) and P-rich oxide (about 150Å thick), have been grown on the same substrate. The surface topography of this surfaces as compared to a clean area, after 1 hour heat treatment in air at 660°C, is shown in Figure 13. As seen, the P-rich oxide is relatively smooth, while large bubbles appeared on the surface with In-rich oxide (inside circle), and on the initially clean area. The bubble formation have previously been reported in the case of thermal oxides on InP grown in dry O_2 at temperatures above 600°C [ref. 14]. The bubbles indicate that the In-rich oxide has softened and has then been pushed away from the InP surface by pressure from beneath the oxide. In the case of the clean surface, the P vapor, which is believed to provide this pressure, breaks the smaller bubbles which form below the thin growing thermal oxide.

This experiment indicates that P-rich oxides could be used as caps during n^+-p or p^+-n InP junction formation in an open tube system. Due to the fact that $In(PO_3)_3$ acts as a good diffusion barrier [ref. 12], we anticipate that the use of P-rich cap layers could be especially beneficial for an open-tube p^+-n InP junction formation. In this case, the passivating P-rich cap not only protects the surface during diffusion, but can also control the depth of acceptor diffusion so as to permit the formation of shallow p^+-n junctions, required for the fabrication of high efficiency solar cells.

Due to the fact that the diffusion temperatures, and time required to form p^+-n InP structures is significantly lower than those in the case of n^+-p junction formation, we anticipate that In accumulation at the defect areas, which we believe introduces a large number of recombination centers, does not occur. Hence, the P-rich cap layer, in this case, could be used as the first layer AR coating in a double or triple layered structure. For the use as a first layer AR coating, $In(PO_3)_3$ has good dielectric properties; that is, a wide bandgap of 6.8 eV [ref. 2], and a resistivity of $10^{13}\Omega$-cm

[ref. 3]. Furthermore, we speculate that a suitable match can be realized with a second layer AR coating material such as MgF_2, both in terms of optimum optical coupling, and a low interface states density.

In conclusion, it appears that P-rich anodic or chemical oxides grown on p-type InP are good candidates for surface passivation, and as protective caps during thermal diffusion. However, more experimental studies are required to understand the complex oxidation process of InP, and to clarify the structural and chemical composition of these oxides as a result of different oxidation conditions and post-oxidation treatments. Further experimental insights on the chemistry of complex systems such as In-P-O-S-Cd(Zn) under various diffusion conditions are needed before designing higher-performance solar cells by this method of junction formation.

References

[1.] G. Hollinger, E. Bergignat, J. Joseph and Y. Robach, J. Vac. Sci. Technol. **A3**, 2082, 1985.

[2.] G. Hollinger, J. Joseph, Y. Robach, E. Bergignat, B. Commere, P. Viktorovitch and M. Froment, J. Vac. Sci. Technol. **B5**, 1108, 1987.

[3.] J. Joseph, Y. Robach, G. Hollinger, P. Ferret and M. Pitaval, *1st. Int. Conf. on InP and Related Materials for Advanced Electronic and Optical Devices*, 1989.

[4.] C. W. Wilmsen, J. Vac. Sci. Technol. **19**, 279, 1981.

[5.] A. Yamamoto, M. Yamaguchi, and C. Uemura, J. Electrochem. Soc.: Solid-State Science and Technology **129**, 2795, 1982.

[6.] Maria Faur, Mircea Faur, Manju Goradia, Chandra Goradia, Douglas Jayne, Navid Fatemi, David J. Brinker, *11th Symposium on Applied Surface Analysis*, 1989. To be published in "Surface and Interface Analysis".

[7.] C. W. Wilmsen and R. W. Kee, J. Vac. Sci. Technol. **14**, 953 1977.

[8.] "Physics and Chemistry of III-V Compound Semiconductor Interfaces", ed. by C. W. Wilmsen, Plenum Press, New York, 1985.

[9.] Maria Faur, Mircea Faur, Manju Goradia, Chandra Goradia, Phillip Jenkins, Douglas Jayne, Sheila Bailey, Irving Weinberg, Extended Abstract submitted for the 2lst IEEE, PVSC, Orlando, Florida, 1990.

[10.] J. F. Wager, Appl. Phys. Lett., **42**, 589, 1983.

[11.] K. A. Bertness, T. Kendelewicz, R. S. List, M. D. Williams, L. Lindan and W. E. Spicer, J. Vac. Sci. Technol. **A4**, 1424, 1986.

[12.] Maria Faur, Mircea Faur, Manju Goradia, Chandra Goradia, D. Jayne, F. Honecy and I. Weinberg, *1st Int. Conf. on InP and Related Materials for Advanced Electronic and Optical Devices*, in press, 1989.

[13.] Mircea Faur, Maria Faur, Chandra Goradia, Manju Goradia, Ralph D. Thomas, David J. Brinker, Navid Fatemi and Frank Honecy, this conference.

[14.] J. J. McLaren, A. Nelson, K. Geib, R. Gann, and C. W. Wilmsen, J. Vac. Sci. Technol. **A1**, 1486 1983.

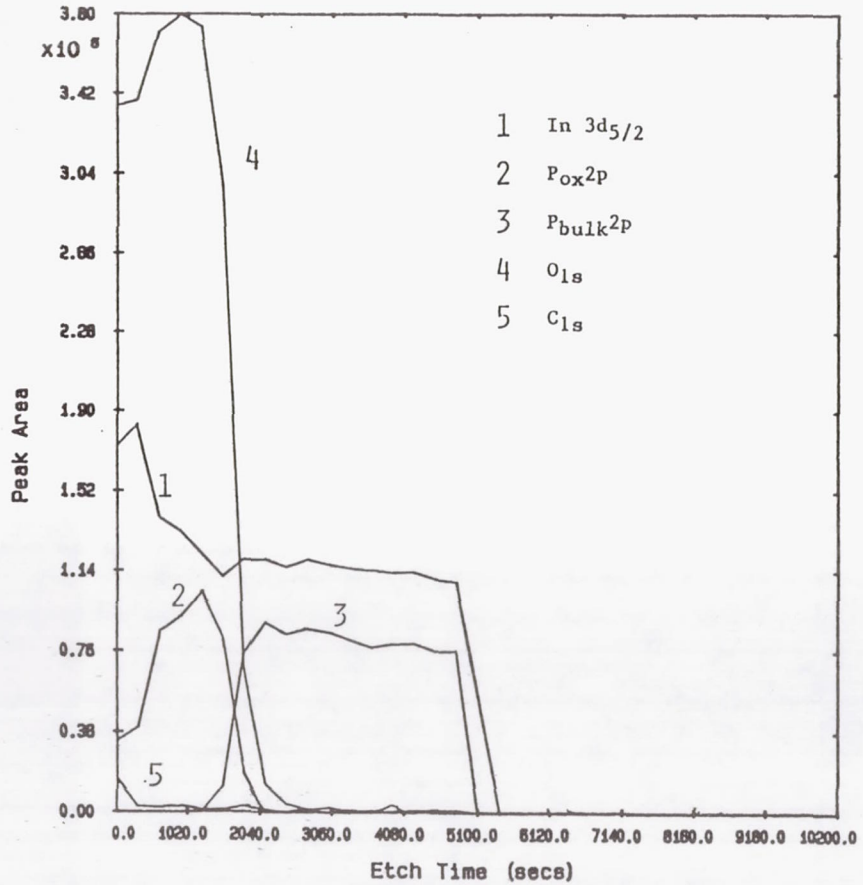

Figure 1. XPS depth profiles of an anodic oxide (about 50nm thick) grown in an O-H_3PO_4:H_2O:ACN (1:200:300) electrolyte under dark conditions at a constant current density (J_c) of 0.25 mA/cm^2 on Cd-doped InP substrate.

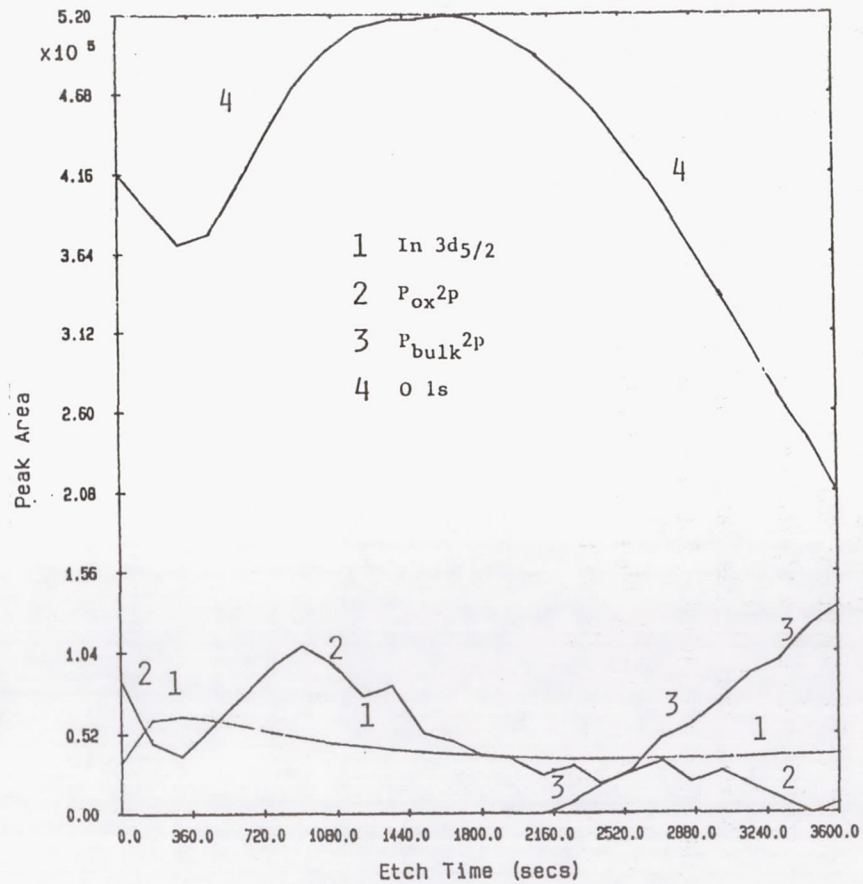

Figure 2. XPS depth profiles (about 90nm thick) grown in similar conditions as indicated in Fig. 1, but at J_c = 0.6 mA/cm^2

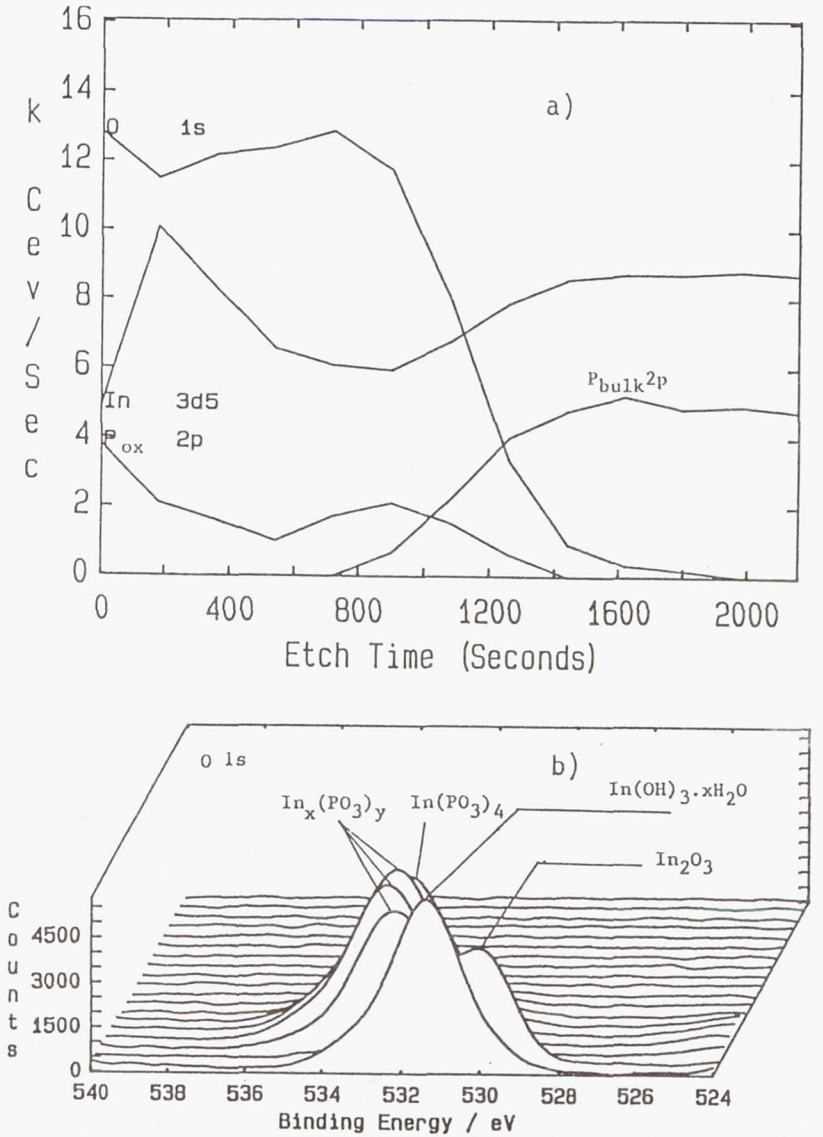

Figure 3. XPS profiles of an anodic oxide (about 30nm thick) grown in O-H_3PO_4:H_2O:ACN (0.1:10:100) under low illumination (about 40 mW/cm^2) at J_c = 0.6 mA/cm^2. a) depth profiles; b) O_{1s} spectra for 23 depths with 180 secs. cyclic sputtering (about 30 Å material removed) and analysis.

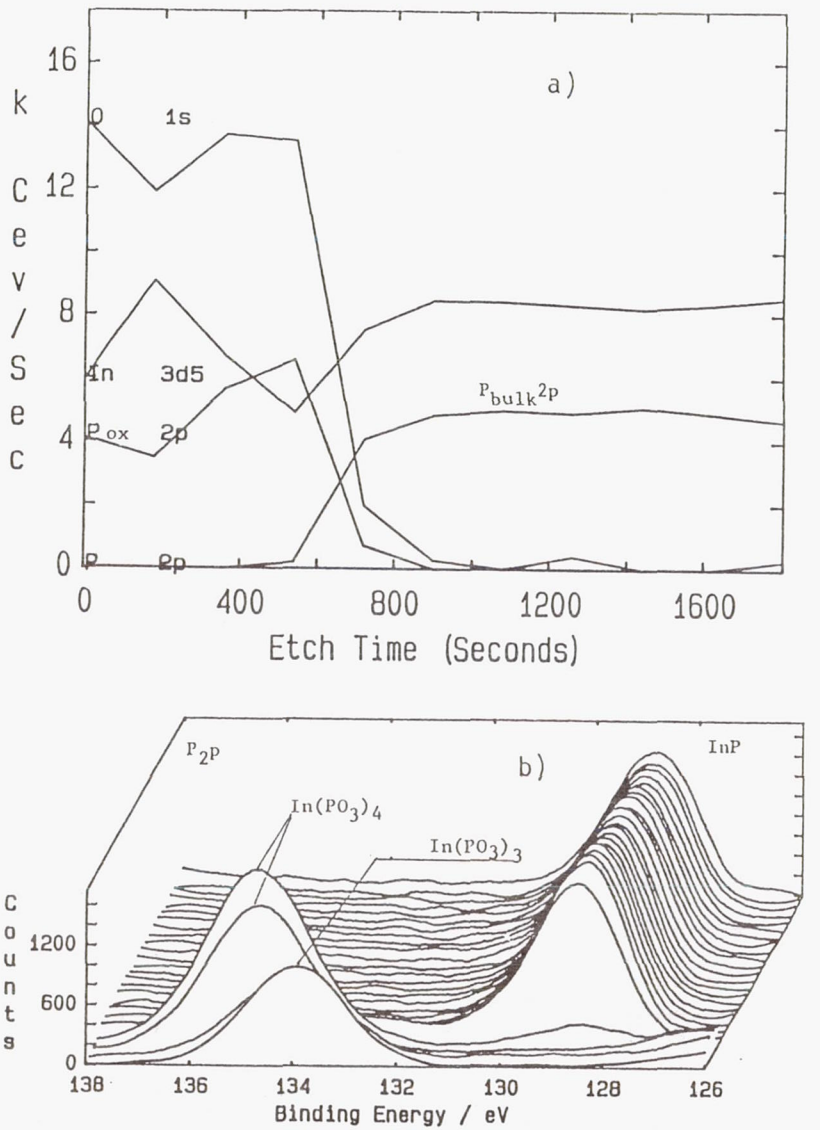

Figure 4. XPS profiles of a P-rich anodic oxide (about 18nm thick) grown in conditions in Fig. 3, but under strong illumination (about 100 mW/cm^2). a) depth profiles; b) P_{2p} spectra after 30 cycles of 180 secs. sputtering and analysis.

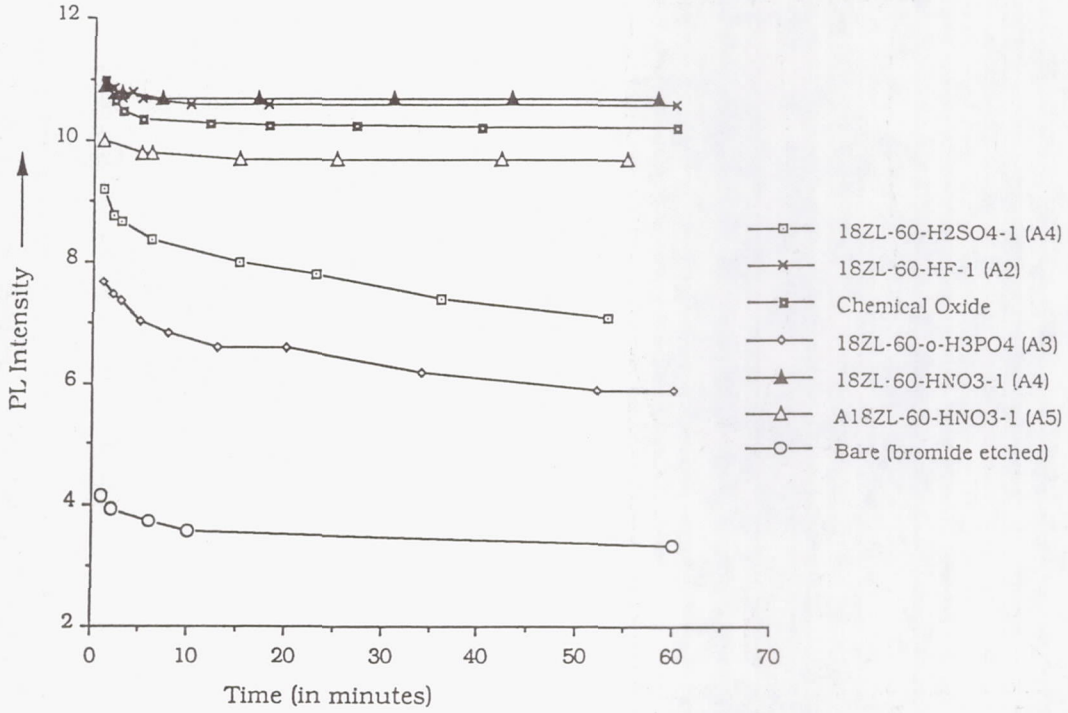

Figure 5. Time dependent PL intensity of p-type InP (Zn-doped to 1.2E18 cm^{-3}) exposed to different etching solutions (15% vol. ratio) at 60°C under strong illumination as compared to the "bare" surface. The chemical treatment was done on degreased surfaces, and after removal of about 10μm layer ("bare" surface) in Br_2-methanol (0.5% Br_2) solution. A5 refers to A4 after annealing in H_2(P ≈ 1,000 torr) at 275°C for 30 min.

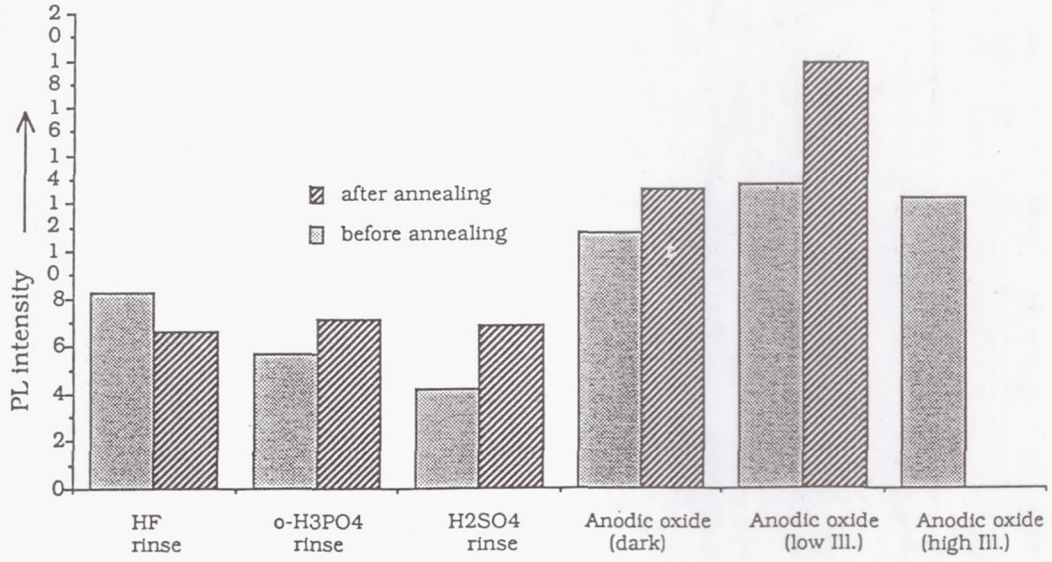

Figure 6. Steady-State PL intensity data after chemical treatment as compared with anodic oxides grown in O-H_3PO_4:H_2O:ACN (1:10:100) solution at constant current density of 1 mA/cm^2 in dark and illumination conditions. Same substrates, chemical treatment and H_2 annealing conditions as described in Fig. 5 have been used.

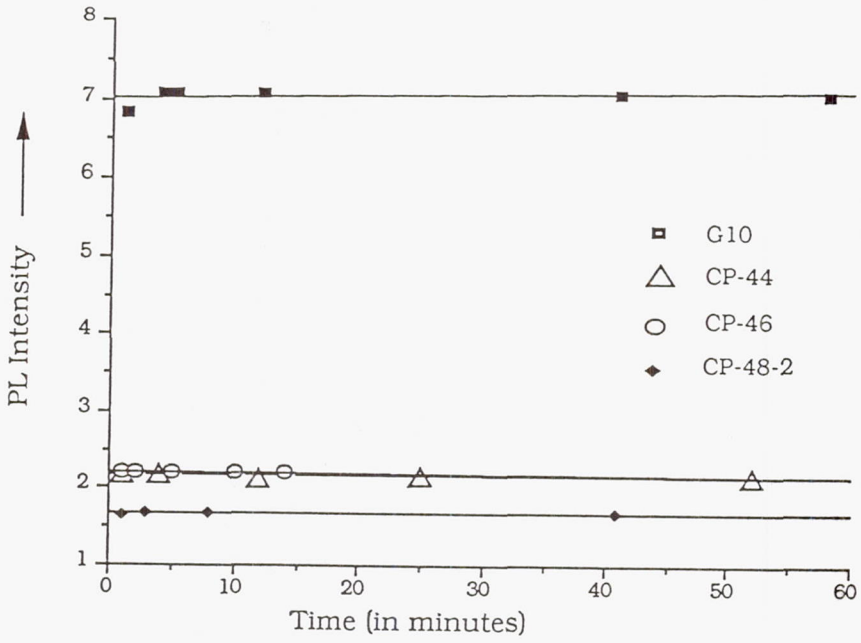

Figure 7. Time dependent PLI of Cd-doped substrates with as-grown anodic oxides. "CP"-series have oxides grown under conditions described in Fig. 2. G10 is grown in 3% citric acid in etylene glycol (1:3) under strong illumination.

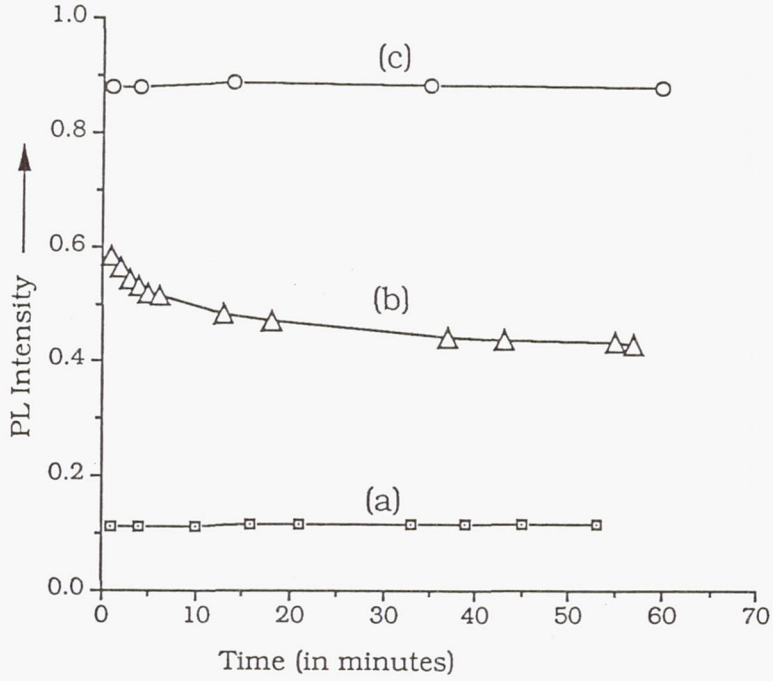

Figure 8. Time-dependent PLI for an anodic oxide grown on Zn-doped (2.6E16cm^2) InP substrates in same conditions as in Fig. 4. a) as grown; b) after annealing the as-grown oxide in H_2 at 275°C for 30 min.; c) after removing the In-rich surface oxide layer (prior to annealing).

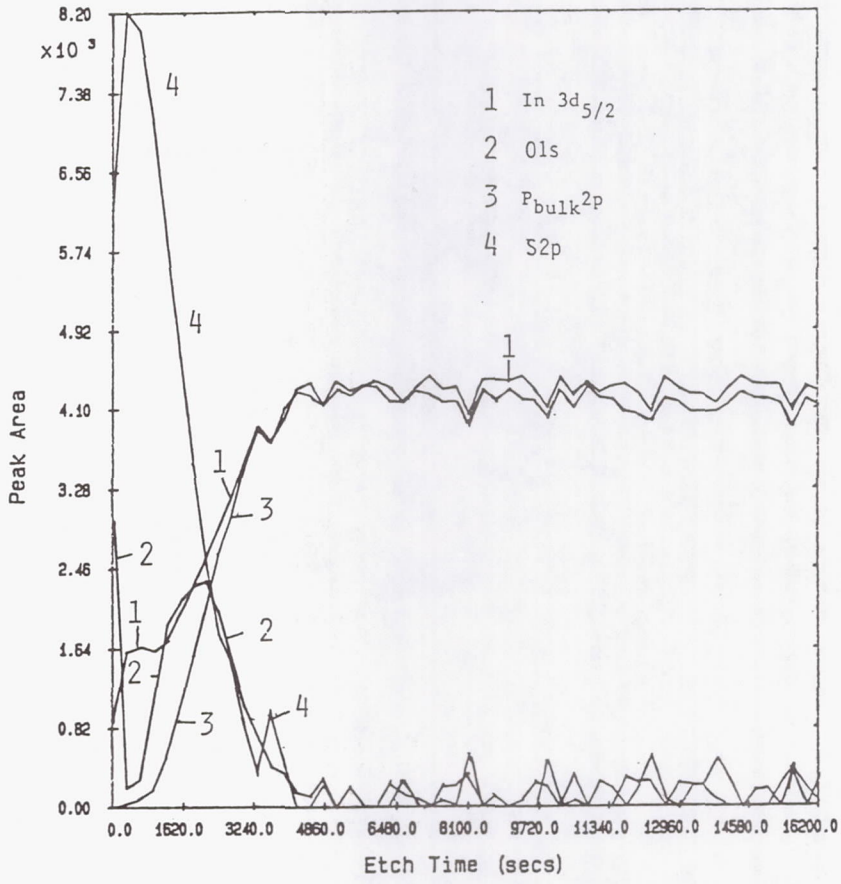

Figure 9. XPS depth profiles of a n^+-p InP structure, S-diffused for 3 hours at 620°C through an anodic oxide as shown in Fig. 2.

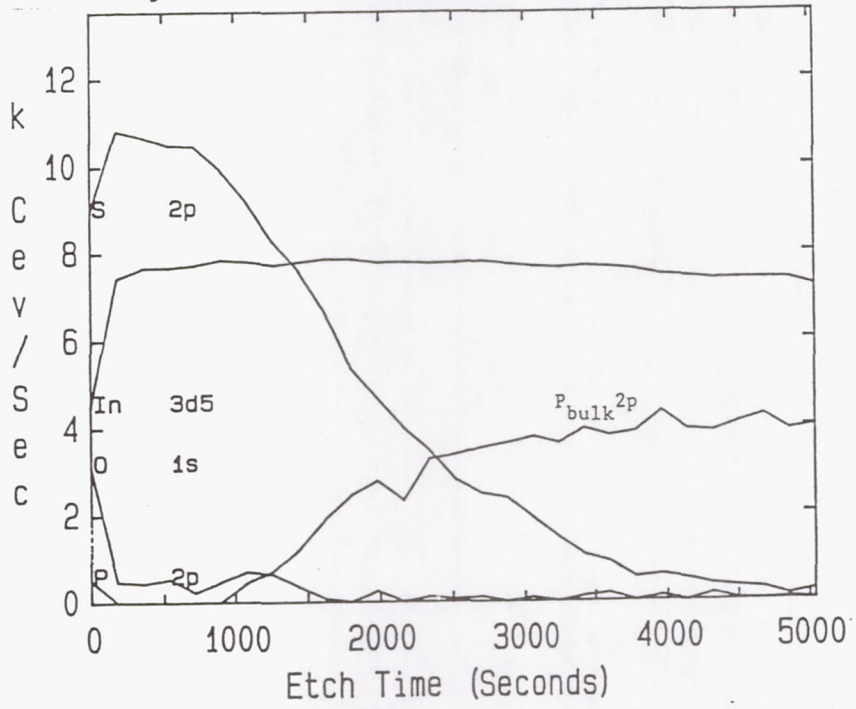

Figure 10. XPS depth profiles of a n^+-p InP structure, S-diffused for 3 hours at 650 °C through an anodic oxide similar to that presented in Fig. 3.

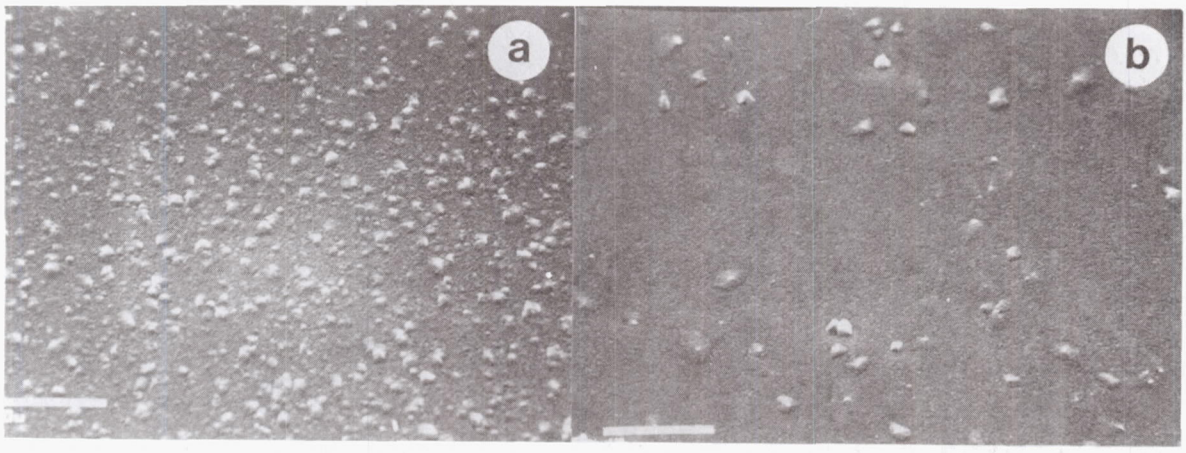

Figure 11. Surface topography after 3 hours S diffusion through a P-rich chemical oxide (about 4nm thick) into a) Zn-doped, and b) Cd-doped substrates.

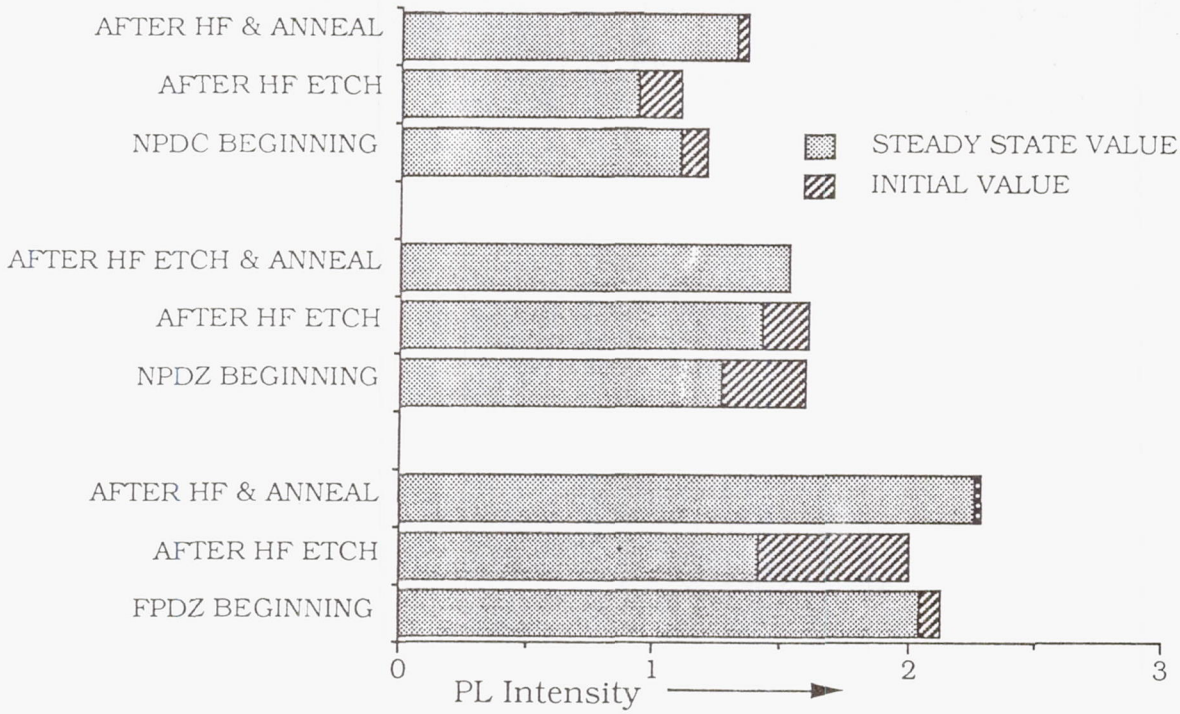

Figure 12. PLI data after S-diffusion into Cd-doped (NPDC) and Zn-doped (NPDZ and FPDZ) substrates for 3 hours at 660°C. FPDZ refers to a pre-diffusion chemical treatment as "A_2" in Fig. 5. NPDZ and NPDC refers to diffusion through a thin P-rich chemical oxide grown as "A_4" in Fig. 5.

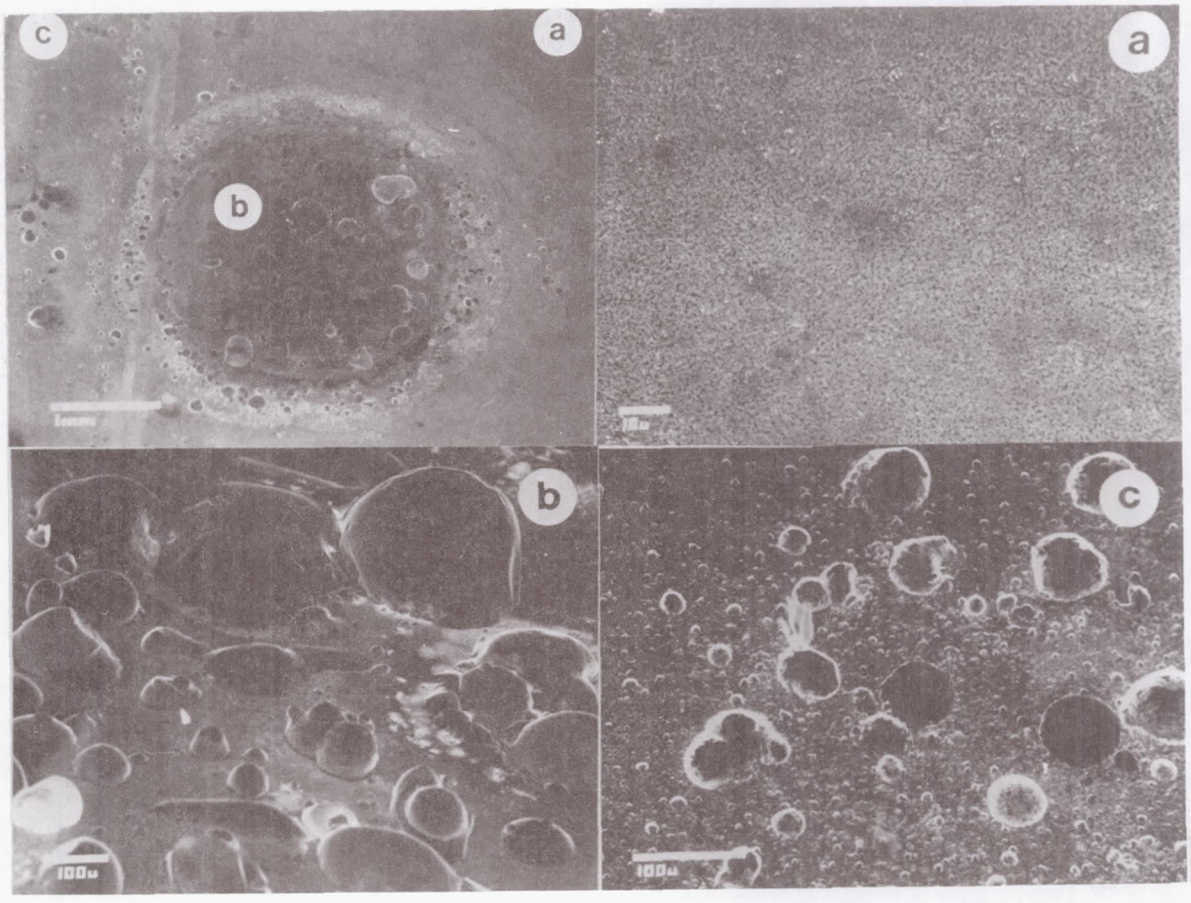

Figure 13. Surface topography of a) P-rich, b) In-rich and c) clean surface after 1 hour heat treatment in air at 660°C.

A Comparative Study of Performance Parameters of n^+-p InP Solar Cells Made by Closed-Ampoule Sulfur Diffusion into Cd- and Zn-Doped p-type InP Substrates

Mircea Faur, Maria Faur, Chandra Goradia and Manju Goradia
*Space Photovoltaic Research Center**
Electrical Engineering Department
Cleveland State University,
Cleveland, OH

Ralph D. Thomas, David J. Brinker, Navid Fatemi** and Frank Honecy
NASA Lewis Research Center
Cleveland OH

Introduction

In previous works [refs. 1,2], we reported a detailed analysis of the InP surface and diffused emitter region of n^+-p InP structures made by thermal diffusion of sulfur into Cd-doped InP substrates. A best 1AM0, 25° efficiency of 14.35% on unoptimized solar cells was obtained. Here we report a comparative study of performance parameters of identically fabricated n+-p InP solar cells made on Cd- and Zn-doped InP substrates with comparable doping and etch pit density. The basic mechanisms which limit the performances of solar cells fabricated on Zn- as compared to Cd-doped substrates are investigated based on structural, compositional and carrier concentration changes in the complex systems In-P-S-O-Zn(Cd) as a result of S diffusion into p-type substrates. Understanding the effects of heat treatment and S diffusion conditions on the above mentioned changes in In-P-S-O-Zn(Cd) systems are essential both in terms of choosing the right substrate, and for optimizing the fabrication steps of n^+-p InP solar cells. The behavior of different species as a result of different processing steps are the key factor to be considered for a better understanding of such complex systems and for a better control of device properties and fabrication. Different diffusing species, e.g. Zn, Cd, S, P, In, on which we report here, have been reported to behave differently in InP and little concensus concerning their diffusion mechanisms and variation with diffusion conditions can be found.

Unlike the relatively large number of papers reporting on acceptor diffusion behavior - especially Zn [refs. 3-6] and, more recently, Cd [refs. 7-9] in InP, very limited information exists on donor behavior, i.e., S diffusion in relation to the other components of In-P-O-S-Cd(Zn) systems. A preliminary investigation of the behavior of such systems under various heat treatment and diffusion conditions, have enabled us 1) to explain the differences in performances of solar cells made on Zn-and Cd-doped

*Funded by NASA Lewis Research Center
**Sverdrup Technology, Inc., Lewis Research Center Group

substrates, and 2) to gather new data on Cd, Zn and S diffusion mechanisms in InP for optimizing the closed ampoule diffusion of sulfur into p-type InP. Part of the results of this study are reported here.

Experimental

A closed-ampoule technique was used to fabricate n^+-p structures by thermal diffusion of sulphur into p-type InP substrates. The surface preparation prior to diffusion, closed-ampoule diffusion environment and conditions, and post-diffusion preparation procedures have been previously reported [ref. 1]. The substrates used were Czochralski (LEC) grown Cd-and Zn-doped from Crystacomm, Inc. and Nippon Mining Co. The doping, etch pit density, and other characteristics of these materials have been measured prior to and/or after heat treatment or diffusion by using Van der Pauw Hall effect and Scaning Electron Microscopy (SEM) data analysis. Atomic and carrier concentration depth profiles have been obtained by Auger Electron Spectroscopy (AES) and electrochemical C-V (ECV) measurements using a Polaron profiler (type PN 420Q). The changes in chemical composition of heat treated or diffused surfaces have been extracted from X-ray Photoelectron Spectroscopy (XPS) data.

Small area n^+-p InP unoptimized solar cells were fabricated under identical conditions, on structures made by thermal diffusion of S into Cd- and Zn-doped substrates. Electron beam evaporated Au-Zn-Au back contacts were sintered in forming gas for 3 minutes at 425°. The front contacts were 2000Å thick Au, evaporated by using photolithographically defined pattern. The grid shadowing was 6.25%. About 800Å thick SiO was used as an anti-reflection (AR) coating. Small area (0.48 cm^2) solar cells were defined by mesa etching.

Results and Discussion

A comparative study of performance parameters of identically fabricated n^+-p InP solar cells made by closed ampoule S diffusion into p-type InP is presented in Table 1. The total area AM0, 25° solar cell performance parameters were measured at NASA LeRC. As seen, the best efficiency is 11.83% for Zn-doped substrates as compared to 14.35% for Cd-doped substrates. For the three diffusion temperatures no significant differences exist between the values of V_{oc} and J_0. However, I_{sc}, FF and R_s vary more substantially for the two substrates. An explanation of these differences is given next in terms of structural, chemical and electrical changes we have observed in In-P-S-O-Zn(Cd) systems after thermal treatment and diffusion.

Heat Treatment Effects

In order to undetand the structural and electrical changes in p-type InP after diffusion, we have heat treated clean Cd-and Zn-doped substrates in evacuated closed

ampoule. As seen in Figure 1, after 3 hours of heat treatment at 660°, the decrease in either P or In surface concentration is relatively small and it is believed to be mainly due to C and O impurities detected at the surface. It is known that InP surface decomposes incongruently at temperatures greater than 356°C [ref.10]. Because a large number of P vacancies (V_P) are created at the surface as an effect, various neutral complexes such as X_{In} V_P or $V_P X_{In} V_P$ are formed [refs. 3,4], where X_{In} represent either Zn_{In} or Cd_{In}. In the $V_P X_{In} V_P$ complex mechanism, one In vacancy, V_{In}, and two P vacancies, V_P, are used up every time an interstitial Zn or Cd atom forms a complex. Since the Zn-doped substrate shows a more severely P depleted region as compared to the Cd-doped one, we assume that a much larger number of neutral complexes are formed in the Zn-doped substrate as compared to the Cd-doped substrate. This is confirmed by the In accumulation at the thin front oxide layer - InP:Zn interface, as seen in Figure 1b.

As previously reported for the InP:Zn substrates [refs. 11-14], an increase in hole density was observed for both Cd-and Zn-doped heat treated substrates, as shown in Figure 2. For Zn-doped substrates the effect was explained in terms of outdiffusion of interstitial Zn donors, thus decreasing the compensation of substitutional Zn acceptors [ref. 13]. This could be the case since the ECV profiles do not seem to follow the variation of In Auger profiles. Hence, the small increase in concentration of substitutional Zn_{In-} acceptors is not expected to account for the relatively large increase in measured acceptor concentration.

In the case of highly doped InP:Zn (1.2 E18 cm^{-3}), however, a very large increase in acceptor concentration appears toward the surface after 3 hours of heat treatment at 660°C as seen in Figure 3. The higher acceptor concentration near the surface with increased background doping can be explained by the increasing substitutional Zn_{In-} concentration added to a constant Zn complex solubility. This could be interpreted as being due to the interaction of singly ionized Zn interstitial not with neutral In vacancies, V_{In}, but with negatively charged In vacancies, V_{In-}, which could be more numerous than neutral vacancies in highly doped p-type InP.

From the above experiments, and assuming a constant Zn solubility which is to be expected for constant new created In and P vacancy concentrations, under similar heat treatment conditions, we concluded that 1) a large accumulation of neutral complexes are expected to appear at the surfaces in the case of low doped materials, while 2) the large accumulation of Zn at the surface in highly doped substrates is mainly due to Zn_{In-} acceptor formation.

Hall effect measurements of bulk acceptor concentration prior to and, after heat treatment at 660°C for 3 hours in the case of low doped Zn-and Cd-doped InP substrates, and 2 hours for the highly Zn-doped substrate, presented in Table 2, show a good agreement with C-V data presented in Figs. 2 and 3. The discrepancy in the case of highly doped substrates is due to differences in heat treatment time, i.e. 3 hours for the case of ECV data and 2 hours in the case of Hall effect data. Also shown

in Table 2 are values of resistivity (ρ) and mobility (μ). As expected with increasing hole concentration both ρ and μ decrease.

From the ECV and Hall effect data it is apparent that the increase in acceptor concentration, as a result of heat treatment is smaller in the case of InP:Cd as compared to InP:Zn of similar doping. This suggests that the interstitial Cd is present in much smaller densities as compared to interstitial Zn since as we have shown before, the density of neutral species also appear to be much smaller in the case of Cd doped materials.

Dislocation Density

The high dislocation density of S diffused InP surfaces are due to: 1) propagation of dislocations initially present in the substrates, 2) formation and propagation of dislocations from precipitates initially present in the crystal and 3) precipitates introduced during diffusion. Taking into consideration that dislocation motion will never occur without breaking crystal bonds, it is reasonable to assume that the bond strength plays an important role in the dislocation motion [ref. 15]. Judging from their high diffusivity, interstitial Zn atoms are not presumed to form strong bonds with host crystal atoms which surround the Zn atoms. Thus, the interstitial Zn atoms will not behave as a pinning point for dislocation motion. If the strength of bonds being formed between doped impurity atoms and sublattice site atoms, which surround the doped impurity atoms, is large enough, propagating dislocations are expected to be pinned at the impurity position. Thus, propagating dislocations under a driving force, i.e. thermal stress introduced during thermal diffusion will be stopped at a position adjacent to the impurities, provided the impurity forms strong bonds with one of the constituent atoms of the host crystal.

We have previously reported [ref. 2] that In_xS_y droplets appear on the surface of InP after closed-ampoule S diffusion into Cd-doped substrates at all diffusion temperatures from 600 to 725°C. These droplets, as seen in Figure 4, accumulate at the defect areas, i.e. at the etch pits at diffusion temperature of up to 700°C (see fig. 4a), and along the microcracks at higher temperatures as can be seen in Figs. 4c and 4d. The droplet density is indicative of dislocation density increase as the diffusion temperature or times increase from 600 to 700°C and from 1 to 4 hours, respectively.

For Zn-doped materials, under similar diffusion conditions, the droplet density has been found to be much higher than in the case of Cd-doped substrates. As seen in Table 3, the increase in dislocation density for Zn-doped substrates, after 3 hours diffusion at 660°C is more than one order of magnitude higher as compared to Cd-doped substrates. The differences observed in the values of EPD_d/EPD_0 ratios for NMC and CCI Zn-doped crystals can be due to inaccuracies in counting the droplets or to a larger number of precipitates initially present in the NMC crystal, probably due to the higher doping concentration.

Prior to diffusion, Cd-and Zn-doped substrates used in this study had comparable etch pit densities (EPD), as seen in Figure 5. The EPDs on virgin surfaces were slightly higher than 2E5/cm^2. However, after surface preparation prior to diffusion, including the removal of about 10μm damaged layer in Br_2-methanol (0.5% Br_2) solution, the EPDs for Zn doped materials were about 5 and 7×10^4/cm^2 and of about 7×10^4/cm^2 for Cd-doped substrates, respectively, as shown in Table 3.

Following a similar post-diffusion surface preparation procedure as reported for the case of Cd-doped substrates [ref. 2] the droplets accumulation from the Zn-doped surfaces could not be removed, as seen in Fig. 6a. For comparison, in the case of Cd-doped substrates, the micrograph in Fig. 4b shows the same location of surface as in Fig. 4a after post-diffusion surface preparation.

SEM analysis of surface topography in the case of Zn-doped substrates, after thinning down the n^+ emitter layer by anodic dissolution,have shown that the In_xS_y precipitate density decreases from about 2×10^7 /cm^2 at the surface to zero at the junction depth. Figure 6c represents a view of surface topography after removal of about 1,200Å thick layer from the surface of Fig. 6a. In contrast, a S diffused Cd-doped substrate, with a 600Å front surface removed, shows no sign of In_xS_y precipitates. The micrograph in Fig. 6b shows the surface dislocatlon density of structure in Fig. 6a, as revealed electrochemically in O-H_3P0_4 (0.5M) solution.

From these experiments it is apparent that the In_xS_y-rich precipitates are present only at the surface in the case of Cd-doped substrates and decrease exponentially from the surface value to zero in the vicinity of the junction in the case of Zn-doped substrates.

The exact composition of In_xS_y precipitates could not be identified, but EDAX and XPS analysis have shown that they are rich in In and S [ref. 2]. From the phase diagram [ref. 16] three stable compounds could be formed in In-S system under the diffusion conditions, e.g. In_2S_3, InS and In_6S_7. However, in the case of Zn-doped substrates, Zn precipltates could appear as a result of heat treatment [refs. 17-18]. We assume that these precipitates contrary, to In precipitates which are believed to concentrate at the surface, can be distributed inside the bulk material. This assumption can provide an explanation for the differences observed in the density and distribution of these precipitates in the case of Zn-and Cd-doped substrates.

AES and ECV Depth Profiles

In Figure 7 are presented S, P and In AES depth profiles after 3 hours closed-ampoule S diffusion into Cd-doped InP substrates at different diffusion temperatures [ref. 2]. As expected the S profiles are temperature dependent and it is clear that the severely P-depleted front surface region is mainly due to the substitution of P by S in the host InP lattice, rather than due to $V_pCd_{In}V_p$ neutral complex formation. For diffusion temperatures of 650 to 700°C, the S concentration is nearly constant

up to depths of several hundred angstroms. The anomalous behavior at 675°C has been explained by the formation at this temperature, of a stable glass-like $In(PO_3)_3$ polyphosphate at the surface, as revealed by XPS data [ref. 2], which acts as a diffusion barrier. The increased concentration of In at the oxide/n^+ interface is assumed to be due, as stated before, to In_xS_y-rich precipitate formation. The S profiles also show an increase in concentration at this location.

In the case of S diffusion into Zn-doped substrates, as seen in Figure 8, P profiles show a more severe loss of phosphorus and, as a consequence, a deeper junction depth, as compared to diffusions into Cd-doped substrates. A deeper junction depth, however, is expected since an increase in diffusion-induced dislocations, which act as P vacancy generators, could form diffusion pipes. However, by increasing the amount of added phosphorus to the ampoule, the phosphorus loss is diminished and, as a consequence, the S profiles vary accordingly. The accumulation of In at the oxide/n^+ interface is associated to the formation of Zn_{In-}, and the In depletion to outdiffusion of interstitial In. The deep accumulation of In is presumed to be due to the diffusion of interstitial In, and In precipitates accumulation at the dislocation areas, due especially to the formation of neutral complexes $V_pCd_{In}V_p$.

The ECV thermal equilibrium majority carrier concentration depth profiles after S diffusion into Cd-doped substrates, have essentially similar shapes as S atomic concentration Auger profiles. However, in the case of Zn-doped substates, the C-V and Auger profiles are quite different. Figure 9 shows two C-V depth profiles after 3 hours S diffusion into the two substrates. As seen, a nearly step diffusion profile is obtained in the case of diffusion into Cd-doped substrate, while a graded profile is seen in the case of diffusion into Zn-doped substrate. The discrepancy is explained based on the differences between the dislocation densities introduced during S diffusion into the two substrates. In the case of diffusion into Cd-doped substrates it seems that most of the S is found in ionized form and appears as a donor. In the case of Zn-doped substrates, however, the departure of C-V profile from a nearly step Auger profile can be explained by assuming that a part of sulfur combines with interstitial In and, probably, Zn and forms stable In_xS_y or ZnS precipitates at the dislocation regions.

External Quantum Efficiency

The last characteristic we discuss here in an attempt to explain the differences between the performance parameters of solar cells fabricated on Zn- and Cd-doped substrates is the external quantum efficiency (EQE).

Figure 10 presents the variation of EQE for solar cells fabricated by 3 hours S diffusion into Cd- and Zn-doped substrates at two diffusion temperatures of 625°C and 660°C.

At the diffusion temperature of 625°C no significant differences could be seen from the EQE variations which could explain the differences in performance parameters shown in Table 1. Then the differences in performance parameters, especially I_{sc} and FF, could be related to an increase observed in the series resistance (R_s) in the case of Zn-doped substrates.

In the case of diffusions at 660°C, however, the EQE variations for the two substrates are in good agreement with differences between the ECV and AES depth profiles and which are explained in terms of a higher dislocation density in the case of Zn-doped substrates. The electrically inactive S, which is incorporated into In_xS_y, and probably, ZnS precipitates at the dislocation regions, will produce a dead layer near the surface. As shown in the previous sections, in the case of Cd-doped substrates, the dead layer is superficial and can be removed by an appropriate post-diffusion surface preparation. In the case of Zn-doped substrates, the dead layer extends well below the surface. This explains the decrease in I_{sc} and increase in R_s since the presence of a dead layer will reduce the collection efficiency by reducing the minority-carrier lifetimes. The decrease in FF is related to the increase in R_s value, which is mainly due to an increased sheet resistivity.

Conclusion

Our preliminary results indicate that Cd-doped substrates are better candidates for achieving high efficiency solar cells fabricated by closed-ampoule S diffusion than Zn-doped substrates. The differences in performance parameters (i.e. 14.35% efficiency for Cd-doped vs. 11.83% in the case of Zn-doped substrates of comparable doping and EPDs) have been explained in terms of a large increase in dislocation density as a result of S diffusion in the case of Zn-doped as compared to Cd-doped substrates. The In_xS_y and probably, ZnS precipitates in the case of Zn-doped substrates, produce a dead layer which extends deep below the surface and strongly affect the performance parameters.

It should be noted that our cells had an unoptimized single layer AR coating of SiO, a grid shadowing of 6.25% and somewhat poor contacts, all contributing to a reduction in efficiency. We believe that by reducing the external losses and further improvement in cell design, efficiencies approaching 17% at 1AM0, 25° should be possible for cells fabricated on these relatively high defect density Cd-doped substrates. Even higher efficiencies, 18-19% should be possible by using long-lifetime substrates and further improving front surface passivation. If solar cells fabricated on Cd-doped substrates turn out to have comparable radiation tolerance as those reported in the case of cells fabricated on Zn-doped substrates, then for certain space missions 18% to 19% efficient cells made by this method of fabrication would be viable.

References

[1.] Mircea Faur, Maria Faur, Chandra Goradia, Manju Goradia, Navid Fatemi, David Brinker and Ralph Thomas, *1st Int. Conf. on InP and Related Materials*, 1989.

[2.] Maria Faur, Mircea Faur, Manju Goradia, Chandra Goradia, Douglas Jayne, Frank Honecy and Irving Weinberg, *1st Int. Conf. on InP and Related Materials*, 1989.

[3.] B. Tuck and A. Hooper, J. Phys. **D8**, 1806, 1975.

[4.] A Hooper and B. Tuck, Solid State Electron. **19**, 513, 1976.

[5.] H. B. Serreze and H. S. Marek, Appl. Phys. Lett. **49**, 210, 1986.

[6.] G. J. van Gurp, P. R. Boudewijn, M. N. C. Kempeners and D. L. A. Tjaden, J. Appl. Phys. **61**, 1846, 1987.

[7.] P.K. Tien and B.I. Miller, Appl. Phys. Lett. 34 **10**, 701, 1979.

[8.] H. Ando, N. Susa and H. Kanbe, IEEE Trans. on Elecl ron Devices, **ED-29**, 1408, 1982.

[9.] K. Ohtsuka, T. Matsui and H. Ogata, Jpn. J. Appl. Phys. **27**, 253, 1988.

[10.] R.F.C. Farrow, J. Phys. **D7**, 2436, 1974.

[11.] K. Tsubaki and K. Sugiyama, Jpn. J. Appl. Phys. **19**, 1185, 1980.

[12.] K. Tsubaki and K. Sugiyama, Jpn. J. Appl. Phys. **19**, 1789, 1980.

[13.] C.C.D. Wong and R.H. Bube, J. Appl. Phys. **55**, 3804, 1984.

[14.] H.S. Marek and H.B. Serreze, Appl. Phys. Lett. **51**, 2031, 1987.

[15.] Y. Seki, H. Watanabe and J. Matsui, J. Appl. Phys. **49**, 822, 1978.

[16.] H.G. Ansell and R.S. Boorman, J. Electrochem. Soc. **118**, 133, 1971.

[17.] S. Mahajan, V.A. Bonner, A.K. Shin, and D.C. Miller, Appl. Phys. Lett. **35**, 165, 1979.

[18.] R.S. Williams, P.A. Barnes, and L.C. Feldman, Appl. Phys. Lett. **36**, 760, 1980.

Table I: Comparison of solar cell performance parameters[a] for cells fabricated on Zn- and Cd-doped substrates

Cell[b]	J_{sc}[c] (mA/cm^2)	V_{oc} (mV)	FF (%)	η (%)	$J_0(A=1)$ (A/cm^2)	R_s (Ω-cm^2)
DZ-3-600	27.96	799	65.4	10.66	8.23E-16	5.15
DC-3-600	29.5	803	76.9	13.28	7.82E-16	2.12
DZ-3-625	27.67	811	68.7	11.24	5.78E-16	3.34
DC-3-625	28.94	809	74.1	12.66	6.08E-16	1.44
PDZ-3-660	26.93	813	74.1	11.83	4.93E-16	5.36
PDC-3-660	30.48	806	80.1	14.35	5.50E-16	1.07

[a] All cell measurements were performed at NASA LeRC, under AM0, 25°C conditions.
[b] Notation DZ(C)-3-X stands for Diffusion into Zn(Cd)-doped substrates for 3 hours at diffusion temperature X(°C). An initial P indicates that substrates were Passivated prior to diffusion.
[c] total cell area 0.6cm × 0.8cm = 0.48cm. $I_{sc} = 0.48 J_{sc}$.

Table 2: Resistivity ρ, mobility μ, and doping N_a for Zn- and Cd-doped substrates from Crystacomm Inc.(CCI) and Nippon Mining Co.(NMC) before and after 3 hours heat treatment (2 hours for NMC crystal) at 660°C in closed-evacuated quartz ampoule.

Vendor	Dopant	Before heat treatment			After heat treatment			$\frac{N_a^h}{N_a^0}$
		ρ_0, $\times 10^{-2}$ Ω-cm	μ_0, cm^2/V-sec	N_a^0, $\times 10^{16}$ cm^{-3}	ρ_h, $\times 10^{-2}$ Ω-cm	μ_h, cm^2/V-sec	N_a^h, $\times 10^{16}$ cm^{-3}	
CCI	Zn	425.5	141.9	1.03	95.9	138.5	4.7	4.54
CCI	Cd	479.7	154.9	1.07	158.1	145.0	2.7	2.52
NMC	Zn	6.7	77.7	120.0	3.7	69.0	246.5	2.05

Table 3: Approximate density of etch pits on p-type InP substrates after removing about 10 μm from the surfaces in Br_2-methanol (EPD_0), and after closed-ampoule S diffusion for 3 hours at 660°C (EPD_d).

Vendor	Dopant	N_a, $\times 10^{16}$ cm^{-3}	EPD_0, $\times 10^4$ cm^{-2}	EPD_d, $\times 10^6$ cm^{-2}	$\frac{EPD_d}{EPD_0}$
NMC	Zn	2.24	5	22	440
CCI	Zn	1.03	7	20	330
CCI	Cd	1.07	7	2.3	29

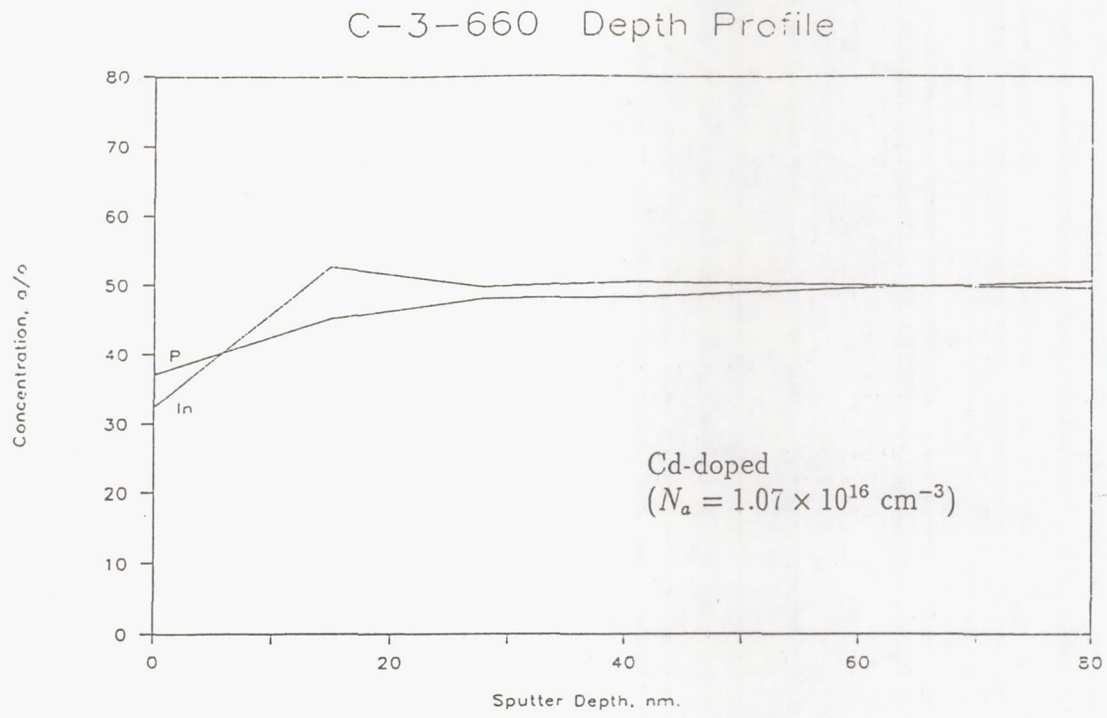

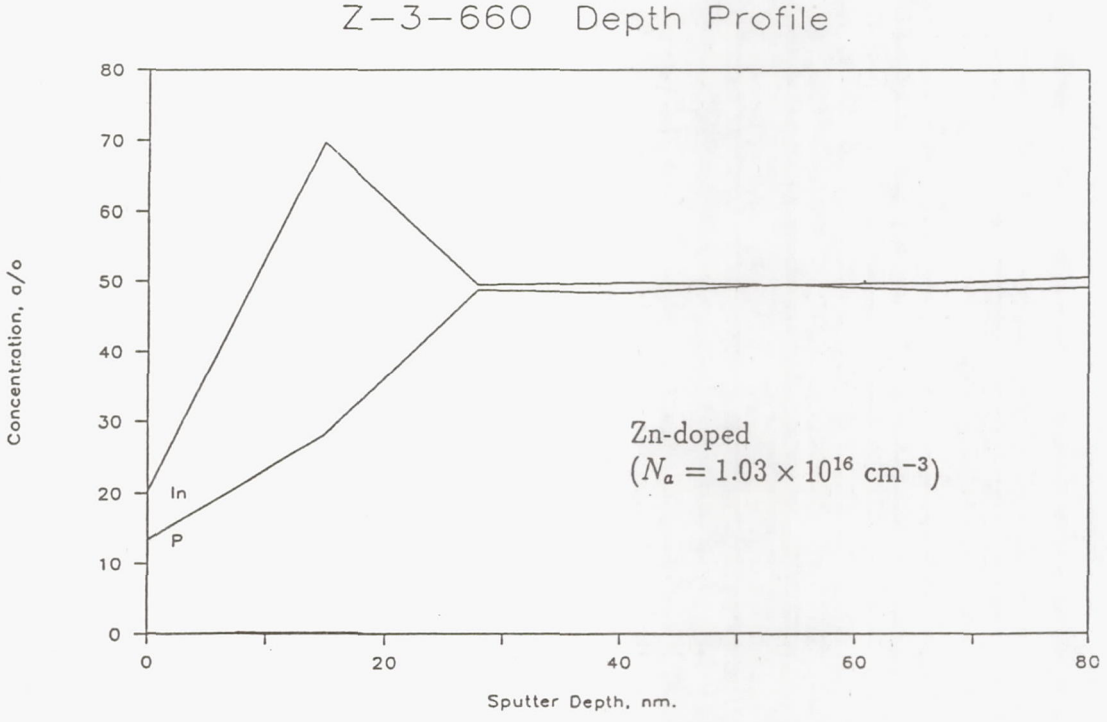

Figure 1. P and In AES profiles after 3 hours closed-ampoule heat treatment of clean Cd- and Zn-doped InP substrates.

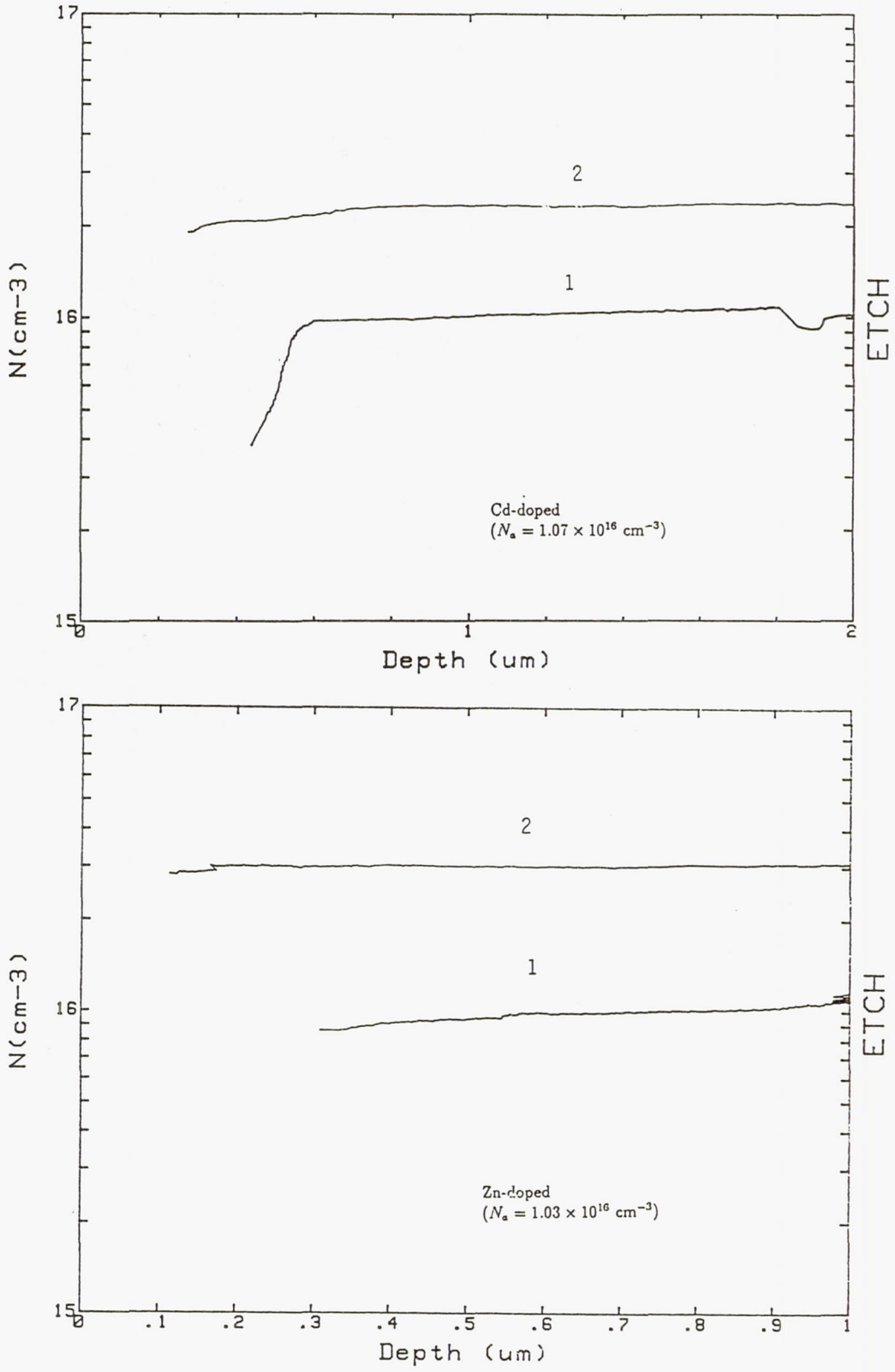

Figure 2. ECV acceptor concentration profiles before (curves 1) and after (curves 2) 3 hours heat treatment at 660°C of clean Cd- and Zn-doped InP substrates.

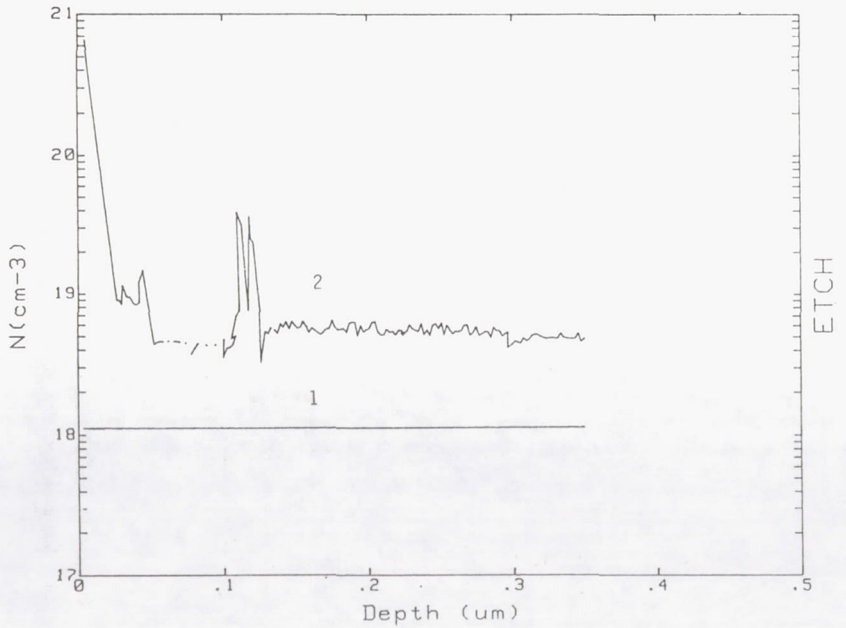

Figure 3. ECV acceptor concentration profiles before (curve 1) and after (curve 2) 3 hours heat treatment at 660°C of Zn-doped ($N_a = 1.2 \times 10^{18}$ cm^{-3}) InP substrates.

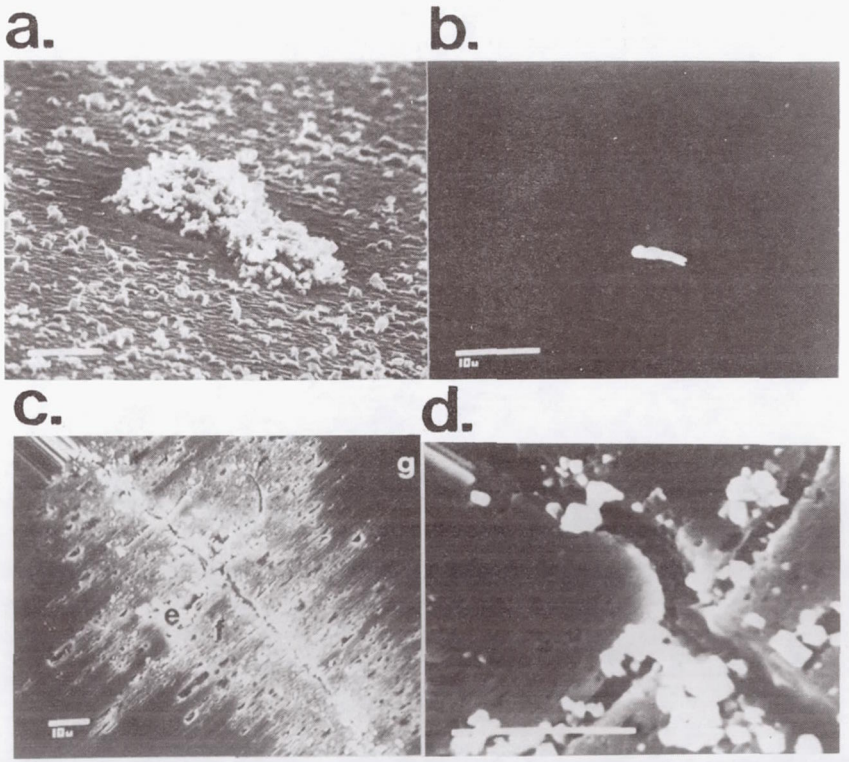

Figure 4. In_xS_y droplet accumulation on surface after 3 hours S diffusion into Cd-doped InP; a) at a temperature of 675°C; b) same region of Fig. 4a after droplet removal; c) at a temperature of 725°C and d) enlarged view of the center region of Fig. 4c.

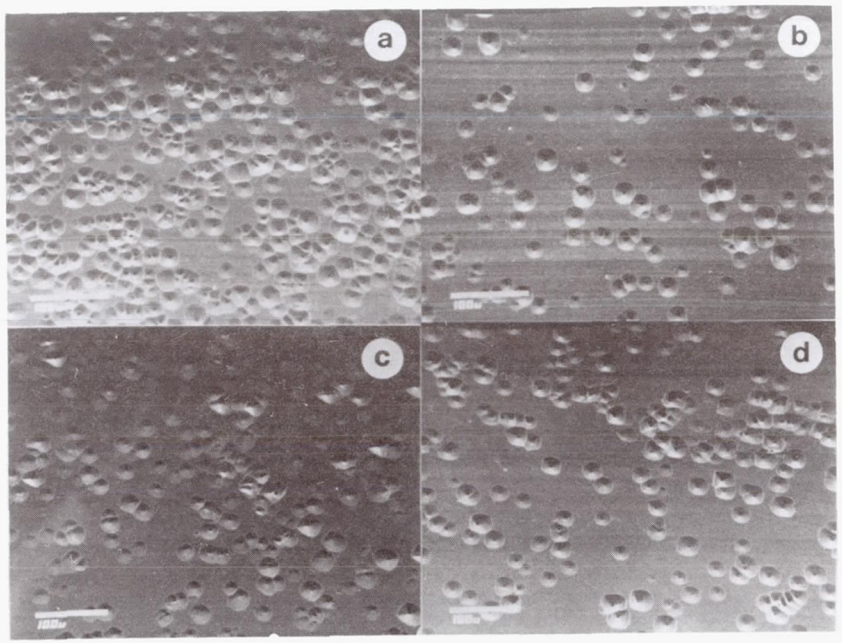

Figure 5. Etch pit density (EPD) revealed after two minutes etching in O-H_3PO_4:HBr (2:1) for a) NMC, Zn-doped (2.24×10^{16} cm^{-3}) InP substrate, b) same substrate after removal of about 10 μm in Br_2-methanol; and CCI, c) Cd-doped (1.07×10^{16} cm^{-3}), and d) Zn-doped (1.03×10^{16} cm^{-3}) after 10 μm removal in Br_2-methanol

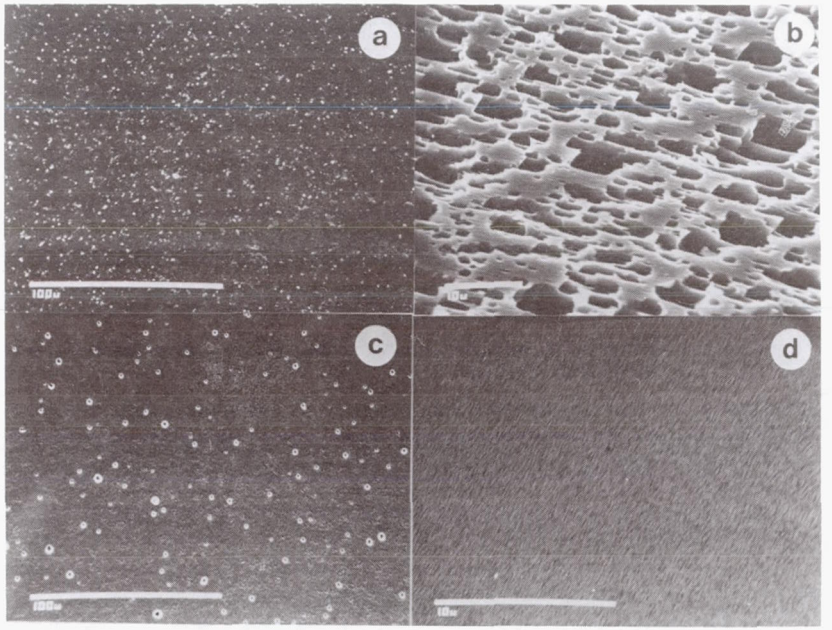

Figure 6. SEM surface topography after 3 hours S diffusion into Zn-doped (1.03×10^{16} cm^{-3}) substrates: a) after same surface treatment as in fig. 4b; b) electrochemically revealed EPD of surface in Fig 6a, in O-H_3PO_4 (0.5M) solution; c) surface in Fig. 6a after anodic disolution to a depth of about 120 nm; d) surface of a n^+p structure S-diffused for 3 hours at 660°C into Cd-doped substrate, after anodic dissolution to a depth of about 60 nm.

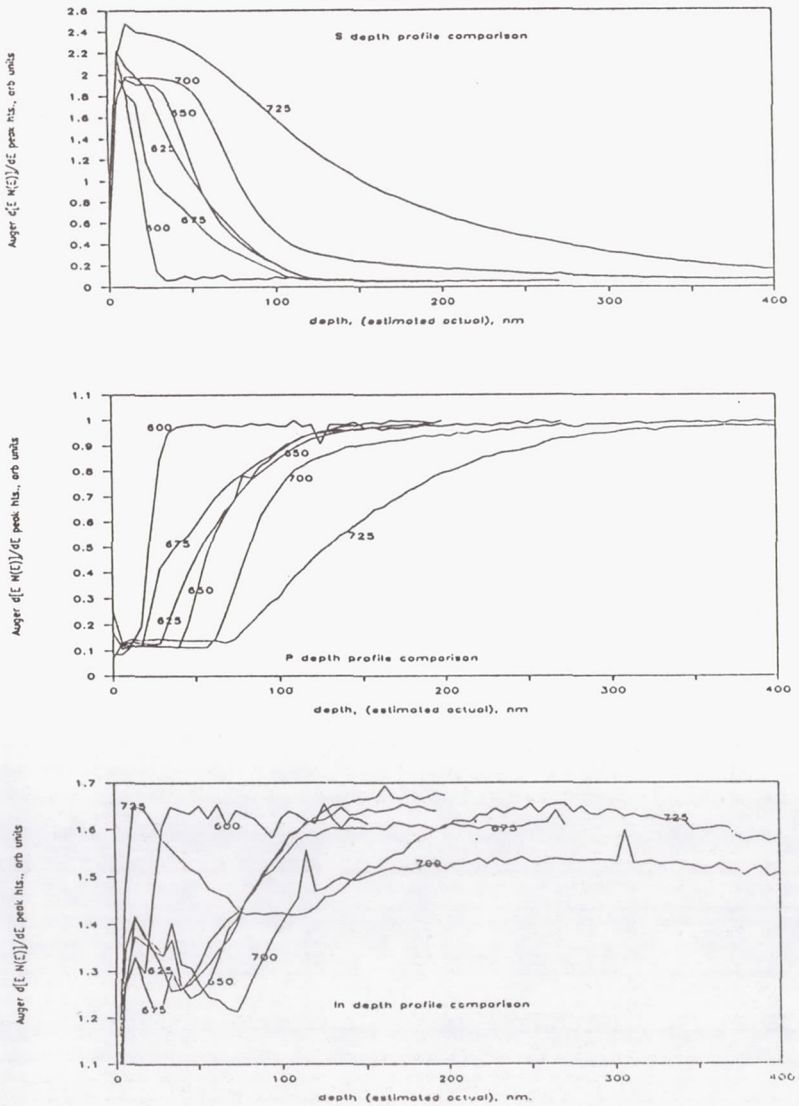

Figure 7. S, P and In AES depth profiles after 3 hours closed-ampoule S diffusion into Cd-doped ($N_a = 1.07 \times 10^{16}$ cm^{-3}) InP substrates, at different diffusion temperatures.

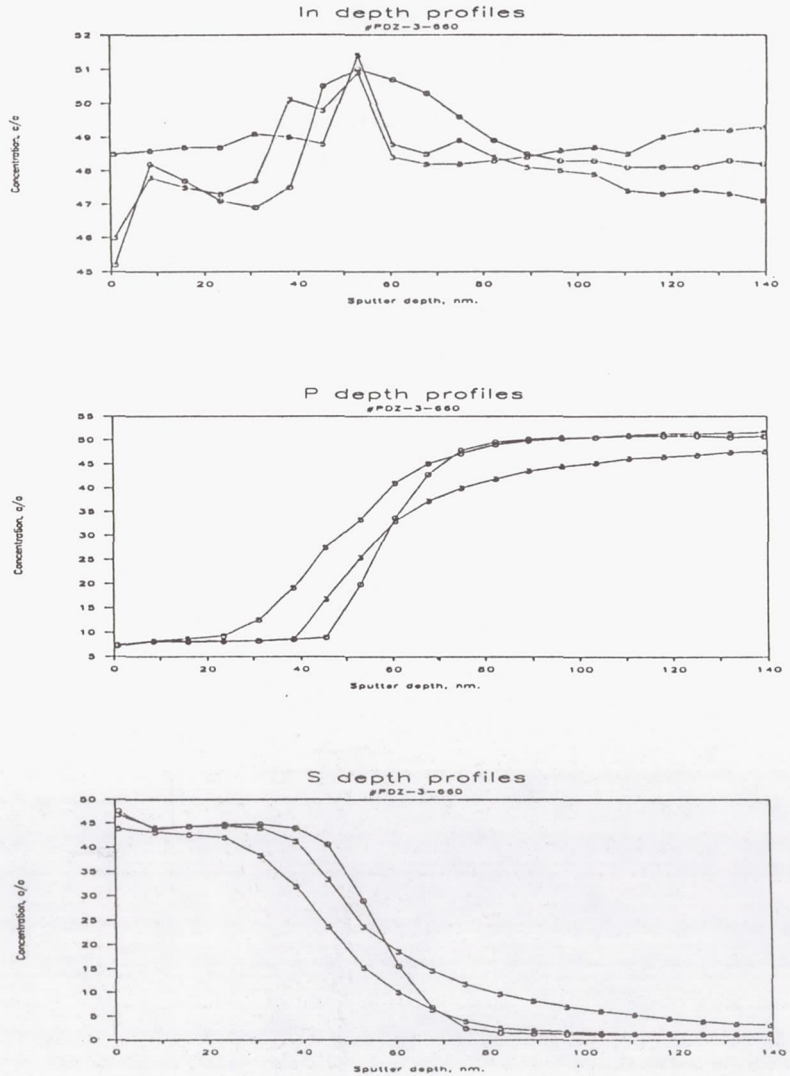

Figure 8. In, P and S AES depth profiles after 3 hours closed-ampoule S diffusion at 660°C. The parameter is the amount of red phosphorus added to the ampoule (in mg).

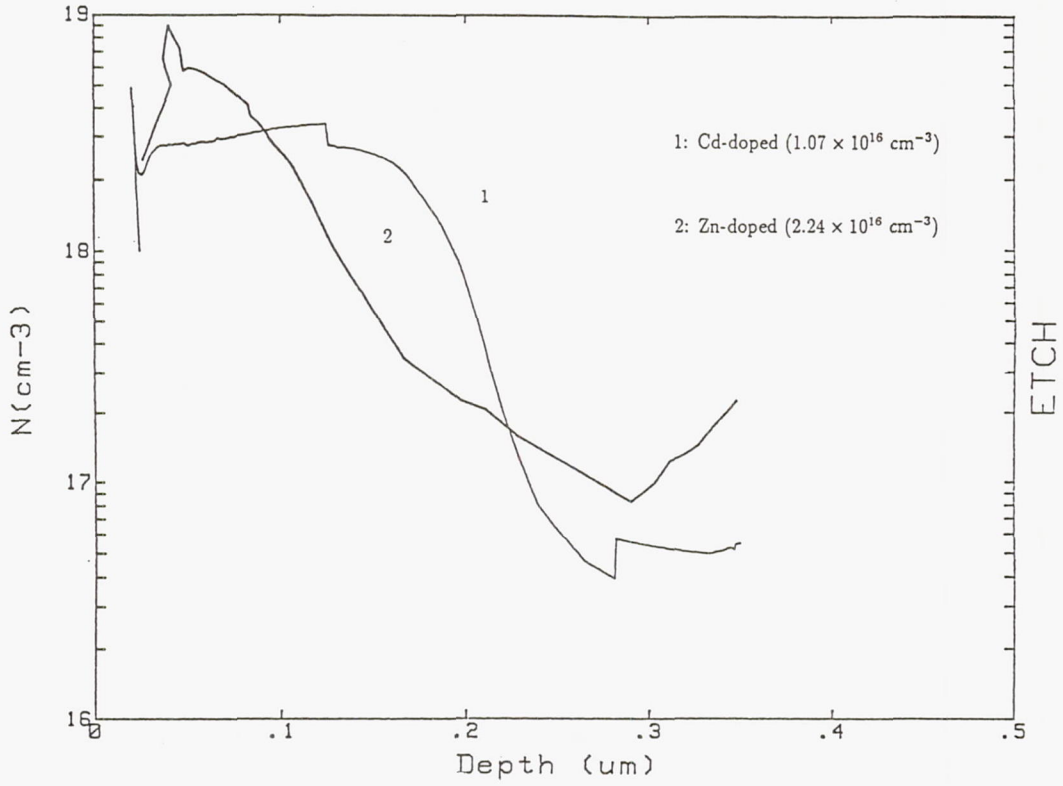

Figure 9. ECV thermal equilibrium majority carrier concentration depth profiles after S diffusion into Cd- and Zn-doped InP substrates, for 3 hours at 660°C.

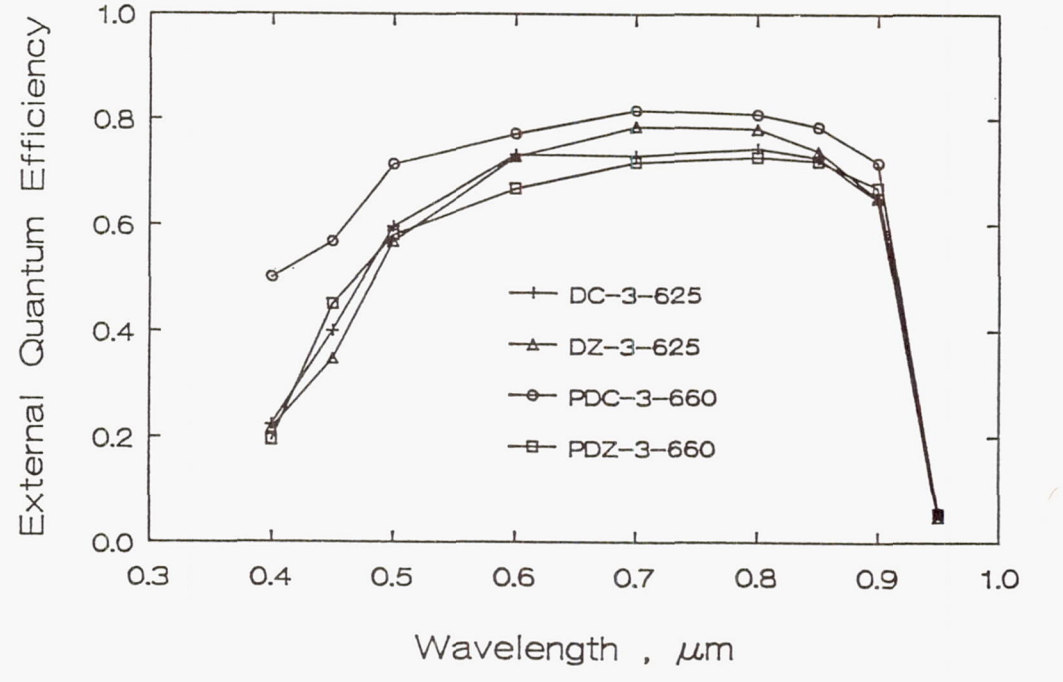

Figure 10. External Quantum Efficiency for solar cells fabricated on Cd- and Zn-doped substrates with performance parameters shown in Table 1.

Session 5
Non-Solar Direct Conversion

Preceding Page Blank

Radioisotope Thermal Photovoltaic Application of the GaSb Solar Cell

M. D. Morgan, W. E. Horne and A. C. Day
Boeing Aerospace and Electronics
Seattle, WA

Introduction

Thermophotovoltaic (TPV) systems have been studied by numerous investigators in the past, due to the possibility of high efficiencies on the order of 30% [refs. 2,3]. In a TPV system solar cells are exposed to the radiant spectrum of an incandescent emitter rather than the solar spectrum. The emitter temperature is chosen so that the peak of its blackbody emission spectrum is close to the optimum wavelength for conversion by the cells, generally near the band edge. Thus, the energy return per absorbed photon may be a factor of two or more greater than it would be for the same cell exposed to the solar spectrum.

The TPV system of ref. 2 consisted of a optical concentrator which focused sunlight on the absorber/emitter, the absorber/emitter which was essentially a blackbody radiator heated by the sun, a reflective cavity used to recycle the unused portion of the radiated blackbody spectrum and silicon solar cells. Due to the nature of the band-gap of silicon, the absorber/emitter had to be maintained at a temperature of 2000 K to 2300 K for high efficiency. The cavity was designed to return energy of a longer wavelength than the band-gap (>1.1 μm for silicon) back to the absorber/emitter to help maintain its equilibrium temperature. The cell, in effect, acted as an optical notch filter absorbing energy from the emitted blackbody spectrum only in that wavelength region where photovoltaic conversion is most efficient. The efficiency of the cell to that portion of the spectrum of wavelength shorter than 1.1 μ then becomes the upper limit of the STPV converter and theory shows that such efficiency can exceed 50 percent [ref. 3]. The study of this system included prototype fabrication and testing. A demonstrated overall efficiency of 13% was achieved using off-the-shelf silicon cells which confirmed the viability of the TPV concept.

Several persistent design challenges arise in attempting to make TPV systems practical. One of these is the necessity of recovering the long wavelength, sub-bandgap energy, usually by cell back-surface reflection. Another arises from temperature limitations on the radiant emitter. Temperatures in excess of 1500 C are needed for efficient operation with silicon cells, which may lead to cavity contamination or be hard to attain with practical heating systems, including solar. Significant progress has been made in some areas, particularly on IR transparent silicon cell technology. However, advances in competing conversion approaches such as tandem cells have reduced the relative advantages of solar-heated TPV.

Preceding Page Blank

If one looks beyond solar heated systems the potential for TPV power is still strong. Many applications now being served by radioisotope thermoelectric generators (RTGs) could be better served with solar cells in place of the thermoelectric elements. These include space power applications in which solar panels are unattractive, including missions to the outer planets, Mars rovers, high radiation orbits, and missions in which array pointing torques may disrupt other spacecraft activities. This paper will explore the possibilities for radioisotope TPV, or RTPV power.

One development which may help to make RTPV power the system of choice for such missions has come directly out of the tandem cell effort. This is the GaSb cell as developed at Boeing for use in its GaAs/GaSb tandem cell [ref. 1]. Recent measurements carried out at Sandia laboratories have established AM1.5 efficiency of 37% for stacked cells under concentration. The GaSb cell itself converts only 8% under an AM0 spectrum, but its voltage, fill factor, and quantum efficiency are such that it is an excellent converter of energy near its 1.7 μm band edge. The efficiency of GaSb cells to wavelengths of 1.5 to 1.6 μm is now approximately 35%. By contrast, RTG systems have only recently exceeded efficiencies of 7% and do not appear likely to go much higher. The next section will discuss the expected efficiency for a RTPV conversion cavity which could be constructed with minimal adaptations to the existing GaSb cell.

Performance Analysis

GaSb Cell Requirements

The sub-bandgap reflectance of a GaSb cell is determined by free-carrier absorption in the bulk as well as by the reflectivity of the rear contact metal [ref. 4]. The substrates now being used are doped to 2.5 x 10^{17}. This is a relatively low doping, but not so low as to make carrier absorption negligible. A cell with lower doping could probably be made successfully. However, the existing substrate material was assumed in making performance estimates. The measured transmission of a wafer 0.28 mm thick is shown in figure 1. The overall transmittance is limited by the air interfaces at front and back and the high index of refraction of the GaSb. However, the curve indicates near theoretical transmittance near the bandgap with free carrier absorption increasing as the wavelength increases. The data are consistent with an absorption coefficient of 5 cm^{-1} at 8 μm and a cubic dependence on wavelength. This is very similar to values determined elsewhere for GaAs. A sub-bandgap reflectivity of 0.95 should be achievable with a suitable metal contact on rear-polished wafers. The net cell reflectance expected is shown in figure 2, with a 1100 C blackbody also shown for reference.

Another important feature of the GaSb cell for this application is its spectral response. Figure 3 shows the normalized spectral response of this cell as compared with the normalized blackbody spectrum at 1100 C. As the operating temperature

increases the effeciency of the system increases as well. However, there always exists the tradeoff between optimum theoretical performance and the reality of having to maintain an emitter at high temperatures.

Configuration

In the first configuration discussed, the PuO_2 General Purpose Heat Source (GPHS) is used as a source of power. The heat source is encased in graphite and iridium, intended to withstand large impact forces without rupture even in the event of catastrophic mission failure or reentry. The 250 W GPHS modules were developed under a multiyear program managed by the Department of Energy. The configuration is based largely on the design of an RTG generator developed for Mars Rover [ref. 7]. The dimensions of a 250 W unit are 3.66 x 3.83 x 2.09 inches, and weigh 1.45 kg. A proposed configuration using sixteen units in a 2 x 2 x 4 stack is shown in figure 4.

The emitter temperature depends on a number of factors, including power output of the isotope, surface to volume ratio of the module stack, and power recycling via solar cells and other surfaces. For a system with electrical output of 573 watts it was found that the cells should cover approximately 30% of the emitter surface to maintain the emitter temperature in the 2 x 2 x 4 configuration. Other surfaces are covered with a multilayer reflective insulation such as Mo/quartz, with a net heat reflectance of 0.98.

There are other isotopes that have suitable characteristics for this application. A listing of these nuclides with some of their properties is shown in table 1. The two candidates that are the most suitable are Curium-244 (Cm-244) and Strontium-90 (Sr-90). And while Actinium-227 and Uranium 232 may be more desirable in their characteristics, the availability of these isotopes appear to be severely limited.

When applying any of the these isotopes to the model, we will attempt to design for a slightly higher emitter temperature. This is because as emitter temperature is increased the efficiency of the system is increased as well. It is found that by increasing the temperature by 9% (from 1100 C to 1200 C) the efficiency is increased by 18%. A schematic of the system utilizing a Sr-90 disk source is shown in figure 5. The dimensions of this system is based on a 500 watts electrical output. As with the GPHS configuration, this features 30% cell coverage with the remaining area a multilayer reflective insulation to provide 98% reflectance of non-absorbed energy back to the emitter. The heat source is 26 cm in diameter and 2.5 cm thick. Terrestial cladding for Sr-90 has been a super alloy of nickel, Hastelloy [ref. 5]. However, for space qualification, materials that will be able to sustain catastrophic failure are required.

Another configuration of interest would be utilized by microspacecraft. These craft would weigh less than 5 kg, meeting mission goals through multiple, frequent launches as opposed to the current approach of highly reliable, component redundant,

single spacecraft. The power needs of the microspacecraft would be met by a small RTPV system employing a higher specific power isotope. This conformation is similar in nature to the GPHS form but on a smaller scale. The total electrical power requirement over 5 years would be about 5 watts [ref. 6]. The heat source would be a cylindrical pellet 1.5 cm in diameter and 1.0 cm thick of Cm-244.

On the negative side of the last two approachs, the use of a new isotopic heat source would require space qualification. This means a substantial expenditure of time, effort and money. And while some of the ground work has already been covered, a program much like that which went into the GPHS qualification would be expected.

Performance Predictions

A computer model of the GaSb TPV conversion cavity was created to test various assumptions regarding cell requirements, efficiency vs. emitter temperature, and system power to weight ratios. The calculation divides the radiant energy spectrum into bins by wavenumber, in intervals of 100 cm^{-1} (approximately 0.03 μm near the band edge). Quantities which are spectrally dependent include cell absorption coefficient based on a free carrier absorption model, emissivity of the radiant emitter, and cell response. For all calculations reported here the emissivity was chosen as 0.85. Selective emitters could also be useful but were not considered here. For the cell, V_{oc} = 0.465 V (as measured at 300 K and 44 suns), fill factor = 0.77, and quantum efficiency = 0.90.

Efficiency as a function of emitter temperature is shown in figure 6 for the system as described above. At any temperature above 850 C the RTPV appears to outperform an RTG system in efficiency; if the overall system has comparable weight, the RTPV should therefore have a substantially higher power density. Discussions with DOE personnel indicate that the GPHS modules should be able to operate as hot as 1100 C without damage to the iridium case. At this temperature the efficiency calculated is 14.4% and the electrical output is 573 watts for sixteen heat sources in a 2 x 2 x 4 stack. The total GPHS weight is 23.2 kg. Calculations were also made for a 1 x 15 stack. This required a lower cell coverage factor to maintain the emitter temperature, about 18%. The resulting efficiency drops to 12.4%, and the output power to 458 watts.

The close relation of the system efficiency with emitter temperature relates to the overlap between the blackbody spectrum and the spectral response of the the cell (See also figure 3). If a heat source other than the GPHS is warrented and higher operating temperatures are possible, significant gains could be achieved. Table 2 outlines the performance of a Sr-90 source and a Cm-244 source and allows a comparison between these systems and the GPHS system. Important points are the specific power of each system and the requirements for a 500 watt output system. The high specific power of Cm-244 gives the capability for much smaller overall systems.

System weights can be estimated by simple analogy with the Mars Rover RTG study carried out by Fairchild [ref. 7]. In that study a 1 x 18 stack gave an electrical output of 280 W BOM. The system weight was 58.67 kg and the specific power was 4.77 watts/kg. The weight is a factor of 2.25 higher than the GPHS weight alone. A similar configuration was assumed for this study except that thermoelectric elements are replaced by cells (lighter weight) and the thermal control system must be made considerably heavier. Otherwise, weights for the canister, insulation, housing, and structural supports should be nearly identical.

In the Mars Rover design the cooling fins operate at about 550 K and the thermal control system contributes 4.7% of the system mass. Modeling of the temperature behavior of the GaSb RTPV predicts that the output will drop by 0.53% per degree near 300 K. The thermal control fins to maintain an RTPV at 300 to 350 K are likely to be larger, perhaps by as much as a factor of five. Including this penalty in our RTPV weight estimate results in a system mass of 61.9 kg and a power to weight ratio of 9.25 watts/kgfor the 2 x 2 x 4 stack configuration. A 1 x 15 stack leads to a weight estimate of 58.0 kg and specific power of 7.90 watts/kg. Either of these power densities is significantly higher than the 4.74 watts/kg now obtainable with thermoelectric generators.

After applying the 500 watt Sr-90 configuration to our model efficiencies and total system power and weights were predicted. The Sr-90 heat source is modeled as a disk of material with a total isotope mass of 6.37 kg. A total power output was modeled at 487 watts at a 17% efficiency and 12.7 watts/kg. However, this system carries with it a heavy radiation dose which is discussed below.

The total mass of the Cm-244 micro-satellite RTPV system is predicted at 100 grams with a electrical output of 6 watts. The small size of the system necessitates the use of more cells per unit area due to the size restriction of the cells themselves; consequently, cell coverage is modeled at 80%. The down side of this is that it will reduce the amount of energy returned to the emitter thus requiring more isotope to maintain the desired temperature. However, by increasing the cell area, the efficiency of the system is boosted to almost 20% at 1200 C.

Source Radiation

Radiation doses are of concern both for material handling by personnel and for long-term degradation of the cells. Personnel protection from gamma doses will involve the same precautions which have been established for RTG missions using the GPHS sources. In addition, both of the alternate isotope candidates have radiation concerns. The Sr-90 material has a high associated gamma dose due to bremsstralung radiation of the emitted β particles. And while this is not expected to be a problem with the cells, there is a real concern associated wth material handling by personnel. The gamma dose is ~1000 R/hr. at 1 meter from the source. This value depends strongly on the Z-number of the isotope cladding material.

Solar cells, however, are known to degrade in neutron environments due to reduced minority carrier lifetimes. Plutonium fuel releases approximately 6000 n/gm-sec at an energy of 1.6 MeV. An RTPV with a 468 watt output requires sixteen modules with 9.54 kg of plutonium oxide, so over a ten year period 1.8×10^{16} neutrons would be released. The cells in the system modeled cover 485 cm^2, which is 30% of the total solid angle of emission. The neutron fluence over ten years is then 1.1×10^{13} n/cm^2. In addition, the Cm-244, while having a low gamma component, has high neutron emission. The neutron emission, due to its spontaneous fission decay, is approximately 2.73×10^5 n/gm-sec. This is about 45 times more neutrons than the PuO_2 emits. The total ten year neutron fluence from 500 watt system with a Cm-244 source is 5.16×10^{13}. Data are not available for neutrons in GaSb, but GaAs test results have shown a power loss of about 15% after exposure to 1×10^{13} n/cm^2 at 1 MeV. Both GaSb and GaAs are direct bandgap materials with short absorption lengths, hence, their response to neutrons should be similar. Therefore, it appears that neutron degradation will be a concern but a manageable one.

The computer modeling discussed here is only the first step in the development of a RTPV power system and we look forward to the many technical challanges that must be hurdled prior to the first working protype.

Conclusions

An examination of an RTPV conceptual design has shown a high potential for power densities well above those achievable with RTG systems. An efficiency of 14.4% and system specific power of 9.25 watts/kg were predicted for a system with sixteen GPHS sources operating at 1100 C. The model also showed a 500 watt system power by the strontium-90 isotope at 1200 C at an efficiency of 17.0% and a system specific power of 11.8 watts/kg. The key to this level of performance is a high-quality photovoltaic cell with narrow bandgap and a reflective rear contact. Recent work at Boeing on GaSb cells and transparent back GaAs cells indicates that such a cell is well within reach.

References

[1.] L. Fraas, J. Avery, V. Sundaram, T. Davenport, and M. ONeill, to be published in IEEE Aerospace and Electronics Systems, November 1989.

[2.] R.M. Swanson and R.N. Bracewell, EPRI ER-478 Progress Report, Research Project 790-1 (1977).

[3.] W.E. Horne and A.C. Day, *Proceedings of 17th Intersociety Energy Conversion Engineering Conference*, 119 (1982).

[4.] J. I. Pankove, *Optical Processes in Semiconductors*, 67, Dover Publications, NY. (1971).

[5.] J.R. Devore, K.W. Haff and J.A. Tompkins, *Proceedings of the American Chemical Society*, 1374 (1986).

[6.] A. Chmielewski, *Proceedings of the 24th Intersociety Energy Conversion Engineering Conference*, 715 (1989).

[7.] A. Schock, T. Or and E. Skrabek, *Proceedings of the 24th Intersociety Energy Conversion Engineering Conference*, 2693 (1989).

Table 1: Listing of suitable radioisotopes for the RTPV application.

Isotope	Half-life (yr)	Compound	Melting Temp. (K)	Watts/gm
Strontium-90	28	SrO	2700	0.453
Curium-244	18	Cm2O3	2400	2.35
Uranium-232	72	UO2	3100	4.22
Actinium-227	22	Ac2O3	---	12.7

Table 2: A comparison of RTPV operating characteristics with different radionuclide source material.

Isotope and/or Configuration	Operating Temperature (C)	Efficiency	Output Power (watts)	Mass (kg)	Watts/kg
GPHS (1x15)	1100	12.4	458	58	7.90
GPHS (2x2x4)	1100	14.4	573	61.9	9.25
Sr-90	1200	17.0	487	41.2	11.8
Sr-90	1200	17.0	49	3.85	12.7
Cm-244	1200	17.0	413	7.56	54.6
Cm-244	1200	19.9	6	0.10	60.0
RTG	1000	7.42	278	58.6	4.74

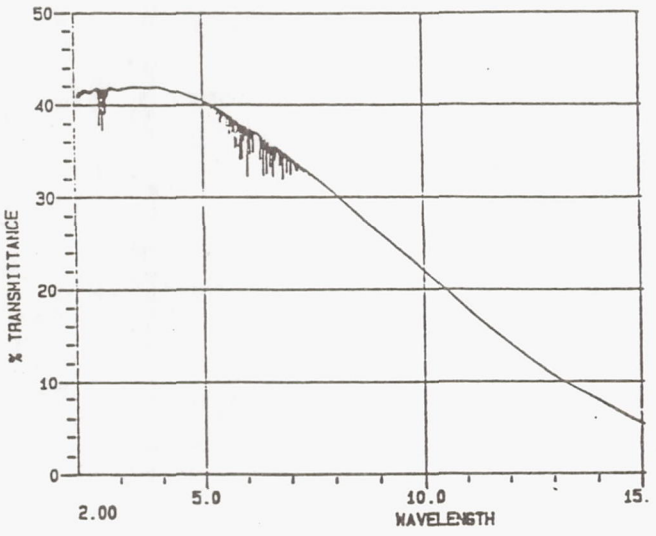

Figure 1: Transmission through a GaSb wafer doped to 2.5 x $10^{17}/cm^3$.

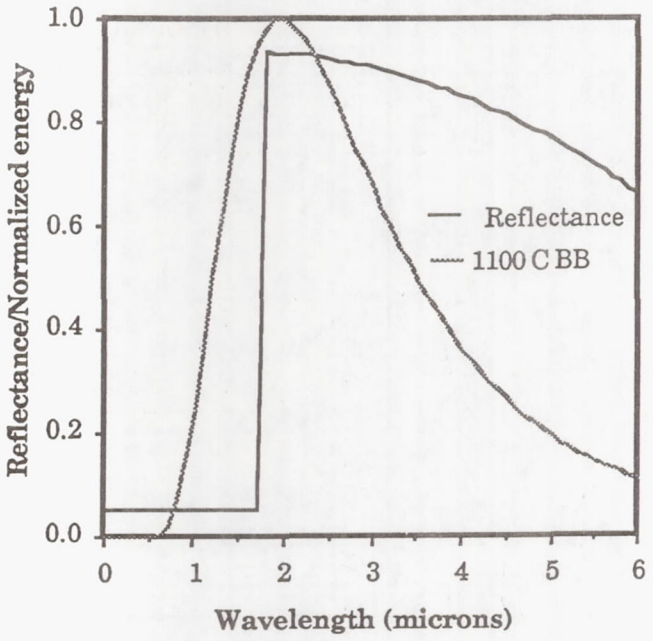

Figure 2: Predicted reflectance of GaSb cell with reflective rear contact. The emission spectrum of a 1100 C blackbody is included for reference.

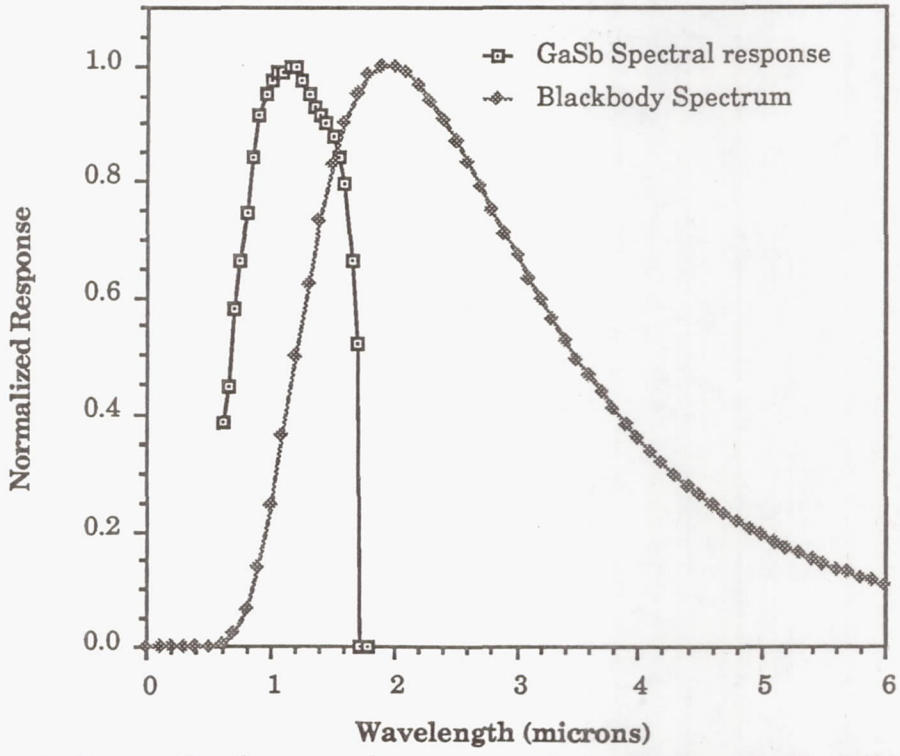

Figure 3 Normalized spectral response of the Boeing GaSb cell and a normalized 1100 C blackbody spectrum.

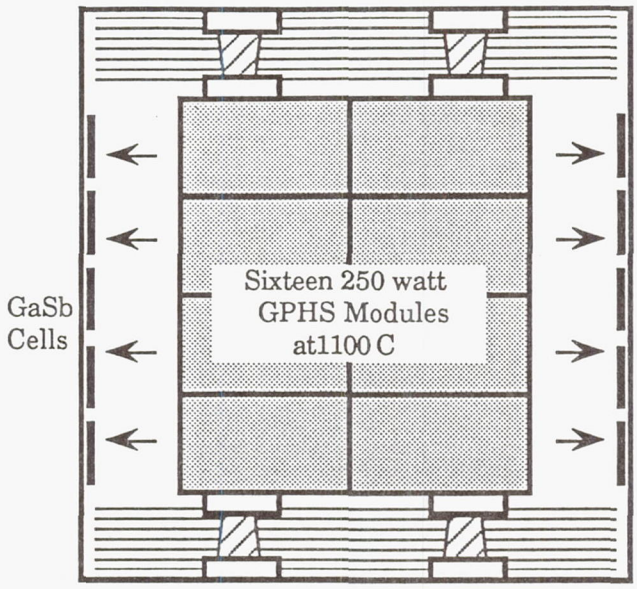

Figure 4. Configuration of an RTPV generator, based on use of GPHS source modules.

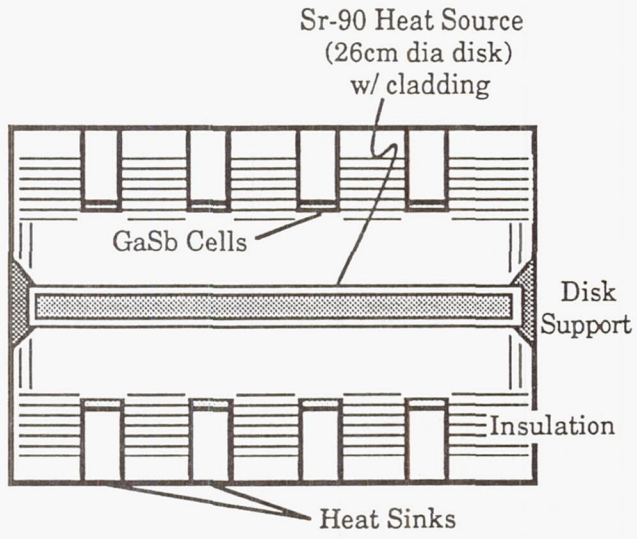

Figure 5: Schematic of a cylindrical 500 watt Sr-90 RTPV system.

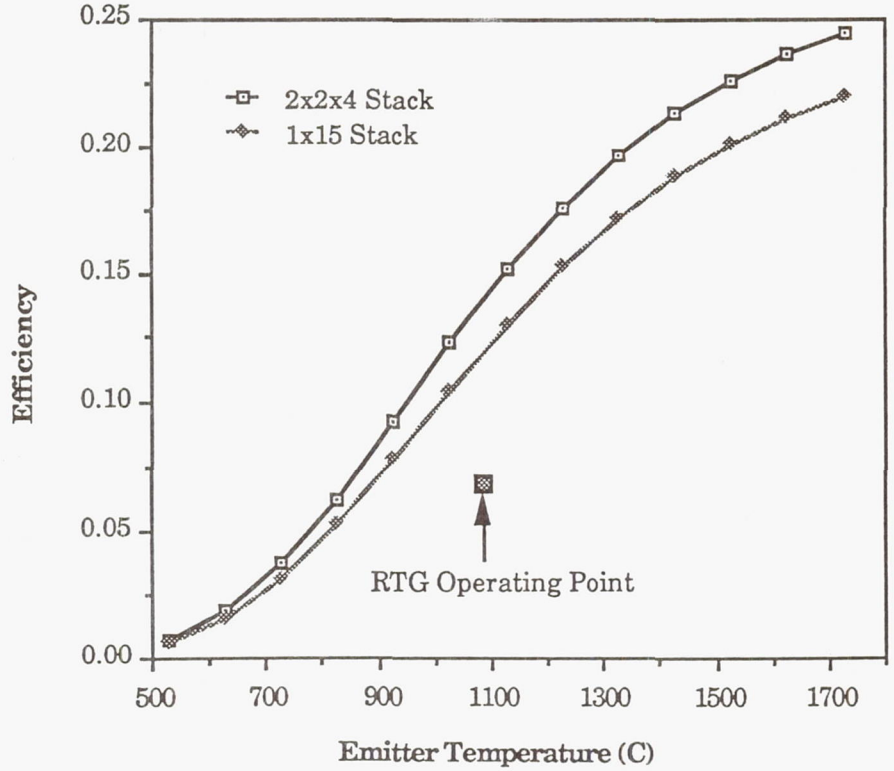

Figure 6: Efficiency of system which utilizes the GPHS verses temperature.

GaP Betavoltaic Cells as a Power Source*

F.S. Pool, P. Stella, B. Anspaugh
Jet Propulsion Laboratory
California Institute of Technology
Pasadena, California

Introduction

Since the launch of the very first satellite, photovoltaics has been the most widely used spacecraft power source. Used not only for earth orbiters, but also for a wide range of interplanetary applications such as a Mercury flyby, Venus orbiters, lunar surface power, and Mars orbiters, photovoltaic systems have demonstrated great versatility. However, photovoltaics are limited by the availability of solar illumination. For missions that operate far from the sun and for those with lengthy non illuminated periods, significant system compromises are required. In some cases the use of non PV power sources, such as the RTG (radio-isotope thermoelectric generator), has been implemented. Extending the range of applications of PV to these more difficult situations has been one of the challenges for PV technology development. Much of that effort has addressed methods for reducing photovoltaic system mass and increasing system conversion efficiency.

For many years the workhorse of space photovoltaics, the silicon solar cell, has been reliably used to power heart pacers in the form of betavoltaics [ref. 1]. The beta cell functions analogously to a solar cell, with the radiant energy of the sun replaced by the emitted electron flux. The emitted high energy electrons (beta particles) from the radioactive source traverse the cell material losing energy and thereby creating electron-hole pairs [ref. 2]. Those carriers within a diffusion length of the junction will be swept across contributing a current. An equivalent circuit for the device is identical to that for a solar cell. Such converters are free from the limitations of a solar light source and can operate where conventional photovoltaics are least capable.

During the past decade the use of microelectronic fabrication methods has allowed the fabrication of a diverse variety of advanced solar cell structures. In view of this progress, an investigation was undertaken in order to ascertain if a significant improvement in betavoltaic conversion efficiency could be realized. In particular the use of a GaP device was evaluated experimentally; GaP is an indirect wide-gap semiconductor [ref. 3]. The purpose of this study was to define the power limitations of current GaP beta cells and examine the efficiency and extent of radiation damage in GaP at the energies of interest.

* This work was performed by the Jet Propulsion Laboratory, California Institute of Technology, under contract to the National Aeronautics and Space Administration.

Experimental

The GaP cells used in this study, shown schematically in Figure 1, were fabricated by Astropower Corporation. GaP was chosen as a cell material because of its wide band gap. It has been shown that device efficiency is a function of band gap, with wide-gap materials possessing higher efficiencies [refs. 1-2]. The GaP cells are a 1cm x 1cm p/n structure grown by liquid phase epitaxy. As a comparison to the performance of the GaP beta cells, Si back surface field 2 cm x 2cm n/p solar cells fabricated by ASEC were exposed to identical conditions.

To approximately evaluate cell performance the average beta energy E_β was chosen for two emitters, Ni^{63} (E_β = 20 KeV, half-life 92 years) and Sr^{90}/Y^{90} (E_β = 200 KeV/ E_β = 900 KeV, half-life 28 years and 62 hours respectively). The latter radioactive source Sr^{90} decays to a daughter nucleus Y^{90} which also undergoes beta decay, hence the notation Sr^{90}/Y^{90}. The Jet Propulsion Laboratory Dynamitron electron accelerator was used as the source of monoenergetic incident electrons at 200 KeV and 40 KeV. A flux $\Phi = 2 \times 10^9$ electron/cm^{2}s, equivalent to a 54 mCurie source (1 Curie = 3.7×10^{10} disintegrations/s), was directed on the cells.

Betavoltaic I-V data was collected with a Tektronix 4052 computer interfaced to the experiment during exposure. Cell efficiencies were calculated as the ratio of maximum power output of the cell to incident power of the electrons

$$\eta = P_{max}/P_e$$

where P_e is the product of the electron flux, energy and cell area. All other parameters such as fill factor, open circuit voltage and short circuit current were determined in the usual way.

Results

In Figures 2 and 3 betavoltaic I-V curves are given for GaP beta cells and Si solar cells. The solid lines refer to the initial exposure and the dotted lines represent cell response after an exposure to a total fluence of 2×10^{12} electrons/cm^2. A summary of the cell characteristics is given in Tables 1-4.

The efficiency of the GaP cells was found to be 9 % at 40 KeV and 5% with exposure to 200 KeV electrons. The reason for the lower device efficiency at 200 KeV is due to the range of the electrons in GaP. At 40 KeV the electrons are stopped within 25 μm, depositing all energy in the active region of the cell. At 200 KeV the incident electrons penetrate approximately 160 μm, depositing a substantial fraction of energy in the substrate, further than a diffusion length (approximately 20 μm) from the depletion region of the cell. A comparison of the GaP cell efficiency to that of Si during exposure demonstrates the effectiveness of GaP over Si in this application. Typical Si heart pacer betavoltaic systems have efficiencies on the order of only 1%.

Power output of the GaP cells was found to be 3.2 μW and 1.2 μW under exposure to 200 KeV and 40 KeV electrons respectively. The limitation in the power output of the cells is primarily a function of the low incident power on the cells. The electron power at a flux of $2 \times 10^9/cm^2s$ is only 65 μW at 200 KeV and 13 μW at 40 KeV. The flux was chosen to represent that from a ideal thin-film source of Ni^{63}, 1 cm $\times$ 1 cm in area and 1 micron thick. A thin-film of the radioactive source is necessary to minimize weight and avoid self-absorption of the emitted beta particles by the source material.

To examine degradation of the cells, betavoltaic I-V data was taken after a prolonged exposure of 1000 seconds at the flux of $2 \times 10^9/cm^2s$ and compared to the initial data. In addition, standard solar I-V and spectral response data were taken as a diagnostic tool to evaluate the cells for radiation damage. GaP suffers a significant degradation in performance after exposure to 200 KeV electrons at a fluence of $2 \times 10^{12}/cm^2$. The beta I-V curve shown in Figure 3 shows a 32% decrease in I_{sc}. Cell degradation is also shown in Figures 4 and 5. A decrease in spectral response is observed at wavelengths greater than 0.43 μm, while the solar I-V shows a reduced I_{sc} of approximately 25%, consistent with the reduced I_{sc} of the beta I-V shown in Figure 3.

By contrast the exposure at 40 KeV produced no observable damage in GaP. The dotted line of Figure 3b is within the error of the experiment. The solar I-V and spectral response data also show no discernable reduction in device performance. The threshold for electron radiation damage in GaP may then be set in the range 40 KeV $< E <$ 200 KeV.

Given the above data it is useful to discuss a model for a power source based on betavoltaics. A system capable of producing power on the order of a few watts is most practical using a high energy beta emitter such as Sr^{90}/Y^{90}. The fundamental limitation is in the power available from the radioactive source and radiation damage to the cell. Due to the density of nickel and low beta energy the maximum source power ideally achieved with Ni^{63} would be on the order of 10 μW. However, Sr^{90} is much less dense (2.6 gm $/cm^3$) and represents an order of magnitude increase in the beta particle energy spectrum. It has been shown that if the source thickness for Sr^{90}/Y^{90} is approximately 1/8 the range of the average energy beta particle (200 KeV) self-absorption may be neglected [ref. 4]. Since Sr^{90} is readily available with activities of 75 Curies/gm, a 1 cm $\times$ 1cm source 35 μm thick would have an activity of about 1 Curie.

For a system based on Sr^{90}/Y^{90}, an estimate of the power available may be made from the average energy of the two emitted Sr^{90}/Y^{90} betas i.e., 550 KeV. A 1 Curie source will produce roughly 3 mW of power. Assuming an efficiency of 9% a cell output power of 0.3 mW would result. To produce 5 watts of power about 16,000 cells would be required. Excluding packaging this system would weigh about 3 kg and occupy a volume of 700 cm^3. Although not an advantageous system in terms of

specific power it represents a battery capable of delivering several watts of power over a period of 25 to 50 years without recharging.

Even with higher cell efficiencies, which are certainly possible, betavoltaic system specific power will still remain low, especially when compared to typical space PV systems. However, it is not intended that betavoltaics compete directly with photovoltaics. Instead the betavoltaic option is better suited to compete with RTGs or batteries. For the latter case, betavoltaics would best match requirements for a long lived, low power, continuous power source.

A possible solution to the problem of radiation damage is to operate the cell at annealing temperatures. A GaP cell could operate at an elevated temperature due to dissipation of radioactive energy not accessed by the device. If annealing properties are rapid in GaP the cells could operate for extended periods under exposure to the high energy electrons discussed above. However, at this time annealing properties of GaP are not known. The possibility of other radiation hard wide-gap materials has not been investigated and could lead to the use of novel materials for this application.

Conclusions

Maximum power output for the GaP cells of this study was found to be on the order of 1 μW. This resulted from exposure to 200 KeV and 40 KeV electrons at a flux of 2×10^9 electrons/cm^{2}s, equivalent to a 54 mCurie source. The efficiencies of the cells ranged from 5% to 9% for 200 KeV and 40 KeV electrons respectively. The lower efficiency at higher energy is due to a substantial fraction of energy deposition in the substrate, further than a diffusion length from the depletion region of the cell. Radiation damage was clearly observed in GaP after exposure to 200 KeV electrons at a fluence of 2×10^{12} electrons/cm^2. No discernable damage was observed after exposure to 40 KeV electrons at the same fluence.

Analysis indicates that a GaP betavoltaic system would not be practical if limited to low energy beta sources ($E_\beta \leq 100$ KeV). The power available would be too low even in the ideal case. By utilizing high activity bet a sources, such as Sr^{90}/Y^{90}, it may be possible to achieve performance that could be suitable for some space power applications. However, to utilize such a source the problem of radiation damage in the beta cell material must be overcome.

References

[1.] L. C. Olson, Energy Conversion**13**, 117, 1972.

[2.] L. C. Olson, *9th Intersociety Energy Conversion Engineering Conference*, 1974.

[3.] W. G. Pfann and W. van Roosbroeck, J. Appl. Phys., **25**, 1422,1954.

[4.] M. B. Panish and H. C. Casey, J. Appl. Phys., **40**, 163, 1969.

Table 1. - GaP Beta I-V Characteristics
Fluence = 2 x 10^9 electrons/cm^2s

cell	E_e(KeV)	J_{sc}(μA/cm^2)	V_{oc}(V)	FF	Eff(%)
10	200	4.1	1.2	0.65	5
8	40	2.3	1.0	0.51	9

Table 2. - Beta I-V Characteristics GaP
Fluence = 2 x 10^{12} electrons/cm^2s

cell	E_e(KeV)	J_{sc}(μA/cm^2)	V_{oc}(V)	FF	Eff(%)
10	200	2.7	1.2	0.64	3
8	40	2.3	1.0	0.52	9

Table 3. - Si Beta I-V Characteristics
Fluence = 2 x 10^9 electrons/cm^2s

cell	E_e(KeV)	J_{sc}(μA/cm^2)	V_{oc}(V)	FF	Eff(%)
119	200	29	128	0.38	2
141	40	8	64	0.25	1

Table 4. - Si Beta I-V Characteristics
Fluence = 2 x 10^{12} electrons/cm^2s

cell	E_e(KeV)	J_{sc}(μA/cm^2)	V_{oc}(V)	FF	Eff(%)
119	200	28	84	0.33	1
141	40	7	60	0.26	1

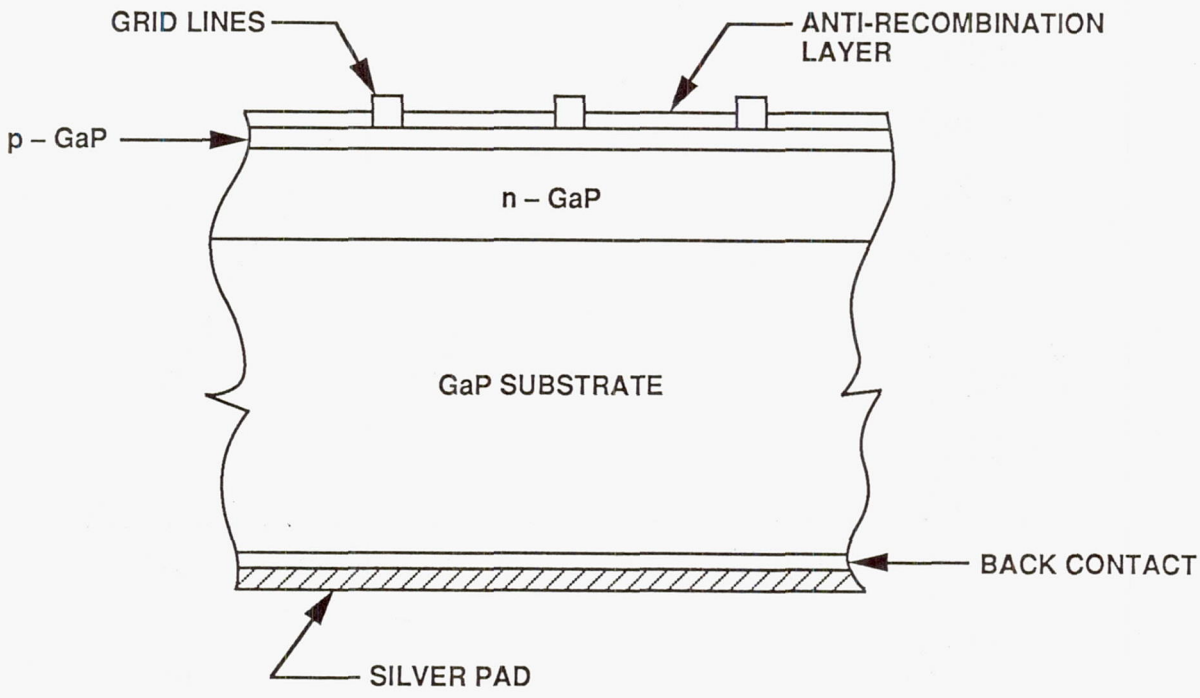

Figure 1. A schematic of the GaP beta cell structure.

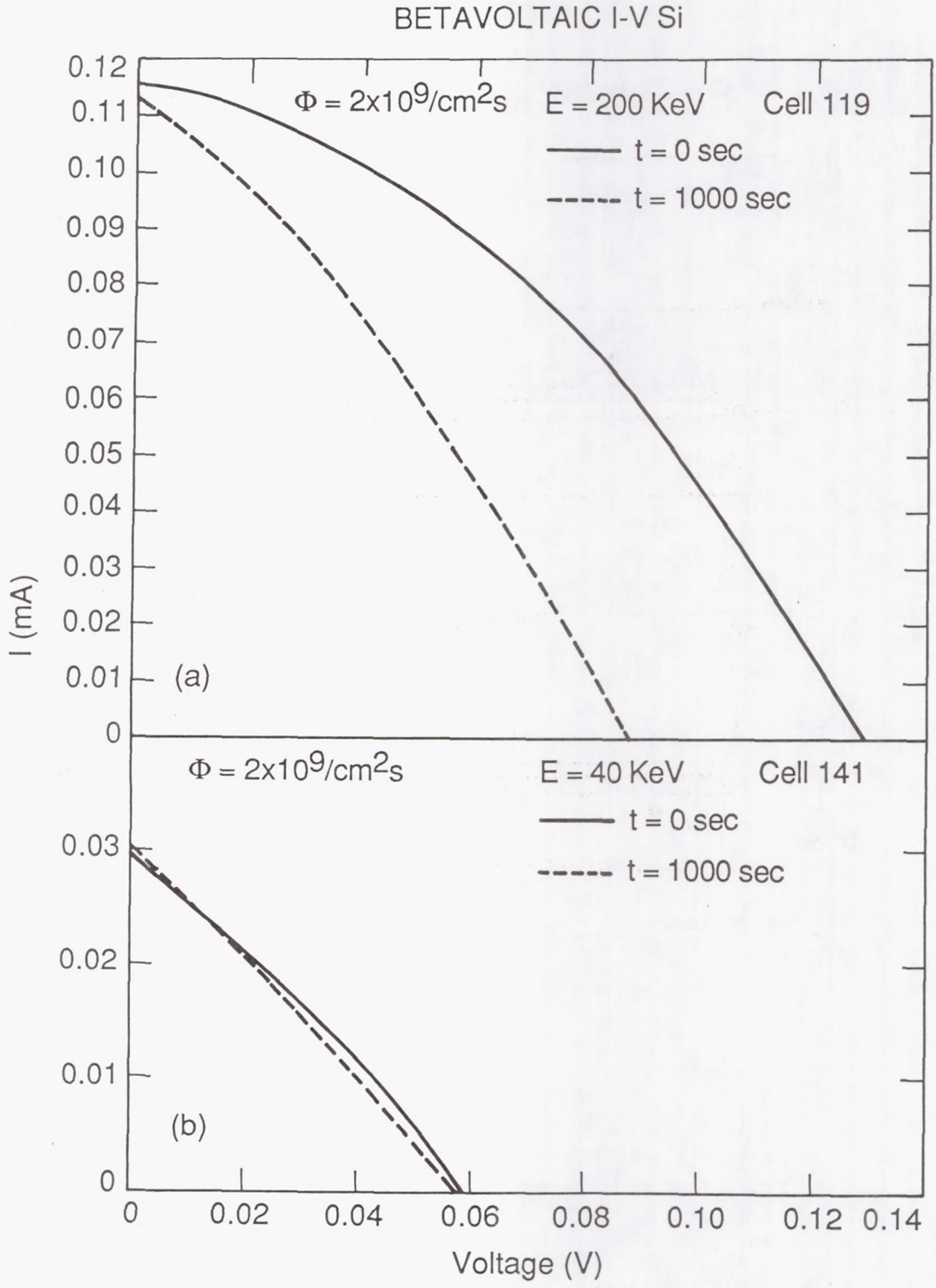

Figure 2. Betavoltaic I-V of Si solar cells for (a) 200 KeV and (b) 40 KeV electron exposures at a flux of 2 x 10^9 electrons/cm^2s.

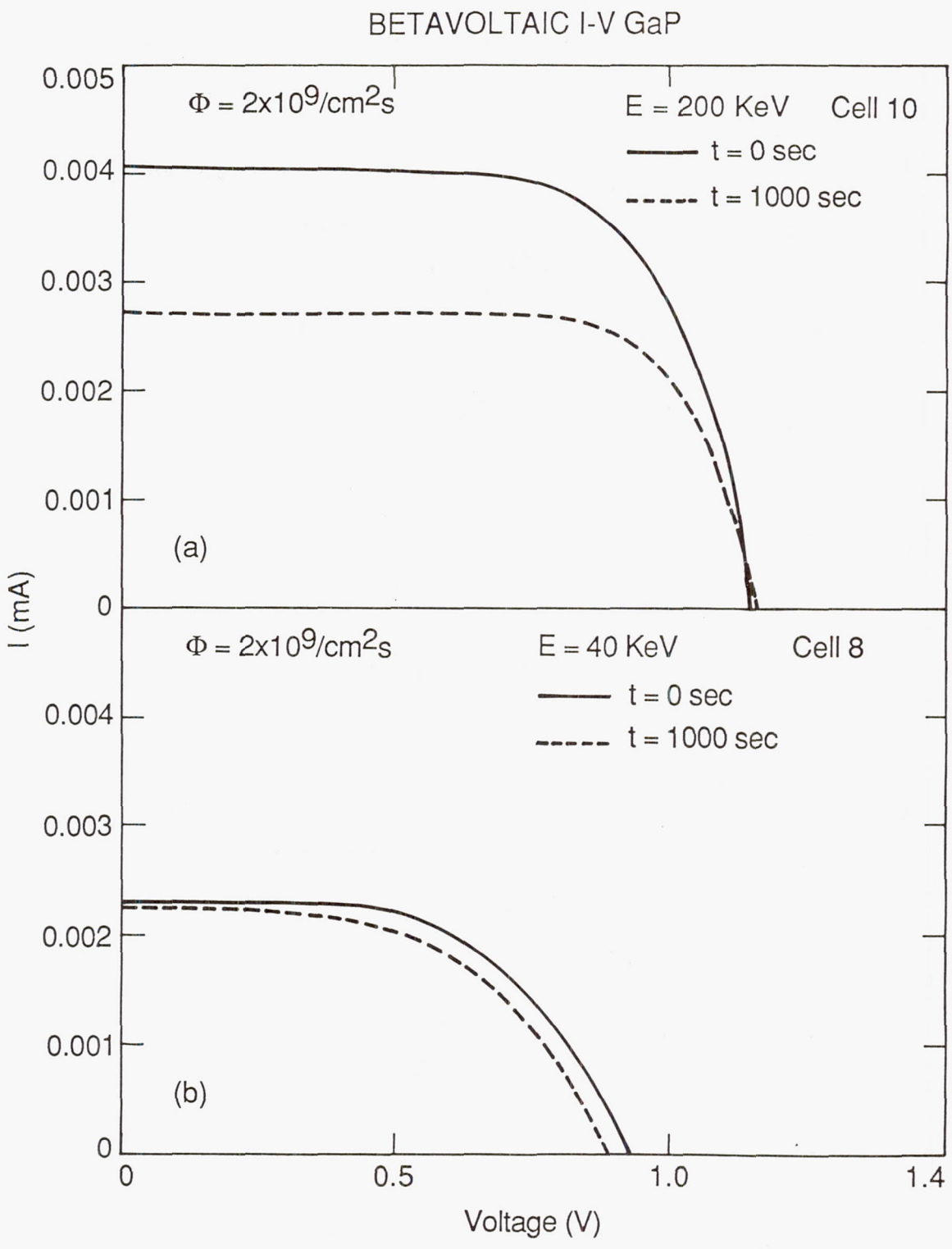

Figure 3. Betavoltaic I-V for GaP beta cells for (a) 200 KeV and (b) 40 KeV electron exposures at a flux of 2 x 10^9 electons/cm^2s.

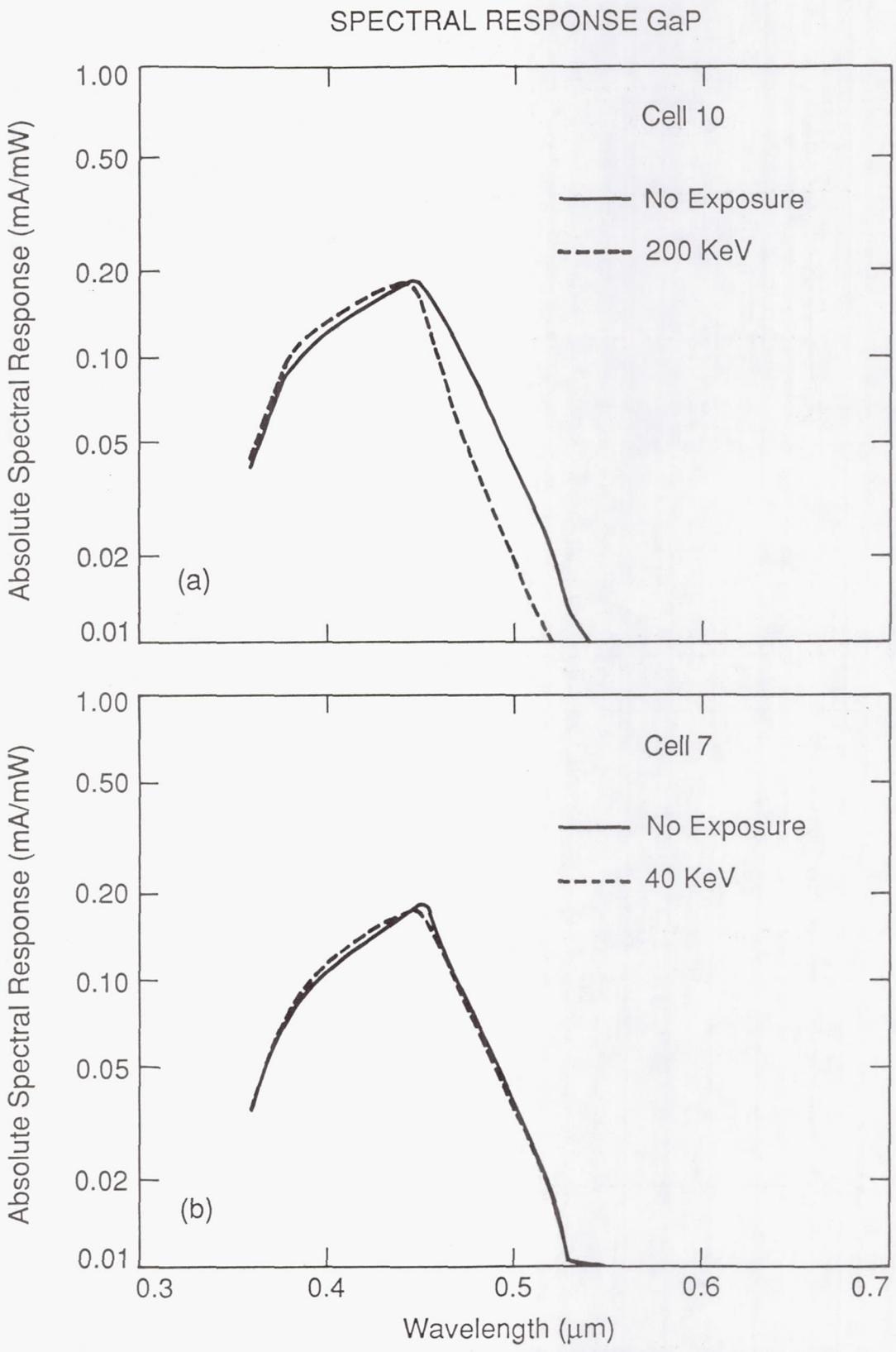

Figure 4. Spectral response of GaP beta cells before and after exposure to (a) 200 KeV and (b) 40 KeV electrons to a total fluence of 2×10^{12} electrons/cm^2s.

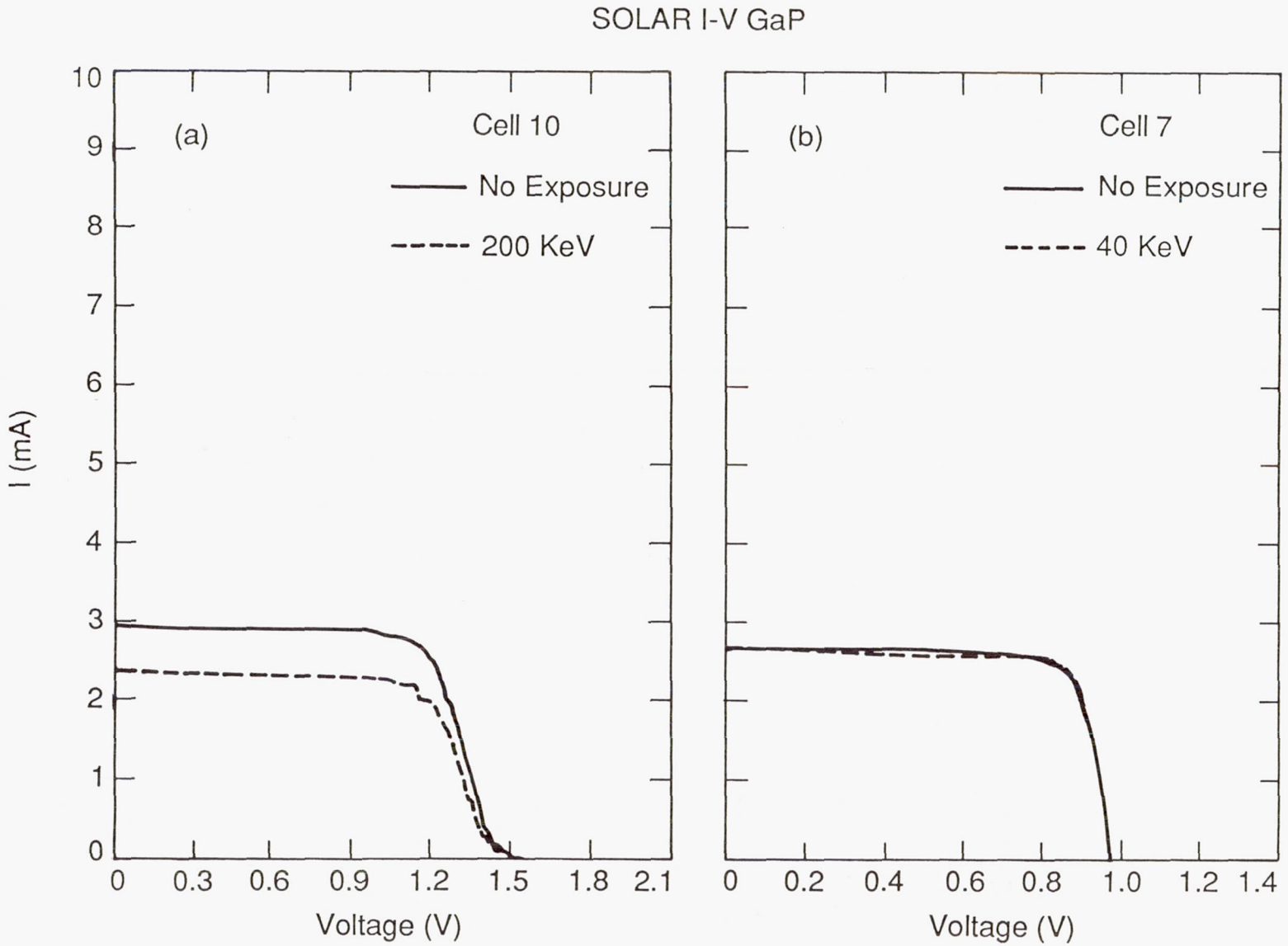

Figure 5. Solar I-V data of GaP beta cells before and after exposure to (a) 200 KeV and (b) 40 KeV electrons to a fluence of 2×10^{12} electrons/cm^2s.

Low Cost Space Power Generation

Randall B. Olsen
Chronos Research Laboratories, Inc.
4186 Sorrento Valley Blvd., Suite H
San Diego, CA

Introduction

Future commercialization of space will be constrained by the high cost of energy. With photovoltaic systems costing about $1,000,000 per electrical kiloWatt, space power is far more expensive than terrestrial power. From the point of view of a potential space manufacturer, the cost of electricity is over $17 per kW-hr or 170 times greater than the terrestrial rate [ref. 1]. Even with new low cost amorphous solar cell technology (or even with zero cost cells), the cost of electrical power will remain very high. The ultimate cost for any space power system is set by transportation costs (see Figure 1).

To achieve orders of magnitude cost reductions in space power, much lighter methods of generating electricity are needed.

A new method of electrical energy generation, pyroelectric conversion, promises to deliver power from a lightweight and inexpensive system.

The advantages of the pyroelectric approach include:

▷ higher power to mass ratio than photovoltaics and even nuclear reactor systems ⇒	LOWEST LAUNCH COST,
▷ active material is a polymer⇒	LOW MATERIALS COST,
▷ all condensed state device⇒	COMPACTNESS,
▷ no pressure vessels⇒	NO EXPLOSIVE HAZARD, LOW MASS CONTAINER,
▷ no single-point failure modes⇒	RELIABLE,
▷ high voltage⇒	EFFICIENT CURRENT COLLECTION AND POWER CONDITIONING,
▷ no toxic fluids⇒	SAFE FOR ASTRONAUTS AND DEVELOPMENT ENGINEERS,
▷ resistant to ionizing radiation⇒	CAN SURVIVE VAN ALLEN BELT RADIATION,

▷ resistant to ionizing radiation⇒	CAN BE USED FOR ORBIT RAISING (e.g. LEO to GEO),
▷ pyroelectric converters can be fashioned into belt radiators⇒	BUILT-IN THERMAL RADIATOR,
▷ with a thermal storage element, pyroelectrics may eventually outperform classical electrochemical batteries⇒	ENERGY STORAGE CAPABILITY,
▷ high voltage⇒	VOLTAGE MATCHED TO ION PROPULSION, and
▷ lowest mass power generation⇒	HIGHEST ACCELERATION FOR AN ELECTRIC PROPULSION SYSTEM.

The pyroelectric approach can convert collected solar heat with an efficiency approaching the Carnot limit. Advanced pyroelectric devices appear capable of exceeding 30% efficiency with materials and device improvements.

The pyroelectric converter generates electricity as a result of thermally cycling capacitor-like elements made of a polymer which will cost about $200 per electrical kiloWatt. This cost is based on the current price of a related polymer which is already commercially available.

Even more important than its inherently low materials cost, the pyroelectric approach offers dollar savings due to its light weight. Since it costs about $3000/kg to put a payload into low earth orbit (LEO) with the Shuttle [ref. 2], systems with high specific power are strongly favored. Figure 1 shows that pyroelectric power is significantly less expensive to place in orbit than photovoltaic, solar dynamic and nuclear power.

Ignoring, for the moment, the safety and reactor cost of the nearest competitor, the pyroelectric approach will clearly be less expensive to put into orbit. The transportation cost savings of a pyroelectric system will be at least $6 million for each 100 kiloWatt system delivered to LEO (compared with nuclear). In light of the Challenger disaster, the cost of assuring the safe delivery of nuclear systems into orbit would certainly be very high. Solar driven pyroelectric systems will be lighter, cheaper to manufacture and less expensive to develop.

When compared with photovoltaics, the pyroelectric approach will save 45 to 87 million dollars in delivery costs per 100 kW system.

Pyroelectric conversion represents an unusual opportunity for advanced power systems. It can provide energy storage, Carnot-limited conversion (heat to electricity), and thermal rejection. Furthermore the pyroelectric approach can provide these functions at very low specific mass and low cost.

In its simplest version, a pyroelectric converter can take the form of a rotating cylinder as shown in Figure 2. A given segment of the cylinder will alternately rotate into and out of the direct sunlight. As a result, the temperature of the segment will rise and fall during each revolution. If an externally applied voltage is raised and lowered in the appropriate phase relation to the temperature oscillation, a substantial amount of electrical power may be produced. Please refer to NASA CR-168727 for more information [ref. 3].

Pyroelectric conversion is a very promising method of making electricity in space (or on Earth). However, present pyroelectric technology must be developed before the promise can be realized. Several fundamental physical and chemical questions have already been successfully addressed.

Perhaps the most important fundamental question remaining regards the lifetime of the active polymer. These new materials had never been studied for more than a few hours of continuous thermal-electrical cycling.

Our objective was to quantify the long term stability of the energy conversion capabilities of a specific pyroelectric copolymer. We measured the thermally induced changes in the electric displacement of the copolymer vinylidene fluoride-trifluoroethylene [P(VDF-TrFE), 60% mol VDF].

We fabricated test specimens from extruded copolymer films and performed thermal-electrical cycling measurements. More specifically, we measured the effects of repetitive thermal and electrical cycling on the electrical polarization and energy density of the copolymer at elevated temperatures (20 up to 100°C).

Fundamentals of Pyroelectric Conversion

The pyroelectric effect is the flow of charge to and from the surfaces of a material resulting from a change in temperature [ref. 4]. This effect may be used for the conversion of heat directly into electrical energy. A pyroelectric converter is a form of heat engine. The thermodynamics of the pyroelectric converter are analogous to the more familiar steam engine with pressure-volume mechanical work replaced by voltage-charge electrical output.

The basic pyroelectric principle is illustrated in Figures 3 and 4. A pyroelectric material is formed into a thin film (shown edge-on in the figures) and sandwiched between two metallic electrodes to form a capacitor-like structure. At low temperature (below the Curie point), the electric dipoles of the pyroelectric material may be easily ordered or polarized by a low applied voltage.

Figure 4 shows that when the ordered pyroelectric slab is heated above its Curie temperature, the electric dipoles become thermally disordered. This causes the voltage on the electrodes to increase dramatically. If the slab electrodes are connected across a load, the high voltage forces the charge to flow through the load. The result

of heating the pyroelectric capacitor is to produce a high-voltage direct-current surge. The current flows only for a short time (the heating period of the slab). To produce more electrical power, the pyroelectric slab must be cooled, re-polarized and then re-heated. Each thermal cycle creates additional electrical energy from heat.

Pyroelectric Conversion Cycle

Figure 5 shows an overlay of the charge-voltage (electric displacement versus electric field) characteristics of a polymer pyroelectric material at two different temperatures. The shaded area of Figure 5 is a pyroelectric conversion cycle, and represents the electrical energy produced in the conversion process. The cycle is an electrical analog of the Ericsson heat engine cycle. It consists of two isothermal portions and two isostress (isoelectrical field) portions. Details of this and other cycles have been presented previously [refs. 5-7].

Poly(vinylidene fluoride-trifluoroethylene), P(VDF-TrFE), was chosen for study because it is the highest performance pyroelectric conversion material known.

Results and Discussion

Figure 8 shows a typical power cycle. Beginning at point 1 in the cold bath at low temperature and low electric field, the electric field was increased isothermally in approximately 1 second to a high value, which resulted in an increased displacement. When the high electric field was reached (point 2), the temperature of the sample was increased by moving it into the hot bath. This resulted in partial thermal depoling of the sample. When the thermal depoling stopped (point 3), the electric field was decreased to its original low value (point 4). Finally, the sample was cooled by moving it into the cold bath which caused the displacement to increase. The cycle was completed when the sample was cooled to its original low temperature (point 5). The apparent difference in displacement between point 5 and point 1 resulted from electrical conduction through the sample during the cycle.

Figure 8 also defines three quantities which describe a power cycle. The depoling displacement change is defined by the warming isofield line from point 2 to point 3. The repoling displacement change is defined by the cooling isofield line from point 4 to point 5. The conduction charge (per unit area) is given by the distance from point 1 to point 5.

To compare the durability of the strengthened samples with unenhanced samples, a pyroelectric power cycle test was applied to both types of specimens. After hysteresis poling (5 cycles), each sample was subjected to thermal cycling between room temperature and 100°C, while simultaneously electrically cycling between 20 and 50 MV/m.

In the case of the unstrengthened samples, no specimen survived more than 10 thermal-electrical cycles before suffering dielectric failure. The lifetime performance of the enhanced samples was dramatically improved. In spite of 24 hours of continuous power cycling, the strengthened sample (Sample A) was still producing electrical power as if it were new. After producing over 13,000 cycles, the power cycling experiment was halted without notable decrease in performance. The lifetime enhancement was a factor of at least 1,300 over the unstrengthened specimens.

Prior to this time, we had never encountered extended lifetime performance at such high electric fields (even with compression molded films). Due to the exceptional performance of these films we decided to try a higher frequency electrical test. We applied 60 Hz electrical cycling to provide many more electrical cycles in a short period of time.

Sample A was then subjected to 60 Hz unipolar voltage (10 to 40 MV/m) at 100°C. After 15 hours of high frequency cycling (3,240,000 cycles) the sample was subjected to power cycling and showed essentially the same displacement change performance as before. This sequence is illustrated in Figure 9.

Next, Sample A was subjected to 60 Hz unipolar voltage (10 to 60 MV/m) at 100°C. After 1 hour of high frequency cycling at this higher electric field, the sample's electrical properties were unaffected. Following a second hour of high frequency (V_{max} = 60 MV/m) cycling, the displacement changes measured in power cycles were found to have been reduced to 2/3 of their original values. This reduction was explained by 1/3 of the specimen becoming electrically disconnected (which agreed with visual observation). After being subjected to 2 more hours of high frequency cycling under these conditions, the sample remained stable.

Sample A was then subjected to 60 Hz unipolar voltage (10 to 70 MV/m) at 100°C. After 2 hours of high frequency cycling to this electric field, the sample's electrical properties were unaffected.

Finally, Sample A was subjected to 60 Hz unipolar voltage (10 to 80 MV/m) at 100°C. After 1 hour of high frequency cycling to 80 MV/m, degradation of the sample's electrical properties were found. The displacement changes had dropped to 25% of their original values. This reduction was explained by 3/4 of the specimen becoming electrically disconnected (again consistent with visual observation - the sample resembled a very highly pocked and cratered lunar surface). At this point the test was terminated.

It is important to note that the specimen degraded only after being subjected to voltages (3500 to 4000 V) which were in excess of the A.C. corona inception voltage (3000 V). Furthermore, the sample degradation appeared to be corona dominated (electrode edges were eroded by the corona process). If the maximum voltage is maintained below the corona inception voltage, this degradation pathway can be minimized if not completely eliminated.

A second sample (Sample B) from the B run was then studied. This sample was subjected to 16 hours of nonstop power cycling (thermal cycling between room temperature and 100°C, while simultaneously electrically cycling between 20 and 50 MV/m). No decrease in pyroelectric performance was detected.

Sample B was then subjected to 60 Hz unipolar voltage (10 to 40 MV/m) at 100°C. After 22 hours of high frequency cycling (4,752,000 cycles) the sample was subjected to power cycling and showed essentially the same displacement change performance as before. This sequence is illustrated in Figure 8.

The upper field limit was raised to 50 MV/m and 60 Hz cycling restarted. The sample was electrically and visually monitored for an additional 12 days. After a total of more than 67 million electrical cycles at 100°C, the electrical properties remained stable. The test was terminated to allow for other experiments. This test ended with no decrease in the pyroelectric performance of the specimen.

A third sample (Sample C) survived an even longer duration test. Sample C was subjected to simultaneous 60 Hz electrical cycling (20 to 30 MV/m) and thermal cycling (35 to 100°C) for 24 hours and showed no decrease in energy output.

Due to safety concerns, the 60 Hz cycling for Sample C was performed at room temperature [ref. 8]. After 1800 hours of continuous 60 Hz cycling, Sample C still provided full pyroelectric energy density when interrupted for an energy production test. The corresponding number of electrical cycles has already exceeded 388 million. We are preparing a dedicated chamber to allow this test to continue beyond the present study.

Summary and Conclusions

The success of this study has given us a method of fabricating durable copolymer films without size limitations. Previously, only compression molded samples (of a few cm^2 in area) were durable enough to generate electrical energy.

The strengthened specimens are very long lived materials. The lifetime was enhanced at least a factor of 1,300 in full pyroelectric conversion cycle experiments compared with extruded, non-strengthened film. The new technique proved so successful that we were not able to fully characterize the lifetime of the resultant copolymer samples.

The lifetime of these new materials is so long that we had to devise accelerated tests to probe their durability. After a total of more than 67 million high voltage electrical cycles at 100° C, the electrical properties of a copolymer sample remained stable. The test was terminated without any detectable degradation to allow for other experiments. One must be cautious in extrapolating to power cycle performance, but 67 million electrical cycles correspond to 2 years of pyroelectric cycling at 1 Hz.

In another series of experiments at reduced temperature and electrical stress, a specimen survived over one-third of a billion electrical cycles during nearly three months of continuous testing.

The radiation-limited lifetimes of the copolymer have been shown to range from several years to millions of years for most earth orbits [ref. 9]. Thus, the pyroelectric copolymer has become a strong candidate for serious consideration for future spacecraft power systems.

References

[1.] Assuming a 10 year lifetime and 5% interest, the annual cost per kiloWatt would be $100,000 for amortization and $50,000 for interest. Since there are 8760 hours in a year, the hourly cost would be $150,000/8760 = $17.12/kW-hr. Terrestrial electrical rates vary, but are of the order of $0.10/kW-hr.

[2.] D. Denais, private communication and Johnson Space Center, July, 1986.

[3.] R. B. Olsen, NASA CR 168272 , 1983.

[4.] M. E. Lines and A. M. Glass, "Principles and Applications of Ferroelectrics and Related Materials", Clarendon, Oxford, 1977.

[5.] R. B. Olsen and D. Evans, J. Appl. Phys **54**, 5941, 1983.

[6.] R. B. Olsen, D. A. Bruno, J. M. Briscoe and E. W. Jacobs, J. Appl. Phys. **57**, 5036, 1985.

[7.] R. B. Olsen, D. A. Bruno and J. M. Briscoe, J. Appl. Phys. **58**, 4709, 1985.

[8.] Our concern was that a thermocouple failure or a heat controller glitch could cause a fire during the long unattended experiment.

[9.] R. B. Olsen, NASA SBIR Phase I Report NAS7-946, 1986.

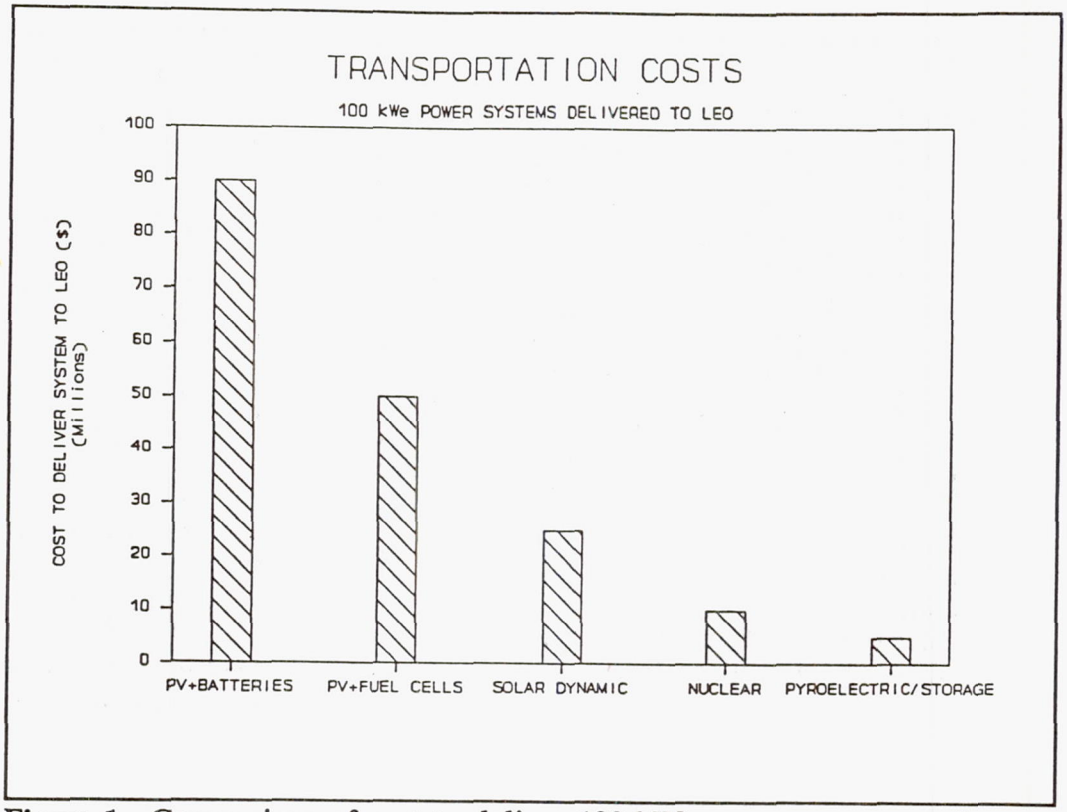

Figure 1. Comparison of cost to deliver 100 kWe power systems to low Earth orbit.

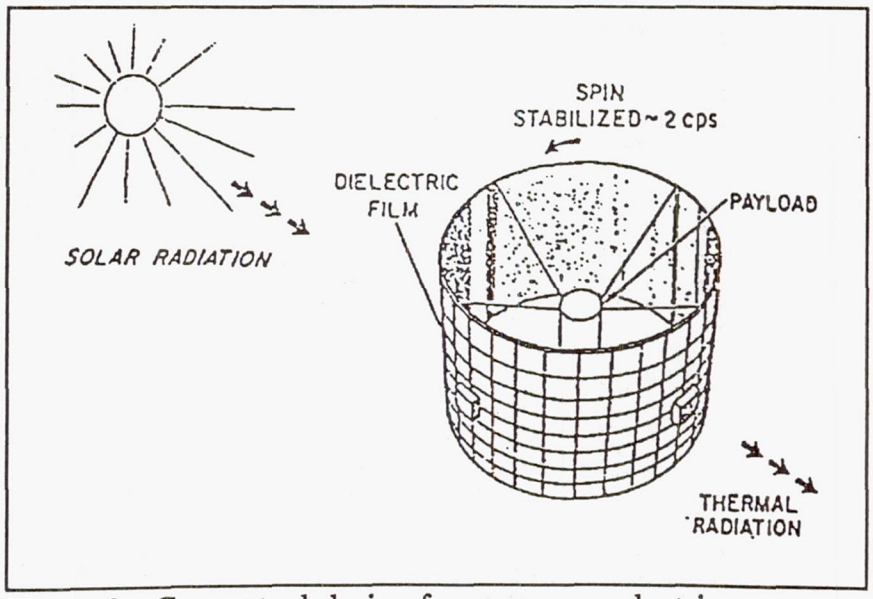

Figure 2. Conceptual design for space pyroelectric converter.

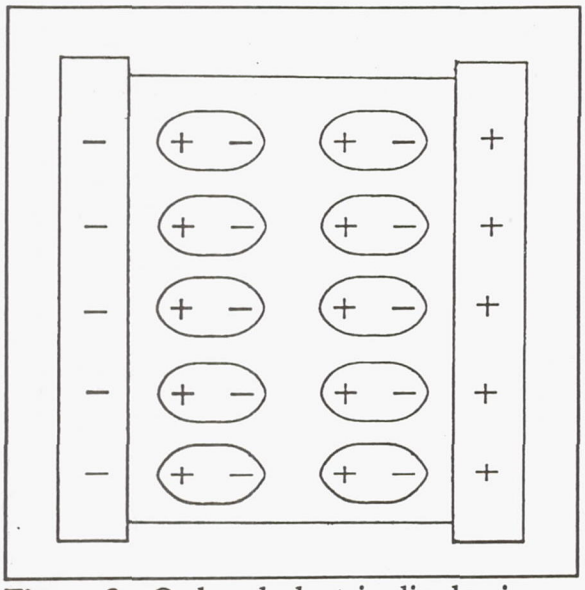

Figure 3. Ordered electric dipoles in a pyroelectric at low temperature.

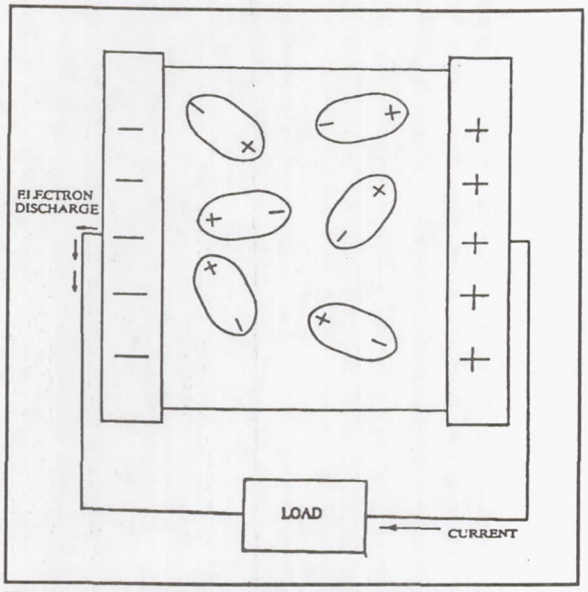

Figure 4. Heating the pyroelectric disorders the dipoles. This drives charge through a load at high voltage.

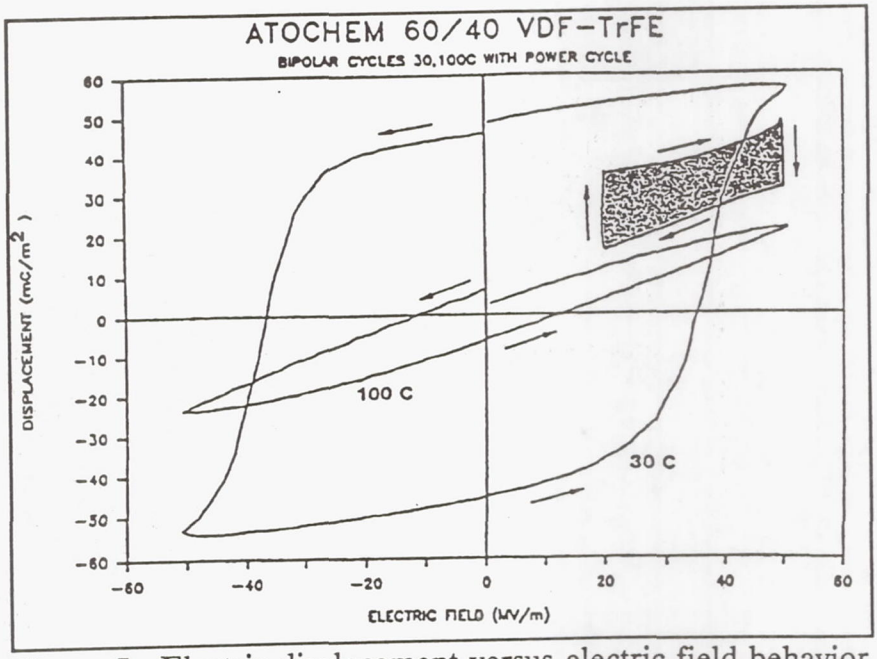

Figure 5. Electric displacement versus electric field behavior of a 60/40 mol % copolymer of vinylidene fluoride and trifluoroethylene.

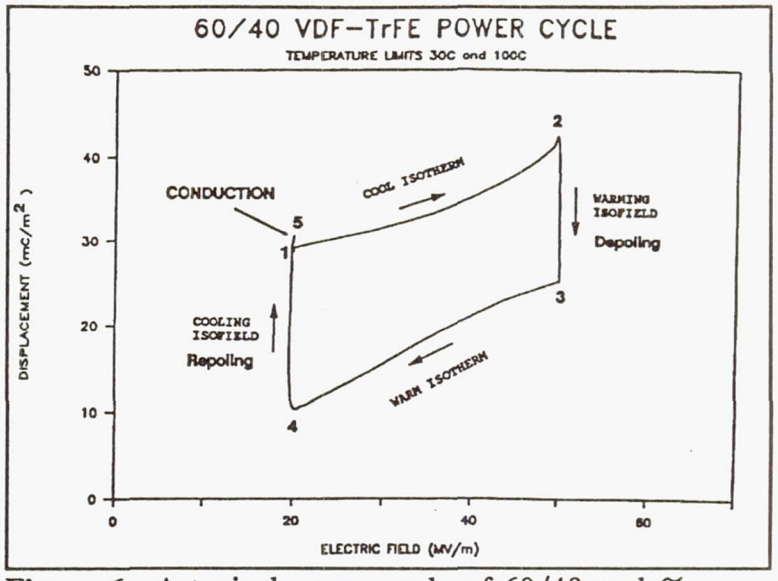

Figure 6. A typical power cycle of 60/40 mol % P(VDF-TrFE). The temperature extremes were 30 and 100 °C.

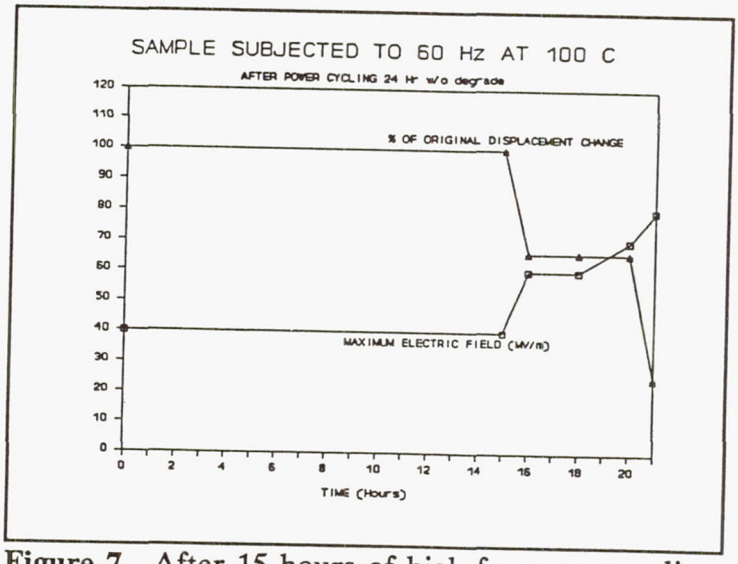

Figure 7. After 15 hours of high frequency cycling, Sample A displayed little change in displacement performance.

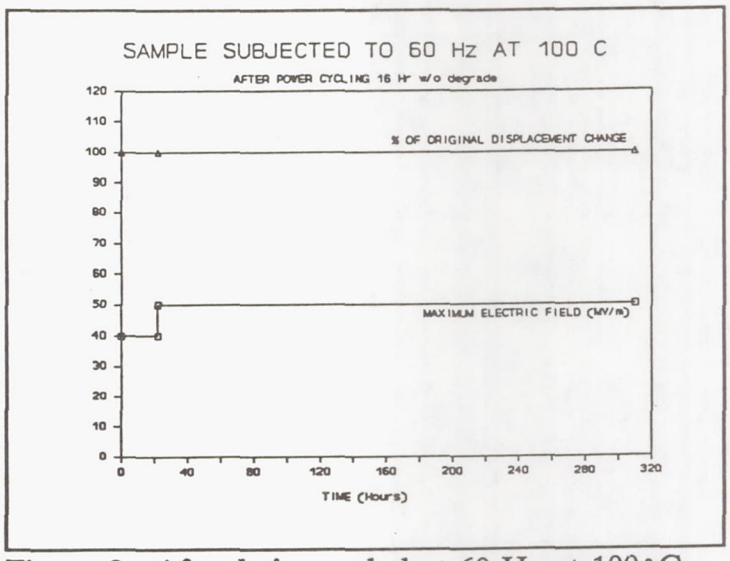

Figure 8. After being cycled at 60 Hz at 100°C for more than 300 hours, Sample B exhibited undiminished pyroelectric properties.

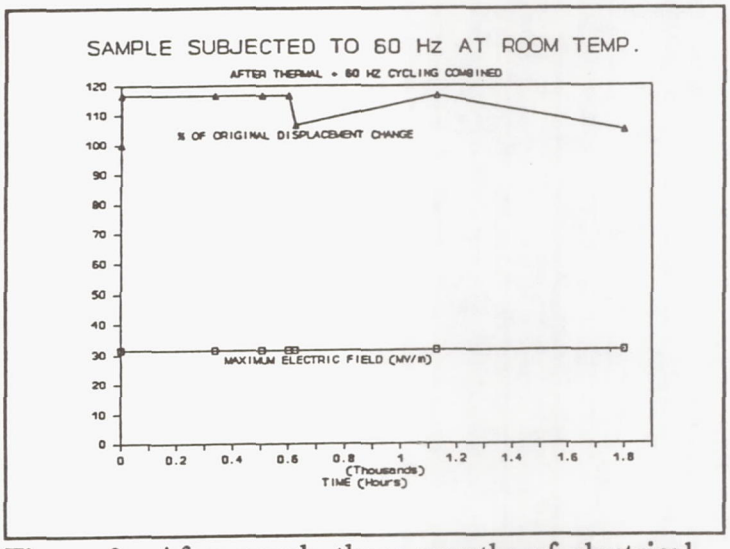

Figure 9. After nearly three months of electrical cycling, sample C exhibited very little degradation in performance.

Session 6
Solar Cell and Array Development

Preceding Page Blank

Spaceflight Performance of Several Types of Silicon Solar Cells on the LIPS III Satellite

J. Silver and D. Warfield
The Solarex Aerospace Division
Rockville, Maryland

Results from exposure of several types of Solarex silicon solar cells to a space environment for nearly two years on the LIPS III satellite are presented. Experiments include standard thickness (10 mil) cells with and without back surface fields, and ultrathin (2 mil) cells also with and without back surface fields. A comparison between a widely used coverslide adhesive, DC 93-500, and a potential alternate is also presented.

The major findings from the data are that the 2 mil cells without a back surface field show the smallest normalized short circuit current degradation and that the 10 mil back surface field cells show the greatest absolute power output for the radiation exposures and temperatures encountered. The new encapsulant (McGhan Nusil CV-2500) exhibits a degradation comparable to DC 93500.

A comparison is made with each of the cell types in this experiment with expectations based on JPL Radiation Handbook data.

Description of Experiments

Ten 2 x 2 cm Solarex silicon solar cells were launched on the LIPS III spacecraft into a nearly circular 1100 km orbit in the spring of 1987, reference 1. Two cells from each of the following groups were included: a) 10 mil BSF (with DC 93-500 adhesive); b) 10 mil BSFR (with McGhan Nusil CV-2500 adhesive); c) 10 mil BSR; d) 2 mil BSFR; e) 2 mil BSR. All of the cells had dual layer antireflective coatings, 12 mil coverslides attached to the cell using DC 93-500 except for b), and titanium/palladium/silver contacts. Each of the cells were fabricated using silicon with 10 ohm-cm bulk resistivity and had an aluminum reflector on the back surface.

Current-voltage characteristics for each of the cells were monitored throughout a 650 day period along with cell temperature and solar constant correction factors. As has been reported for other LIPS III data, reference 2, anomalous fluctuations in current were observed for each of the groups. However, relative comparisons between each of the groups and expectations for each of the groups can be made.

Results

Measured short circuit current degradation with time in orbit is shown in Figures 1-4. The data is corrected for variations in solar constant and temperature. Expected

Preceding Page Blank

degradation curves based on a fluence of 2.28 x 1013 equivalent 1 MeV electron/cm2 fluence per year are shown for each cell type (except for the 2 mil BSR for which no data was available).

As expected, the 2 mil cells show the smallest normalized short circuit current degradation. The 10 mil BSF cells show the greatest relative power degradation. However, for the radiation levels and temperatures encountered in orbit, the 10 mil BSFR cells still maintain the highest total power output. Since the 10 mil BSR cells do not have a back surface field, their relative current output degraded more slowly than the BSFR cells. Both solar cell/coverslide adhesives used for the 10 mil BSFR cells performed comparably.

Solarex vertical junction cells were also present on this spacecraft. This carries special significance as it is the first successful flight test of covered vertical junction cells and demonstrates the effectiveness of a new covering technique. As reported previously, reference 3, these cells showed comparable degradation to planar 10 mil BSFR cells for the environmental conditions seen to date. The vertical junction cells, however, are expected to be capable of improved relative power output as radiation fluence levels increase.

All of the Solarex cells in this experiment have survived 9599 thermal cycles as of this writing with no observed failures.

References

J. G. Severns, R. M. Hobbs, N. P. Elliott, R. H. Towsley, R. W. Conway and G. F. Virshup, "LIPS III-A Solar Cell Test Bed in Space", l9th IEEE Photovoltaic Specialist Conference, 1988, p. 801.

J. G. Severns, R. W. Conway, B. J. Faraday and R. M. Hobbs, "Flight Experience with LIPS-III", 24th IECEC Proceedings, 1989, p. 399

R. L. Statler, "The Effects of Space Environment on Silicon Vertical Junction Solar Cells on the LIPS-III Satellite", 24th IECEC Proceedings, 1989, p. 405.

Fig. 1

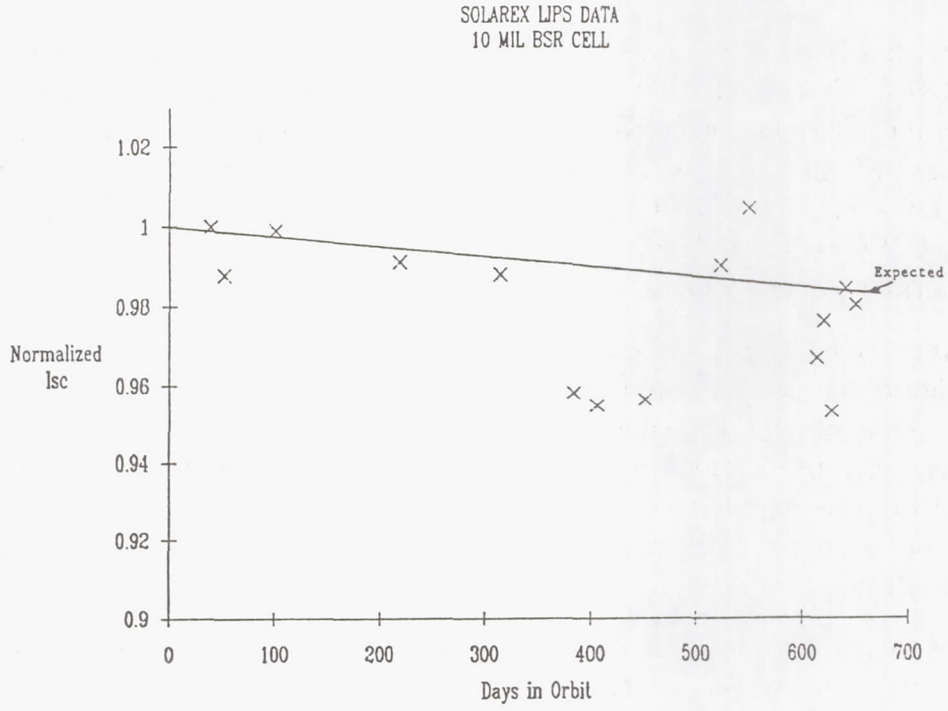
SOLAREX LIPS DATA
10 MIL BSR CELL
Normalized Isc
1.02
1
0.98
0.96
0.94
0.92
0.9
Expected
0
100
200
300
400
500
600
700
Days in Orbit

Fig. 2

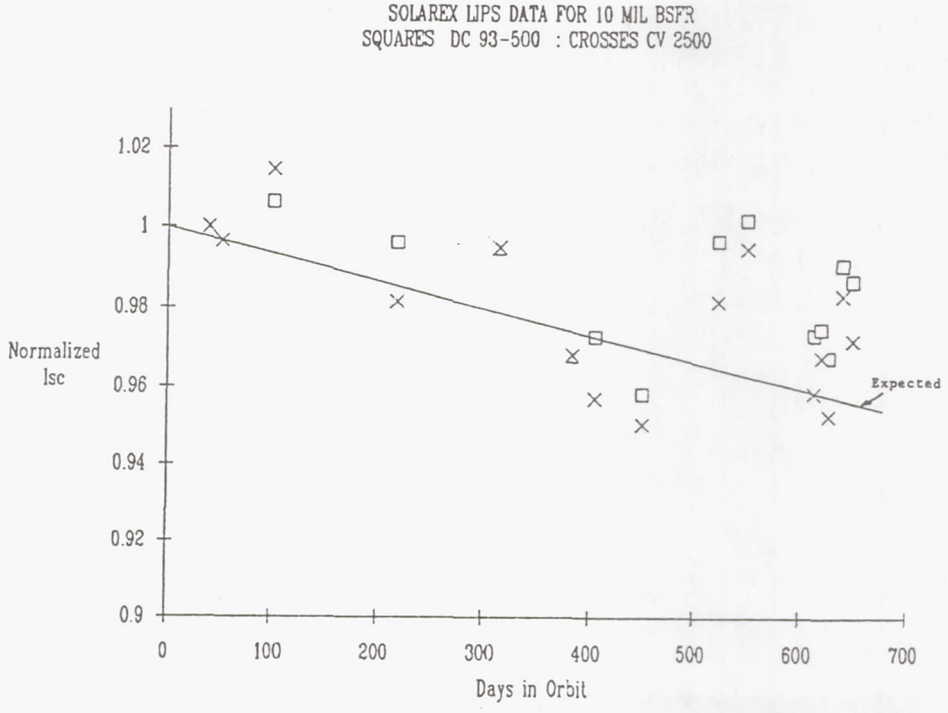
SOLAREX LIPS DATA FOR 10 MIL BSFR
SQUARES DC 93-500 : CROSSES CV 2500
Normalized Isc
1.02
1
0.98
0.96
0.94
0.92
0.9
Expected
0
100
200
300
400
500
600
700
Days in Orbit

Fig. 3

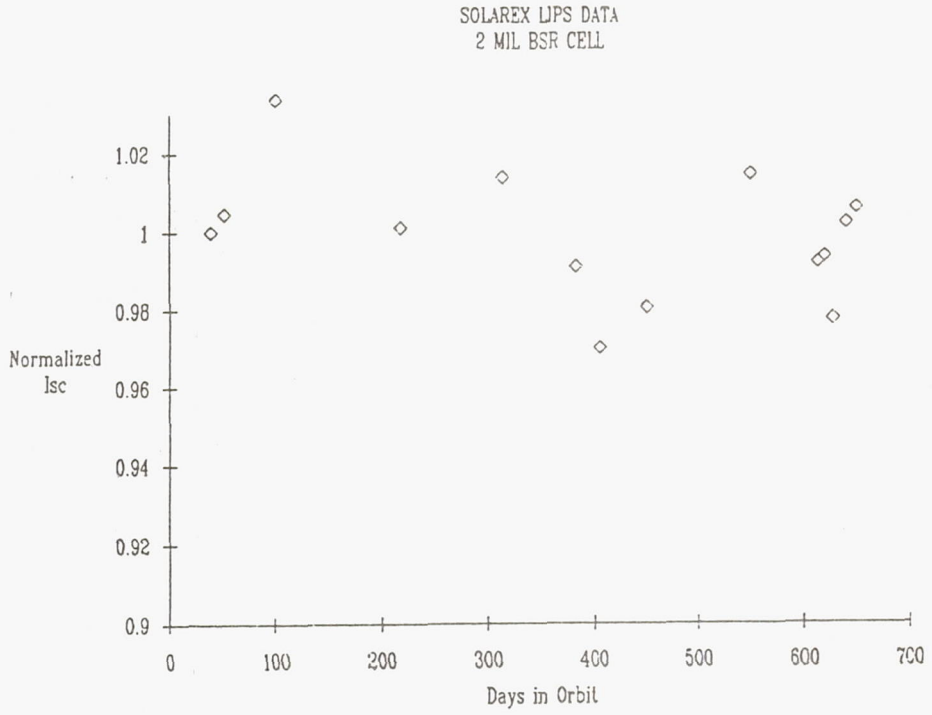
SOLAREX LIPS DATA
2 MIL BSR CELL
Normalized Isc
1.02
1
0.98
0.96
0.94
0.92
0.9
0
100
200
300
400
500
600
700
Days in Orbit

Fig. 4

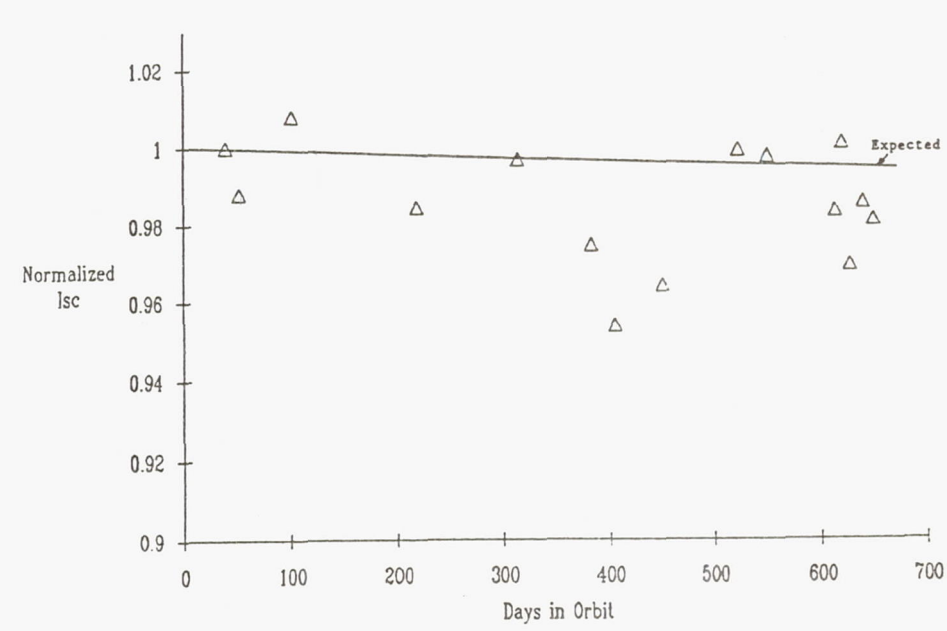
SOLAREX LIPS DATA
2 MIL BSFR CELL
Normalized Isc
1.02
1
0.98
0.96
0.94
0.92
0.9
Expected
0
100
200
300
400
500
600
700
Days in Orbit

Annealing Characteristics of Irradiated Hydrogenated Amorphous Silicon Solar Cells

J. S. Payson, S. Abdulaziz, Y. Li and J. R. Woodyard
Institute for Manufacturing Research
and
Department of Electrical and Computer Engineering
Wayne State University
Detroit, MI

Introduction

Hydrogenated amorphous silicon (a-Si:H) solar cells have recently been proposed as candidates for future advanced space solar cell arrays based primarily on its high specific power density and radiation tolerance [ref. 1]. The purpose of this work is to report on our investigations of the radiation resistance properties of a-Si:H solar cells.

Past work shows that the effect of 1.00 MeV proton irradiation on a-Si thin film alloy solar cells is to degrade the efficiency mainly through degradation of the short-circuit current and the fill-factor [ref. 2]. Changes in the short-circuit current become noticeable at a fluence of about 1E12 cm^{-2} and decrease to about zero at 1E15 cm^{-2}. The initial efficiency can be restored by annealing the device at about 160°C for various times depending on the fluence, i.e., the higher fluences require longer times to completely restore the efficiency of the solar cell. No room temperature annealing of irradiated solar cells has been reported.

We have recently irradiated a-Si:H thin films in order to elucidate the effect of proton irradiation on the intrinsic layer of the solar cell [ref. 3]. Thin films of 1.0 and 1.5 micrometer thicknesses were irradiated with 1.00 MeV proton fluences in the range of 1E11 to 1E15 cm^{-2}. The optical and electrical properties of the films were measured. Photothermal Deflection Spectroscopy (PDS) was used to measure the sub-band-gap optical absorption; the dependence of the steady-state photoconductivity on photon flux was measured. 1.00 MeV proton irradiation produced an increase in the sub-band-gap absorption. The sub-band-gap optical absorption was modelled using a convolution method with a density of states function with a peak at about 1.35 eV below the conduction band edge and a full-width at half-maximum of about 0.1 eV. Large decreases in the photoconductivity were also observed. The slope of the photoconductivity versus intensity did not change with irradiation, suggesting that the form of the density of states above the Fermi level was not drastically changing. Room temperature annealing of the sub-band-gap absorption was observed; large changes were observed over a period of nineteen days at room temperature. Following the room temperature anneals, the samples were annealed for one hour at 175°C and the sub-band-gap absorption was restored to its original level for most of the

samples. The sub-band-gap absorption of one sample, however, was below its initial level even though the sample had been annealed prior to irradiation. This effect was also observed in our earlier 2.00 MeV helium ion irradiation studies of a-Si:H thin films [ref. 4].

The purpose of this study is to determine whether state-of-the-art solar cells have different radiation resistance properties than cells used in past studies. The reason for raising the question is thin films which exhibited room temperature annealing [ref. 3] were fabricated using state-of-the-art technology. No room temperature annealing of the cells fabricated and studied in 1985 [ref. 3] was reported. Hence, there is a question of the role of the changing solar cell fabrication technology on radiation resistance and annealing characteristics. Additionally, we wish to determine if thin film properties can be correlated with solar cell behavior.

Experimental

Two sets of solar cells were used in this study. One set, referred to as "old cells", consists of four solar cells which were used in a previous study of the radiation resistance of a-Si:H alloy solar cells [ref. 2]. The second set of three cells was recently fabricated and is referred to as "new" cells. The old cells were fabricated in 1985 using the Plasma Enhanced Chemical Vapor Deposition (PECVD) method which was characteristic of the prototype manufacturing technology at that time. The new cells employ current research level PECVD solar cell fabrication technology; this technology was also used in our recent studies of degradation and annealing effects of proton irradiated thin films [ref. 3]. The structure of both sets of cells is ITO/mircrocrystalline $p^+/i/n^+$/stainless steel and the active areas are in the range of 0.8 to 1.0 cm^{-2}; ITO serves as the top electrical contact and anti-reflection coating. The old cells have a grid of screen-printed silver paint, whereas, one of the new cells has a 1000 Angstrom thick Au grid while the other two new cells do not have grids. The efficiencies of the cells were 6-8% under AM1.5 global illumination. One major difference between the old and new cells is the thickness of the intrinsic layers. The new cells were fabricated to produce about the same short-circuit current as the old cells; improvements in material quality result in an intrinsic layer thickness in the new cells which is about one-half the old cells. The intrinsic layer thickness of the old and new cells were 500 and 250 nm, respectively The new cell open-circuit voltage is also about ten percent greater than the old cells. Using an optimum intrinsic layer thickness the state-of-the-art technology may be used to produce single junction solar cells with about 10% efficiency under global AM1.5 illumination.

Prior to irradiation each solar cell was annealed at 190°C for 90 minutes, and the current-voltage characteristics, I-V, measured at room temperature in the dark and under illumination. The illumination source was an ELH lamp filtered through a heat-absorbing filter. The intensity was set using a crystal silicon standard which was calibrated in the AM0 simulator at the NASA Lewis Research Center; the illumination

was adjusted to produce the same crystal silicon short-circuit as produced in the AM0 simulator. Due to the spectral mismatch between AM0 and the ELH lamp, the currents observed in the amorphous silicon solar cells were about 70% of what would be obtained under true AM0 illumination. For this reason, we will only discuss changes in the normalized short-circuit current, I_{sc}, open-circuit voltage, V_{oc}, and fill-factor, FF.

The samples were uniformly irradiated with 1.00 MeV protons under a vacuum of 1E-6 Torr to fluences of 1.25E14 and 1.25E15 cm^{-2} using currents of about 50 nanoamperes. The irradiations were carried out with the cells in the dark at room temperature which was approximately 25°C. Half of the cells were irradiated under open-circuit conditions and the other half under short-circuit conditions. Following irradiation the cells were stored in the dark at room temperature and the I-V characteristics measured at various time intervals in order to assess the effect of room temperature annealing. Isochronal anneals, of one hour duration, were also performed at temperatures of 50, 100 and 150°C; the anneals were performed in a vacuum of 1E-7 Torr. The annealing apparatus was well characterized to insure that the sample temperature was the same as the measured temperature and that the ramp times were much less than the annealing times. Upon completion of the isochronal anneals the cells were annealed at either 190 or 200°C for an hour in an attempt to restore the original I-V characteristics.

Results

The effect of 1.00 MeV protons on the I-V characteristics of old and new solar cells is show in figures 1 and 2 . The uncertainty in the I-V measurements corresponds to the symbol sizes used in the figures. Figure 1 shows the effect of a 1.25E14 cm^{-2} fluence on old cell, O-5, and new cell N-3. Notice that the original I_{sc} and FF of cell O-5 and cell N-3 are quite similar. However, cell N-3 has a larger V_{oc} than cell O-5. The effect of the irradiation is to markedly decrease the I_{sc} and FF. Figure 1 shows that cell O-5 degrades much more than cell N-3. Figure 2 shows the effect of a 1.25E15 cm^{-2} fluence of 1.00 MeV protons on old cell, O-6, and new cell, N-6. Again, note that the I_{sc} of both the old and new cells are about the same before irradiation. The FF of cell N-6 appears to be lower than cells O-5, O-6 and N-3. The reason for this apparent discrepancy is cell N-6 does not have a top grid; the ohmic loss in the ITO layer for the collected current results in a low FF for cell N-6. However, the initial V_{oc} of cell N-6 in figure 2 is about the same as the V_{oc} for cell N-3 shown in figure 1. Figure 2 shows the serious irradiation induced degradation of the I_{sc} and FF for cells O-6 and N-6. There is also a marked decrease in the V_{oc} for both cells O-6 and N-6 following irradiation, with the V_{oc} of cell O-6 decreasing more than cell N-6. As with cells O-5 and N-3, the I-V characteristics of cell O-6 degrade more than cell N-6. Figures 1 and 2 show that 1.00 MeV protons with fluences of 1.25E14 and

1.25E15 cm^{-2} produce greater degradation in the I-V characteristics of old cells as compared to new cells.

The effect of annealing on the normalized I_{sc} was investigated at annealing temperatures, T_a=25, 50, 100, 150 and 190°C. The normalized short-circuit current, $I_{sc}(t)/I_{sc}(0)$, is defined as the short-circuit current, $I_{sc}(t)$, at various times, t, following irradiation divided by the short-circuit current before irradiation, $I_{sc}(0)$. We were concerned about the effect of light induced instabilities and annealing on the I-V characteristics of the cells. The effect of the I-V measurements on the cells was explored by carrying out several measurements of the I-V characteristics at one time; in every case the I-V measurements were within the uncertainty of the measurements showing that the normalized I_{sc} was not affected by the I-V measurements.

The effect of annealing on the normalized I_{sc} of old cells, O-5, O-6, and O-9, and new cells, N-5 and N-6, is shown at the top of figure 3 for 1.00 MeV proton fluences of 1.25E14 and 1.25E15 cm^{-2}. Cells O-6, N-5 and N-6 were stored at room temperature in the dark following irradiation for 242, 235 and 260 hours, respectively. The I-V characteristics of the cells were measured at the times shown in figure 3 in order to determine the effect of annealing at T_a=25°C on the normalized I_{sc}. Figure 3 shows the normalized I_{sc} of cell O-6 did not change during 242 hours at T_a=25°C. However, there is considerable annealing of the normalized I_{sc} of cells N-5 and N-6 during the 235 and 260 hour periods, respectively, at T_a=25°C. The normalized I_{sc} increased between 0.1 and 0.15 during the T_a=25°C anneals. It is clear that for a 1.00 MeV fluence of 1.25E15 cm^{-2}, the two new cells anneal more readily at T_a=25°C than the old cell .

Following the T_a=25°C anneals, cells O-6, N-5 and N-6 were isochronally annealed at T_a=100°C for one-hour intervals; the I-V characteristics were measured after each one-hour anneal. Figure 3 shows the time and temperature of the anneals, and the changes in the normalized I_{sc}. The normalized I_{sc} of all three cells increased between 0.2 and 0.4 during the five 100°C isochronal anneals. At the end of the 100°C anneals, the normalized I_{sc} of cell O-6 was about 0.25 while the normalized I_{sc} of cells N-5 and N-6 were about 0.75. Improvements in the FF were also noted for the new cells. Following T_a=100°C anneals, the cells were stored in the dark at room temperature. A final one-hour anneal at T_a=190°C restored the normalized I_{sc} of cells N-5 and N-6 to within 5% of the pre-irradiation values However, a one-hour anneal at T_a=190°C restored the normalized I_{sc} of cell O-6 to within 10% of the pre-irradiation value; an additional one-hour anneal at 200°C restored the normalized I_{sc} of cell to the original value.

The role of 1.00 MeV proton fluence on the annealing of the normalized I_{sc} of two old cells is shown at the bottom in figure 3. Old cells, O-5 and O-9, were irradiated to fluences of 1.25E14 and 1.25E15 cm^{-2}, respectively, and annealed at T_a=25, 150 and 190°C. Annealing for about 330 hours following irradiation at T_a=25°C produced an increase of about 0.1 in the normalized I_{sc} of cell O-5. The change is less than the new

cells which were irradiated with an order of magnitude higher fluence. The recovery in the normalized I_{sc} of cell O-9 is less than 0.02 during a 308 hour T_a=25°C anneal. The results of cell O-9 agree with those of cell O-6 also shown at the top of figure 3; cell O-6 was also irradiated to a fluence of 1.25E15 cm^{-2}. Room temperature annealing effects for the old cells which were irradiated to 1.25E15 cm^{-2} with 1.00 MeV protons may be considered to be negligible. Both of the old cells, O-5 and O-9, were annealed at T_a=150°C for one- hour intervals beginning 308 and 332 hours after irradiation, respectively; their annealing behavior is different and suggests that the higher level fluence introduces different defect structures. The first one-hour T_a=150°C anneal of cell O-5 produced a change of about 0.6 in the normalized I_{sc}; the second one-hour anneal does not produce a change in the normalized I_{sc}. The T_a=150°C anneals of cell O-9 produce a continuing increase in the normalized I_{sc}. The first T_a=150°C one-hour anneal of cell O-9 produced an increase of about 0.5 in the normalized I_{sc}; the second one-hour anneal increased I_{sc} about 0.15 and the third one-hour anneal produced an increase of about 0.05. Following the T_a=150°C anneals, the cells were stored at room temperature in the dark except for the time during which the I-V measurements were carried out; the measurements show there is no further room temperature annealing of the normalized I_{sc}. At about 350 hours following irradiation, cells O-5 and O-9 were annealed at T_a=190°C for one hour. The T_a=190°C anneals resulted in slight improvements the normalized I_{sc} but did not restore the original I-V characteristics. A final one-hour T_a= 200°C anneal restored the original I-V characteristics to within about 5%. Additional observations on another old cell showed that T_a=50°C anneals of a cell irradiated to 1.25E14 cm^{-2} produced negligible changes in the normalized I_{sc} following about 280 hours of T_a=25°C annealing.

Figure 4 shows the detailed I-V characteristics under illumination for new cell, N-3, prior to irradiation, and at various times following irradiation during the T_a=25°C anneals; the I-V characteristics following a final one-hour T_a=190°C is also shown. The first I-V measurement on cell N-3 following the 1.00 MeV proton irradiation was at 48 hours and shows that the effect of a fluence of 1.25E 14 cm^{-2} is to cause a decrease of about 30% in the normalized I_{sc}. There are significant increases in I_{sc} for T_a=25°C at 163 and 212 hours following irradiation. The I_{sc} is within a few percent of the pre-irradiated value after 212 hours of T_a=25°C annealing. The open-circuit voltage and fill factor are however not restored. The effect of a one-hour T_a=190°C anneal is to restore the FF and V_{oc} to the original values; the annealing increased I_{sc} to a value approximately 20% greater than the value prior to irradiation.

Discussion

One of the purposes of this work is to evaluate the radiation resistance of cells fabricated using current research technology, referred to as new cells, with cells fabricated in 1985, referred to as old cells. The results shown in figures 1 and 2 show that the new cells have radiation resistances that are far superior to the old cells. The

new cells degrade less than the old cells for 1.00 MeV proton fluences even when the fluences are an order of magnitude greater. There are two major known differences between the new and old cells which are believed to be due to the materials used in the fabrication of the solar cells.

The first device material difference between the new and old cells is the improvements make it possible to fabricate thinner single junction solar cells with the same efficiencies as the older thicker cells. This is believed to be due to the fact that the new materials result in increased collection efficiencies of the new cells. Increased collection efficiencies are inferred from the relationship between cell current and thickness. The new and old cell currents are about the same under AM1.5 global illumination while the cell thicknesses differ by about a factor of two. The new cells are between 250 to 300 nanometers thick, whereas the old cells are between 500 to 600 nanometers thick. However, figures 1 and 2 show that the I_{sc} are about the same. The increased radiation resistance of the new cells suggests that thickness may be an important parameter. Earlier work by Woodyard and Hanak [ref. 6] showed that tandem junction solar cells are more radiation resistant than single junction devices. Since the individual intrinsic layers of tandem junction solar cells are thinner than those of single junction cells, they suggested that the improved radiation resistance of the tandem cells was due to the fact that the intrinsic layers were thinner. We also suggest that one of the reasons for the improved radiation resistance of the new cells is due to the fact that the cells are thinner than the old cells.

The second material dependent difference between the new and old cells is the current fabrication technology results in solar cells with increased V_{oc}. The V_{oc} increase is about 0.1 V as shown in figure 1. The improved V_{oc} is a result of improved materials. These improved materials may result in better solar cells for many reasons including, among other things, better junction interfaces, wider band-gap p^+ and n^+ layers, and fewer electrically active defect centers in the cell layers. The reasons for these improvements are not well understood but are probably related to the structure of the material and the role of hydrogen. We have studies in progress with the objective of separating the role of material structure and hydrogen by fabricating cells under different conditions and controlling the hydrogen concentration through annealing and hydrogenation schedules.

The work reported in this paper does not support the point of view that the only reason for the good radiation resistance of solar cells fabricated from a-Si:H based alloys is the poor initial efficiency and quality of the device material. The point of view suggests that the reason for the good radiation resistance is the virgin material has a high level of intrinsic defects and the cell parameters do not decrease until the radiation induced defects exceed the intrinsic defects. Those with this point of view suggest that this will occur at a higher fluence than for cells fabricated with good material. This work shows that as the quality of the a-Si:H material increases, both the cell parameters and radiation resistance improve. We conclude that it is

possible the improved radiation resistance of the new solar cells is due to the improved material quality. In order to understand the role of cell thickness and material quality, device simulation studies must be carried out using numerical models which include fundamental device parameters, such as the density of electronic states and device structure. This is a subject of intense interest in this and other laboratories. We believe that a definitive and quantitative relationship between cell thickness, material properties and radiation resistance can be developed by solar cell modelling studies. To this end, we have solar cell modelling work in progress and will report on these studies in the future. A combination of material properties and thickness are probably important in determining the radiation resistance of a-Si:H alloy based solar cells.

Several points are to be emphasized concerning the annealing results shown in figures 3 and 4. The first is that both new and old solar cells show room-temperature annealing effects. The rate of annealing appears to be dependent upon the total number of radiation induced defects as evidenced by the decrease in the normalized I_{sc}. That is, if the light I-V characteristics are about the same following irradiation, then the rate of annealing appears to be similar. A comparison of N-5 and O-5 in figure 3 illustrates this point. This hypothesis must however be tested over a very much larger range of fluences. The annealing rate is temperature dependent; the rate for T_a=100°C is greater than the T_a=25°C rate. An analysis of the figure 3 data suggests there are at least two types of defects and/or annealing mechanisms. One type appears to operative at T_a <150°C and the other at T_a >190°C. This effect has been reported earlier [ref. 6] and was suggested as being due to different defect structures. We are no closer to understanding this effect except that room temperature annealing also raises the possibility that the T_a <150°C annealing may be due to defects resulting from electronic stopping effects. Electronic stopping was excluded in the earlier work because the degradation in cell efficiency followed the changes in nuclear stopping power.

These investigations were also carried out to determine if our earlier PDS studies with thin films of a-Si:H could be used to predict solar cell characteristics [ref. 4]. In the earlier work, we observed room-temperature annealing of the sub-band-gap optical absorption; we also observed that irradiation and annealing produced lower sub-band-gap optical absorption than a virgin film. As discussed above, the room temperature annealing of solar cells was observed, suggesting the usefulness of the PDS observations. This work shows that irradiation with subsequent annealing results in a higher cell efficiency than the virgin cell. The convincing evidence is figure 4 which shows a 20% improvement in the normalized I_{sc} following irradiation and annealing. This observation is also in agreement with our PDS predictions. Based on our PDS investigations and density of states model [ref. 4], we suggest the increase in the normalized I_{sc} results from a decrease in the density of states within the mobility gap of the intrinsic layer; the decrease reduces the number of recombination centers. The reduction in the number of recombination centers increases the carrier collecting efficiency and normalized I_{sc}.

Conclusions

We have shown that 1 MeV proton irradiation with fluences of 1.25E14 and 1.25E15 cm^{-2} reduces the normalized I_{sc} of a-Si:H solar cell. Solar cells recently fabricated showed superior radiation tolerance compared with cells fabricated four year ago; the improvement is probably due to the fact that the new cells are thinner and fabricated from improved materials. Room-temperature annealing was observed for the first time in both new and old cells. New cells anneal at a faster rate than old cells for the same fluence. From the annealing work it is apparent that there are at least two types of defects and/or annealing mechanisms. One cell had improved I-V characteristics following irradiation as compared to the virgin cell. The work shows that the PDS and annealing measurements may be used to predict the qualitative behavior of a-Si:H solar cells. We anticipate that our modelling work will quantitatively link thin film measurements with solar cell properties.

Quantitative predictions of the operation of a-Si:H solar cells in a space environment will require a knowledge of the defect creation mechanisms, defect structures, role of defects on degradation, and defect passivation and annealing mechanisms. We have work in progress to develop the engineering data and knowledge base for justifying space flight testing of a-Si:H alloy based solar cells.

References

[1.] Joseph Wise and Cosmo Baraona, *Proc. of the Space Photovoltaic Research and Technology Conference*, Nasa Conference Publication 2475, 355, 1986.

[2.] Joseph J. Hanak, Art Myatt, Prem Math and James R. Woodyard, *Proc. of the Eighteenth IEEE Photovoltaic Specialists Conference*, 1718, 1985.

[3.] J. Scott Payson, Yang Li and James R. Woodyard, *Amorphous Silicon Technology-1989, Materials Research Society Symposia Proceedings*, Edited by A. Madan, M. J. Thompson, P.C. Taylor, Y. Hamakawa and P.G. LeComber **149**, 321, 1989.

[3.] J. J. Hanak, Englade Chen, C. Fulton, A. Myatt and J.R. Woodyard, *Proc. of the Space Photovoltaic Research and Technology Conference*, NASA Conference Publication 2475, 99, 1986.

[4.] James R. Woodyard and J.J. Hanak, *Amorphous Silicon Semiconductors-Pure and Hydrogenated, Materials Research Society Symposia Proceedings*, Edited by D. Adler, A. Madan, Y. Hamakawa and M. Thompson **95**, 533, 1987.

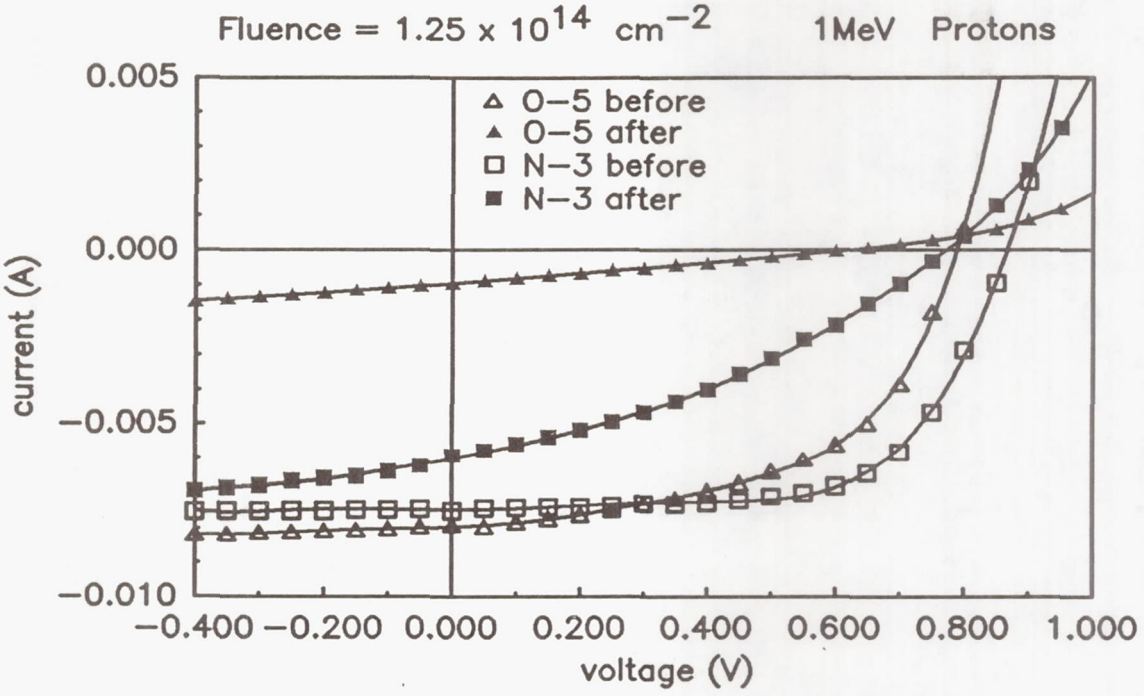

Figure 1. Light I-V characteristics of old cell, O-5, and new cell, N-3, before and after irradiation with a 1.00 MeV proton fluence of 1.25E14 cm-2

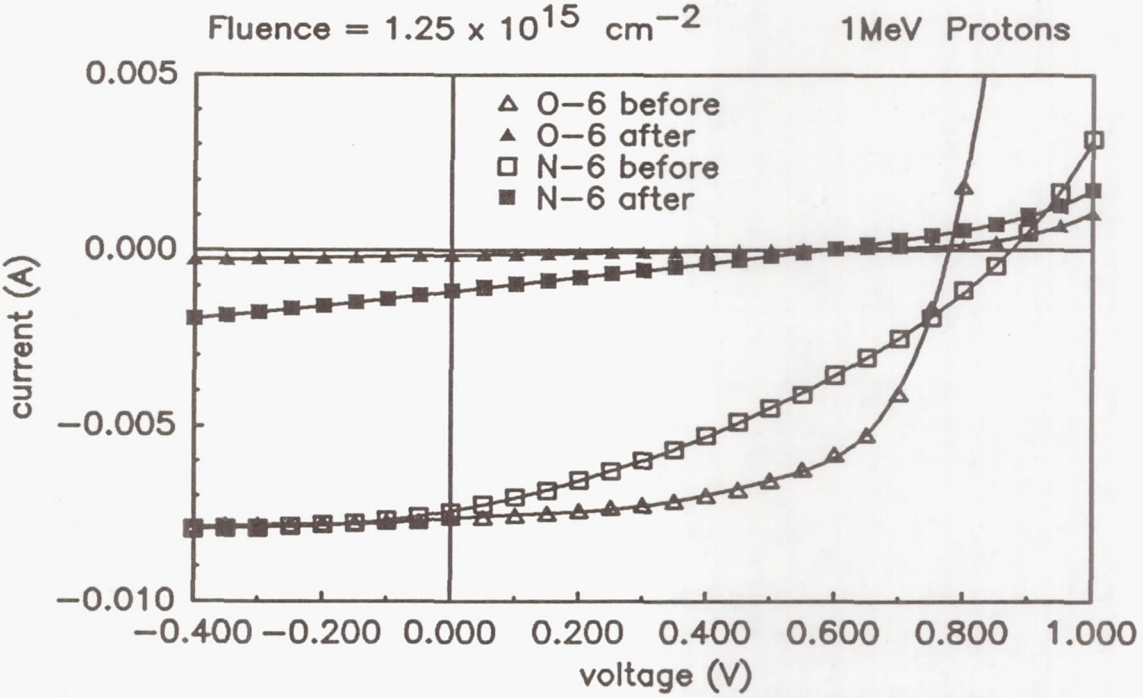

Figure 2. Light I-V characteristics of old cell, O-6, and new cell, N-6, before and after irradiation with a 1.00 MeV proton fluence of 1.25E15 cm-2

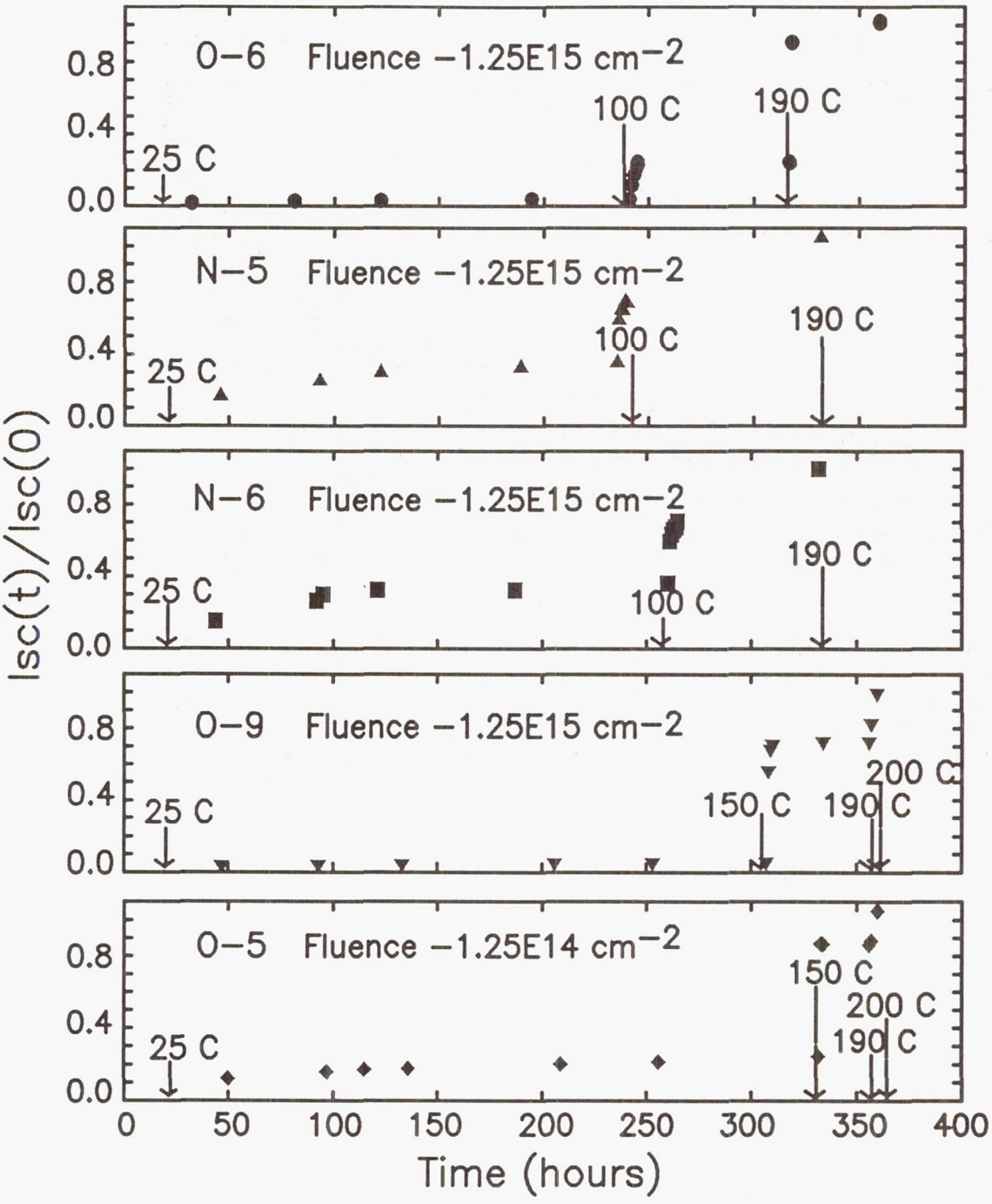

Figure 3. Annealing characteristics of the normalized Isc following irradiation with 1.00 MeV protons. The fluence was 1.25E14 cm-2 for cell O-5 and 1.25E15 cm-2 for cells O-6, O-9, N-5 and N-6. The annealing temperatures were 25 °C for the times shown. One-hour 100, 150, 190 and 200 °C anneals were carried out at the times shown by the arrows.

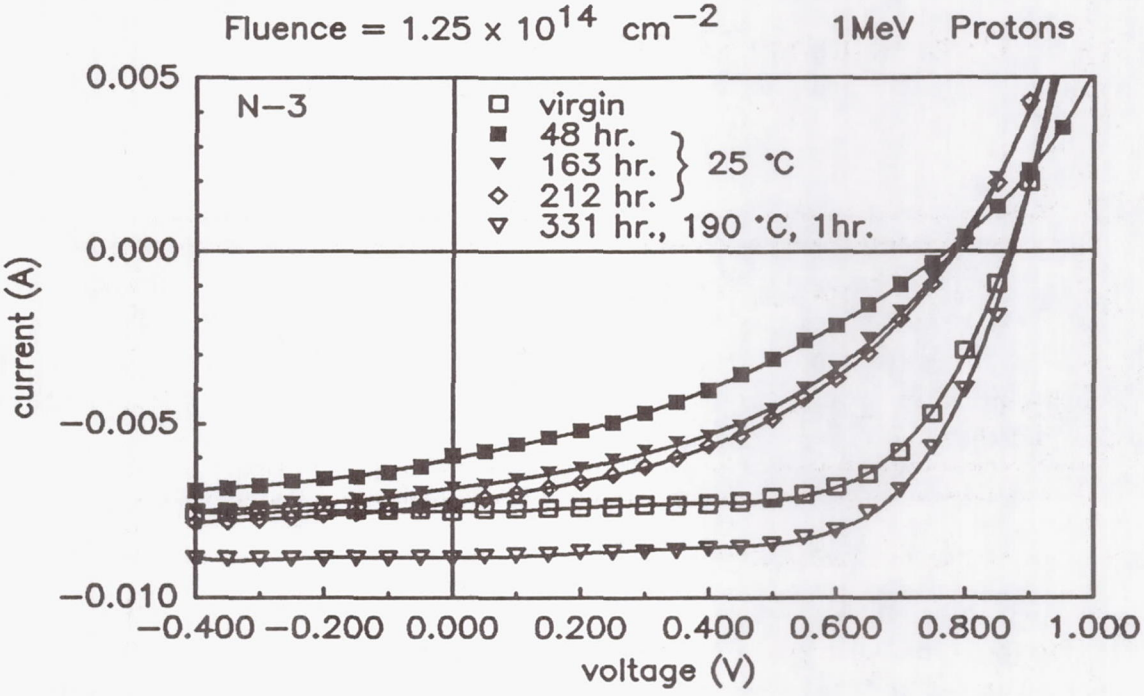

Figure 4. Light I-V characteristics of new cell, N-3, before and after irradiation with a 1.00 MeV proton fluence of 1.25E14 cm-2. The I-V characteristics were measured at various times during a 331 hour anneal at 25 °C and then after a one-hour anneal at 190 °C.

Optimization and Performance of Space Station Freedom Solar Cells

S. Khemthong, N. Hansen and M. Bower
Applied Solar Energy Corporation
City of Industry, CA

High efficiency, large area and low cost solar cells are the drivers for Space Station solar array designs. The manufacturing throughput, process complexity, yield of the cells and array manufacturing technique determine the economics of the solar array design. This paper describes the cell efficiency optimization of large area (8cm by 8cm), dielectric wrapthrough contact solar cells. The results of the optimization are reported and the solar cell performance of limited production runs is reported.

Introduction

The Space Station solar cell is a shallow diffused N on P silicon solar cell with back surface field manufactured from P-type, boron doped, single crystal silicon with a base resistivity of 7 to 14 Ohm-cm. The cell size is 8cm × 8cm and the nominal thickness is 8 mils.

Both N and P contacts are located on the back side of the solar cell. The N contacts are wrapped through four interior holes, isolated from the P contacts by SiO_2 dielectric layer. The cell is equipped with a gridded back and a back side optical coating, designed to optimize transmission of solar energy in the range of 1.1 to 2.5 micrometer. This IR transmission allows the solar cell to operate at low temperature and improve on-orbit electrical performance. The coverglass is a 5 mils thick ceria-doped borosilicate glass. The top surface of the coverglass is optically coated with UV reflecting coating designed to reject UV radiation and reduce solar absorptance. The solar cell and coverglass are bonded together with an optically clear DC93-500 adhesive.

The original cell efficiency requirement was approximately 12.8 percent. Since then, the requirement was raised to as high as 14.4 percent and the final efficiency was negotiated to 14.1% (2420mA at 495mV). In early 1988, ASEC developed the required solar cells. Since the standard cell for simulator calibration for this newly developed cell was not available, ASEC chose one of the in-house standard cells to calibrate the solar simulator to evaluate these new cells. In summer of 1988 a balloon flight standard cell for this newly developed cell was flown by JPL. The cells were then retested electrically using the new balloon flight standard cell and found that the solar cells were 3.4 percent below the requirement of the specifications.

Cell Efficiency Optimization

It was obvious that cell efficiency optimization was required to achieve the requirement of the specifications. ASEC worked to optimize the cell efficiency. The cell efficiency goal of 14.5% under production conditions was set. Table 1 shows the performance status prior to optimization and the goal for optimization.

The approach for optimization was to fine-tune the existing process using production equipment and personnel under close supervision by engineers and production management. This process reduced production transfer time. The production personnel were part of the optimization team from the start and many of the potential start-up problems were reduced.

V_{oc} Optimization

The achieved V_{oc} of 615.5 mV was considered good. It was felt that some marginal improvement can be achieved by optimizing the back surface field process. Boron nitride diffusion process is used to form the back surface field for this program. The V_{oc} optimization process was to vary the boron diffusion temperature while keeping all other processes unchanged. Three (3) boron diffusion temperatures were chosen, baseline temperature, 25°C above baseline temperature and 50°C above baseline temperature. For simplicity, 2x4cm top-bottom contact cells were made for these experiments. Two sets of experiments were carried out to assure repeatability. The AMO electrical output for all three type of cells were evaluated to determine V_{oc} improvement.

I_{sc} Optimization

It was determined that I_{sc} improvement of 3 to 4% could be achieved. I_{sc} optimization included designing a new front grid mask to reduce gridline shadowing and series resistance. This new front mask design included:

- Reduction of metalization dot size around the wrapthrough holes.
- Reduction of gridline width, and
- Increase gridline density to handle solar cell with shallow junction.

An improved photoresist process was proposed to be used in manufacturing of Space Station cell. This improved photoresist process allows narrow and tall gridlines to be formed on solar cells with clean and sharp edges, and reduced shadowing. With new mask design and implementation of improved photoresist process, it was estimated that cell efficiency improvement approximately 3% would be achieved.

The next area of I_{sc} optimization was to reduce the solar cell junction depth further and to fine-tune the AR coating to match the junction depth. The junction

depth experiment was performed by diffusing the N + junction at 25° and 50° below the baseline diffusion temperature. 2x4cm solar cells with baseline BSF were made and evaluated electrically. Particular attention was paid to the improvement of short circuit current without sacrificing the loss in curve filled factor.

CFF Optimization

The CFF Optimization included:

- Improved CVD dielectric
- Improved wrap-through hole geometry

The dielectric layer in and around the wrapthrough holes must fulfill several functions. It must be impermeable to reduce any possible shunting paths caused when the wrapthrough metal layers are deposited. In addition, the dielectric layer which is present under the N welding pads must not degrade during the welding pulse, or impair the adhesion of the welded contact. Three CVD dielectric systems, APCVD, LPCVD and PECVD were considered. It was determined that an APCVD system would be a suitable system for ASEC due to the nature of the CVD dielectric process, and this system is now used.

It was also determined that the wrapthrough hole geometry needed improvement. After laser drilling of the holes, the silicon damage silicon surfaces were removed by chemical etching. This chemical etching also smoothed the surface and rounded the wrapthrough holes allowing good coverage of dielectric material in and around the wrapthrough hole, thus reduce shunting paths caused when wrapthrough metal layers are deposited. Figure 1 shows a typical wrapthrough hole geometry after optimization.

Production of Optimized Cell

Upon completion of the optimization process, limited prototype solar cells were made to verify the optimization results. The verification process was successful and documentations were established.

The first production quantity required for delivery was 970 assemblies. This production run was carried out with full documentation. The production line was closely monitored by engineers and supervision to assure smooth production flow.

Solar Cell Performance

Figure 2 shows the open circuit voltage distribution of 558 solar cell assemblies tested under AMO condition and 28°C. The solar simulator was calibrated using a Space Station balloon flight standard cell flown late this summer. The open circuit voltage ranges from 590mV to 630mV with an average of 618.9mV. The average V_{oc} met the established goal of 618 mV. Figure 3 shows the I_{sc} distribution for the same 558 cell assemblies. The I_{sc} distribution is tightly controlled with an average of 2733mA (43.6mA/cm2). The average I_{sc} is 5% above the established goal. Figure 4 shows the efficiency distribution of the same 558 cell assemblies. The efficiency ranges from 13.1% to 15.4% with an average of 14.6% (2495mA at 495 mV). The efficiency of the cell is well above the requirement of the specification of 14.1%. Figure 5 shows the typical spectral response of a typical Space Station solar cell showing good response in both the blue and red regions. The Space Station solar cell has currently undergone qualification tests. Electron radiation test and high temperature soak test are completed and passed the qualification test. The remainder of the qualification will be completed by the end of November. Figure 6 shows the results of lMeV electron radiation.

Table 1: Solar Cell Performance Status Prior to Optimization and Optimization Goal

Electrical Parameters	Status Prior to Optimization	Optimization Goal
Voc (mV)	615.5	618
Isc (mA)	2516	2600
CFF (%)	74.7	76.5
EFF (%)	13.7	14.5

FIGURE 1

Typical Wrapthrough Hole Profile of Space Station Cell

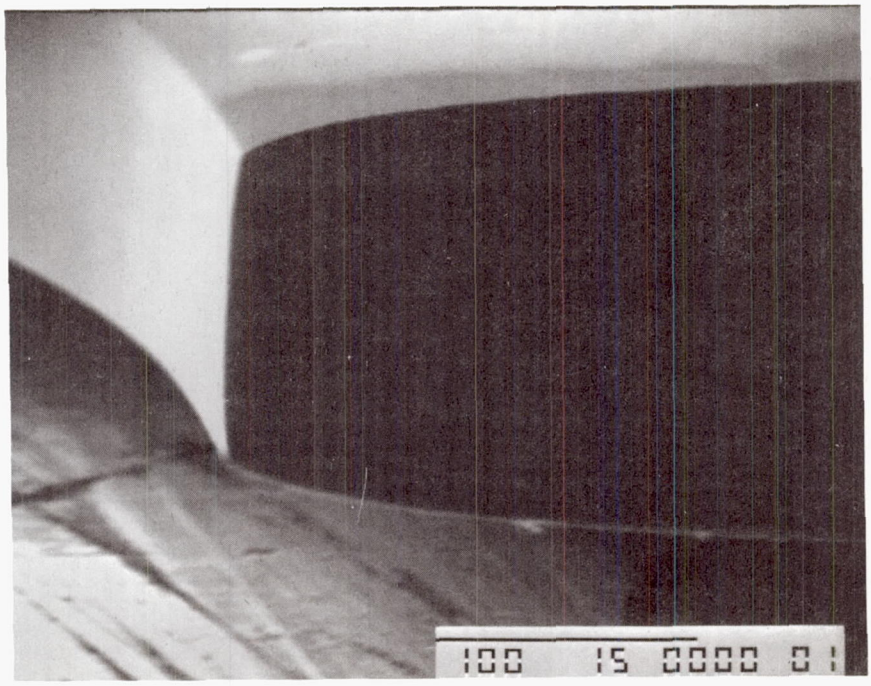

Figure 2

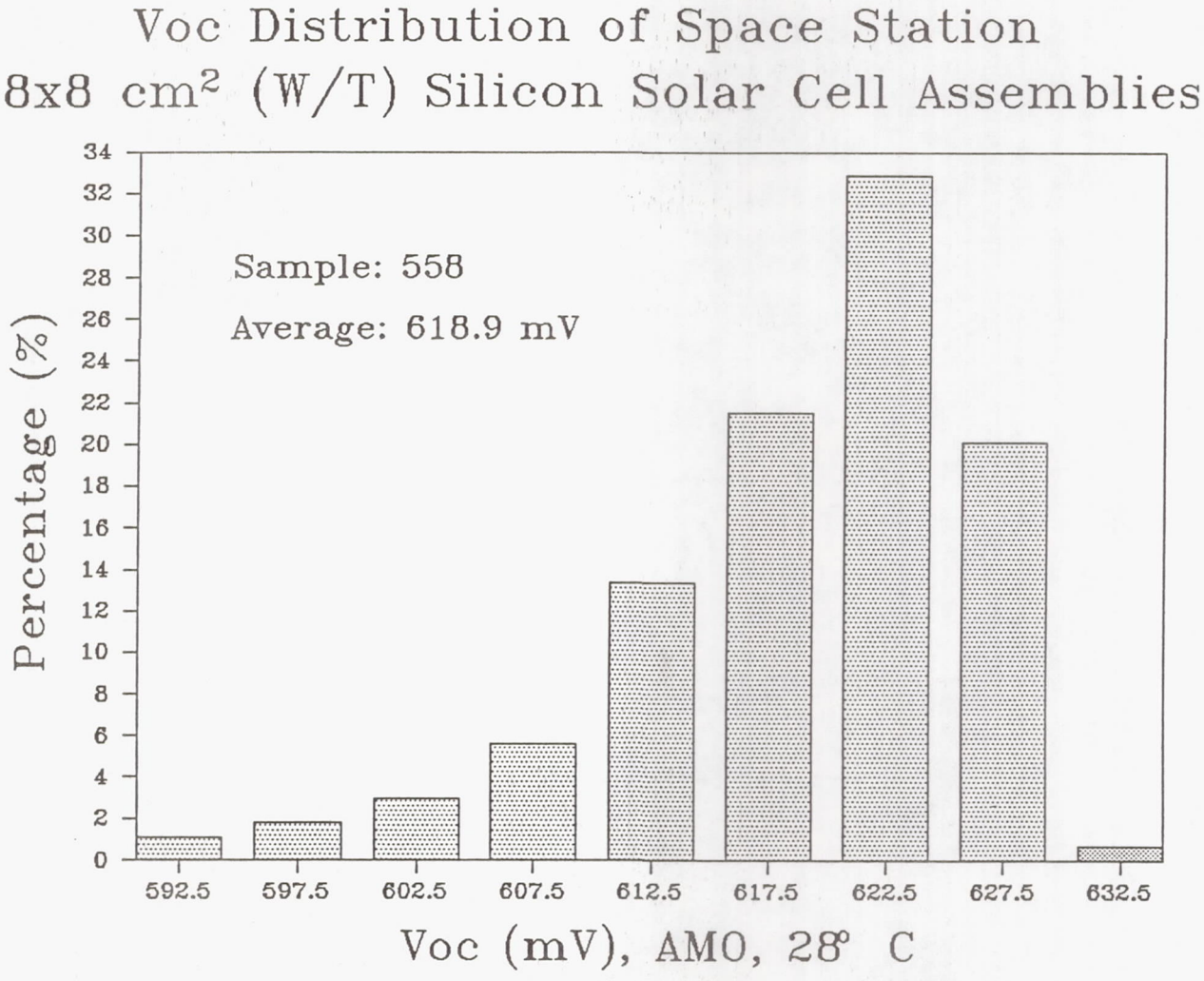
Voc Distribution of Space Station
8x8 cm² (W/T) Silicon Solar Cell Assemblies
Sample: 558
Average: 618.9 mV
Percentage (%)
0
2
4
6
8
10
12
14
16
18
20
22
24
26
28
30
32
34
592.5
597.5
602.5
607.5
612.5
617.5
622.5
627.5
632.5
Voc (mV), AM0, 28° C

Figure 3

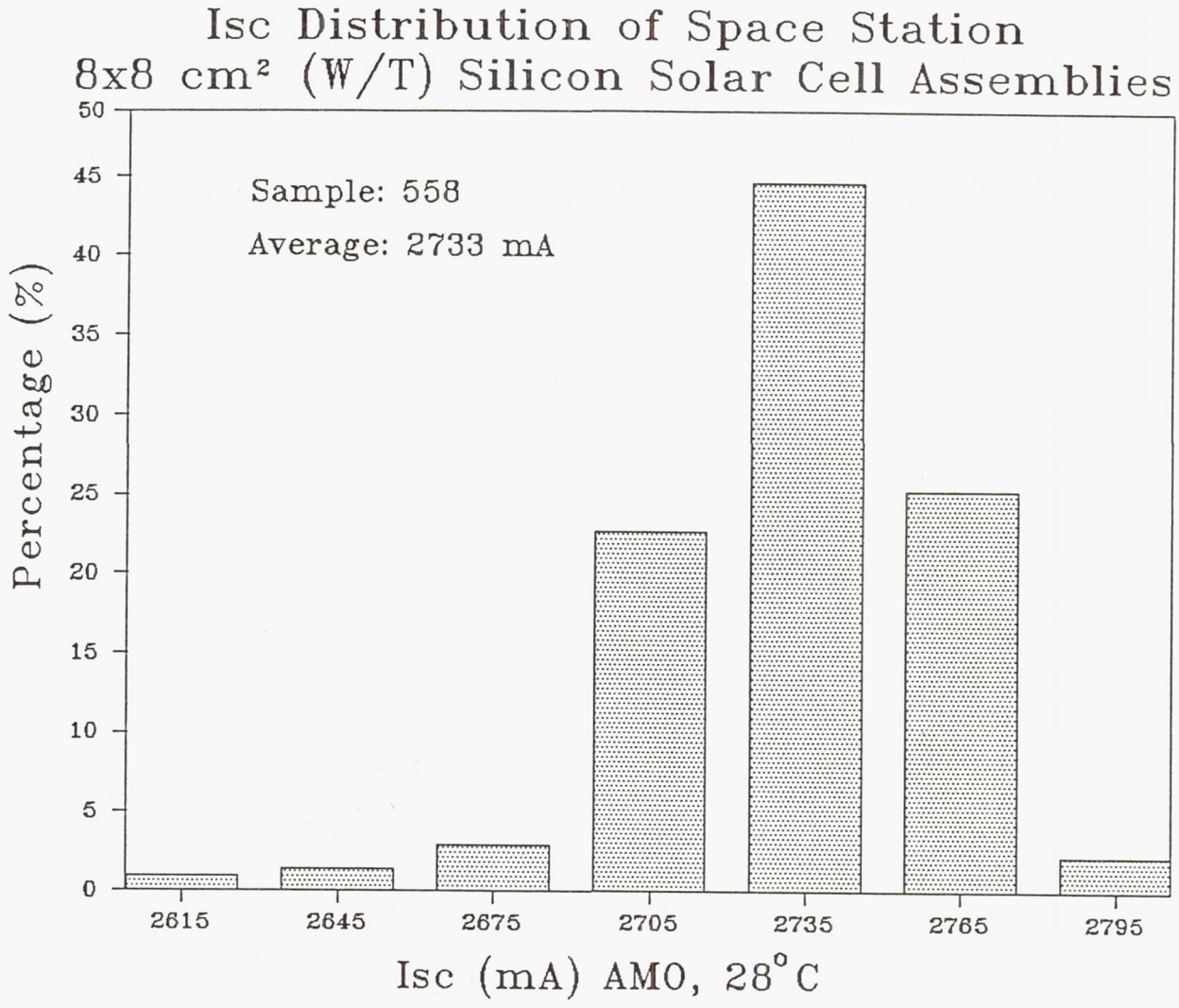
Isc Distribution of Space Station
8x8 cm² (W/T) Silicon Solar Cell Assemblies
Sample: 558
Average: 2733 mA
Percentage (%)
50
45
40
35
30
25
20
15
10
5
0
2615
2645
2675
2705
2735
2765
2795
Isc (mA) AM0, 28°C

Figure 4

Efficiency Distribution of Space Station 8x8 cm² (W/T) Silicon Solar Cell Assemblies

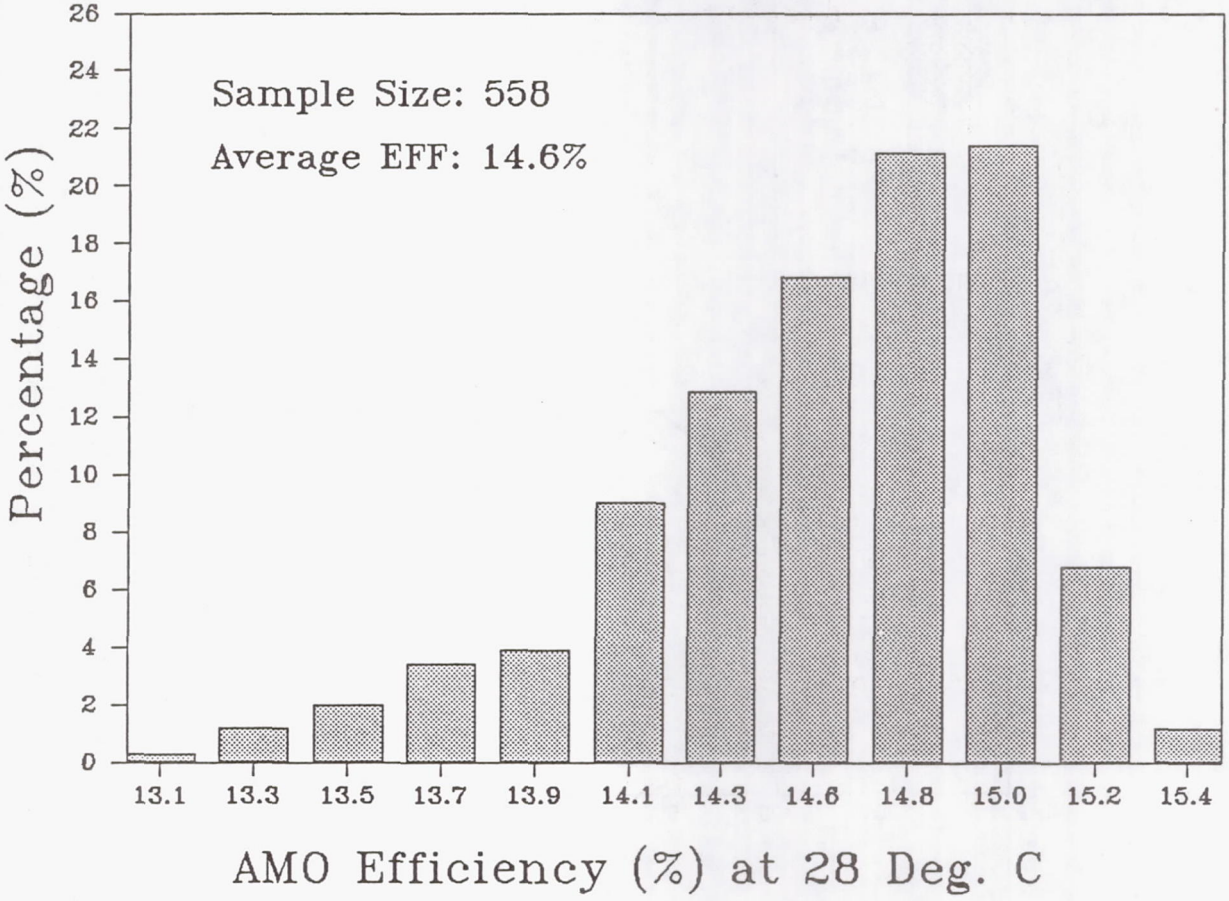

FIGURE 5

Typical Spectral Response for Space Station Solar Cell

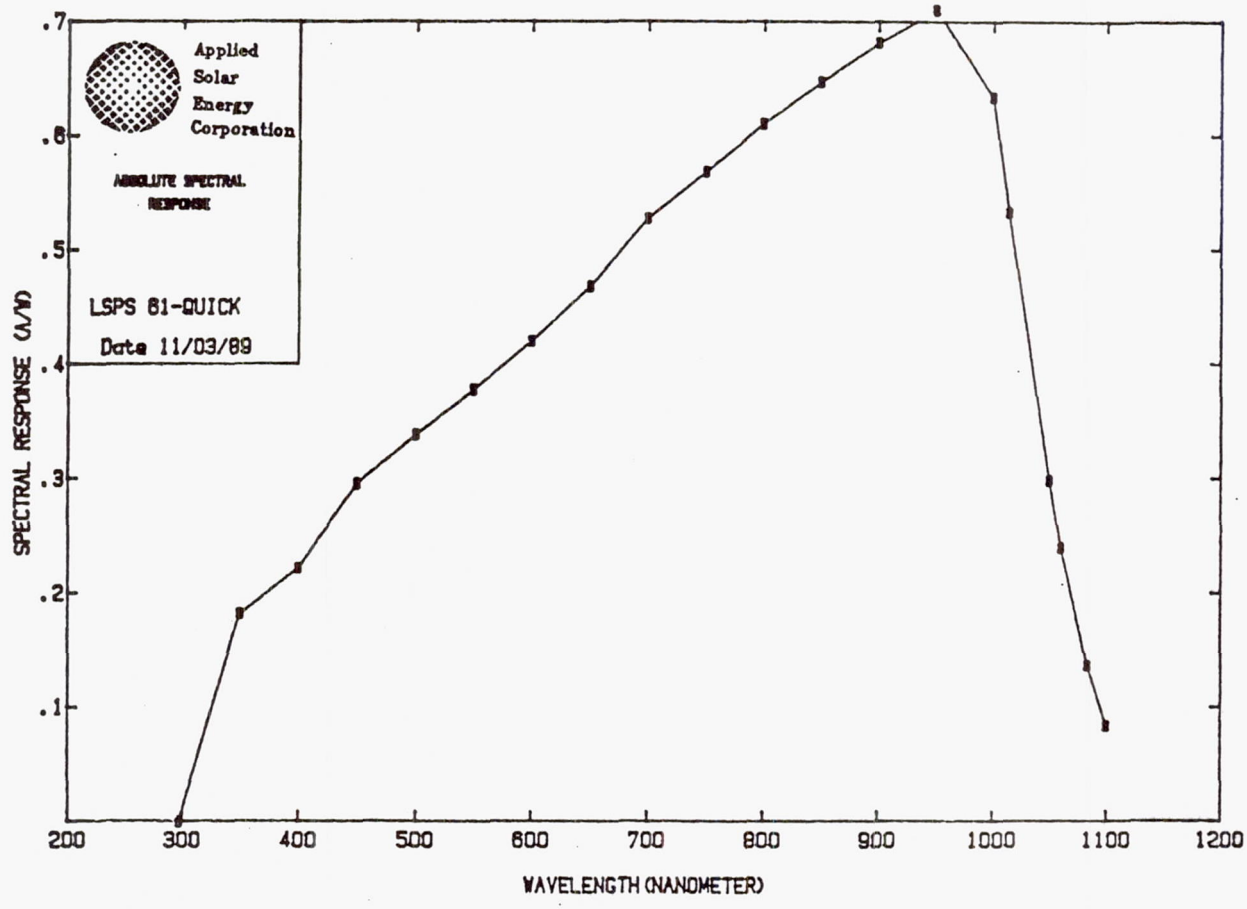

FIGURE 6

1 MeV Electron Radiation Results for Space Station Solar Cell

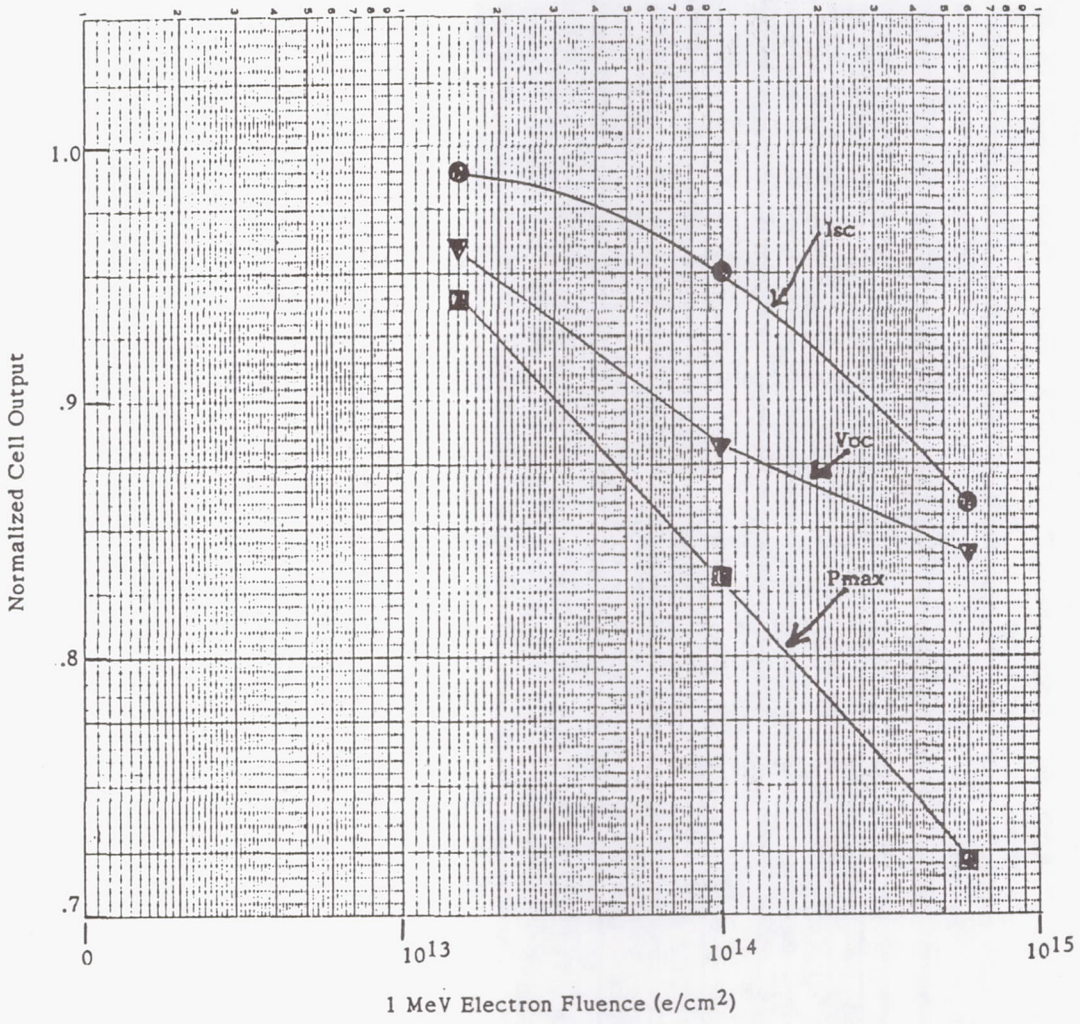

Thermal Cycle Testing of Space Station Freedom Solar Array Blanket Coupons

Bryan K. Smith
Jet Propulsion Laboratory
NASA Lewis Research Center
Cleveland, Ohio

David A. Scheiman *
Sverdrup Technology, Inc.
Cleveland, Ohio

Lewis Research Center is presently conducting thermal cycle testing of solar array blanket coupons that represent the baseline design for Space Station Freedom. Four coupons were fabricated as part of the Photovoltaic Array Environmental Protection (PAEP) program, NAS 3–25079, at the Lockheed Missiles and Space Company. The objective of the testing is to demonstrate the durability or operational lifetime of the solar array welded interconnect design within a Low Earth Orbit (LEO) thermal cycling environment. Secondary objectives include the observation and identification of potential failure modes and effects that may occur within the solar array blanket coupons as a result of thermal cycling. The paper presented describes the objectives, test articles, test chamber, performance evaluation, test requirements, and test results for the successful completion of 60,000 thermal cycles.

Introduction

The primary objective of the thermal cycle test is to demonstrate the durability or operational lifetime of the solar array welded interconnect design within a LEO thermal cycling environment. Secondary objectives include the observation and identification of potential failure modes and effects that may occur within the solar array blanket coupons as a result of thermal cycling.

This document describes the objectives, test articles, test chamber, performance evaluation, test requirements, and test results to date for the thermal cycle testing of solar array blanket coupons at NASA LeRC.

Power for Space Station Freedom will be generated by four photovoltaic power modules that each employ two solar array wings. The solar array wings are comprised of two blankets that each are an assembly of active solar panels. An active solar cell panel contains 200 solar cells connected in series. Each solar cell is attached to the underlying circuit interconnects by 10 welded contact points.

* Work performed under NASA Lewis Research Center contract NAS 3–25266.

The solar cell to circuit weldments and copper interconnects are subjected to thermally induced stresses as a result of temperature excursions experienced each orbit. Freedom will orbit the earth approximately once every 90 minutes which results in 6,000 thermal cycles a year, or 90,000 thermal cycles for the array over a period of 15 years. This cycling will cause stresses on the blanket materials and will, over time, result in structural fatigue of panel components.

The solar array blanket is a combination of materials with different Coefficients of Thermal Expansion (CTE). Although the copper interconnect and the silver contact points on the solar cell, where the weld is made, have a similar CTE, the adjacent blanket materials, adhesives, and silicon cells do not (Fig. 1). Consequently, the resultant effects at the weld joint, due to mismatches in the adjacent material's CTEs and the composite metallurgical properties of the weld are difficult to predict and warrant the physical testing of a blanket sample.

Test Article Description

The test articles were fabricated as part of the Photovoltaic Array Environmental Protection (PAEP) program, NAS 3-25079, at the Lockheed Missiles and Space Co. (LMSC), Inc., Sunnyvale, California. Four thermal cycle coupons were fabricated using the same design, materials, and manufacturing processes that are presently the baseline for Space Station Freedom (Fig. 3).

Each test coupon contains four 8 cm by 8 cm silicon solar cells with coverglasses. The cells were manufactured as part of an advanced development program, NAS 3-24672, at Spectrolab Inc. The coverglass is bonded to the solar cell with Dow Corning (DC) 93-500 adhesive. The cells are an N-on-P type silicon cell with a boron back surface field and a 10 ohm-cm nominal base resistivity. The back collection grids and the N-type and P-type interconnect contact points are both deposited layers of aluminum, titanium, palladium, and silver. The back side of the cell has six positive and four negative contact points (Fig. 4).

Prior to fabricating the deliverable thermal cycle coupons, the PAEP program completed a weld optimization task using a parallel gap resistance welder. The task determined the voltage, emissivity, and IR sensing settings that are used to control the weld pulse energy and the weld pulse duration on the LMSC production welder. The parallel gap resistance welding utilizes two closely space electrode tips that make contact with the copper interconnect on one side of the array panel. The electrodes pass a current through the copper circuit and underlying solar cell metal contacts causing the metals to join through resistance welding. The welding was performed using a constant voltage power supply that regulates the current during welding to compensate for variations in the resistance occurring in or across the weld. Pull tests, photomicrographs, and illumination tests were used to evaluate the quality of actual solar cell to copper interconnect welds. From this effort a weld schedule was selected

that exhibited the statistically highest pull strengths and showed no obvious failure mechanisms such as gross melting, voids, or cracking.

The coupon substrate is comprised of two layers of silicon dioxide coated Kapton [ref. 2] with a copper circuit between. The copper circuitry is thermally bonded to the first layer of Kapton with a polyester adhesive. The solar cells are welded to the copper circuitry through access holes in the first layer of Kapton. The second sheet of Kapton is bonded with DC 93–500 to the exposed circuitry, the first sheet of Kapton, and the solar cells through access slots in the first layer of Kapton. The coupons are also configured with aluminum foil covered Kapton hinges and hinge pins. The aluminum foil was determined to be the most effective method of protecting the panel hinges from atomic oxygen.

For thermal cycling, the test articles are mounted to metal frames using springs. The springs maintain a tension that simulates the on orbit solar array assembly conditions and isolates the samples from any adverse affects that may be caused by the frames.

Test Chamber Description

The test chamber (Fig. 2) is designed to cycle a test article between the temperature extremes encountered by spacecraft orbiting the earth. The thermal cycling chamber consists of two smaller chambers that each maintain a constant hot and cold temperature of +85°C and –115°C, respectively. The switching temperatures of the test frames are set at +70°C and –90°C. Once a switching temperature is achieved, the frame and coupon move to the opposite side of the chamber. The typical cycle time for one complete cycle is between 3–4 minutes, depending on the number of test frames in the chamber at a given time.

The thermal cycling chamber is basically an insulated box with an oven and a freezer. The oven is heated electrically using two 500 W resistance heaters which provide radiative and convective heat transfer to the samples. The freezer is cooled using liquid nitrogen which is fed into the chamber through a series of holes in a 1/4 inch copper tube. The liquid nitrogen boils off creating nitrogen gas which cools the chamber and also provides an inert atmosphere. As a result of this, the oven chamber is also provided with a nitrogen environment. Temperatures of the chambers are monitored by centrally located thermocouples interfaced to a computer which turns the heaters and liquid nitrogen on or off as required. The system is capable of temperature extremes as high as +125°C ± 10°C as low as –180°C ± 10°C.

Up to four 8 in.× 8 in.× 1/2 in. solar array test articles can be tested simultaneously. Each test article is mounted to a removable frame which slides between the hot and cold sides of the chamber. Each frame is independently monitored by a thermocouple attached to the test article. Cycle counts are maintained by the computer and printed hourly. The temperature swing of any test article can be plotted

graphically against time if desired. Cycling will stop automatically at a predetermined cycle count, at which time, the test frames can be removed from the chamber for performance measurements and visual inspection.

This method of thermal cycling allows for a more rapid cycling than can be achieved in a vacuum chamber with much lower maintenance and operational costs. Both of these issues are rationale for using an inert atmosphere chamber. Atmosphere thermal cycling does tend to be equal or more severe than when cycling in a vacuum [ref. 3].

Test Requirements

Phase I

A test chamber characterization shall be run and recorded to determine the thermal environment and the thermal gradients that exist within each side of the test chamber.

The coupons shall be mounted in a manner that represents the on–orbit tensions of the solar array blanket. Equally tensioned springs should be used along at least one side of the coupon.

The coupons shall be attached to the test fixture frame along the sides of the hinge pins only.

The coupon should be oriented in the test fixture frames so that the largest thermal gradient across the coupon is perpendicular to the longest series run in the copper circuitry. This will minimize the thermal gradients across a single cell's interconnected weldments during the test.

Electrical leads from the coupon shall be attached to the fixture frame such that any forces directly applied to the lead during measurement will not compromise the lead-to-coupon connection or result in any external forces on the coupon.

Phase II

The test chamber shall cycle between -90°C ± 10°C and +70°C ± 10°C.

Both the upper and lower chamber temperatures shall be monitored throughout the test. Coupon temperatures shall be monitored by attaching a thermocouple to a single point on the coupon.

Cycling time shall be between 3 and 5 minutes per cycle.

A record of events that may have occurred shall be kept where the experiment exceeded the experimental design limits.

Electrical measurements, visual inspections including low power magnification, and any other NonDestructive Evaluation (NDE) techniques shall be made after the following number of cycles: 0, 3000, 6000, 12000, 18000, 24000, 30000, 42000, 60000, 72000, 84000, 90000.

Once the testing has begun, the time taken to measure and inspect the coupons out of the chamber should be kept to an absolute minimum.

All test coupons should be photographed before cycling and at any point during the test that specifically illustrates a failure mode and/or effect.

Solar Cell Performance Evaluation

Performance of the test article is measured by the range of its power output under illumination. This electrical output is characterized as an I-V curve (current vs. voltage). The I-V curve is generated by varying a load resistance on the solar cell or array from 0 to infinity ohms while the cell is under illumination. The illumination is the equivalent sunlight or solar spectrum that would be seen in space. The solar constant or air mass zero (AM0) is 136 mW/cm^2 for the IV flash reference. The following key factors from the IV curve are used in the performance evaluation:

1) I_{sc} short circuit current (AMPS)
2) V_{oc} open circuit voltage (VOLTS)
3) I_{max} maximum power current (AMPS)
4) V_{max} maximum power voltage (VOLTS)
5) P_{max} maximum power ($V_{max}I_{max}$, WATTS)
6) F.F. fill factor, < 1 ($V_{max}I_{max}/P_{max}$)

7) Efficiency peak efficiency P_{max}/(light intensity $\times$ cell area)

(The cell area is the surface area of the cell being illuminated).

SSF solar array test articles' I-V curves are obtained by flash testing. Flash testing is performed by using a short burst of light (xenon arc lap) with a normalized AM0 spectrum and ramping an increasing load on the cell during that burst. Using this method a complete I-V curve is generated in about 1.5 milliseconds. This flash test provides curve data with virtually no heat being generated in the cells under test. Under this condition, test repeatability is very good and data comparisons can be made. If a weld failure were detected, series resistance in the cell would increase. Series resistance would most prominently affect the slope of the curve between the P_{max} point and V_{oc}.

Solar Cell Visual Inspection

In addition to performance characteristics, the solar cells undergoing thermal cycling are visually inspected and mapped. This consists of looking at the cell under

10× magnification with incident light at varying angles. Because of the glass and reflective nature of the cell, light angles are varied to detect any notable flaws in the surface of the cell or glass. These flaws are noted in their respective locations on a paper image of the cell. Each flaw is marked with a letter designation and subscripted to indicate the time the flaw was first seen. In the SSF solar array test articles, both the front and back sides are mapped, the front being the cell face and the back having the actual welds and interconnects. The following flaws are noted:

1) B - break/crack in cell surface
2) C - break/crack in cover glass
3) V - void
4) W - wrinkle in copper interconnect
5) A - adhesive (visible lines/bubbles)

6) Any other suspicious or nonconformity in the cell array, i.e., air bubbles, glue, peeling

Visual mapping and subscripted notations are performed for each of the coupons at all scheduled intervals. Ultimately, the visual inspection is used to observe any trends that would lead to the performance degradation in the cells or trace the origin of any possible failures that may have occurred.

Status to Date

All of the four array test articles have completed 60,000 cycles which is approximately 10 years in LEO. All of these samples show no significant signs of electrical degradation or failure.

Electrical performance of the arrays has been unchanged within the accuracy of the test equipment (2%). Measurements were taken at 0, 3000, 6000, 12000, 18000, 24000, 30000, 42000, 48000, and 60000 cycles. The ratio of maximum power over initial maximum power has remained consistent. Any weld failures or catastrophic cracks would cause a significant change in the coupon output.

Visual inspection of the coupons at 10× magnification has revealed very slight changes in the cells. Fine cracks have been detected in the cell and coverglass. Most of the cell and coverglass cracks were observed before cycling and only tended to elongate fractionally during the first 12000 cycles. These changes in the cells are viewed as creating no severe consequence to the integrity of the cells.

The backside of the coupon or interconnect side has exhibited a change in the copper interconnects, Kapton, and adhesive layers. Within the first 12000 cycles a movement of the copper and Kapton was observed. The copper went from being flat to having a large number of ripples. This out of plane rippling, resulting from initial thermal stresses, has actually become a stress relief path for subsequent thermal cycling. Depending on how the copper was applied, more ripples occurred in some

areas than in others. Rippling of the copper interconnects has run up to some of the weld connections on the cells.

The adhesive also appears to have become elongated. This elongation is exhibited by round voids in the adhesive that have become oval in shape. After 12000 cycles all of the motion in the copper, Kapton, and adhesives stabilized and does not appear to have affected the weld joints. After 48000 cycles some of the rippling appeared to have decreased in size and the adhesive looks as if crystallization has taken place in some localized areas. The adhesive bonds within the coupons will be carefully watched for any delaminations or bonding failure that might occur as a result of cycling.

Table 1 contains flash test results to date for the four thermal cycle coupons; SSFSA–1, SSFSA–3, SSFSA–4, and SSFSA–5. All of the data indicates that the performance has been unchanged throughout the cycling. At this time, the achievement of the 90000 thermal cycle goal appears to be feasible.

References

[1.] Jet Propulsion Laboratory: Solar Cell Array Design Handbook Volume II. NASA, October 1976, pp. 7.11–4,5.

[2.] Kapton is a registered trademark of E.I. DuPont de Nemours and Co., Inc.

[3.] Rauschenbach, H.S.: Solar Cell Array Design Handbook. Van Nostrand Reinhold Company. 1980. pp.402–403.

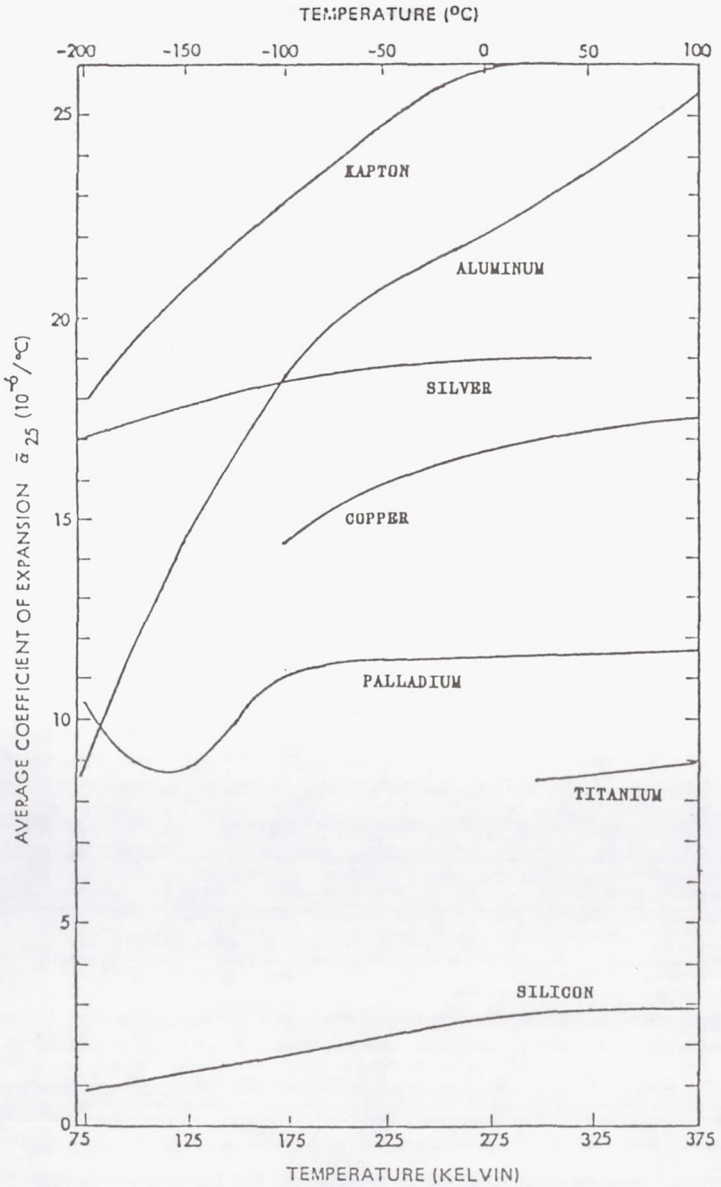

Fig. 1 CTE (Coefficient of Thermal Expansion) Versus Temperature for Materials Used on SSf Array[1]

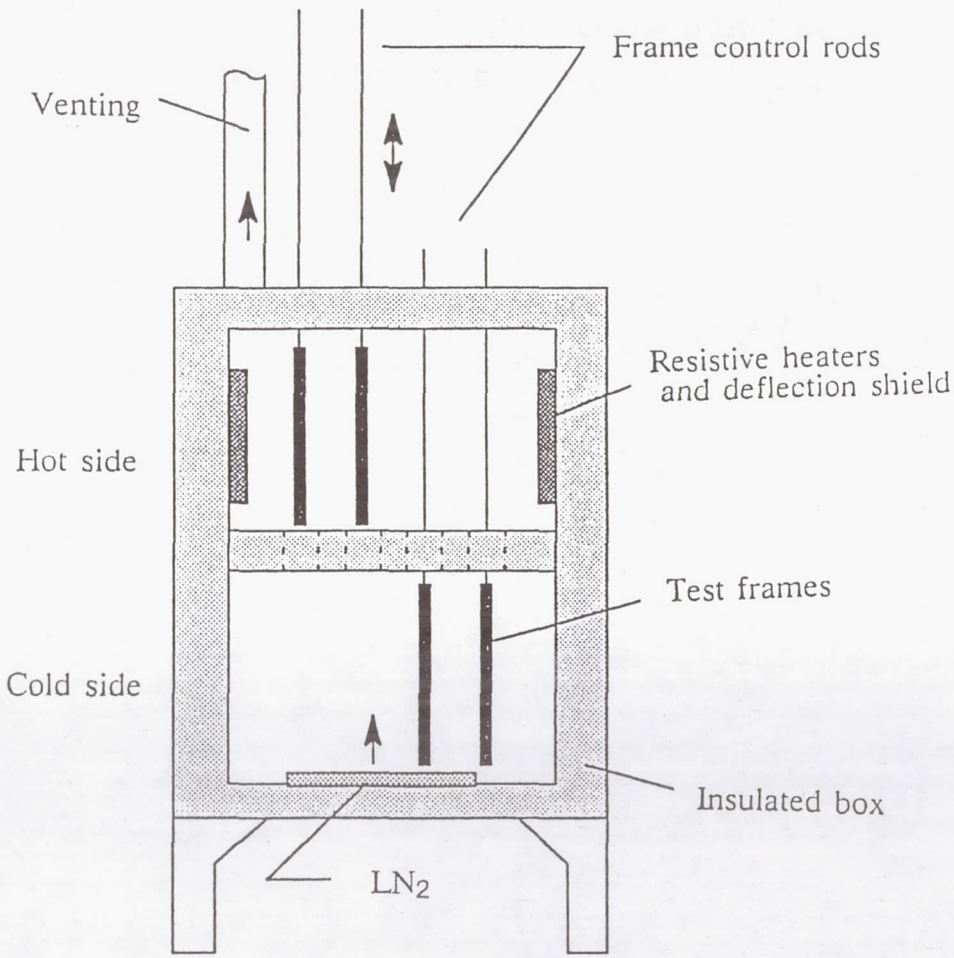

Fig. 2 **Thermal Cycle Test Chamber**

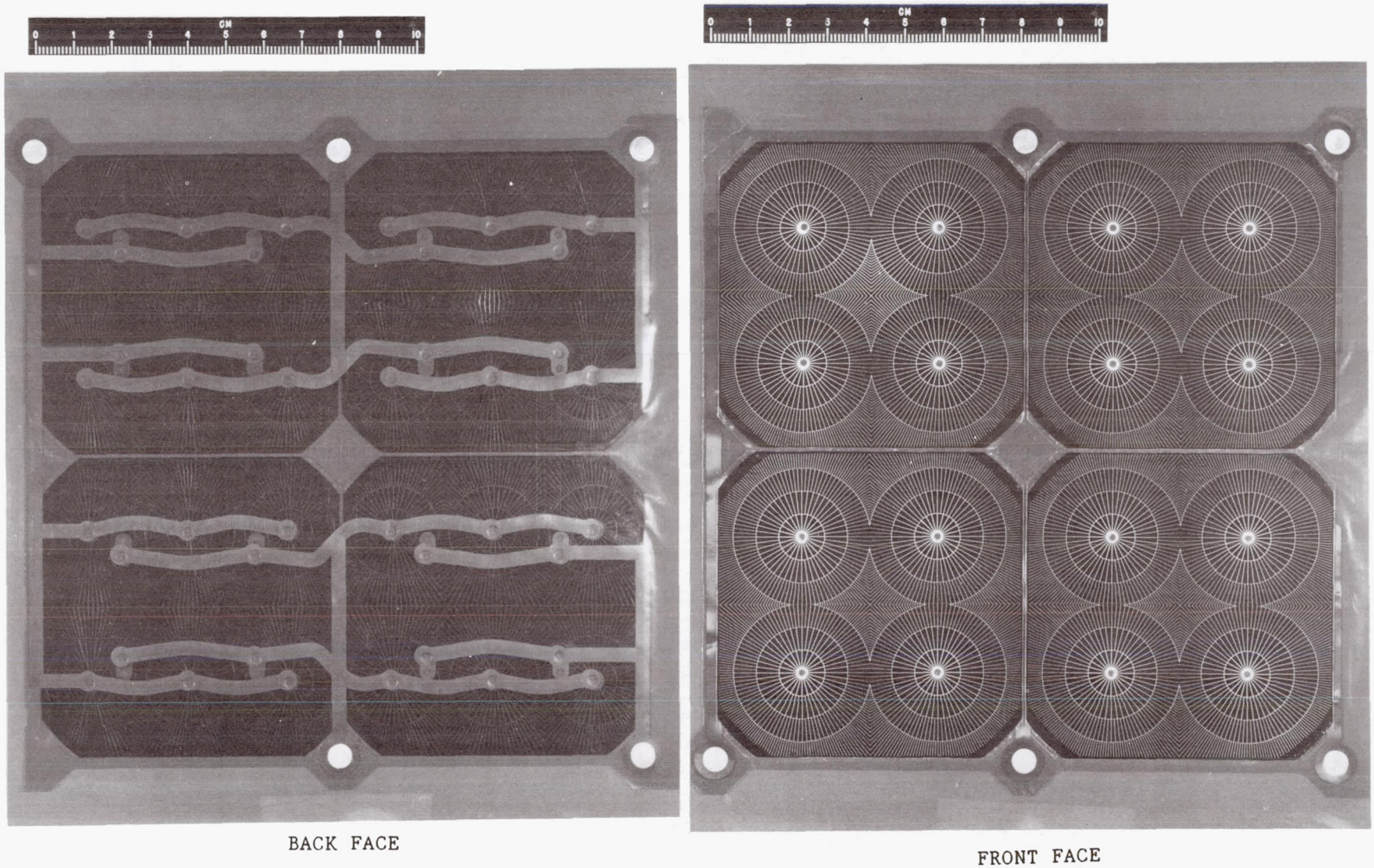

Fig. 3 Test Article Solar Array Blanket Coupons

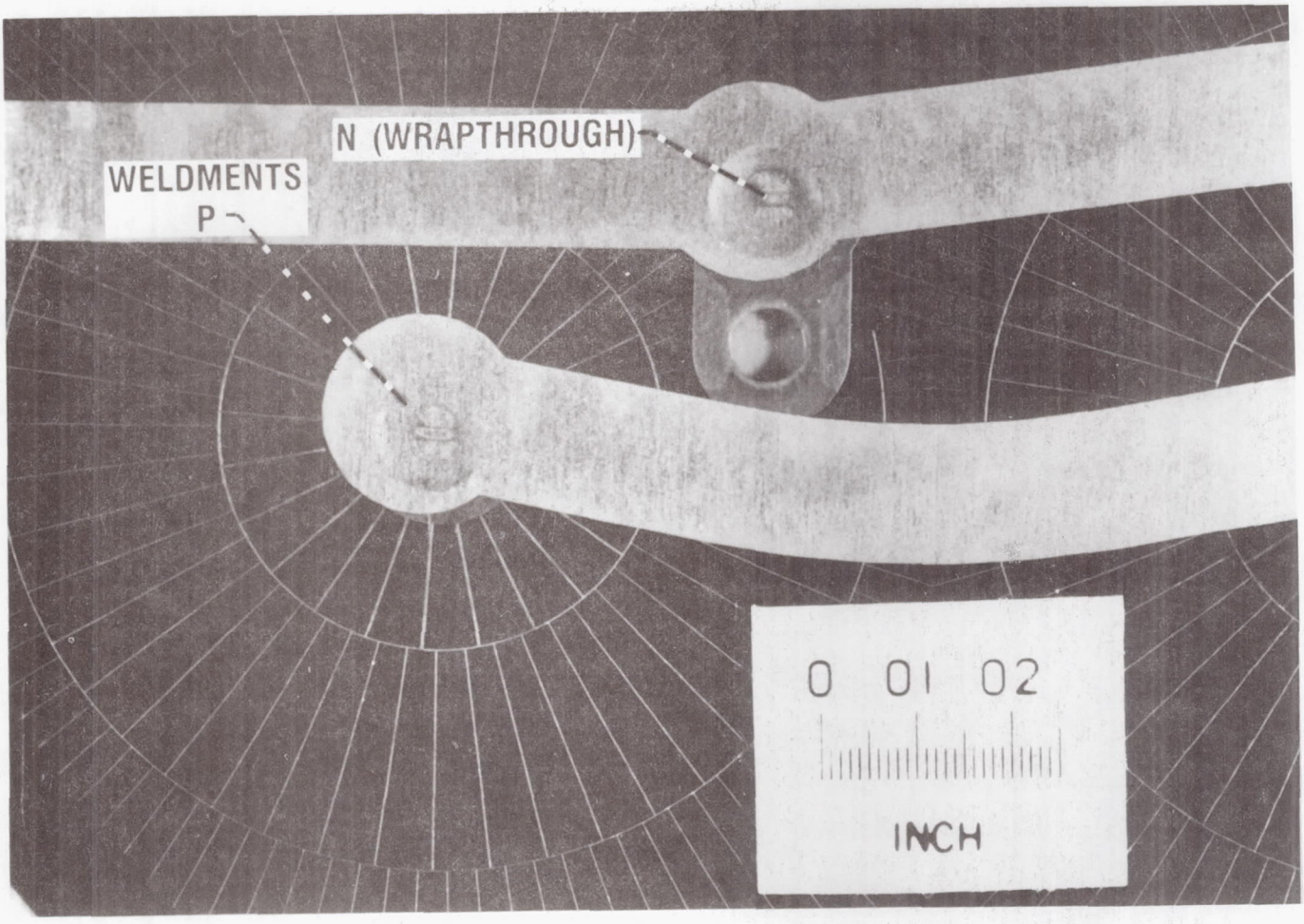

Fig. 4 Close-up view of copper interconnect weld contact points, shown is one P-weld and one N-weld contact.

Space Station Thermal Cycling Modules

Table I: I-V Data 4-cells in series arrays.

A-51 (standard reference cell AMO I_{SC}= .1518 Amps)

Date	3/02/89	4/06/89	4/24/89	5/08/89	5/24/89	6/09/89	7/09/89	7/25/89	8/21/89
Isc	0.1529	0.1519	0.1514	0.1517	0.1518	0.1519	0.1520	0.1518	0.1517
Isc/Isc0	1.0072	1.0007	0.9974	0.9993	1.0000	1.0007	1.0013	1.0000	0.9993

Date	3/02/89	4/06/89	4/24/89	5/08/89	5/24/89	6/09/89	7/09/89	7/25/89	8/21/89
Cycles	0	6000	12000	18000	24000	30000	42000	48000	60000
SSFSA-3									
I_{sc}	2.7080	2.6855	2.7361	2.6446	2.6698	2.6733	2.7272	2.6893	2.6772
V_{oc}	2.4530	2.5073	2.4917	2.4885	2.4829	2.5162	2.4803	2.5136	2.5192
I_{max}	2.4290	2.3754	2.4744	2.3466	2.4095	2.3829	2.4292	2.4131	2.4038
V_{max}	1.8480	1.9066	1.8582	1.9140	1.8520	1.9264	1.8892	1.9239	1.9140
P_{max}	4.4880	4.5287	4.5979	4.4875	4.4624	4.5904	4.5893	4.6425	4.6008
F.F.	0.676	0.673	0.674	0.677	0.673	0.682	0.678	0.687	0.682
Effic.	13.2	13.3	13.63	13.2	13.2	13.5	13.5	13.7	13.6
P/P_0	1.0000	1.0091	1.0245	0.9999	0.9943	1.0228	1.0226	1.0344	1.0251
SSFSA-4									
I_{sc}	2.7070	2.6703	2.7331	2.6612	2.6519	2.6654	2.7274	2.6886	2.6759
V_{oc}	2.4470	2.4559	2.4783	2.4774	2.4722	2.5127	2.4724	2.5058	2.5097
I_{max}	2.4740	2.4228	2.4337	2.4027	2.3405	2.3993	2.4336	2.4148	2.4368
V_{max}	1.8360	1.8669	1.9152	1.8842	1.9152	1.9289	1.9053	1.9450	1.9115
P_{max}	4.5430	4.5230	4.6610	4.5272	4.4827	4.6279	4.6368	4.7038	4.6580
F.F.	0.686	0.690	0.688	0.687	0.684	0.691	0.688	0.698	0.694
Effic.	13.4	13.3	13.7	13.3	13.2	13.6	13.7	13.9	13.7
P/P_0	1.0000	0.9956	1.0260	0.9965	0.9867	1.0187	1.0206	1.0354	1.0253

Date	3/02/89	5/23/89	6/09/89	7/10/89	7/24/89	8/21/89	9/25/89	10/23/89
Cycles	0	6000	12000	24000	30000	42000	54000	66000
SSFSA-1								
I_{sc}	2.6870	2.6571	2.6752	2.7133	2.6983	2.6611	2.6463	2.6493
V_{oc}	2.5125	2.4910	2.5294	2.4865	2.5179	2.5247	2.4960	2.4928
I_{max}	2.3790	2.3990	2.4083	2.4354	2.4212	2.3978	2.3820	2.3927
V_{max}	1.9115	1.8756	1.9276	1.9090	1.9363	1.9425	1.9053	1.9028
P_{max}	4.5475	4.4994	4.6422	4.6493	4.6882	4.6577	4.5385	4.5528
F.F.	0.674	0.680	0.686	0.689	0.690	0.693	0.687	0.689
Effic.	13.4	13.3	13.7	13.7	13.8	13.7	13.4	13.4
P/P_0	1.0000	1.9894	1.0208	1.0224	1.0309	1.0242	0.9980	1.0012
SSFSA-5								
I_{sc}	2.6776	2.6643	2.6809	2.7156	2.7026	2.6828	2.6516	2.6561
V_{oc}	2.4766	2.4767	2.5097	2.4769	2.5087	2.5152	2.4851	2.4827
I_{max}	2.3782	2.3966	2.3704	2.4599	2.3994	2.3991	2.3670	2.3324
V_{max}	1.8756	1.8446	1.9202	1.8520	1.9289	1.9140	1.8892	1.9214
P_{max}	4.4605	4.4206	4.5516	4.5559	4.6281	4.5919	4.4717	4.4815
F.F.	0.673	0.670	0.676	0.677	0.683	0.681	0.679	0.680
Effic.	13.1	13.0	13.4	13.4	13.6	13.5	13.2	13.2
P/P_0	1.0000	0.9911	1.0204	1.0214	1.0376	1.0295	1.0025	1.0047

The Advanced Photovoltaic Solar Array (APSA) Technology Status and Performance

Paul M. Stella
Jet Propulsion Laboratory
California Institute of Technology
Pasadena, CA

Richard M. Kurland
TRW Space & Technology Company
Redondo Beach, CA

Introduction

In 1985, the Jet Propulsion Laboratory, under sponsorship of the NASA Office of Astronautics and Space Technology, initiated the Advanced Photovoltaic Solar Array (APSA) program. The program objective is to demonstrate a producible array system by the early 1990s with a specific performance of at least 130 W/kG (beginning-of-life) as an intermediate milestone towards the long range goal of 300 W/kG. The APSA performance represents an approximately four-fold improvement over existing rigid array technology and a doubling of the performance of the first generation NASA/OAST SAFE flexible blanket array of the early 1980s.

Technology Status

The first phase of the APSA program developed preliminary designs through contracts with TRW and LMSC. In order to allow for a subsequent comparison and evaluation of the two designs a number of ground rules were established through a consensus agreement. These requirements established the operational environment for the array design (geosynchronous-10 years lifetime), the baseline size (approximate 10 kW with scaleability from 5 to 25 kW), and a number of additional mechanical and electrical characteristics. At the completion of the design phase, TRW was selected to implement prototype hardware development. The prototype hardware effort was identified as phase II. Due to funding constraints phase II was divided into an A and B effort. Phase IIA began in 1987 and was completed in 1988. Phase IIB began in January, 1989, and is expected to be completed in early 1990. A schedule for phase IIB is shown in figure 1. An additional phase will be added to develop any necessary array upgrades and to perform ground testing and evaluation.

The prototype hardware being developed during phase II is essentially a foreshortened version of the approximately 5 kW TRW wing design developed during phase I. The configuration of the APSA is similar to the SAFE array flown on the shuttle in 1984; it is a flexible fold out wing with deployment and structural support

attained through the use of a rear side mounted coilable longeron mast. The APSA wing design is based on a flexible foldable blanket element called a SPA, or solar panel assembly. The full size wing consists of 13 SPAs, each covered with 5760 thin 2x4 cm^2 silicon solar cells. The prototype wing will include two SPAs and the mast is reduced in length accordingly. Cell coverage is reduced to a total of 1440 cells with the remaining SPA areas covered by mass simulating aluminum wafers. The lid and pallet structure (also referred as the blanket housing) and the mast canister are equal in size to the full scale wing design. A sketch of the prototype wing is shown in figure 2.

During phase IIA, the flexible blanket, consisting of two SPAs, along with additional leader, or lid/pallet attachment, panels was successfully assembled by TRW. Thin silicon cells were provided by all three space solar cell vendors, ASEC, Solarex, and Spectrolab, and 50 micron thick CMZ glass cell covers were provided by Pilkington. In addition a lightweight canister/mast system was provided by AEC Able Engineering. Appropriate tests were performed on all assemblies to verify mass estimates and mechanical performance projections.

At present phase IIB is well underway. As shown in figure 1, the remaining tasks include fabrication of the blanket housing (lid/pallet structure and tiedown/release mechanisms), integration of all wing components, and a ground deployment to verify prototype form, fit, and function. Component development tests have recently been completed on a narrowed version of the blanket housing. These tests included an exposure of the latched housing to an acoustic environment 6 db higher than present shuttle requirements. No structural problems were identified and the blanket housing test article has been subjected to repeated latch and unlatch tests prior to and after testing without any anomalous results. A photograph of the blanket housing test hardware is shown in figure 3. As a result of these tests, fabrication of the full size blanket housing has commenced.

A key demonstration for the integrated wing will be a ground deployment which will verify the unlatching of the tie down mechanisms and the deployment of the mast/blanket system. Particular care is required in conducting such a test in the earth's gravity environment. Consequently, a fixture has been prepared to support the wing assembly both during the stowed and deploying phases. The fixture has been designed to minimize frictional forces on the wing supports which would otherwise interfere with the deployment. Figure 4 is a photograph of the fixture with the APSA blanket attached. Mockup lid and pallet endplates are attached for a manual deployment (without the mast/canister assembly) to verify low friction blanket motion.

One additional test which is presently underway is being supported by NASA-LeRC. A small module fabricated by TRW to the APSA blanket design is undergoing extensive thermal cycling in the LeRC fast thermal cycling chamber. At present 3000 GEO type thermal cycles have been completed without significant electrical change.

The module is presently being subjected to an additional LEO type thermal cycles. To date 18,000 of the LEO cycles have been completed without any degradation.

APSA Performance

At the end of the phase I design effort array electrical and mechanical performance estimates were made for a ten year geosynchronous mission. These have been updated to include the results of hardware fabrication and design changes in the phase II effort. Table 1 shows both sets of performance estimates along with the initial phase I contract performance goals. The result of the phase II work has been to increase both wing power and mass somewhat (for example, a slightly thicker and more efficient silicon cell is presently used). Although there has been some reduction in APSA specific performance it still exceeds the goal of 130 W/kG. It should be noted that the mass and specific performance values include a ten percent contingency. Part of that contingency is due to design uncertainty and will be reduced when the prototype hardware is completed.

The APSA electrical performance has been examined for two missions which would benefit from the use of a lightweight array. These include the initial GEO orbit and a LEO-GEO transfer orbit as might occur with solar electric propulsion. Table 2 presents results for a ten year GEO mission and compares the baseline APSA design (3 mil shielding front and rear) with some options. The options include a more heavily shielded APSA, a conventional rigid array (using thin silicon cells), and an extrapolation of APSA using thin film copper indium diselenide(CIS) cells rather than silicon cells. It should be noted that the CIS option is based upon preliminary data obtained with development cells. However it does serve to indicate what is possible with the use of a relatively moderate efficiency, radiation resistant, thin film cell, even if such a cell eventually is composed of some other material. For the GEO application it is clear that no significant benefit follows from increased APSA shielding or the use of rigid array technology. Both provide for a modest reduction in array area, but both incur a significant mass penalty. The use of the advanced thin film material cell will, in contrast, save mass and area and probably cost.

A more dramatic result is seen in table 3, where a similar analysis is performed for a possible LEO-GEO transfer lasting 200 days. The transfer orbit was calculated by assuming the performance of a solar electric ion propulsion system. In this case increased APSA shielding will lead to fairly substantial reductions in required array area, as will the use of a conventional rigid array. These area reductions will most likely provide for array cost reductions. However, in all cases the baseline APSA array will still be the lightest option, an important factor for a SEP mission where increased array mass will require a corresponding decrease in payload, or an increased transit time which would in turn lead to further array degradation. The best option is that of the APSA using the thin film cell, for not only is it the lightest but it also has the

least area. The importance of the development of such lightweight cells for future APSA versions is clear, particularly where substantial radiation will be experienced.

Flight Readiness

The present APSA program has as its objective, the ground testing and verification of a prototype lightweight wing assembly. The prototype is not intended to be flight hardware, inasmuch as program constraints could not support flight hardware fabrication. At the same time, the fabrication of the prototype has been accomplished with sufficient design development to address potential manufacturing difficulties and identify any unsuspected design weaknesses. As a result it is felt that design maturity will be sufficient to allow for a subsequent flight design and manufacturing effort. Figure 5 is a suggested schedule for flight hardware effort that could commence at the end of phase III. Obviously a number of assumptions are included since any actual flight application will have its own unique set of requirements. The schedule is for the fabrication of a single wing of the present APSA size (5.8 kW) and includes detail design task to meet flight requirements and appropriate qualification testing. It is estimated that an additional wing could be fabricated by adding an additional 4-6 months of schedule time. Allowing one year for the procurement cycle suggests that the APSA type lightweight wing could be ready for launch in the mid 1990s.

Conclusion

The APSA is nearing completion of the prototype fabrication and ground test effort. It is likely that the specific power goal of 130 W/kG or greater will be achieved. A flight test could be possible by the mid 1990s.

Lightweight and relatively radiation resistant arrays can provide significant advantages over conventional rigid arrays for a number of mission applications, both in BOL and EOL(end- of-life) performance. The development of advanced lightweight thin film, radiation resistant, solar cells is key to extending the advantages of the present APSA technology well into the next century. Such cells may allow future arrays to provide EOL specific power values appreciably higher than present day BOL values.

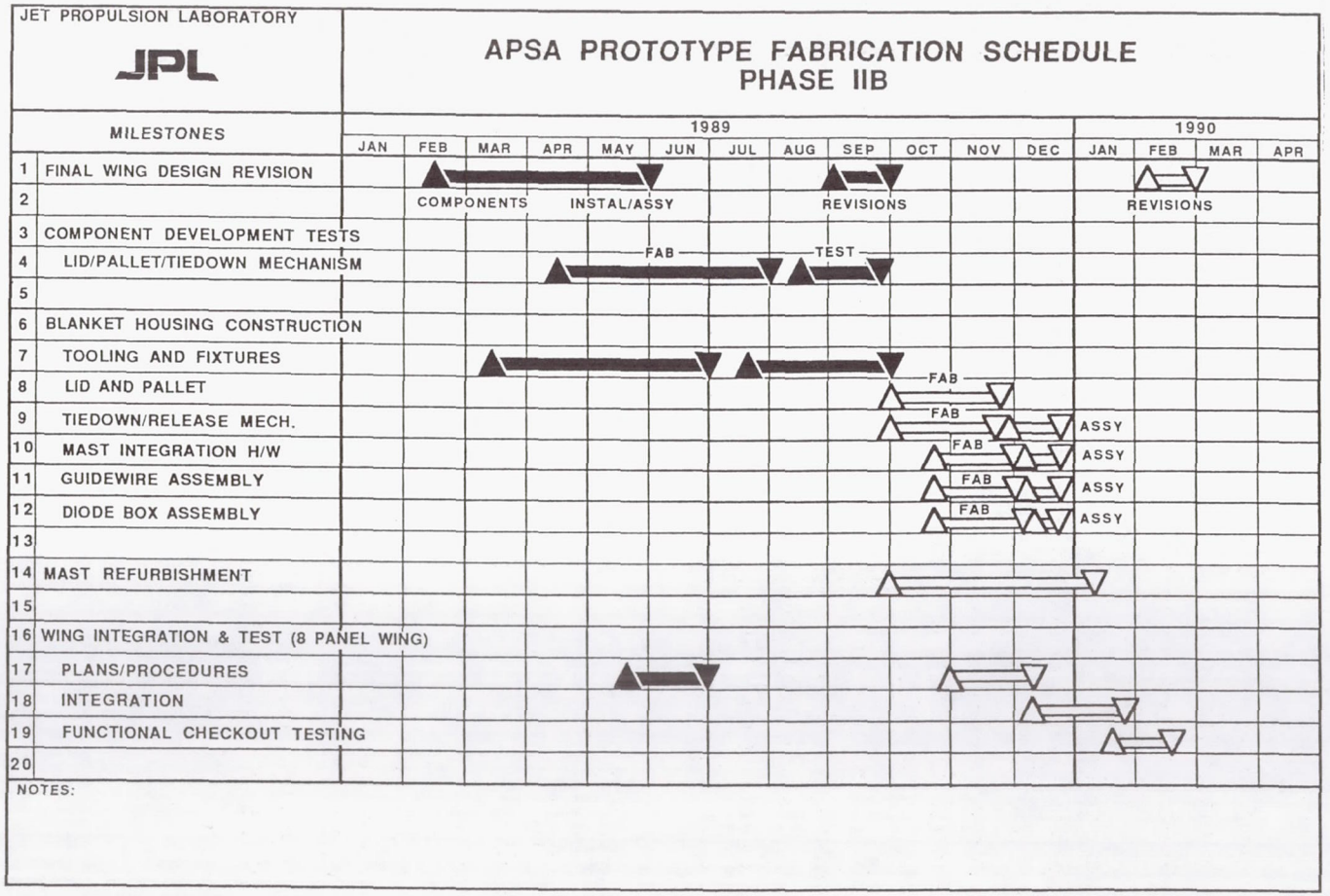

Figure 1: APSA Prototype Fabrication Schedule
Phase IIB

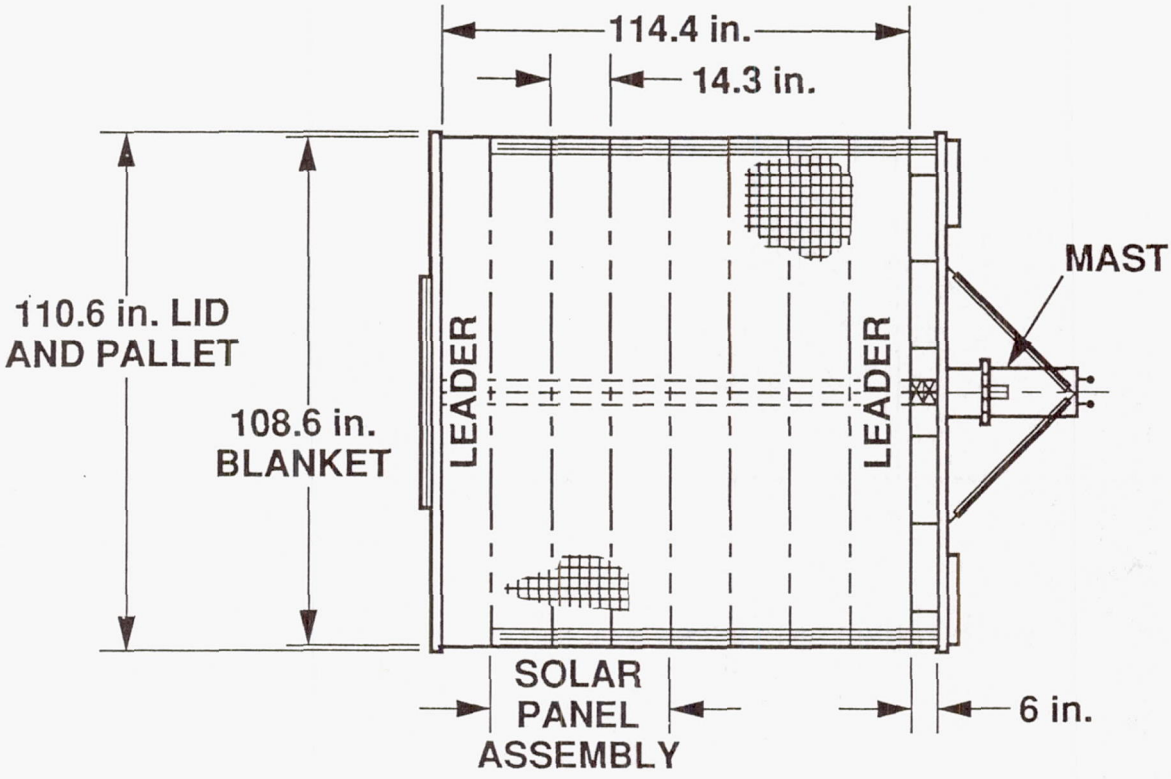

Figure 2: APSA Prototype Wing Configuration

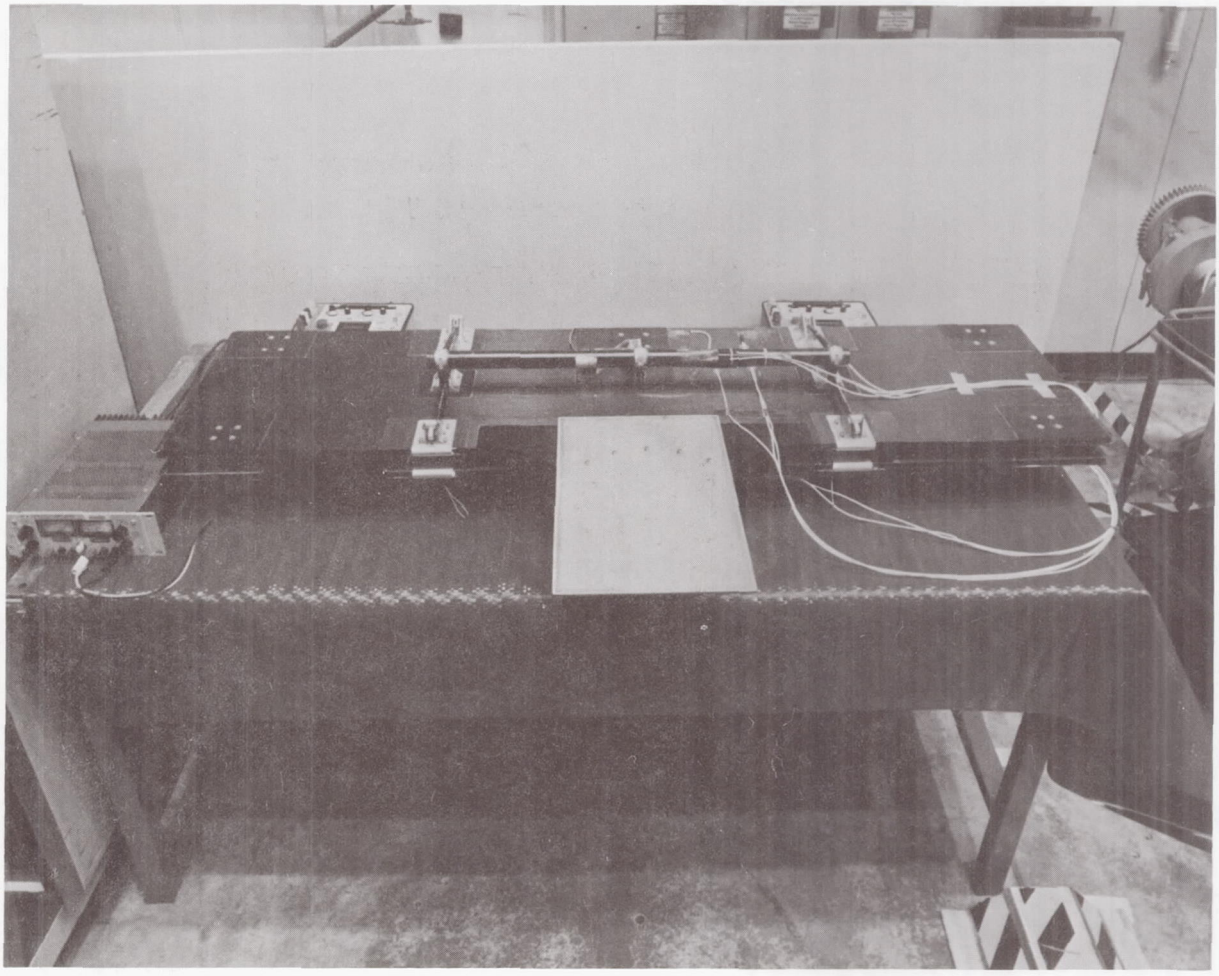

Figure 3: APSA Blanket Housing Development Test Hardware

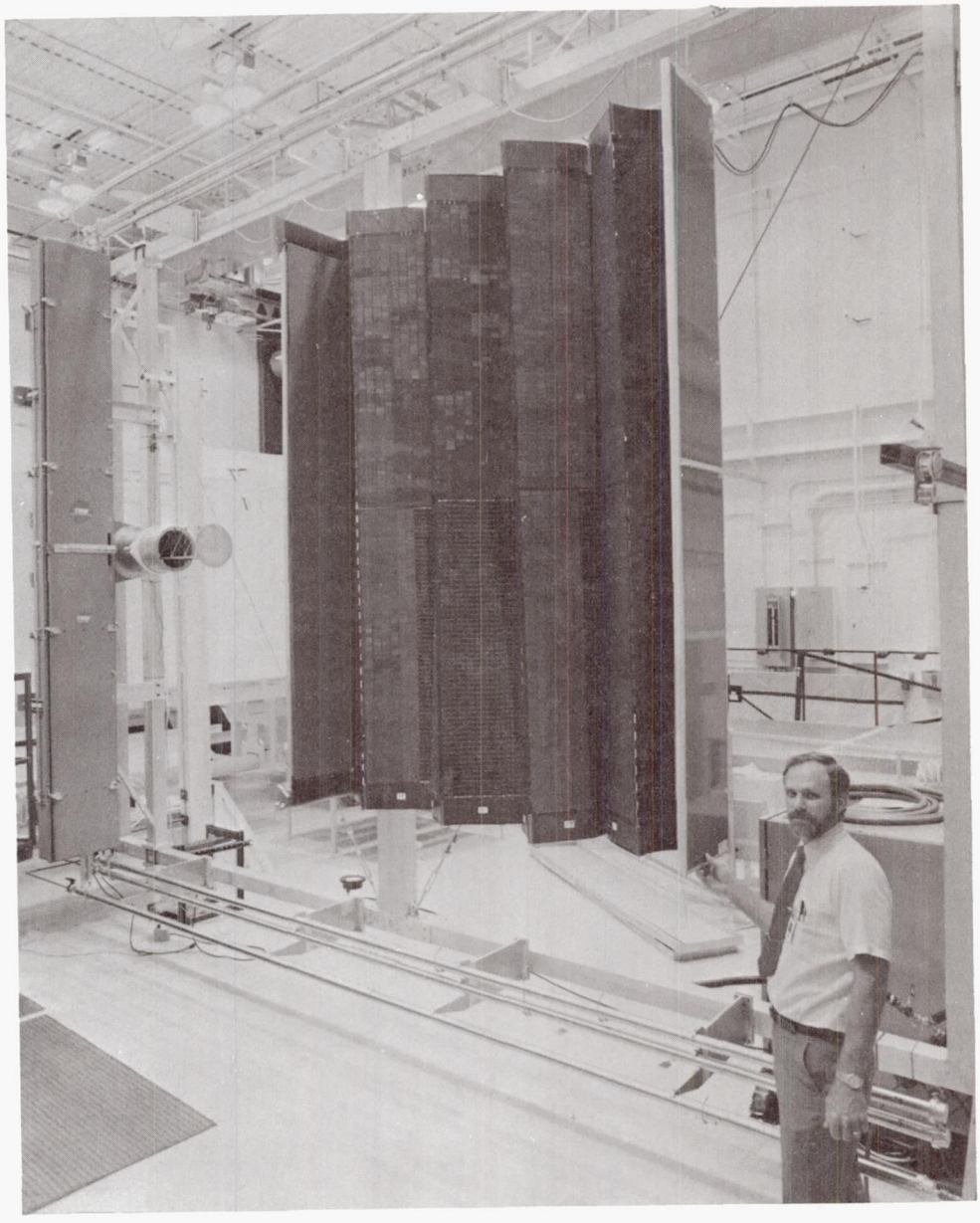

Figure 4: APSA Prototype Blanket on Deployment Test Fixture

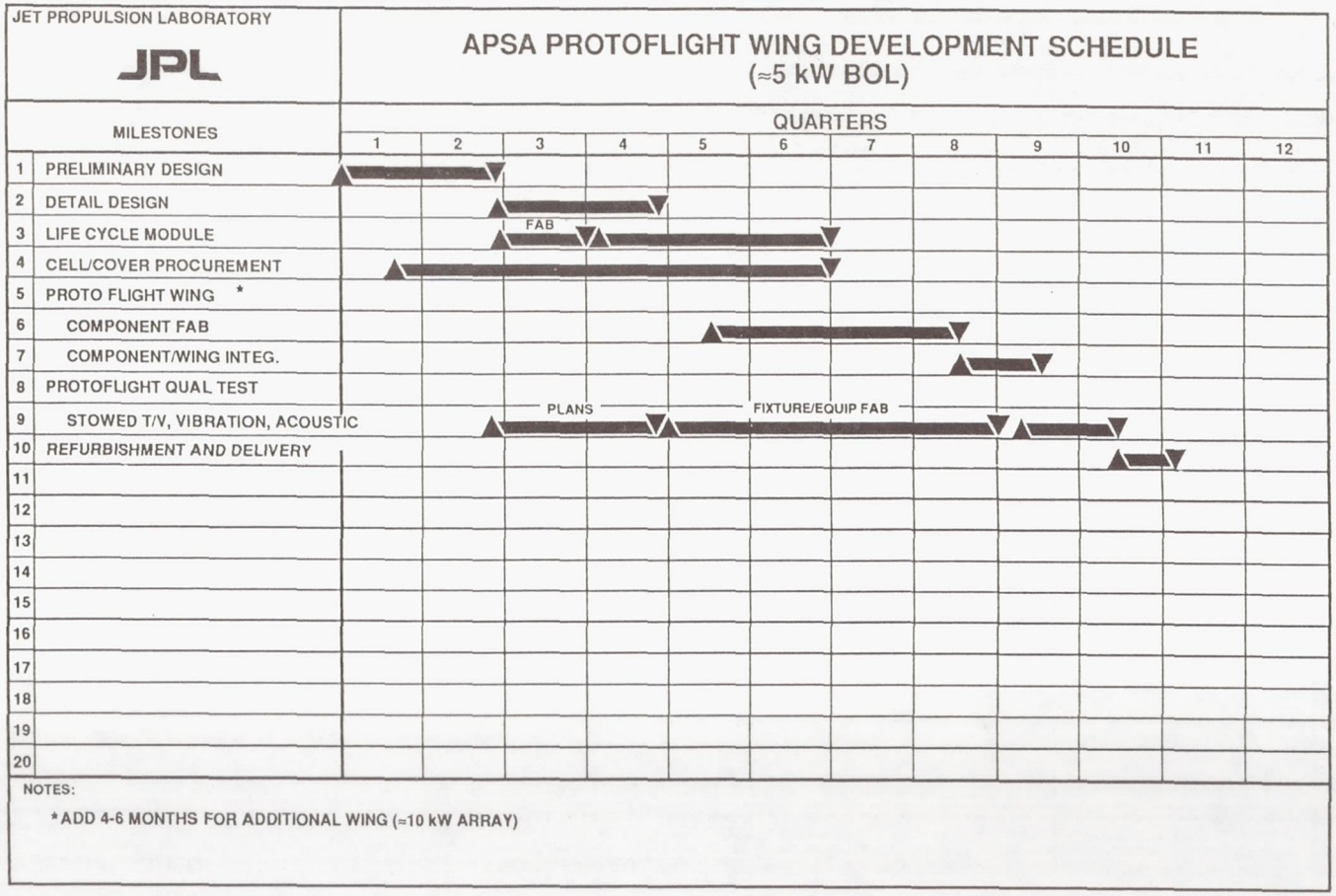

Figure 5: Baseline Schedule for APSA Flight Test Wing

PARAMETER	1986 GOAL	PHASE I 1986 ESTIMATE	PHASE II 1989 ESTIMATE
BOL POWER (GEO)	10 kW (2 WINGS)	10.4 kW	10.6 kW
EOL POWER (GEO)	NOT SPECIFIED; 8 kW IMPLIED BY EOL SPECIFIC POWER GOAL	7.4 kW	7.7 kW
BOL SPECIFIC POWER AT EQUINOX	>130 W/kg	136.1 W/kg*	131.5 W/kg*
EOL SPECIFIC POWER AT EQUINOX	>105 W/kg	96.7 W/kg*	93.8 W/kg*
EOL POWER DENSITY AT EQUINOX	>110 W/m_2; REFERENCE AREA NOT SPECIFIED	94.6 W/m_2**	98.9 W/m_2**
BOL OC VOLTAGE	<200 volts	210 volts	214 volts
WING WEIGHT	NOT SPECIFIED	38.2 kg*	41.1 kg*
DEPLOYED FREQUENCY	>0.01 Hz; 0.1 Hz PREFERRED	0.10 Hz	0.14 Hz (BENDING) 0.12 Hz (TORSION)
DEPLOYED STIFFNESS	>0.001 g; 0.01 g PREFERRED	0.015 g	0.015 g

* INCLUDES 10 PERCENT WEIGHT CONTINGENCY

** BASED ON TOTAL PANEL AREA WITH HARNESS

Table 1: APSA Electrical and Mechanical Performance

	SPECIFIC PERFORMANCE (W/kg)		RELATIVE AREA FOR SAME EOL POWER (≈7 kW)
	BOL	EOL	
APSA (3 mil SHIELD) *	130	94	1.00
APSA (6 mil SHIELD) *	95	73	0.94
CONVENTIONAL RIGID (12 mil COVER)	25	20	0.90
APSA ($CuInSe_2$) ** EST.	165	155	0.95

* FRONT AND REAR SIDE EQUIVALENT SHIELDING
** ASSUME 11% CELL EFFICIENCY, 3 mil SHIELDING FRONT AND REAR, SILCON DAMAGE EQUIVALENCE

Table 2: APSA Specific Performance 10 Years GEO

	SPECIFIC PERFORMANCE (W/kg)		RELATIVE AREA FOR SAME EOL POWER (≈7 kW)
	BOL	EOL	
APSA (3 mil SHIELD) *	130	50	1.00
APSA (6 mil SHIELD) *	95	45	0.81
APSA (12 mil SHIELD) *	65	38	0.63
CONVENTIONAL RIGID (12 mil COVER)	25	17	0.57
APSA ($CuInSe_2$) ** EST.	165	130	0.56

* FRONT AND REAR SIDE EQUIVALENT SHIELDING
** ASSUME 11% CELL EFFICIENCY, 3 mil SHIELDING FRONT AND REAR, SILCON DAMAGE EQUIVALENCE

Table 3: APSA Specific Performance - 200 Day LEO to GEO Spiral Orbit

Integral Bypass Diodes in an Amorphous Silicon Alloy Photovoltaic Module

J.J. Hanak* and H. Flaisher**
Sovonics Solar Systems, Inc.
Troy, MI

Thin-film, tandem-junction, amorphous silicon (a-Si) photovoltaic modules have been constructed in which a part of the a-Si alloy cell material is used to form bypass protection diodes. This integral design circumvents the need for incorporating external, conventional diodes, thus simplifying the manufacturing process and reducing module weight.

Introduction

When connecting photovoltaic cells in series, each cell is potentially vulnerable to damage caused by inadvertent application of a reverse bias having a voltage equal to the sum of the voltages produced by the other cells in the string. This occurs either when the cell is shaded while the others are illuminated, or if the current of the cell is not matched well to that of the other cells. This reverse voltage, if sufficiently high, can cause breakdown, leading to irreversible damage in the shaded cell. To protect against this event, diodes are usually connected across one of several cells in order to prevent build-up of this reverse voltage (see Figure 1). These "bypass" diodes are necessary, but they lead to increased cost and complexity in module fabrication and they add extra weight to the module, which can reduce significantly the power-to-weight ratios, particularly for an ultralight module. Accordingly, alternative solutions to solar cell protection are in order. Integral bypass diodes, made of the same material and on the same substrate as the solar cell are particularly attractive for this purpose. Previous examples of integral diode design exist for individual monocrystalline silicon cells, which incorporated the bypass diode on a portion of the wafer [see, e.g., refs. 1 and 2]. Recently, thin film integral bypass diodes made of a-Si have been described by Ishihara et al. [ref. 3].

Current Affiliations:

*APOGEE Corporation, P.O. Box 1459 Welch Ave. Station, Ames, Iowa 50010 and, Iowa State University, Institute for Physical Research and Technology, Ames, Iowa 50011. Telephone: 515/294-2296

**NIR Systems, 2441 Linden Lane, Silver Spring, MD 20910.

The purpose of this paper is to describe our experimental results on integral, tandem-junction a-Si bypass diodes protecting a series string of a-Si tandemjunction solar cells and to evaluate them for potential use in ultralight space PV arrays. We have found the current-carrying capability of the a-Si alloy diodes to be excellent, allowing the diode to be fabricated on a relatively small area of the active solar panel.

Results and Discussion

Determination of Damage Induced by Reverse Bias in Unprotected a-Si Alloy Cells

At first we conducted experiments to determine the minimum number of a-Si alloy solar cells connected in series that would lead to module damage upon shadowing of one of the cells. The experiments have been conducted on modules consisting of commercially available Sovonics tandem-junction, n-i-p/n-i-p cells, 14.5 cm^2 in area, deposited on a stainless steel substrate and encapsulated in a flexible polymer. Series strings from two to 32 such cells were made, short-circuited, exposed to AM1.5 illumination, and selected cells were shadowed one at a time. The unshaded cells thus applied external reverse bias of 1.6 to 49.6 V to the shaded cell.

The minimum number of cells per string in which damage was observed was four; in this case a decrease of 300 mV in V_{oc} as well as a decrease in the fill factor took place. With larger number of cells per string the damage was progressively more frequent and more severe.

A shadowing experiment has also been made on a monolithic [ref. 4], Ultralight^{tm} [refs. 5 and 6] module consisting of 120 tandem-junction cells, each 6.3 cm in area (12 cells per series string x 10 strings in parallel). After shadowing of all cells, 10 cells at a time, the V_{oc} decreased by 2.8 V from 16 V to 13.2 V.

In still another experiment over 350 such 6.3 cm^2 cells were connected in series, generating V_{oc} in excess of 500 V. Without bypass diode protection, several of the cells sustained visible burns just by operating the module in the sunlight without shadowing.

These experiments clearly indicate that bypass diode protection is desirable with a-Si alloy cells across at least every 3 tandem-junction cells connected in series and preferably across every cell.

Determination of Current Carrying Capacity of a-Si Alloy Tandem-Junction Diodes

Next, we carried out tests to determine the maximum current which these diodes, made of tandem-junction, a-Si alloy cell material, could carry without heating up to temperatures which could damage either them or other parts of the module, such as

the encapsulant. To do this, the diodes were made having an area of 1.28 cm^2 and a top contact of silver paste covering completely the transparent indium tin oxide electrode. The diodes being tested were placed in a small oven and the instantaneous I-V curve was scanned at various temperatures. One typical result is shown in Figure 2. (The temperature coefficient (dV/dT) in Figure 2 is approximately 20 mV/°C, which is larger than expected [ref. 7]. This behavior will be addressed in a future publication.) The diodes were then placed at ambient temperature and a DC voltage was applied until the diode reached its steady-state operating temperature. The I-V curve was then scanned and the diode temperature was deduced by correlation of this scan to one of the scans in Figure 2. It was found that the diodes were capable of passing an instantaneous current of 7 amps/cm^2 at 6 volts. They were able to sustain in excess of 1-1.5 amps/cm^2 at 2.53 volts without exceeding a temperature of approximately 100°C in air.

Demonstration of Effective Protection of PV Modules with a-Si Alloy Bypass Diodes

In order to test the effectiveness of the diodes in a module, we performed a test aimed at demonstrating that as the cell was progressively shadowed, less current was generated by the cell, while an increasing amount of current was passing through the diode. The circuit shown in the inset of Figure 3 was constructed with a standard, 2.5 watt module consisting of seven cells interconnected in series and protected with conventional silicon diodes. One of these diodes was removed and replaced with an a-Si alloy, tandem-junction diode having a multilayer structure similar to that of the cells used in the module. The size of each cell was 74 cm^2 while that of the a-Si diode was 1 cm^2, so that the ratio of the diode area to that of the module was 1.4%. The module was then exposed to near-AM1 solar irradiation and with the output leads of the module shorted, the current generated by the module and the current passing through the a-Si alloy bypass diode were measured (I_1 and I_2 in Figure 3). Figure 3 reflects the desired result that increasing shadowing effects both a decrease in cell current (obtained by subtracting I_2 from I_1) and an increase in diode current. The string current (I_1) remains essentially independent of shadowing, as is required for a module which is properly protected. The nonlinearity in the curves for weak shadowing arises form the finite turn-on voltage of the diode. Since the diode has a tandem junction, its turn-on voltage is approximately twice that of a single junction diode. Therefore, until sufficient shadowing and concomitant build-up of reverse voltage occurs, current will not flow through the bypass diode and will instead flow through the shadowed cell, causing a reduction in the total string current.

Protection of Large a-Si Alloy Cells with Integral a-Si Alloy Diodes

After this test, we fabricated a module in which the diodes were integrally formed. The module consisted of four giant tandem n-i-p/n-i-p cells, each having an area of 1430 cm^2. Diodes were created on a 6.25% portion of each of these cells and were

separated from the active cell area by etching through the top conductive layer to form a thin border line. The bypass diode on a given cell substrate was connected so as to protect the cell on the adjacent substrate.

Figure 4 shows the I-V curve for the module both with and without shading of one of the cells. Note first that there is a difference of about 1.7 V in open circuit voltage between the two curves (6.6 V-4.9 V); this is consistent with the fact that the contribution of the shaded cell (1.6 to 1.7 V) is removed upon shading. At voltages less than that at open circuit, the discrepancy in voltage between the two curves is approximately 4 V. This occurs because the voltage in the cell string does not sufficiently bias the diode (thus decreasing its conductivity), causing the diode to act as an internal resistance. For example, for a module output voltage of 2 V, the diode would be forward biassed 2.9 V (4.9 V-2 V). From Figure 2, this corresponds to 1 to 5 amps, depending on temperature, which is consistent with the string current of 3 A generated during shading (Figure 4). It is this factor which is also responsible for the decrease in the fill factor for this curve.

Figure 4 also shows that the original I-V trace is essentially reproduced after the shading has been removed, signifying that the diodes had indeed protected the module. (The reduction in V_{oc} of about 0.1 V is probably due to a slight heating of the module [ref. 7].) Considering the diode current-carrying capability discussed above, one could optimally construct an integrally, diode-protected version of one of these large cells with about 10 cm^2, or 0.7% (10 cm^2 /1430 cm^2) of the cell area devoted to the bypass diode.

Another, similar, two-cell module containing integrated bypass diodes was connected in series to a Sovonics MP140 panel (consisting of 14 cells, each 1430 cm^2 in area, all connected in series) and exposed to direct sunlight to produce a total array I_{sc} of 10.2 A and V_{oc} of 24.9 V. Each of the cells in the two-cell module was sequentially shaded while the whole array was held at short circuit. The I_{sc} and V_{oc} readings with one cell shaded were 10.13 A and 23.3 V. Note that the difference in V_{oc} readings is 1.6 V, (24.9 V-23.3 V), again signifying a reduction in voltage by an amount equal to the V_{oc} of the shaded cell. Once again, no degradation in either the short circuit current or open circuit voltage of the module was observed after the shading was removed. Without bypass diodes damage by such a high reverse bias (23.3 V) would be expected to occur and even more readily in the large cells used in the present test because of the 20 to 200 times larger photocurrent generated by these large cells.

Finally, it is useful to compare the behavior of the thin film, a-Si alloy tandem-junction diode with its conventional silicon diode counterpart. Figure 2 shows that 3 to 4 V bias is needed in order for the a-Si diodes to pass 5 amps. This value compares with about 1.2 V for a conventional silicon diode. This fact may make the use of thin film diodes advantageous, since short passivation of a-Si alloy tandem junction solar cells is optimally carried out by applying a reverse bias of about 5 V. Therefore, an

occasional build-up of several volts on a cell during shadowing may actually act to repair any shorts which may exist within the cell [ref. 8]. We have demonstrated this feature in a separate experiment. We have also shown that in general, this reverse bias voltage is not sufficiently high to create new shorts by causing cell breakdown; these shorts are typically created above about 5 V.

Conclusions

In conclusion, we have shown that protection of a-Si alloy tandem junction photovoltaic cells in solar panels against reverse bias voltage can be achieved through the use of integrated bypass diodes made of the same materials as the solar cells. Protection of a cell area as large as 1430 cm^2 has been demonstrated. This capability has important implications on the design and manufacture of ultralight, monolithic arrays for potential space applications [refs. 5 and 6] as well as in arrays utilizing "giant" cells [ref. 9]. It will also have a substantial impact on the reliability and production cost of any amorphous silicon alloy panels, using either single junction or multijunction cells.

References

[1.] C. H. Cox, III, D. J. Silversmith and R.W. Mountain, *Proc. 16th Photovoltaic Specialists' Conf.*, 834, IEEE, New York (1982).

[2.] M. A. Green, E. S. Hasyim, S. R. Wenham and M. R. Willison, *Proc. 17th Photovoltaic Specialists' Conf.*, 513, IEEE, New York (1984).

[3.] Ishihara et al., U.S. Patent No. 4,638,109, issued January 20, 1987.

[4.] J. J. Hanak, Solar Energy, **23**, 145 (1979).

[5.] J. J. Hanak, *Proc. 18th Photovoltaic Specialists' Conf.*, 89, IEEE, New York (1985).

[6.] J. J. Hanak, L. Walter, D. Dobias, and H. Flaisher, *8th Space Photovoltaic Research and Technology (SPRAT) Conf.*, 99, NASA Conference Publication 2475 (1986).

[7.] C. R. Osterwald, T. Glatfelter and J. Burdick, *Proc. 19th Photovoltaic Specialists' Conf.*, 188, IEEE, New York (1987).

[8.] J. J. Hanak, *Proc. 14th Photovoltaic Specialists' Conf.*, 623, IEEE, New York, (1980).

[9.] J. J. Hanak, L. Walter, D. Dobias and H. Flaisher, *DGLR/AIAA/JSASS 20th International Electric Propulsion Conference*, 121 (1988); and *Space Photovoltaic Research and Technology (SPRAT) Conference*, 162, NASA Conference Publication 3030 (1986).

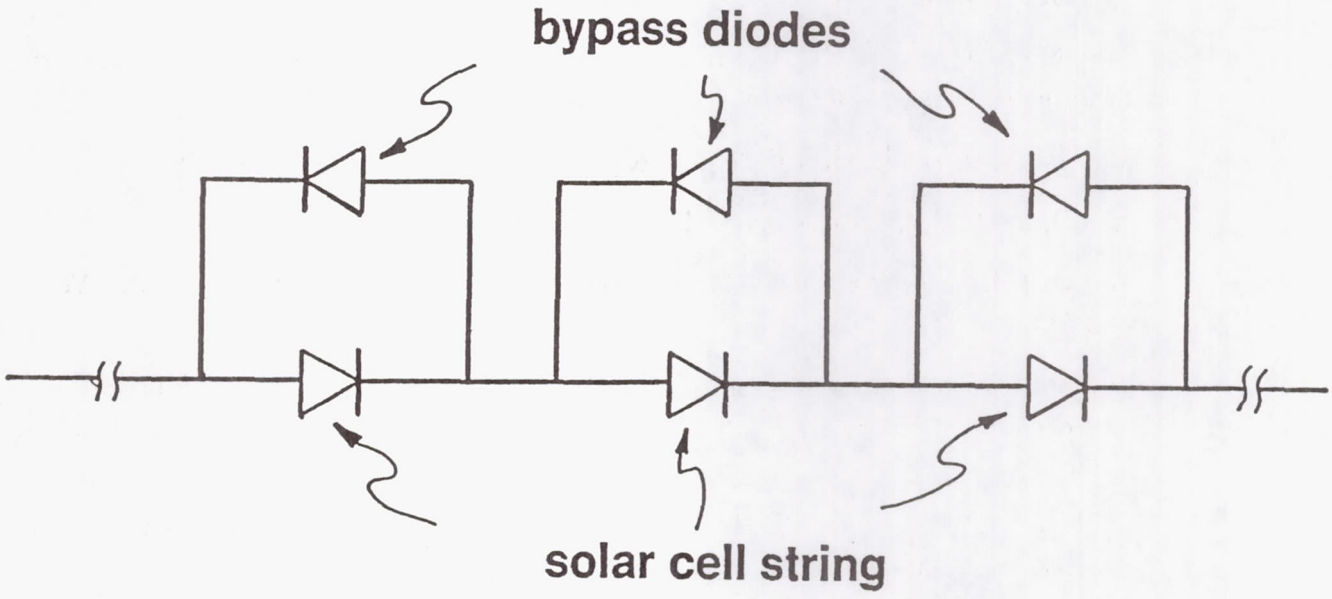

Figure 1 Schematic diagram showing how bypass diodes are connected to a string of solar cells (also represented as diodes).

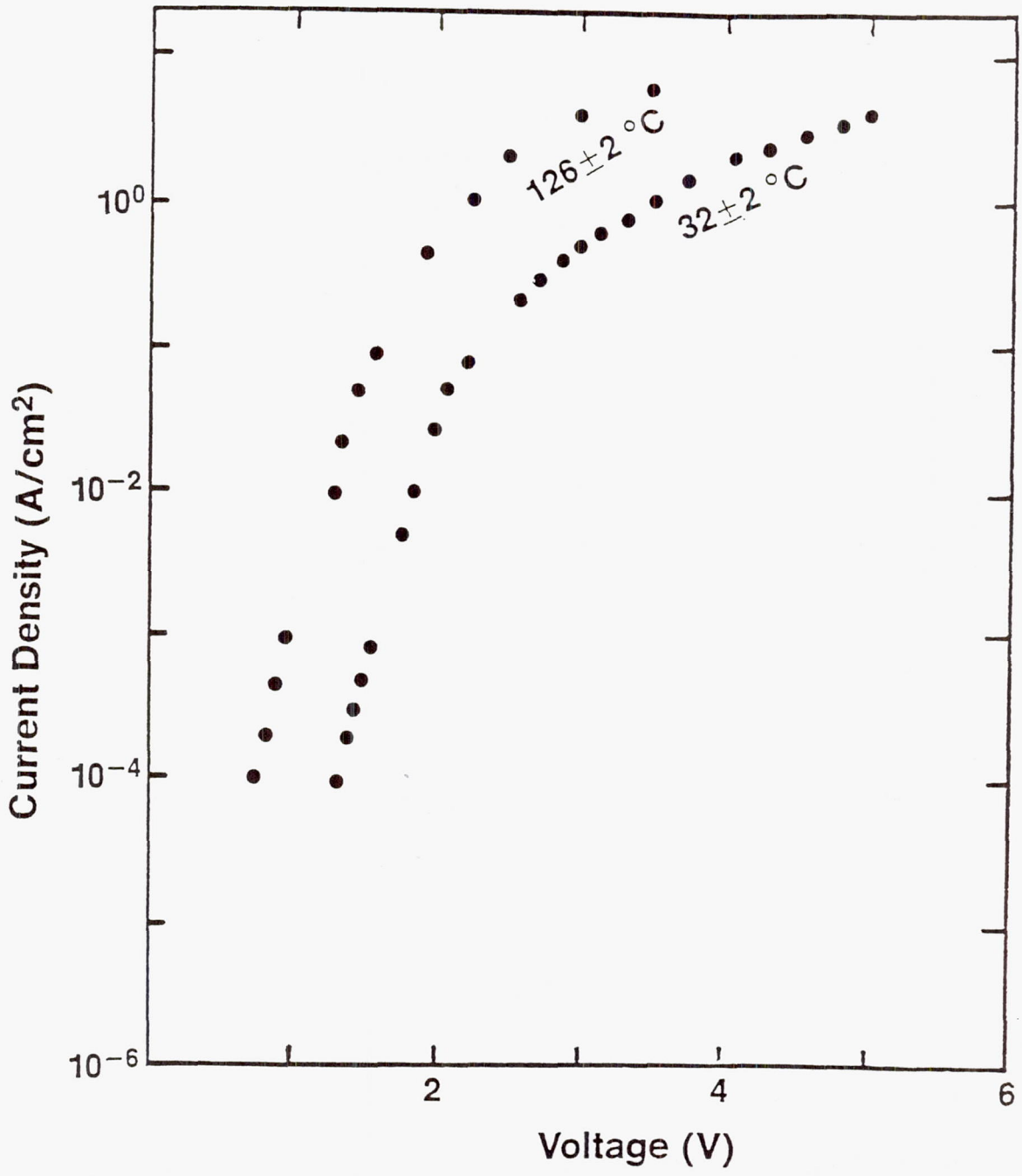

Figure 2 Typical dark I-V characteristics for an a-Si alloy tandem-junction cell, recorded at two temperatures.

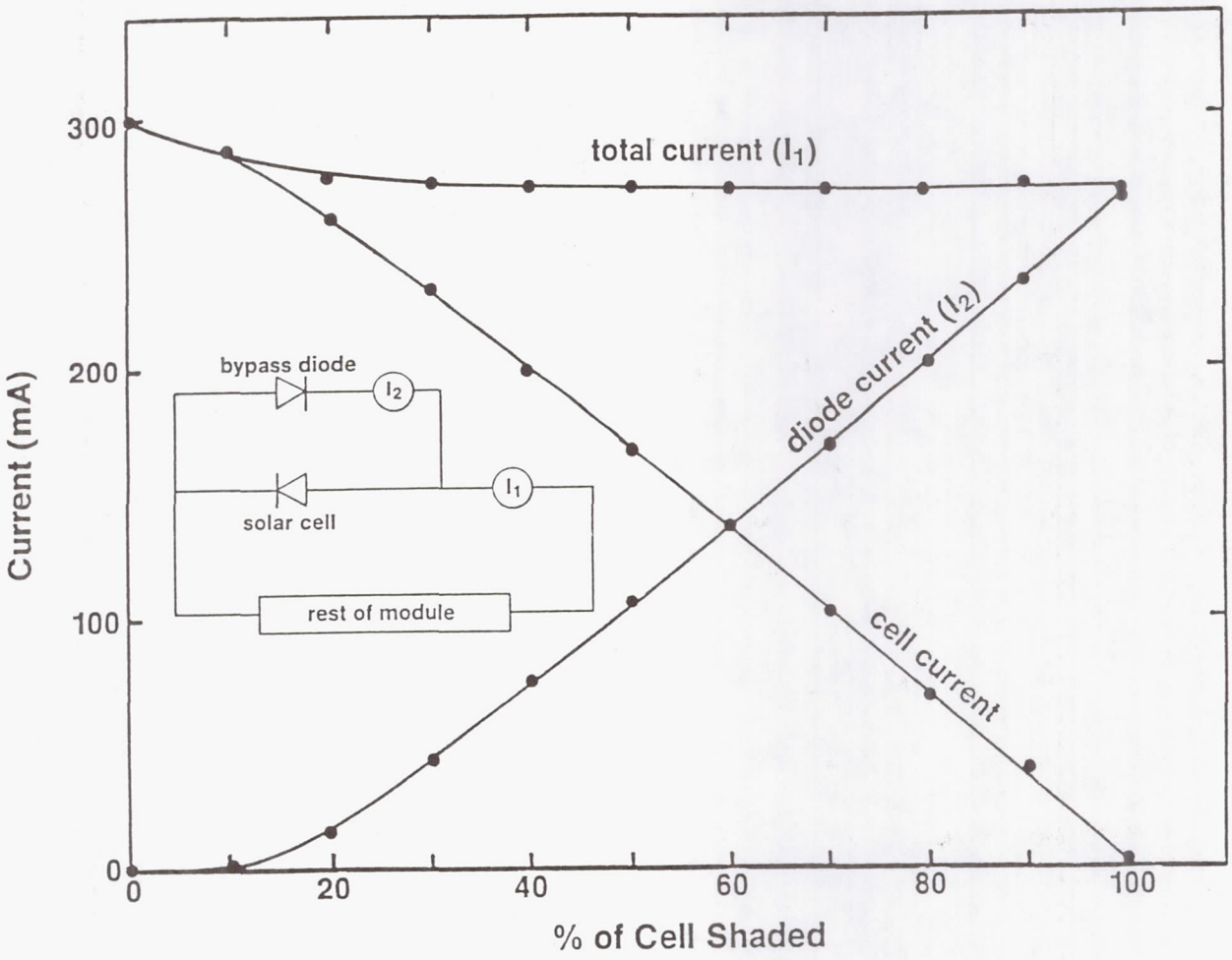

Figure 3 Total, diode and cell current vs. percentage of the cell shaded, using an a-Si alloy tandem-junction bypass diode. The cell current was obtained by subtracting the diode current from the total current, which were measured using the circuit shown in the inset.

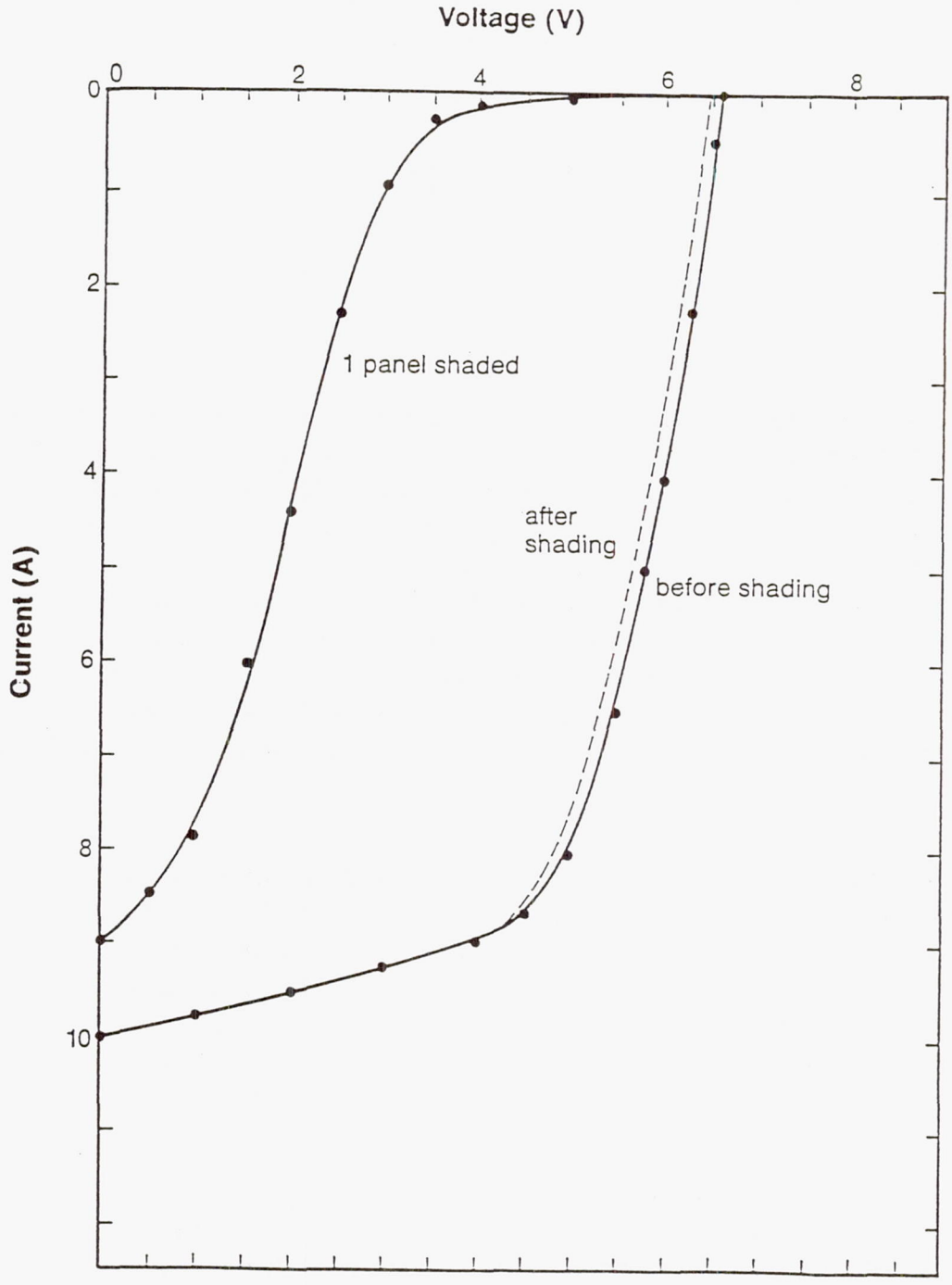

Figure 4 Current vs. voltage for a four-cell module protected with a-Si alloy tandem junction diodes (AM1 intensity). The dotted line represents the scan carried out after the shading of one of the cells.

Mini-Dome Fresnel Lens Photovoltaic Concentrator Development

Mark J. O'Neill
ENTECH, Inc.
DFW Airport, TX

Michael F. Piszczor, Jr.
NASA Lewis Research Center
Cleveland, OH

Introduction

Since 1986, our organizations have been actively developing a new high-performance, light-weight space photovoltaic concentrator array [refs. 1-6]. This development work is being done under Small Business Innovation Research (SBIR) contracts funded by NASA and SDIO. The new array is the first space photovoltaic concentrator system to use a refractive optical concentrator in the form of a unique, dome-shaped, point-focus, Fresnel lens [refs. 7-9]. The new array is also the first space photovoltaic concentrator system to utilize prismatic cell covers to eliminate gridline obscuration losses [refs. 10-11]. By combining these new array features with state-of-the-art cell technology, we anticipate substantial improvements over present space power systems in both array power density (watts/square meter) and specific power (watts/kilogram).

The three most critical elements of the new array are the lens, the prismatic cell cover, and the photovoltaic cell. During 1987 and 1988, prototypes of the latter two elements were successfully developed and tested [refs. 5-6]. The prismatic cover has provided cell performance enhancement levels in close agreement with predictions. Likewise, the prism-covered cell performance has matched predictions. In fact, gallium arsenide cells made by Varian have achieved over 24% efficiency (at 100 AM0 suns irradiance and 25C) after prismatic cover application, the highest single-junction space cell efficiency yet measured by NASA Lewis, as we described at the last SPRAT Conference.

Since the last SPRAT Conference, the master tooling required to make the third critical element of the new array, the mini-dome Fresnel lens, was completed. This state-of-the-art diamond-turned tooling was made to ENTECH specifications by 3M Company. During 1989, prototypes of the mini-dome lens optical concentrator have been successfully made from this tooling and tested. Outdoor test results, fully discussed in later paragraphs, confirm that the mini-dome lens will provide excellent optical efficiency levels. In fact, the first prototype flexible silicone rubber lens achieved 86% net optical efficiency.

Also since the last SPRAT Conference, we have also been adapting the prismatic cell cover technology to Boeing's new mechanically stacked multi-junction (MSMJ)

cell, which is fully compatible with the mini-dome lens concentrator approach. Boeing's new cell (fully described in another paper at this SPRAT Conference [ref. 12]) includes a transparent gallium arsenide (GaAs) top cell and a gallium antimonide (GaSb) bottom cell, with both cells using prismatic covers to eliminate gridline obscuration losses. These stacked cells have recently achieved over 30% AM0 efficiency (at 25C and 100 suns irradiance) in simulator testing. This new MSMJ cell technology has excellent long-term implications for the mini-dome lens concentrator array.

The following paragraphs provide an update on the mini-dome lens concentrator array development program.

System Description

Since the mini-dome Fresnel lens concentrator array has been described in previous papers [refs. 1-6], only a brief description of the new concentrator system will be presented here. Figure 1 shows an individual dome lens photovoltaic concentrator module. The square-aperture dome lens focusses sunlight onto a state-of-the-art concentrator cell (i.e., a single-junction gallium arsenide cell or a tandem MSMJ cell). An optically clear silicone rubber prismatic cell cover is bonded to the upper surface of each cell to eliminate gridline obscuration losses. A high-thermal-conductivity dielectric layer is used to bond the cell assembly to the aluminum backplane radiator. Top and bottom electrical contacts are used to join cells into desired series/parallel circuits. The 200 micron thick radiator and the 150 micron thick aluminum honeycomb structure are bonded together to form a rigid assembly, which is coated with a white thermal control coating (with high infrared emittance and low solar absorptance).

Each individual dome lens module provides an operational power output of about 0.4 watt. Multiple modules are integrated into a larger panel, capable of providing tens or hundreds of watts, as shown in Figure 2. The individual dome lenses are placed within the square slots forming the honeycomb, with the top of each lens located below the top of the honeycomb after assembly. Thus, panels can be stacked on top of one another, without touching the lenses, thereby allowing compact stowage of multiple panels. To form multi-kilowatt arrays, the panels have been designed for use with existing automatically deploying space structures, such as the Astro Aerospace extendible support structure (ESS) [ref. 13], as shown in Figure 3. Such structures have been designed for deploying and supporting other space photovoltaic concentrator panels, such as the TRW mini-Cassegrainian concentrator (MCC) [ref. 14]. Due to its higher power density, the dome lens concentrator (DLC) will require a smaller array size than the MCC concentrator, as shown in the lower portion of Figure 3.

Figure 4 shows the ENTECH/Varian GaAs concentrator cell geometry and performance after prismatic cover application. NASA Lewis measured the cell efficiency to be over 24% at 25C and 100 AM0 suns, and about 22% at 100C and 100 AM0 suns.

Similar performance can be expected for a transparent version of the GaAs cell, forming the top cell in a tandem MSMJ assembly, as Boeing will report at this SPRAT Conference [ref. 12]. When a prismatically covered GaSb cell is placed beneath such a transparent GaAs cell, a boost efficiency of about 9% is currently attainable, based on recent simulator measurements for a GaSb cell under a GaAs filter [ref. 12].

Figure 5 shows the baseline mini-dome Fresnel lens configuration. The shape of the lens corresponds to a unique geometry which provides minimal reflection loss for each prism, and thus maximal transmittance for the lens [ref. 7]. Also, this design provides a smaller solar image, smaller optical aberrations, and greatly improved manufacturing tolerances, compared to other concentrator designs [ref. 8]. The lens has a 4.0 cm focal length and a 3.7 cm square aperture (13.7 sq.cm. in area). The lens is designed to focus incident sunlight onto a 0.4 cm diameter cell (0.126 sq.cm. active area), the same size cell as that used in the TRW MCC reflective space concentrator [ref. 14].

The lens irradiance profile can be tailored by selecting the appropriate angle for each of the individual prisms comprising the lens, such that the individual prism images overlap to provide the desired irradiance distribution across the focal plane. For the present lens, the prism angles have been optimized to form an image over a small 0.26 cm diameter circular portion of the cell, to allow the module to tolerate a 1 degree tracking error without appreciable loss in performance [ref. 6]. Figure 6 shows this lens design approach, including the photon flux distribution over the cell with and without a sun-tracking error. To provide this smaller image size, the predicted peak irradiance at the center of the cell is about 400 suns, which is quite tolerable for the cell under consideration [ref. 6]. The predicted optical efficiency of the lens is above 90%, comparable to ENTECH's terrestrial photovoltaic concentrator lenses. The optical efficiency could be further improved by applying anti-reflection coatings to the lens surfaces.

The lens materials have been selected to provide good optical performance, as well as durability in the orbital environment. The ceria-doped microglass superstrate is the same material which has been used for cover slides on one-sun photovoltaic cells in space. The clear silicone RTV substrate is the same material which has been used as an adhesive to bond cover slides to one-sun photovoltaic cells in space. Diamond-turned master tooling, which is used to mold the silicone rubber Fresnel lens, was delivered to ENTECH by 3M Company in late 1988. Prototype silicone rubber lenses have since been successfully made and tested, as highlighted in a later paragraph. Glass superstrate thermal forming experiments have been underway for several months at both ENTECH and outside vendor facilities. While the glass forming appears to be straightforward, the best methods of manufacturing such microglass domes have not yet been selected.

The following paragraphs discuss recent test results on the key components of the mini-dome space photovoltaic concentrator system.

Key Component Test Results

In 1988, NASA Lewis tested several of the latest gallium arsenide cells (made by Varian of Palo Alto, California) under simulated space sunlight, before and after prismatic cover application by ENTECH. Test results (at 100 AM0 suns irradiance and 25C) for one of these cells are shown in Figure 4. The cells utilize a parallel gridline geometry, with grids about 12 microns wide on 127 micron centers. After prismatic covering, the cell efficiency increased about 11%, due principally to a 12% short-circuit current increase. This performance enhancement matches expectations for the prismatic cover in this application. The 24% cell efficiency of Figure 4 is the highest single-junction space cell efficiency measured by NASA Lewis to date. This same prism-covered cell achieved about 22% efficiency at 100 AM0 suns and 100C, the expected operational conditions on orbit for the mini-dome lens array. Thus, prototype cells and prism covers have demonstrated performance levels in close agreement with early predictions [refs. 1-2].

In 1989, Boeing has achieved over 30% AM0 efficiency in simulator tests of their GaAs/GaSb MSMJ cell system, which includes prismatic covers on both the top and bottom cells. This unprecedented efficiency was achieved at 100 AM0 suns irradiance and 25C cell temperature, as fully described in another paper at this conference [ref. 12]. This MSMJ cell is ideally suited for use in the mini-dome lens panel, where it will provide a significant array performance improvement, as discussed in a later paragraph.

During 1989, we have obtained the first test data on the mini-dome Fresnel lens. Prototype silicone rubber lenses, without the microglass superstrates, have been successfully molded. A typical lens is shown in Figure 7, with centimeter graph paper in the background. Figure 8 shows a prototype lens focussing actual sunlight onto a test gallium arsenide cell. This cell is a 1985-vintage Cassegrainian concentrator cell made by Applied Solar Energy Corporation (ASEC) and furnished to ENTECH by NASA Lewis. The cell has a radial gridline pattern, not compatible with the prismatic cover, and a short-circuit current response typical of ASEC cells of that vintage [ref. 15]. The test results reported below were all obtained with the same heat sink-mounted ASEC cell, by measuring its short-circuit current response under three different irradiance conditions: (i) one direct normal sun irradiance; (ii) the full circular aperture dome lens irradiance (Figure 8); and (iii) the masked dome lens irradiance (Figures 9 and 10), which simulated the square aperture of the mini-dome lens discussed in previous paragraphs. The full dome lens has an aperture diameter of about 5.5 cm. Since the lens was made of flexible silicone rubber without the microglass superstrate needed for rigidity, its thickness was increased to about double the 200 micron (8 mil) design value of Figure 5, to make the dome self-supporting. For testing, the dome lens was adhesively bonded to an acrylic sheet, with a hole in the sheet to allow the focussed sunlight to travel from the lens to the cell. The hole was cut with an available saw with a 5.4 cm diameter, slightly smaller than the

full dome lens aperture. Since the hole was smaller than the lens aperture, some ray blockage occurred during the full dome lens testing. For the more important testing, with a 3.7 cm square aperture surrounded by an opaque mask placed in front of the dome lens, ray blockage by the undersized hole was negligible.

Figure 11 summarizes the outdoor test results for the prototype silicone mini-dome Fresnel lens. The data columns of Figure 11 include lens aperture area (two bracketing values for the full dome lens test); cell active area; geometric concentration ratio (GCR), which is the ratio of lens aperture area to cell active area; the cell short-circuit current (ISC); net concentration ratio (NCR), which is the ratio of the ISC produced with the lens in place to the ISC produced at one-sun with only direct normal insolation reaching the cell; and optical efficiency, which is the ratio of NCR to GCR. Note that the full dome lens had a measured optical efficiency between 81% and 85%, depending on whether the gross lens aperture area or the mounting plate hole area is used as the true aperture for the test. More importantly, note that the masked square aperture lens had a measured optical efficiency of 86%.

The measured 86% optical efficiency for the first prototype square-aperture lens is less than the predicted value (>90%) for production lenses. However, the prototype lens was much thicker than production lenses; the prototype lens was self-supporting, rather than rigidized by a microglass superstrate; the lens and cell were hand-aligned with two bolts (Figure 8), rather than precisely aligned with fixtures; and the prototype was hand-pointed at the sun. We believe that each of these factors contributed to a slight lowering of performance for the prototype lens. Despite these prototype shortcomings, the focal spot produced by the lens on the small cell appeared to match predictions and the measured optical efficiency was a respectable value.

Current Array Development Status

Now that the three key array components have been successfully tested, project activities are now directed toward the fabrication and testing of several multi-module panels during the next few months. These prototype panels will use our baseline design, which includes the key elements summarized in Figure 12. The total mass of the baseline panel equates to about 2.4 kg/sq.m, with most of the panel mass being attributable to the microglass lens superstrate and the aluminum honeycomb/radiator assembly. In addition to this near-term baseline panel, we are also developing a longer-term, ultra-light panel for SDIO applications. The microglass superstrate in the baseline panel is primarily a monatomic oxygen shield for low earth orbit (LEO) applications. In higher orbits, which are of great interest to SDIO, the glass should become unnecessary, since oxygen is no longer present. In addition, the aluminum radiator thickness can be reduced from 200 microns to 50 microns, with only a 30C increase in cell operating temperature, based on conservative thermal analyses. Likewise, the aluminum honeycomb thickness can be reduced from 150 microns to 50

microns, while still providing adequate stiffness, based on preliminary structural analyses. With only these three changes in design, the panel mass should be reduced from 2.4 kg/sq.m. to about 1.0 kg/sq.m. Pending the successful fabrication and testing of several prototype baseline panels, we will initiate prototype fabrication of the ultra-light SDIO panels.

Updated Array Performance Estimates

Figure 13 summarizes our latest performance estimates for the mini-dome Fresnel lens array, based on the recent test results for prototype cells and lenses discussed above. Using measured efficiency values for GaAs cells and mini-dome lenses, the near-term baseline array should provide an on-orbit efficiency of 17%, corresponding to a power density of 230 w/sq.m. As previously discussed, the baseline panel mass is about 2.4 kg/sq.m. The previously described automatically deploying ESS structure has a mass of 0.7 kg/sq.m., when designed to support the relatively heavy TRW MCC concentrator panels [ref. 13]. Adding this value to the panel mass provides an array mass of 3.1 kg/sq.m., which equates to a specific power of 74 w/kg for the baseline array.

The second column of Figure 13 corresponds to the substitution of the Boeing MSMJ cell for the single-junction GaAs cell in the baseline panel. This single change raises the array efficiency to 22%, the corresponding power density to 300 w/sq.m., and the specific power to nearly 100 w/kg. These values are based on a GaSb cell boost efficiency of 8% (at 25C), which was achieved by Boeing earlier this year [ref. 12]. The calculated GaSb boost efficiency at operating temperature is based on an estimated fractional power/temperature coefficient 2.3 times as high as for the GaAs cell, to reflect the correspondingly lower open-circuit voltage of the GaSb cell (i.e., 0.49 volts versus 1.14 volts at 25C and 100 suns).

The third column of Figure 13 includes the ultra-light panel mass reductions discussed in a previous paragraph. In addition, the ESS structure mass estimate has been reduced to conservatively include the effect of reduced loads due to the drastically reduced panel mass. Also, a slight improvement in GaSb cell performance is included, since a 9% room-temperature boost efficiency has already been measured for GaAs-filtered cells [ref. 12]. Finally, the lens efficiency is expected to improve to 90% with the application of antireflection coatings to the lens surfaces. These small lens and cell performance gains offset the higher cell operating temperature, to retain the 300 w/sq.m. power density of the previous column. With the drastically reduced mass, the specific power increases to more than 200 w/kg.

In summary, recent prototype cell and lens test results indicate that near-term array performance goals of 300 w/sq.m. and 100 w/kg are feasible, and that a longer-term goal of 200 w/kg is reasonable.

References

[1.] M. J. O'Neill et al, Phase I Final Report, NASA Contract No. NAS3-24871, ENTECH, Inc., DFW Airport, TX, (1986).

[2.] M. J. O'Neill and M. F. Piszczor, *Proc. 8th NASA SPRAT Conference*, 119 (1986).

[3.] M. J. O'Neill and M. F. Piszczor, *Proc. 19th IEEE-PVSC*, 479 (1987).

[4.] M. F. Piszczor and M. J. O'Neill, NASA Technical Memorandum 100101 (also presented at 22nd IECEC), (1987).

[5.] M. F. Piszczor and M. J. O'Neill, *Proc. 9th NASA SPRAT Conference*, 308 (1988).

[6.] M. J. O'Neill and M. F. Piszczor, *Proc. 20th IEEE-PVSC* (1988).

[7.] M. J. O'Neill, "Solar Concentrator and Energy Collection System," U.S. Patent No. 4,069,812, 1978.

[8.] M. J. O'Neill, *ISES/Atlanta*, 531 1979.

[9.] M. J. O'Neill et al, *ISES/Phoenix*, 510 (1980).

[10.] M. J. O'Neill, U.S. DOE Report No. DOE/ER/80126-1 (1985).

[11.] M. J. O'Neill, "Photovoltaic Cell Cover for Use with a Primary Optical Concentrator in a Solar Energy Collector," U.S. Patent No. 4,711,972 (1987).

[12.] J. E. Avery et al, this conference.

[13.] M. Mobrem, Final Report, NASA Contract No. NAS8-36043, Astro Aerospace Corp., Carpinteria, CA (1985).

[14.] R. E. Patterson, Final Report, NASA Contract No. NAS8-35635, TRW, Inc., Redondo Beach, CA (1985).

[15.] K. Chang, *13th Sandia Photovoltaic Concentrator Project Integration Meeting (SAND85-0791)*, 157 (1985).

Fig. 1 - Mini-Dome Lens Concentrator Module

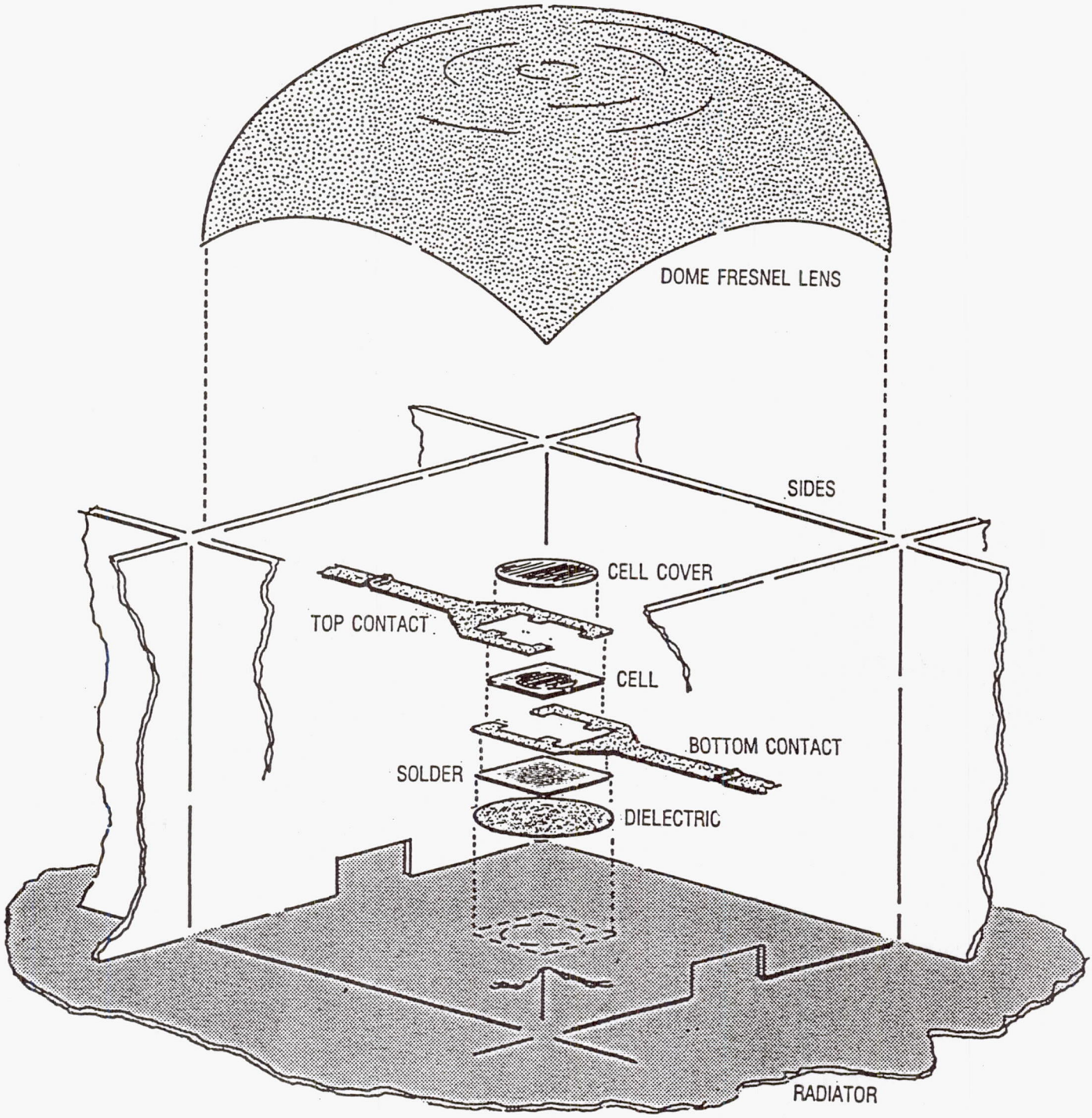

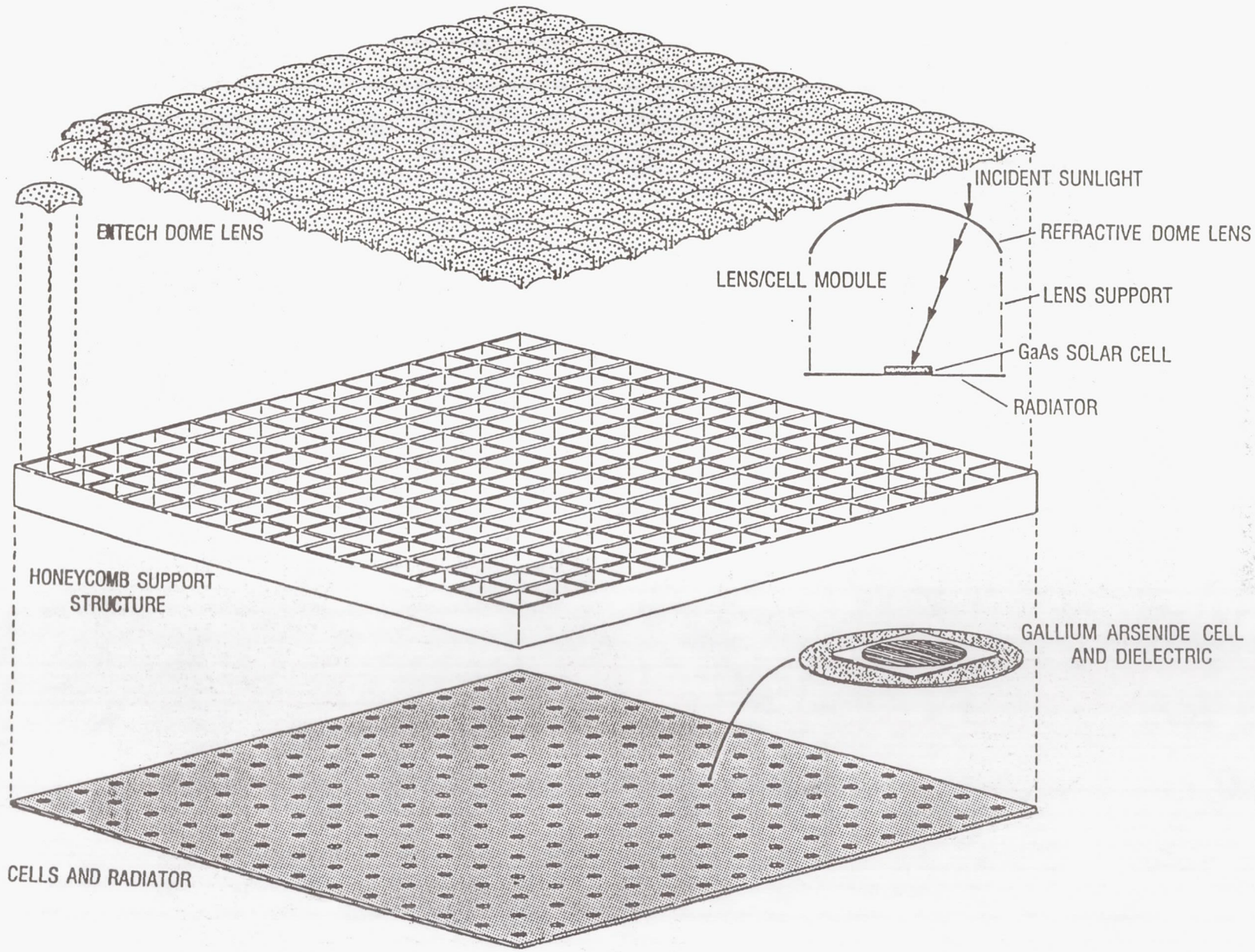

Fig. 2 - Mini-Dome Lens Concentrator Panel

Fig. 3 - Mini-Dome Lens Concentrator Array

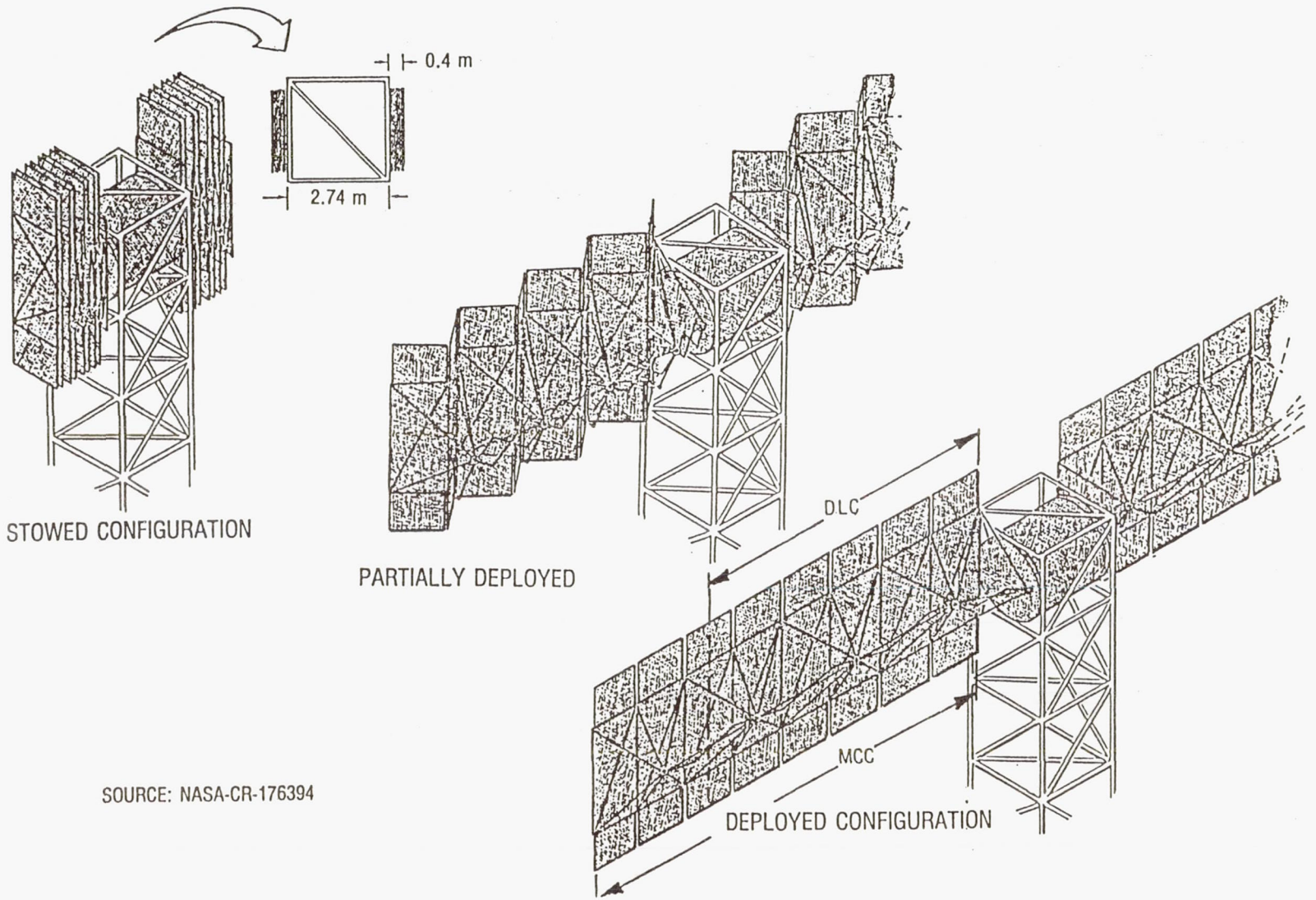

SOURCE: NASA-CR-176394

Fig. 4 - ENTECH/Varian GaAs Cell

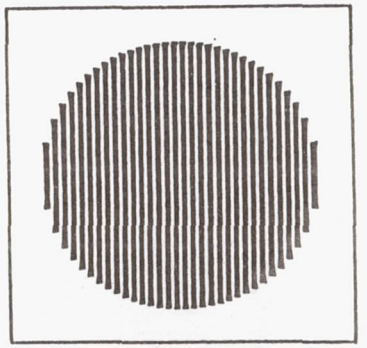

GEOMETRY
Total Area: Square, 0.5 cm per side.
Active Area: Circle, 0.4 cm diameter.

METALLIZATION
Gridlines: 31 parallel lines on 127 micron centers, each 12 microns wide by 5 microns tall.
Busbar: Continuous around cell periphery.

PREDICTED VS. MEASURED CELL PERFORMANCE AT STANDARD TEST CONDITIONS

(100 Uniform AM0 Suns, 25C Cell Temperature)

Parameter	Predicted Value	NASA-Measured Value
Short-Circuit Current:	0.415 amp	0.423 amp
Open-Circuit Voltage:	1.154 volts	1.143 volts
Fill Factor:	87.5 %	86.1 %
Cell Efficiency:	24.3 %	24.2 %

PREDICTED VS. MEASURED CELL EFFICIENCY AT ORBITAL OPERATING TEMPERATURE

(100 Uniform AM0 Suns, 100C Cell Temperature)

Predicted Cell Efficiency: 21.7%
NASA-Measured Cell Efficiency: 21.9%

Fig. 5

LAMINATED CERIA MICROGLASS/SILICONE RTV MINI-DOME FRESNEL LENS

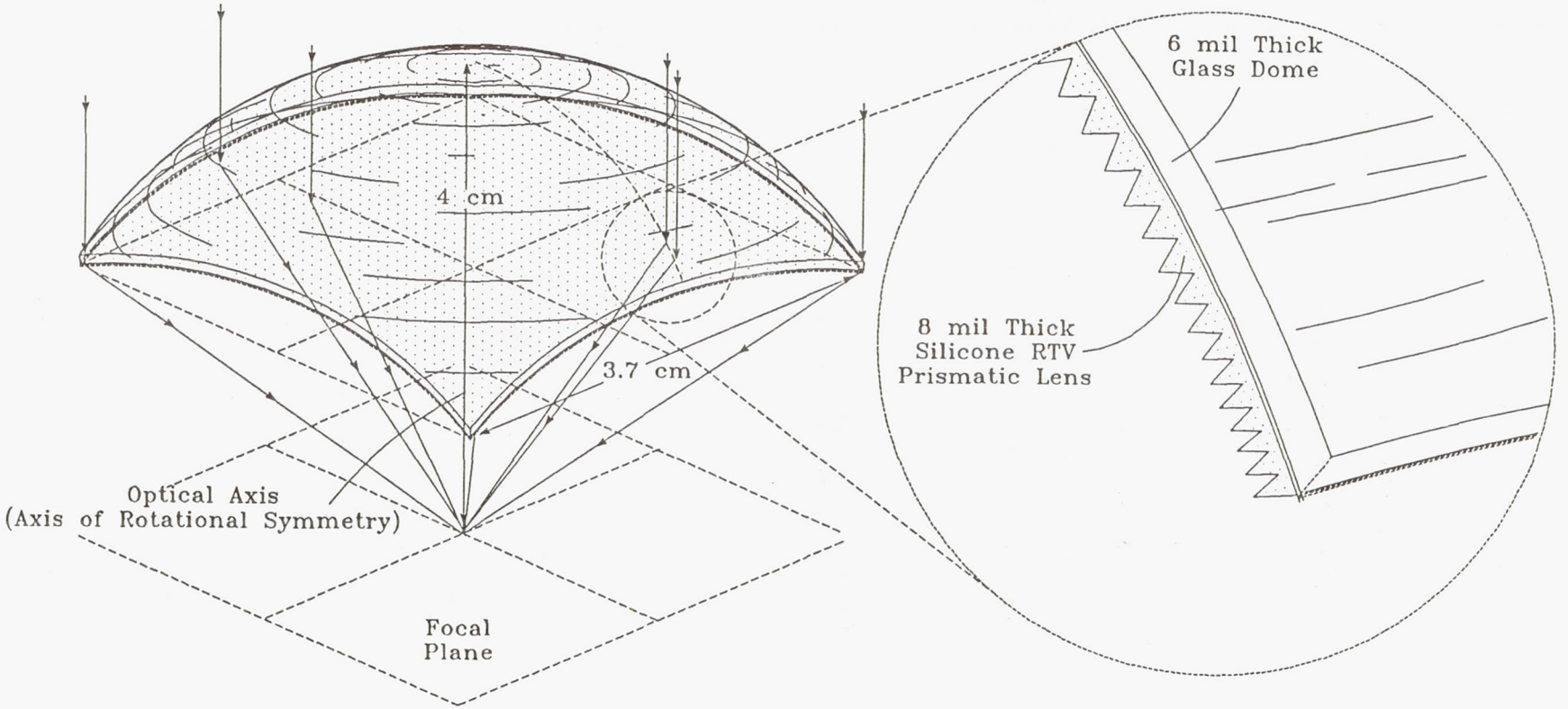

Fig. 6 - Lens Design Approach and Predicted Performance

NUMERICAL RESULTS

IRRADIANCE OVER 0.40 CM SQUARE

1	1	0	0	0	1	0	2
1	0	6	53	67	10	4	1
1	8	170	150	277	287	13	1
0	63	286	253	274	309	93	0
0	86	312	299	273	326	78	0
1	12	332	391	258	178	9	0
0	4	15	97	82	9	1	1
0	1	0	0	0	1	2	0

4000 RAYS OUT OF 4000
OPTICAL EFFICIENCY TO ACTIVE AREA = .933

4000 RANDOM RAY INTERCEPTS
(ACTIVE AREA CIRCLE DIAMETER = 0.4 CM)

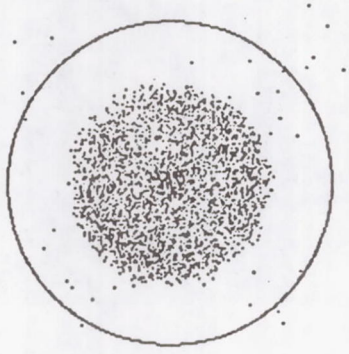

No Tracking Error

NUMERICAL RESULTS

IRRADIANCE OVER 0.40 CM SQUARE

0	0	10	5	57	72	15	5
0	0	31	117	164	303	205	10
0	0	67	281	186	269	365	98
0	0	67	349	295	263	400	87
0	5	15	307	431	210	142	5
0	5	0	10	119	113	15	0
0	0	0	0	0	0	0	0
0	0	0	0	0	0	0	0

1000 RAYS OUT OF 1000
OPTICAL EFFICIENCY TO ACTIVE AREA = .934

1000 RANDOM RAY INTERCEPTS
(ACTIVE AREA CIRCLE DIAMETER = 0.4 CM)

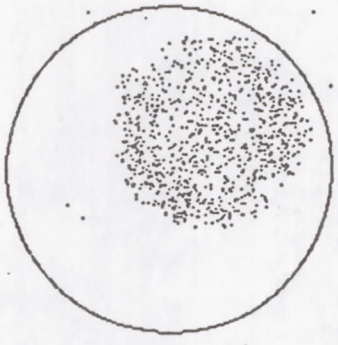

1 Degree Tracking Error

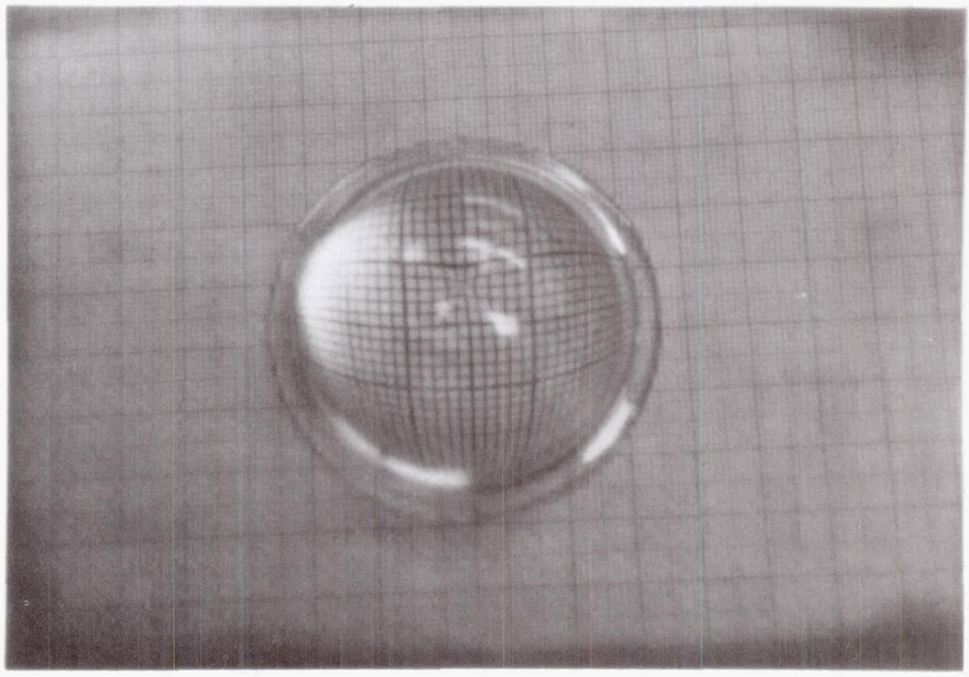

Fig. 7 - Prototype Silicone Rubber Lens

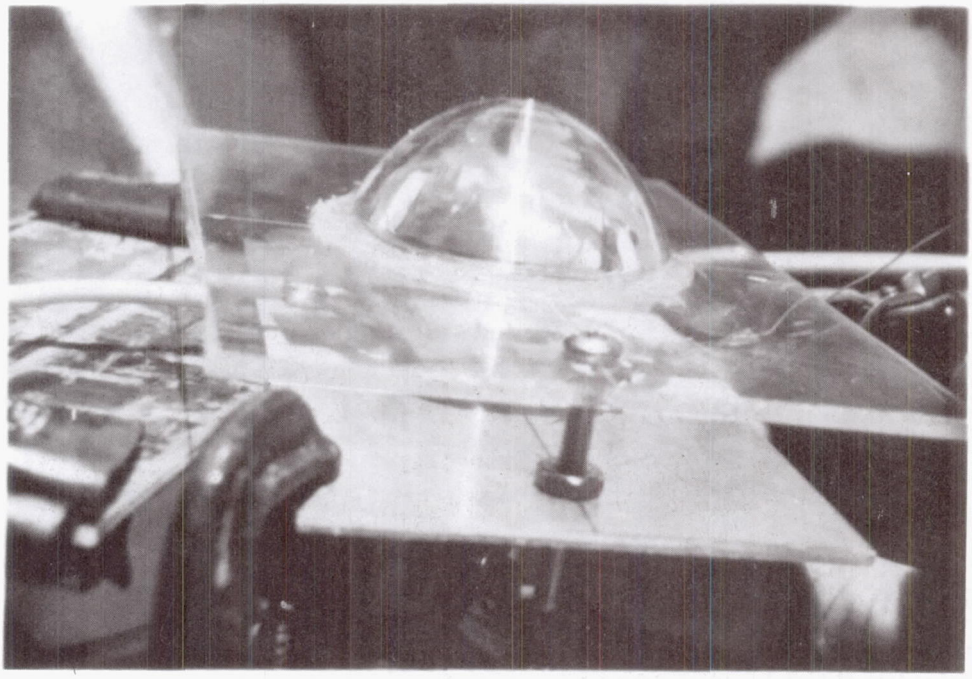

Fig. 8 - Prototype Lens Focussing on Cell

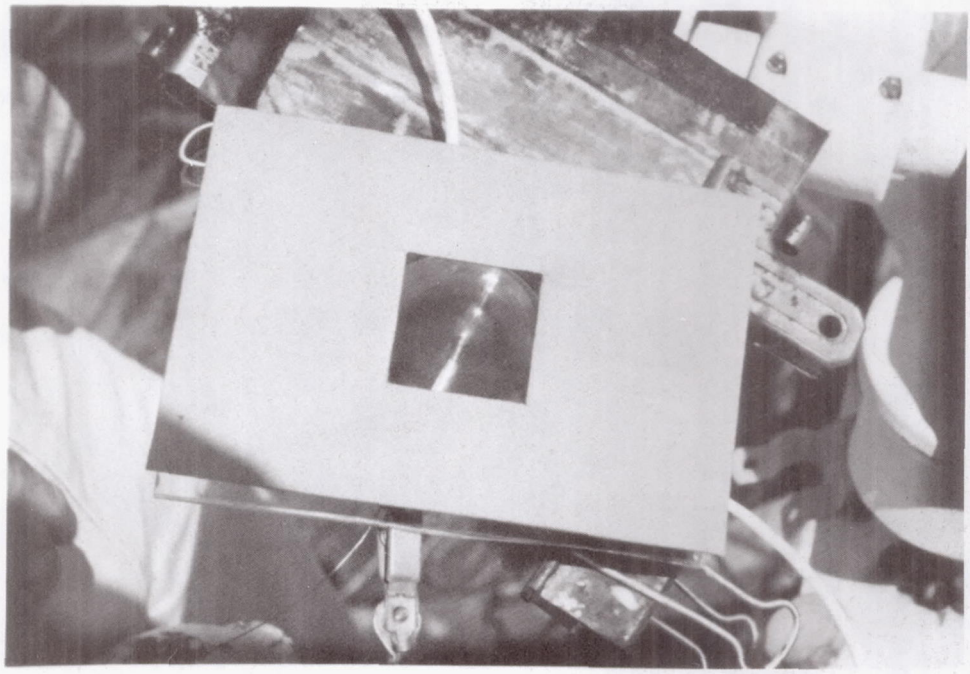

Fig. 9 - Square Aperture Mask for Prototype Lens

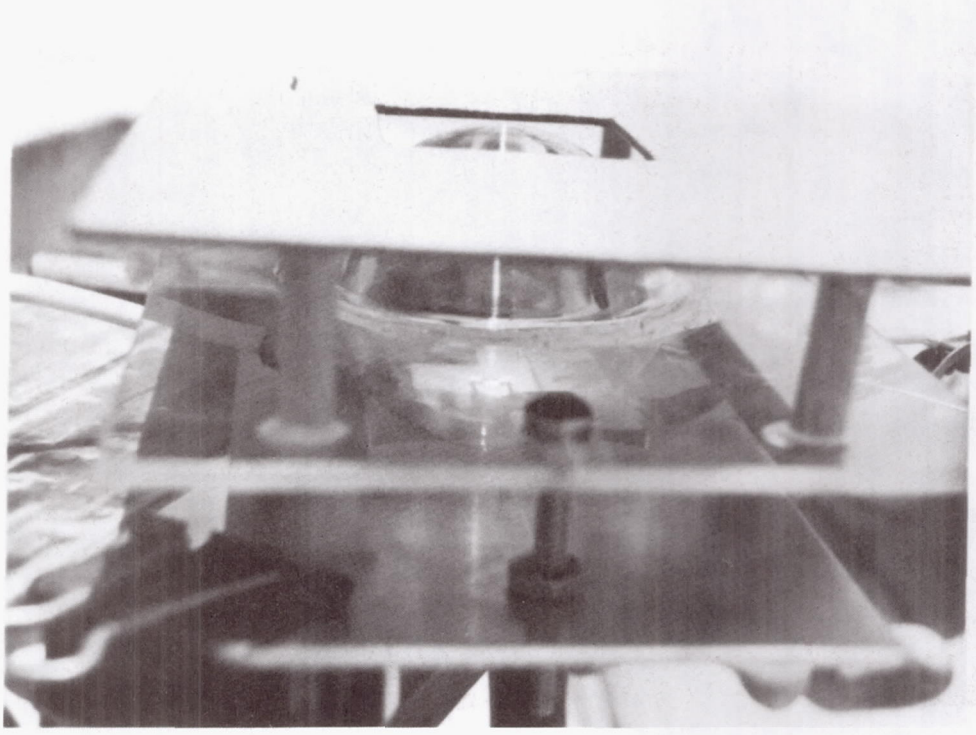

Fig. 10 - Square Aperture Lens Focussing on Cell

TEST DESCRIPTION	LENS APERTURE AREA (SQ.CM.)	CELL ACTIVE AREA (SQ.CM.)	GCR	ISC* (MA)	NCR (SUNS)	OPTICAL EFFICIENCY
ONE-SUN RESPONSE	N/A	0.126	1X	2.92*	1	100%
FULL DOME LENS						
USING 5.4 CM DIAMETER HOLE AREA IN LENS MOUNTING PLATFORM	22.9	0.126	182X	451*	154	85%
USING 5.5 CM DIAMETER TOTAL LENS APERTURE AREA	23.8	0.126	189X	451*	154	81%
MASKED SQUARE LENS (3.7 CM X 3.7 CM)	13.7	0.126	109X	274*	94	86%

* NORMALIZED TO 1000 W/SQ.M. DIRECT NORMAL INSOLATION.

Fig. 11 - Summary of Outdoor Test Results for Silicone Mini-Dome Fresnel Lens and 1985-Vintage ASEC GaAs Cassegrainian Concentrator Cell

Element	Material	Density (g/cu.cm.)	Thickness (cm)	Surface Area/Panel Area	Mass/Panel Area (kg/sq.m.)
Lens Superstrate	Microglass	2.50	0.015	1.30	0.49
Lens Prisms	Silicone	1.00	0.015*	1.30	0.19
Radiator	Aluminum	2.77	0.020	1.00	0.55
Cell/Cover/Mount	GaAs et al	5.70	0.046	0.02	0.05
Honeycomb	Aluminum	2.77	0.015	2.20	0.91
Radiator Coating	Alumina	3.88	0.001	2.00	0.08
Miscellaneous			7.5% of Above Total		0.17
TOTAL					2.44

* Silicone Base Thickness = 0.010 cm
Silicone Prism Thickness = 0.010 cm (But Half Void)
Effective Silicone Thickness = 0.015 cm

Fig. 12 - Mass Breakdown for Baseline Mini-Dome Lens Panel

Fig. 13

MINI-DOME FRESNEL LENS ARRAY - UPDATED PERFORMANCE ESTIMATES

BASED ON RECENT TEST RESULTS FOR PROTOTYPE CELLS AND LENSES

ITEM	BASELINE ARRAY	NEAR-TERM ARRAY	LONGER-TERM ARRAY
CELL TYPE	GAAS	GAAS + GASB	GAAS + GASB
CELL EFF. AT 25C	24%	24% + 8% = 32%	24% + 9% = 33%
CELL OPERATING TEMP.	100C	100C & 100C	130C & 130C
CELL EFF. AT OPER. TEMP.	22%	22% + 6% = 28%	21% + 6% = 27%
LENS EFFICIENCY	86%	86%	90%
PACKING FACTOR	97%	97%	97%
MISMATCH/WIRING FACTOR	93%	93%	93%
ARRAY EFFICIENCY	17%	22%	22%
POWER DENSITY (W/SQ.M.)	230	300	300
PANEL MASS (KG/SQ.M.)	2.4	2.4	1.0
STRUCTURE MASS (KG/SQ.M.)	0.7	0.7	0.4
ARRAY MASS (KG/SQ.M.)	3.1	3.1	1.4
SPECIFIC POWER (W/KG)	74	97	214

NOTE: MEASURED PERFORMANCE PARAMETERS FOR PROTOTYPE CELLS AND LENSES ARE UNDERLINED.

Workshop Summaries

Preceding Page Blank

Preceding Page B...

Mechanical vs. Monolithic Multijunction Cells

John Fan
Kopin Corporation
Taunton, MA

Preceding Page Blank

WORKSHOP 1
MECHANICAL vs. MONOLITHIC MULTIJUNCTION CELLS

1. **WHAT IS KNOWN ABOUT RADIATION DAMAGE IN THE TWO TYPES OF CELLS?**
   - MORE RADIATION DAMAGE DATA NEEDED
   - NEED SPECTRAL RESPONSE AS FUNCTION OF RADIATION DAMAGE
   - NEED MORE PROTON DAMAGE DATA

2. **HOW MANY TERMINALS CAN BE USED - 2, 3, OR 4?**
   - DESIGNS FOR 2, 3, OR 4 EXIST AND ARE REASONABLE
   - NEED A TERM FOR THE SOLAR CELL ASSEMBLY SUCH AS PV ELEMENT
   - VOLTAGE - MATCHING LOOKS LIKE A VERSATILE APPROACH

3. **WHAT ARE THE ISSUES WITH AR COATINGS AND/OR OPTICAL COUPLING?**
   - MORE COMPLICATED FOR MECHANICAL STACK
   - TRADE-OFF FOR EASIER EPITAXY

WORKSHOP 1
MECHANICAL vs. MONOLITHIC MULTIJUNCTION CELLS

4. **IS THERE A PREFERRED CONFIGURATION - (PLANAR, CONCENTRATOR MONOLITHIC OR MECHANICAL STACK, 2, 3, OR 4 TERMINALS)**
   - PV ELEMENT TERMINALS SHOULD BE 2
   - PLANAR vs CONCENTRATOR TOO SOON TO TELL
   - MONOLITHIC vs MECHANICAL: MONOLITHIC, LATTICE-MATCHED SYSTEM MAY BE PREFERABLE IN LONG TERM
   - IT IS NOT CLEAR THAT A MONOLITHIC APPROACH OFFERS HIGHER SPECIFIC POWER
   - THERE ARE THERMAL ISSUES IN MECHANICALLY STACKED CONCENTRATORS

5. **WHAT IS KNOWN ABOUT TEMPERATURE EFFECTS? WHAT WORK NEEDS TO BE DONE?**
   - CONCENTRATION RATIO, TEMPERATURE HAVE A BIG EFFECT ON MEASURMENTS
   - SPECTRAL RESPONSE CURVES AT APPROPRIATE TEMPERATURE IS IMPORTANT
   - BIGGER PROBLEM IS THE LACK OF PROPER SIMULATOR

WORKSHOP 1
MECHANICAL vs. MONOLITHIC MULTIJUNCTION CELLS

6. **WHAT SHOULD BE DONE ABOUT TESTING MBG CELLS? ARE SIMULATOR RESULTS RELIABLE?**
   - FULL SPECTRUM SIMULATORS ARE NEEDED
   - CALIBRATION STANDARDS ARE NECESSARY
   - NASA SHOULD BE PLANNING A CALIBRATION STANDARDS PROGRAM FOR MBG CELLS
   - NEED CENTRAL PLACE FOR RELIABLE TESTING

7. **WILL THERE BE OR ARE THERE PRODUCTION YIELD PROBLEMS SPECIFIC TO MBG CELLS?**
   - MAYBE FOR LATTICE MISMATCHED MONOLTHIC APPROACHES
   - LATTICE-MATCHED AND MECHANICAL STACK APPROACHES HAVE YIELD ISSUES THAT ARE DIFFERENT BUT ABOUT THE SAME LEVEL OF DIFFICULTY.

WORKSHOP 1
MECHANICAL vs. MONOLITHIC MULTIJUNCTION CELLS

8. WHAT ARE PROJECTED COSTS (PER WATT) FOR VARIOUS TYPES?

- TOO SOON TO ANSWER

9. WHAT ARE THE ARRAY/SYSTEM LEVEL BENEFITS AND ISSUES? ARE THERE WEIGHT AND AREA ADVANTAGES?

- IF EFFICIENCY IS REALIZED, YES
- TOO SOON TO TELL WHETHER MONOLITHIC IS BETTER THAN MECHANICAL STACK

10. ARE ULTRA LIGHT WEIGHT THIN FILM MBG CELLS FEASIBLE

- NEED TO DEFINE ULTRA LIGHT WEIGHT
- 200 W/kg IN 5 YRS. FOR ARRAY LOOKS FEASIBLE
- 750 W/kg IN 2 YRS. FOR CELLS LOOKS FEASIBLE

PV ELEMENT

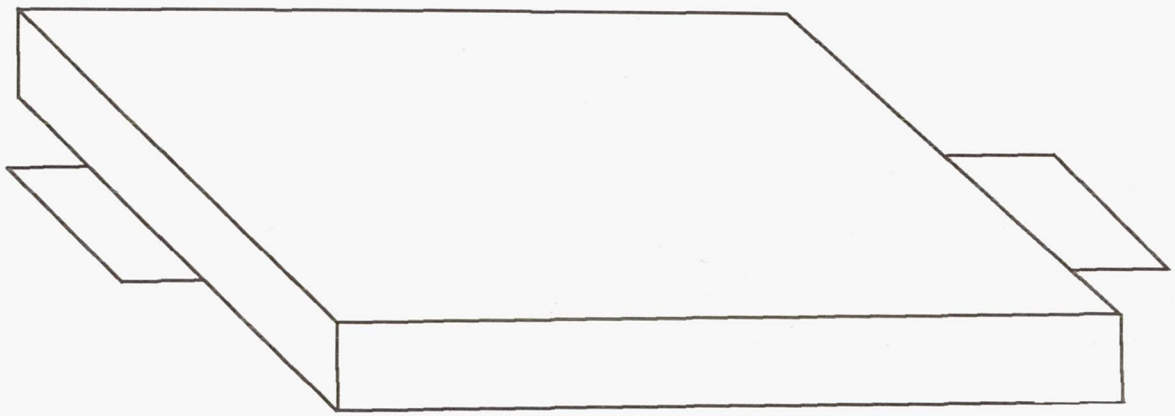

- ABOUT SAME SIZE AS A CELL
- WELL-KNOWN CHARACTERISTICS (SPEC'S)
- FITS INTO ARRAY "SOCKET"
- INTERNAL PARTS NOT SPECIFIED EXPLICITLY

Strategy in Space Flight Experiments

Dean Marvin
Chemistry and Physics Laboratory
The Aerospace Corp.
Los Angeles, CA

James Severns
Naval Research Laboratory
Washington, D.C.

The Workshop consisted of approximately 40 people, representing universities, government contractors, and DOE and DOD agencies. The main topics of the workshop were evaluation of both the need for flight testing of solar array hardware and the opportunities for such testing.

Motivation for Flight Testing

The effect of the space environment on silicon solar cells is reasonably well established. Extensive compilations of radiation degradation are contained in the JPL Solar Cell Radiation Handbook. The accuracy of these ground test data have been verified by flight tests and data from operational systems over the past 30 years. However, the data are more sparse for gallium arsenide and indium phosphide, and almost non-existent for advanced cell materials, such as copper indium diselenide, aluminum gallium arsenide, and indium gallium arsenide. In addition, there has been little flight testing of multijunction cells. There will be more ground radiation testing of devices using these materials as development proceeds, and confirmation of the observed behavior by flight testing is needed. One workshop attendee expressed the opinion that "the flight test is not so much to verify the effects that were identified on the ground, but rather to discover the effects that were not identified".

At the array level discussion centered on the issues of spacecraft charging effects and array dynamics. As new array structures such as light weight or concentrating systems are developed, space testing is needed in these areas. The complex geometry of concentrating photovoltaic arrays makes prediction of plasma interaction very difficult. Flight experiments such as PASP-Plus are essential for assessing array behavior. The design used in many light weight arrays generates new paths for plasma interaction that must be evaluated under realistic conditions. The dynamics of array deployment and response to maneuvers cannot be reproduced in general testing in the one g environment. It was concluded that large area, light weight array designs would benefit from flight tests. The SAFE array test on the shuttle is an example of the beneficial information obtained.

From the customer's point of view, flight heritage hardware is always desirable. The NASA technology maturity scale requires flight-proven performance at level 7

and beyond. The Air Force position is not as formalized, but acceptance of advanced technology by System Program Offices is always facilitated by the presence of encouraging flight data. The acceptance of radically new photovoltaic technology has not been a major issue over the past 20 years because of the success of silicon technology in meeting program needs. However, it promises to take on a higher profile in the next ten years as system requirements exceed the capability of silicon solar cells and competing technologies are closely scrutinized.

Bus Options

The relationship of the flight experiment to the spacecraft as a whole determines the cost of the experiment. At the low cost limit a test panel mounted on an existing vehicle might fly for only the integration expense plus the panel fabrication cost. As discussed below in the Planning section, there are many opportunities for this type of experiment that can be exploited. The major issues are finding a ride to an appropriate orbit and a spacecraft which can support the experiment power, temperature, weight and telemetry requirements.

A more expensive option is a piggy-back flight such as the Living Plume Shield (LIPS) experiments. The cost here is higher because the experiment must be self supporting. However, it offers tailored support to the experiment, reduced spacecraft interface problems, and a paid-for launch vehicle. Since cost of the launch operations far exceeds the cost of all but the largest experiments, this is still an important advantage.

The most costly option is the dedicated flight experiment such as The Combined Radiation Release Experimental Satellite (CRRES) and the Long Duration Exposure Facility (LDEF). In return for paying the entire cost of launch, vehicle procurement, and payload development, the experimenter can select the mission profile that best suits the goals of the program.

Planning

The methods of flight test planning generated the most discussion of any topic in the Workshop. It was clear that better communications between hardware builders (both cell and array level) and those who are aware of flight opportunities would be beneficial. Planning and prioritizing of flight tests for all three military services are handled by the Air Force Space Test Program. However, this process can accommodate only a very small number of programs each year. There is an office at NASA/HQ which tracks scheduled launches many years in advance and disseminates this information to potential users. Many attendees at the Workshop were unaware of this information.

The consensus of the group was that a listing of appropriate NASA and DOD spacecraft which might accommodate flight test hardware should be made available to government contractors. This information is already tracked by NASA/HQ and STP, and the opportunities would be better utilized if the information were disseminated. It would then be up to the individuals involved to discuss the feasibility of an experiment. After some discussion it was clear that many spacecraft have extra area on the solar array (in the case of TDRSS, 50 ft^2 !) which could accommodate an appropriate experiment.

An additional conclusion was that a National effort to insure regular flight opportunities should be made. This could take the form of an LDEF-scale spacecraft launch every 2-3 years. Such a capability would be suitable for either a number of small experiments, or a larger panel or array level test. The British government has such a capability in their Space Technology Research Vehicle (STRV) run by The Royal Aircraft Establishment–Farnborough. STRV-1 is to be launched in 1991 but is still accepting proposals. STRV-2 is scheduled for 1993-4, and STRV-3 is under discussion for the 1993-5 time frame. For the near term it was pointed out that the US Commerce Dept. encourages scientific collaboration with NATO partners, and a number of opportunities exist.

A workshop at last year's SPRAT on Space Environmental Effects concluded that "space flight tests will be needed in the future as far as can be imagined, because of the inadequacy of simulating the complex combined environment of space". This workshop concludes that this need will be best accommodated by a deliberate, improved communication between the civilian and military agencies who fund spacecraft programs and the community of researchers who are developing advanced technologies for those spacecraft.

CONCLUSIONS OF FLIGHT EXPERIMENT WORKSHOP

FLIGHT EXPERIMENTS ARE IMPORTANT:

- NASA LEVEL 9 MATURITY DEMANDS FLIGHT-PROVEN PERFORMANCE.
- MILITARY PROGRAMS GENERALLY INSIST ON FLIGHT HERITAGE.
- SOME PROPERTIES CANNOT BE GROUND TESTED--ARRAY DEPLOY/REDEPLOY MECHANISMS, ARRAY CHARGING/DISCHARGING EFFECTS.

CAVEATS:

- ORBIT MUST BE REPRESENTATIVE (E.G., ECLIPSE CYCLE, RADIATION DOSE). NEGATIVE RESULTS ARE NOT HELPFUL.
- HARDWARE MUST BE FULLY DEVELOPED: CAN'T MODIFY AFTER FLIGHT, CAN'T FLY POOR SAMPLES.
- POOR PERFORMANCE IN TEST CAN BE MAJOR SETBACK FOR A TECHNOLOGY. (GaAs ON LIPS 2)
- DELAY BETWEEN HARDWARE FREEZE AND RECEIPT OF DATA CAN MAKE RESULTS PASSE'.

CONCLUSIONS OF FLIGHT EXPERIMENT WORKSHOP (CONTINUED)

FLIGHT EXPERIMENT COORDINATION:

- MANY NASA SATELLITES AND CERTAIN DARPA, USAF, AND EUROPEAN PROGRAMS OPEN TO DISCUSSION OF FLIGHT TEST CO-PAYLOADS.
- SOME FLIGHTS PAID FOR BY AF/STP.

PRIMARY CONCLUSION:

- AN OFFICE WITH A NATIONAL PERSPECTIVE ON FLIGHT TEST OF ADVANCED TECHNOLOGIES IS SORELY NEEDED TO COORDINATE OPPORTUNITIES.
- MANY SATELLITES HAVE ROOM FOR SMALL AUXILIARY PAYLOADS, BUT THEY ARE NOT ACTIVELY ADVERTISED.
- MEDIUM SCALE TESTS, E.G., PANELS, ENVIRONMENT DIAGNOSTICS MUST BE PLANNED WELL IN ADVANCED. MAKE USE OF KNOWLEDGE THAT REGULAR LAUNCHES OF CERTAIN SPACECRAFT OCCUR.
- LARGE-SCALE, DEDICATED SPACECRAFT, E.G., LDEF SHOULD BE PLANNED EVERY 2-3 YEARS. NEEDED FOR ARRAY AND MECHANISM TESTING.

Non-Solar Direct Conversion

W. E. Horne
Boeing Aerospace
Seattle, WA

TPV
Concepts and Applications

- Solar heated (orbital missions)

- Solar heated with thermal storage (orbital missions)
  - may double subsystem specific power for some missions

- Isotope heated--interplanetary/surface probes/modular microsatellites
  - decreased fuel requirement from RTG
  - increased radiator size

- Nuclear heated--large power supplies (surface or orbital)
  - efficiency may require line emitter
  - low temperture radiator

Key Performance Limiters

- PV cell
  - Low band gap
  - IR reflective
  - High near bandgap response

    GaSb

    InGaAs

    Ge
- Thermal emitter
  - Line emitter desirable

    Most are vacuum incompatible

    Require hermetic sealed system
- Radiator size
  - Sheet radiator beneficial

Recommended Future Work

- PV cell optimization
- Selective emitter development
- Performance demonstration
- Radiator development

Betavoltaics (Particle Voltaics)

Concepts and Applications

- Micropower (5-10 Watts may be practical limit)
- Point power sources
- Miniature satellites
- Surface probes

Key Performance Limiters

- Source self absorption
  - Solution:
    Increase area & stack
    Alpha emitter doped into semiconductor
- Radiation damage
  - Solution:
    Heavy atom compounds
    Thermal annealing
- External/background radiation environment

Recommended Future Work

- Investigate high bandgap/high-Z cells
  - SiC
  - Diamond
  - ZnSe
  - ZnS
- Explore sources vs. new semiconductor candidates
- Explore doping isotopes directly into lattice

Pyroelectric

Concepts/Applications

- Huge spinning sheet (extended structure)

- Compact recuperated system

  - Large (>10 kW) low-cost/light weight
  - Low drag orbits
  - Surface power/thermal sources (bottoming cycles)

Key Performance Limiters

- Low upper temperature limits

  Solution: efficient radiator to lower bottom temperature

- Radiation (?)

- Mechanical pumps and sophisticated PMAD

Recommended Future Work

- Small scale working demo
- Explore advanced materials
- Space systems trade studies

Indium Phosphide Solar Cells

I. Weinberg, Chairman
NASA Lewis Research Center
Cleveland OH

The indium phosphide working group considered the folowing questions.

1. What appears to be the most fruitful directions for InP solar cell research?

2. What can be done to decrease cell cost?

3. What can be done to increase cell efficiency?

4. What measurements are needed for a better understanding of cell performance?

5. n/p vs p/n? Is the question settled? If not what should be done?

6. What is known about SRV?

7. Which areas in radiation effects require additional effort?

8. What are the major problems in cell contacting?

9. Should the present level of InP solar cell research in the U.S.A. be maintained, increased or decreased?

With regard to research directions, the working group recommended continued or additional effort on increasing cell efficiency, reducing cost and the production of larger area cells. Considering the latter it was felt that scale up was not a problem and that high efficiency cells with areas comparable to the present GaAs cells appeared to be feasible.

Suggestions for reducing cell cost included heteroepitaxial growth on cheaper, sturdier substrates such as silicon or germanium, use of processes, such as CLEFT and peeled film technology, which enable one to reuse the presently used, expensive, InP substrate. It was suggested that new crystal growth techniques, to replace the presently used LEC method of crystal growth, could be helpful in reducing substrate cost. With respect to the latter an increase in the number of suppliers, by introducing more competitive pricing, would possibly tend to reduced substrate cost as would the more obvious procedure of procuring large quantities of substrates in a single order. Obviously this would depend on the capability and necessity of producing large quantities of solar cells or on initiation of a Mantech program.

To increase cell efficiency, there is a need for lattice matched window materials in order to reduce the SRV. Semiconductors suggested for this application included AlAsSb and AlInAs with components in the appropriate proportions. The development of multibandgap cells is an obvious direction to take in attaining higher

efficiencies. While this would not necessarily lead to higher efficiencies for InP per se it could result in higher efficiency multicomponent cells, one component of which would be InP. Improved substrate material is a necessity in these efforts. Research directed at higher efficiency should also have as a goal the maintenance of high radiation resistance while at the same time yielding high BOL efficiencies.

Measurements needed for a better understanding of cell performance include absorption coefficients at wavelengths greater than 0.85 micrometers, minority carrier lifetimes, diffusion lengths, SRV and experimental determinations of heavy doping effects. Although there is presently some activity in several of these measurement areas, there is a need for determinations over a wide range of dopant concentrations. Also wherever feasible it would be desirable to perform measurements on the actual solar cell structures.

The question of which configuration is preferable, n/p or p/n, is still undecided. Although several modelling efforts have yielded slightly higher theoretical efficiencies for the p/n configuration, additional experimental results are needed in order to make an intelligent choice. One would have greater confidence in the modelling results if more accurate input parameters were available. It was pointed out that, because of the lower emitter sheet resistance, the n/p configuration was preferrable for shallow junction cells. Furthermore, the problem of contacting p–type material needs to be considered in making the final choice. In addition, the few experiments in which both configurations were compared show a slightly lower radiation resistance for the p/n configuration at the higher 1 MeV electron and 10 Mev proton fluences.

Considering surface recombination velocity, there is a need for making this difficult measurement on actual solar cell surfaces. Modelling calculations suggest values approaching 10^7cm/sec for the surface of heavily doped emitters. Although measurements on heavily doped InP, using photoluminescence, indicate values approaching this magnitude there is a need for direct measurements, if feasible, on actual solar cell emitter surfaces. It was pointed out that older measurements, which yielded SRV's in the 10^3–10^4 cm/sec range, were obtained on InP which was cleaved in vacuum. Hence, the need for real world measurements.

In the area of radiation effects, there is a need to obtain data over a wide range of energies for both protons and electrons. Additional annealing experiments are required, especially with regard to photon annealing. Flight experiments are a necessity and every effort should be made to seek out and utililize flight opportunities as they arise. Defect studies should be expanded to obtain a more definitive answer to the reasons for the superior radiation resistance of InP.

The working group concluded that InP solar cell research in the US should be at least maintained at its present level and preferrably increased. The group surfaced a requirement for increased university participation in the areas of crystal growth, cell fabrication and analysis. In addition to strengthening the present program, this

would result in graduates trained in the special requirements presented by growth of InP crystals and cell processing. In addition the present program would benefit from increased activity in surface passivation and improvements in base substrate material quality.

Space Cell Theory and Modeling

James Hutchby
Research Triangle Institute
Research Triangle Park, NC

The workshop on PV Theory and Modeling was attended by about thirty people drawn from the industrial, government and academic communities

Discussed during the workshop were current concerns in cell modeling, both general and material-specific, a discussion of PC-1D, a commercial PV modeling computer code, and future issues. The major points discussed at the workshop are displayed in the following viewgraphs.

Current Issues in Cell Modeling--GaAs

Physics

- Anomalous Log I vs V behavior at P_{max}
- Reverse Bias Breakdown Mechanism(s)
- Dominant Defect Structures Governing Radiation Damage Effects

Parameters

- Minority Carrier Parameters

  (determine directly from minority carrier measurements)

Current Issues in Cell Modeling--InP

Physics

- Heavy Doping Effects
  - -Bandgap Narrowing
  - -Optical Absorption Coefficient
- Anomalously Low V_{oc} ?
- Surface Recombination

Parameters

- Many important parameters not well known
  - n_i, (N_D, N_A)
  - L_n, L_p, τ_n τ_p (N_D, N_A)
  - S_n, S_p $(N_D, N_A, \ldots)$

PC - 1D V.2

Description

- One-dimensional solar cell model
- Numerical
- Runs on IBM-PC; User-friendly
- Steady-state and transient analysis
- Si, GaAs, AlGaAs built-in models; also user-specified models

Validation

- Si predictive, GaAs near-predictive

Issues

- Absorption Coefficient vs. temperature needs more work

Future Issues

New problems for modeling

- Light-trapping cells
- Thin films

Theory and Modeling--Conclusions

GaAs

- Physics appears to be well understood
- Accurate modeling requires material/process specific parameter measurements
- Radiation induced defects not understood

InP

- Physics needs more work
  - heavy doping effects
  - low V_{oc}
  - surface recombination
- Many inportant parameters need better measurements

Thin films

- Physics--uncertain
- Parameters--not well known

Invited Paper

Preceding Page Blank

Cryogenic Reactant Storage for Lunar Base Regenerative Fuel Cells

Lisa Kohout
NASA Lewis Research Center
Cleveland OH

CRYOGENIC REACTANT STORAGE FOR LUNAR BASE REGENERATIVE FUEL CELLS

LISA L. KOHOUT

NASA LEWIS RESEARCH CENTER
CLEVELAND, OHIO

CRYOGENIC REACTANT STORAGE FOR LUNAR BASE REGENERATIVE FUEL CELLS

OBJECTIVE

TO DETERMINE THE IMPACT OF CRYOGENIC REACTANT STORAGE ON THE MASS OF AN ALKALINE REGENERATIVE FUEL CELL POWER SYSTEM FOR LUNAR APPLICATION

i.e. DOES STORING THE REACTANT CRYOGENICALLY, INCLUDING A REFRIGERATION PLANT AND EXTRA SOLAR ARRAY TO POWER IT, RESULT IN A LOWER OVERALL SYSTEM MASS THAN CONVENTIONAL PRESSURIZED GAS STORAGE?

THE CARROT: CRYOGENIC STORAGE TAKES MUCH LESS TANK WEIGHT PER POUND OF REACTANT THAN GASEOUS STORAGE

THE STICK: CRYOGENIC STORAGE REQUIRES A REFRIGERATION PLANT AND EXTRA POWER

CRYOGENIC REACTANT STORAGE FOR LUNAR BASE REGENERATIVE FUEL CELLS

APPROACH

MODEL A CONVENTIONAL RFC POWER SYSTEM FOR A MANNED LUNAR INSTALLATION

REPLACE THE GASEOUS HYDROGEN AND OXYGEN STORAGE TANKS WITH LIQUEFACTION UNITS AND CRYOGENIC STORAGE TANKS

CONSIDER 20 kW AND 250 kW SYSTEMS

RFC vs. Batteries for Varied Darkside Periods

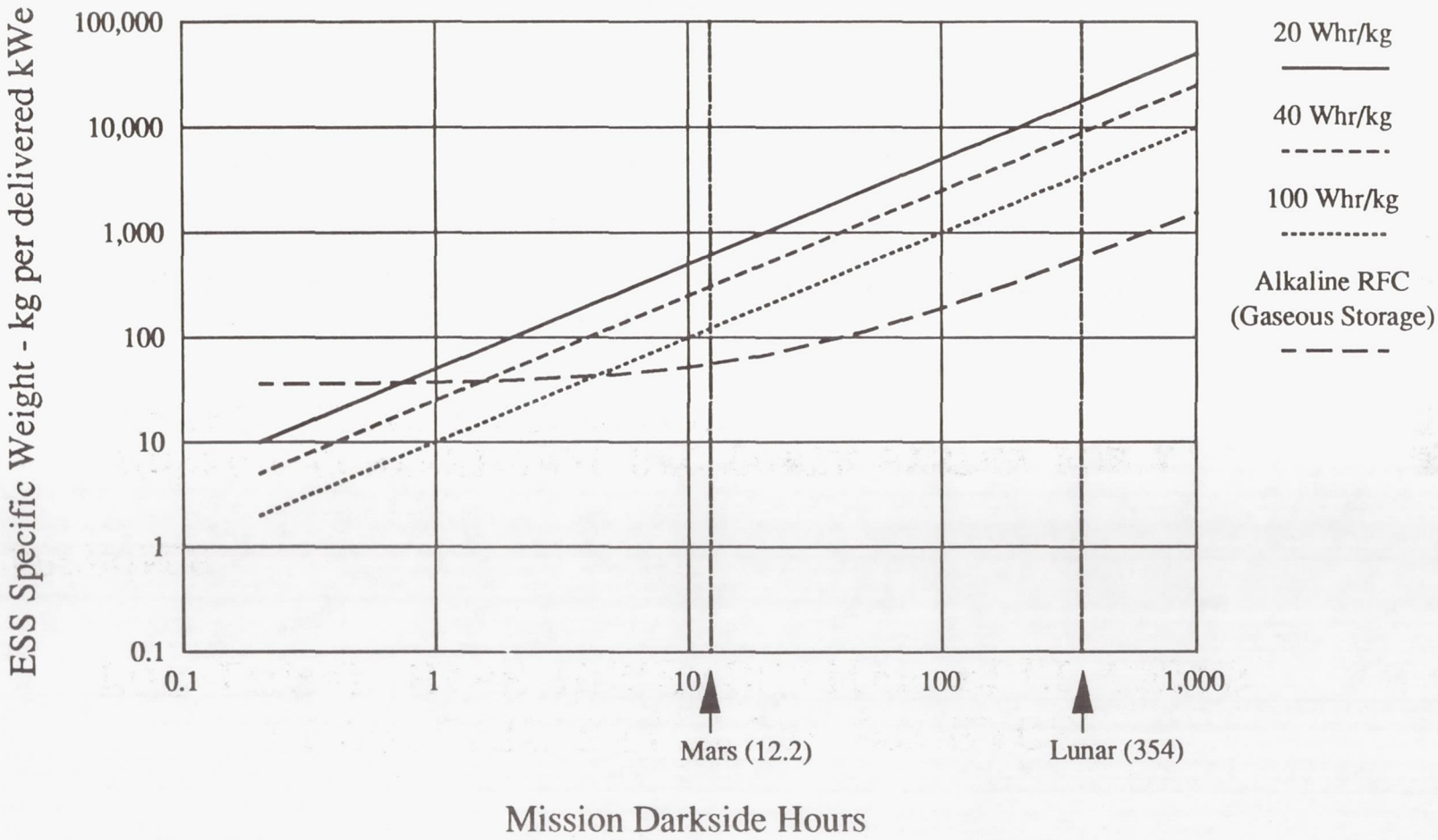

CONVENTIONAL REGENERATIVE FUEL CELL SYSTEM (REACTANTS STORED AS PRESSURIZED GASES)

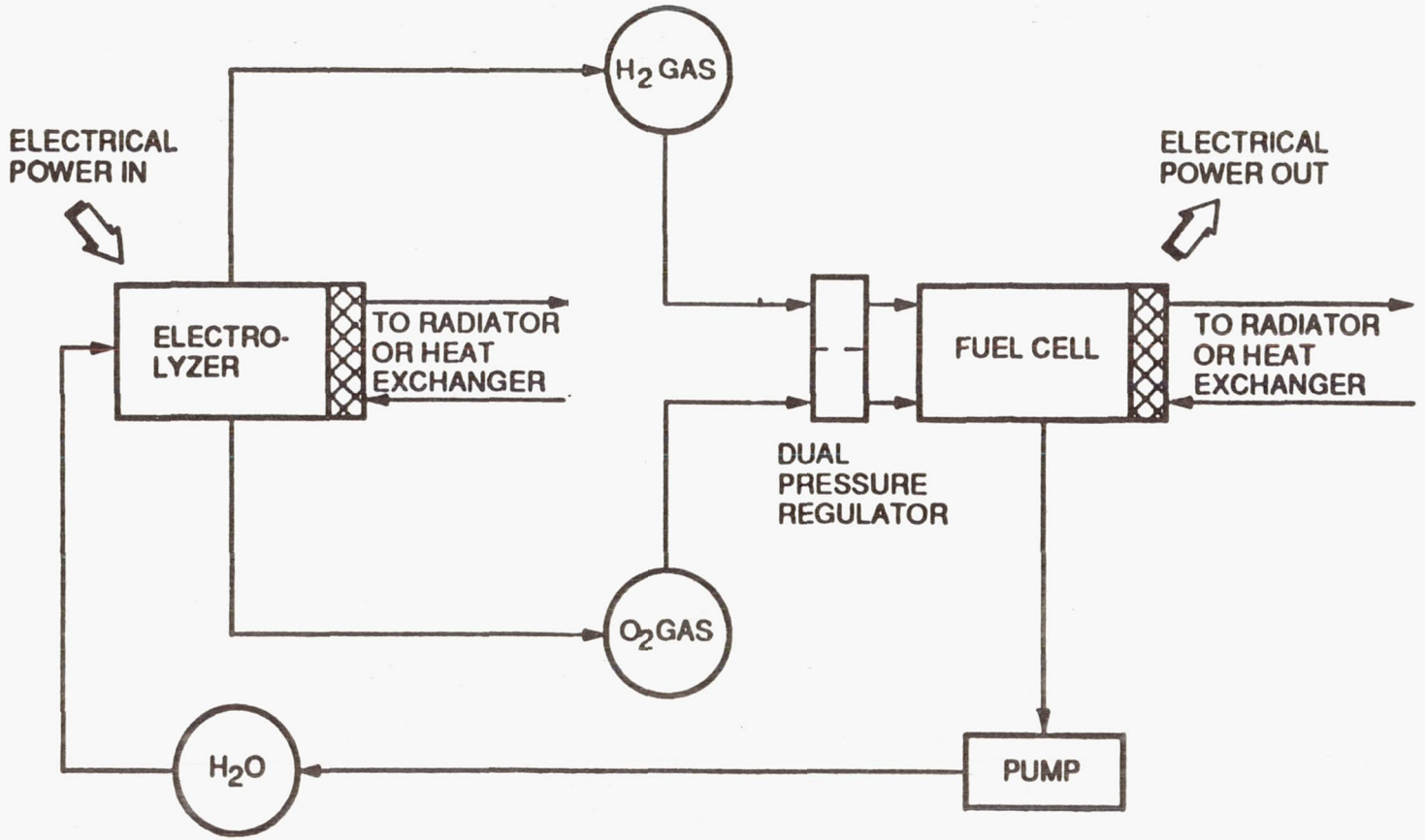

COMPARISON OF MASS BREAKDOWNS FOR A 250 kW REGENERATIVE FUEL CELL SYSTEM

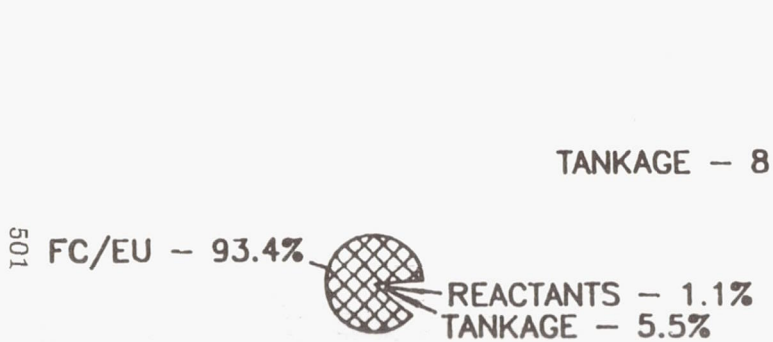

LEO RFC
(~0.5 HR. STORAGE)

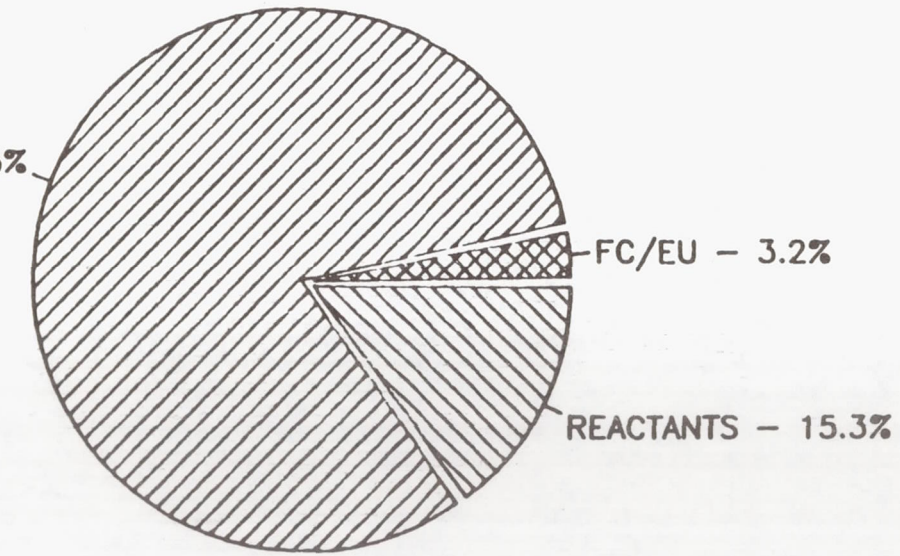

LUNAR RFC
(~330 HR. STORAGE)

(INCONEL TANK MATERIAL)

MASS BREAKDOWN FOR A 250 kW LUNAR REGENERATIVE FUEL CELL SYSTEM

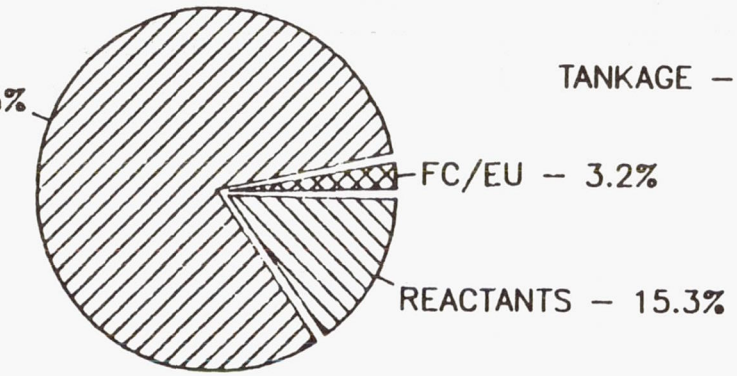

INCONEL TANKS

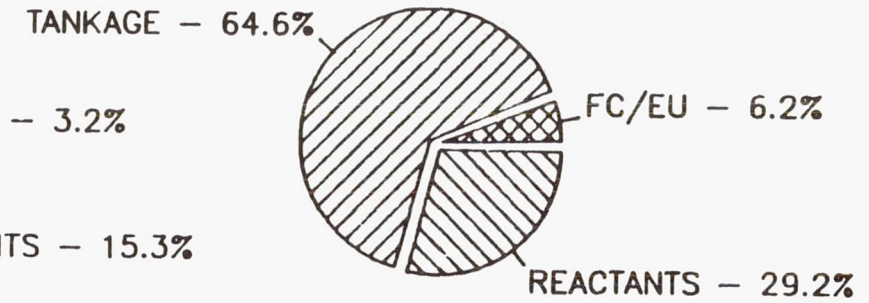

KEVLAR TANKS

CONVENTIONAL REGENERATIVE FUEL CELL SYSTEM (REACTANTS STORED AS PRESSURIZED GASES)

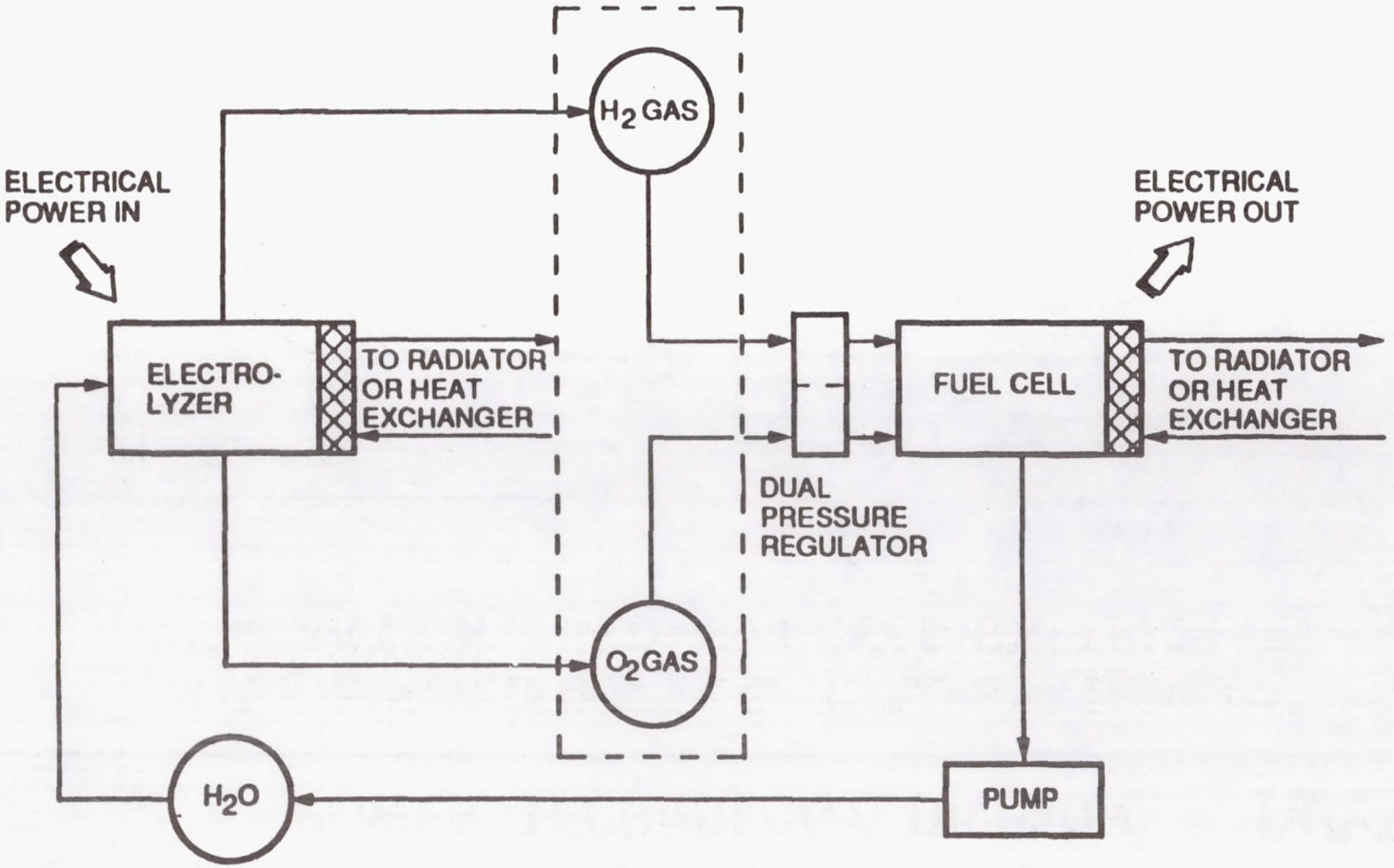

REGENERATIVE FUEL CELL SYSTEM (REACTANTS STORED AS CRYOGENIC FLUIDS)

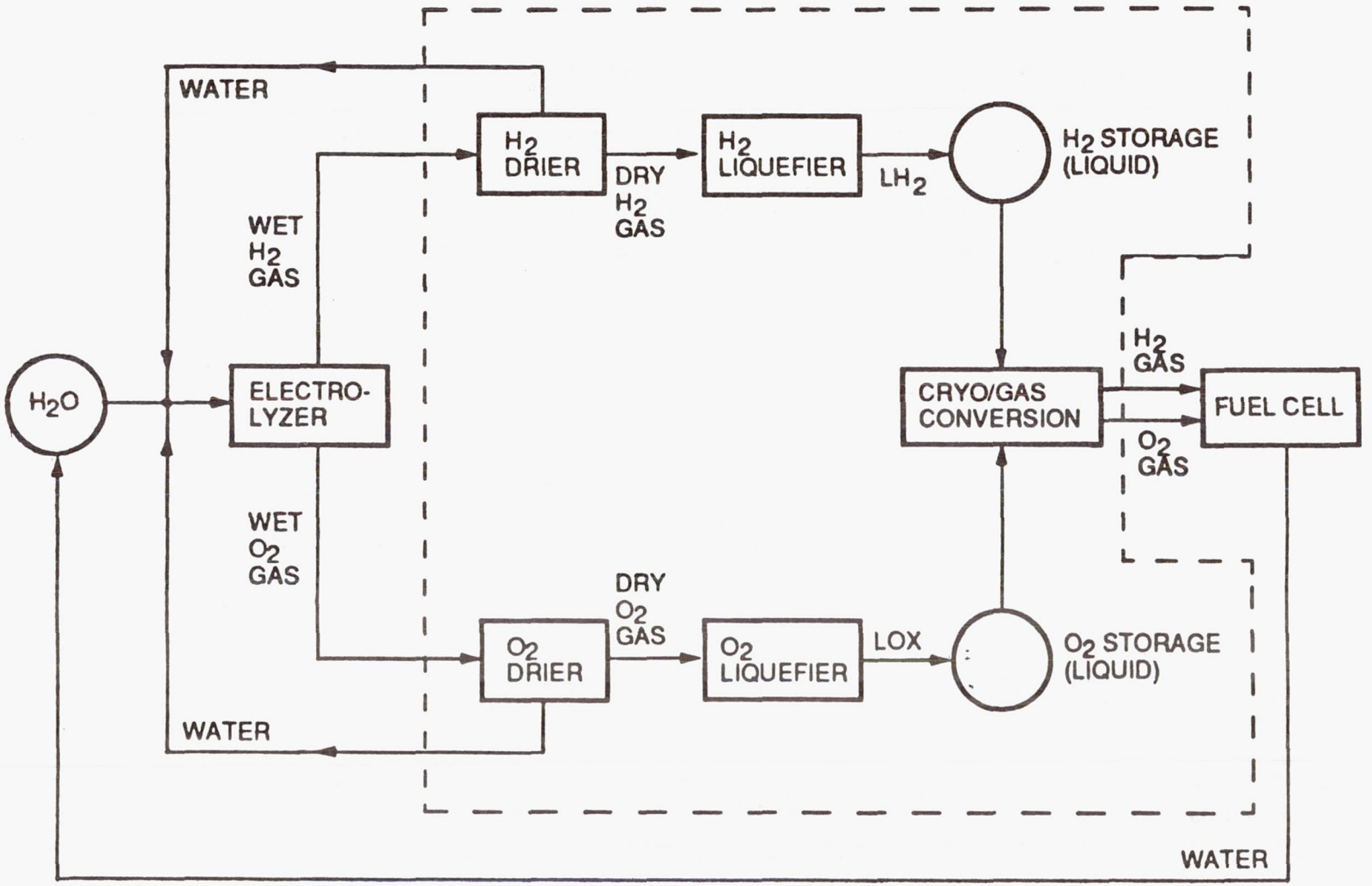

MODELING OF FUEL CELL / ELECTROLYZER SUBSYSTEM

- MODELED USING CODE DEVELOPED AT NASA LEWIS BY M. HOBERECHT AND L. RIEKER

- OPERATING CONDITIONS

FUEL CELL	
CELL ACTIVE AREA	930 SQ.CM.
OPERATING TEMPERATURE	355 K
OPERATING PRESSURE	0.4 MPa
CURRENT DENSITY	161 mA/SQ.CM.
ELECTROLYZER	
CELL ACTIVE AREA	930 SQ.CM.
OPERATING TEMPERATURE	355 K
OPERATING PRESSURE	2.2 MPa
CURRENT DENSITY	161 mA/SQ.CM.

MODELING OF DRYING AND LIQUEFACTION SUBSYSTEMS

PRIMARY REFERENCE FOR PRODUCTION OF CRYOGENS IN SPACE:

"IN-SPACE PROPELLANT PROCESSING USING WATER DELIVERED AS SHUTTLE CONTINGENCY PAYLOAD," E.H. BOCK AND J.G. FISHER, GENERAL DYNAMICS CONVAIR DIVISION, 1978.

SCENARIO

- SHUTTLE DELIVERS WATER STORED AS CONTINGENCY PAYLOAD TO ON-ORBIT PROPELLANT PROCESSING FACILITY
- AT PROCESSING FACILITY, WATER IS ELECTROLYZED AND PRODUCT GASES LIQUEFIED AND STORED AS CRYOGENS
- CRYOGENS USED AS PROPELLANTS FOR SPACE-BASED OTV

REFERENCE DESCRIBES THE DEFINITION AND PRELIMINARY DESIGN OF THE PROPELLANT PROCESSOR SUBSYSTEMS INCLUDING DRYING, LIQUEFACTION, AND STORAGE

GASEOUS HYDROGEN/OXYGEN DRYING SYSTEM

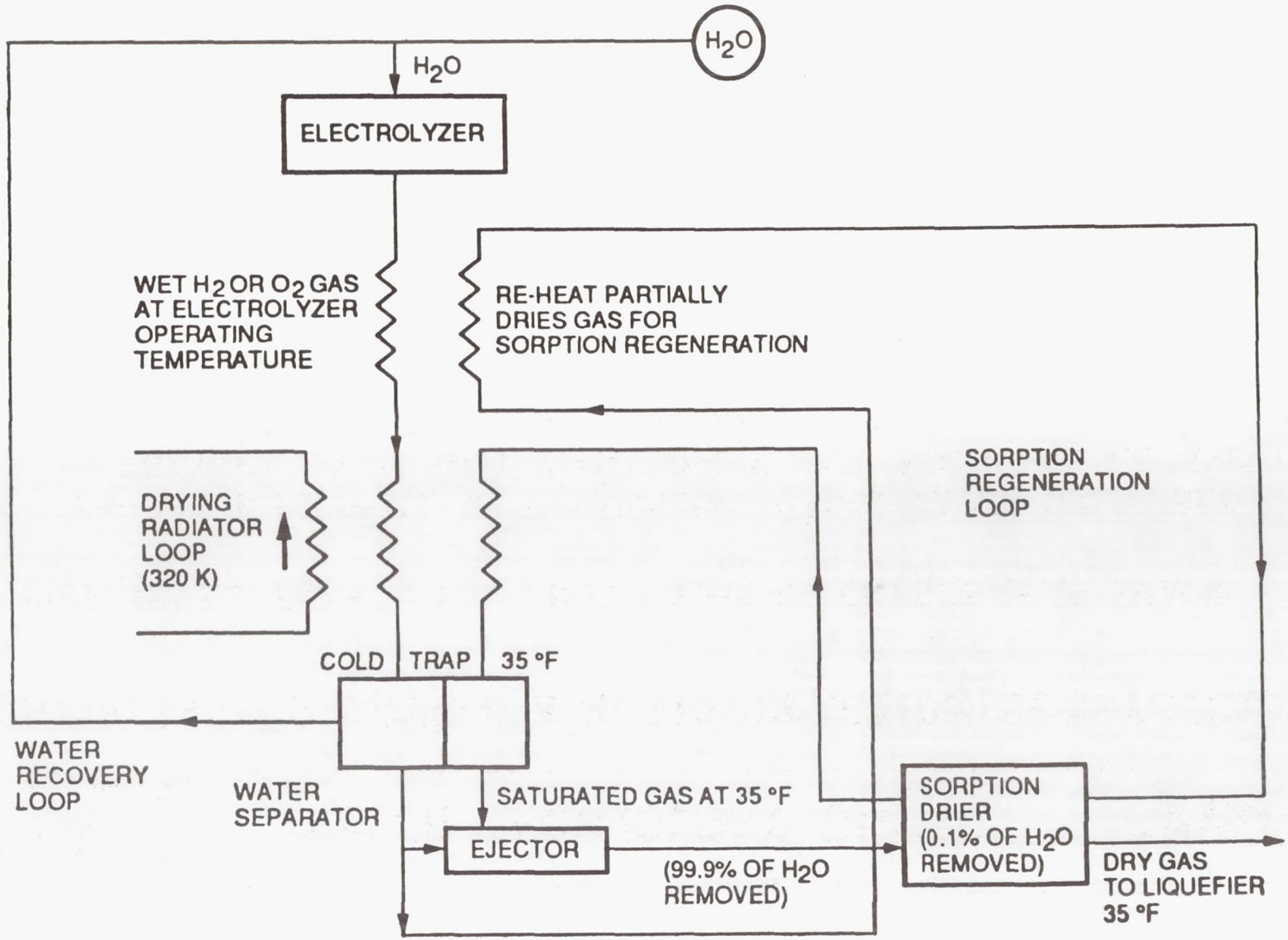

MODELING OF HYDROGEN/OXYGEN LIQUEFACTION SYSTEM

- UTILIZES REVERSED BRAYTON CYCLE FOR LIQUEFACTION
- LIQUEFIES H2/O2 GAS AS WELL AS BOIL-OFF FROM STORAGE TANKS
- EQUIPMENT REQUIRED FOR HYDROGEN AND OXYGEN LIQUEFACTION IS SIMILAR EXCEPT THAT TWO REFRIGERATION STAGES ARE REQUIRED FOR HYDROGEN

REVERSED BRAYTON LIQUEFACTION CYCLE

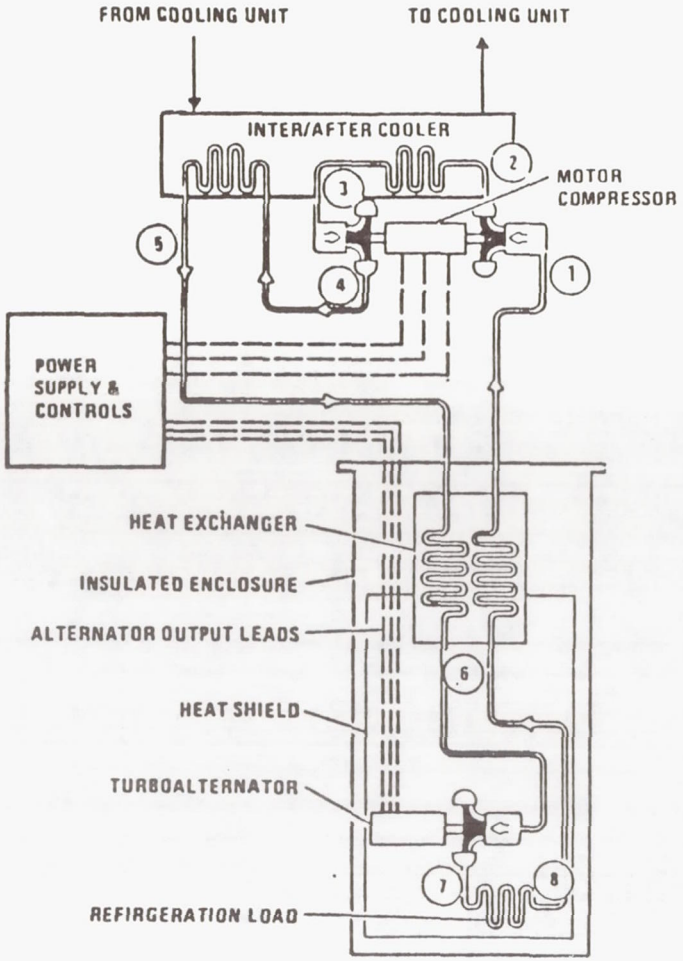

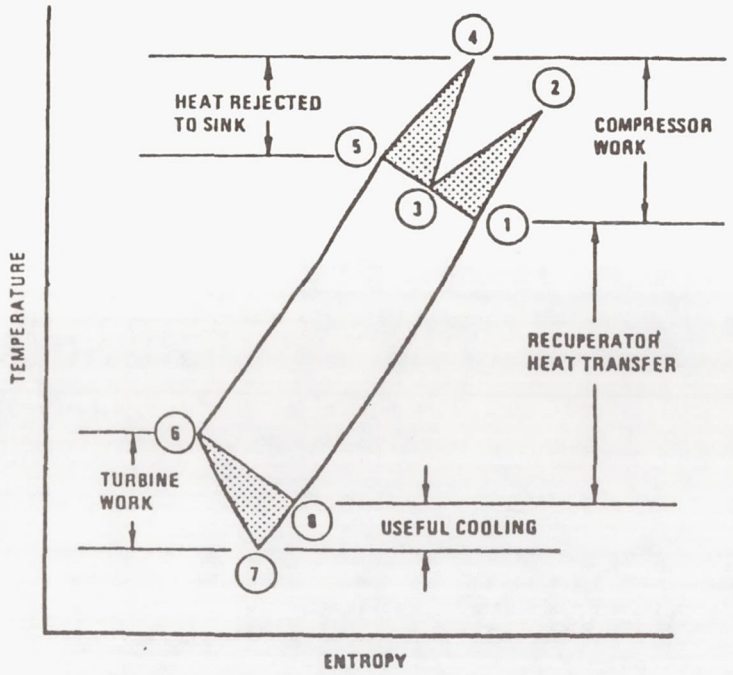

REFRIGERATION CYCLE

MODELING OF CRYOGENIC REACTANT STORAGE TANKS

- BASED ON BEECHCRAFT DESIGN

  SPACE STATION EXPERIMENT DEFINITION:
  LONG-TERM CRYOGENIC FLUID STORAGE

- ALUMINUM INNER PRESSURE VESSEL AND OUTER SHELL

- 90 LAYERS OF MULTILAYER INSULATION AND 2 VAPOR COOLED SHIELDS PLACED BETWEEN CONCENTRIC INNER AND OUTER SHELLS

- 5% REACTANT RESIDUAL ALLOWED

- ADDITIONAL 10% TANK VOLUME ALLOWED TO ACCOMMODATE MAXIMUM ACHIEVABLE FILL LEVEL

SCHEMATIC OF CRYOGENIC STORAGE TANK

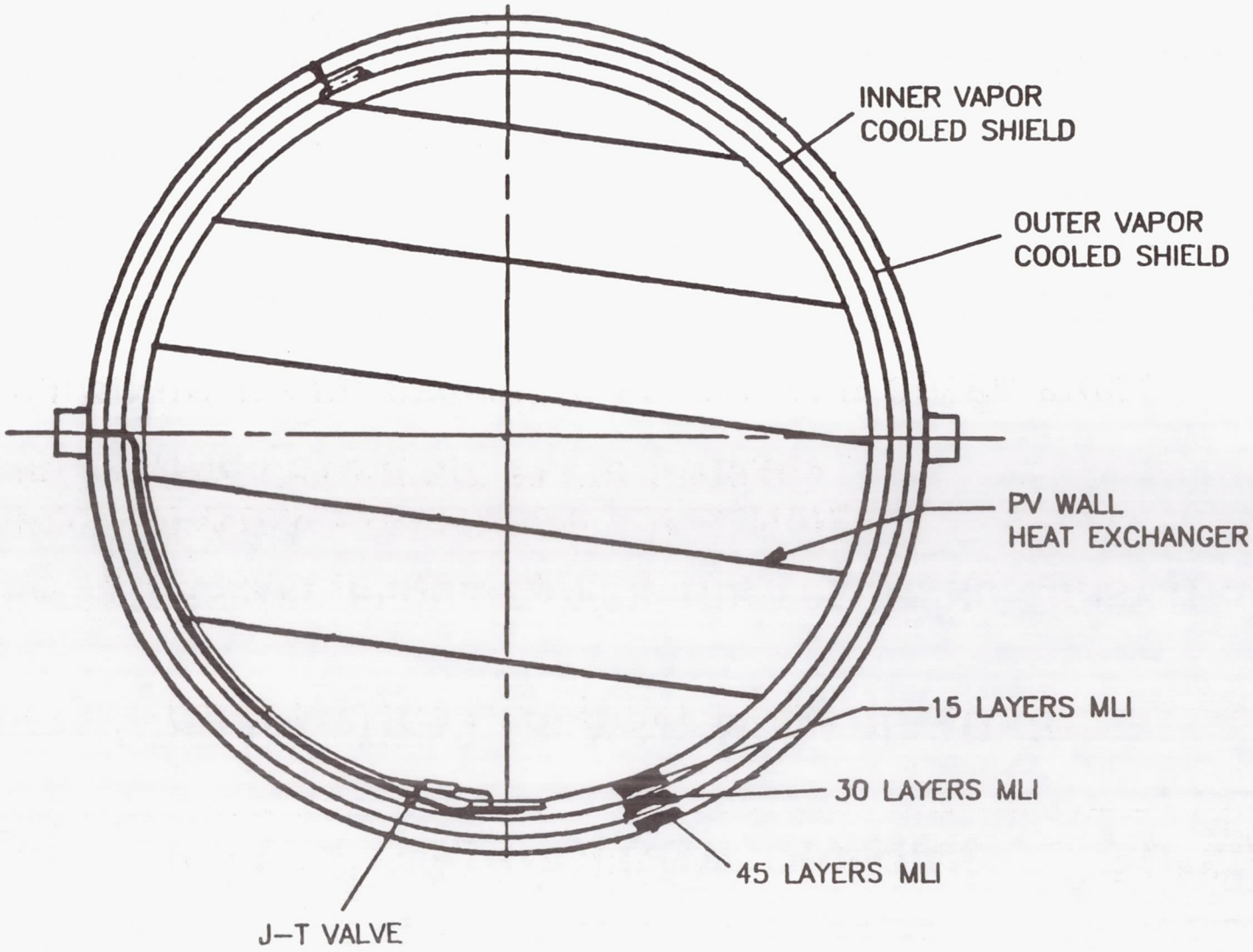

MODELING OF SUBSYSTEM RADIATORS

- RADIATORS ARE REQUIRED FOR THE FOLLOWING SUBSYSTEMS:
  - FUEL CELL
  - DRYING
  - OXYGEN LIQUEFACTION
  - HYDROGEN LIQUEFACTION
- ALL RADIATORS EXCEPT FUEL CELL RADIATOR WERE SIZED BASED ON REJECTION TEMPERATURES AND APPROXIMATED HEAT LOADS FROM BOCK AND FISHER REFERENCE
- FUEL CELL RADIATOR WAS SIZED BASED ON REJECTION TEMPERATURE AND HEAT LOAD FOUND FROM RFC CODE
- DAYTIME SINK TEMPERATURE OF 220 DEG K WAS USED (VERTICAL ORIENTATION OVER SURFACE SHEET)

SCHEMATIC OF RADIATOR WITH GROUND COVER SHEET

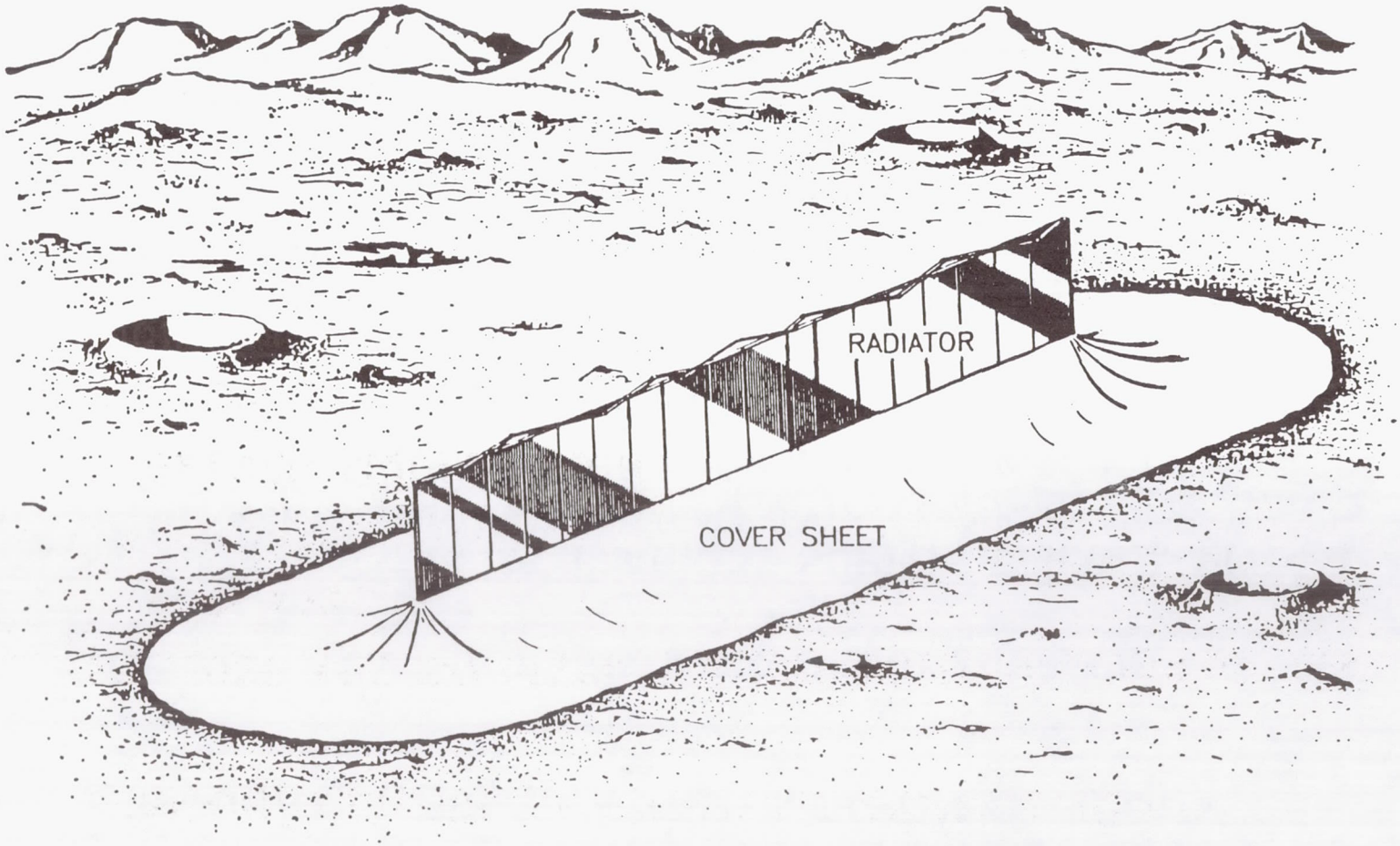

REFERENCE: "A METHOD FOR REDUCING THE EQUIVALENT SINK TEMPERATURE OF A VERTICALLY ORIENTED RADIATOR ON THE LUNAR SURFACE", D. BIEN AND D. GUENTERT, NASA LERC, 1968

MODELING OF SOLAR PHOTOVOLTAIC ARRAY

- GaAs SUN-TRACKING ARRAY ON LUNAR SURFACE
  - INCLUDES ARRAY BLANKET, SUPPORT FRAME, PIVOTS, TRACKING MOUNT, AND WIRING HARNESS

EFFICIENCY	22.512 %
SPECIFIC POWER*	123 W/KG
SPECIFIC MASS	2.48 KG/SQ.M.

* (@ 22.512% EFFICIENCY, 110 DEG.C.)

BREAKDOWN OF POWER REQUIREMENTS
250 kW SYSTEM

COMPONENT	POWER TO BE SUPPLIED BY PV ARRAY (kW)
ELECTROLYZER	400.0
H2/O2 DRIERS	2.0
H2 LIQUEFACTION UNIT	123.5
O2 LIQUEFACTION UNIT	71.3
BASELINE POWER TO USER	250.0
TOTAL POWER TO BE DELIVERED BY PV ARRAY:	846.8
REQUIRED ARRAY AREA:	2780 SQ.M. (2134 SQ.M. W/O CRYO STORAGE)

250 kW LUNAR SURFACE POWER SYSTEM COMPARISON

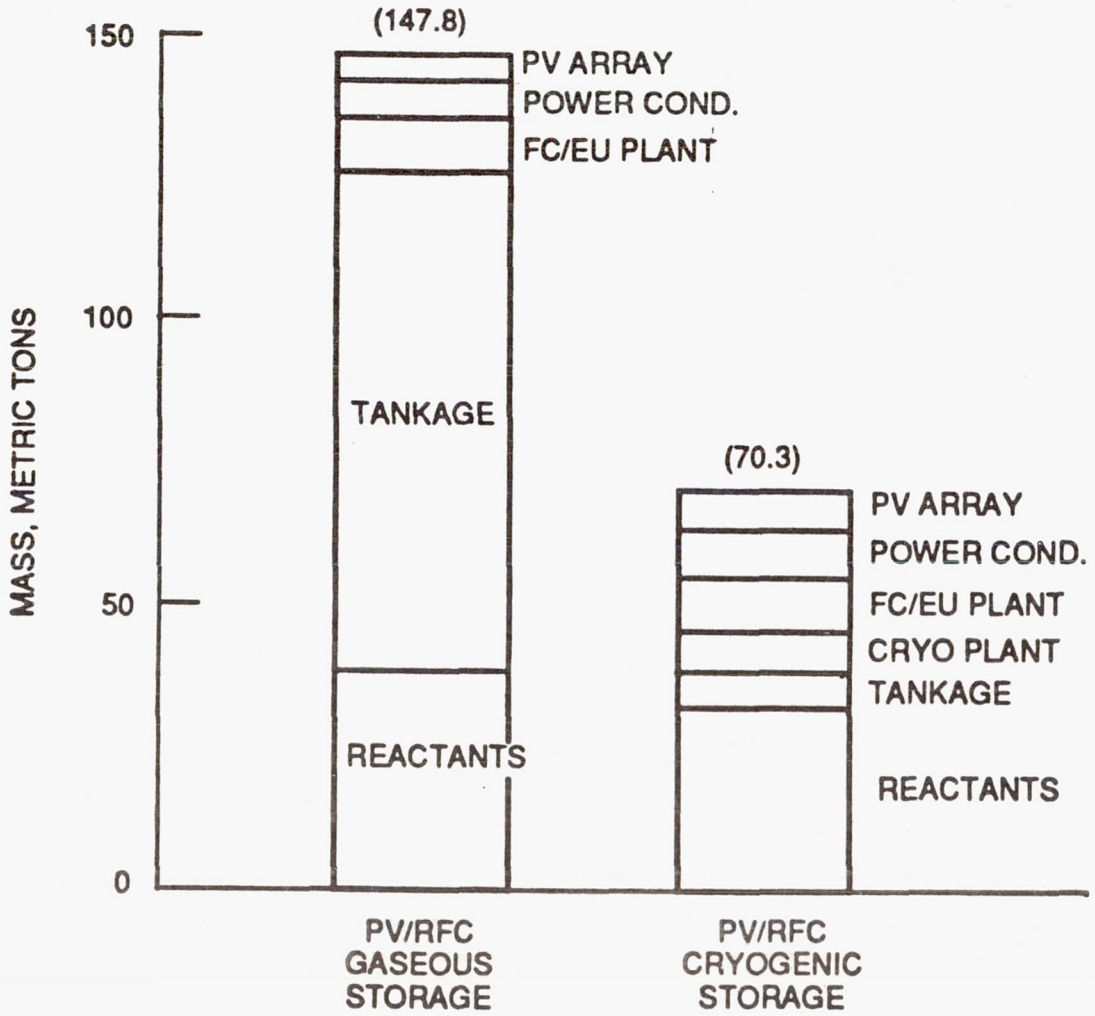

COMPARISON OF REACTANT STORAGE TANK SIZES 250 kW SYSTEM

	GASEOUS STORAGE (KEVLAR)	CRYOGENIC STORAGE
HYDROGEN TANK		
MASS OF H2 (M.T.)	4.40	3.59
RADIUS (M)	9.0	INNER SHELL: 2.4 OUTER SHELL: 2.6
VOLUME (CU.M.)	2969	56
OXYGEN TANK		
MASS OF O2 (M.T.)	34.9	28.5
RADIUS (M)	7.1	INNER SHELL: 1.9 OUTER SHELL: 2.0
VOLUME (CU.M.)	1485	27

(BASED ON SINGLE TANK PER REACTANT)

20 kW LUNAR SURFACE POWER SYSTEM COMPARISON

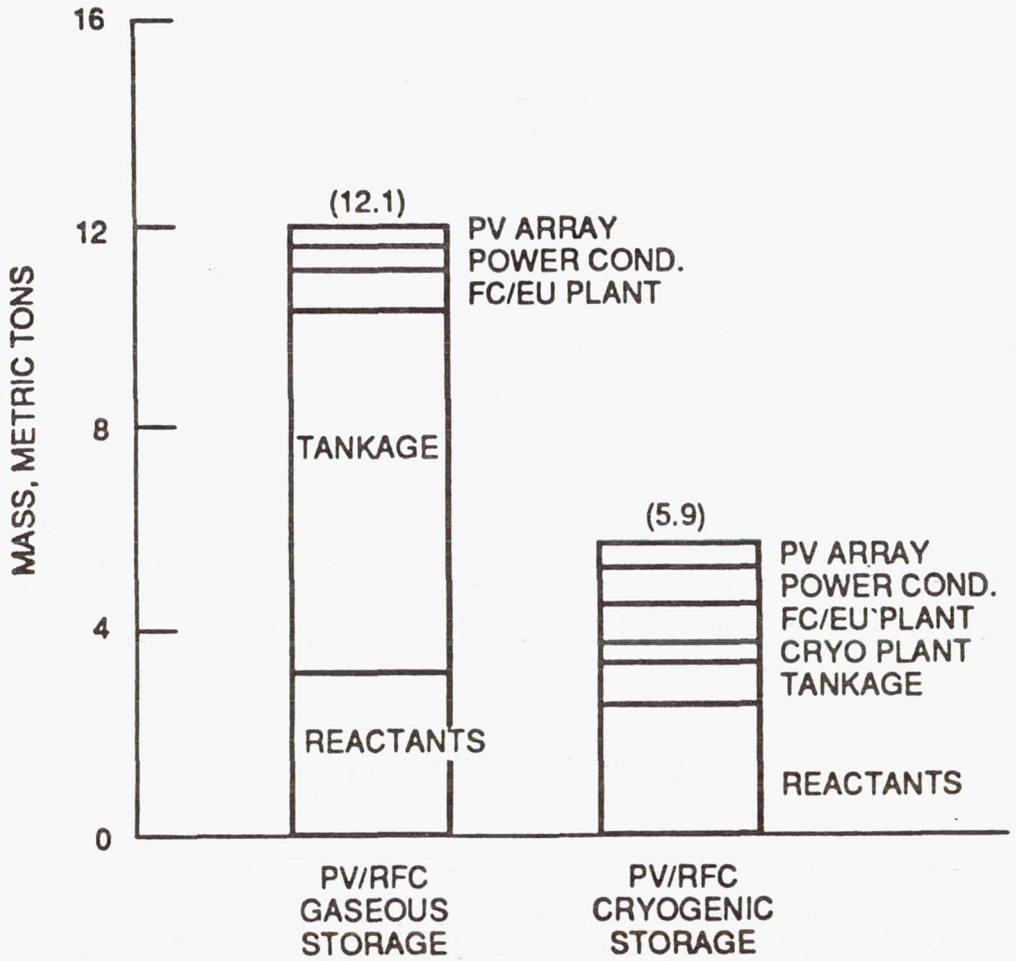

CONCLUSIONS

- CRYOGENIC REACTANT STORAGE APPEARS TO HAVE A MAJOR BENEFIT FOR LUNAR SURFACE REGENERATIVE FUEL CELL ENERGY STORAGE SYSTEMS

- REDUCTION IN TANK WEIGHT MORE THAN COMPENSATES FOR THE ADDITIONAL WEIGHT OF LIQUEFACTION PLANTS, RADIATORS, AND PV ARRAYS

- FOR SOLAR PV/RFC POWER SYSTEMS UTILIZING CRYOGENIC STORAGE, THE RESULTING OVERALL MASS REDUCTION IS APPROXIMATELY 50 PERCENT (COMPARED WITH GAS STORAGE USING FILAMENT WOUND PRESSURE VESSELS)

- SYNERGISTIC USER BENEFITS ALSO EXIST – THE CRYO RFC SYSTEM CAN PROVIDE LOX AND LH2 ON-SITE FOR OTHER USES (REFUELING, PROPELLANTS, ETC.)

AREAS FOR FURTHER STUDY

- SCALABILITY OF THE LIQUEFACTION PROCESS COMPONENTS
- OPTIMIZATION OF SUBSYSTEMS
- CRYOGEN–FUEL CELL INTERFACE
- INFRASTRUCTURE CONSIDERATIONS
- RELIABILITY/REDUNDANCY TRADE–OFFS

NASA
National Aeronautics and Space Administration

Report Documentation Page

1. Report No.	2. Government Accession No.	3. Recipient's Catalog No.
NASA CP-3107		

4. Title and Subtitle	5. Report Date
SPACE PHOTOVOLTAIC RESEARCH AND TECHNOLOGY—1989	January 1991
	6. Performing Organization Code

7. Author(s)	8. Performing Organization Report No.
	E-5728
	10. Work Unit No.
	506-41-11

9. Performing Organization Name and Address	11. Contract or Grant No.
National Aeronautics and Space Administration Lewis Research Center Cleveland, Ohio 44135-3191	
	13. Type of Report and Period Covered
	Conference Publication

12. Sponsoring Agency Name and Address	14. Sponsoring Agency Code
National Aeronautics and Space Administration Washington, D.C. 20546-0001	

15. Supplementary Notes

16. Abstract

The Tenth Space Photovoltaic Research and Development conference was held at NASA Lewis Research Center from November 7 to 9, 1989. The papers and workshop summaries presented in this volume report remarkable progress on a wide variety of approaches in space photovoltaics, for both near and far term applications. Papers were presented in a variety of technical areas, including multi-junction cell technology, GaAs and InP cells, system studies, cell and array development, and non-solar direct conversion. Five workshops were held to discuss the following topics:

- Mechanical versus Monolithic Multi-Junction Cells
- Strategy in Space Flight Experiments
- Non-Solar Direct Conversion
- Indium Phosphide Cells
- Space Cell Theory and Modeling

All presented papers, as well as summaries of the five workshops, are included in this volume.

17. Key Words (Suggested by Author(s))	18. Distribution Statement
Space power Photovoltaic cells Solar cells Solar arrays	Unclassified – Unlimited Subject Category 20

19. Security Classif. (of this report)	20. Security Classif. (of this page)	21. No. of pages	22. Price*
Unclassified	Unclassified	524	A22

NASA FORM 1626 OCT 86

*For sale by the National Technical Information Service, Springfield, Virginia 22161

☆U.S. GOVERNMENT PRINTING OFFICE: 1991-527-064/26013